Experimental and Numerical Studies of Mist Cooling with Thin Evaporating Subcooled Liquid Films

A Dissertation
Presented to
The Academic Faculty

by

Vladimir Novak

In Partial Fulfillment
Of the Requirements for the Degree
Doctor of Philosophy in Mechanical Engineering

Georgia Institute of Technology
May 2006

Experimental and Numerical Studies of Mist Cooling with Thin Evaporating Subcooled Liquid Films

Approved by:

Dr. Said I. Abdel-Khalik, Chair
School of Mechanical Engineering
Georgia Institute of Technology

Dr. Sheldon M. Jeter
School of Mechanical Engineering
Georgia Institute of Technology

Dr. Daniel W. Tedder
School of Chemical and Biomolecular Engineering
Georgia Institute of Technology

Dr. S. Mostafa Ghiaasiaan
School of Mechanical Engineering
Georgia Institute of Technology

Dr. W. Russell Callen, Jr.
School of Electrical and Computer Engineering
Georgia Institute of Technology

Date Approved: March 29, 2006

This thesis is dedicated to my wife Martina

ACKNOWLEDGEMENTS

The completion of this thesis would not have been possible were it not for the support of many individuals. First, I would like to thank my advisor Dr. Said I. Abdel-Khalik for supporting my research and providing guidance throughout my time in the thermal hydraulic laboratory at Georgia Tech. I would like to thank Dr. Seungwon Shin for modifying the KIVA-3V computer program and guidance in KIVA-3V numerical modeling. The assistance of Dennis Sadowski is also greatly appreciated for his help in the lab and finding solutions to many problems. I would also like to thank Kevin G. Schoonover for his assistance and insight in many aspects of this project.

I would like to thank my committee members, Dr. S. Mostafa Ghiaasiaan, Dr. Sheldon M. Jeter, Dr. W. Russell Callen, Jr., and Dr. Daniel W. Tedder for their advice and recommendations. A special thanks is given to Dr. S. Mostafa Ghiaasiaan for his guidance in literature review during the early phases of my project.

I would like to thank many individuals with whom I have worked and who have contributed to my experience during my Ph.D. research. Thanks to Michael J. Kohl, Joerg Stromberger, Ramiro-Rivera, Fahd Abdel-All, Chad Dillon, Tony Jones, Timothy P. Koehler, Celine Lascar, Joseph Hu, and Lorenzo Crosatti.

Most importantly I wish to thank my wife, Martina Novak who has supported and encouraged me during my studies and my parents Ljubica and Kuzman Novak, and sister Jasna, who helped me to identify what I want in life and to achieve it.

TABLE OF CONTENTS

LIST OF TABLES

LIST OF FIGURES

NOMENCLATURE

0.1 Variables

ACcurrent	AC current
ACvoltage	AC voltage
A_o	Quantity that is zero in laminar and unity in turbulent calculations
A_w	Inside wall area of the heated test section
α	Thermal diffusivity
δ	Wall thickness
$C_{\varepsilon 1}$	k-ε turbulent model constant (1.44)
$C_{\varepsilon 2}$	k-ε turbulent model constant (1.92)
$C_{\varepsilon 3}$	k-ε turbulent model constant (– 1.0)
C_p	Constant pressure specific heat
C_s	Constant (1.5)
C_μ	Empirical constant (0.09)
D	Diameter
d	Test section hydraulic diameter
DCcurrent	DC current
DCvoltage	DC voltage
ε	Turbulent kinetic energy dissipation rate
F	Rate of momentum exchange between the two phases
g	Gravitational acceleration vector

h	Heat transfer coefficient
I	Specific internal energy
$\mathbf{I}$	Unit dyadic second order tensor
I_{eff}	Effective current
K	Thermal conductivity
k	Turbulent kinetic energy
k_c	Coverage factor
$\dot{m}$	Fluid flowrate
μ	First coefficient of viscosity
λ	Second coefficient of viscosity
p	Pressure
Pr_k	k-ε turbulent model constant (1.0)
Pr_ε	k-ε turbulent model constant (1.3)
Pr	Prandtl number
q'''_w	Volumetric wall heat generation rate
q_w	Uniform wall heat flux based on the inside surface area
Q	Energy source due to spray (in terms of total energy change of droplets and work done by the droplets to continuous phase)
ρ	Density
Sc_t	Turbulent Schmidt number
T	Fluid temperature
t	Time
T_b	Calculated bulk temperature of the gas
T_{in}	Inside wall surfaces temperatures

T_{inlet}	Test section inlet gas temperature
T_{out}	Outside wall surfaces temperatures
T_w	Wall temperature
τ	Viscous stress tensor
$\mathbf{u}$	Fluid velocity vector
U_A	Uncertainty A
U_B	Uncertainty B
U_C	Combined uncertainty (uncertainty C)
V_{eff}	Effective voltage drop along the heated test section
W	Negative work of the turbulent eddies on dispersed droplets
x	x-coordinate
y	y-coordinate
z	z-coordinate
z	Test section axial location
$z_{unheated}$	Unheated test section length

0.2 Subscripts and Superscripts

g	Gas (subscript)
s	Source term due to spray (superscript)
T	Tensor transpose (superscript)

0.3 Acronyms

AC	Alternate Current

A/D	Analog to Digital (card)
ALE	Arbitrary Lagrangian Eulerian (method)
CFD	Computational Fluid Dynamics
DC	Direct Current
EES	Engineering Equation Solver
FB	Force Balance
FG	Fixed Geometry (nozzle)
GA	Gas-Assisted (nozzle)
HTC	Heat Transfer Coefficient
ID	Inner Diameter
IFE	Inertial Fusion Energy
ITS	Integrated Tiger Series
KrF	Krypton Fluoride (gas)
MTE	Minimum Total Energy
NRL	Naval Research Laboratory
PC	Personal Computer
PLC	Power Line Circle
PVC	Polyvinyl Chloride
RH	Relative Humidity
RTD	Resistance Temperature Detector
SEE	Standard Error of Estimate
SMD	Sauter Mean Diameter
SSD	Sample Standard Deviation

SW	South West
US	Ultrasonic (nozzle)

SUMMARY

An experimental and numerical investigation has been conducted to examine steady, internal, nozzle-generated, gas/liquid mist cooling in vertical channels with ultra-thin, evaporating subcooled liquid films. Interest in this research has been motivated by the need for a highly efficient cooling mechanism in high-power lasers for inertial fusion reactor applications. The aim is to quantify the effects of various operating and design parameters, viz. liquid atomization nozzle design (i.e. spray geometry, droplet size distribution, etc.), heat flux, liquid mass fraction, film thickness, carrier gas velocity, temperature, and humidity, injected liquid temperature, gas/liquid combinations, channel geometry, length, and wettability, and flow direction, on mist cooling effectiveness.

A fully-instrumented experimental test facility has been designed and constructed. The facility includes three cylindrical and two rectangular electrically-heated test sections with different unheated entry lengths. Water is used as the mist liquid with air, or helium, as the carrier gas. Three types of mist generating nozzles with significantly different spray characteristics are used. Numerous experiments have been conducted; local heat transfer coefficients along the channels are obtained for a wide range of operating conditions. The data indicate that mist cooling can increase the heat transfer coefficient by more than an order of magnitude compared to forced convection using only the carrier gas. The data obtained in this investigation will allow designers of mist-cooled high heat flux engineering systems to predict their performance over a wide range of design and operating parameters.

Comparison has been made between the data and predictions of a modified version of the KIVA-3V code, a mechanistic, three-dimensional computer program for internal, transient, dispersed two-phase flow applications. Good agreement has been obtained for downward mist flow at moderate heat fluxes; at high heat fluxes, the code underpredicts the local heat transfer coefficients and does not predict the onset of film rupture. For upward mist flow, the code underpredicts the local heat transfer coefficients and, contrary to experimental observations, predicts early dryout at the test section exit.

CHAPTER I

INTRODUCTION

Mist cooling with thin evaporating liquid films is a highly efficient heat transfer mechanism with heat transfer coefficients even greater than those accruing in nucleate boiling [Sun and Hewitt (2001)]. These high heat transfer coefficients are due to the phase change at the interface between the evaporating liquid film and the mist core. A thin liquid film that covers a heated surface insures a very low thermal resistance and provides evaporative media, while the fine mist core droplets continuously feed the liquid film preventing a film breakdown. This cooling method keeps surfaces with very high heat fluxes at relatively low temperature. Therefore, it is used in many thermally demanding applications. Industrial and technical problems such as nuclear power plant emergency cooling, design of compact heat exchangers, and cooling of electrical and electronic devices, etc., use this cooling method. The specific interest of this study is in nozzle-generated mist cooling with ultra-thin subcooled evaporating liquid films, with the application in cooling of the high average power lasers (HAPL) designed to initiate a thermonuclear fusion reaction.

1.1 Background

In thermonuclear fusion, two light weight nuclei are combined at high temperatures and densities to produce energy typified by Einstein's famous equation, $E = mc^2$. Fusion is the power source of the Sun. If fusion could be harnessed on Earth, the power plants would have nearly unlimited fuel. There are also no chemical by-products,

and limited long-term radioactive waste. The payoffs are so large that numerous scientific institutions worldwide have been working on this problem. However, after almost 50 years the solution is still elusive and challenging.

Recently, the U.S. Naval Research Laboratory (NRL) has spearheaded an inertial confinement approach that appears to be very promising [Sethian, *et al.* (2004)]. In this approach, an array of high-energy krypton fluoride (KrF) gas lasers symmetrically and directly illuminates a cryogenic target, i.e. a pellet of fuel that has been injected into a reactor chamber. The target is a spherical shell of deuterium and tritium, 4 mm in diameter and 0.4 mm thick. As the laser beams illuminate the surface of the shell, it is rapidly heated and high-pressure plasma is formed. A rocket-like blowoff of this plasma is ejected from the surface of the shell, forcing an inwardly focused compression wave propagating towards the center of the fuel. The fuel is compressed to such high densities (40 x solid) and temperatures (100 million ^{o}C) that a localized hot spot in the center undergoes thermonuclear ignition. The resulting thermonuclear burn wave rapidly propagates radially outward through the compressed fuel releasing many times the input energy, which is then converted to electrical energy in a conventional steam turbine. The basic for this process are shown in Figure 1.1 [Lawrence Livermore National Laboratory (1997)]. Once the fuel is burned, the process is repeated. Because the target is confined by its own inertia, this is in a class of fusion concepts known as inertial fusion energy (IFE).

Experiments and computations at the Naval Research Laboratory show that this approach is scientifically viable and should provide sufficient energy release for a fusion reactor. A laser for a fusion power plant must fire nearly five times per second for several

years and meet stringent cost and efficiency requirements. The Electra Laser Program at NRL has as its goal development of a KrF gas laser that can meet these requirements.

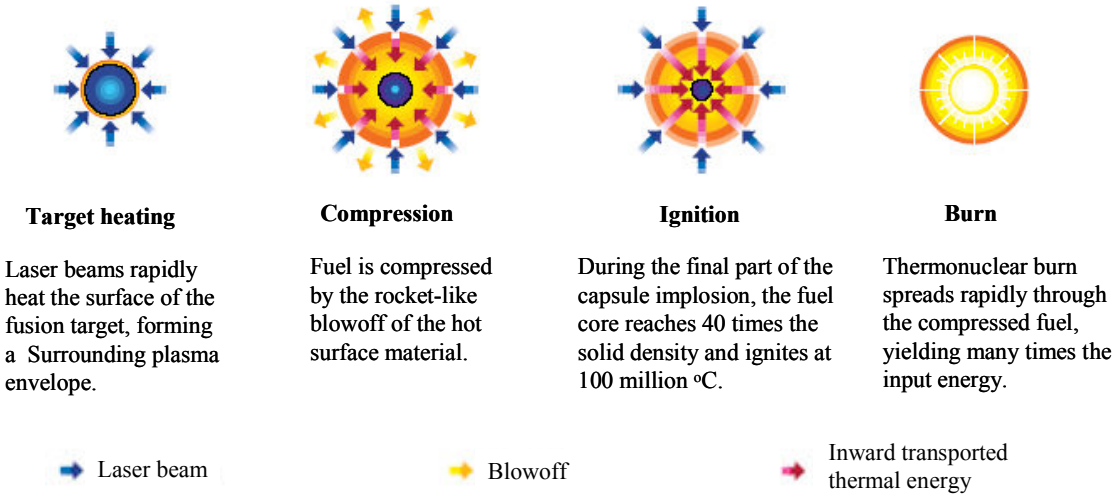

Figure 1.1 Schematic of the stages of inertial confinement fusion using lasers

1.1.1 Components of the Electra KrF Laser

Figure 1.2 shows the Electra laser, i.e. the first-generation high-energy electron beam pumped krypton fluoride gas laser, that NRL has built explicitly for this task, [Sethian, *et al.* (2004)]. Electra will run at 5 Hz with a laser output of 400 to 700 Joules and a pulse width of nearly 10 ns. This will be large enough to develop technologies that can be scalable to the 50 kJ to 150 kJ lasers needed for a fusion power plant beam line. For example, in one reactor concept under consideration, there would be 60 beam lines with each line producing energy of 50 kJ to produce a 3 MJ laser that would hit a pellet of fuel.

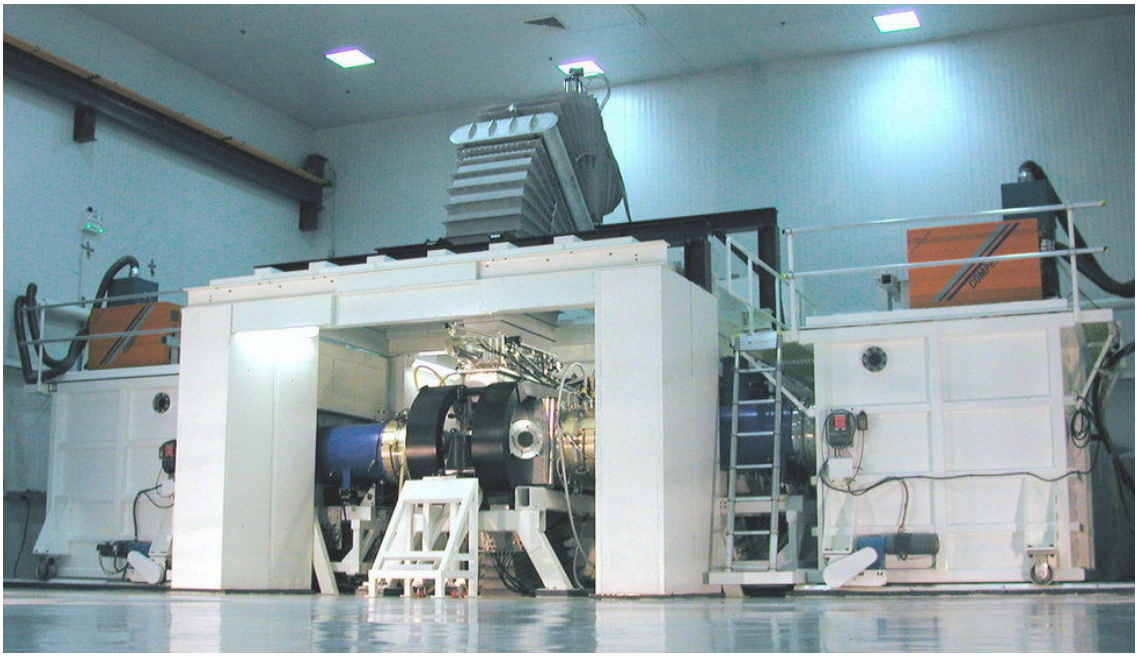

Figure 1.2 Electra - the krypton fluoride (KrF) laser built by NRL

The fundamental components of the Electra laser are shown in Figure 1.3. Electra is an excimer (*exc*ited di*mer*) laser based on a molecular electronic transition to a ground state which immediately dissociates. Generation of an intense KrF laser beam begins with applying the voltage from a pulsed power system to a field emission vacuum diode (cathode) to create the electron beam. The beam passes through two (or one depending on a design) thin foils that isolate the diode from the pressurized krypton and fluorine laser cell gases. This process is simultaneously occurring on both laser cell sides. When the electron beams excite the krypton and fluorine gases to the excited KrF* gas, it is triggered with low power solid-state input laser to emit an amplified laser beam. The fundamental wavelength of the KrF laser is ultraviolet at 248 nm. The laser cell has an amplifier window with highly transparent anti-reflective coatings through which the amplified laser beam leaves the cell, and a recirculator to cool and quiet the laser gas

before the next emission event. The recirculator drives the laser gas vertically upward at approximately 7.5 m/s. Each side foils have a supporting structure known as a "hibachi" because of its grill-like shape. Typically, the hibachi consists of a series of parallel vertical ribs.

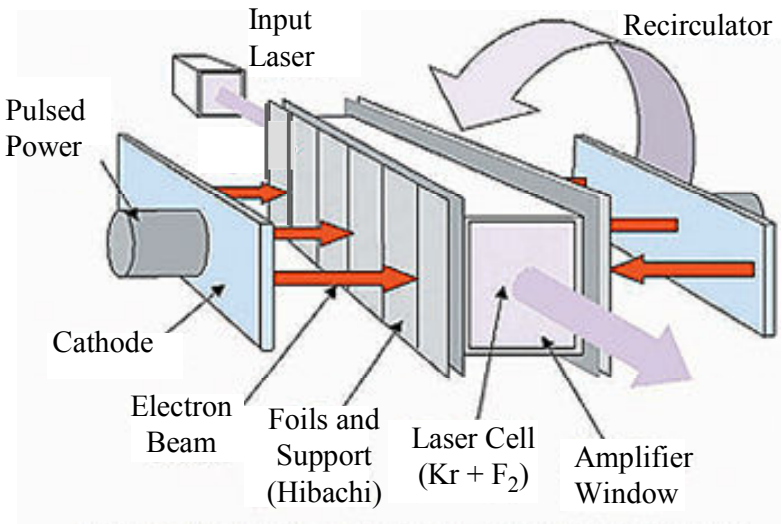

ENERGY + (Kr + F_2) → (KrF)* + F → (Kr +F_2) + hν (248 nm)

Figure 1.3 The fundamental krypton fluoride (KrF) lasers components

A generic, top view hibachi structure is shown in Figure 1.4. The hibachi structure (or ribs) supports a thin pressure foil (facing laser gas at 1.3 to 2.0 atmospheres) and anode foil (facing the hard vacuum of the electron beam diode).

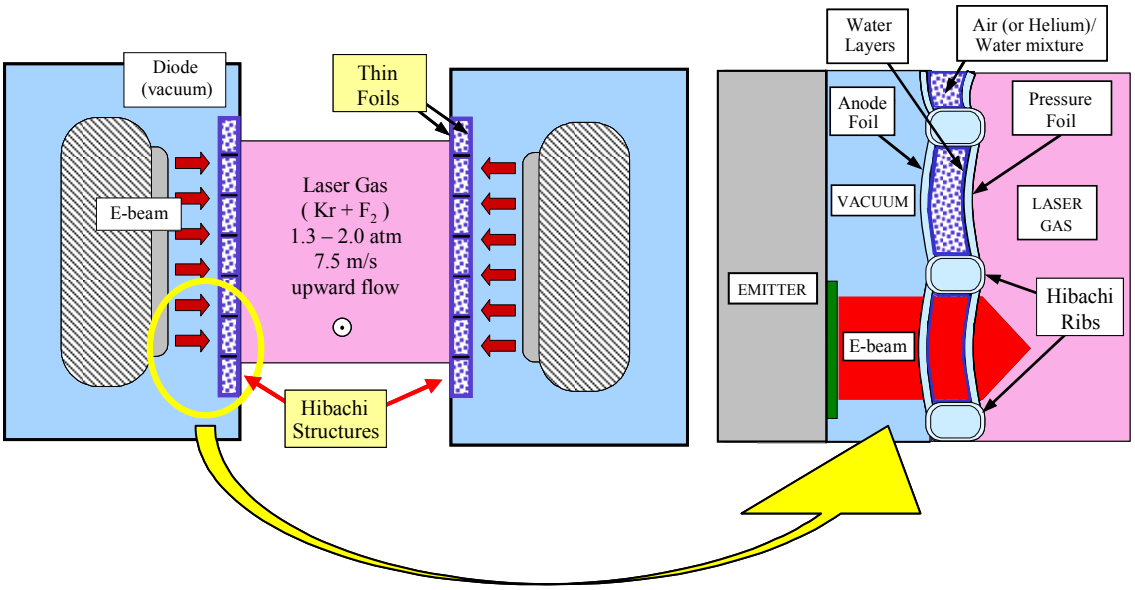

Figure 1.4 A generic hibachi structure with two foils (top view)

The hibachi structure and foils must meet the following requirements [Novak, *et al.* (2005)]:

1. Maximize transmission efficiency of electrons into the laser gas (75 % minimum).
2. Lifetime of > 10^8 shots, projected; (two years at 5 Hz between major maintenance).
3. Power to cool both hibachis should be less than 5 % of the total system power.
4. Must operate in an environment of hydrodynamic shock (pressure rise induced by the electron beam as it deposits its energy into the laser gas), fluorine, X-rays, UV light (must have low UV reflectivity), electrons and probably hydrofluoric acid.

5. Withstand the electron beam parameters: 500 kV, 100 kA, 30 cm x 100 cm area, 33 A/cm^2 average, 100 ns flat top with 40 ns rise and 80 ns fall; the required electrical power during this short interval is about 50 GW, equivalent to 25 kW over one second with 5 pulses .

Materials used for hibachi foils are: titanium, aluminum, stainless steal, silicon and alloys such as HAVAR (42 % Co, 20 % Cr, 13 % Ni + Fe, W, Mo, Mn).

Cooling the hibachi thin foils and structure in a manner consistent with the design criteria listed above is one of the main technical challenges of the laser system development, and that is where the need for this thesis research appears. There are several options for cooling the hibachi structure and foils [Giuliani, *et al.* (2005)].

1. Cooling the pressure foil with the flowing laser gas,
2. Cooling the foils by conduction to water-cooled support ribs,
3. Radiative cooling. In order for this to work the foil has to get to a rather high temperature (probably 600-800 ^{o}C) which may limit its lifetime,
4. Cool the entire assembly using high pressure (20 psig) forced helium flow between the two foils,
5. Pulsed spray cooling of the foils with spray nozzles mounted on the hibachi rib structure, and
6. Cooling the entire structure with a downward flowing helium/water or air/water nozzle-generated mist with ultra-thin evaporating liquid films, at an intermediate pressure (~ 1 atmosphere) between the two foils.

The first three options require only a single-foil, while the last three require a two-foil arrangement. Experiments have shown that the first three options cannot sufficiently

cool the hibachi structure and the foil [Giuliani, *et al.* (2005)]. Among the last three schemes, mist cooling with ultra-thin liquid films (option 6) is best suited for the Electra hibachi. It can provide nearly an order of magnitude enhancement in the heat transfer coefficients over those for forced convection to a gas coolant (option 4), as shown in Novak, *et al.* (2005) and Giuliani, *et al.* (2005). It is also considerably simpler and more reliable than the pulsed spray approach (option 5). The high heat transfer coefficients produced by mist cooling with ultra-thin liquid films make it possible to operate with moderate carrier gas velocities, thereby reducing the cooling system power requirement to meet the less than 5 % design constraint. Design simplicity and reliability are necessary to meet the lifetime goal of more than 10^8 shots.

One of the primary concerns about the use of mist cooling in Electra is the loss of electron beam transmission efficiency due to absorption and scattering in the additional foil and the two-phase, albeit highly-voided, coolant, together with the ultra-thin liquid films expected to form on the cooled foil surfaces. Preliminary calculations using the Integrated Tiger Series (ITS) of Monte Carlo electron transport algorithms developed by Halbleib, *et al.* (1992) suggest that the transmission efficiency in a full-scale IFE system with electron beam energy of 800 keV, and helium/water mist cooling with ultra-thin liquid films, can be greater than 75 % [Swanekamp (2004)].

1.2 Experimental and Numerical Approach

The motivation for this research lays in the need to keep the hibachi foils temperature low. At this time, it is believed that a maximum average foil temperature below 150 ^{o}C is adequate, since above that temperature fluorine starts to react with some of the foil materials. However, the lower the temperature the better it is. If it is assumed that 25 % of the total 25 kW averaged electron beam power going through 30 cm x 100 cm hibachi window is absorbed evenly by both hibachi foils, it is equivalent to heating each foil with uniform continuous heat flux of 10 kW/m^2. The attenuation of electrons depends on the foils' material and thickness. For example, stainless steal attenuates electrons more than titanium, which attenuates them more than aluminum. Choosing a foil material is not as trivial task as it might appear. Their mechanical strength is important, as they have to sustain a significant force exerted on them by the pressure difference between the laser gas and hard vacuum. In addition, the electron beam attenuation depends on the liquid film thickness. A thicker film of water would attenuate more electrons. However, even if 38 % of the total averaged electron beam power is absorbed evenly by both foils, which is not expected according to Swanekamp (2004), it would be equivalent to having a uniform continuous heat flux of 15 kW/m^2, which can be removed easily with the nozzle-generated air/water mist cooling with ultra-thin evaporating subcooled liquid films. For a continuous 15 kW/m^2 heat flux, 15 m/s average air velocity, 15 % water mass fraction, and prototypical hibachi channel case, the film temperatures would not exceed 55 ^{o}C. This is why only subcooled liquid films are considered in the experimental study.

The focus of this thesis research is on steady, turbulent, nozzle-generated, gas/liquid mist flow cooling in vertical channels with ultra-thin, evaporating subcooled liquid films and constant heat flux. Instead of repeating this all over again, shorter titles such as nozzle-generated mist cooling with thin evaporating subcooled liquid films, or just mist cooling are used in the rest of this thesis. In addition, the nozzle-generated and spray mist terms are used interchangeably. In order to complete this research, an experimental and numerical approach has been undertaken.

The purpose of the experimental approach is to measure using laboratory experiments, the local heat transfer coefficients for nozzle-generated mist cooling with thin evaporating subcooled liquid films at conditions suitable for the Electra hibachi structure. This knowledge can then be used to quantify and optimize various operating and design parameters involved in this cooling system. A hibachi structure with mist cooling can then be confidently designed and built according to this optimization prior to actual full-scale testing within the Electra laser.

The purpose of the numerical approach is to obtain a mechanistic, three-dimensional model that would be able to predict the Electra hibachi foils' response under prototypical pulsed operating conditions, including their temperature history and overlying liquid film thickness.

Aside from the specific application described above, the data and models obtained in this investigation will allow designers of mist-cooled high heat flux engineering systems to predict their thermal performance over a wide range of design and operational parameters.

1.3 Objectives of this Thesis

There are two main objectives in this thesis study:

1. To gain a better understanding of this method of cooling. The aim is to quantify the effect of various operating and design parameters, viz. the gas/liquid combination, carrier gas velocity, temperature, and inlet humidity, liquid mass fraction, film thickness, injected liquid temperature, liquid atomization nozzle design (i.e. spray geometry, droplet size and distribution, and droplet velocity/spray momentum), heated test section length, unheated entrance length and its surface wettability, channel geometry, flow direction, and heat flux on mist cooling effectiveness.
2. To validate a mechanistic, three-dimensional, two-phase flow model based on the KIVA-3V computer code [Amsden (1997) and (1999)] by comparing its predictions with experimental heat transfer data for the nozzle-generated mist cooling with thin evaporating subcooled liquid films.

1.4 Overview of the Thesis

The remainder of this thesis is organized as follows. Chapter II presents the literature review with emphasis on nozzle-generated mist cooling with thin evaporating subcooled liquid films, traditional annular-mist cooling, and liquid film instability. Chapter III describes in detail the experimental apparatus used for the laboratory experiments including the three cylindrical and two rectangular test sections, as well as the experimental procedures and data acquisition. It covers the assumptions made in processing the data and describes the data processing codes. The experimental results and

discussions are presented in Chapter IV. Effects of various operating and design parameters on heat transfer performance are analyzed in detail. Chapter V gives the numerical simulation description, including modifications made to model the experimental apparatus, and comparisons between code predictions and experimental data. The conclusions to be drawn from this research and recommendations for future research are presented in Chapter VI.

CHAPTER II

LITERATURE REVIEW

A wealth of information exists on mist flow cooling in external and internal flows with and without film formation. This literature review will focus on heat transfer in internal two-phase mist flows with film formation. These flows are known for their superior cooling performance as they can maintain surfaces with very high heat fluxes at relatively low temperatures.

As stated in Chapter I, the focus of this study is on nozzle-generated mist cooling with thin evaporating subcooled liquid films. It is important to note that the mist flow in this study always has two components, a non-condensable gas component and a vapor/liquid component. In addition, the liquid films produced by the spray mist are subcooled; evaporation takes place at the interface between the liquid film and the non-condensable gas in the channel core. However, when discussing internal mist flows with liquid films, the first such flow that comes to mind is the annular-mist flow, and the associated two-phase forced convection heat transfer, also called forced convection evaporation. This flow is traditionally co-current, one component, and saturated upward flow in vertical tubes. There are important differences between what traditionally is called annular-mist flow and the flow studied in this thesis. The flow examined here is "two-component" versus the "single-component" flow in traditional annular mist flow; among the important differences between these two flows are the film temperature and thickness, and droplet size, concentration and origin. Although, there is a clear differentiation between these two flows, an understanding of the traditional annular-mist

flow and the associated two-phase forced convection boiling is important for a better understanding of the present study, because the heat transfer mechanisms are essentially the same, assuming that bubble nucleation does not occur at the wall. In both cases, the heat is removed by forced convection from the heated surface to the liquid film/gas interface, where evaporation occurs. In addition to evaporation, which is the main heat removal mechanism, some heat is removed from the walls by the liquid film heating process. This is true for both, the saturated and subcooled film cases. The mist and the liquid film characteristics of the traditional annular-mist flow and the nozzle-generated mist flow are responsible for the difference in cooling performance of these two flows. These various differences and similarities, advantages and disadvantages, and other characteristics are presented and analyzed here.

2.1 Nozzle-Generated Mist Cooling with Thin Evaporating Subcooled Liquid Films

Nozzle-generated mist cooling with thin evaporating subcooled liquid films is a more-recent research topic. Unlike the traditional annular-mist flow, which has been studied for nearly 60 years, work on nozzle-generated mist cooling began only twenty years ago. Hence, fewer heat transfer studies on this subject have been reported in the literature.

Lee, Yang and Hsyus (1994) experimentally studied nozzle-generated mist cooling with ultra-thin subcooled water films for upward flow. They used a square channel with a cross section of 41 mm x 41 mm, and 185 cm long. At 86 cm from the channel entrance there was 25 cm long test section. Two sides of the test sections were

transparent and the other two eclectically heated. They used a laser-Doppler anemometer system to measure droplet size, concentration, velocity, trajectory, and liquid film thickness. An air-assisted nozzle was used to generate the mist. The wall heat flux was varied form 1.5 kW/m^2 to 53 kW/m^2, while the air centerline velocity was varied from 4 m/s to 32 m/s; the ambient mean droplet concentration was varied from 0.05 kg/m^3 to 0.09 kg/m^3. Measured mean droplet diameter varied from a few microns to 200 μm. Using the laser-Doppler anemometer system, the water film thickness was estimated to be 50 μm to 100 μm. They observed the best cooling performance when the droplet Sauter mean diameter (SMD) was in the range of 30 μm to 80 μm. They explained this with the appearance of dry patches in the film when droplets were smaller than 30 μm, and with the film being too thick, thus increasing the wall temperature when droplets were bigger than 80 μm. One might think a similar behavior is to be expected for the downward flow case. However, the actual droplet size range is probably different due to the gravity effect, which in general results in a thinner liquid film as shown later [Ueda and Tanaka (1974), and Ueda and Nose (1974)]. They measured a heat transfer enhancement as high as seven times, i.e. a seven times higher heat transfer coefficient than the corresponding value for the air flow only. The enhancement improved with increasing droplet concentration and heat flux. The measured droplet concentration was highest in the center of the channel, and then gradually decreased towards the channel walls. They measured the longitudinal and transverse velocity of droplets and air, and concluded that the slip between them is very small.

Yang and Lee (1991) theoretically studied the same flow configuration as in Lee, Yang and Hsyus (1994). They theoretically analyzed the dimensionless deposition

coefficient using a new unified theoretical approach for the entire transverse flow region from the turbulent core to the quasi-laminar region next to the boundary wall. The proposed analytical model showed satisfactory agreement with the experimental results. They found that the heat transfer enhancement increased with increasing droplet deposition rate and Reynolds number. As they explained, the key to the best cooling performance was in the ultra-thin liquid film evaporation, which was maintained by the continuous deposition of the optimal size droplets. The optimal droplet size was directly related to the optimal droplets transverse migration caused by the dynamic interaction between the phases in a turbulent mist flow. The main role of the mist core was to feed the thin evaporating film at the rate and with the droplet size range that would prevent formation of either dry patches or a thick liquid film.

Lee, Issapour, Yang and Cho (1990) studied experimentally and theoretically nozzle-generated mist cooling for a very similar arrangement as in Lee, Yang and Hsyus (1994). The direction of the flow was upward and the temperatures were subcooled. The difference was that the test section was 57 mm x 254 mm stainless steel plate, only 0.25 mm thick, placed at the center of a square cross section channel (127 mm x 127 mm). They varied the droplet Sauter mean diameter from 6 μm to 82 μm, and used the same instrumentation as in Lee, Yang and Hsyus (1994). This time they measured the film thickness to be approximately 100 μm for all of the experiments. They observed that 30 μm droplets were moving the most vigorously toward the wall. This size droplets achieved the highest droplet deposition rate and heat transfer enhancement. Their theoretical droplet deposition rate results showed satisfactory agreement with the experimental results.

Lee and Hanratty (1988) examined the differences in droplet deposition onto dry and wet surfaces. Their test section was a 50.8 mm diameter pipe (either ground brass or Plexiglas). Droplets 50 μm in diameter were used, with a co-current 155 μm thick water film. They found that the presence of the water film on the wall impedes deposition. As the most likely explanation, they suggested that the droplets bounced off the liquid film and did not coalesce with it.

Šikalo, Delalić and Ganić (2002) experimentally studied droplet deposition in vertical upward air-water nozzle-generated mist flow. They used stainless steel and Plexiglas test sections with different air flow rates, liquid concentrations, and mean droplet diameters. They showed that for poor surface wettability (i.e. high contact angle as in Plexiglas), a high liquid film flow rate, and thus thicker film, was necessary to form a continuous liquid film around the periphery of the test section. Therefore, materials with high surface wettability (i.e. low contact angle as in stainless steal) could have continuous liquid film at smaller film flow rates. In addition, the higher surface wettability increased the liquid film length. They also pointed out that the droplet size affected the way the droplets travel in the mist core. Large droplets with large momentum ejected from the liquid film into the gas phase, as in annular-mist flow, travel relatively unaffected by the gas turbulence and do not change direction before they impact the wall opposite to the place of ejection. This mechanism of deposition is called direct impaction (non-turbulent) mechanism. Small droplets with low momentum, as in spray mist flow, are influenced by the gas turbulence; therefore, the mechanism of deposition is called diffusion (turbulent) deposition. They observed that by increasing a droplet concentration, the droplet deposition coefficient increases too, resulting in a longer test

section portion covered with the liquid film. In addition, they defined the droplet coalescence ratio to the wall as the ratio between flow rates of coalesced droplets and droplets impacted on the wall, and showed that the droplets coalescence ratio is much higher for a dry wall case than for a liquid film case, i.e. the wet surface tended to increase droplet rebound. The same phenomenon was reported in the study by Lee and Hanratty (1988). Because of this, dry walls have a higher droplet deposition coefficient than wet walls assuming all other variables are the same. This higher deposition coefficient does not mean that there are more droplets hitting a dry wall than a wall covered with a liquid film, but that fewer of them stay on a liquid film than on a dry wall. The measured droplet coalescence ratio was equal to 1 for the dry wall case, and it ranged form 0.05 to 0.2 for the liquid film case. Since it takes longer for surfaces with poor wettability to form a continuous liquid film around the periphery of the test section, they have higher droplet coalescence ratio for longer time and hence, higher droplets deposition coefficient than dry surfaces with good wettability. In addition, they explained that higher droplet coalescence ratios were observed in annular-mist flows due to the larger droplet impact angles caused by both, the direct impaction deposition mechanism and the large amplitude disturbance waves associated with thicker liquid films.

Kitagawa, Torii and Nishino (1998) studied experimentally and theoretically spray mist cooling with liquid films in vertical pipes with co-current upward flow. They recognized that there was a fundamental difference in the heat transfer mechanisms for single-component mist flow of steam and water, and two-component mist flow of air and water. In the case of steam-water flow, the bulk temperature of the heated section is basically maintained at the saturation temperature appropriate for the flow pressure. The

evaporation rate is expressed simply in terms of the wall heat flux and the evaporation latent heat. On the other hand, in the air-water flow, the bulk temperature can vary independently of the saturation temperature and the resistance of heat and mass transfer at the gas-liquid interface plays an important role. Their theoretical study predicted that near the entrance region, almost 90 % of the mass flow rate of water ended up on the wall. A heat transfer enhancement ratio as high as seven was observed experimentally. Their model predicted higher heat transfer coefficients compared to the experimental values while the liquid film remained intact. However, it did not predict where film breakdown occurred, i.e. when the rivulet flow regime started.

Mori, Hijikata and Yasunaga (1982) experimentally studied the cooling of gas turbine blades using water mist generated by injecting water through a very small tubule of 0.4 mm ID. The injected water was at room temperature. Straight and coiled test sections with 1.8 mm ID were used. Both test sections were electrically heated. Most of the experiments were done with a heat flux of 200 kW/m^2. They reported heat transfer enhancement of about ten while the water film remained intact. Test section wall temperatures were below the saturated temperature as long as the film was unbroken. As soon as the film became unstable, the wall temperatures increased significantly, up to 500 ^oC. They observed three different wall temperature regions, i.e. liquid film, traditional mist flow and single-phase region. The mist flow region had the highest axial wall temperature gradient. In experiments with a coiled tube, the secondary flow and body force influenced film breakdown location for the opposite sides as well as wall temperatures even in the single-phase region.

O'Rourke and Amsden (1996) conducted a numerical study of particle-based wall liquid film dynamics in spray flows. Their particle numerical method was incorporated into the KIVA-3V code [Amsden (1997)] to model the dynamics and evaporation of wall liquid films, and was primarily intended for port-injection spark ignition engines. Later it was improved with models for splash velocities of secondary droplets, impingement pressure spreading, particle momentum and energy, gravitational terms, and other miscellaneous corrections, and included into the KIVA-3V Release 2 [see Amsden (1999)]. It is a goal of this study to validate this numerical code (KIVA-3V) for internal spray mist cooling with thin subcooled evaporating films applications (see Chapter V).

2.2 Annular-Mist Flow and Two-Phase Forced Convection

Annular-mist flow is one of several flow regimes observed in internal forced convection boiling in vertical heated ducts. Internal forced convection boiling is commonly referred to as two-phase flow and is characterized by rapid changes from liquid to vapor in the flow direction, which traditionally is upward. The sequence of the flow regimes is as follows. As a subcooled liquid flows in a vertical heated duct, the heat transfer to the liquid is by single-phase forced convection. However, once the liquid near the walls reaches the saturation temperature, bubbles appear on the duct inner walls. They are carried into the mainstream of the liquid flow. The vapor bubbles and the liquid form a bubbly flow regime, which is the first two-phase flow regime in this sequence. As the volume fraction of the vapor increases, individual bubbles coalesce to form first a "churn" and then a "slug" flow regime. At higher void fractions, annular, annular-mist, and mist flow regimes are observed. The vapor core and the saturated liquid film that

moves along the inner duct surface characterize the annular flow regime. The liquid film removes the heat coming from the duct walls by evaporation. As the quality of the two-phase flow increases, the velocity of the vapor core increases too, hence it shears liquid droplets off the liquid film. When the liquid droplets and the vapor form a mist core, the annular-mist flow regime is established. The mist core moves at much larger velocity than the liquid film. In general, the annular-mist flow regime has a thinner liquid film than the annular flow, since the annular-mist flow has a faster core of moving gas phase with a considerable amount of water droplets. The mist flow regime has only a mixture of vapor and droplets with no liquid film on the wall. The wall temperature in the mist flow regime is much higher than the saturation temperature. Therefore, traditional mist flow cooling has nothing in common with the mist cooling mechanism studied in this thesis, except for the name mist cooling. When all of the droplets evaporate, the mist flow regime vanishes; at that point, there is only superheated vapor, which is further heated by single-phase forced convection. The heat transfer mode in annular and annular-mist flow regime is two-phase forced convection. Its main characteristic is the evaporating liquid films. No other two-phase flow regime has this heat transfer mode. Forced convection evaporation can coexist with nucleate boiling (within the film), but it can also exist alone. However, nucleate boiling cannot coexist without some forced convection evaporation.

Some of the early empirical heat transfer correlations for two-phase forced convection in vertical tubes for upward one component flows, that are used even today because of their simplicity and reasonable accuracy, were developed in the past fifty years. Examples of such correlations are given by Dengler and Addoms (1956), and Guerrieri and Talty (1956). One of the first important analytical studies on co-current

upward, one component, two-phase forced convection was done by Hewitt (1961). It was based on a study of downward flow condensation done by Dukler (1959). Pletcher and McManus (1968) conducted one of the earliest experimental study on horizontal annular two-phase flow of two components. They measured both the local and average heat transfer coefficients. In 1970, Hewitt and Hall-Taylor (1970) summarized all relevant work up to that point into a book on annular and annular-mist flow and two phase forced convection heat transfer. They presented results showing the hydraulic differences, e.g., film thickness and film flow rate, between the cases when all droplets were introduced into the gas flow through a small pipe located at the centerline of a duct, and when they were entrained by the gas from a wavy liquid film.

Ueda and Tanaka (1974) conducted an experimental study of liquid film flow in the annular and annular-mist flow regimes for downward flow in vertical tubes. In order to establish those flow regimes, they used air and water at room temperature. Their test sections were a 28.8 mm ID transparent acrylic pipe, and a 29.9 mm ID stainless steel pipe. The water was introduced into a test section through a 29 mm ID porous sintered pipe, instantly forming a liquid film. Ueda and Nose (1974) modified the experimental apparatus of Ueda and Tanaka (1974) to study upward flow in vertical tubes. They ran the same experiments and did the same analysis for the upward flow case. For downward flow cases, they used superficial air velocities from 0 to 56 m/s, while for upward flow cases, the air velocity varied from 10 m/s to 45 m/s. The total water flow rate ranged from 0.25 l/min to 18 l/min for both flow directions. These annular-mist water flow rates are significantly higher than the water flow rates used in nozzle-generated mist flows. These studies showed several differences for the upward and downward flow cases. They

observed two film layers, viz. a continuous liquid sublayer and a disturbed wavy layer. The continuous liquid sublayer was laminar. Its thickness was calculated from data obtained in heat transfer experiments. It was assumed that all of the thermal resistance was in the continuous liquid layer due to its cross sectional temperature difference. The disturbed wavy layer had a nearly uniform temperature due to its turbulent nature and therefore did not increase the thermal resistance of the liquid film. The continuous liquid sublayer thickness for the downward flow case varied from 500 μm at a gas Reynolds number of 20,000, to 50 μm at a gas Reynolds number of 100,000. For the upward flow case, it varied from 350 μm to 50 μm for the same gas Reynolds number range. The thickness of the continuous liquid sublayer was relatively insensitive to the liquid flow rate, i.e. ± 10 μm for the higher, and ± 50 μm for the lower gas Reynolds numbers. These thicknesses were approximately the same as those obtained by others who used the same measurement technique. The disturbed wavy layer thickness was measured by a contact probe technique. This thickness was considerably larger for the upward flow case when the gas velocity was low. However, with high gas velocities it was about 1-1.5 times that of the downward flow case. The disturbed wavy layer thickness for upward flow ranged from 150 μm to 7000 μm, while for downward flow it ranged from 120 μm to 3000 μm, at the corresponding gas Reynolds numbers as for the laminar sublayer. It should be noted that these disturbed layer thicknesses are not the mean values but the peak values of turbulent waves. Droplet concentration was measured by collecting droplets at the test section exit. The highest droplet concentration was measured in the center of the pipe. It then gradually decreased to its minimum near the wall. The observed droplet deposition mechanism was direct impaction. Droplet entrainment and their momentum were higher

at higher air flow rates. According to this study, it is obvious that there cannot be any entrainment from the thin films with low gas Reynolds numbers, as is the case in this study. They concluded that for the traditional two-phase flow, if there were less than 1 % of total water mass flow rate present as water droplets, the flow regime was annular; for water flow more than 1 % an annular-mist flow regime was present. Their data showed that annular-mist flow in general had a thinner liquid film than annular flow. The mean liquid film thickness was obtained by accumulating the liquid film at the test section exit and then back calculating it. This mean thickness was considerably thinner for the down flow case. As the air velocity was increased, the mean film thickness became closer for these two cases. At the superficial air velocities of 25 m/s to 30 m/s the mean thicknesses were the same. However, their experiments showed a slightly thinner mean film thickness for the upward flow case at superficial velocities higher than 30 m/s. For the case of 15 m/s superficial air velocity and 0.25 l/min water flow rate, which is equivalent to a 30 % water mass fraction for 15 m/s air flow rate, the mean liquid film thickness for the downward flow was 180 μm, while for the upward flow it was 380 μm. Therefore, for these same operating parameters the liquid film thickness for the upward flow case had more than twice that for downward flow. In this thesis study, the closest case to that mentioned above is the case with a 15 m/s superficial air velocity and 15 % water mass fraction. As will be shown in Chapter V, the numerically estimated mean liquid film thickness for this case is 60 μm. Since the mean liquid film thickness in downward flow changes nearly linearly with the water flow rate [Ueda and Tanaka (1974)], extrapolating their data would yield a 90 μm thick liquid film for the 15 m/s air and 15 % water case. This 30 μm difference in mean film thickness suggests that there is more liquid present as

mist core droplets in nozzle-generated mist flow than in annular-mist flow. Since the mean droplet size is much smaller in nozzle-generated mist flow than for traditional annular-mist flow (see for example Lee, Yang and Hsyus (1994), and Fore, Ibrahim and Beus (2002)), one could conclude that the droplet concentration in nozzle-generated mist flow is much higher than in annular-mist flow. In these two studies, the thickest mean liquid film thickness was reported for the upward flow case (1.9 mm) with 10 m/s air and 18 l/min water flow rates, while the thinnest was for the downward flow case (90 μm) corresponding to the case with 56 m/s air and 0.25 l/min water flow rates. The minimum heat transfer coefficient they reported was of the order of 10,000 W/m^2K, while the maximum was nearly 32,000 W/m^2K.

Jayanti and Hewitt (1997) conducted a numerical investigation of the hydrodynamics and heat transfer of wavy thin film in downward flows. They neglected the presence of a gas beyond the gas-liquid interface and assumed no gas shear stress as well. They showed that the film thickness, rather than the turbulent film waves, is most important for obtaining higher heat transfer rates in these flows. They also showed that the ratio of the wave velocity and the average film velocity is about three and that the average flow velocity in a wavy film flow is slightly greater than that for a smooth film flow with the same flow rate. However, the effect of the velocity difference on the heat transfer was shown to be very small.

Ganić and Rohsenow (1977) performed experimental and theoretical studies showing that two-phase forced convection has higher heat transfer rates than nucleate boiling. They summarized the results of several previous studies regarding droplet deposition and rebound from the surface depending on the normal velocity of the droplet,

size of the droplet, and temperature of the surface. They divided droplets into high and low impact velocity droplets, and the wall temperature into a high and low regimes. If a droplet velocity perpendicular to the wall were lower than 1.8 m/s, it was considered as a low impact velocity droplet. Additionally, if the wall temperature exceeded the minimum film boiling temperature, they considered it a high temperature wall. In the case when a big droplet (diameter of the order of several millimeters or more) with a high impact velocity hits a high temperature wall, it partially stays on the wall and partially rebounds into the main stream due to escaping vapor bubbles (nucleate boiling). Sometimes, however rarely reported, due to a very small thickness of the formed liquid layer and the very high temperature gradient in it, nucleation is prevented. In the case when a small high impact velocity droplet approaches a high temperature wall, a vapor layer forms between the droplet and the wall, and rebounds the tiny droplet without even letting it touch the wall surface. When a low impact velocity droplet hits a high temperature wall, the liquid layer formed from the deposited droplet is found to be in a film boiling-like state. In the case of low impact velocity droplet and a low temperature wall, as is the case in this study, a liquid layer is formed. This layer is then heated up to the wall temperature; it then cools the wall as it evaporates. They also noted that surfaces with a smaller contact angle, i.e. higher wettability, would spread the deposited droplet further apart and therefore increase the heat transfer from the wall. Since the behavior and the further existence of the liquid layer formed from the deposited droplet was mostly determined by the wall temperature, they concluded that the wall temperature was the most important variable associated with this problem.

Barbosa, Kandlbinder and Hewitt (2002) conducted and experimental and numerical investigation of two-phase forced convective boiling of ternary mixtures at high qualities. They used n-pentane/n-hexane/iso-octane mixture as a working fluid. Experiments were carried out in an 8.58 m long, 25.4 mm ID, electrically heated test section. Their predictions were obtained by applying the effective diffusivity, and interactive method, and they showed a good agreement with experimental data. They reported that the temperature difference across the liquid film thickness. i.e. from the wall to the liquid film/gas interface, varied from 20 ^{o}C at the test section entrance to 15 ^{o}C at the test section exit. A temperature difference between the liquid film/gas interface and the gas core was reported to be vary 1-2 ^{o}C at the entrance to 20 ^{o}C at the test section exit.

Barbosa, Hewitt and Richardson (2003) conducted a theoretical study of the influence of droplet interchange on evaporation and condensation of a multicomponent mixture in two-phase forced convection. They concluded that the liquid contained in the liquid film plays a major role in the heat transfer process, while the liquid contained in the droplets of the mist core has a negligible role. They wrote,

"Due to the distribution of the liquid phase within the pipe, the temperature driving force across the liquid film is much higher than that at the vicinity of a droplet. Therefore, in real annular flow, with a significant fraction of the liquid entrained as droplets, not all of the liquid plays a significant role in phase change."

Sun and Hewitt (2001) experimentally studied forced convection evaporation and condensation of steam/water in a vertical tube; their main objective was to examine whether the hypothesis of secondary nucleation proposed by Mesler (1977) was important in annular-mist flow. Their test section was 3.3 m long with a 9.5 mm ID. It used fluid heating in order to avoid any ambiguity in the evaporation experiments that

could come from electrical hating. At high qualities, in annular-mist flow, the interface is traversed by disturbance waves and is impinged upon by droplets from the mist core. Mesler argued that these processes lead to the entrainment of small bubbles into the liquid film which then grow due to the film superheat, significantly contributing to the heat transfer rate. Mesler described this process as secondary nucleation, and suggested that it is because of the secondary nucleation and not the forced convection evaporation, that the heat transfer coefficient increases after the nucleate boiling dominant segment. Sun and Hewitt proved this hypothesis wrong, and therefore unimportant, for annular-mist flow by comparing their forced convection evaporation and condensation results. In this paper they reported,

"In the annular flow regime, two complementary mechanisms coexist for heat transfer, namely heat transfer resulting from nucleate boiling in the liquid film and heat transfer resulting from convection from the tube surface to the interface, where evaporation occurs. As the film thins along the tube, forced convection becomes more dominant since, with the increasing heat transfer coefficient, the wall temperature falls and the intensity of nucleate boiling decreases."

Therefore, they reconfirmed that forced convection evaporation is superior to nucleate boiling. They reported heat transfer coefficients as high as 50,000 W/m^2K. Typical heat fluxes used were in the range 50-100 kW/m^2.

Suzuki, Hagiwara and Sato (1983) numerically studied the heat transfer and flow characteristics of two-phase, two-component, annular flow with wavy-laminar thin liquid films heated at low heat flux. They employed a simple model for the wave mass transfer effects on momentum, and heat and mass transfer. In order to account for the wave effect directly, they substituted experimental data for the two-wave parameters appearing in their model. The wall heat flux was assumed to be low enough so that evaporation did not significantly affect the gas phase flow pattern. Their theoretical results agreed very well

with the existing experimental data for heat transfer, axial pressure gradient and mean liquid film thickness in this particular annular flow situation. Based on this method, a warning was given on the usage of the existing traditional annular flow heat transfer empirical formulae for the wavy-laminar thin liquid films case. They believed the reason for this was due to differences in the liquid films obtained in these flows; the liquid films studied were wavy-laminar thin liquid films while in the general case these liquid films were either thick or they had liquid Reynolds number higher than the critical value. This conclusion is of particular importance for this thesis study since the wavy-laminar thin liquid film could resemble nozzle-generated liquid films.

Jayanti and Hewitt (1997) used computational fluid dynamics techniques to calculate flow and heat transfer through a wavy liquid film driven by gas shear. The geometry and flow conditions specified were typical of conditions encountered in traditional annular flows. Their results showed that the flow in the substrate layer was laminar while that in the disturbance wave region was turbulent leading to a local enhancement of the transfer coefficients.

Various numerical techniques and models have been proposed for annular-mist, mist, and forced convection evaporation heat transfer; these include analytical two-phase flow models, two-dimensional finite-difference models, separated flow models, and others [Fu and Klausner (1997), Petukhov and Zlokazov (1991), Nakabe and Yamanaka (1985), and Matida and Torii (1995)].

Experimental studies on generation, size distribution, and concentration of droplets in annular-mist flow include those by Tatterson, Dallman and Hanratty (1977), Kataoka, Ishii and Mishima (1983), Kocamustafaogullari, Smits and Razi (1994), and

Fore, Ibrahim and Beus (2002). All of these studies clearly showed that the size of droplets in traditional annular-mist flow is much larger; sometimes as much as two order of magnitude larger than the size of droplets obtained by atomizing nozzles in spray mist cooling applications. Fore, Ibrahim and Beus (2002) reported that Sauter mean droplet diameter range was from 298 μm to 1060 μm, while the maximum droplet size range was from 754 μm to 3078 μm. The corresponding superficial velocities for both lower range diameters were 0.031 m/s for the liquid film and 20.7 m/s for the gas; the corresponding values for the upper range diameters were 0.122 m/s for the liquid film and 4.6 m/s for the gas. These studies also reported that the main droplet entrainment mechanisms in annular-mist flow were: roll-wave shearing off, wave undercutting, droplet impingement, and liquid bridge disintegration. The liquid bridge disintegration and wave undercutting mechanisms produce the biggest size droplets [Tatterson, Dallman and Hanratty (1977)]. However, none of these processes is typical for nozzle-generated mist flow.

Mastanaiah and Ganić (1981) studied experimentally and theoretically the post dryout region of air-water dispersed flow. Their test section was an electrically heated 12.95 mm ID vertical stainless steel tube with a length of 889 mm. The average wall heat flux was varied from 6.4 kW/m^2 to 36.2 kW/m^2. Their data suggested that the two-phase thermal entrance length decreased with increasing wall temperature, and was higher than the entrance length for the singe-phase flow. They reported single-phase thermal entrance lengths of 10 to 15 tube diameters, while for the traditional mist flow their data showed them to be from 30 to 50 tube diameters. It was found that the local two-phase heat transfer coefficient decreased increasing wall temperature and that the effectiveness of

wall-to-drop heat transfer depended mainly on the wall superheat for surface temperatures below the minimum film boiling temperatures.

Akagawa, Fujii and Murata (1984) experimentally studied swirling annular-mist two-phase flow in a 40 mm ID and 5 m long tube. The swirling was induced by a swirler inserted into the inlet of the test section. They investigated the behavior of the liquid film and entrained droplets in a non-swirling and swirling downward annular-mist air-water flow in order to find ways to maintain the liquid film longer on the tube wall. Measured values for the liquid film thickness, wave velocity, length and frequency of disturbance, base liquid film flow rate, entrained droplets flow rate, and disturbance wave flow rate were reported.

2.3 Liquid Films Instability

In order to fully understand the liquid films' evaporative cooling process, one must understand the phenomena leading to liquid films instability. A wealth of information exists on liquid films instability. For clarity, studies of liquid films instability are divided into three groups; the first group covers free falling liquid films without heat transfer. The second group covers free falling liquid films with heat transfer, and finally the third group covers sheared liquid films with and without heat transfer. Clearly, the case of sheared liquid films with heat transfer is the most important in this thesis study.

Two theoretical approaches have been commonly used to study liquid films instability. The first approach involves a force balance (FB) at the point of liquid stagnation, which forms after the film breakdown. The criterion for a stable configuration, i.e. liquid film flow versus rivulet flow, is the balance of inertial and

interfacial forces. If the inertial forces are dominant, the stable configuration is liquid film flow. However, if the interfacial forces are dominant, rivulet flow will form. The results of this approach are strongly dependent on the contact angle of the liquid at stagnation point.

The second approach is commonly referred to as the Minimum Total Energy (MTE) model for the stable liquid rivulets forming after a film breakup. The total energy of rivulets is the sum of the liquid kinetic energy and the interfacial energies at the liquid-solid and liquid-gas interfaces. It is assumed that the stable flow configuration will exist at the minimum of the total energy function.

2.3.1 Free Falling Liquid Films without Heat Transfer

For free falling films without heat transfer, the liquid films either break into rivulets before they fully develop or they do not break at all. The forces involved in this case are: stagnation (or decelerating) force, body force, surface tension force, and wall shear force. The body and wall shear force are usually insignificant. Therefore, the balance of stagnation and surface tension force determines if the liquid film would break or not, as shown in theoretical studies by Hartley and Murgatroyd (1964) for the case of a flat surface, and by Hughes and Bott (1998) for the case of a vertical tube.

2.3.2 Free Falling Liquid Films with Heat Transfer

There are two different types of free falling liquid films with heat transfer. Here, liquid films could be saturated or subcooled. Forces involved in saturated liquid films are the same as those for free falling films without heat transfer, except for the addition of

vapor thrust caused by liquid film evaporation. The vapor thrust is not a significant force, except for liquid metal films as shown the in theoretical study by Zuber and Staub (1966). Fujita and Ueda (1978) and Hewitt and Lacey (1965) showed that saturated liquid films would break either because of liquid film starvation, i.e. the film is depleted to zero flow due to evaporation, or because of bubble nucleation in the liquid film, i.e. localized nucleate boiling, where the formation and bursting of the vapor domes are significant enough to create a dry patch. Whether film starvation or nucleation is going to occur depends on many factors such as, wall temperature, heat flux, wall surface condition (micro-roughness, oxidation), film thickness, etc. However, as discussed later for the sheared saturated liquid films, liquid film starvation is more common.

Forces involved in subcooled liquid films are the same as those for the saturated liquid films, except for the addition of the thermocapillary force (i.e. the Marangoni force). Temperature differences along the subcooled liquid film surface, caused by, e.g. waves with thinner-wormer and thicker-colder regions, local diversion from the normal droplet deposition, or local heat flux non-uniformity, cause local variations of the surface tension. These local surface tension variations create thermocapillary forces, which are commonly referred to as the Marangoni effect. Thermocapillary forces create a lateral flow diversion and further local film thinning. Thinner segments of the film become even wormer and therefore increase the thermocapillary forces even more. Finally, the thinner segments of the liquid film rupture due to sufficient heat flux that evaporates locally very thin film or the continuous lateral flow diversion, and form dry patches. This film breakdown mechanism is called thermocapillary breakdown, and is different from the film burnout or dry out mechanisms, which occur in saturated liquid films. In

thermocapillary film breakdown, a dry patch extends not only downstream but also upstream since the boundary of the dry area depends on the absolute surface tension, which is much greater than the differential surface tension causing the Marangoni effect. According to Fujita and Ueda (1978), the critical film thickness for thermocapillary breakdown is about one quarter of the main film thickness. Due to the Marangoni effect, the heat fluxes required to rupture subcooled liquid films are much lower than those for saturated liquid films as shown by Hoke and Chen (1992) and Fujita and Ueda (1978). Hoke and Chen (1992) measured that a stable free falling liquid film thickness was thicker than 55 μm even for as low as 0.3 kW/m^2 heat flux. In addition, they did not report a significant change in the breakdown heat flux for 50 ^oC and 75 ^oC subcooled liquid films. Ganić and Getachew (1986) showed that surfaces with higher wettability could resist thermocapillary breakdown better than non-wetting surfaces. El-Genk and Saber (2002) derived an expression for the critical film thickness as a function of Marangoni number.

Subcooled as well as saturated liquid films eventually rupture provided that the heated surface is long enough. However, their breakdown mechanisms are different since subcooled liquid films usually do not reach saturated temperatures due to the Marangoni effect. The importance of the Marangoni effect depends on the amount of subcooling when the liquid film is formed. If the liquid film is subcooled just a few degrees Celsius, it is very likely it will become saturated, where the Marangoni effect vanishes. For more subcooled liquid films, e.g. 50 ^oC, the Marangoni effect is greater and probably detrimental in the film breakdown mechanism.

2.3.3 Sheared Liquid Films with and without Heat Transfer

In addition to the forces describes in the previous cases, sheared liquid films are subjected to two additional interfacial forces, namely, the free surface shear force and form drag force (i.e. the aerodynamic shape force at the small step in the film). McPherson (1970) showed that the form drag force is not significant and can be neglected, while Murgatroyd (1965) showed that the interfacial forces could be as much as twenty times greater than the film inertial forces. Therefore, the free surface shear force enhances liquid film stability, and enables the film to become much thinner before it breaks. The film breakdown mechanisms are the same as those for in free falling liquid films, with the film breakdown delayed.

In the sheared, heated, and saturated liquid films case, even though the film breakdown mechanisms are the same as those for the free falling, heated, and saturated liquid films case, the fact that the liquid films become much thinner favors film starvation over bubble nucleation breakdown. Sun and Hewitt (2001) explained that in thin sheared saturated liquid films, forced convection evaporation becomes dominant over nucleate boiling. Therefore, bubble nucleation is less likely to occur and cause a film breakdown. The film simply continues to evaporate until it breaks due to starvation. Studies of sheared liquid films have been reported by Hartley and Murgatroyd (1964), Hughes and Bott (1998), and Hewitt and Lacey (1965); these studies point to the more complex phenomena taking place in these film flows as opposed to those discussed earlier for the low-shear cases.

2.4 Single-Phase Flow Convection

In order to confirm the accuracy of the experimental data obtained in this investigation, experiments were performed using single-phase forced convection to the carrier gas. Comparisons were then made between the measured heat transfer coefficients and predictions of the widely-used empirical correlation of Reynolds, Swearingen and McEligot (1969), and the analytical solution of Notter and Sleicher (1972). In addition to confirming the validity of the experimental methodology, the measured heat transfer coefficients for single-phase cooling were used to estimate the enhancement ratio, i.e. the ratio between the heat transfer coefficients for mist cooling and those obtained using the carrier gas alone.

2.5 Summary

The high heat transfer coefficients observed in annular-mist and spray mist flows are primarily due to the phase change which takes place at the liquid film/gas interface. Liquid films in annular-mist flow are frequently one to two order of magnitude thicker than in spray mist cooling (see for example Lee, Yang and Hsyua (1994), and Ueda and Nose (1974)). This is mostly caused by the higher liquid flow rates present in annular-mist flow, where the film thickness can be as much as several millimeters. In addition, the films are generally turbulent, with roll-waves and droplet entrainment. On the other hand, liquid films in spray mist cooling are laminar and flat with, possibly, small ripples, and no droplet entrainment. They are very thin, between 50 μm and 100 μm, which results in very low thermal resistance. This ensures a high temperature at the film/gas interface, which is desirable for film evaporation. Therefore, from the film thickness

standpoint, spray mist cooling offers a lower thermal resistance. However, due to evaporation, liquid films in annular-mist flow eventually become very thin as they approach the starvation stage, but that thickness is not typical for the entire length of the annular-mist flow regime.

The droplet size in annular mist flow is also one to two order of magnitude larger than that for spray mist cooing (see for example Lee, Yang and Hsyua (1994), and Fore, Ibrahim and Beus (2002)). In spray mist cooling, at the channel entrance, all of the liquid is contained within the mist core as tiny droplets, which deposit on the walls as they flow along the channel. The main function of these very small droplets (30 μm to 80 μm diameter) is to establish and continuously feed a very thin and uniform liquid film along the channel surface, therefore preventing a film breakdown. This could not be done with the larger droplets. On the other side, in annular-mist flow almost all of the liquid is present within the liquid film, from which droplets as large as 1000 μm are entrained into the gas core. Figure 2.1 shows a typical annular-mist flow regime situation, while Figure 2.2 shows two photos of spray mist taken in this thesis study, which show a dense fine mist core spray, and a thin liquid film with some ripples. These characteristics make spray mist cooling more attractive for high heat flux evaporative cooling systems.

The droplet concentration in annular-mist flow is lower that in spray mist cooling. A higher droplet concentration allows a thin liquid film to exist over a longer portion of the channel, thereby delaying film rupture and producing a higher overall heat transfer rate.

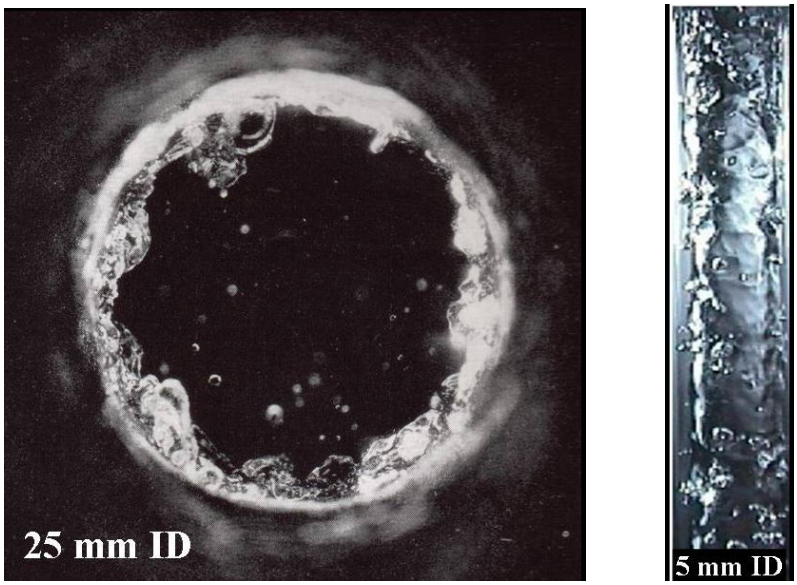

Figure 2.1 Traditional annular-mist flow regime: axial view (left) [Hewitt and Hall-Taylor (1970)], side view (right) [Verberk (2005)]

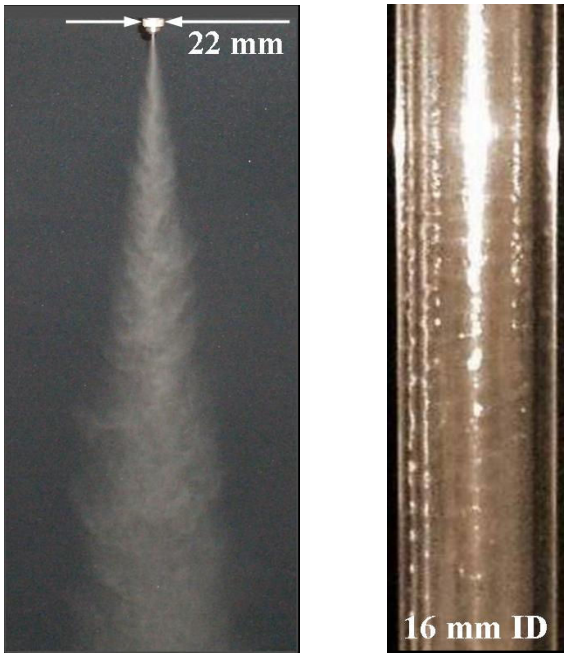

Figure 2.2 Nozzle-generated spray mist (left), thin liquid film side view (right)

The liquid film in annular-mist flow is maintained at the saturation temperature, while the film in spray mist cooling is subcooled. Usually, due to Marangoni effect, the subcooled liquid film generated by spray mist never reaches the saturation temperature before breaking down. The liquid film temperature significantly improves surface evaporation, and hence the heat transfer coefficient; therefore, if all other factors are equal, annular mist flow would have a higher heat transfer coefficient than nozzle generated mist flow. Concerns regarding liquid film stability for nozzle generated mist flow are more evident for long channels. This is due to the fact that for nozzle-generated mist cooling, as the flow proceeds along the channel, the nozzle effects (i.e. very thin film, very small droplet size and high droplet concentration) die off. When that occurs, the film becomes unstable and a rivulet flow regime quickly forms, thereby significantly reducing the heat transfer coefficient.

Even though considerable knowledge regarding spray mist cooling has accumulated over the past two decades, this study expands on such knowledge by examining additional effects including the effects of nozzle design, channel geometry, flow direction, unheated entrance length and its wettability, inlet gas humidity, injected water temperature, and carrier gas properties. The data obtained in this study will provide a deeper understanding of the phenomena taking place in nozzle-generated mist cooling. These data will allow designers of mist-cooled high power systems to predict the system behavior under different design and operational conditions, thereby allowing the system design to be optimized.

CHAPTER III

EXPERIMENTAL APPARATUS AND PROCEDURES

3.1 Experimental Apparatus

The purpose of this investigation is to quantify the effects of various operating and design parameters, namely, the gas/liquid combination, carrier gas velocity, temperature, and inlet humidity, liquid mass fraction, film thickness, injected liquid temperature, liquid atomization nozzle design (i.e. spray geometry, droplet size distribution, and droplet velocity/spray momentum), heated test section length, unheated entrance length and its surface wettability, channel geometry, flow direction, and heat flux on mist cooling effectiveness. To this end, an experimental apparatus has been designed, constructed, and instrumented to allow variation and control of these parameters. Specifically, the experimental apparatus has been designed to meet the following functional requirements:

(1) Provide a carrier gas (room temperature air or helium) to the heated channel at a controlled mass flow rate, and humidity.

(2) Provide a liquid (water) to an atomizing nozzle (placed at the channel inlet) at a controlled flow rate and temperature.

(3) Provide the means to accommodate different channel geometries, i.e. different channel cross sections (rectangular or cylindrical), hydraulic diameters, heated length, and unheated entry length.

(4) Provide the means to accommodate different atomizing nozzle designs to produce a wide range of mist characteristics.

(5) Provide the means to heat the test section and precisely control the surface heat flux over a wide range of power inputs.

(6) Provide the means to allow the gas/mist mixture to flow either upward or downward through the test section.

(7) Provide the means to measure the local heat transfer coefficient along the channel for the entire range of design and operating parameters.

A schematic diagram and a photograph of the experimental apparatus are shown in Figure 3.1 and 3.2, respectively. The system is designed to operate in a once-through mode with either air or helium as the carrier gas and water as the atomizing liquid.

3.1.1 Gas Supply System

Air is supplied from the house line, while helium is supplied by a pallet of 12 high-pressure gas cylinders (Figure 3.3). Figure 3.1 corresponds to air/water operation; for helium/water operation, the supply line is connected to the pressure regulator of the pressure gas cylinders. Referring to Figure 3.1, the supply gas is first pressure-regulated and filtered before being divided into two streams. Most of the gas (or all of it if a gas-atomized nozzle is not used) flows through the main line (horizontal leg in SW corner of Figure 3.1). When a gas-atomized nozzle is used, a small fraction of the gas flow is directed to the atomizing nozzle placed at the test section inlet (vertical leg in SW corner of Figure 3.1) by opening valve "*A*". When a fixed geometry or an ultrasonic nozzle is used, valve "*A*" is closed. The main gas flow can be either directly supplied to the test section inlet (valve "*B*" open and valves "*C*" and "*D*" closed), or, alternatively, it can be

humidified before being supplied to the test section inlet (valve "*C*" open and valve "*B*" and "*D*" closed).

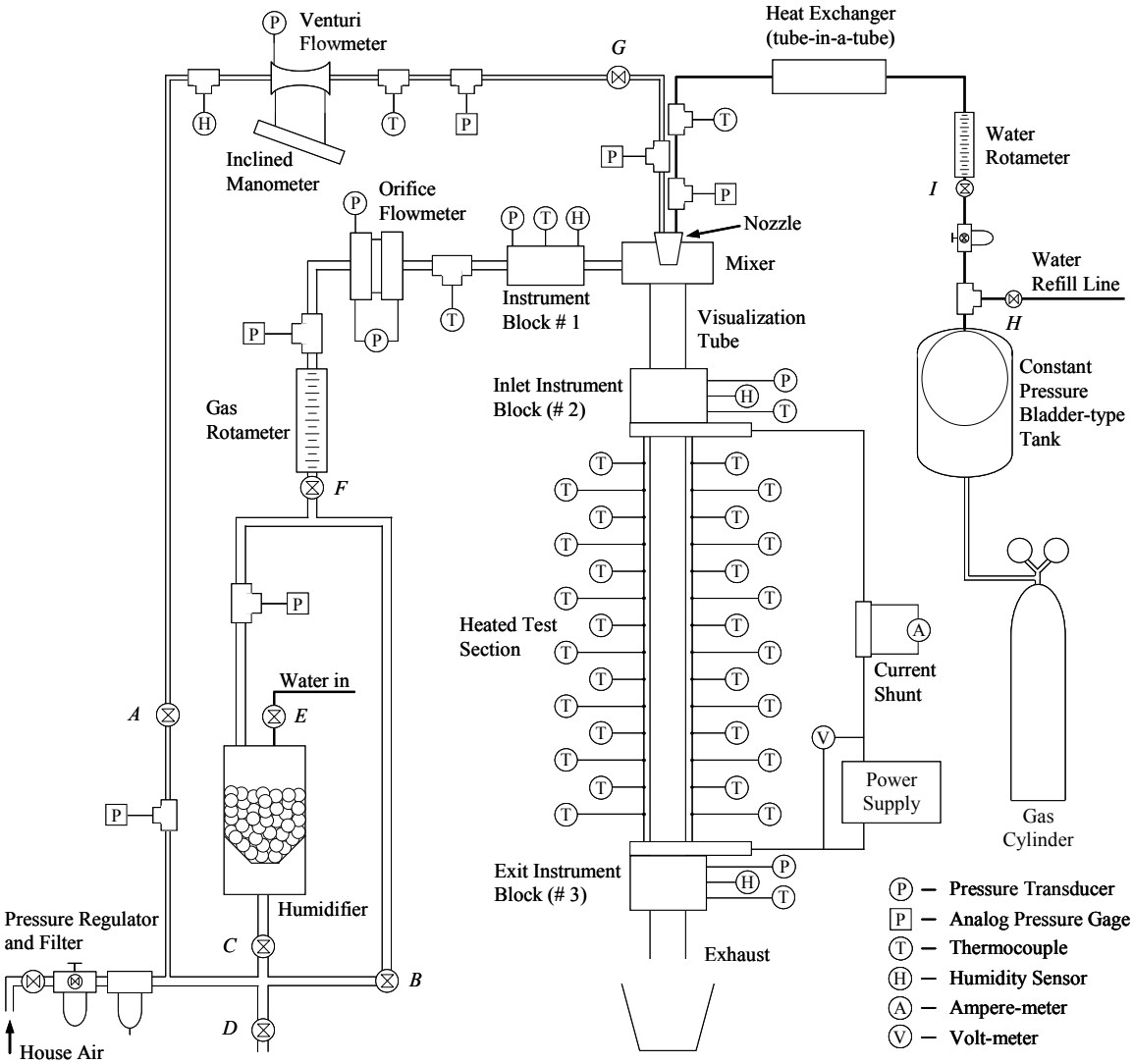

Figure 3.1 Schematic Diagram of the Experimental Apparatus

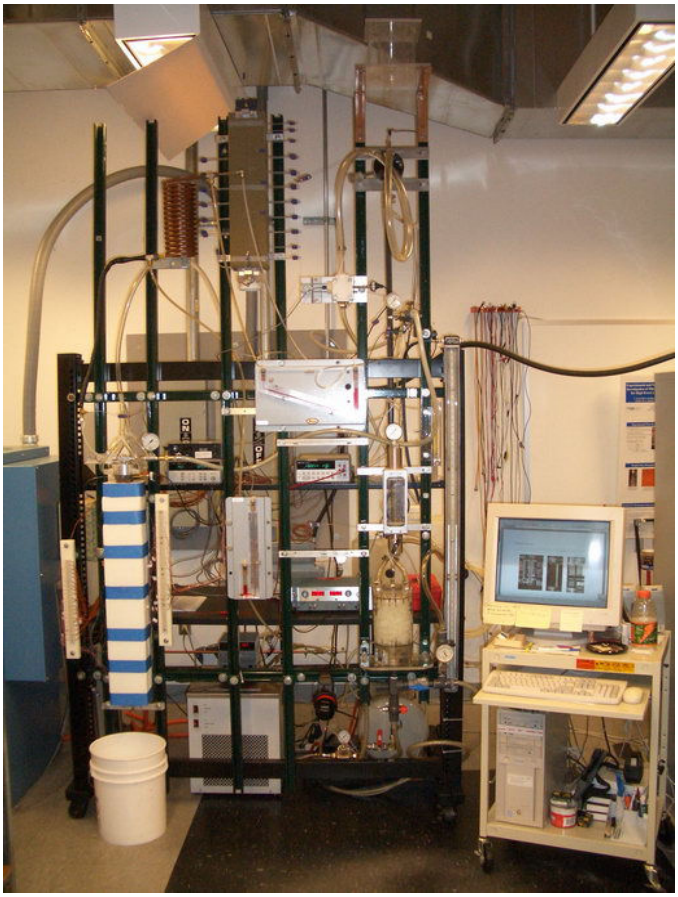

Figure 3.2 Photograph of the experimental apparatus

Figure 3.3 High-pressure helium cylinders used for helium/water experiments

The humidifier is an 11.5 cm ID, 19 cm long acrylic vessel containing a packed bed of acrylic balls with different diameters (1.3 cm, 1.9 cm and 2.5 cm). A photograph of the humidifier is shown in Figure 3.4. When operational, it is filled with liquid water up to the mid-level; water is periodically supplied to the humidifier by opening valve "*E*". When gas flows through the humidifier, the water level swells to the top. The acrylic balls serve to increase the surface area for evaporation, so that the gas exiting the humidifier is nearly fully saturated (100 % relative humidity). When not in use, the humidifier can be drained by opening valve "*D*".

Figure 3.4 The humidifier

Before entering the test section, the carrier gas flows through a rotameter (Brooks Instrument Division 1110CK11CMDAGK) to provide a visual indication of the flow rate. A needle valve "*F*" at the rotameter inlet is used to adjust the gas flow rate. The gas flow rate is precisely measured using a calibrated orifice flowmeter (Figure 3.5) manufactured

by Gerrand Engineering (model ¾" B-5) with the orifice manufactured by Meriam (bore 0.315 in, line 3/4 , series 300, material 316 SS, S/N 647640-S1). Measurements made at the orifice flowmeter include the gas pressure upstream of the orifice, the gas temperature downstream of the orifice, and the differential pressure across the orifice. The upstream gage pressure is measured using a differential pressure transducer (Omega PX26-030DV), while the pressure differential is measured using a differential pressure transducer (Omega PX26-015DV). The downstream gas temperature is measured using an E-type thermocouple probe (Omega EMQSS-062E-12). Type E thermocouples are used for all temperature measurements in this experiment, while all absolute pressures are obtained by adding measured gage pressures to the room pressure measured by an absolute pressure transducer (Omega PX302-015AV).

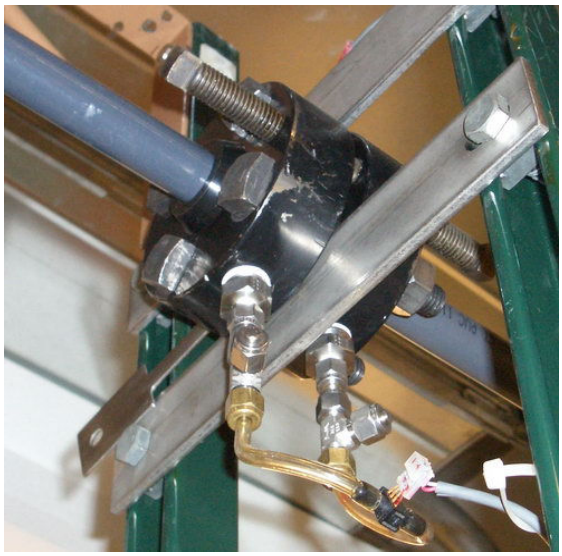

Figure 3.5 The orifice flowmeter

The carrier gas leaving the orifice is directed to a Teflon "instrument block" (16 mm ID, 9 cm long, 7.5 cm wide and 3.8 cm thick) before entering the test section. At that point,

the temperature (Omega EMQSS-062E-12), pressure (Omega PX180-015GV), and relative humidity (Honeywell HIH-3610-003) are measured using miniature transducers. Figure 3.6 shows a schematic of the Teflon instrument block # 1, while Figure 3.7 is a photograph. It is designed to prevent the humidity sensor from wetting, which is important to prevent false high readings. The same instrument block design is used at both the inlet and exit of the test section. After passing through the instrument block, the main gas line splits into four equivalent lines that connect to the supply mixer placed at the test section inlet.

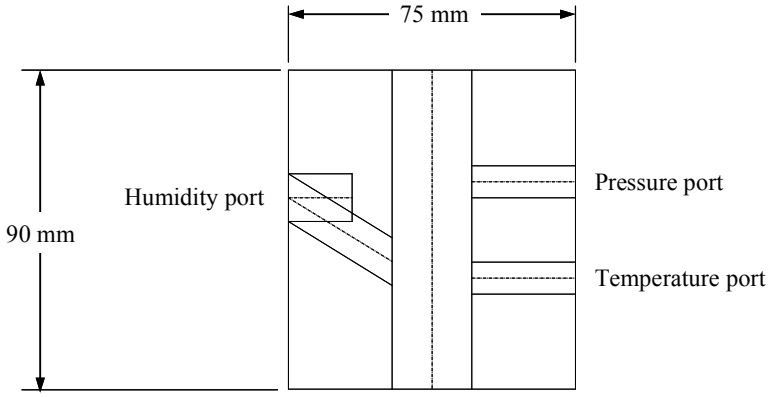

Figure 3.6 The Teflon instrument block # 1 schematic

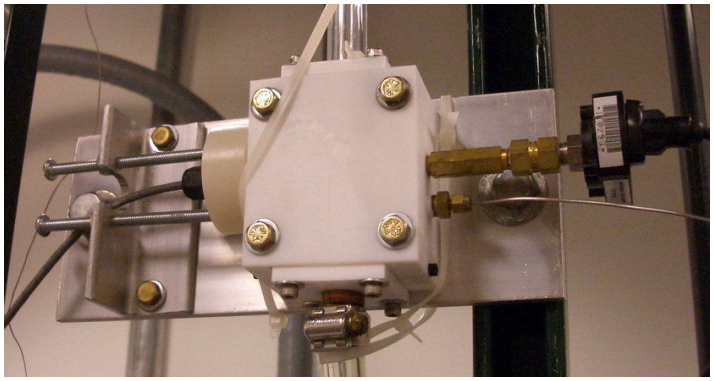

Figure 3.7 Photograph of the Teflon instrument block # 1

As indicated earlier, when a gas-atomized nozzle is used, a small gas stream is diverted from the main supply to the nozzle. The flow rate through the gas-atomized nozzle supply line is measured using a Venturi flowmeter (Lambda Square CBV075); a photograph is shown in Figure 3.8. Measurements made at the Venturi flowmeter include the upstream gage pressure (Omega PX180-060GV), downstream temperature (Omega EMQSS-062E-12), and upstream relative humidity (Honeywell HIH-3610-003). An inclined manometer (Dwyer 244) is used to measure the pressure drop across the Venturi. A needle valve "*G*" after the Venturi flowmeter is used to adjust the gas flow rate. After passing through the needle valve "*G*", the gas-atomized nozzle supply line goes directly to the gas-atomized nozzle, which is mounted atop the mixer at the test section inlet. Immediately before the gas-atomized nozzle supply line connects to the nozzle, an analog gage is used to provide a visual indication of the atomization gas pressure; this is an important parameter for determining the mean droplet size. The gas used to atomize the water exits the nozzle together with the water mist into the mixer where they are combined with the main line gas before entering the test section.

Figure 3.8 The Venturi flowmeter

3.1.2 Water Supply System

Figure 3.1 includes a schematic of the water supply circuit; all water lines are made of vinyl tubing. Distilled water from a 10-gallon reservoir (not shown on the system schematics) is pumped into a constant pressure bladder-type tank (TEEL 4P833A), shown in Figure 3.9. The maximum rated pressure of the water supply tank is 100 psig. A constant pressure (usually set to 40 psi) is maintained within the tank using a regulated air cylinder or a house line. The system is designed so that the tank can be refilled with water even while it is in use, so that the experiment can be operated for many hours without stopping. This can be accomplished by opening valve "*H*" and starting the pump to transfer water from the 10-gallon reservoir to the bladder-type supply tank. Distilled water is used in all of the experiments.

Figure 3.9 The constant pressure tank

The water discharged from the supply tank flows through a calibrated water rotameter (Brooks Instrument Division 1355K1BH0F6CG) shown in Figure 3.10, where the water flow rate is controlled by a needle valve "*I*". Before reaching the nozzle, the water supply line flows through a coiled tube-in-a-tube heat exchanger (Parker Hannifin DHTC-SS-4) shown in Figure 3.11, connected to a constant temperature bath (Fischer Scientific 9500) – Figure 3.12. The constant temperature bath can precisely regulate the water temperature at the nozzle inlet between nearly 0 ^{o}C and 100 ^{o}C. Immediately after the water line leaves coiled heat exchanger, it goes to the nozzle at the test section inlet. This very short portion of the water line is insulated in order to control the water inlet temperature. At the nozzle connection point, the water temperature is measured using an E-type thermocouple probe (Omega EMQSS-062G-6), while the gage pressure is measured by an analog-type Bourdon pressure gage.

Figure 3.10 The water rotameter

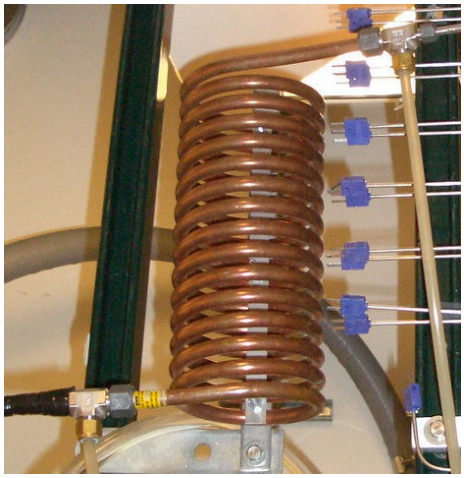

Figure 3.11 The coiled heat exchanger

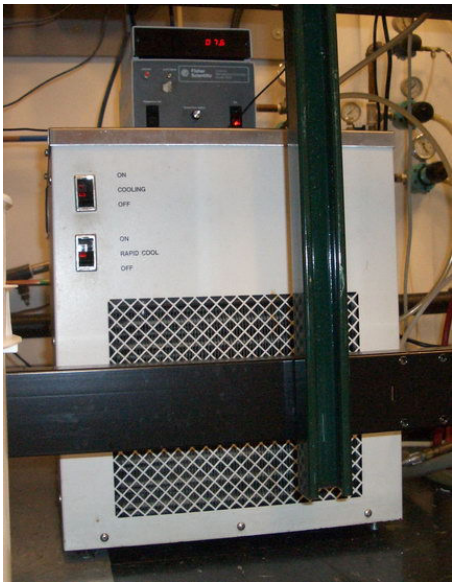

Figure 3.12 The constant temperature bath

3.1.3 Nozzles

Three types of nozzle have been used in this investigation, namely, a gas-atomized nozzle (Spray Systems 1/8J-SS+SU22B-SS), a fixed geometry hydraulic nozzle

(HAGO M1), and an ultrasonic nozzle (Sono-Tek 8700-48). Figures 3.13, 3.14, and 3.15 show these three nozzles, respectively.

Figure 3.13 The gas-assisted nozzle

Figure 3.14 The fixed geometry hydraulic nozzle

Figure 3.15 The ultrasonic nozzle

These nozzles cover a wide range of spray geometry, spray velocity and droplets size distribution. The gas-assisted nozzle uses pressurized gas for droplet atomization; the fixed geometry hydraulic nozzle atomizes droplets by forcing high-pressure water through a small orifice; while the ultrasonic nozzle atomizes droplets with the oscillating tip of the nozzle.

The gas-assisted nozzle produces a high-velocity, full-cone spray with a cone angle of nearly 18 degrees. The Sauter mean droplet diameter for the gas-assisted nozzle can be controlled from as low as few microns to nearly 100 μm. The droplet size distribution is controlled by varying the gas pressure inside the gas-assisted line; higher gas pressure produces smaller droplets.

The fixed geometry hydraulic nozzle produces a low velocity, full-cone spray with a cone angle of 80 degrees. Depending on the water flow rate (which is a function of the water line pressure) it can produce droplets with Sauter mean diameter of nearly 20 μm to 40 μm. This nozzle does not provide any droplet size distribution control for a fixed water flow rate. Only by changing the water flow rate, i.e. the water line pressure, a droplet size distribution can be changed.

The ultrasonic nozzle produces a nearly mono-disperse cylindrical spray with negligible axial velocity. It produces droplets with Sauter mean diameter of 80 μm to 85 μm. This nozzle does not provide any control over the droplet size distribution. Depending on the electrical power input to the ultrasonic generator, either it atomizes the droplets within the stated size range with a cylindrical spray shape, or it creates significantly larger single droplets of unknown diameter when the power is too high; the latter condition has never been observed in this study.

The experimental data obtained in this investigation show that the gas-atomized nozzle produces the best performance, while the fixed geometry nozzle produces the poorest performance.

Figure 3.16 The ultrasonic nozzle power generator

3.1.4 Flow Mixer and Visualization Section

Figure 3.17 shows a schematic diagram of the flow mixer placed at the test section inlet. The mixer consists of a top and bottom plate. The plates are sealed together using an O-ring. The top plate is designed to mount a nozzle at its center. Each of the three nozzle used has its specially designed top mounting plate. The same bottom plate is used for all nozzles. It is designed to mix the main line gas with the nozzle-generated mist. It has four openings through which the main gas lines are connected. Four inlet lines are used, 90^{o} apart, to ensure good directional flow uniformity. The four main gas streams combine at the center of the bottom plate, then turn 90 degrees downward towards test section. As the gas flows axially, it is mixed with the co-currently flowing droplet stream generated by the nozzle. The mixture flows through an unheated entrance

length before entering the heated test section. The entry length serves as a flow visualization tube, which is used to visually study gas/water mist flow and water film behavior (viz. film stability, presence of waves, film and mist spray concentricity, etc.) prior to entering the heated test section.

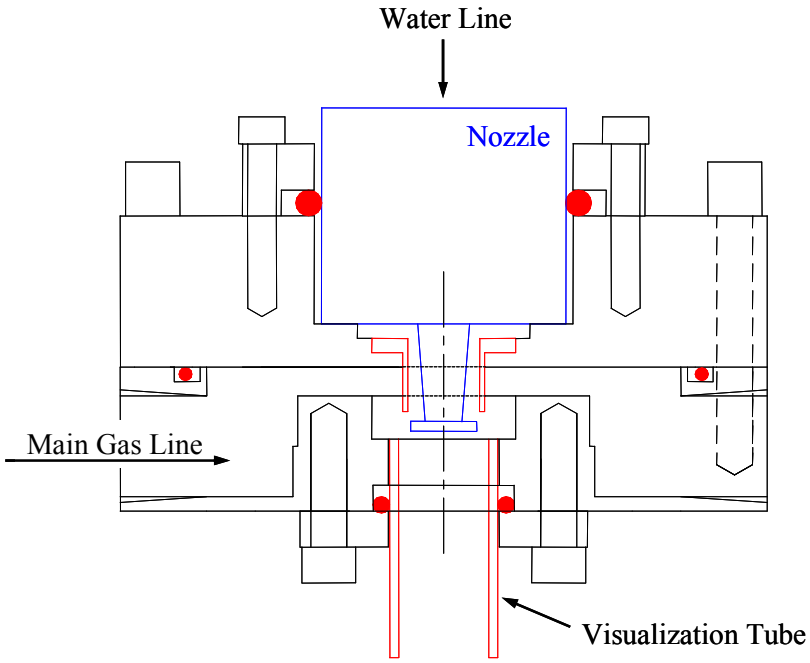

Figure 3.17 The mixer schematic

The visualization tube is an acrylic, glass, or transparent polyvinyl chloride (PVC) tube. These different materials are chosen in order to study the effect of surface wettability on film formation and stability. Experiments have shown that the glass tube had the best characteristics and provided the most stable film due to its relatively small contact angle and high wettability. Two 16 mm ID acrylic tubes are used, with a length of either 61.5 cm or 7.5 cm. Four glass tubes are used. Two of them have 17 mm inner

diameter and are 61.5 cm and 7.5 cm long. The other two have 27 mm inner diameter and are 7.5 cm and 68.5 cm long. Two transparent PVC tubes are used. Both of them have 25.4 mm inner diameter and are 7.5 cm and 68.5 cm long. Different tube lengths have been used to study the effect of the unheated entry length on heat transfer and liquid film breakdown. The mixer and a 7.5-cm long visualization tube are shown in figure 3.18.

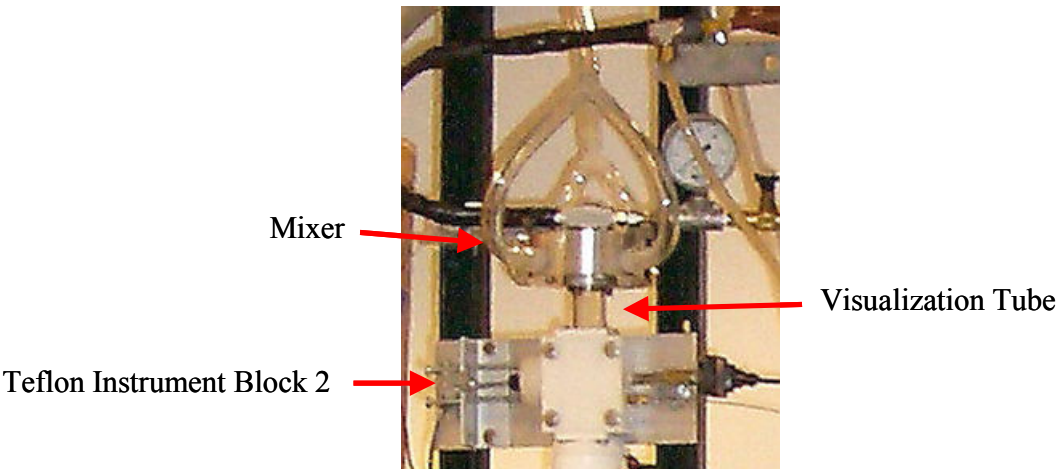

Figure 3.18 The mixer, visualization tube and inlet instrument block

3.1.5 Test Section Inlet Instrument Block

An inlet instrument block is placed between the unheated visualization tube and the test section inlet. Two designs are used for the inlet instrument block. For the cylindrical test sections, the block has the same design as the Teflon instrument block # 1 described earlier, and is referred to as Teflon instrument block # 2, (Figure 3.18). It has the same inner diameter as the cylindrical test section in use and is 9 cm long, 7.5 cm wide and 3.8 cm thick. Therefore, there are three versions of Teflon Instrument block # 2,

one for each test section/visualization tube combination; this way a smooth transition is provided from the visualization tube inner diameter (chosen to be as close to the test section inner diameter as possible), to the heated test section. The visualization tube is connected to the instrument block by inserting its bottom 25 mm into the instrument block; sealing is done by an O-ring placed around the visualization tube 25 mm from its bottom end. This smooth transition is important in order not to disturb the flow and formation of a thin liquid film. Teflon Instrument block # 2 is equipped with miniature transducers to measure the centerline wet bulb temperature (Omega EMQSS-062E-12), the gage pressure (Omega PX180-015GV), and the relative humidity (Honeywell HIH-3610-003) of the mist stream as it enters the test section. Similar to instrument block # 1, it is designed to prevent the humidity sensor from wetting.

For the rectangular test sections, the inlet instrument block has a different design (Figure 3.19). It accommodates the sudden expansion from the cylindrical visualization tube cross section to the rectangular cross section of the heated test section. For the first used rectangular test section used in this study, the inlet instrument block is 5 cm long with 16 mm ID. This instrument block is designed to be used with the visualization tube in the same manner as Teflon instrument block # 2. This “long” design caused liquid film breakdown since the film is already formed inside the instrument block and is then “broken” at the sudden expansion to the heated test section, where big droplets are sheared off at the expansion edge. In order to overcome this problem, the inlet instrument block for the second rectangular test section is designed to be 3.8 cm long with 15 mm ID and no visualization tube. This causes only a small portion of the spray droplets to impact the instrument block walls before they enter the heated test section. The “rectangular

instrument blocks" are made of PVC and are equipped with miniature transducers that measure only the temperature and pressure (Omega EMQSS-062E-12 and PX180-015GV, respectively).

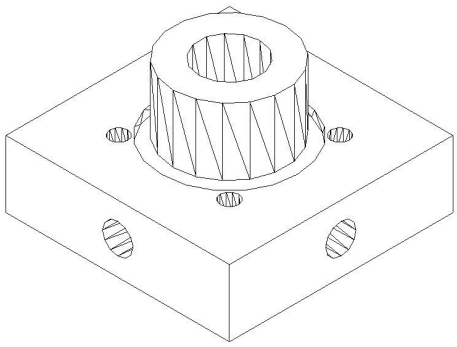

Figure 3.19 The rectangular test section inlet instrument block

3.1.6 Heated Test Sections

Five electrically-heated test sections have been used in this investigation, two of which have rectangular cross sections with prototypical Electra hibachi channel dimensions, while the other three are cylindrical. The test sections are electrically heated by a DC rectifier with 3 phase AC 60Hz input, and an output range of 0-18 V and 0-2500 A (Figure 3.20) manufactured by Rapid Power Technologies (#1198224).

Each test section is equipped with Chromel-constantan, 30-gauge, thermocouples (type E) attached to the heated wall along the flow direction to measure the outside surface wall temperature distribution. The thermocouples are electrically isolated from the ohmically-heated channel walls to eliminate measurement errors due to voltage gradient along the wall.

Figure 3.20 The DC rectifier - power supply

For most axial locations, multiple thermocouples (two for cylindrical test sections and four for rectangular test sections) are placed at diametrically-opposed locations in order to check azimuthal uniformity of the wall temperature. A large difference between the thermocouple readings at the same axial location indicates film rupture. Under these conditions, the temperature indicated by the thermocouple on the dry side quickly reaches or exceeds the saturation temperature; when such condition exists, the DC power supply is shut off. All thermocouples used in this study were individually calibrated, except for the self-adhesive thermocouples used to measure wall temperatures in the second rectangular, and second and third cylindrical test sections. Calibration of these thermocouples would damage their adhesive; fortunately, they are manufactured as high accuracy thermocouples with manufacturer-supplied calibrations. To minimize conduction error, the self-adhesive thermocouples lead wires are wound once around the test section before radially penetrating the insulation. The thermocouples used on the

other two test sections could not be wound due to their design. Detailed descriptions of the various test sections are given below.

3.1.6.a First Rectangular Test Section

The first rectangular test section is shown in Figures 3.21 and 3.22. It has two heated sides made of Hastelloy X strips, 0.25 mm thick (simulating the Electra hibachi foils), 40 mm wide, 622 mm long, and 20 mm apart, backed by 19 mm thick Teflon plates which serve as external insulation and provide the means to maintain a fixed geometry along the entrance channel length.

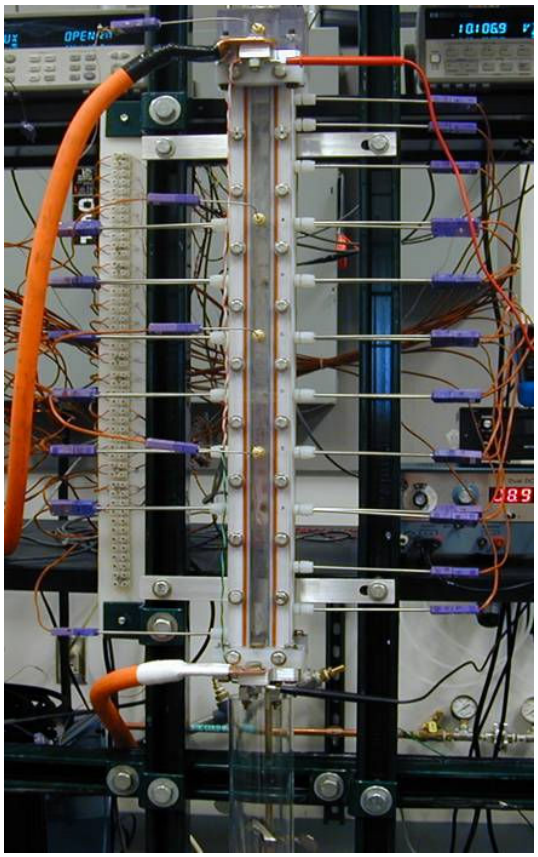

Figure 3.21 First rectangular test section with insulation removed

The other two sides of the channel are unheated and are made of transparent polycarbonate plates, 58.6 mm wide and 12.7 mm thick (simulating the hibachi ribs). The four walls produce a rectangular channel with a 40 mm x 20 mm cross section along the entire 622 mm length. Sealing is achieved by an O-ring placed between the Teflon and polycarbonate plates. The polycarbonate sides enable flow visualization within the heated test section. This is the only test section that has this feature.

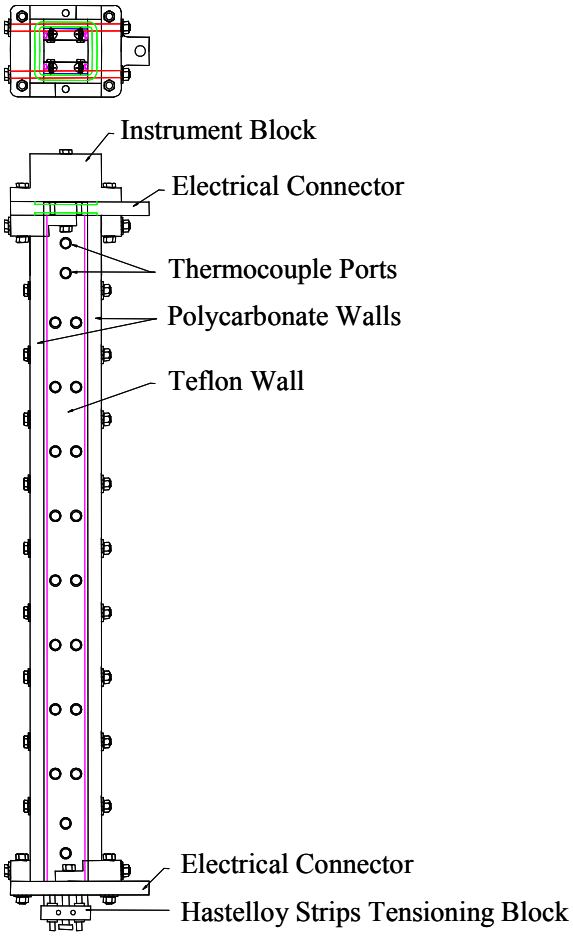

Figure 3.22 The first rectangular test section schematic

During the experiments, the test section is surrounded by additional insulation made of 28 mm thick rigid PVC foam. However, when the PVC foam insulation is in place, the flow visualization capability is lost. Thirty thermocouple probes (Omega EMQSS-125G-6) are used to measure the temperature distribution of the two heated walls. Four thermocouples are placed at each of six main cross sections along the middle part of the test section, two on each heated side symmetrically spaced, while only one wall thermocouple is placed at each of three different elevations at both ends of the test section placed at the center of the heated side. The first three instrumented locations are 25.4 mm, 52.7 mm, and 98.1 mm away from the test section inlet. The next six wall temperature measurement locations represent the main instrumented cross sections spaced 63.5 mm apart. At those six cross sections, in addition to the heated wall temperature probes, thermocouple probes (Omega EMQSS-062G-6) are inserted through the unheated polycarbonate walls to measure the centerline coolant temperature (i.e. centerline wet bulb temperature) of the gas/liquid mist. The last three instrumented wall temperature locations are placed 59.1 mm, 104.5 mm, and 131.8 mm further down from the last main instrumented cross section.

This test section design has two drawbacks, which prompted the development of an alternate test section design. First, the wall thermocouples are not permanently attached to the metal foil but are only pressed against it. Their tips are coated with a soft thermally conductive paste (Omega OB-200) to help provide better thermal contact. However, uncertainty regarding the effectiveness of such thermal contact made it difficult to accurately and repeatably measure the wall temperature. Second, to enhance contact between the probes and the heated wall, large probes (3.2 mm diameter) are used; these

probes proved to be too large to accurately measure the very thin hastelloy strips temperatures. These two problems, cause the heat transfer coefficients measured using this test section to be overestimated. Hence, an alternative test section design has been used.

3.1.6.b Second Rectangular Test Section

The second rectangular test section is made of a thin-walled 304 Stainless Steel channel; all four sides are ohmically heated by passing an electrical current through the channel walls. Figure 3.23 shows the second rectangular test section. The inner test section dimensions are 16.6 mm x 35.6 mm, while the wall thickness is 1.24 mm. This test section is 889 mm long and is insulated with 51 mm thick melamine foam. The outside wall temperatures are measured at eleven different cross sections along the flow direction, using 37 fast response self-adhesive thermocouples (Omega SA1-E). These thermocouples are especially designed for measuring temperature of thin walls, thus removing the problems mentioned for the first rectangular test section. In addition to the use of electrically nonconductive self-adhesive backing that these thermocouples have, they are also pressed against the outside wall surface, first with Teflon and then fiberglass tape, and finally with high temperature resistant tie wrap, thus providing a good thermal contact between the thermocouple beads and the metal walls. (This method is used whenever the self-adhesive thermocouples are used in this study.)

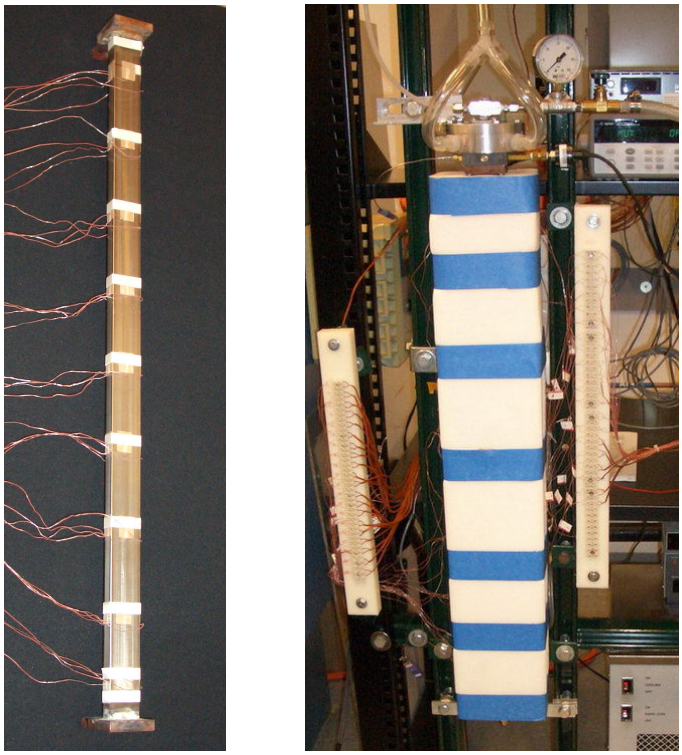

Figure 3.23 The second rectangular test section without the insulation (left), and including the insulation (right)

All thermocouples are attached along the centerline of each instrumented wall at a particular cross section. The first cross section is located 12.7 mm away from the test section entrance, and has only one thermocouple attached to one of the narrower channel walls. The second instrumented cross section is 38.1 mm further down and has four thermocouples measuring all four sides' temperatures. The next seven instrumented cross sections are 101.6 mm apart with four thermocouples at each elevation (one on each side). The tenth instrumented cross section is 76.2 mm further downstream; it has three thermocouples to measure the temperature of the two wider sides and one of the narrower sides. The last instrumented cross section is 25.4 mm lower and has only one thermocouple attached to one of the narrower sides.

3.1.6.c First Cylindrical Test Section

The first cylindrical test section (Figure 3.24) is made of a thin-walled Hastelloy C-276 tube with inner diameter of 16 mm, and length of 610 mm. Center-less grinding was used to reduce the tube wall thickness to 0.635 mm. This was necessary to increase the wall resistance thereby reducing the current required to achieve the desired maximum heat flux. It is insulated with a melamine foam pipe insulation, 25 mm thick, with a thin PVC jacket. Twenty thermocouples (Omega 5TC-TT-E-30-36) are cemented to the tube outer surface using a highly conductive paste (Omega OB-600). The wall temperatures are measured at thirteen different axial locations, 51 mm apart, starting with the first cross section, which is 51 mm below the test section entrance, two thermocouples are attached on the opposite sides of every other instrumented cross section; the rest of the cross sections have only one thermocouple. Close examination of this test section revealed a drawback. Due to machining tolerances, the tube's 0.635 mm thickness was not azimuthally uniform. Hence, ohmic heating causes one side of the tube to be hotter than the other. To eliminate this problem, two other cylindrical thermocouples has been constructed.

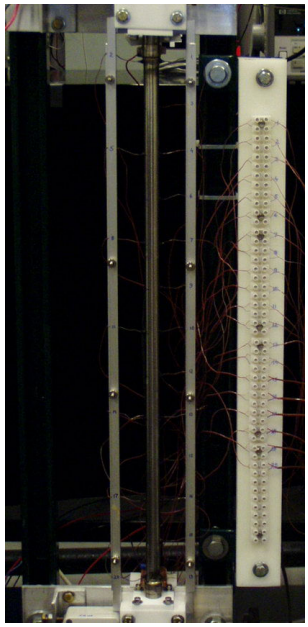

Figure 3.24 The uninsulated first cylindrical test section

3.1.6.d Second Cylindrical Test Section

The second cylindrical test section (Figure 3.25) is made of a thin-walled 316 Stainless Steel tube with inner diameter of 17.3 mm, and a length of 882 mm. The wall thickness is 0.889 mm with excellent azimuthal uniformity. The tube is insulated with a melamine foam pipe insulation, 38 mm thick, with a thin PVC jacket. The outside wall temperature is measured at twenty different axial locations using 37 fast response, self-adhesive, thermocouples (Omega SA1-E), which are further pressed against the pipe wall in the same manner previously described for the second rectangular test section. By doing so, excellent contact between the thermocouple beads and the tube wall is achieved. The first two and the last instrumented cross section have only one thermocouple measuring the wall temperature. Each of the other seventeen instrumented cross sections has two thermocouples positioned 180^{o} apart from each other. The first cross section is 38.1 mm

away from the test section entrance, while the next two are 25.4 mm apart further down further down. The third through eighteenth instrumented cross section are spaced 50.8 mm apart, while the nineteenth and twentieth cross sections are 38.1 mm and 25.4 mm further down, respectively.

Figure 3.25 The insulated second cylindrical test section

3.1.6.e Third Cylindrical Test Section

The third cylindrical test section is made of a thin-walled 316 Stainless Steel tube with inner diameter of 23.6 mm, and a length of 1052 mm. The wall thickness is 0.889 mm with excellent azimuthal uniformity. It is insulated with a melamine foam pipe insulation, 25 mm thick, with a thin PVC jacket. The outside wall temperature is measured at twenty different cross sections using 37 fast response thermocouples with

self-adhesive backing (Omega SA1-E), which are further pressed against the pipe wall as described earlier. The process of attaching the self-adhesive thermocouples and insulation is demonstrated in Figure 3.26.

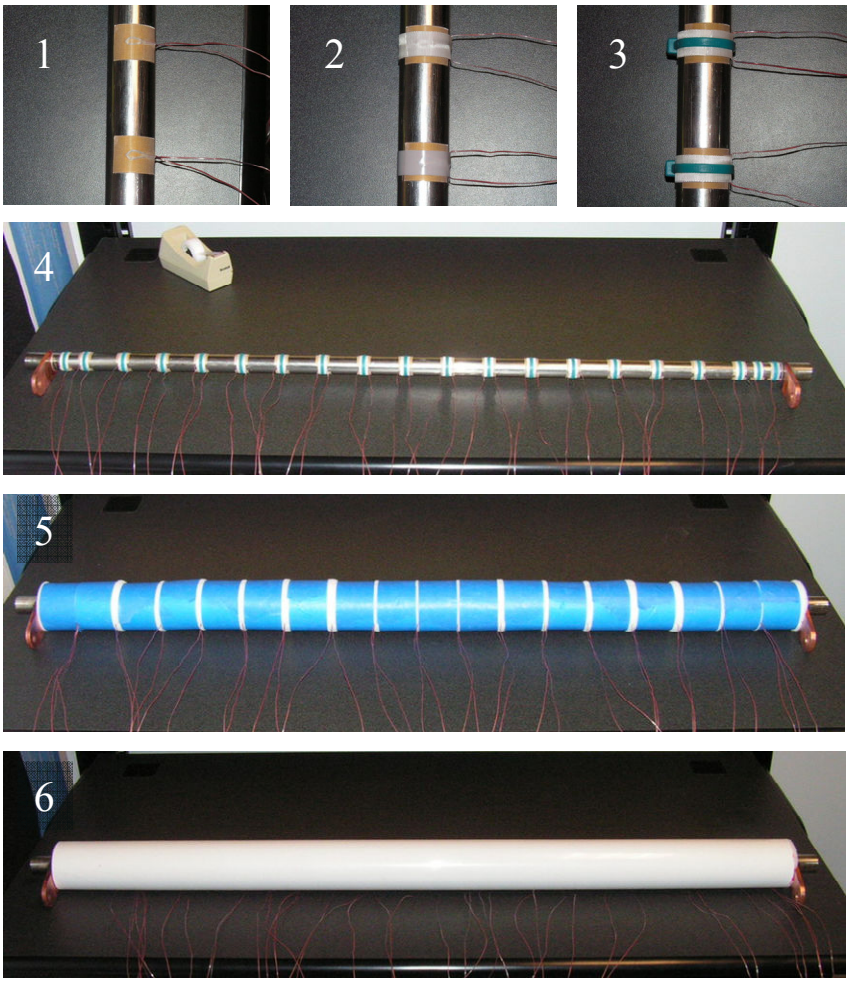

Figure 3.26 Attaching self-adhesive thermocouples and insulation

The first two and the last instrumented cross section have only one thermocouple measuring the wall temperature. Each of the other seventeen cross sections have two thermocouples each positioned 180^{o} apart from each other. The first instrumented cross

section is 12.7 mm away from the test section entrance, while the next two are 25.4 mm apart further down. The third through nineteenth instrumented cross section are spaced 58.4 mm apart, while the twentieth cross section is 22.9 mm further down.

All five test sections used in this study are significantly longer than the Electra hibachi structure. This allows the mist flow to reach fully-developed conditions. Additionally, the use of different unheated flow visualization pipe lengths, makes it possible to quantify the effects of entry conditions on local heat transfer.

3.1.7 Test Section Exit

A Teflon instrument block (instrument block # 3) is placed at the exit of each of the three cylindrical test sections exit. It is identical to Teflon instrument block # 2. It includes miniature transducers to measure the centerline wet bulb temperature (Omega EMQSS-062E-12), gage pressure (Omega PX180-015GV), and relative humidity (Honeywell HIH-3610-003) of the mist flow exiting the test section. The two rectangular test sections use an exit instrument block similar to their inlet instrument block. All experiments are run in a once-through mode with unrestricted discharge to the atmosphere, so that the pressure inside the test sections is essentially atmospheric. For the downward flow experiments with air as the carrier gas, the test section vents directly to the atmosphere. However, when helium is used as the carrier gas it is separated from the water in a sealed T-tube glass separator (Figure 3.27) from where it is ducted to a fume hood. For upward flow experiments, only air/water mist is used with cylindrical test sections. Water is separated from the air at the test section exit using the separator shown

in Figure 3.28. This separator allows the excess moisture to be removed without flooding the test section.

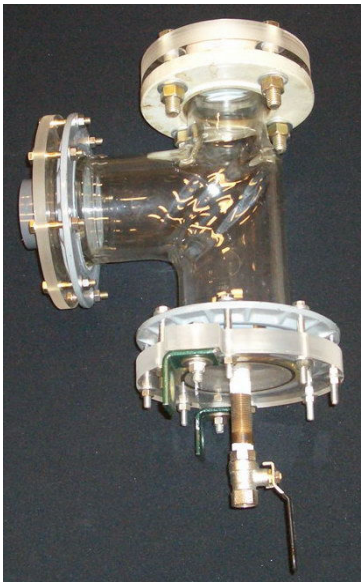

Figure 3.27 The Helium separator

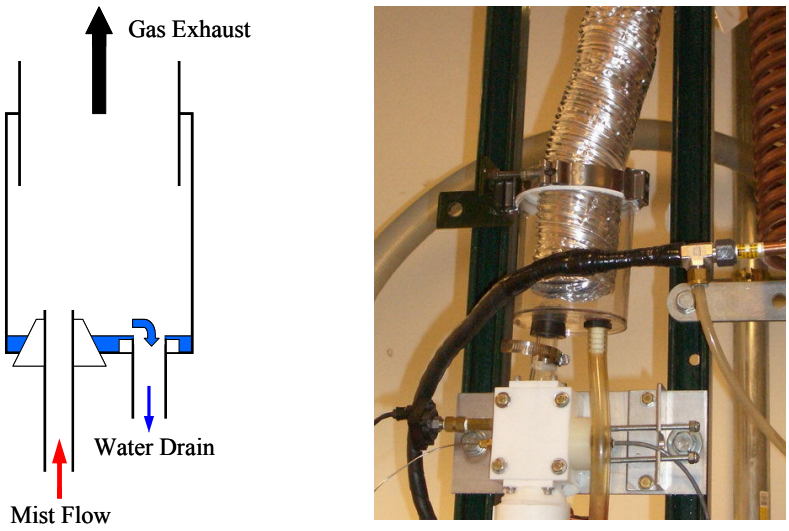

Figure 3.28 The water separator, a cross section drawing (left), photograph (right)

3.1.8 Data Acquisition System

The data acquisition system consists of a data acquisition unit, PC, their interconnection and various software that runs it. A 60-channel data acquisition unit (Agilent model #34970A with three, 20-channel each, A/D cards #34901A) shown in Figure 3.29 is used to monitor individual channels on its display for the entire duration of the experiments. More importantly, it is used to collect the data from transducers connected to all of the 60-channels. The Agilent data acquisition unit is connected to a PC. The communication between the unit and the PC is done through a RS-232 serial cable. Agilent BenchLink Data Logger software package is used to configure the unit and monitor the transient data on a PC display. After steady sate is reached, a Visual Basic code is used to once again configure the unit and control data acquisition. It also computes the time-average values of the various parameters and stores the data into an Excel sheet. Extensive post-processing of the data is done with the help of Engineering Equation Solver (EES) and Excel. Only steady state data are stored for each experiment; these data represent an average of 6 to 15 consecutive measurements collected over nearly 7 to 20 minutes.

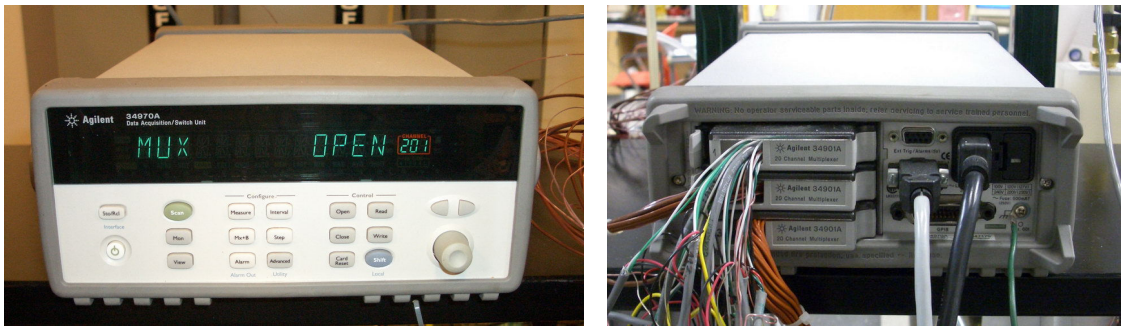

Figure 3.29 60-channel data acquisition unit, front side (left) and back side (right)

3.1.9 Power Input and Heat Losses

Since the outside wall surface temperature is measured, the inside surface temperature is calculated. A bulk gas temperature of the mist flow is calculated using an energy balance. The ambient heat loss and electrode conduction losses have been estimated and found to be relatively minor (1-2 %), as discussed in the data processing assumptions, so that nearly all the power input is removed by the flowing mist. The outside insulation surface temperature and room temperature used in estimating ambient heat loss are measured using 2 fast response self-adhesive thermocouples (Omega SA1-E). The power input is measured by measuring the effective voltage drop along the heated length of the test section and the effective current. As an additional check, the measured power input is compared to the product of the square of the effective current and the calculated test section resistance, corresponding to the measured wall temperature profile. Both power measurements essentially give the same measured power. Uniform heat flux is calculated by dividing the power input by the inner surface area of the heated portion of the test section. The effective voltage drop along the heated test section is measured directly using the Agilent data acquisition unit (model #34970A with A/D card #34901A). The effective current is measured using a 600 amps DC shunt (Deltec Company MKB-600-100) (Figure 3.30). Both the effective voltage drop and effective current are measured using a 4-wire method since the current running through the test section is half rectified AC current with nearly 360 Hz, as measured by an oscilloscope. The use of the DC shunt with close connectors (~ 2 cm apart) is appropriate since the current frequency is not higher than 360 Hz and the effective amperage is less than 600 A. This ensures that electromagnetic interference with the measured signal is

insignificant, as specified by the shunt manufacturer. The shunt is cooled with a fan to ensure negligible temperature variation.

Figure 3.30 The DC shunt and fan

3.1.10 Test Matrix

For all five test sections and three atomizing nozzles, experiments have been conducted with either air/water or helium/water mists using different gas velocities, inlet humidity, water inlet mass fractions (i.e. film thicknesses), water inlet temperatures, unheated entry section lengths and their wettability, and heat loads. The effects of inlet gas temperature and relative humidity were examined by comparing the results for experiments with widely different ambient (i.e. supply) temperatures, and with or without the humidifier, respectively (see Table 3.1). Both upward and downward flow experiments were performed using the three cylindrical test sections; only downward

flow experiments were conducted using the two rectangular test sections. For all experiments, only distilled water is used as a mist liquid.

Air/water tests have been performed with average inlet air velocities of approximately 5 m/s, 10 m/s, 15 m/s and 30 m/s, and water mass fractions of 5 %, 10 %, 15 %, 19 %, etc. The temperature of the water supplied to the nozzle, i.e. the water injection temperature, was varied; values of 2 ^{o}C, 22 ^{o}C, 55 ^{o}C and 95 ^{o}C have been used. Helium/water experiments have been performed with an average helium inlet velocity of 24 m/s and 30 m/s and water mass fractions of ~ 20 %, 40 % and 60 %; for the 30 m/s case these water injection rates nearly match those for the 15 m/s air/water tests (5 %, 10 %, and 15 %). A water injection temperature of 22 ^{o}C has been used for all helium/water experiments. Air/water experiments are run for both downward and upward flow, while only downward flow experiments are run for the helium/water case. Different unheated entry section lengths (3.8–75 cm) have been chosen to produce either thermally-developing flow or hydraulically-and-thermally developing flow inside the heated portion of the test section. For a given set of gas/liquid flow conditions, experiments have been conducted at different wall heat flux inputs (~ 0 to 51 kW/m^2) to quantify the effect of heat flux on the heat transfer coefficients. In all experiments, however, the wall temperature has been maintained below the saturation temperature to avoid local boiling, thus assuring that the heat transfer is driven by liquid film evaporation. A list of the test parameters used in this investigation is given in Table 3.1.

Table 3.1 List and ranges of operating and design parameters used in this investigation

Carrier Gas	Air Helium
Mist Liquid	Distilled water
Gas Velocity	Air: 5 m/s, 6 m/s, 10 m/s, 15 m/s, 30 m/s Helium: 24 m/s, 30m/s
Inlet Gas Temperature	Nearly 19 ^{o}C - 24 ^{o}C
Inlet Gas Relative Humidity	Nearly zero - 40 %
Water Fraction	Air: 5 %. 10 %, 15 %, 19 %, (up to 209 %) Helium: ~ 20 %, 40 %, 60 %
Water Injection Temperature	2 ^{o}C, 22 ^{o}C, 55 ^{o}C, 95 ^{o}C
Heat Flux	Nearly zero - 51 kW/m2
Flow Direction	Upward flow Downward flow
Nozzles	Gas-atomized nozzle Ultrasonic nozzle Fixed geometry nozzle
Droplet Size Distribution	30-55 μm droplet size optimization for the gas-atomized nozzle
Cylindrical Channels ID and Length Effects	16 mm ID – 610 mm long 17.3 mm ID – 882 mm long 23.6 mm ID – 1052 long
Rectangular Channels ID and Length Effects	20 mm x 40 mm – 622 mm long 16.6 mm x 35.6 mm – 889 mm long
Unheated Entry Length and Wettability	3.8 cm - 75 cm; acrylic, PVC, and glass

3.2 Experimental Procedure and Data Processing

The procedure of running the mist cooling experiments starts with configuring all 60 channels of the Agilent data acquisition unit by the Agilent BenchLink Data Logger installed on a PC. The configuration of a channel consists of defining a type of the signal to be measured, signal range, decimal accuracy and measurement duration. Figure 3.31 shows the configuration interface for the first 20-channel A/D Agilent card, while Figure 3.32 shows the configuration interfaces for the second and third 20-channel A/D Agilent cards used in this study. These two figures correspond to the third cylindrical test section and provide an overview of all 60 transducer signals which are electronically collected during an experiment.

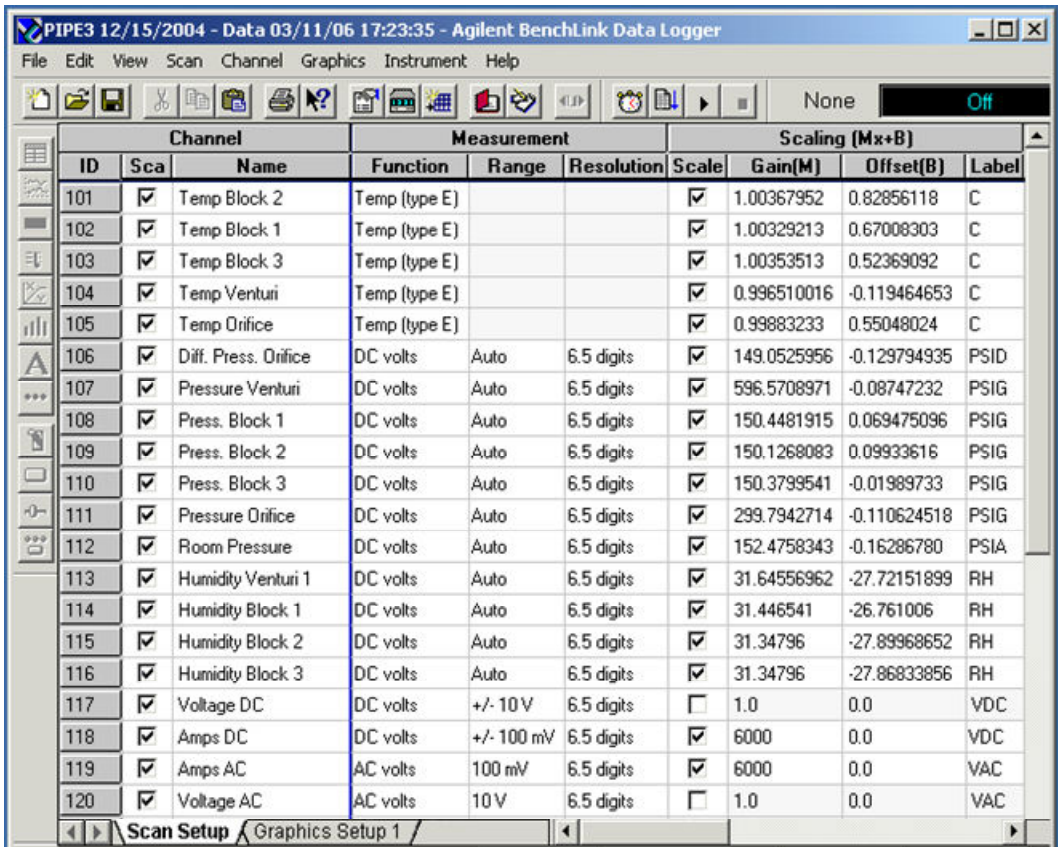

Figure 3.31 Configuration interface for the first 20-channel A/D Agilent card

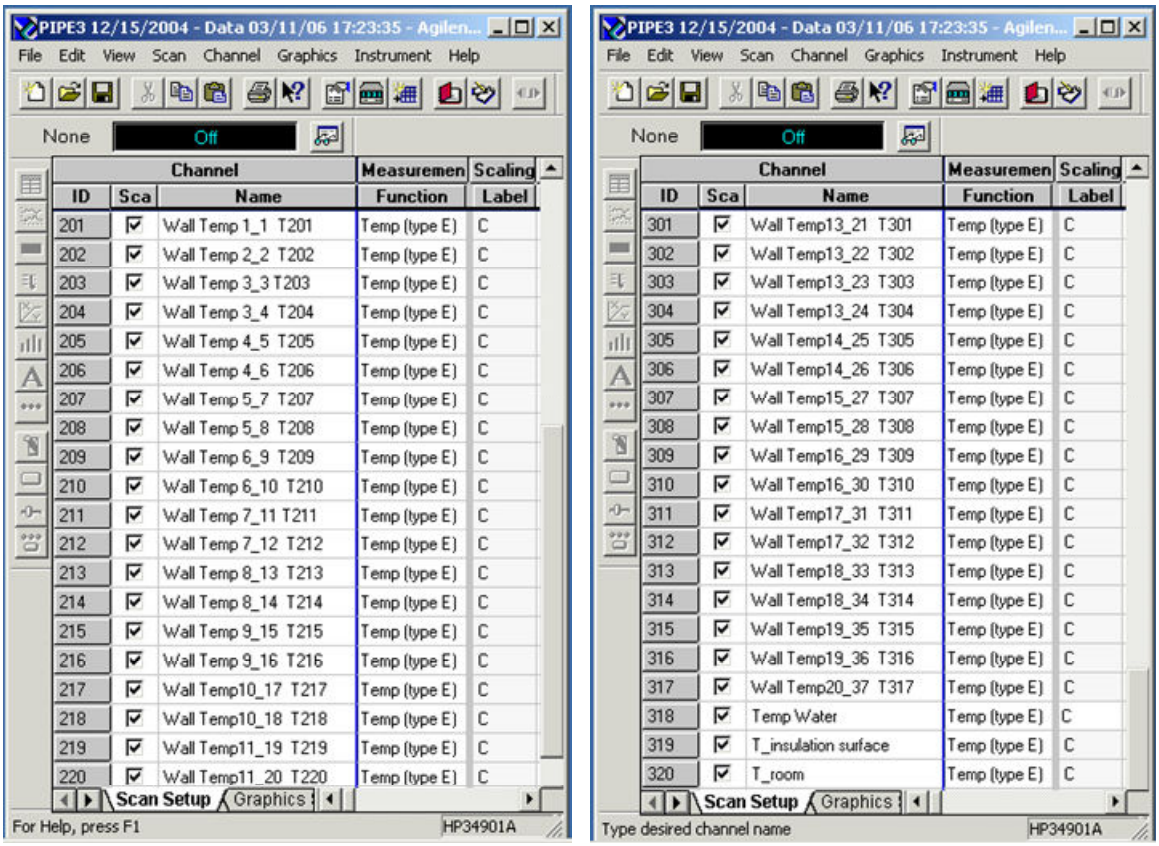

Figure 3.32 Configuration interface for the second (left) and third (right) 20-channel A/D Agilent cards

In general, the highest decimal accuracy is used, and the measurement duration is set to 2 Power Line Cycles (PLC). However, all pressure measurements and all three instrument blocks temperature measurements use 10 PLC measurement durations in order to average turbulence fluctuations. The power, current, and voltage measurements are set to 10 PLC for DC voltage signals and middle band (band 20) for AC voltage signals in order to average DC rectifier – power supply frequency (nearly 360 Hz as measured by an oscilloscope). Once the configuration is completed, the Agilent BenchLink Data Logger is used to calibrate and monitor the transient data in real time. Nearly all of the 60 channels are tabulated and for some of the more important ones, e.g. wall temperatures,

the time history is plotted. Figure 3.33 shows the Agilent BenchLink Data Logger monitoring interface.

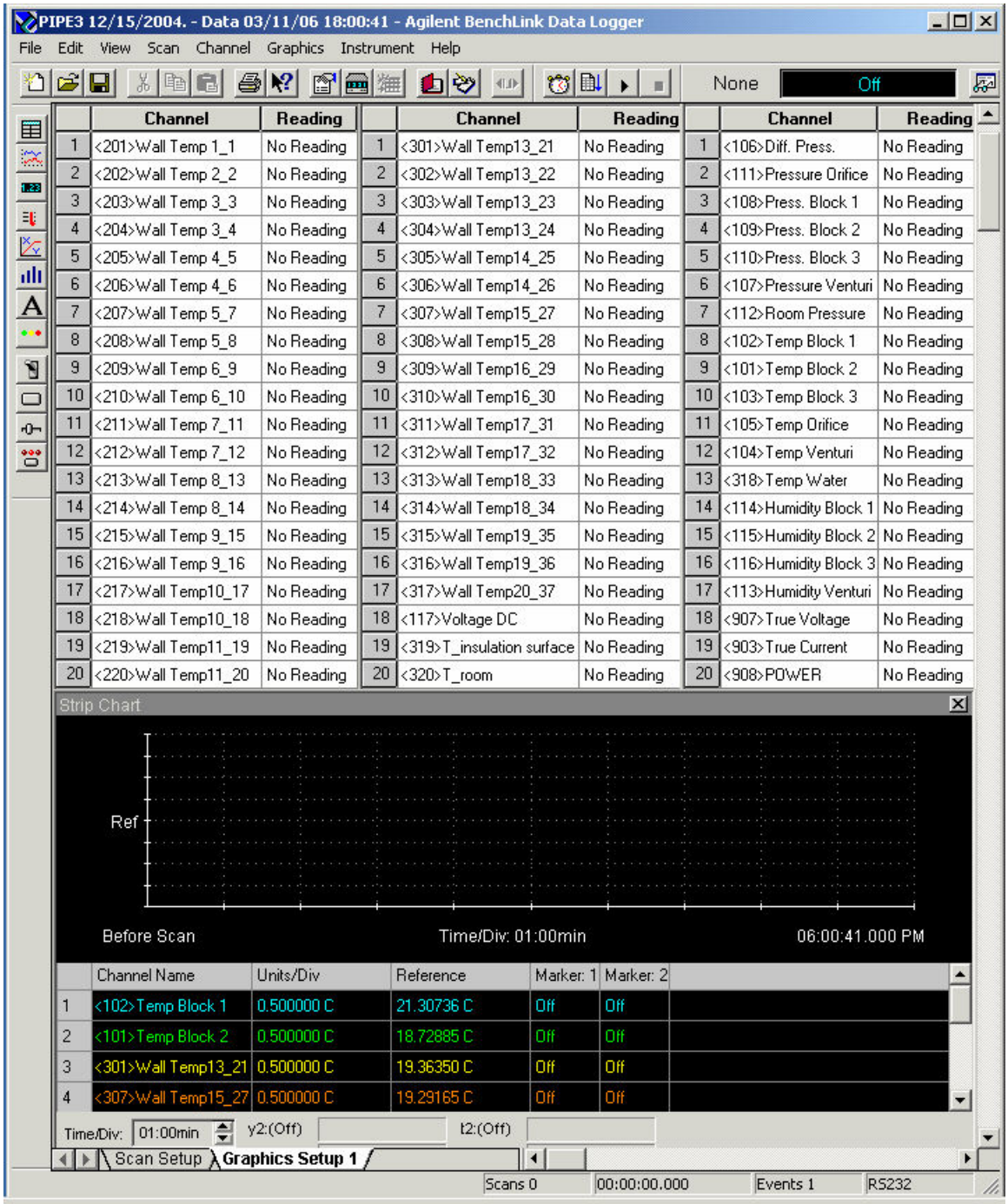

	Channel	Reading
1	<201>Wall Temp 1_1	No Reading
2	<202>Wall Temp 2_2	No Reading
3	<203>Wall Temp 3_3	No Reading
4	<204>Wall Temp 3_4	No Reading
5	<205>Wall Temp 4_5	No Reading
6	<206>Wall Temp 4_6	No Reading
7	<207>Wall Temp 5_7	No Reading
8	<208>Wall Temp 5_8	No Reading
9	<209>Wall Temp 6_9	No Reading
10	<210>Wall Temp 6_10	No Reading
11	<211>Wall Temp 7_11	No Reading
12	<212>Wall Temp 7_12	No Reading
13	<213>Wall Temp 8_13	No Reading
14	<214>Wall Temp 8_14	No Reading
15	<215>Wall Temp 9_15	No Reading
16	<216>Wall Temp 9_16	No Reading
17	<217>Wall Temp10_17	No Reading
18	<218>Wall Temp10_18	No Reading
19	<219>Wall Temp11_19	No Reading
20	<220>Wall Temp11_20	No Reading

	Channel	Reading
1	<301>Wall Temp13_21	No Reading
2	<302>Wall Temp13_22	No Reading
3	<303>Wall Temp13_23	No Reading
4	<304>Wall Temp13_24	No Reading
5	<305>Wall Temp14_25	No Reading
6	<306>Wall Temp14_26	No Reading
7	<307>Wall Temp15_27	No Reading
8	<308>Wall Temp15_28	No Reading
9	<309>Wall Temp16_29	No Reading
10	<310>Wall Temp16_30	No Reading
11	<311>Wall Temp17_31	No Reading
12	<312>Wall Temp17_32	No Reading
13	<313>Wall Temp18_33	No Reading
14	<314>Wall Temp18_34	No Reading
15	<315>Wall Temp19_35	No Reading
16	<316>Wall Temp19_36	No Reading
17	<317>Wall Temp20_37	No Reading
18	<117>Voltage DC	No Reading
19	<319>T_insulation surface	No Reading
20	<320>T_room	No Reading

	Channel	Reading
1	<106>Diff. Press.	No Reading
2	<111>Pressure Orifice	No Reading
3	<108>Press. Block 1	No Reading
4	<109>Press. Block 2	No Reading
5	<110>Press. Block 3	No Reading
6	<107>Pressure Venturi	No Reading
7	<112>Room Pressure	No Reading
8	<102>Temp Block 1	No Reading
9	<101>Temp Block 2	No Reading
10	<103>Temp Block 3	No Reading
11	<105>Temp Orifice	No Reading
12	<104>Temp Venturi	No Reading
13	<318>Temp Water	No Reading
14	<114>Humidity Block 1	No Reading
15	<115>Humidity Block 2	No Reading
16	<116>Humidity Block 3	No Reading
17	<113>Humidity Venturi	No Reading
18	<907>True Voltage	No Reading
19	<903>True Current	No Reading
20	<908>POWER	No Reading

	Channel Name	Units/Div	Reference	Marker: 1	Marker: 2
1	<102>Temp Block 1	0.500000 C	21.30736 C	Off	Off
2	<101>Temp Block 2	0.500000 C	18.72885 C	Off	Off
3	<301>Wall Temp13_21	0.500000 C	19.36350 C	Off	Off
4	<307>Wall Temp15_27	0.500000 C	19.29165 C	Off	Off

Figure 3.33 Agilent BenchLink Data Logger monitoring interface

The next step is to adjust the flow conditions to the desired values. The main carrier gas line, and, if used, the gas-assisted line, flow rates are adjusted. For the main line, this is done by first, setting the line gas pressure to the required pressure and then fine-tuning it with a needle valve (valve "*F*" in Figure 3.1) at the gas rotameter inlet. The gas rotameter is used for a visual indication of the flow rate. However, the precise value of the main line gas flow rate is calculated by an experimental data processing code in Engineering Equation Solver (EES), using the gage and differential pressures and the gas temperature measured at the orifice flowmeter, along with the relative humidity measured in instrument block # 1. The experimental data processing code written in Engineering Equation Solver will be discussed later. Depending on the desired gas relative humidity, the main gas line in this process is either configured to by-pass or include the humidifier. The gas-assisted line flow rate is adjusted by setting the line pressure to nearly 41-42 psi (for reference purposes) and then fine-tuning it to the desired atomization pressure with a needle valve located immediately upstream of the nozzle. The precise gas-assisted line gas flow rate is calculated by the same experimental data processing code in Engineering Equation Solver using the gage and differential pressures, gas temperature, and relative humidity measured at the Venturi flowmeter. After the desired gas flow rates are set, the water flow rate is adjusted using water rotameter. The desired water temperature is controlled by adjusting the set point for the constant temperature bath. At this point, the air and water are allowed to flow for a short time until the liquid film is established throughout the entire test section length. At that point, the DC rectifier – power supply is turned on. The power input, i.e. the test section heat flux, is adjusted manually by gradually increasing the supply current/voltage to the desired level. While this is being

done, the measured test section wall temperatures are closely monitored in order to prevent excessive heating due to potential film breakdown. Should that occur, the power is either turned off or maintained at the same level. In order to make this process easier, the wall temperatures are plotted and the power input is calculated by the Agilent BenchLink Data Logger in real time. The power input calculation is the only calculation done by the Agilent BenchLink Data Logger. Power is calculated using the 4-wire power measurements since the power supply – DC rectifier operates at nearly 360 Hz, as measured on an oscilloscope. Therefore, DC and AC voltage measurements are taken for both the electrical current from the power supply and the voltage drop across the test section length. The equation used for the 4-wire power measurements calculation is:

$$Power = \sqrt{ACvoltage^2 + DCvoltage^2} \cdot \sqrt{ACcurrent^2 + DCcurrent^2} \qquad (3.1)$$

Once the desired power input is set, the experiment is allowed to operate for several minutes until steady state conditions are reached. During that time, the wall temperatures are monitored. The criterion for steady state is that the average wall temperatures at all instrumented locations do not change by more than 0.25 ^{o}C within the last 2 minutes. This is determined by the Agilent BenchLink Data Logger. When steady state conditions are reached, the Agilent BenchLink Data Logger is closed and an Excel sheet with a Visual Basic Macro code (code is shown in Appendix A.1) is opened since only one of them can be connected to the Agilent data acquisition unit at a time. The Visual Basic code run from its Excel sheet is now used to configure (in the same manner as explained earlier) and control all of the 60 channels of the Agilent data acquisition

unit. While the Visual Basic code is running, the wall temperature monitoring is done on the Agilent data acquisition unit display only. The data acquisition procedure controlled by the Visual Basic code involves sequential scanning of all 60 channels which takes several seconds. The scanned data is then transferred to a PC and stored into its Excel sheet. As soon as this is done, the next sequential scan of the 60 channels is taken. The code repeats this cycle 6-15 times as specified in the code's configuration subroutine. The number of cycles used is determined by the wall temperature oscillations. If the liquid film is stable, fewer cycles are used. However, if dry patches are present, more cycles are repeated in order to obtain a good average reading. After the scanning is completed and all of the sequentially measured data are stored, the Visual Basic code time-averages the readings for each channel and redistributes them into a pre-designed table in the same Excel sheet.

Following the Visual Basic code processing, the pre-designed table calibrates the data, and if needed, converts them into their physical units. It also calculates the inside wall temperatures from the measured outside wall temperatures. The inside wall temperatures are calculated using a solution for one-dimensional steady state conduction with heat generation and an adiabatic boundary condition on one side. Since the test section walls are very thin compared to their radius, a one-dimensional solution in Cartesian coordinates is used:

$$T_{out} - T_{in} = q'''_w \cdot \frac{\delta^2}{2K} \tag{3.2}$$

Here, T_{out} and T_{in} are the outside and inside wall surfaces temperatures, respectively, q'''_w is the volumetric wall heat generation rate, δ is the wall thickness, and K is the wall thermal conductivity. The outer surface of the test section is assumed to be adiabatic,

which is a reasonable assumption as confirmed by an overall energy balance. The outside and inside wall surfaces temperature difference varied from less than 0.1 ^{o}C to nearly 2.2 ^{o}C in for the highest heat flux used in this study (51.1 kW/m^2). The calculated inside wall temperatures based on the two or four thermocouple readings at each axial location are averaged; the averaged values are used in the local heat transfer coefficient calculation. Depending on the specified number of cycles, the Visual Basic data acquisition process, along with initial processing in the Excel sheet, takes about 7-20 minutes to be completed.

An example of an Excel sheet with pre-designed table and 60-channel 8-cycle run for the 23.6 mm ID circular test section (PIPE 3) is presented in Figure 3.34 (not all 60 channel 8-cycles are shown in the figure). It is noted that the Venturi differential pressure and water rotameter readings (typed in red) are not electronically recorded. Instead, they are manually recorded. However, these variables are generally very stable and are continuously monitored; therefore, their manual readings are treated as averaged readings. It is also noted that for the test run shown in Figure 3.34, the difference between the outside and inside wall temperature is only 0.38 ^{o}C (see channel <Temp 211> 7_11) even thou the heat flux is 8.89 kW/m^2, which is considered to be near the film breakdown range for this test run. It is also interesting to note that the thermocouple readings at the diametrically opposed locations indicate higher wall temperatures on one side of the channel along the first half of the heated length; this suggests a nozzle misalignment effect, which is discussed in Chapter IV.

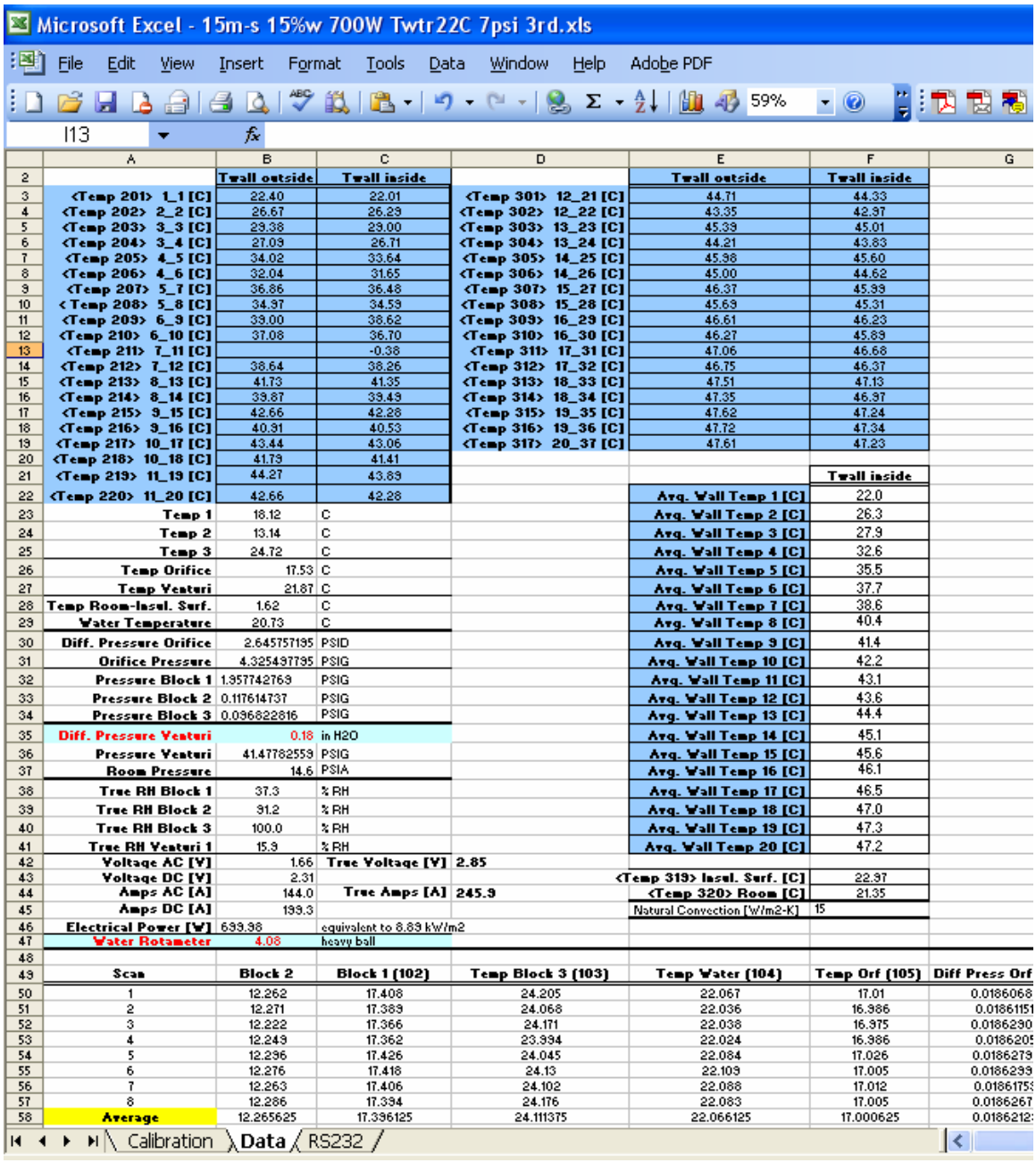

Microsoft Excel - 15m-s 15%w 700W Twtr22C 7psi 3rd.xls

File Edit View Insert Format Tools Data Window Help Adobe PDF

59%

I13

	A	B	C	D	E	F	G
2		Twall outside	Twall inside		Twall outside	Twall inside	
3	<Temp 201> 1_1 [C]	22.40	22.01	<Temp 301> 12_21 [C]	44.71	44.33	
4	<Temp 202> 2_2 [C]	26.67	26.29	<Temp 302> 12_22 [C]	43.35	42.97	
5	<Temp 203> 3_3 [C]	29.38	29.00	<Temp 303> 13_23 [C]	45.39	45.01	
6	<Temp 204> 3_4 [C]	27.09	26.71	<Temp 304> 13_24 [C]	44.21	43.83	
7	<Temp 205> 4_5 [C]	34.02	33.64	<Temp 305> 14_25 [C]	45.98	45.60	
8	<Temp 206> 4_6 [C]	32.04	31.65	<Temp 306> 14_26 [C]	45.00	44.62	
9	<Temp 207> 5_7 [C]	36.86	36.48	<Temp 307> 15_27 [C]	46.37	45.99	
10	< Temp 208> 5_8 [C]	34.37	34.59	<Temp 308> 15_28 [C]	45.69	45.31	
11	<Temp 209> 6_9 [C]	39.00	38.62	<Temp 309> 16_29 [C]	46.61	46.23	
12	<Temp 210> 6_10 [C]	37.08	36.70	<Temp 310> 16_30 [C]	46.27	45.89	
13	<Temp 211> 7_11 [C]		-0.38	<Temp 311> 17_31 [C]	47.06	46.68	
14	<Temp 212> 7_12 [C]	38.64	38.26	<Temp 312> 17_32 [C]	46.75	46.37	
15	<Temp 213> 8_13 [C]	41.73	41.35	<Temp 313> 18_33 [C]	47.51	47.13	
16	<Temp 214> 8_14 [C]	39.87	39.49	<Temp 314> 18_34 [C]	47.35	46.97	
17	<Temp 215> 9_15 [C]	42.66	42.28	<Temp 315> 19_35 [C]	47.62	47.24	
18	<Temp 216> 9_16 [C]	40.31	40.53	<Temp 316> 19_36 [C]	47.72	47.34	
19	<Temp 217> 10_17 [C]	43.44	43.06	<Temp 317> 20_37 [C]	47.61	47.23	
20	<Temp 218> 10_18 [C]	41.79	41.41				
21	<Temp 219> 11_19 [C]	44.27	43.89			Twall inside	
22	<Temp 220> 11_20 [C]	42.66	42.28		Avg. Wall Temp 1 [C]	22.0	
23	Temp 1	18.12	C		Avg. Wall Temp 2 [C]	26.3	
24	Temp 2	13.14	C		Avg. Wall Temp 3 [C]	27.9	
25	Temp 3	24.72	C		Avg. Wall Temp 4 [C]	32.6	
26	Temp Orifice	17.53	C		Avg. Wall Temp 5 [C]	35.5	
27	Temp Venturi	21.87	C		Avg. Wall Temp 6 [C]	37.7	
28	Temp Room-Insul. Surf.	1.62	C		Avg. Wall Temp 7 [C]	38.6	
29	Water Temperature	20.73	C		Avg. Wall Temp 8 [C]	40.4	
30	Diff. Pressure Orifice	2.645757195	PSID		Avg. Wall Temp 9 [C]	41.4	
31	Orifice Pressure	4.325497795	PSIG		Avg. Wall Temp 10 [C]	42.2	
32	Pressure Block 1	1.957742769	PSIG		Avg. Wall Temp 11 [C]	43.1	
33	Pressure Block 2	0.117614737	PSIG		Avg. Wall Temp 12 [C]	43.6	
34	Pressure Block 3	0.036822816	PSIG		Avg. Wall Temp 13 [C]	44.4	
35	Diff. Pressure Venturi	0.18	in H2O		Avg. Wall Temp 14 [C]	45.1	
36	Pressure Venturi	41.47782559	PSIG		Avg. Wall Temp 15 [C]	45.6	
37	Room Pressure	14.6	PSIA		Avg. Wall Temp 16 [C]	46.1	
38	True RH Block 1	37.3	% RH		Avg. Wall Temp 17 [C]	46.5	
39	True RH Block 2	31.2	% RH		Avg. Wall Temp 18 [C]	47.0	
40	True RH Block 3	100.0	% RH		Avg. Wall Temp 19 [C]	47.3	
41	True RH Venturi 1	15.9	% RH		Avg. Wall Temp 20 [C]	47.2	
42	Voltage AC [V]	1.66	True Voltage [V]	2.85			
43	Voltage DC [V]	2.31			<Temp 319> Insul. Surf. [C]	22.97	
44	Amps AC [A]	144.0	True Amps [A]	245.9	<Temp 320> Room [C]	21.35	
45	Amps DC [A]	193.3			Natural Convection [W/m2-K]	15	
46	Electrical Power [W]	633.36	equivalent to 8.83 kW/m2				
47	Water Rotameter	4.08	heavy ball				
48							
49	Scan	Block 2	Block 1 (102)	Temp Block 3 (103)	Temp Water (104)	Temp Orf (105)	Diff Press Orf
50	1	12.262	17.408	24.205	22.067	17.01	0.0186068
51	2	12.271	17.389	24.068	22.036	16.986	0.01861151
52	3	12.222	17.366	24.171	22.038	16.975	0.0186230
53	4	12.249	17.362	23.994	22.024	16.986	0.0186205
54	5	12.296	17.426	24.045	22.084	17.026	0.0186279
55	6	12.276	17.418	24.13	22.103	17.005	0.0186239
56	7	12.263	17.406	24.102	22.088	17.012	0.0186175
57	8	12.286	17.394	24.176	22.083	17.005	0.0186267
58	Average	12.265625	17.396125	24.111375	22.066125	17.000625	0.0186212

Calibration | Data | RS232

Figure 3.34 Excel sheet with pre-designed table and 60-channel 8-cycle run data for an experiment using the 23.6 mm ID circular test section (PIPE 3), featuring a Visual Basic Macro data acquisition code

Following calculation of the average steady state inside wall temperatures, the Excel sheet with the Visual Basic Macro code is saved and closed, and the Agilent BenchLink Data Logger reopened again; the entire data acquisition procedure is then repeated for

another set of variables, e.g. a different heat flux, gas velocity, water mass fraction, etc. However, in general, only one parameter is varied at a time in order to isolate its effect. The original experimental, averaged, electronically and visually recorded data saved in the Excel sheet are later processed by an experimental data processing code in Engineering Equation Solver. The most important variables calculated by the Engineering Equation Solver code, namely the bulk gas temperature distribution along the channel and the heating power (i.e. electrical power reduced by heat losses), are then copied together with the averaged inside wall temperatures to a master processing Excel sheet for the entire test section, where the final data processing, including calculation of the uniform wall heat flux and local heat transfer coefficients, are done. Figure 3.35 shows a small window of a master processing Excel sheet. In the master processing Excel sheet, the local heat transfer coefficients are plotted, along with the inside wall and bulk gas temperatures; they are also compared with values from previously-completed experiments. These plots are shown and discussed in Chapter IV.

The local heat transfer coefficient h is calculated using the relation:

$$h = \frac{q_w}{\left(T_w - T_b\right)} \tag{3.3}$$

where q_w is the uniform wall heat flux based on the inside surface area, T_w is the local value of the average inside surface temperature, and T_b is the calculated bulk temperature of the gas at the same axial location.

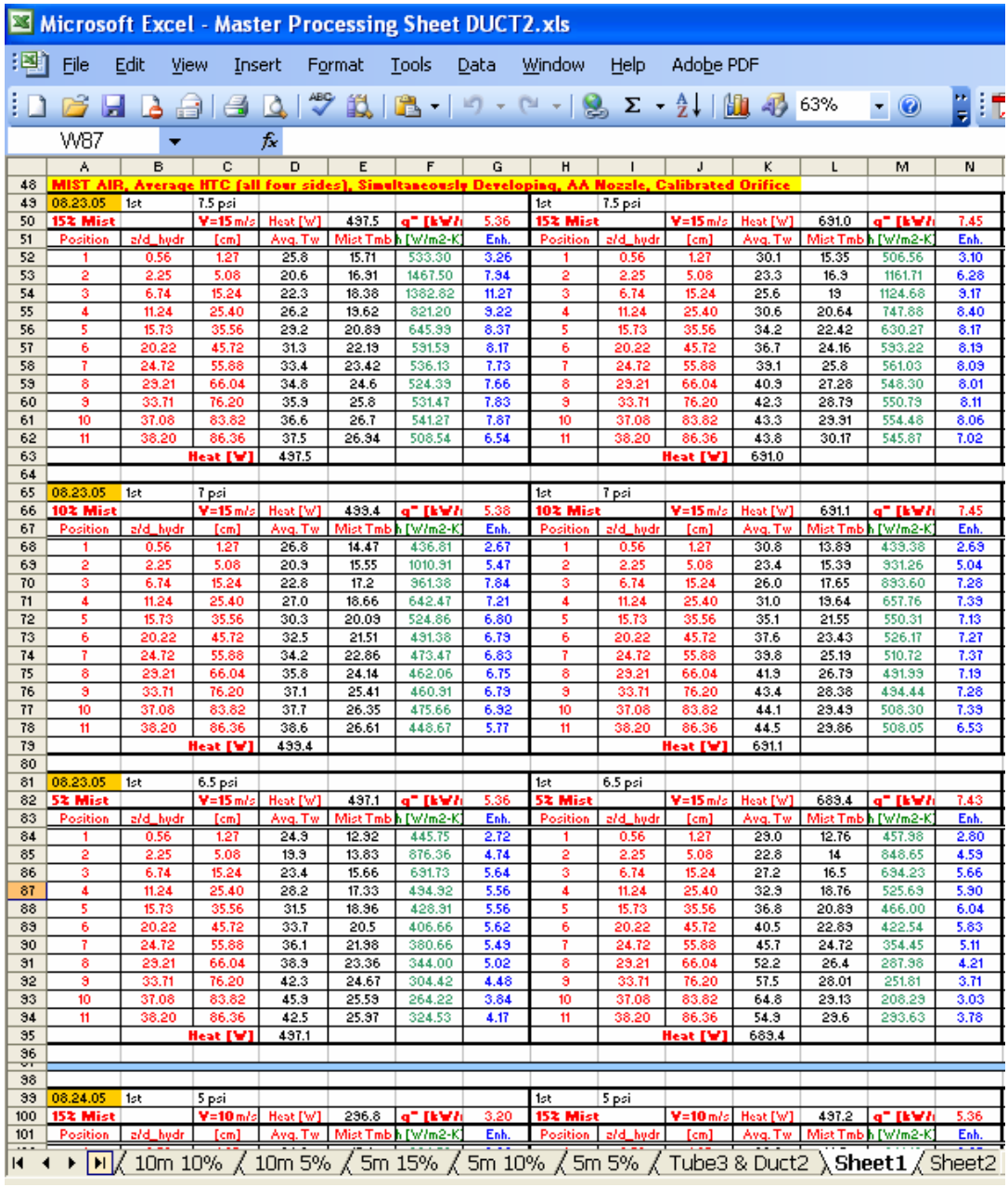

Microsoft Excel - Master Processing Sheet DUCT2.xls

File Edit View Insert Format Tools Data Window Help Adobe PDF

W87

	A	B	C	D	E	F	G	H	I	J	K	L	M	N
48	MIST AIR, Average HTC (all four sides), Simultaneously Developing, AA Nozzle, Calibrated Orifice													
49	08.23.05	1st	7.5 psi					1st	7.5 psi					
50	15% Mist		V=15 m/s	Heat [W]	497.5	q" [kW/	5.36	15% Mist		V=15 m/s	Heat [W]	691.0	q" [kW/	7.45
51	Position	z/d_hydr	[cm]	Avg. Tw	Mist Tmb	h [W/m2-K]	Enh.	Position	z/d_hydr	[cm]	Avg. Tw	Mist Tmb	h [W/m2-K]	Enh.
52	1	0.56	1.27	25.8	15.71	533.30	3.26	1	0.56	1.27	30.1	15.35	506.56	3.10
53	2	2.25	5.08	20.6	16.31	1467.50	7.34	2	2.25	5.08	23.3	16.9	1161.71	6.28
54	3	6.74	15.24	22.3	18.38	1382.82	11.27	3	6.74	15.24	25.6	19	1124.68	9.17
55	4	11.24	25.40	26.2	19.62	821.20	9.22	4	11.24	25.40	30.6	20.64	747.88	8.40
56	5	15.73	35.56	29.2	20.89	645.99	8.37	5	15.73	35.56	34.2	22.42	630.27	8.17
57	6	20.22	45.72	31.3	22.19	591.59	8.17	6	20.22	45.72	36.7	24.16	593.22	8.19
58	7	24.72	55.88	33.4	23.42	536.13	7.73	7	24.72	55.88	39.1	25.8	561.03	8.09
59	8	29.21	66.04	34.8	24.6	524.39	7.66	8	29.21	66.04	40.9	27.28	548.30	8.01
60	9	33.71	76.20	35.9	25.8	531.47	7.83	9	33.71	76.20	42.3	28.79	550.79	8.11
61	10	37.08	83.82	36.6	26.7	541.27	7.87	10	37.08	83.82	43.3	29.91	554.48	8.06
62	11	38.20	86.36	37.5	26.94	508.54	6.54	11	38.20	86.36	43.8	30.17	545.87	7.02
63			Heat [W]	497.5						Heat [W]	691.0			
64														
65	08.23.05	1st	7 psi					1st	7 psi					
66	10% Mist		V=15 m/s	Heat [W]	493.4	q" [kW/	5.38	10% Mist		V=15 m/s	Heat [W]	691.1	q" [kW/	7.45
67	Position	z/d_hydr	[cm]	Avg. Tw	Mist Tmb	h [W/m2-K]	Enh.	Position	z/d_hydr	[cm]	Avg. Tw	Mist Tmb	h [W/m2-K]	Enh.
68	1	0.56	1.27	26.8	14.47	436.81	2.67	1	0.56	1.27	30.8	13.89	439.38	2.69
69	2	2.25	5.08	20.9	15.55	1010.91	5.47	2	2.25	5.08	23.4	15.39	931.26	5.04
70	3	6.74	15.24	22.8	17.2	961.38	7.84	3	6.74	15.24	26.0	17.65	893.60	7.28
71	4	11.24	25.40	27.0	18.66	642.47	7.21	4	11.24	25.40	31.0	19.64	657.76	7.39
72	5	15.73	35.56	30.3	20.09	524.86	6.80	5	15.73	35.56	35.1	21.55	550.31	7.13
73	6	20.22	45.72	32.5	21.51	491.38	6.79	6	20.22	45.72	37.6	23.43	526.17	7.27
74	7	24.72	55.88	34.2	22.86	473.47	6.83	7	24.72	55.88	39.8	25.19	510.72	7.37
75	8	29.21	66.04	35.8	24.14	462.06	6.75	8	29.21	66.04	41.9	26.73	491.99	7.19
76	9	33.71	76.20	37.1	25.41	460.91	6.79	9	33.71	76.20	43.4	28.38	494.44	7.28
77	10	37.08	83.82	37.7	26.35	475.66	6.92	10	37.08	83.82	44.1	29.49	508.30	7.39
78	11	38.20	86.36	38.6	26.61	448.67	5.77	11	38.20	86.36	44.5	29.86	508.05	6.53
79			Heat [W]	493.4						Heat [W]	691.1			
80														
81	08.23.05	1st	6.5 psi					1st	6.5 psi					
82	5% Mist		V=15 m/s	Heat [W]	497.1	q" [kW/	5.36	5% Mist		V=15 m/s	Heat [W]	689.4	q" [kW/	7.43
83	Position	z/d_hydr	[cm]	Avg. Tw	Mist Tmb	h [W/m2-K]	Enh.	Position	z/d_hydr	[cm]	Avg. Tw	Mist Tmb	h [W/m2-K]	Enh.
84	1	0.56	1.27	24.9	12.92	445.75	2.72	1	0.56	1.27	29.0	12.76	457.98	2.80
85	2	2.25	5.08	19.9	13.83	876.36	4.74	2	2.25	5.08	22.8	14	848.65	4.59
86	3	6.74	15.24	23.4	15.66	691.73	5.64	3	6.74	15.24	27.2	16.5	694.23	5.66
87	4	11.24	25.40	28.2	17.33	494.92	5.56	4	11.24	25.40	32.9	18.76	525.69	5.90
88	5	15.73	35.56	31.5	18.96	428.91	5.56	5	15.73	35.56	36.8	20.89	466.00	6.04
89	6	20.22	45.72	33.7	20.5	406.66	5.62	6	20.22	45.72	40.5	22.89	422.54	5.83
90	7	24.72	55.88	36.1	21.98	380.66	5.49	7	24.72	55.88	45.7	24.72	354.45	5.11
91	8	29.21	66.04	38.9	23.36	344.00	5.02	8	29.21	66.04	52.2	26.4	287.38	4.21
92	9	33.71	76.20	42.3	24.67	304.42	4.48	9	33.71	76.20	57.5	28.01	251.81	3.71
93	10	37.08	83.82	45.9	25.59	264.22	3.84	10	37.08	83.82	64.8	29.13	208.29	3.03
94	11	38.20	86.36	42.5	25.97	324.53	4.17	11	38.20	86.36	54.9	29.6	293.63	3.78
95			Heat [W]	497.1						Heat [W]	689.4			
96														
98														
99	08.24.05	1st	5 psi					1st	5 psi					
100	15% Mist		V=10 m/s	Heat [W]	296.8	q" [kW/	3.20	15% Mist		V=10 m/s	Heat [W]	497.2	q" [kW/	5.36
101	Position	z/d_hydr	[cm]	Avg. Tw	Mist Tmb	h [W/m2-K]	Enh.	Position	z/d_hydr	[cm]	Avg. Tw	Mist Tmb	h [W/m2-K]	Enh.

10m 10% | 10m 5% | 5m 15% | 5m 10% | 5m 5% | Tube3 & Duct2 | Sheet1 | Sheet2

Figure 3.35 Master processing Excel sheet

3.2.1 Experimental Data Processing Code

Most of the experimental data processing is done by the experimental data processing code written in Engineering Equation Solver. Some additional, less extensive, processing, along with plotting, is done in Excel as already discussed.

There are several versions of the experimental data processing code; the main version has been used to process the mist cooling experimental data. A copy of the code is included in Appendix A.2, along with an example of the calculated results. Other data processing codes that address particular cases or tasks are briefly discussed here as well, and are also included in Appendices A.3-A.5.

The main version of the experimental data processing code is used to determine the thermodynamic state at each experimental measurement location, the gas and water flow rates, and the heating power. The input into the code include all of the averaged electronically and visually recorded data saved in a corresponding Visual Basic code Excel sheet (i.e. various pressure/pressure drop readings, flow and inside wall temperatures, humidities, electrical power, and water rotameter reading). The code first calculates various gas and water flow rates, namely, the gas flow rates through the Venturi (if the gas-assisted nozzle is used) and orifice flowmeters, and the water flow rate through the water rotameter. The equations used in to calculate the gas flow rates from the Venturi and orifice flowmeters raw data are given by Miller (1996). The thermodynamic states and velocities at instrument blocks # 1 and # 2 are then calculated. Heat losses to the room by the natural convection are estimated using the measured values of room temperature and the temperature of the outer surface of the insulation at the mid-point elevation of the test section. The natural convection heat losses, together

with losses to the electrical connections at the both ends of the test section, are subtracted from the measured electrical power to determine the actual heating power. The calculated heating power is used to determine the surface heat flux in the master processing Excel sheet assuming it to be uniform along the entire heated length; it is also used in the energy equation to calculate the bulk gas temperature distribution. For the each axial location where the test section wall temperature is measured, a bulk gas temperature is calculated using a control volume energy equation. The control volume inlet is taken to be at the instrument block # 2 where, the mist temperature, relative humidity and pressure are measured. The control volume exit is placed at the specific axial location where the wall temperature is measured. The other control volume boundary is at the test section wall, across which the uniform heat flux is transferred into the control volume. The assumptions made in calculating the energy balance, and in general, are discussed later (see section 3.2.2). The calculated bulk gas temperatures, inside wall temperatures, and uniform heating power are later used in the master processing Excel sheet to calculate the local heat transfer coefficients as already discussed. The code also calculates the mass fractions of oxygen, nitrogen, and water vapor, which are used as inputs for the numerical simulation performed using the modified KIVA-3V code.

Other versions of the experimental data processing code include those for air single-phase forced convection experiments, alternate heating power calculation method, and helium gas/water mist cooling and single-phase convection. There are two versions of the code for air single-phase convection. They both follow the same procedure as the main mist cooling version, however the water flow rate through the water rotameter is set to zero. In addition, they calculate the single-phase heat transfer coefficient in the fully

developed region using the Dittus-Boelter and Gnielinski correlations [Kakac, Shah and Aung (1987)], and local heat transfer coefficients along the test section length. The only difference between the two code versions is that one uses a correlation proposed by Reynolds, Swearingen and McEligot (1969), while the other uses a theoretical turbulent Graetz problem solution by Notter and Sleicher (1972). These two processing code versions are included in Appendices A.3 and A.4, respectively. A version of the processing code which is used to check the accuracy of the power and the heat flux measurements, is essentially the same as the main version, except for the control volume energy balance calculations. Instead of calculating the total heating power by multiplying the effective current and voltage drop along the test section length, the local heating rate (power input per unit length) is calculated by multiplying the square of the effective current by the appropriate test section resistance evaluated at the local wall temperature. In the first method which is used in the main processing code version the average heat flux is calculated while in the second method the local heat flux is calculated. This second method code version is included in Appendix A.5. The helium gas processing code versions are essentially identical to the air gas versions, except that they use the helium properties provided by the Engineering Equation Solver.

3.2.2 Data Processing Assumptions

Several assumptions have been made in processing the experimental data. First, it is assumed that the gas in the mist flow is fully saturated (i.e. 100 % RH) as soon as it reaches the heated portion of the test section and that it remains to be fully saturated as it is heated while flowing along the entire heated channel length. This assumption is

believed to be appropriate due to presence of liquid droplets in the core together with the heat flux from the electrically heated channel walls which results in significant evaporation at the film/carrier gas interface. This assumption is verified by the fact that the Teflon Instrument block # 3 (exit instrument block), located downstream of the heated test section always measures 100 % relative humidity. The Teflon instrument block # 2 (inlet instrument block), located upstream of the heated test section portion often reads 100 % relative humidity as well. However, depending on the injected water mass fraction, gas flow rate, nozzle used and droplets size distribution it could measure nearly as low as 55 %, e.g. in the fixed geometry hydraulic nozzle case. In general, a lower relative humidity is present at the heated test section inlet when lower water fractions and gas flow rates, are used, along with larger droplet sizes.

The second assumption is that the relative humidify, inside the inlet instrument block of the second rectangular test section is 100 %. This assumption is necessary since the inlet relative humidity for that test section was not measured. It is believed to be reasonable since only the gas-atomized nozzle with optimal droplet size, and high gas and water flow rates are used for the second rectangular test section, DUCT 2. In addition, for single-phase convection it is assumed that the relative humidity inside the inlet instrument block of the same test section is nearly zero. Data for the first rectangular test section, DUCT 1, are not presented because of uncertainties in the measured wall temperatures (see section 3.1.6.a).

The third assumption is that the average water film temperature at each axial location is an average of the local inside wall temperature and the gas bulk temperature at that location. This assumption is supported by the fact that the water film interface with

the wall has the same temperature as the wall, and the water film interface with the misty gas core is at the saturated temperature of the gas (i.e. gas bulk temperature) since its assumed relative humidity is 100 %. Water droplets inside of the gas core are assumed to have the same temperature as the saturated gas (i.e. gas bulk temperature). The only location where this water temperature assumption is not used is at the instrument block # 2 where the temperature of all the water is equal to the wet bulb temperature measured at that location.

The fourth assumption is that the pressure drop along the test section is linear since the pressure difference between pressure transducers readings at the inlet and exit instruments blocks is negligible; the pressure along the test section is nearly atmospheric for all experiments performed in this study. Even if the pressure were assumed to be constant and equal to the atmospheric pressure along the entire length, it would not make a significant difference in the experimental results.

The fifth assumption is that natural convection heat transfer coefficient on the outside of the insulated test section is 15 W/m^2K, and that losses to the electrical connectors at both end of the test section are 0.2 % of the total power input; the assumed value for the natural convection heat transfer coefficient is based on estimates made using the correlation given by Churchill and Chu [Incropera and DeWitt (1996)]. Heat loses to the electrical connectors were estimated using observed axial temperature gradients near the test section ends.

CHAPTER IV

EXPERIMENTAL RESULTS AND DISCUSSIONS

In this chapter, the experimental data obtained in this investigation are presented and discussed. An extensive test matrix has been used. Five different test sections and three atomization nozzle designs have been tested. Experiments have been conducted with either air/water or helium/water mists over wide ranges of operating parameters including the flow orientation, carrier gas velocities, injected water mass fraction, surface heat flux, carrier gas inlet temperature and humidity, injected water temperature, channel geometry and length, and unheated entry length and surface wettability. A total of over 1,500 experiments have been conducted. The majority of these tests pertain to downward flow of air/water mists because of its direct relevance to the Electra KrF laser application.

A listing of the experimental data is given in Appendix B. It contains the data obtained using the second cylindrical test section (PIPE 2), third cylindrical test section (PIPE 3), and second rectangular test section (DUCT 2). Data obtained using the first cylindrical test section (PIPE 1) are not reported due to concerns regarding the non-uniformity of the wall thickness i.e. the wall heat flux produced by ohmic heating. Additionally, data obtained using the first rectangular test section (DUCT 2) are not reported due to concerns regarding possible over estimation of the measured heat transfer coefficients, due to underestimation of the wall temperatures as a result of poor thermal contact between the wall and thermocouple probes. Because of the large number of experimental runs, it was not practical to report them all. Many of the experimental runs at a given set of conditions were repeated to check for consistency. Also many of the

experiments at a given set of test conditions were repeated using different test sections. Therefore, in order to limit the size of the Appendices, selected data which best represent the encountered and studied phenomena are presented.

4.1 Single-Phase Flow

In order to confirm the accuracy of the experimental measurements and data analysis techniques, experiments were performed using single-phase forced convection to the carrier gas. Comparisons were then made between the measured heat transfer coefficients and predictions of the widely-used empirical correlation of Reynolds, Swearingen and McEligot (1969), and the analytical solution of Notter and Sleicher (1972). Both, the correlation and the analytical solution are for thermally developing turbulent flow, i.e. the turbulent Graetz problem. Figure 4.1 and Figure 4.2 show typical comparisons between the experimental data and predictions of the empirical correlation and analytical solution. The x-ordinate represents the non-dimensional axial heated test section position z normalized by the hydraulic diameter d, while the y-ordinate represents the local heat transfer coefficient. The data shown in Figure 4.1 pertain to the second cylindrical test section (PIPE 2, ID = 17.3 mm), with an average inlet velocity of 15 m/s and wall heat flux of 3.18 kW/m^2. The unheated length is 7.5 cm long acrylic tube. The data shown in Figure 4.2 pertain to the third cylindrical test section (PIPE 3, ID = 23.6 mm), with an average air velocity of 15 m/s and wall heat flux of 2.88 kW/m^2. The unheated length is a 68.5 cm long glass tube. The inlet Reynolds number for these two experiments are 1.7×10^4 and 2.3×10^4, respectively, which fall within the applicable ranges of the model and the correlation.

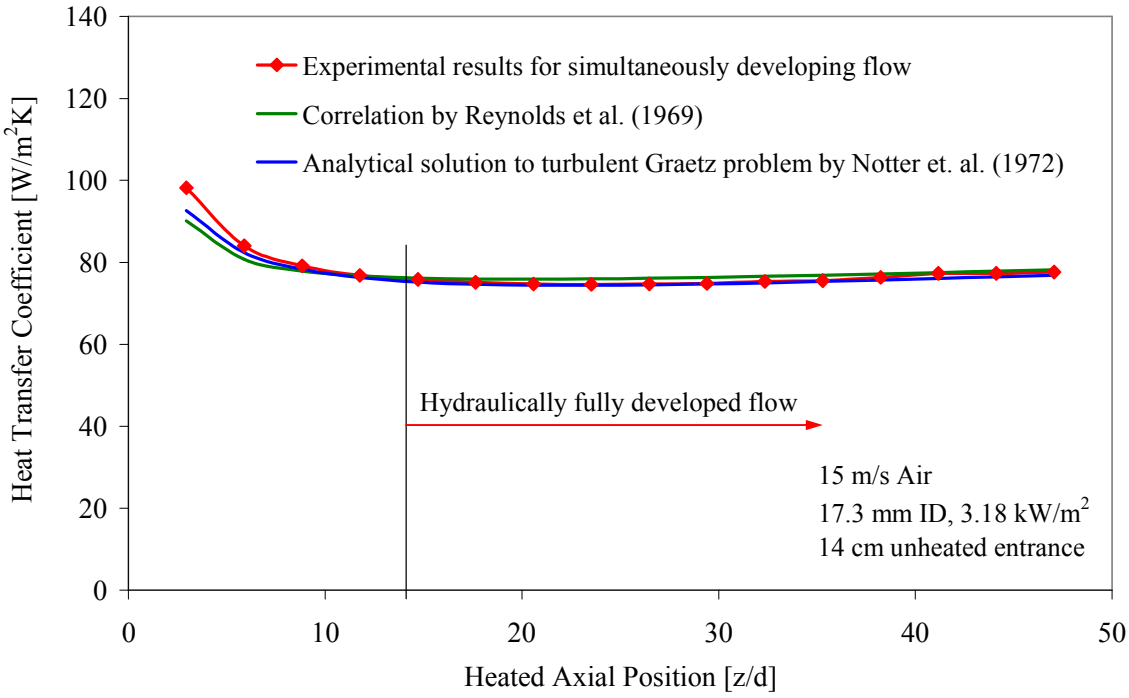

Figure 4.1 Comparison between experimental values of the heat transfer coefficient and predictions of the empirical correlation and analytical solution for cylindrical tube with short entry length

In calculating the heat transfer coefficient using the correlation of Reynolds, Swearingen and McEligot (1969), the Gnielinski correlation [Kakac, Shah and Aung (1987)] is used to calculate the fully developed Nusselt number in Figure 4.2, while in Figure 4.1 the fully-developed value predicted by the analytical solution of Notter and Sleicher (1972) is used. Figures 4.1 and 4.2 demonstrate the excellent agreement between the measured heat transfer coefficients and the predictions of well established models and correlations.

In addition to confirming the validity of the experimental methodology, the measured heat transfer coefficients for single-phase cooling were used to estimate the enhancement ratio, i.e. the ratio between the heat transfer coefficients for mist cooling and those obtained using the carrier gas alone.

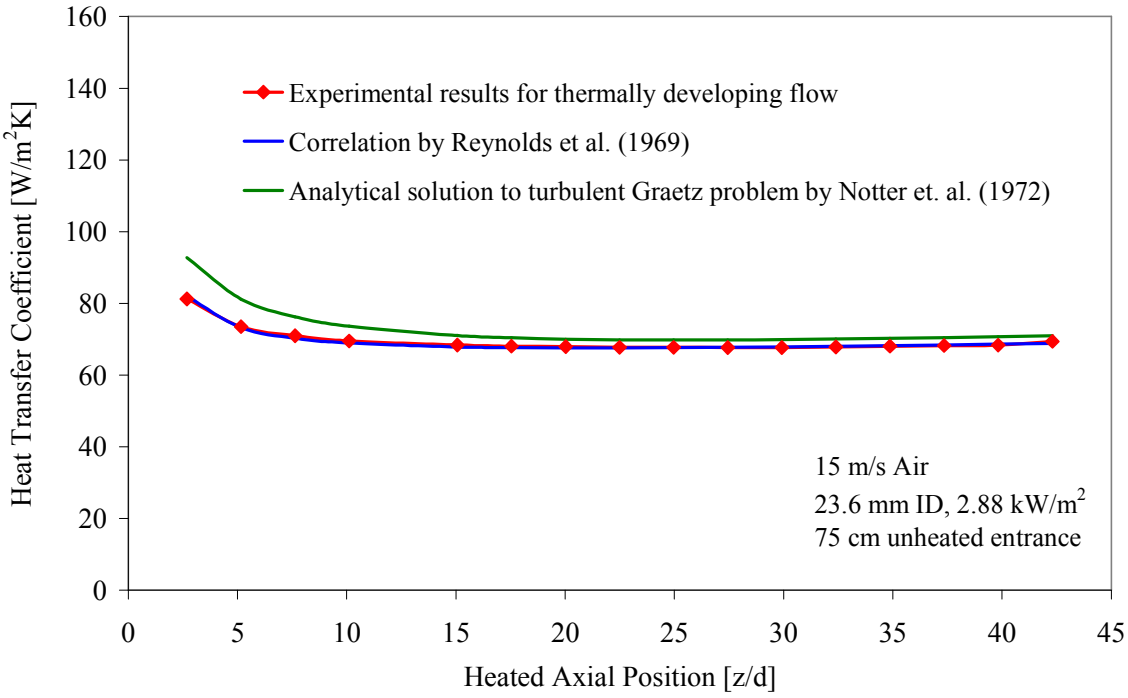

Figure 4.2 Comparison between experimental values of the heat transfer coefficient and predictions of the empirical correlation and analytical solution for cylindrical tube with long entry length

The experimental values of the local heat transfer coefficients shown in Figures 4.1 and 4.2 were calculated by dividing the measured value of the wall heat flux by the difference between the measured wall temperature and the local average bulk temperature calculated using an energy balance. Figure 4.3 shows a typical "measured" time-and-circumference-average inside wall temperatures along test section PIPE 3, along with the calculated gas bulk temperatures. The inside surface "measured" wall temperature was determined by correcting the measure outside surface temperature for the temperature drop across the tube wall using a one-dimensional condition model.

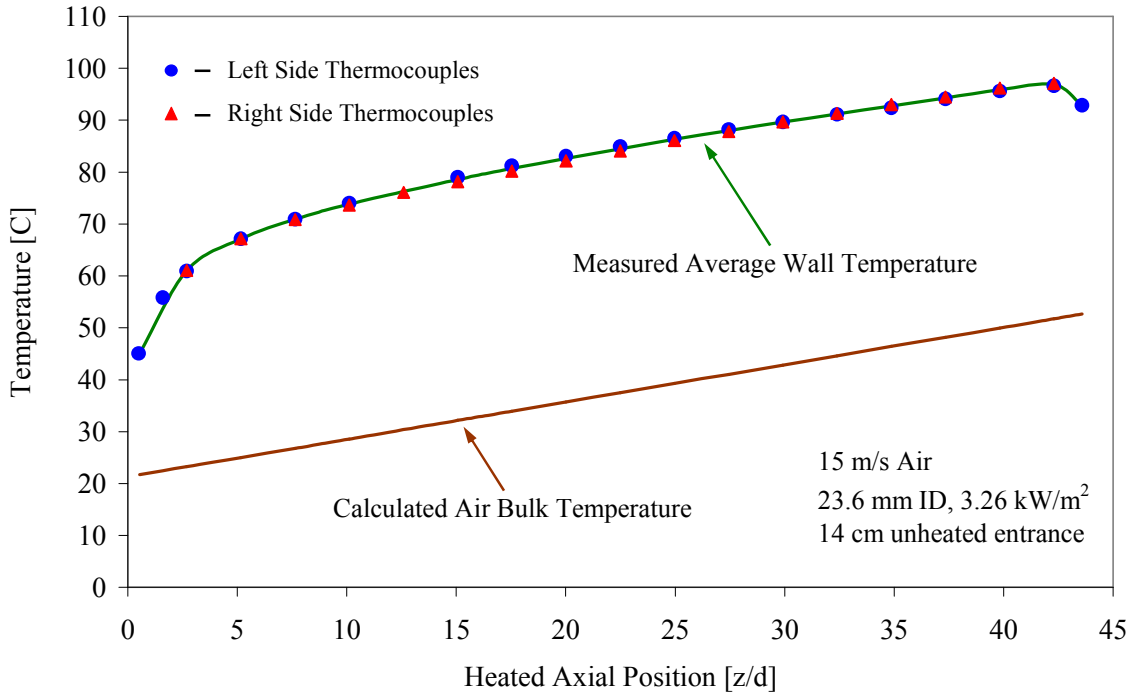

Figure 4.3 Variation of the "measured" time-and-circumference-average inside wall and calculated air bulk temperatures for air flow only in a cylindrical tube with a short unheated entry length

For most of the instrumented axial locations, two thermocouples were attached to the tube wall at diametrically opposed positions. The data in Figure 4.3 clearly show the azimuthal variation in wall temperature are relatively small, thereby confirming uniformity of the wall thickness. The last instrumented axial location (z/d = 43.6) shows a sudden drop in wall temperature; this is to be expected of end effects caused by axial heat conduction to the electrical power cable connection. To avoid errors associated with end effects, the end thermocouples in all test sections were not used to calculate the local heat transfer coefficient. This end effect is also expected to be present at the inlet of the test section; therefore, the thermocouple at the first instrumented elevation (z/d = 1.6) was not used to calculate the local heat transfer coefficient. Figure 4.3 also shows that

there is only one thermocouple at the axial location corresponding to z/d = 12.6. The second thermocouple at that elevation failed during experiments. Hence, local heat transfer coefficient data are not reported for that elevation. Local heat transfer coefficient data are reported only when both thermocouples are present at the instrumented axial location and indicate consistent measurements. The same approach was used on all test sections. Differences between the readings of two diametrically opposed thermocouples at the same axial location can be attributed to either azimuthal non-uniformity in heat flux (due to variation in wall thickness) or non-uniformity of the heat transfer coefficient caused by film instability and liquid rivulet formation. In general, for either single phase experiments or mist cooled experiments with a stable liquid film, the differences between the indicated temperatures by any two diametrically opposed thermocouples was less than 2 ^{o}C.

4.2 Heat Flux Uniformity

The walls of the test section are ohmically heated. Nominally, the wall thickness is uniform; hence one would expect the heat flux to be uniform. However, temperature variations along the test section are an inherent part of the experiment. Such temperature variations can result in variations in the local electrical resistivity, and hence, the heat flux. Therefore, analyses have been performed to check the extent by which the local heat flux varies from its uniform (i.e. average) values, and the impact of such deviations on the measured heat transfer coefficients. Two methods were used to calculate the local heat flux and the corresponding heat transfer coefficient. In the first method the electrical power input to the test section was calculated by multiplying the measured effective

current and voltage drop across the test section. The average heat flux was then calculated by dividing the input power by the inner test section surface area. The local heat flux was assumed to be equal to the average heat flux, which, in turn, was used to calculate the local heat transfer coefficient. In essence, this method assumes that the wall cross sectional area (through which the current flows) is uniform and that the wall material resistivity is independent of temperature.

In the second method, the effect of local temperature on resistivity was accounted for. Here, the local input power was calculated as the product of the effective current squared and the local resistance of the test section. For this method, the test section had to be divided into segments between two adjacent instrumented locations in order to account for the change in electrical resistivity of the test section walls as the wall temperature changes. The effective current through the test section was measured in the same manner as in the first method. The measured wall temperature at each thermocouple location was used to determine the local specific resistivity for the test section material. This, in tern, was used to determine the wall resistance per unit length at each instrumented location. The local power dissipated per unit length and therefore, the local heat flux for the each segment was then calculated. Figure 4.4 shows the heat transfer coefficient obtained by these two independent local heat flux measurement methods. The agreement was excellent proving the accuracy of the uniform heat flux assumption.

Uncertainty A and the combined uncertainty (see Appendix G) of the heat transfer coefficient are shown in Figure 4.4 for the case in which the electrical power input to the test section was calculated by multiplying the effective current and voltage drop.

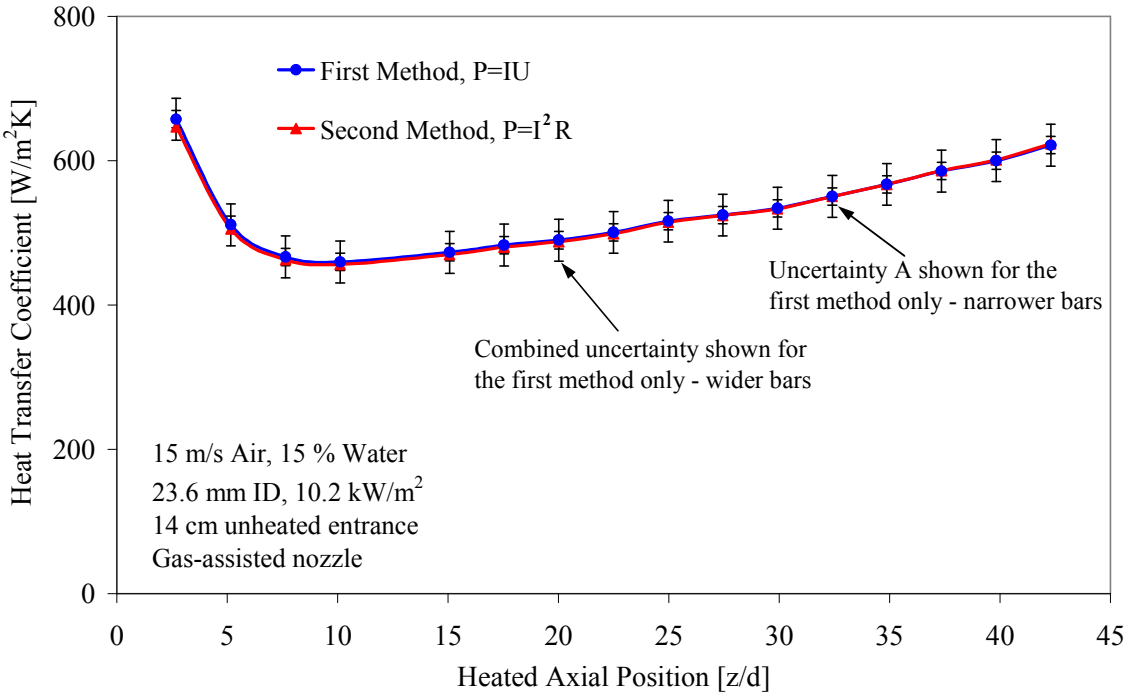

Figure 4.4 Calculated values of the local heat transfer coefficient with and without accounting for wall resistivity changes with temperatures

4.3 Repeatability of Experimental Data

In order to gain confidence in the experimental data, numerous experiments were duplicated to examine their repeatability. Figure 4.5 demonstrates such repeatability. It pertains to downward air/water mist flow with an average inlet air velocity of 15 m/s and injected water mass fraction of 15 %. These experiments were conducted using the 23.6 mm ID circular test section (PIPE 3) with a 7.5 cm long unheated acrylic visualization section. Experiments were conducted at three different heat fluxes, of approximately 3.9, 6.4, and 8.9 kW/m^2. Each experiment was repeated at nearly identical heat flux. The resulting values of the local heat transfer coefficients were highly repeatable (Figure 4.5). It should be noted, however, that the heat fluxes used in all six experiments in Figure 4.5

are sufficiently low so that film breakdown did not occur, as evidenced by the lack of azimuthal variations in temperatures.

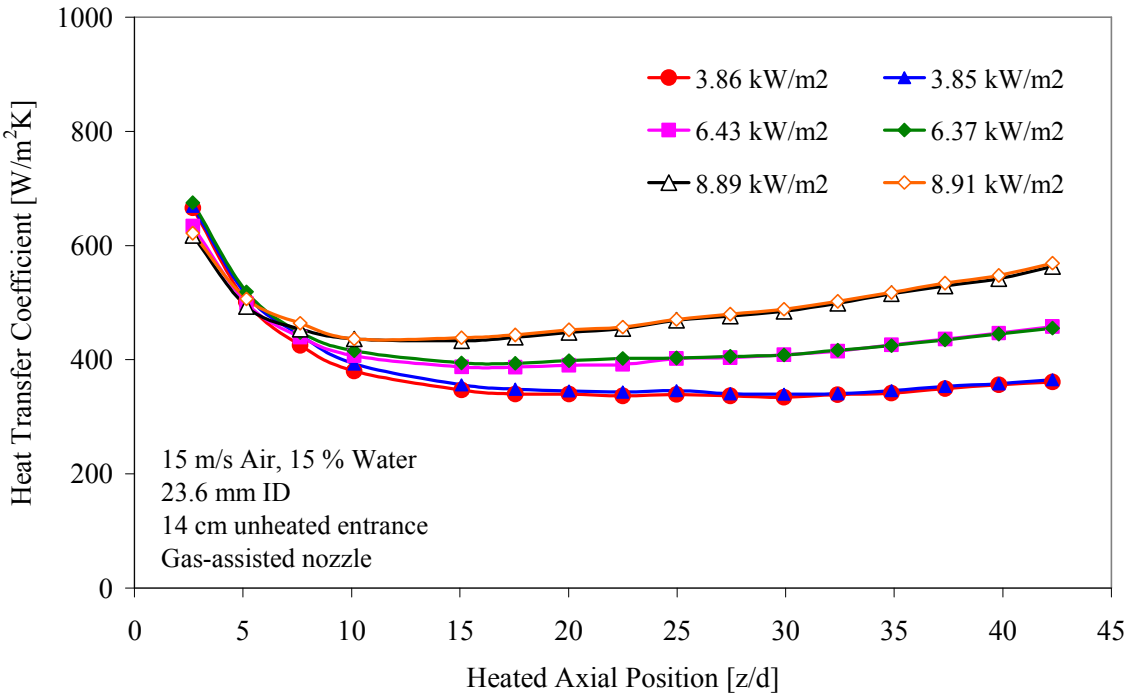

Figure 4.5 Experimental data demonstrating repeatability of the data at low heat fluxes (prior to film breakdown)

4.3.1 Effect of Film Breakdown

As the heat flux increases the film becomes unstable and breakdown occurs. This effect is manifested through observation of large temperature differences between the two diametrically opposed thermocouples near the channel exit. At, or near, the heat flux value at which the film becomes unstable, significant variations in the local heat transfer coefficient are observed downstream of the film breakdown point. Here, the film can fluctuate between a stable flow with full wall coverage, to unstable film with dry patches,

and finally, a rivulet flow. This situation is demonstrated in Figure 4.6, where the local heat transfer coefficients are shown for two experiments at the heat flux corresponding to film instability. Both experiments are conducted using the 23.6 mm ID circular tube (PIPE 3) with an inlet air velocity of 15 m/s, a water mass fraction of 15 %, and a nominal heat flux value of 12.75 kW/m^2. The film breakdown point, can be clearly seen as the local heat transfer coefficient suddenly decreases below its previously fully-developed value (Figure 4.6). It should be noted that significant azimuthal variations in the heat transfer coefficient are to be expected beyond the film breakdown point as the wall temperature varies significantly between the wetted and unwetted regions. For all data presented in the thesis, the local heat transfer coefficients are based on the arithmetic average wall temperature measured by the thermocouples (two or four) placed at each instrumented elevation. Clearly, beyond the film breakdown point these "locally averaged" heat transfer coefficients may not be repeatable as the liquid rivulet randomly moves thereby causing significant variations in the azimuthal temperature distribution.

As the heat flux is further increased, only the ruptured film case is observed, as can be seen in Figure 4.7. Under these conditions the rivulet flow regime dominates along a large fraction of the test section length where the resulting liquid film and rivulet position and thickness constantly vary.

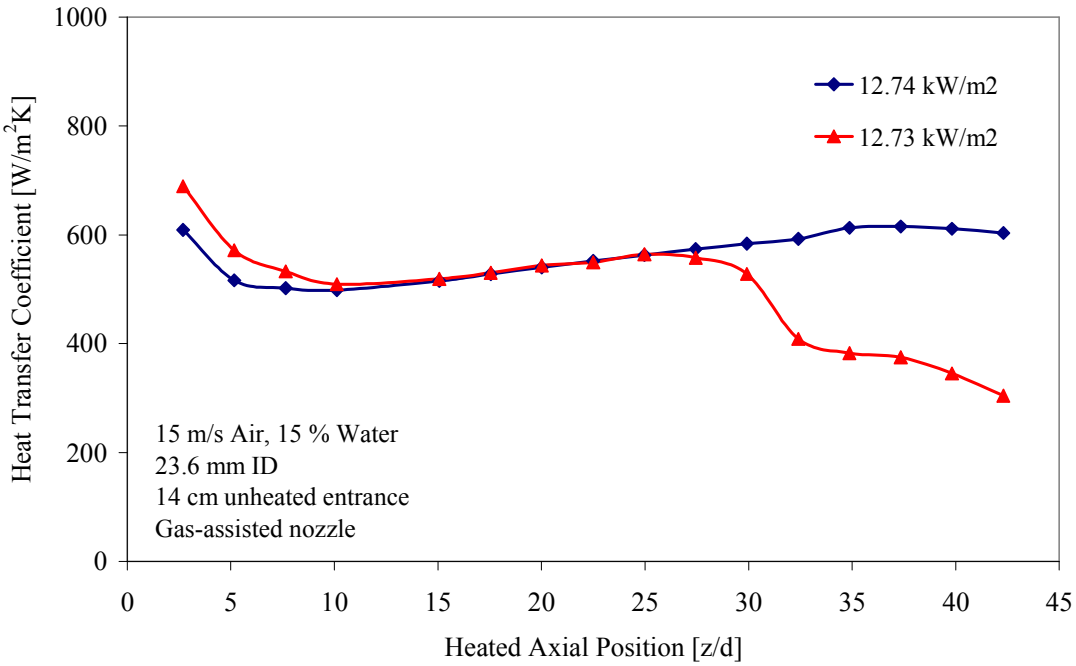

Figure 4.6 Effect of film breakdown on the measured values of the local heat transfer coefficient at high carrier gas velocity

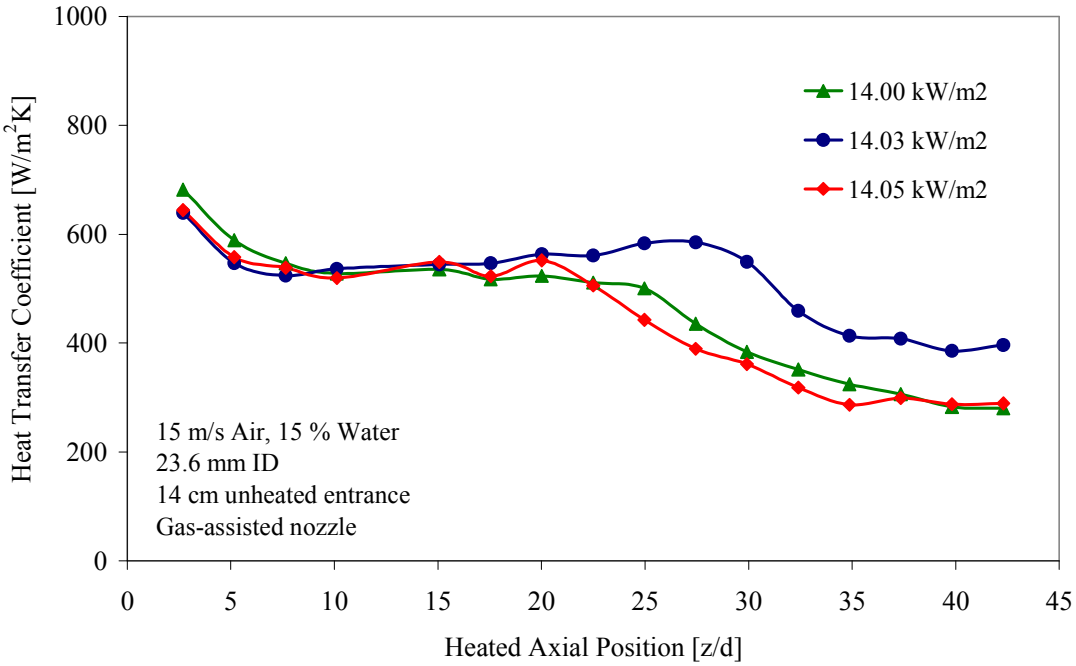

Figure 4.7 Effect of film breakdown and instability on the measured heat transfer coefficient at elevated heat fluxes and high carrier gas velocity

The extent of variation in the local heat transfer coefficient following film breakdown becomes less pronounced as the carrier gas velocity decreases. This can be seen in Figure 4.8, which corresponds to experiments conducted using the 23.6 mm ID circular tube (PIPE 3) with an inlet air velocity of 5 m/s and a water mass fraction of 5 % at different heat fluxes. These data show good repeatability for both stable and ruptured film conditions.

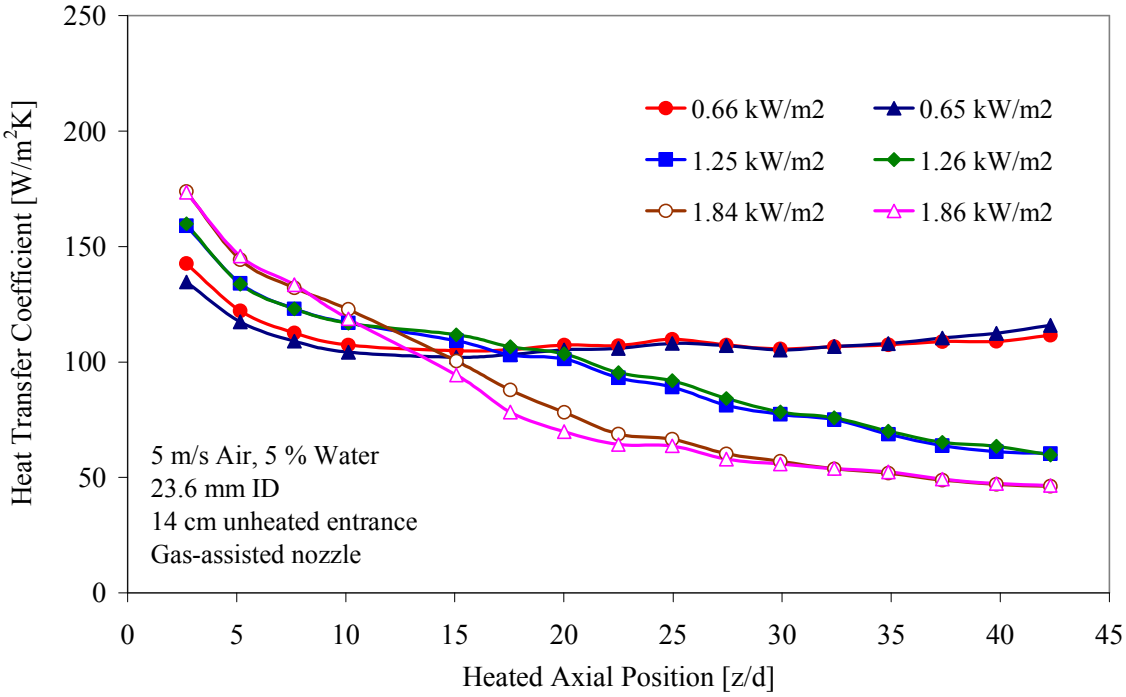

Figure 4.8 Experimental data demonstrating repeatability of the data for both stable and ruptured film conditions at moderate carrier gas velocities

4.3.2 Effect of Nozzle Alignment

Nozzle alignment can significantly impact the measured heat transfer coefficients. This is particularly evident for the gas-assisted nozzle, where misalignment from the test

section center line by only a few degrees can significantly impact the resulting wall temperature distribution, and hence, the heat transfer coefficients. When misaligned, the high gas jet momentum produced by this nozzle could preferentially deposit more droplets onto one side of the test section, thereby reducing the wall temperature due to the higher film flow rate. The data suggest that the temperature of the other side of the wall would not significantly increase above its value for the well aligned gas-assisted nozzle case. Nevertheless, the net effect of misalignment is a slightly reduced average wall temperature at that cross section, which produces a higher heat transfer coefficient. This affect is most pronounced near the entrance of the test section. An example of this effect can be seen in Figure 4.6, where the circumferential wall temperature difference at the entrance region was up to 3 ^{o}C for the 12.73 kW/m^2 heat flux case, and around 1 ^{o}C for the 12.74 kW/m^2 heat flux case. The affect of nozzle misalignment decreases as the flowing mist further proceeds along the heated channel; for the case shown in Figure 4.6, nearly identical values for the fully developed heat transfer coefficients are reached at z/d $\approx$ 17. It should be noted that nozzle misalignment may also contribute to early film breakdown due to film thickness non-uniformity. This could be seen in Figure 4.9 where non-uniform azimuthal temperatures and film breakdown are observed at lower heat flux than that shown in Figure 4.6. Aside from its direct impact on liquid film uniformity, the azimuthal temperature differences produced by film thickness non-uniformity further enhance film instability due to the Marangoni effect. Therefore, nozzle misalignment generally hastens film breakup; the effect becomes more pronounced as the extent of misalignment increases. Azimuthal temperature differences of nearly 10 ^{o}C have been observed in experiments using a highly misaligned gas-assisted nozzle with only two 2

^{o}C axial temperature difference between two neighboring elevations (nearly 5 cm apart). For cases with such high azimuthal temperature gradients, thermocapillary film breakdown could occur even at low heat fluxes.

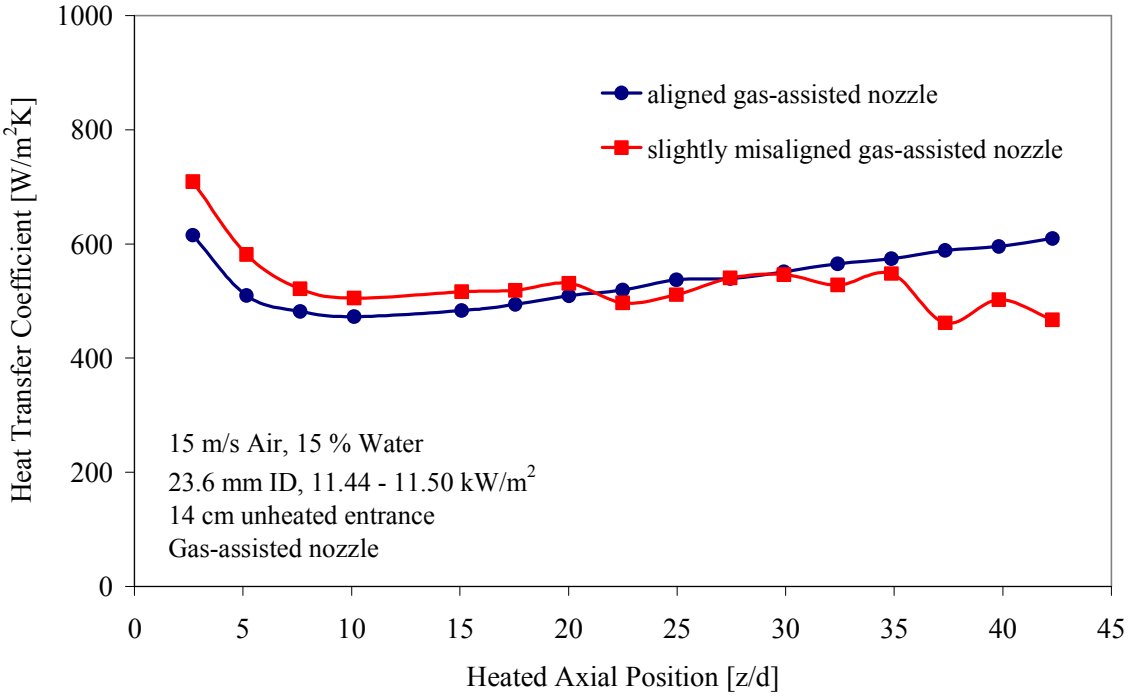

Figure 4.9 Effect of nozzle misalignment on the local heat transfer coefficients and film breakdown

As indicated earlier, nozzle misalignment effects were primarily observed when the gas-assisted nozzle was used. Nozzle misalignment effects were not observed with either the ultrasonic or fixed geometry hydraulic nozzle. This is caused by the low-momentum sprays generated by these nozzles, as well as the manner in which they were mounted into the mixer. The manner in which the gas-assisted nozzle was assembled into the mixer made it possible for the nozzle axis to be slightly misaligned, while the other

nozzles were more rigidly mounted. Nevertheless, it should be noted that the nozzle alignment, i.e. spray axis alignment, is an important operational parameter particularly at high heat fluxes where film breakdown may be of concern. At low heat fluxes, i.e. when film breakdown is not of concern, the effect of nozzle alignment may not be discernible.

These results point to the importance of using multiple thermocouples at the same axial location to detect any azimuthal variations in temperature. The use of two diametrically-opposed thermocouples at each instrumented axial location in cylindrical test sections was deemed to be adequate in this study; however, clearly better diagnostics would have been achieved if additional thermocouples were used at each instrumented axial location.

4.3.3 Effect of Ambient Temperature

While the test section itself is well insulated, variations in the ambient temperature caused the carrier gas inlet-temperature to change thereby affecting the heat transfer coefficient. An increase in the inlet carrier gas temperature enhances evaporation at the liquid film/mist interface, thereby increasing the heat transfer coefficient. Figure 4.10 clearly demonstrates this effect; these data pertain to the 17.3 mm ID circular tube (PIPE 2) with an inlet carrier gas velocity of 15 m/s and a 15 % water mass fraction. Consistently higher heat transfer coefficients are obtained as the ambient temperature, i.e. the gas inlet temperature increases. Additional discussion regarding the effect of inlet carrier gas temperature is given elsewhere in this chapter.

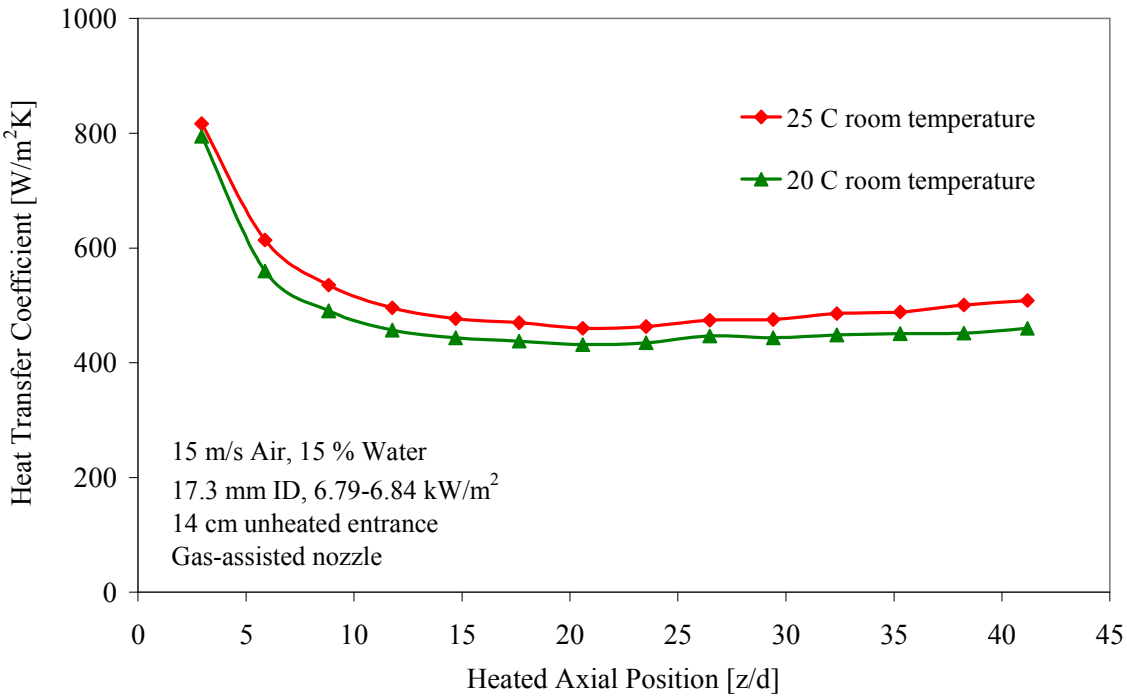

Figure 4.10 Effect of ambient temperature on measured values of local heat transfer coefficient

4.3.4 Effect of Heat Flux History

It was observed that the liquid film was more resistant to rupture if sequentially performed experiments were run with gradually increasing heat flux (i.e. increments from low to high rather than from high to low). It appears that a gradual increase in the heat flux results in a better film temperature uniformity than the case where power is instantaneously set to provide the desired heat flux directly from zero. A gradual heat flux increase apparently slows down the Marangoni effect and thus the associated thermocapillary film breakdown. Therefore, all the results presented here were obtained gradually increasing the heat flux in sequential experiments from very low heat fluxes to their desired maximum values.

The above discussion of data repeatability points to the need for meticulous attention to detail when conducting experiments for internal spray mist cooling with thin evaporating subcooled liquid films.

4.4 Effect of Nozzle Design

Three types of nozzle are used in this study, namely, gas-assisted, ultrasonic, and fixed geometry hydraulic nozzle. These three nozzles cover a wide range of spray geometry, spray velocity and droplets size distribution. The gas-assisted nozzle uses pressurized gas for droplet atomization; the ultrasonic nozzle atomizes droplets with the oscillating tip of the nozzle, while the fixed geometry hydraulic nozzle atomizes the water by forcing high-pressure water through a small orifice. In this section, the spray characteristics of the three nozzles are first presented. The effect of nozzle type on the heat transfer coefficients for both downward and upward mist flow are then described.

4.4.1 Spray Characteristics

The gas-assisted nozzle produces a high-velocity, full-cone spray with a cone angle of nearly 18 degrees, as shown in Figure 4.11. The Sauter mean droplet diameter for the gas-assisted nozzle can be controlled from as low as few microns to nearly 100 μm (see Appendix E); the droplet size distribution is controlled by varying the atomizing gas pressure. A higher gas pressure produces smaller droplets.

The ultrasonic nozzle produces a nearly mono-disperse cylindrical spray with negligible axial velocity, as shown in Figure 4.12. It produces droplets with Sauter mean diameter (SMD) of 80 μm to 85 μm. This nozzle does not provide any control over the

droplet size distribution. Depending on the electrical power input to the ultrasonic generator, either it atomizes the droplets within the stated size range with a cylindrical (i.e. narrow cone) spray shape, or it creates significantly larger single droplets of unknown diameter when the power is too high; the latter condition has never been observed in this study.

The fixed geometry hydraulic nozzle produces a low velocity, full-cone spray with a cone angle of 80 degrees, as shown in Figure 4.13. Depending on the water flow rate which is controlled by the water line pressure, it can produce droplets with Sauter mean diameter of nearly 20 μm to 40 μm. This nozzle does not provide any droplet size distribution control for a fixed water flow rate. Only by changing the water flow rate, i.e. the water line pressure, a droplet size distribution can be changed (see Appendix E).

Figure 4.11 The gas-assisted nozzle spray shape

Figure 4.12 The ultrasonic nozzle cylindrical spray shape

Figure 4.13 The fixed geometry hydraulic nozzle spray shape

4.4.2 Downward Mist Flow

In this section, the effect of nozzle design on the heat transfer coefficients for downward mist flow is discussed. Figure 4.14 shows the heat transfer coefficients using these three nozzles at their optional performance condition. The data pertain to the 23.6 mm ID circular tube (PIPE 3) with a 14 cm long unheated entry length.

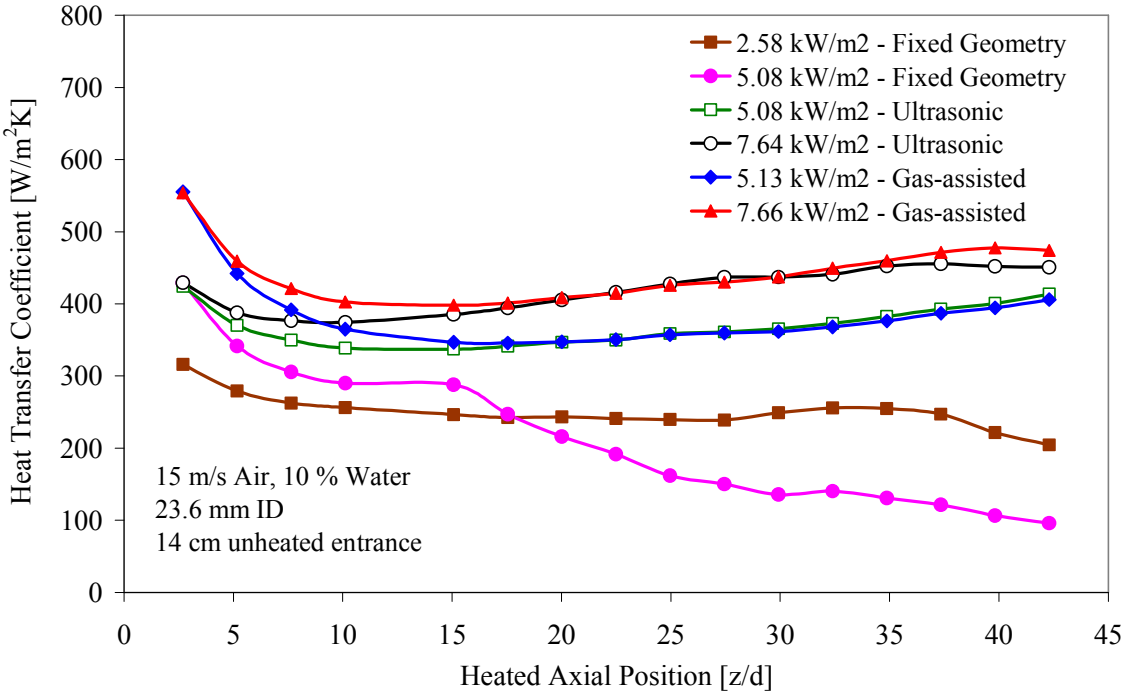

Figure 4.14 Effect of nozzle design on the heat transfer coefficient for downward mist flow in a circular channel

At the wall heat fluxes examined, the fully developed values for the heat transfer coefficients obtained using the gas-assisted and ultrasonic nozzles are nearly identical. Higher entrance region heat transfer coefficients are obtained with the gas-assisted nozzle due to the significantly higher turbulence intensity caused by its high velocity jet. The

lower heat fluxes used in this experiments are sufficiently low so that no film breakdown takes place along the entire tube length. Indications of early film breakdown can be seen for the ultrasonic nozzle near the end of the test section for the highest heat flux value in Figure 4.14 while the data for the gas-assisted nozzle show almost no indication of film breakdown. This is believed to be due to narrow angle and high velocity spray provided by the gas-assisted nozzle which assures nearly uniform droplet deposition on the liquid film along the entire length of the test section. The ultrasonic nozzle has a narrow angle spray; however, the mist produced by that nozzle has considerably less forward momentum compared to that produced by the gas-assisted nozzle as it is advected by the atomizing gas stream. Therefore, the ultrasonic nozzle provides less uniform droplet deposition along the channel length, which in return, could result in an uneven film thickness and thermocapillary breakdown further down in the test section. Early breakdown of the liquid film obtained with the ultrasonic nozzle versus the gas-assisted nozzle is more easily visible when the longer unheated entry length (visualization tube), i.e. 68.5 cm glass tube is used. This can be seen in Figure 4.15. These data pertain to downward mist flow in a 23.6 mm ID circular tube (PIPE 3) with a 75 cm long unheated entry length. The inlet air velocity is 15 m/s while the water mass fraction is 15 %. For the ultrasonic nozzle case, film breakdown clearly occurs at a heat flux of ~ 8.9 kW/m^2. At lower heat fluxes, both nozzles produce essentially the same fully developed heat transfer coefficient.

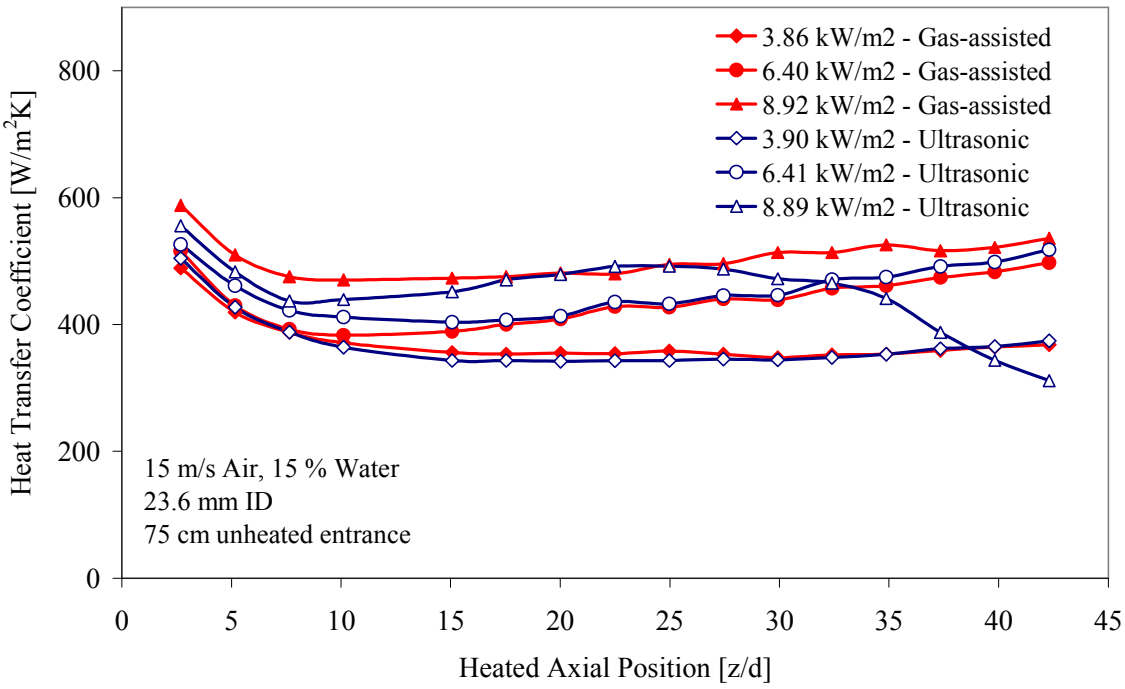

Figure 4.15 Effect of nozzle design on the heat transfer coefficient for downward mist flow in a circular pipe with a long unheated entry length

These data suggest that the narrow-angled cone and high velocities spray produced by the gas-assisted nozzle provides the fastest and the most uniform droplet film deposition mechanism ensuring film stability over the entire length of the test section.

Experiments conducted using the fixed geometry nozzle resulted in film breakdown near section exit at a very low heat flux (2.58 kW/m^2). The location of the film breakdown point moves progressively closer to the test section inlet as the high flux is increased. For a heat flux of 5.08 kW/m^2, the fixed geometry nozzle film broke as early as z/d = 15, i.e. only one third of the way along the channel length, while the liquid films for experiments with the ultrasonic and gas-assisted nozzles remained intact through entire length of test section. The Sauter mean diameter of nearly 32 μm generated by the fixed geometry nozzle in this run is not believed to be the reason for this poor mist

cooling performance; instead, the large spray cone angle (80 degrees) is believed to be the reason for the observed behavior. The large spray cone angle causes most of the droplets to be deposited onto the unheated visualization tube. This means that there are not enough droplets in the mist core to deposit on the wall and provide a uniform film further down along the test section, which is important for film thickness uniformity. The lack of continuous droplet deposition on the film surface makes it more susceptible to thermocapillary breakdown along the heated test section. This problem is exacerbated by the presence of the instrument block at the test section inlet. Nevertheless, it is believed that even if the instrument block were not present, the fixed geometry nozzle would have the smallest chance of providing a stable liquid film along the entire length of the test section.

Figure 4.16 shows the effect of nozzle design on the wall temperature distributions for downward mist flow in a circular tube. The data corresponds to the same experiments shown in Figure 4.14. As one would expect, for fully developed conditions with the same heat flux, the wall temperatures for experiments using the gas-assisted and ultrasonic nozzles are nearly identical. As explained earlier, slightly higher temperatures (i.e. lower heat transfer coefficients) are observed in the entrance region when the ultrasonic nozzle is used compared to those with the gas assisted nozzle. For experiments with a heat flux of ~ 5 kW/m^2, the data obtained using the fixed geometry nozzle follows closely the ultrasonic nozzle data until the liquid film breaks down approximately one third of the way down the channel. At that point, the fixed geometry nozzle wall temperature quickly rises above that for the ultrasonic nozzle due to a film breakdown. While the wall temperature in the entrance region is nearly the same for both cases, the

heat transfer coefficient in the fixed geometry nozzle experiment is lower than that for the ultrasonic nozzle at the same axial location. This may seem contradictory, however, the calculated bulk temperature for the ultrasonic nozzle experiment was higher than that for the fixed geometry case (see Figure 4.17).

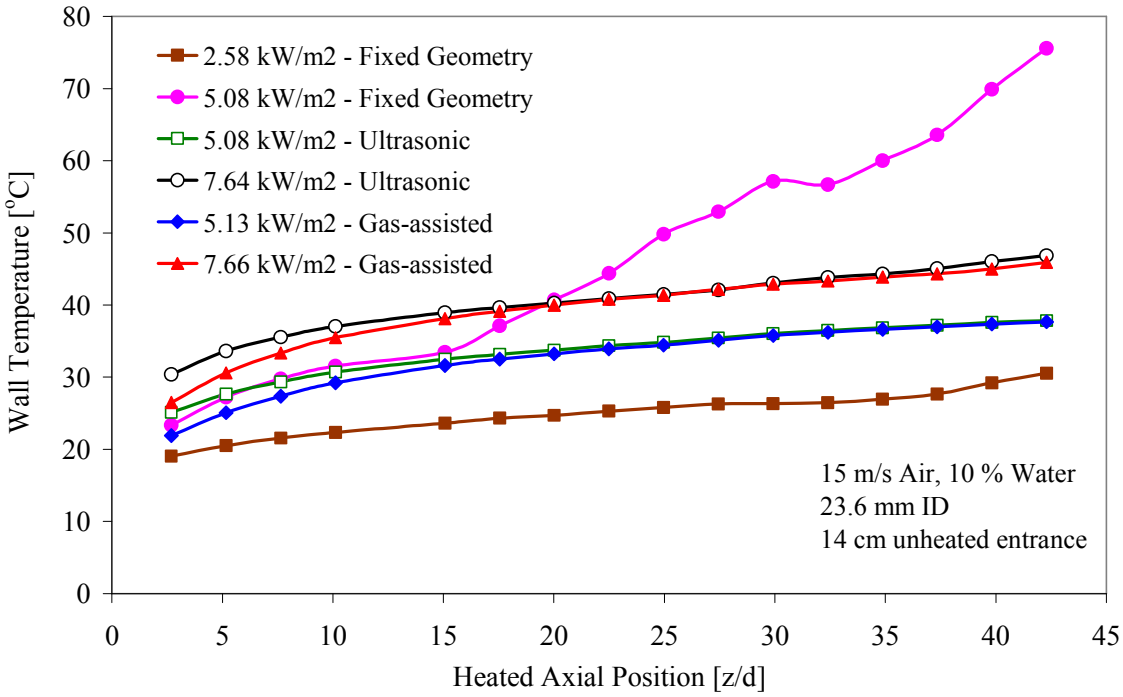

Figure 4.16 Effect of nozzle design on the wall temperature distribution for downward mist flow in a circular channel

The lower bulk temperatures obtained in the fixed geometry nozzle experiment were caused by the lower inlet temperature and humidity measured at the entrance instrument block. Before reaching the heated test section, i.e. within the visualization tube and entrance instrument block, adiabatic air humidification takes place. The injected water droplets play a major role in humidifying the incoming air due to their high surface area.

However, along the heated length saturation is maintained primarily by evaporation at the liquid film/gas interface.

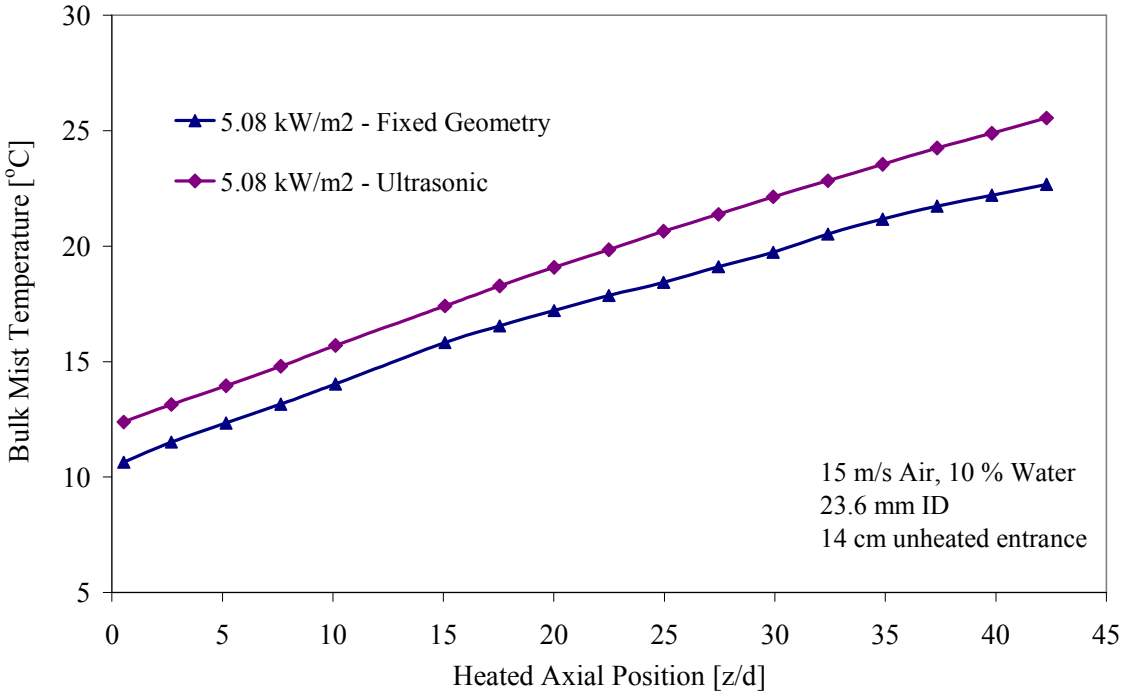

Figure 4.17 Variation of coolant bulk temperature with axial location for downward mist flow with either fixed geometry or an ultrasonic nozzle

4.4.3 Upward Mist Flow

In this section, the effect of nozzle design on the heat transfer coefficients for upward mist flow is discussed. The ultrasonic nozzle was not used in the internal upward mist cooling experiments due to electrical concerns in case of flooding. Figure 4.18 shows the heat transfer coefficients obtained using the gas-assisted and fixed geometry nozzles at their optimal performance condition. The data pertain to upward flow within the 17.3 mm ID circular tube (PIPE 2) with a short (14 cm long) unheated entry length.

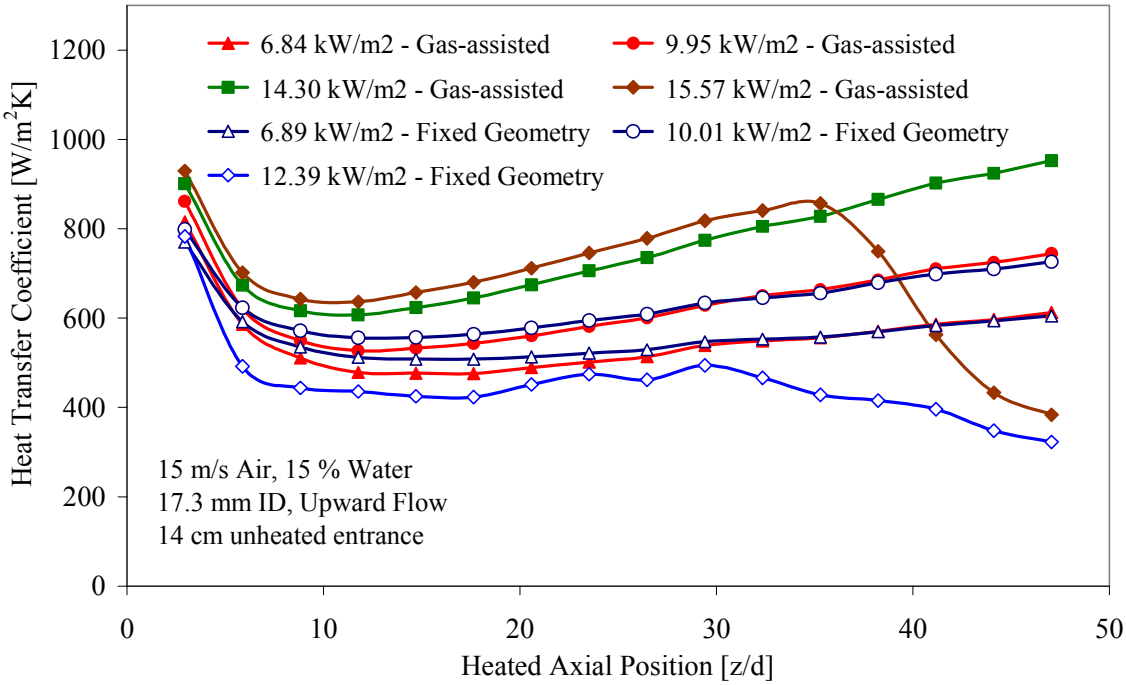

Figure 4.18 Effect of nozzle design on the heat transfer coefficients for upward mist flow in a circular channel

The data correspond to an inlet gas velocity of 15 m/s with a water mass fraction of 15 % at different wall heat fluxes. The results show that, in general, the local heat transfer coefficients obtained with upward mist flow are generally higher than those obtained with downward flow at the same flow conditions (Figure 4.14). Significant improvement in performance is observed for the fixed geometry nozzle where the heat transfer coefficients matched those obtained with the gas-assisted nozzle up to the heat flux corresponding to film breakdown (12.4 kW/m^2). At that point, the heat transfer coefficient for the fixed geometry case decreases over the entire length of the tube. Film breakdown for the gas-assisted nozzle case was observed at a significantly higher heat flux (15.5 kW/ m^2). The estimated mean droplet size generated by the fixed geometry nozzle at the water flow rate used in these experiments is 37 µm. As was the case for

downward mist flow, early film breakdown for the fixed geometry nozzle case is attributed to its large cone angle spray which results in early droplet deposition near the test section inlet with insufficient droplet deposition near the test section exit resulting in premature film breakdown. Nevertheless, the liquid film remains stable at much higher heat fluxes than those observed for the downward flow case. Film stability for the gas-assisted nozzle case was also observed at significantly higher heat fluxes than those for the same flow conditions with downward flow.

Figure 4.19 shows the effect of nozzle design on the wall temperature distributions for upward mist flow in a circular tube. The data correspond to the two lower heat flux experiments in Figure 4.18, where film stability is maintained along the entire pipe length for both nozzle designs.

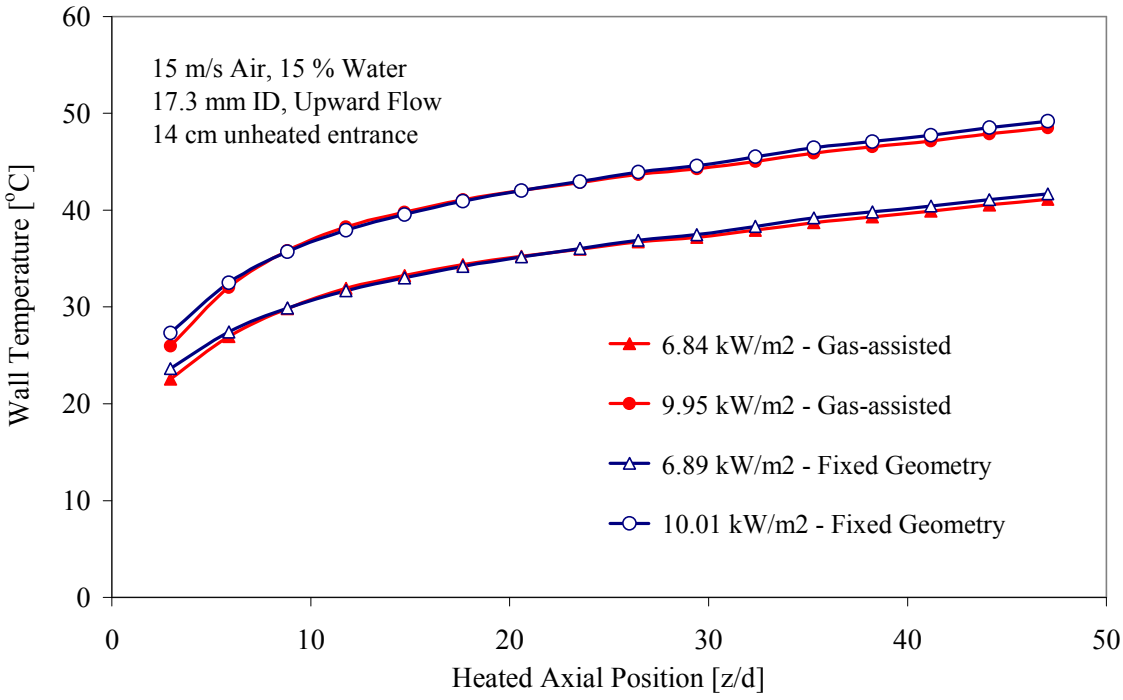

Figure 4.19 Effect of nozzle design on the wall temperature for upward mist flow in a circular channel

As expected, nearly identical wall temperature distributions along the entire tube length are obtained for both nozzle designs. The results obtained in this section point to the importance of flow direction (upward versus downward) on the behavior of mist flow and the resulting heat transfer coefficients. Additional discussion pertaining to the effect of flow orientation will be presented later in this chapter.

4.5 Effect of Droplet Size

In this section, the effect of droplet size on the heat transfer effectiveness of mist cooling will be discussed. Only the gas-assisted nozzle is used in droplet size optimization, since the ultrasonic and fixed geometry hydraulic nozzles do not allow the droplet size to be independently controlled. The mean droplet diameter for the gas-assisted nozzle can be controlled by varying the atomizing gas stream flow rate. Sauter mean droplet diameters ranging from ~ 10 to 100+ μm can be readily obtained. The Sauter mean diameter values reported here are obtained by linear extrapolation from manufacturer supplied performance data. Here the effect of droplet diameter on the resulting heat transfer coefficients for both downward and upward mist flow will be discussed.

4.5.1 Downward Mist Flow

Figures 4.20 and 4.21 show the effect of droplet size on the heat transfer coefficient for downward mist flow in a 23.6 mm ID circular tube (PIPE 3) with a short (14 cm long) unheated entry length. Figure 4.20 corresponds to a carrier gas inlet velocity of 10 m/s and a water mass fraction of 10 % at a heat flux of 5.1 kW/m^2, while Figure

4.21 corresponds to a velocity of 10 m/s and a water mass fraction of 15 % at a heat flux of ~ 6.3 kW/m^2. Droplet sizes ranging from ~ 20 to 70 μm are used. These data show that the heat transfer coefficient in the entry and fully-developed regions are slightly affected by the droplet size. However, the onset of film breakdown at a given heat flux is strongly affected by the droplet diameter. The data point to the existence of an optimal droplet diameter range where film breakdown is preserved; droplet sizes smaller than or greater than that optimal diameter range result in early film breakdown. This is an intriguing result, in as much as it points to the existence of two separate effects which cause film breakdown on both ends of the droplet size spectrum.

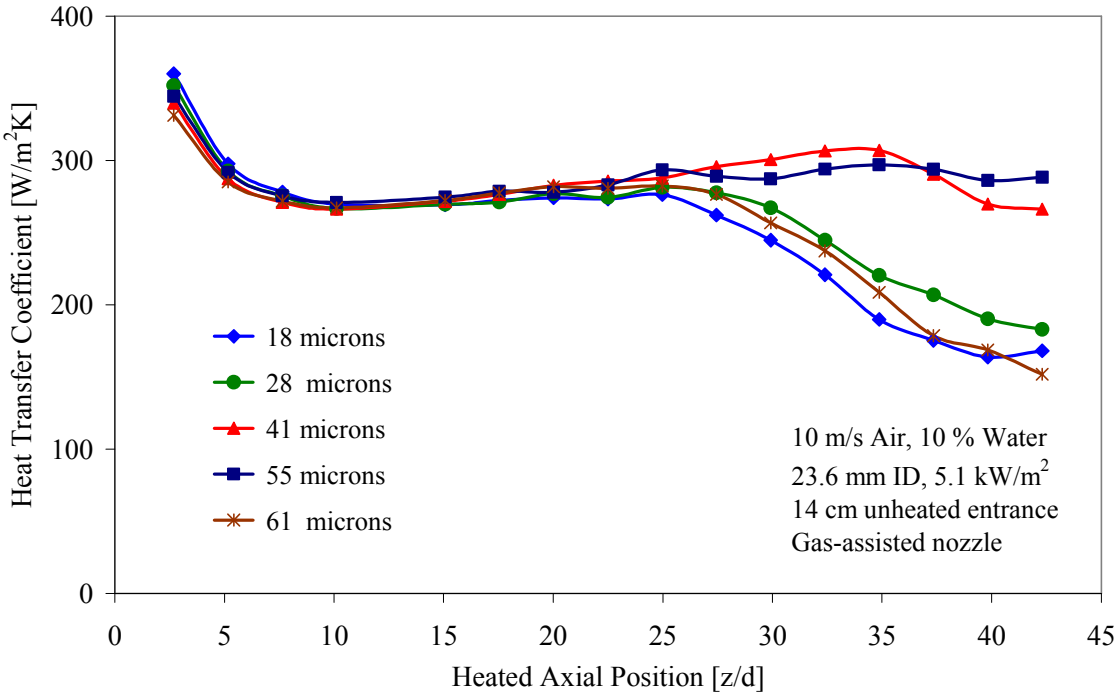

Figure 4.20 Effect of droplet diameter on liquid film stability for downward mist flow in a circular tube

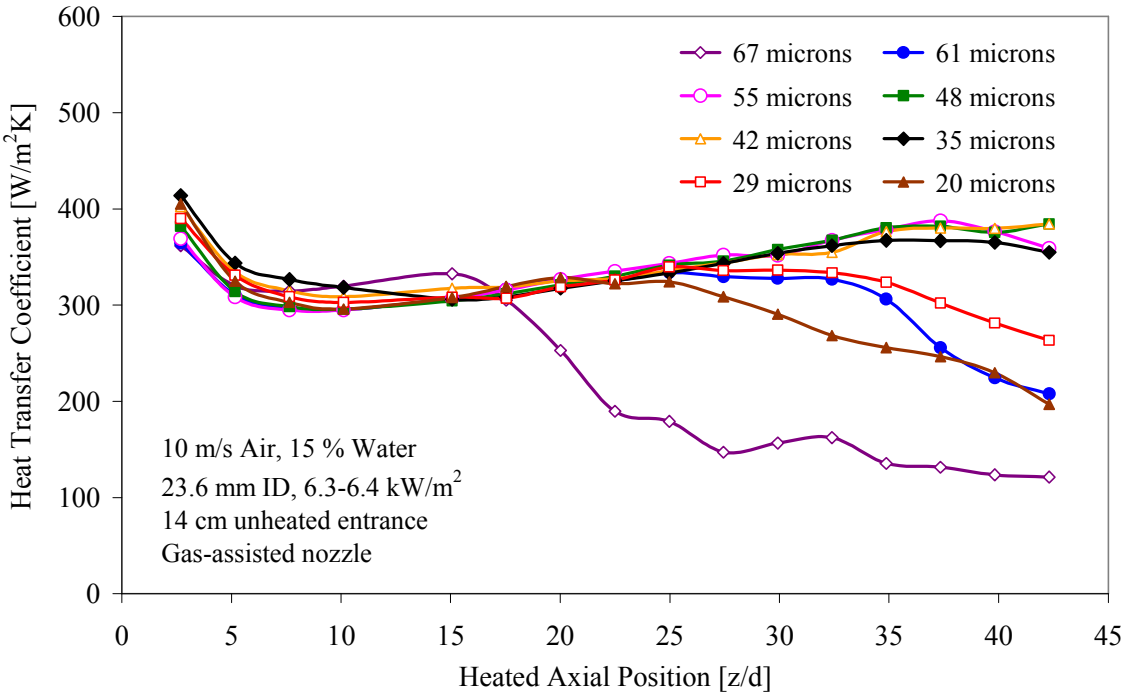

Figure 4.21 Effect of droplet diameter on liquid film stability for downward mist flow in a circular tube

Similar results are shown in Figures 4.22 and 4.23 for an air velocity of 15 m/s and water mass fractions of 10 and 15 % at heat fluxes of 8.9 and 6.8 kW/m^2, respectively. Again, these data show that the heat transfer coefficients in the entry and fully-developed regions are only slightly affected by the particle diameter. However, the droplet mean diameter significantly impacts liquid film breakdown. Outside an optimal diameter range of ~ 30 to 55 μm, early film breakdown occurs, while experiments within the optimal droplet diameter range have a stable liquid film along the entire heated length.

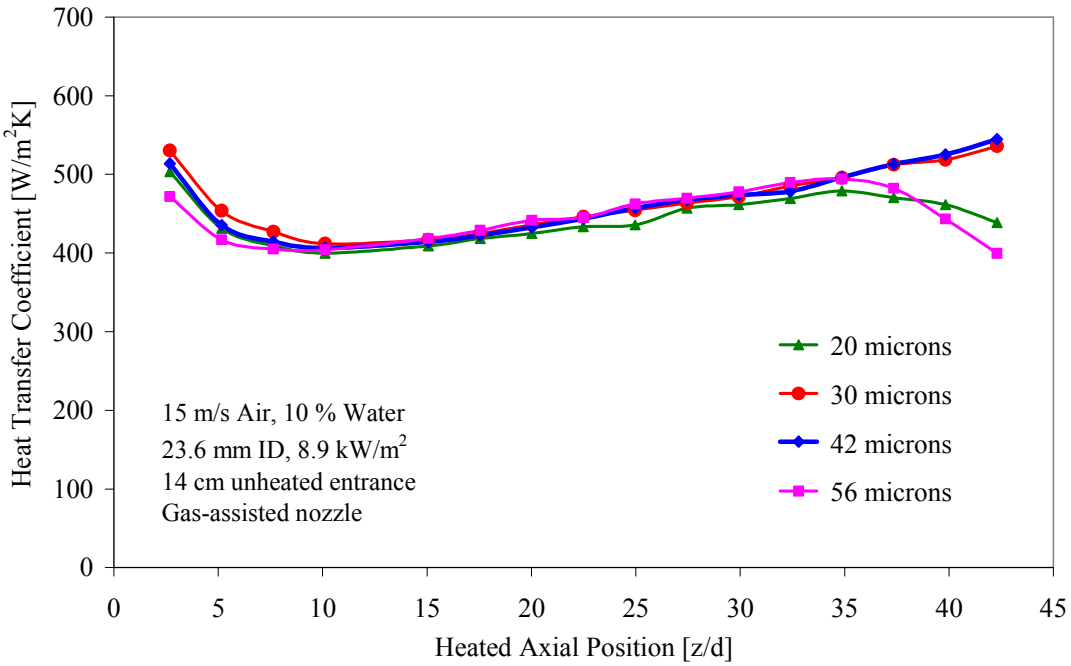

Figure 4.22 Effect of droplet diameter on liquid film stability for downward mist flow in a circular tube

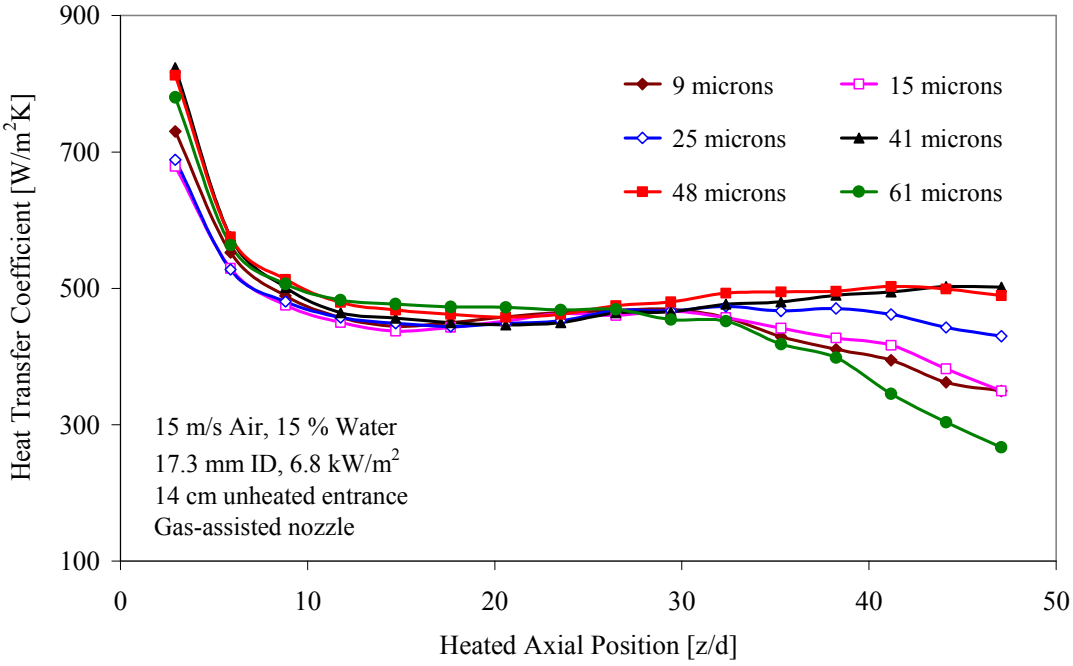

Figure 4.23 Effect of droplet diameter on liquid film stability for downward mist flow in a circular tube

Therefore, all of the results presented in this study for the gas-assisted nozzle, except these presented in this section, correspond to experiment performed using the optimal droplets size range, usually in the 32 μm to 42 μm range, in order to insure consistency of the data.

Early film failure with small droplet diameters can be attributed to the fact that small droplets can be produced when the atomizing gas flow rate is high. For example, for a mean droplet diameter of 20 μm, the atomizing gas velocity at the nozzle exit is nearly 200 m/s. This suggests that liquid film breakdown occurs because a significant fraction of the liquid droplets leaves the test section without depositing on the liquid film; this hypothesis is supported by the results of Lee, Yang and Hsyus (1994). Reduced droplet deposition produces a thinner liquid film which is less resistant to thermocapillary breakdown. The atomizing gas velocity corresponding to the optional droplet size is nearly half of that for 20 μm droplets. This reduces the likelihood of droplet "losses" at the exit, as the drag forces on the droplets reduce slip between them and the surrounding carrier gas (≈ 15 m/s), thereby enhancing droplet deposition along the entire heated length.

For large droplet diameters, i.e. droplet diameters above the optimal range, the atomizing gas velocity is significantly lower. The droplets lower initial velocity coupled with their larger diameters means that the drag forces imposed by the slower carrier gas will quickly reduce slip and prevent the droplets from independently penetrating farther down along the test section. This, in turn, means that the droplets will quickly deposit on the liquid film near the test section inlet, thereby "starving" the downstream region of the test section. This effect allows thermocapillary breakdown to occur sooner or at lower

heat fluxes, as can be clearly seen in Figure 4.24, where the experiment using large droplet diameters (~ 69 μm) has a higher heat transfer coefficient at the entrance region compared to that for the experiment using a near optimal droplet diameter (~ 44 μm) at the same heat flux. However, nearly one third of the way along the test section the heat transfer coefficient for the larger droplet diameter case rapidly decreases signifying early film rupture, while the smaller diameter case shows a stable liquid film with fully-developed heat transfer coefficient along the entire heated length. It should be noted that in addition to increased droplet deposition in the entry region, the smaller number of droplets in the entry region due to larger droplets may also enhance liquid film evaporation to possibly lower relative humidity surrounding gas, thereby further reducing the wall temperature.

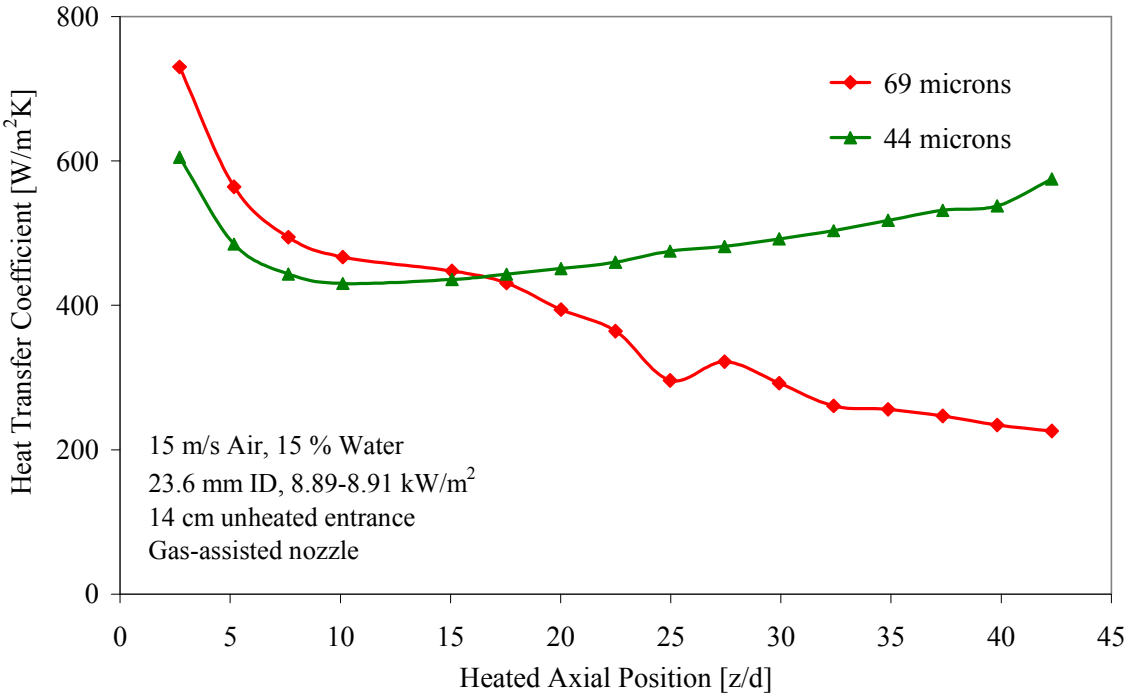

Figure 4.24 Effect of droplet diameter on liquid film stability for downward mist flow in a circular tube

The suggestion offered by Lee, Yang and Hsyus (1994) that the "large" droplets and/or the evaporating liquid film create a vapor cushion between the large droplets and the film surface which decreases the droplet deposition effectiveness does not seem to be realistic here since the wall temperatures in this experiment do not exceed 50 ^{o}C at the entrance region or 75 ^{o}C near the exit, which are significantly lower than the temperatures needed for that effect.

Figure 4.25 shows photographs of the spray pattern produced by the gas-assisted nozzle at the water flow rate corresponding to the case with 15 m/s air and 15 % water mass fraction for a tubular test section with 23.6 mm ID (Figure 4.24): The atomizing gas flow rate (i.e. inlet pressure) was varied to obtain the indicated droplet mean diameters, viz., 8, 36, and 69 μm.

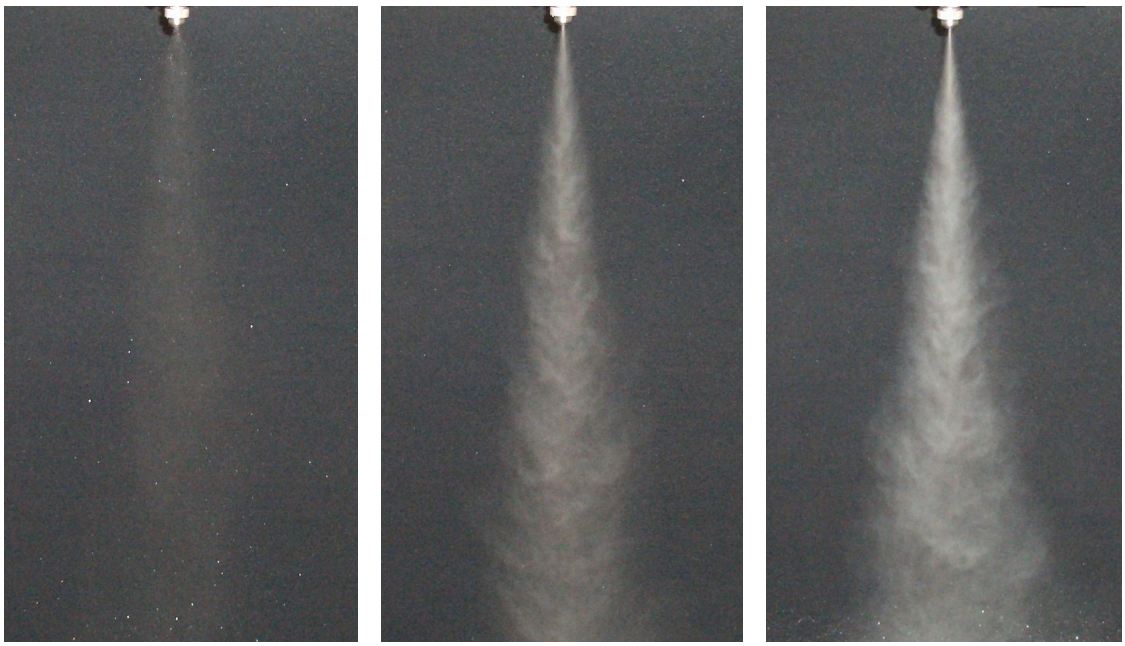

Figure 4.25 The gas-assisted nozzle spray pattern for 69 μm (left), 36 μm (middle), and 8 μm (right) droplet size

As can be seen, the large droplet spray pattern does not penetrate very far down stream of the nozzle because of the low atomizing gas velocity at the nozzle exit, while the small droplet spray clearly penetrates much farther despite the fact that the surrounding gas is stationary, as compared to the co-flowing, albeit slow, carrier gas in the actual channel. Nevertheless, the idea that extremely small droplets are not advantageous because of excessive carryover at the exit, is consistent with the experimental observations.

The indicated droplet size near the upper limit of the examined range may not be exact because of uncertainty in the linear extrapolation used to extract the values from manufacturer data at the corresponding low atomizing air pressures in the gas-assisted line. The pressures used to generate the droplets with extrapolated droplet diameter of 55 μm and above range from 1-3 psi (e.g. a gas pressure of 1 psi is needed for the 69 μm spray in Figure 4.25), where the droplet atomization process could be significantly diminished or even disabled when compared to the optimal atomization gas pressure namely, 5-7 psi (e.g. a gas pressure of 6 psi is needed for the 36 μm spray in Figure 4.25). The sparse nature of the nozzle performance data provided by the manufacturer (Table 4.1) makes it difficult to pinpoint the value of mean droplet diameter at all operating conditions. Additionally, the fact that the ultrasonic nozzle produces 80 μm to 85 μm droplets but performs essentially as well as the optimized gas-assisted nozzle is another reason for this uncertainty. Therefore, the extrapolated droplets size for the low atomizing air pressures could be significantly smaller than the real size.

Table 4.1 Sauter Mean Diameter [μm], (extrapolated diameters shown in bold)

Pressure	Liquid			
Gas	1	2	5	10
1	**70**	**73**		
2	**63**	**66**		
3	**56**	**59**		
4	**49**	**52**	64	
5	**42**	**45**		
6	**35**	**38**	47	62
7	**28**	**31**		
8	**21**	**24**	34	50
9	**17**	**20**		
10	**13**	**16**	26	42

Figure 4.26 shows the droplet size effect in a significantly longer test section, i.e. PIPE 2 with a 68 cm long unheated entry length. The data pertain to an inlet air velocity of 15 m/s air flow and 15 % water mass fraction with nearly the same heat flux (6.8 kW/m^2). The droplet size was varied from 22 to 56 μm by varying the atomizing gas flow rate (i.e. nozzle inlet pressure). The data indicate that the optimal droplet size range remains unchanged. Experiments with droplet sizes of 34 and 41 μm show a stable liquid film along the heated length, while those with either a smaller or larger droplet diameter experienced film breakdown one third to one half of the way along the heated length.

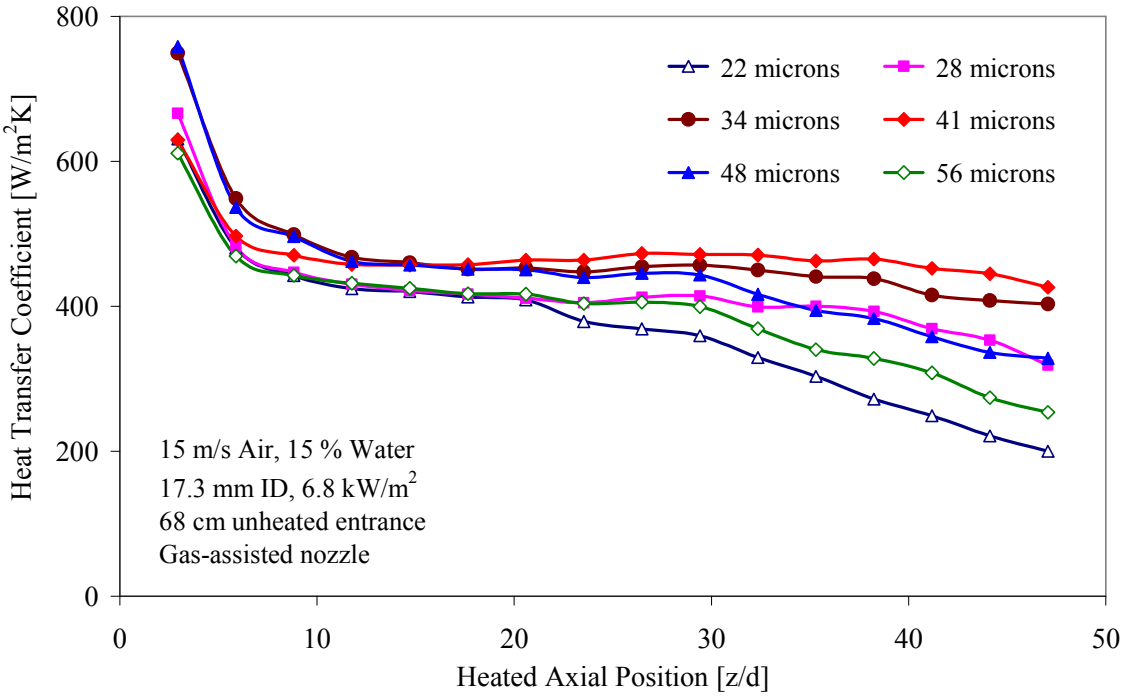

Figure 4.26 Effect of droplet diameter on liquid film stability for downward mist cooling in a circular tube with a long unheated entry length

Figure 4.27 shows a photograph of the droplet size distribution corresponding to the most frequently used optimal Sauter mean diameter of 42 μm. This picture was taken under a microscope. The droplets were collected by sliding a paraffin waxed glass plate a foot away from the nozzle through a mist spray that freely expanded into the room. Wax (paraffin) was used due to its known high contact angle with water (109 degrees). Therefore, nearly perfect half spheres of water were formed on the waxed glass plates. Therefore the diameters shown in the photograph are larger that the actual droplet diameters by nearly 26 % (~ $2.0^{0.33}$). The photograph was taken only a few seconds after collecting the droplets; nevertheless, it is possible that extremely small droplets may had

already evaporated before the slide was placed in the microscope to capture the image shown in Figure 4.27.

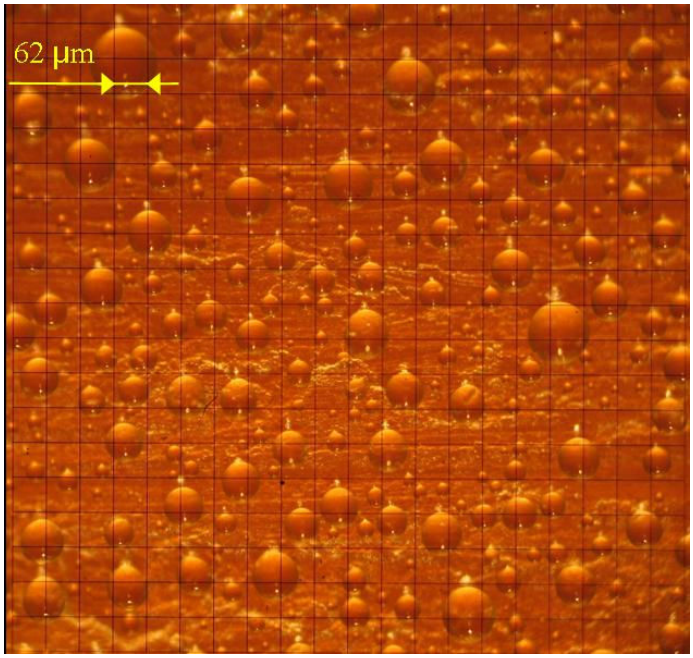

Figure 4.27 Photograph of the droplet size distribution for the spray produced by the gas-assisted nozzle at a Sauter mean diameter of 42 µm

4.5.2 Upward Mist Flow

Experiments have been conducted to determine the effect of droplet size on the local heat transfer coefficient for upward mist flow. Figure 4.28 shows typical results corresponding to flow in a 17.3 mm ID circular tube (PIPE 2) with a short (14 cm long) unheated entry length. The data pertain to an inlet gas velocity of 15 m/s and a water mass fraction of 15 %. These data exhibit a completely different behavior than that observed for downward flow. Specifically, the optimal diameter range appears to be

significantly wider than that for downward mist flow. Nearly identical values of the local heat transfer coefficient are observed for droplet size ranging from 16 μm to 100+ μm. No film breakdown was observed in any of the eases except for the smallest examined droplet size (8.0 μm SMD).

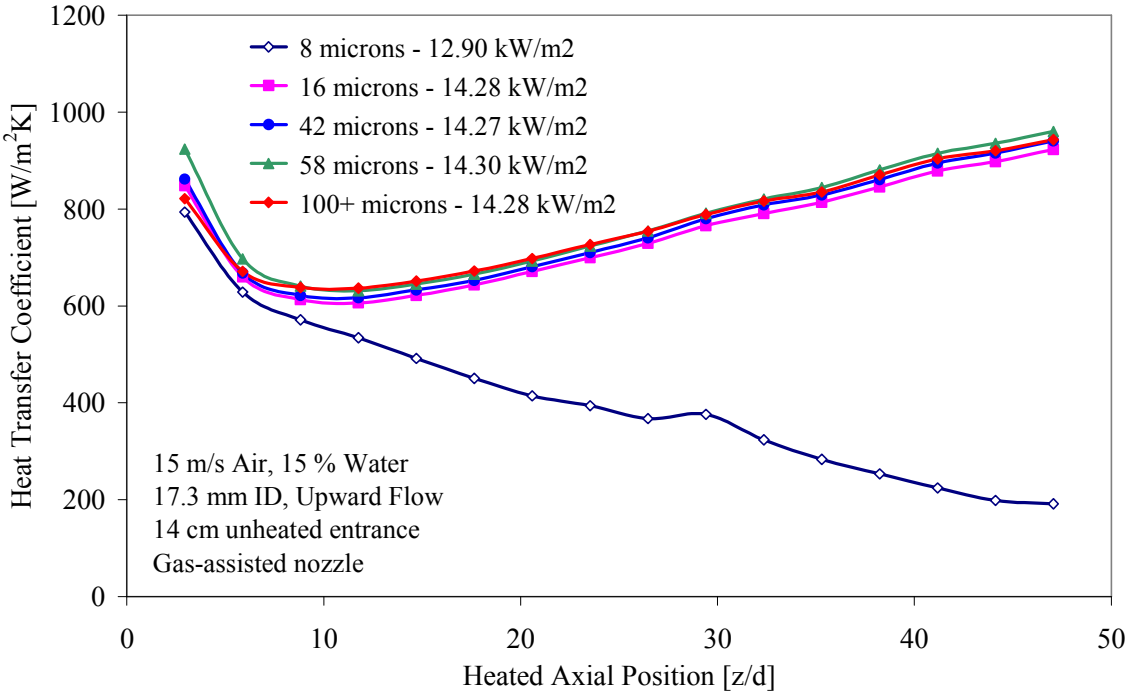

Figure 4.28 Effect of droplet size on local film stability and the local heat transfer coefficients for upward mist flow in a circular tube with a short unheated entry length

For experiments without film breakdown, the heat transfer coefficient increased slightly as the droplets size increased. It appears that gravitational effects tend to balance the non-uniform droplet deposition associated with large droplet sizes which was the reason for film breakdown for downward flow cases. This effect will be discussed in

detail later in this chapter (see section 4.15). Film breakdown occurs when extremely small droplets are used because of the extremely high atomizing gas velocity at the nozzle exit (260 m/s for 8 μm SMD), which decreases the droplet deposition rate and increases the rate of liquid loss through the test section exit, thereby creating considerably thinner films which are more susceptible to thermocapillary breakdown.

4.6 Effect of Heat Flux

Unlike the case of single-phase forced convection where the heat transfer coefficient does not depend on heat flux, the heat transfer coefficient for mist flow with their evaporating films is strongly dependent on the wall heat flux. The heat transfer coefficient increases with increasing heat flux, provided that the liquid film remains intact. This is because a higher heat flux increases the liquid film temperature, thereby enhancing the evaporation process at the liquid film-gas interface, resulting in higher heat transfer coefficients, i.e. lower thermal resistance. This is the reason why saturated liquid films cool better than subcooled liquid films, as explained in Chapter II. Figure 4.29 shows the effect of heat flux on the local heat transfer coefficient for downward mist flow in a 23.6 mm ID circular tube (PIPE 3) with a short (14 cm long) unheated entry length. The data correspond to an inlet average air velocity of 15 m/s with a 15 % water mass fraction. The gas-assisted nozzle is used with atomizing gas flow (i.e. pressure) corresponding to the optimal droplet mean diameter (~ 42 μm SMD). Different heat fluxes range from ~ 3.3 to 14.6 kW/m^2.

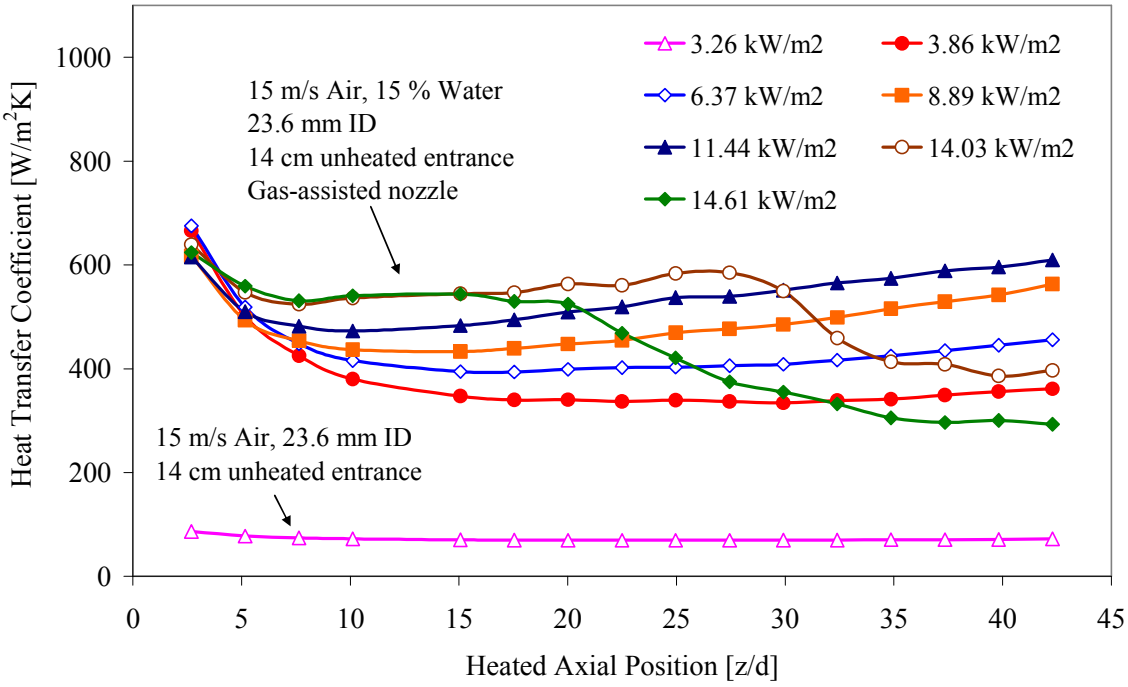

Figure 4.29 Effect of wall heat flux on the local heat transfer coefficient for downward mist flow in a circular tube with a short unheated entry length

Figure 4.29 also shows the local heat transfer coefficients obtained for single phase forced convection when only the carrier gas is used. This provides a clear evidence of the extent of enhancement in heat transfer achieved by mist cooling. The data clearly shows that the heat transfer coefficient for air/water mist flow increases with increasing wall heat flux provided that the liquid film remains intact. As the heat flux increases the film becomes unstable and breakdown occurs. The breakdown point signifies the formation of rivulet flow which causes a sudden decrease in the local heat transfer coefficient as shown in Figure 4.29 for the cases with heat fluxes of 14.03 and 14.61 kW/m^2. As the heat flux increases, the breakdown point moves closer to the test section entrance, as is typical in thermocapillary film breakdown. Therefore, the length of the channel is an

important parameter impacting the effectiveness of mist cooling. For short channels, film breakdown may not occur along the entire channel length even at elevated heat fluxes, i.e. downward mist flow is most suitable for high heat flux applications with short channels. Figure 4.29 shows that following the entrance region and establishment of fully-developed conditions, the heat transfer coefficient continues to increase due to enhanced evaporation caused by the increasing liquid film temperature as the film flows downward along the heated channel, coupled with the thinning of the liquid film. The increase in heat transfer with heat flux and with distance along the channel in the fully-developed region provide unambiguous proof that the heat transfer process is evaporation-driven. Further evidence is provided by the increasing slope of the fully developed local heat transfer coefficient lines as the heat flux increases. Figure 4.30 shows variations of the local measured wall temperatures and calculated bulk temperatures for the mist cooling cases shown in Figure 4.29. The measured wall temperatures represent both time and circumferential average values at each axial location. As the heat flux increases both the local wall temperature and bulk temperatures increase. It is these elevated wall temperatures which produce the higher heat transfer coefficients shown in Figure 4.29. The wall temperatures would have been even higher if the heat transfer coefficients had not increased due to the higher evaporation rates. For a given heat flux the local temperature difference between the wall and the mist decreases as the flow proceeds along the channel, provided that the film remains intact. Figure 4.30 clearly shows the rapid temperature rise associated with film breakdown at elevated heat fluxes near the test section exit. The dry patches associated with the rivulet flow regime

produce large azimuthal temperature gradients, and hence, higher average wall temperatures at these axial locations.

For a given heat flux, the calculated local bulk temperatures increases nearly linearly with position along the channel. The values are calculated using a steady state energy balance between the inlet and each axial location. The energy balance accounts for the enthalpy flux of the excess liquid at each location, while assuming the carrier gas in the core to be saturated (i.e. 100 % relative humidity). This causes the rate of increase in bulk temperature to slightly decrease as the flow proceeds along the heated channel.

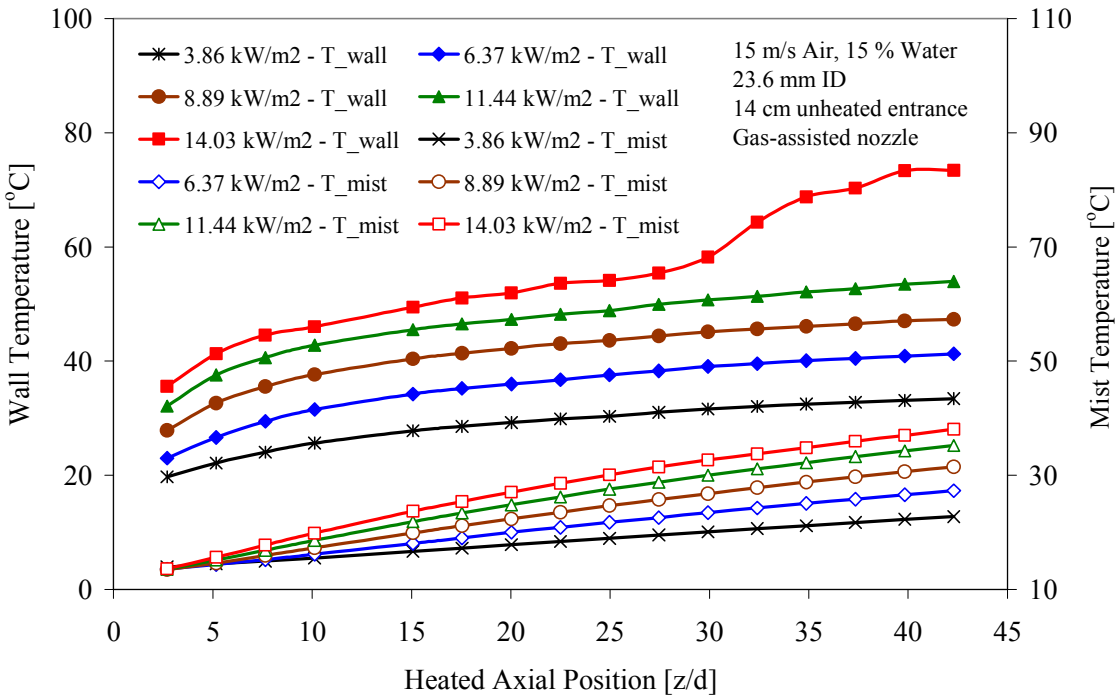

Figure 4.30 Effect of wall heat flux on the measured wall temperatures (top) and calculated bulk temperatures (bottom) for downward mist flow in a circular tube with a short entry length

As the bulk temperature increases, the local wall temperature also increases, consistent with the local heat transfer coefficient variations described earlier. For a given set of flow conditions, higher heat fluxes will always result in higher wall temperatures despite the increase in heat transfer coefficients.

At elevated heat fluxes, e.g. the case with a wall heat flux of 14.03 W/m^2, film breakdown at some point along the heated length causes the wall temperatures to rapidly increase signifying a rapid reduction in the local heat transfer coefficient. Nevertheless, the heat transfer coefficient remains significantly higher than the case of single-phase forced convection with the carrier gas alone. This can be seen in Figure 4.29. It can also be seen in Figure 4.31 where the wall and coolant bulk temperature distributions are shown for the air-only case at a heat flux of 3.26 kW/m^2 and the downward mist cooling case at a heat flux of 14.03 kW/m^2. The fact that the heat transfer coefficient after film breakdown remains higher than the corresponding single-phase value for air only indicates that liquid dryout (i.e. film starvation) is not the cause of the observed wall temperature rise for mist cooling; instead, the temperature rise is caused by film instability and transition to a rivulet flow regime.

It should be noted that the heat transfer coefficient values calculated for the post-film-breakdown region, are based on the time-and-circumferential average value of wall temperature (i.e. the average value of two diametrically opposed thermocouple readings). As expected, significant differenced of the readings of the two diametrically opposed thermocouples were obtained following the onset of rivulet flow. Hence, large azimuthal variations in the local heat transfer coefficients at these axial locations would be expected. The limited number of instrumented azimuthal locations (two) at each axial

elevations suggest that the true azimuthally-averaged heat transfer coefficients may be significantly different than these shown here. Nevertheless, the values shown here indicate the extent of deterioration in local heat transfer. More importantly, they can pinpoint the location of film breakdown for different operating conditions, which is important to know if and when mist cooling is being considered for a system with long coolant channels.

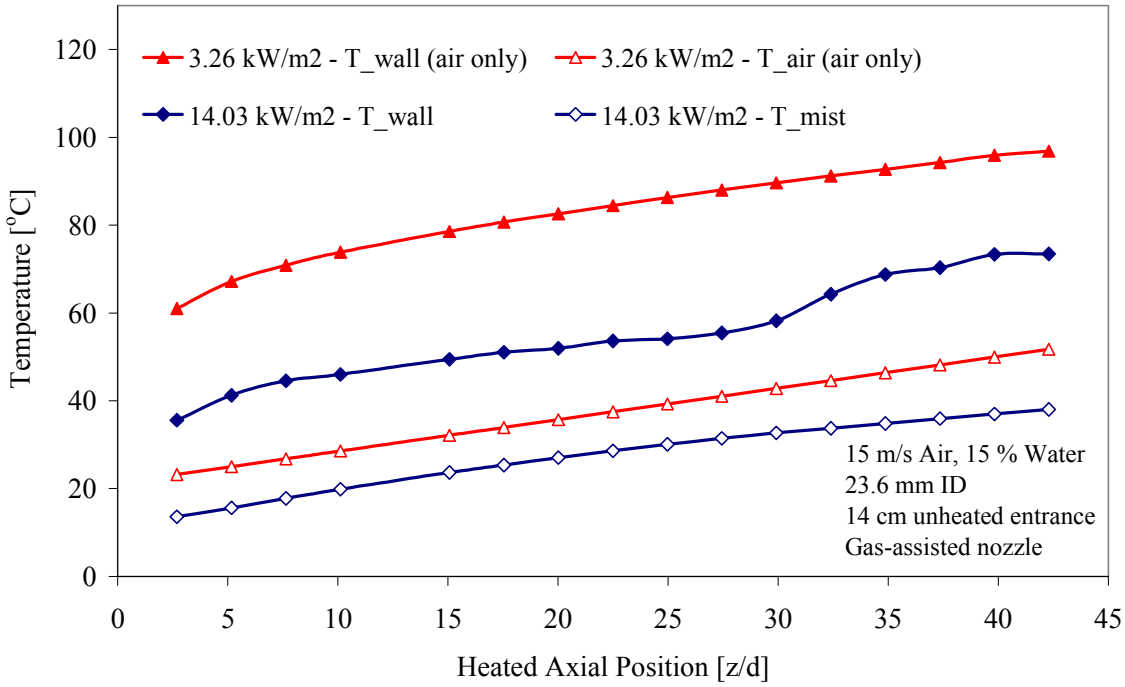

Figure 4.31 Wall and bulk temperature distributions for single-phase forced convection and downward mist flow in a circular tube with a short entry length

The data shown in Figure 4.29 have been used to calculated the corresponding enhancement ratios; i.e. the ratio between the local heat transfer coefficient and the corresponding value for single-phase forced convection using the carrier gas alone.

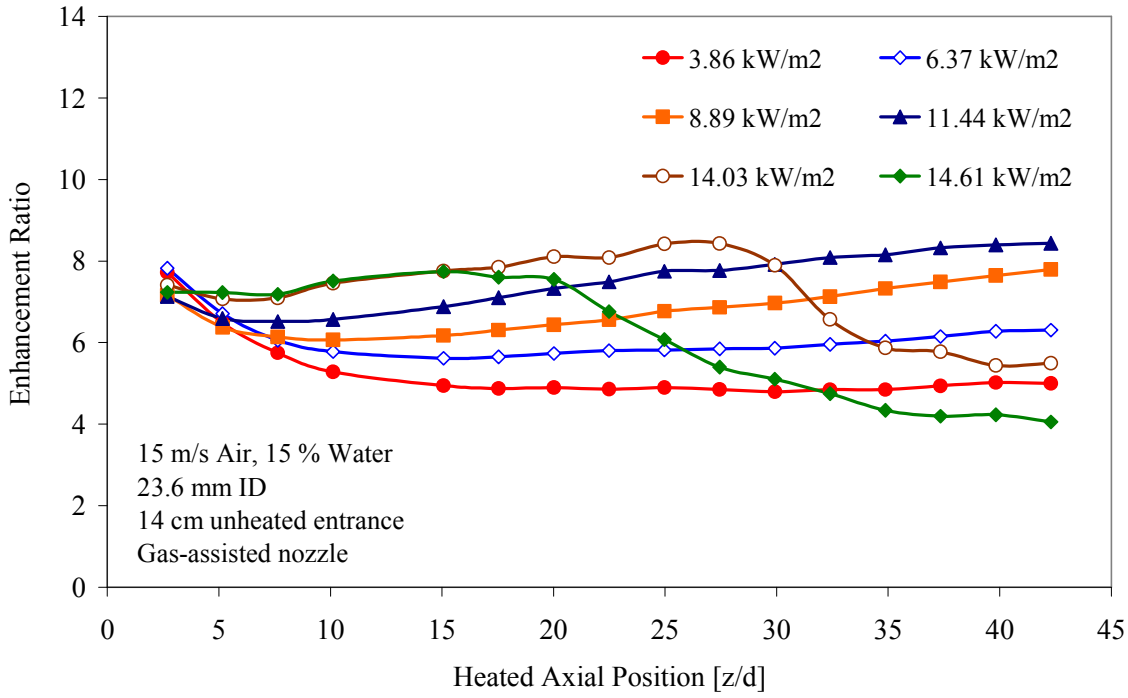

Figure 4.32 Effect of wall heat flux on the enhancement ratio for downward mist flow in circular tube with a short entry length

Enhancement ratios ranging from ~ 5.0 to 8.0 are obtained as the heat flux is increased. These results essentially mirror the changes in local heat transfer coefficients described above, inasmuch as the local single-phase heat transfer coefficient only drops slightly along the heated length.

In order to investigate the evaporation process at elevated wall temperatures, significantly higher carrier gas velocities and somewhat higher water mass fractions are used to insure film stability at those elevated temperatures. For this purpose, experiments have been conducted at a carrier gas velocity of 31.5 m/s and a water mass fraction of 19 %. The data shown in Figure 4.33 pertain to downward mist flow in a 23.6 mm ID circular tube (PIPE 3) with a short unheated length (14 cm). The atomizing gas flow rate (i.e. pressure) is adjusted to produce the optimal mean droplet diameter (~ 42 μm SMD)

corresponding to the water flow rate used. The experiments are conducted at elevated heat fluxes ranging from 12.4 to 51.1 kW/m^2. Figure 4.33 shows the resulting values of the local heat transfer coefficients; the corresponding wall temperatures are shown in Figure 4.34, while the calculated bulk temperatures are shown in Figure 4.35. Figure 4.33 also shows the local heat transfer coefficients obtained for single phase forced convection when only the carrier gas is used (4.5 kW/m^2 case). Again, it provides a clear evidence of the extent of enhancement in heat transfer achieved by mist cooling.

The data shows that as the heat flux increases, the heat transfer coefficients significantly increase; values over 2,200 W/m^{2}K are obtained near the test section exit at the highest heat flux (51.1 kW/m^2). This is clearly due to the enhanced evaporation obtained with increasing wall temperature (i.e. film interface temperature), coupled with the ability of the higher temperature carrier gas to contain more vapor when it is fully saturated. These two effects are the reason for the more rapid increase (i.e. higher slope) in heat transfer coefficient as the mist proceeds along the heated length (Figure 4.33) at elevated heat fluxes.

Figure 4.34 shows that the wall temperatures will always increase as the heat flux increases; it is these higher wall temperatures which result in the higher heat transfer coefficients due to enhanced evaporation. The wall temperatures would have been significantly higher without such enhancement. The non-linear dependence of the evaporation rate on temperature causes a less-than-proportional increase in wall temperature rise as the heat flux is increased. The enhancement becomes more pronounced at elevated heat fluxes; an enhancement ratio of nearly 18 has been obtained at a heat flux of 51.1 kW/m^2.

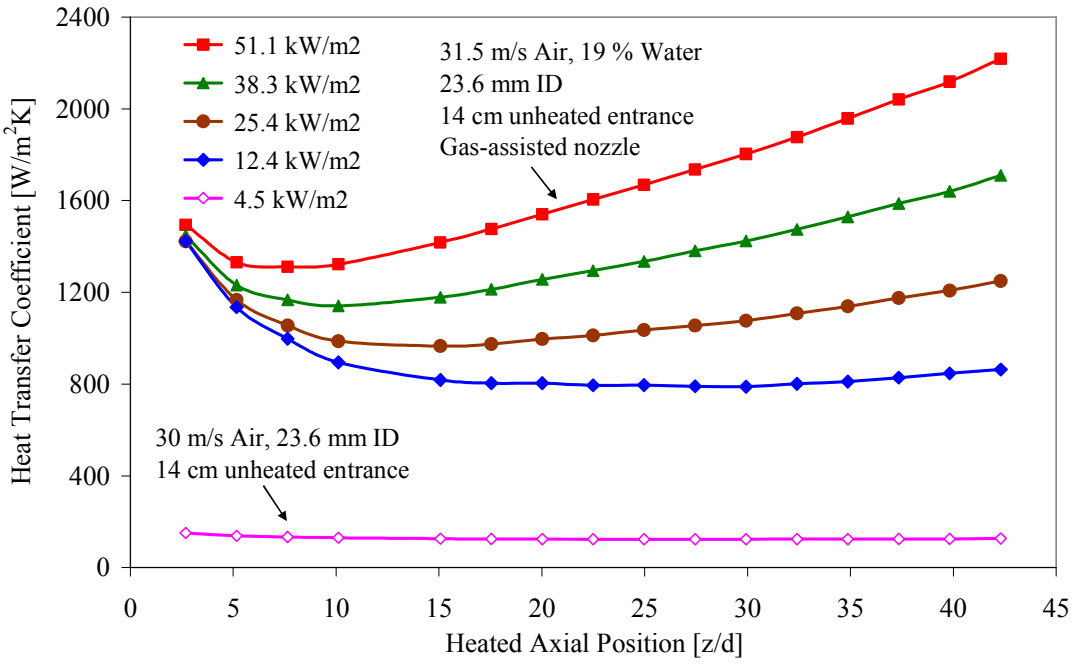

Figure 4.33 Variations of the local heat transfer coefficient for downward mist flow in a circular pipe at elevated wall heat fluxes

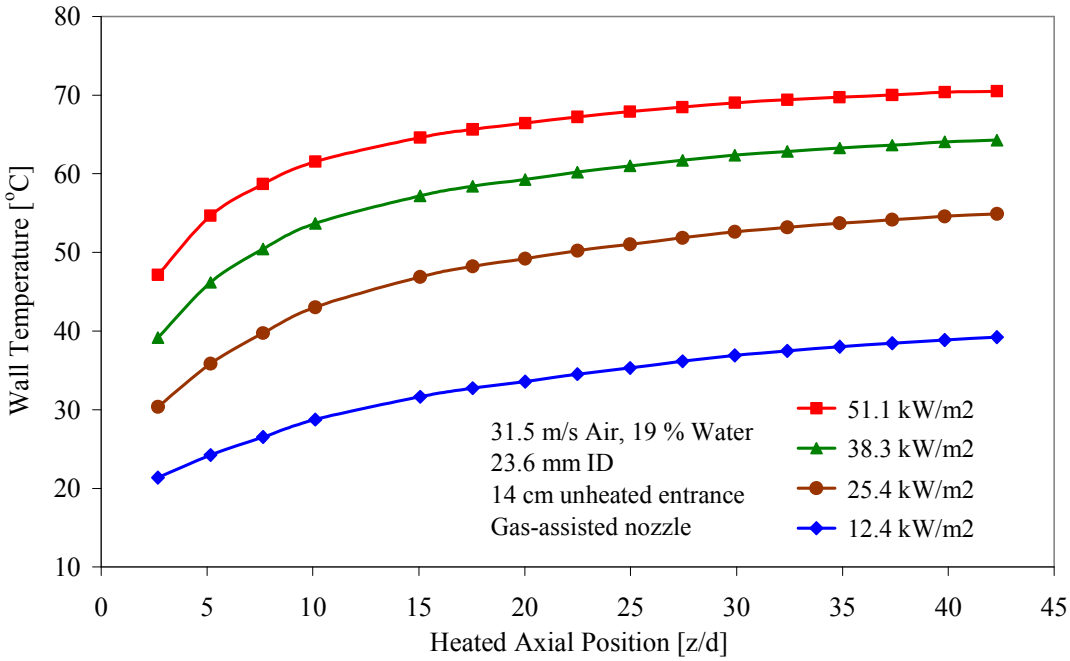

Figure 4.34 Variations of the wall temperature distribution for downward mist flow in a circular pipe at elevated heat fluxes

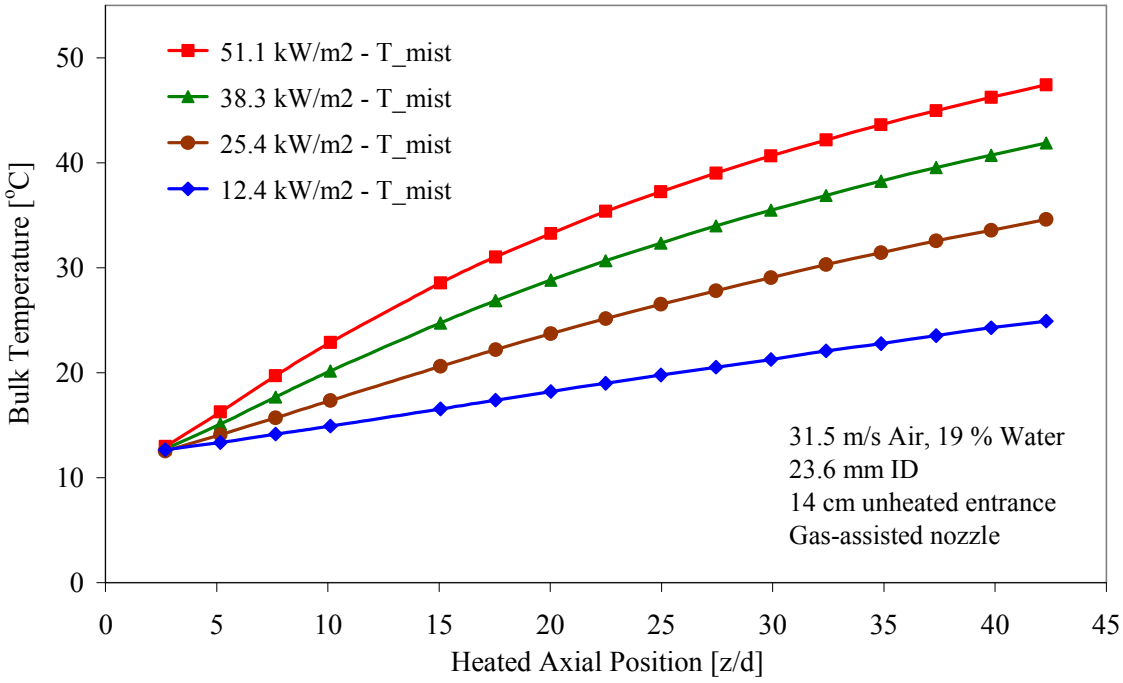

Figure 4.35 Variations of the calculated bulk temperature distribution for downward mist flow in a circular pipe at elevated heat fluxes

4.7 Effect of Water Mass Fraction

The injected water mass fraction, i.e. the ratio between the injected water mass flow rate and the mass flow rate of the carrier gas, is one of the most important parameters affecting the performance of internal mist cooling. Obviously, as long as there is enough water to form a thin water film on a test section walls, the evaporation would occur and heat transfer enhancement would result. However, since the nozzle generated liquid films are generally subcooled liquid films, the Marangoni effect plays an important role in film stability. Having a slightly thicker liquid film than the critical film thickness for thermocapillary breakdown would provide a more stable (i.e. more durable), but still thin, film which is needed for improved heat transfer. The effect of the injected water

mass fraction is demonstrated here for the case of downward mist flow in a 23.6 mm ID circular tube (PIPE 3) with a short (14 cm long) unheated entry length. The data pertain to experiments with an average carrier gas inlet velocity of 15 m/s; injected mass fractions of 5, 10, and 15 % have been used. To demonstrate the effect of water mass fraction on film stability, experiments have been conducted at different heat fluxes for each of the examined water mass fractions. All experiments were conducted using the gas-assisted atomizing nozzle with an atomizing air flow rate (i.e. pressure) corresponding to the optimum mean droplet diameter (~ 42 μm SMD).

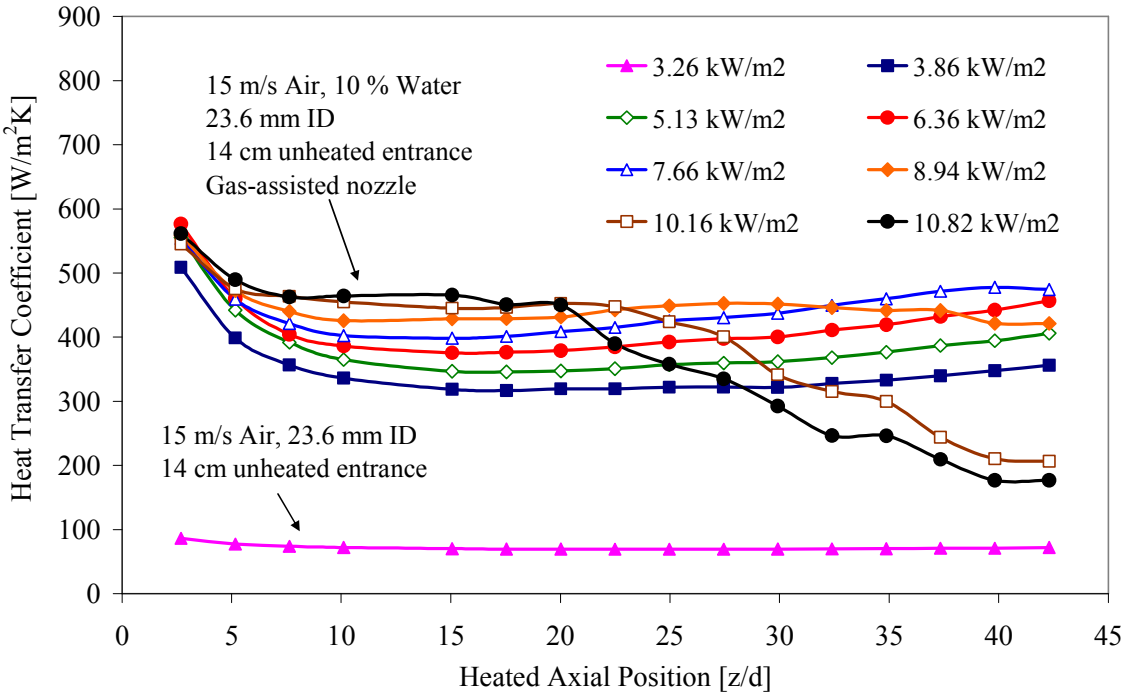

Figure 4.36 Effect of wall heat flux on local heat transfer coefficient for downward mist flow in a circular tube with an average air velocity of 15 m/s and water mass fraction of 10 %

Figure 4.36 shows variations of the local heat transfer coefficient with heat flux for and average inlet air velocity of 15 m/s and water mass fraction of 10 %. The corresponding data for a mass fraction of 15 % was previously shown (Figure 4.29). Comparison between the data shown in Figures 4.29 and 4.36 clearly indicate that for the same heat flux, the local heat transfer coefficient in the entry region decreases by ~ 10 % as the water mass fraction is decreased from 15 % to 10 %. More importantly the data indicate that as the injected liquid mass fraction decreases, the heat flux at which liquid film breakdown occurs also decreases. The data shown in Figure 4.36 suggest that a dry patch begins to form at the test section exit at a heat flux of 7.66 kW/m^2 and that significant fraction of the test section length is covered with dry patches at a heat flux of 8.94 kW/m^2, as evidenced by the reduction in heat transfer coefficient. Unstable dry patches, i.e. dry patches which intermittently rewetted, may not reduce the local heat transfer coefficient; instead they may simply decrease the rate at which the heat transfer coefficient increases along the channel length. On the other hand, stable dry patches, i.e. those which are not rewetted, would reduce the local heat transfer coefficient; however, they do not spread upstream or downstream as in rivulet flow. In this study, the formation of stable dry patches is considered to be the first indication of liquid film instability. For permanent dry patches to spread and turn into rivulet flow, a higher heat flux is needed as can be seen in Figure 4.36 for the 10.16 kW/m^2 heat flux case. In that case, a significant decrease in the heat transfer coefficient is observed along the remaining channel length.

It is important to note that there is little difference in the effectiveness of mist cooling with water mass fractions of 10 % and 15 % at the same heat fluxes as long as the liquid film remains intact. This can be seen in Figure 4.37 where the local heat transfer

coefficients at low heat fluxes with either 10 % or 15 % water mass fraction are shown. A slight enhancement in the local heat transfer coefficient in the entrance region is observed at a higher water mass fraction for heat fluxes of ~ 3.9 and 6.4 kW/m^2. However, the difference becomes vanishingly small as fully developed conditions are reached. This is consistent with the wall and bulk temperature distributions shown in Figure 4.38 where virtually identical temperatures are reached in the later half of the test section. This points to the fact that, regardless of the flow conditions, mist cooling will be effective as long as stable thin liquid film is maintained along the entire heated surface.

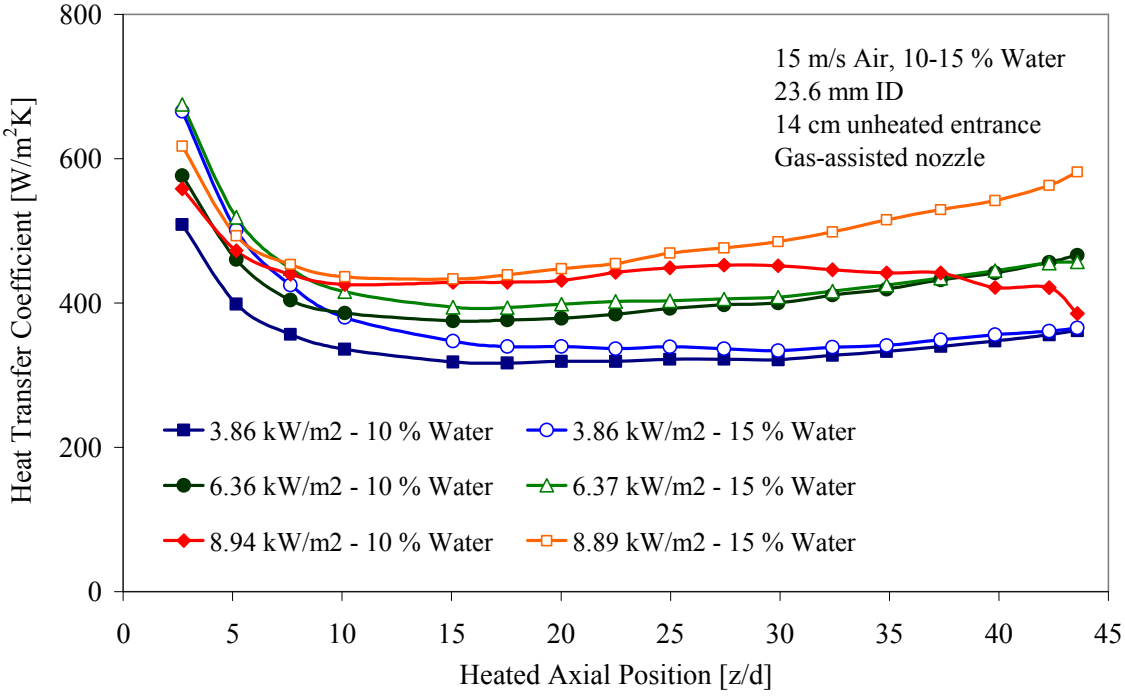

Figure 4.37 Effect of heat flux and injected water mass fraction on the heat transfer coefficients for downward mist flow in a circular tube

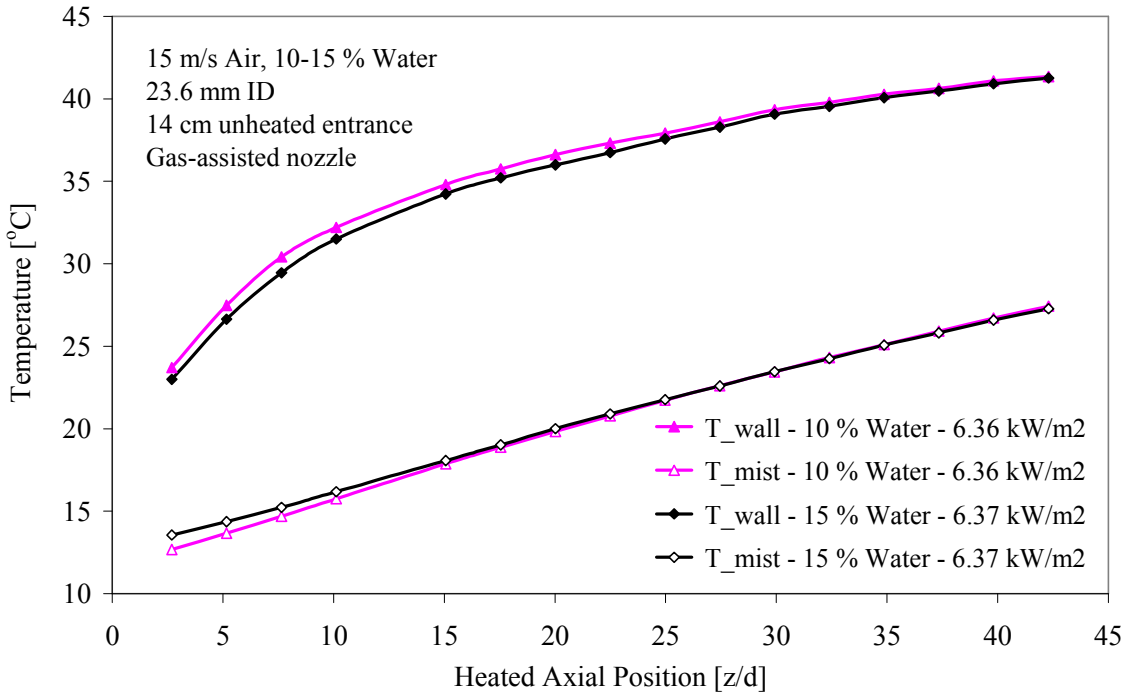

Figure 4.38 Effect of injected water mass fraction on the wall and bulk temperatures distributions for downward mist flow in a circular tube

The difference in the film thickness between the 10 % and 15 % water mass fraction cases is small enough in these two low heat flux cases that it does not introduce noticeable thermal resistance increase in the heat transfer from the test section walls to the liquid film/carrier gas interface where the evaporation process is occurring. The slightly higher heat transfer coefficient for the 15 % water mass fraction cases, may be attributed to the higher convective heat removal capability of the liquid film itself particularly near the test section inlet. The effect of thinner liquid film (with lower mass fractions) manifests itself farther downstream where improved heat transfer may be obtained with lower mass fractions as long as the liquid film remains intact. This effect is very slight, however, as evident by the "line crossing" of the 10 % and 15 % cases in

Figure 4.37 for a heat flux of 6.4 kW/m^2. In general, for mist cooling with subcooled liquid films, a small reduction in film thickness will likely not show its heat transfer benefits unless the test section is of considerable length. Furthermore, due to the strong Marangoni effect for thin (50 μm to 100 μm) subcooled liquid films, it is possible that a thermocapillary breakdown may occur before the film thickness benefits could show their affect. The 8.9 kW/m^2 heat flux cases shown in Figure 4.37 are a good example of that effect. Due to the higher heat flux, the entrance region difference in heat transfer coefficients for the 10 % and 15 % water mass fractions is reduced since the liquid film temperature is increasing faster in the 10 % water mass fraction case, which enhances evaporation early on in the test section, thereby reducing the advantages of the increased (15 %) water mass fraction case. After the entrance region, the heat transfer coefficients for the 10 % water case rapidly approaches those for 15 % water case. However, approximately one third of the way along the heated length, evidence of dry patch formation first appears thereby preventing any further increases in the local heat transfer coefficient. The local heat transfer coefficient eventually begins to decrease as film breakdown progresses and the rivulet flow regime is established. The data shown in Figures 4.29, 4.36 and 4.37, suggest that higher water mass fractions provide enhanced heat transfer. More importantly however, with higher mass fractions, film breakdown is delayed until the heat flux reaches a considerably higher value, since thicker films are more resistant to the Marangoni effect, and can delay thermocapillary breakdown to higher heat fluxes, thereby yielding higher heat transfer coefficients. Hence, it can be concluded that slightly thicker liquid films (i.e. larger injected liquid mass fractions) are preferred since they produce high heat transfer coefficients and, more importantly,

postpone film breakdown until a much higher heat flux is reached. The enhancement in local heat transfer coefficients is particularly evident in short channels. Strictly speaking, however, for the Electra hibachi structure, because of beam attenuation considerations, the optimum conditions are reached when using the lowest mass fraction which can assure film stability over the entire heated length at the maximum expected heat flux. However, uncertainty over the exact mass value of mass fraction corresponding to film breakdown makes it prudent to use a higher liquid injection rate.

The wall and bulk temperature distributions corresponding to the experiments presented in Figure 4.36 for a 10 % water injection mass fraction are shown in Figure 4.39. These results show similar behavior to those corresponding to the 15 % water mass fraction experiments presented in Figure 4.30. Again, the calculated bulk temperatures increase nearly linearly with distance along the flow direction; these values are, again, calculated using an energy balance between the inlet and each axial location. They account for the enthalpy flux of the excess liquid at each location and assume the carrier gas in the core to be saturated (100 % relative humidity). As the bulk temperature increases, the local wall temperature also increases consistent with the local heat transfer coefficient variations shown in Figure 4.36. The first indication of dry patch formation near the test section exit is observed at a heat flux of 8.94 kW/m^2. For that case, a slightly higher rate of increase in wall temperature is observed near the end of the heated section which signifies slightly decreased heat transfer conditions. When the heat flux is further increased to 10.16 kW/m^2, the data shows clear evidence of film breakdown beginning near the middle of the heated test section. These results are qualitatively similar to those shown in Figure 4.30 for the case of 15 % water mass fraction, except for the fact that the

onset of film instability occurs at a significantly lower heat flux when the water mass fraction is reduced.

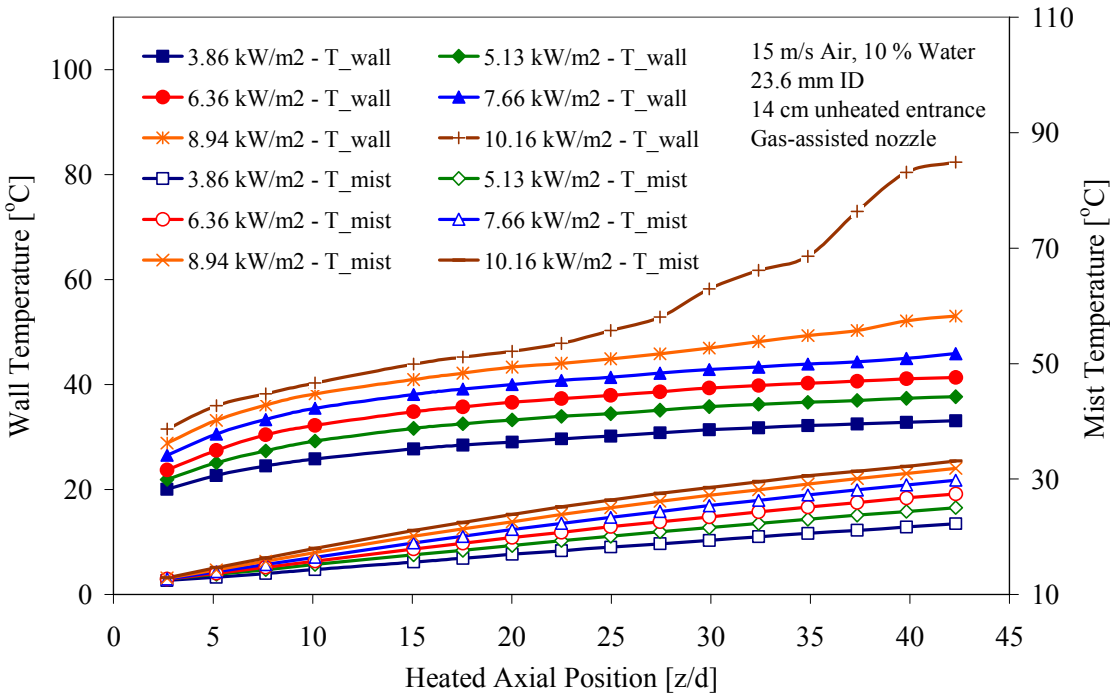

Figure 4.39 Effect of wall heat flux on the measured wall temperatures (top) and calculated bulk temperatures (bottom) for downward mist flow in a circular tube with a short entry length

The calculated enhancement ratios for the heat transfer coefficient data in Figure 4.36 are shown in Figure 4.40. These results correspond to an injected water mass fraction of 10 %; the maximum enhancement ratio after the entrance region in this case is 6.7, as compared to 8.4 in Figure 4.32 for the case of 15 m/s air velocity with 15 % water mass fraction. This lower enhancement is primarily due to the lower heat fluxes at which the experiments were conducted because of film breakdown limitations; additional reduction in the enhancement ratio can be attributed to the lower water flow rate, which

reduces the forced convection cooling contribution provided by the liquid film itself. Therefore, unlike the case of saturated liquid films where a thinner film is desirable for better cooling performance, thinner films may not always produce the highest heat transfer coefficients in nozzle-generated subcooled thin liquid films, which are also more susceptible to breakdown by thermocapillary forces.

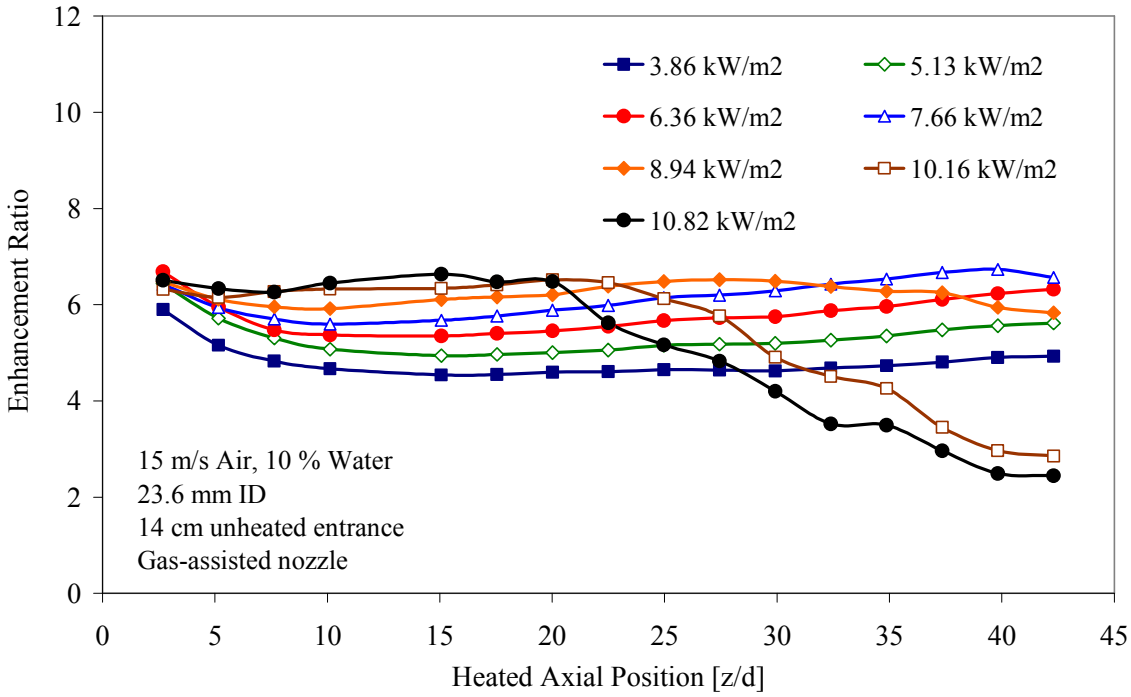

Figure 4.40 Effect of wall heat flux on the enhancement ratio for downward mist flow in a 23.6 mm ID circular tube with an air velocity of 15 m/s and 10 % injected water mass fraction

Figure 4.41 shows the local heat transfer coefficients for downward mist flow in a 23.6 mm ID circular tube (PIPE 3) with short (14 cm long) unheated length using an even lower injected water mass fraction. The data pertain to experiments with an average carrier gas inlet velocity of 15 m/s with an injected water mass fraction of 5 %. Again,

the atomization air flow rate (i.e. pressure) supplied to the nozzle corresponds to the optimum mean droplet diameter (42 μm SMD). The corresponding enhancement ratios are given in Figure 4.42. Again, these data are qualitatively similar to those presented earlier for water mass fractions of 10 % and 15 %. They show that the heat transfer coefficient in the entry region is slightly reduced (~ 10 % compared to those for the case of 10 % water mass fraction) as the water injection rate is reduced. More importantly, they show that dry patch formation and establishment of rivulet flow occur at even lower heat fluxes compared to those for the case of 10 % water mass fraction.

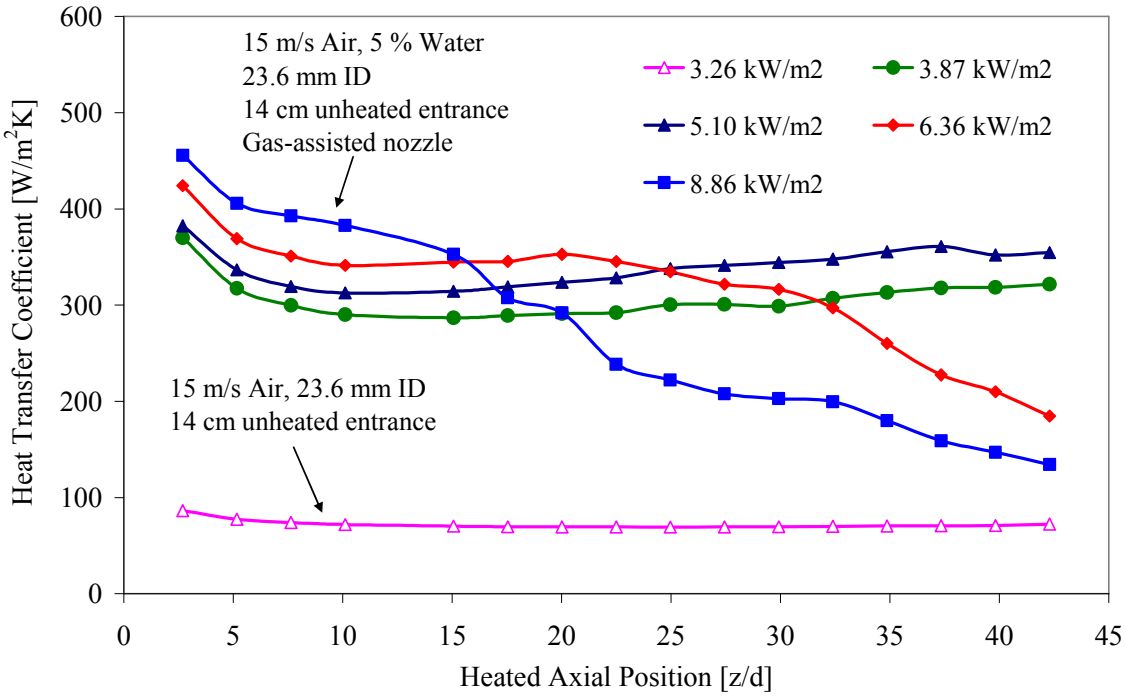

Figure 4.41 Effect of wall heat flux on the local heat transfer coefficients for downward mist flow in a 23.6 mm ID circular tube with 15 m/s air velocity and 5 % injected water mass fraction

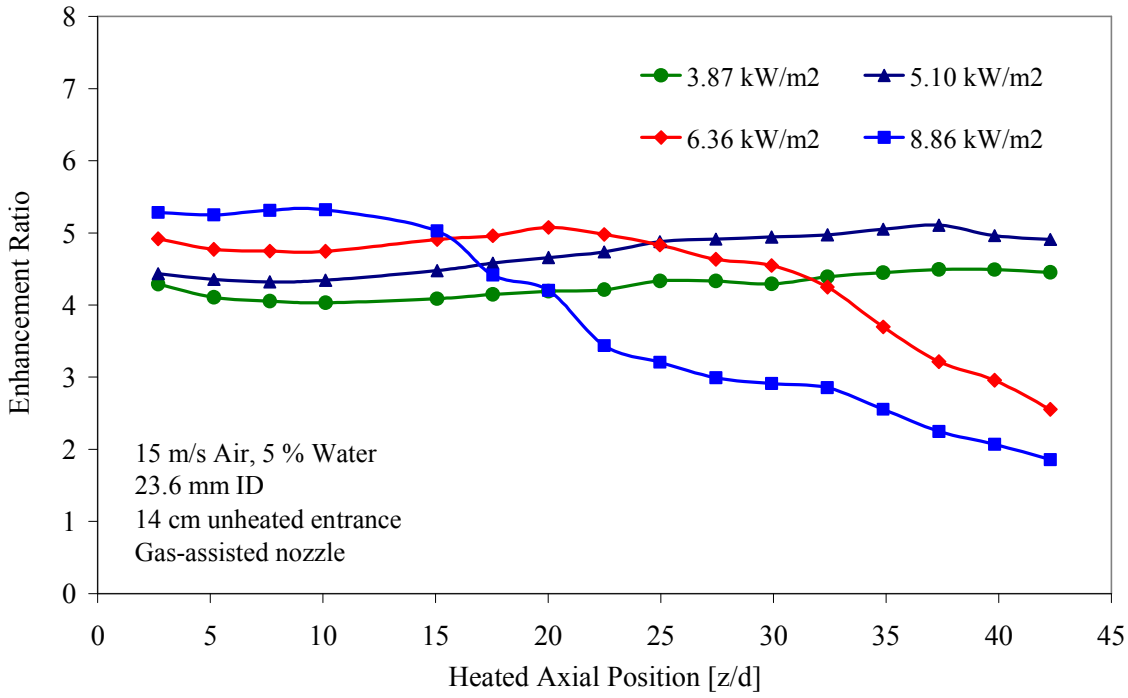

Figure 4.42 Effect of wall heat flux on the enhancement ratio for downward mist flow in a 23.6 mm ID circular tube with 15 m/s air velocity and 5 % injected water mass fraction

The highest enhancement ratio obtained in this case is 5.1, as compared to 6.7 and 8.4 for the cases with 10 % and 15 % water mass fractions, respectively. Again, this is primarily due to the lower heat fluxes at which the 5 % water mass fraction experiments have to be conducted in order to prevent film breakdown; additional reduction in the enhancement ratio can be attributed to the lower film flow rate which reduces the forced convection contribution of the liquid film itself.

In order to provide a more consistent comparison between the cooling effectiveness to be achieved with different water mass fractions for a given carrier gas velocity, comparison has been made between the highest achievable values of local heat transfer coefficient without film breakdown anywhere along the channel. This clearly

corresponds to the maximum heat transfer coefficient obtained at the highest heat flux at which the test section can be operated with that mass fraction at the point when stable dry patched are first formed. The data shown in Figures 4.29, 4.36, and 4.41 were used to extract those values; heat transfer coefficients of 362, 478, and 613 W/m^2K were obtained for water mass fraction of 5 %, 10 %, and 15 %, respectively. The corresponding heat flux values at which these peak heat transfer coefficients were observed were approximately 5.10, 7.67, and 12.74 kW/m^2, respectively (see Figure 4.43).

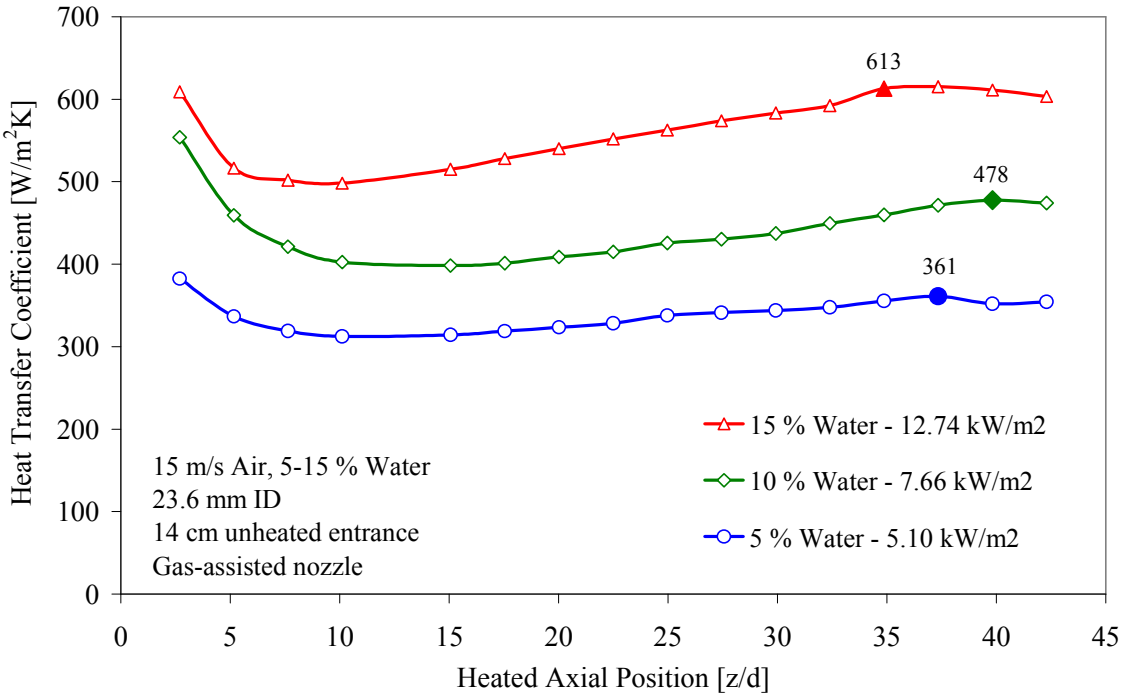

Figure 4.43 Effect of injected water mass fraction on the local heat transfer coefficients for downward mist flow in a 23.6 mm ID circular pipe with a short entry length (14 cm). The heat fluxes correspond to the onset of film instability at each water mass fraction

Figure 4.44 shows variation of the maximum achievable local heat transfer coefficient with the injection water mass fraction; all other variables, except the wall heat flux, are kept the same. The results show a nearly linear relationship between the maximum achievable local heat transfer coefficient and the injected water mass fraction. These results pertain to the 23.6 mm ID tube with a short unheated entry length (14 cm) and 15 m/s average inlet air velocity. Similar monotonic, nearly-linear, variations have been observed for other test conditions (e.g. a different carrier gas velocity).

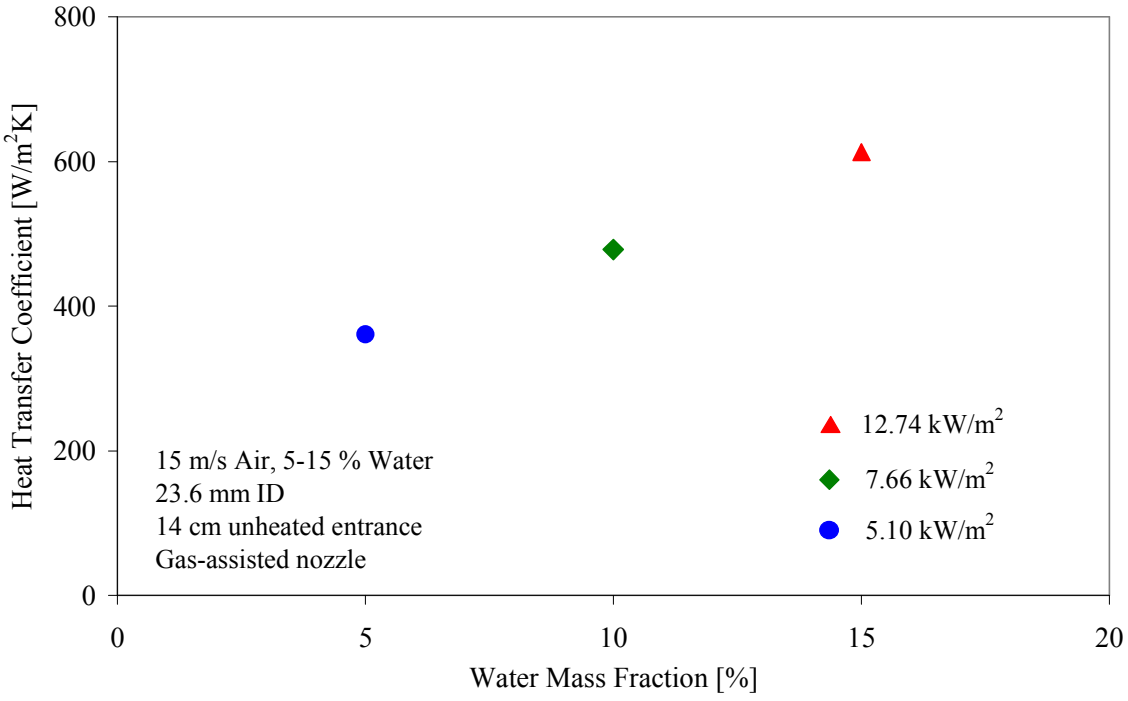

Figure 4.44 Variation of the maximum achievable local heat transfer coefficient with injected water mass fraction for downward mist flow in a 23.6 mm ID circular tube with a short entry length at a carrier gas velocity of 15 m/s

The results presented so far support the conclusion that for a given heat flux, increasing the water injection rate enhances heat transfer and improves film stability by delaying thermocapillary breakdown to higher heat fluxes. One may argue that such a trend cannot maintained indefinitely since the liquid film thickness increases with the water injection rate which increases the conduction component of the overall thermal resistance between the wall and the flowing mist core. In other words, one would expect that for a given heat flux and carrier gas velocity the local heat transfer coefficients near the test section exit would eventually decrease as the injected water mass fraction increases. Figure 4.45 shows the wall, inlet wet bulb, air and water line temperatures for experiments conducted using 17.3 mm ID circular tube (PIPE 2) with a short unheated entry length (14 cm). The carrier gas inlet velocity and heat flux were kept constant at 6 m/s and 0.62 kW/m^2, respectively. The injected water mass fraction was varied from 10 % to more than 200 %. In all cases, however, the atomizing gas flow rate (i.e. pressure) was adjusted to produce the optimum droplet size (~ 42 μm SMD). The wall temperatures at two specific axial locations, namely z/d = 17.6 and 26.5, are shown.

The main air line temperature is plotted in order to confirm that conditions had not changed during these five independent runs. The temperatures of the atomization gas line and the water line were nearly the same and were also unchanged during the experiments. The inlet wet bulb temperature is measured by a thermocouple located in the entrance instrument block. It indicated that the lowest inlet wet bulb temperature is achieved for the 10 % water injection case, since the air humidification process before the heated test section is adiabatic.

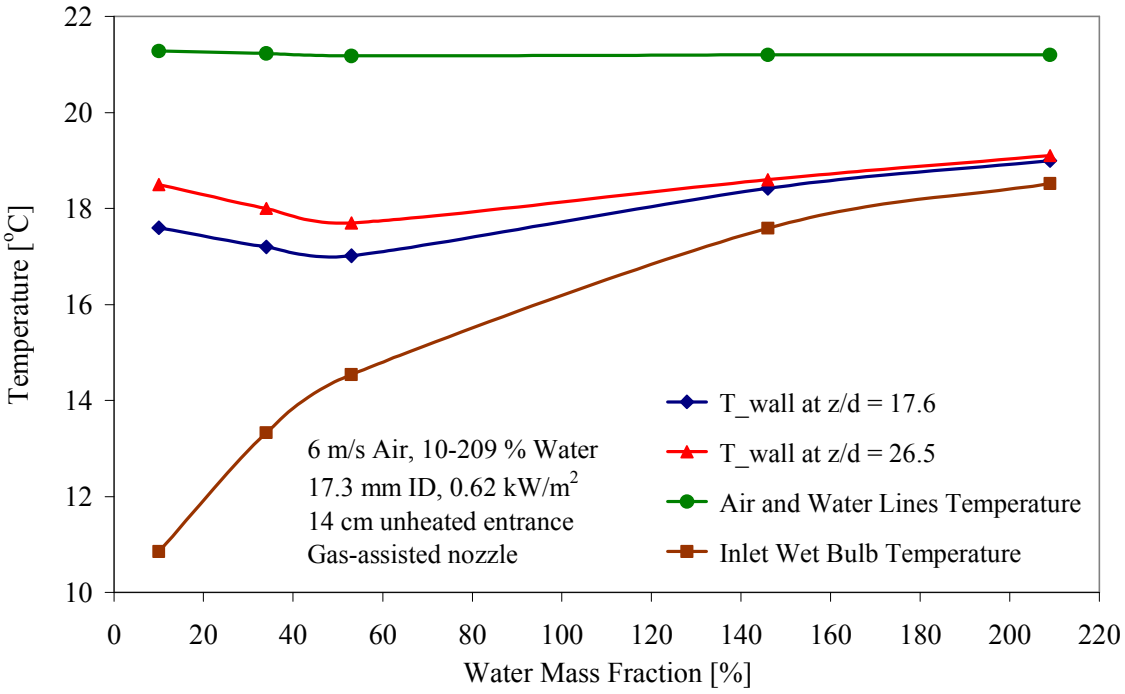

Figure 4.45 Variations of the wall, inlet wet bulb, air and water line temperatures with injected water mass fraction for downward mist flow in a circular pipe at a constant carrier gas velocity (6 m/s) and wall heat flux (0.62 kW/m^2)

The wall temperatures at heated axial positions z/d = 17.6 and z/d = 26.5 are plotted as a function of water mass fraction to demonstrate the liquid film thickness effect. For the conditions used in these experiments, as the water mass fraction increases from 10 % to nearly 55 % the wall temperatures at these two axial locations decrease indicating a higher local heat transfer coefficient. However, as the liquid mass fraction is further increased, the local wall temperatures at these two locations increase, signifying a reduced heat transfer coefficient due to the increased film thickness. The limited number of data points makes it difficult to exactly pinpoint the point at which the lowest wall temperatures are reached. Nevertheless, these data demonstrate the postulated hypothesis

with regard to the effect of increasing film thickness. The relatively low values of carrier gas velocity and wall heat flux use in these experiments were dictated by the capabilities of the test apparatus to provide the necessary water flow at the maximum examined mass fraction. For the main application of interest hear, namely, mist cooling of the Electra hibachi foils, operation is expected at water mass fractions well below those corresponding to the point of minimum wall temperatures; low water flow rates are desirable from a beam attenuation stand point, which suggests operation at the lowest water mass fraction which can confidently assume the presence of a continuous water film over the entire heated surface.

4.8 Effect of Carrier Gas Velocity

The effect of the carrier gas velocity, i.e. carrier gas flow rate for a given test section flow area and inlet density, can be studied from two perspectives, namely, while keeping either the same water flow rate or the same water mass fraction. Experiments have been conducted to quantify these effects.

4.8.1 Constant Water Mass Flow Rate

Experiments aimed at quantifying the effect of carrier gas velocity while maintaining the same water injection rate are first described. Figure 4.46 compares the case of an average carrier gas inlet velocity of 10 m/s with an injected water mass fraction of 15 % against the case of an inlet carrier gas velocity of 15 m/s with an injected water mass fraction of 10 %. The data pertains to downward mist flow through a 23.6 mm ID circular tube (PIPE 3) with a short unheated entry length (14 cm). Two heat flux

values, viz. ~ 5.1 and 7.6 kW/m^2, are used. In all cases, the atomizing gas flow rate (i.e. pressure) was selected to produce the optimum mean droplet diameter (~ 42 μm SMD).

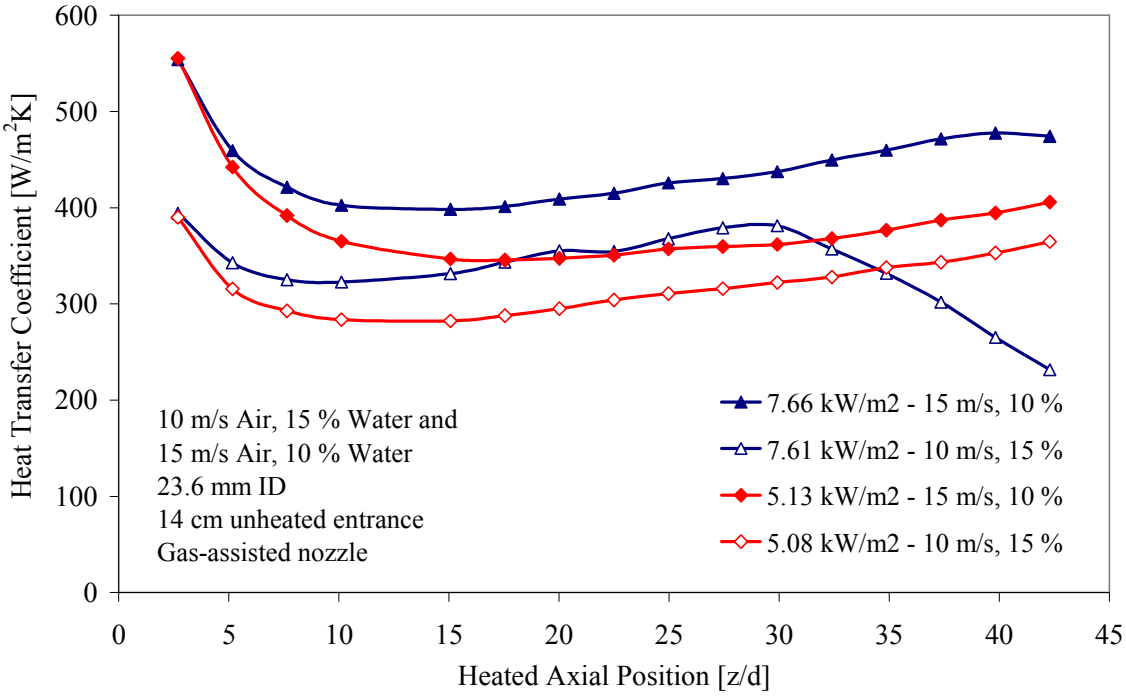

Figure 4.46 Variation of the local heat transfer coefficient in a circular tube for downward mist flow with carrier gas velocity for a constant injected water mass flow rate and heat flux

Assuming the average velocity in the co-current flowing liquid film to be proportional to the carrier gas velocity suggests that the liquid film thickness is proportional to the injected water mass fraction. Therefore, the 10 m/s air/15 % water case would be expected to have a thicker liquid film than the 15 m/s air/10 % water case. The difference in film thicknesses between those two cases is comparable to that for the 15 m/s air/15 % water and 15 m/s air/10 % water cases shown in Figure 4.37, which produce nearly the same value for the fully-developed heat transfer coefficient. Hence, one may conclude

that the difference in film thicknesses for these two cases is not the reason for the large difference in heat transfer coefficients observed in Figure 4.46. Additionally, a change in gas velocity from 10 to 15 m/s would result in a relatively small increase (~ 20 W/m^2K) in the single phase forced convection heat transfer coefficient. Therefore, the results shown in Figure 4.46 show that for mist flow increasing the gas velocity while keeping the same water injection rate results in significantly higher heat transfer coefficients. This effect can be attributed to the ability of the higher gas flow rate to absorb more vapor, which enhances the film evaporation process, and therefore, significantly increases the heat transfer coefficients. The data also show that for the same liquid mass flow rate and wall heat flux, an increase in the carrier gas velocity promotes film stability. This can be readily seen by comparing the higher heat flux cases (7.6 kW/m^2) shown in Figure 4.46; film breakdown is clearly evident at the lower (10 m/s) gas velocity, while a stable film is maintained along nearly the entire heated length for the higher velocity (15 m/s) case. This can be impacted by two effects; namely, the lower wall temperature obtained at the higher gas velocity (see Figure 4.47), and the increased shear forces acting on the liquid film. Despite the lower wall temperature for the 15 m/s velocity case, i.e. despite the lower vapor pressure at the liquid film/gas core interface, higher vapor mass flux may result because of the increase in mass transfer coefficient at the interface and the ability of the increased carrier gas flow rate to accommodate higher vapor flow rates.

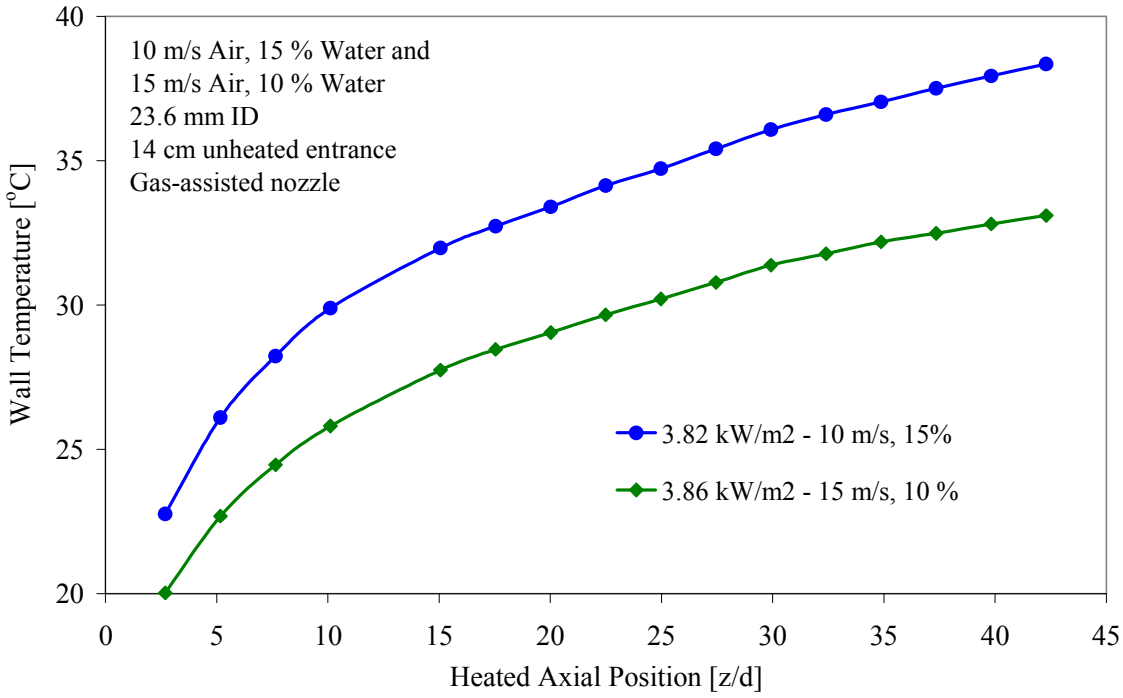

Figure 4.47 Variation of the wall temperature distribution with carrier gas velocity for downward mist flow with constant water injection flow rate and wall heat flux

While it is not readily evident, the data shown in Figure 4.48 suggests that even though the case with 15 m/s air velocity and 10 % water mass fraction has a higher heat transfer coefficient and a lower wall temperature, it shows the signs of the first liquid film instability, i.e. stable dry patches, at a lower temperatures than the case with 10 m/s air velocity and 15 % water mass fraction. This suggests that a thicker liquid film is more resistant to the onset of breakdown than a thinner film, assuming they both have the same wall temperature and film flow rate. Therefore, for this case, the film thickness appears to be more important than the shearing force at the film/gas interface.

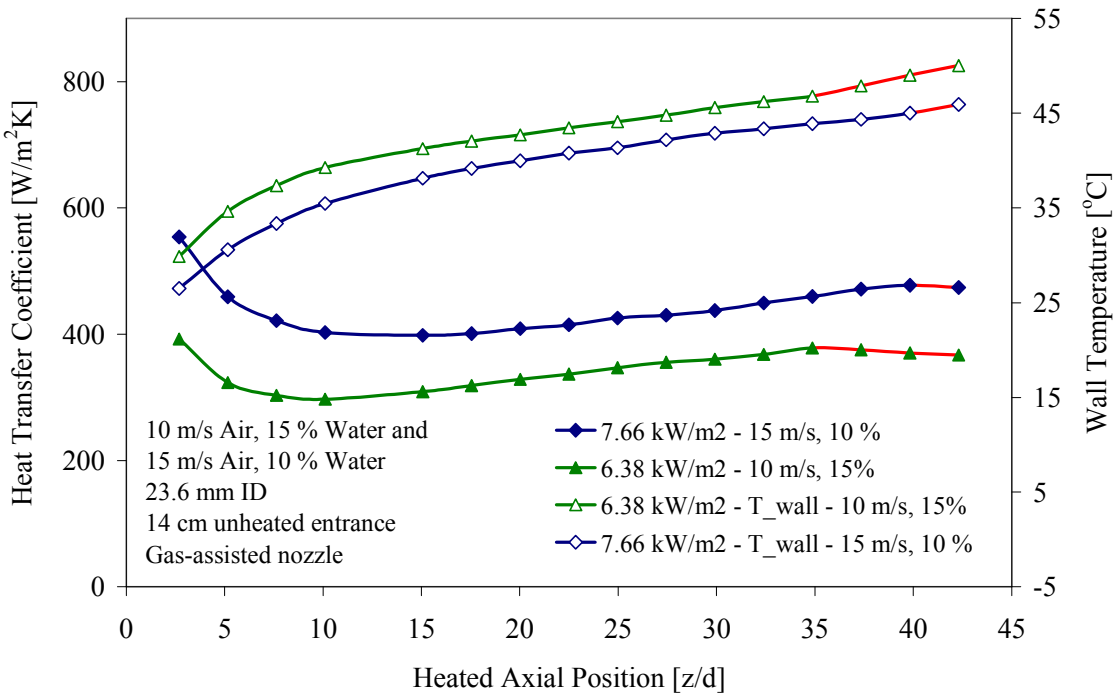

Figure 4.48 Variation of the heat transfer coefficient and wall temperature with carrier gas velocity for downward mist flow with constant water injection flow rate and wall heat flux

Figure 4.49 shows the enhancement ratios corresponding to heat transfer coefficient data given in Figure 4.46. The case with 10 m/s air velocity and 15 % water has significantly higher enhancement ratios than those for the case with 15 m/s air velocity and 10 % water mass fraction. This effect is primarily due to the fact that the forced convection heat transfer coefficient against which the mist cooling heat transfer coefficients are compared, is nearly 30 % lower for the 10 m/s air velocity case than the corresponding value for 15 m/s.

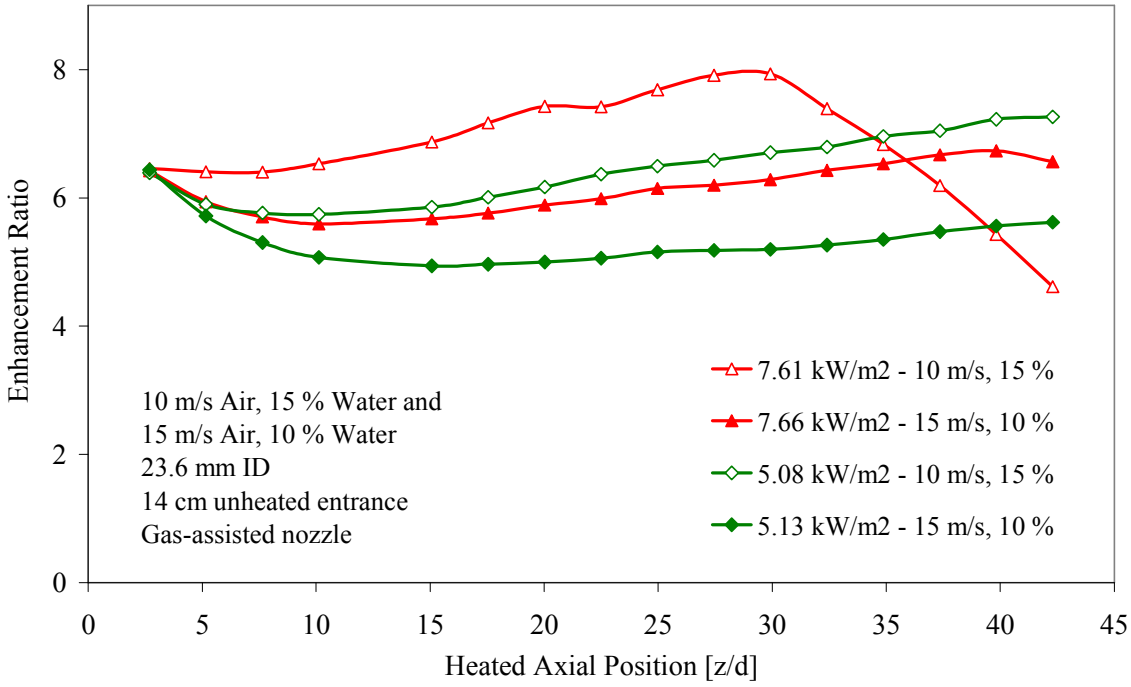

Figure 4.49 Variation of enhancement ratio for downward mist flow an a circular pipe with carrier gas velocity with constant water injection flow rate and wall heat flux

4.8.2 Constant Water Mass Fraction

Assuming the average velocity in the co-current flowing liquid film to be proportional to the carrier gas velocity suggests that the liquid film thickness is proportional to the injected water mass fraction. Hence, comparison has been made between experiments where the carrier gas velocity is varied while keeping the same injected water mass fraction. Figure 4.50 compares the local heat transfer coefficient values for three different carrier gas velocities (5, 10, and 15 m/s) with a 15 % injected water mass fraction. The data pertains to downward mist flow in a 23.6 mm ID circular tube (PIPE 3) with a short (14 cm) unheated entry length. As expected, the 15 m/s case

has the highest heat transfer coefficient followed by the case with 10 m/s, and finally the 5 m/s case. It should be noted that since the injected water mass fraction is kept constant, the injected water mass flow rate for the 15 m/s case is 50 % higher than that for the 10 m/s case and three times higher than that for the 5 m/s case. The low water mass flow rate for the 5 m/s case caused the liquid film to readily rupture midway along the channel length even though the heat flux was lower than the other two cases (~ 3.2 versus 3.8 kW/m^2).

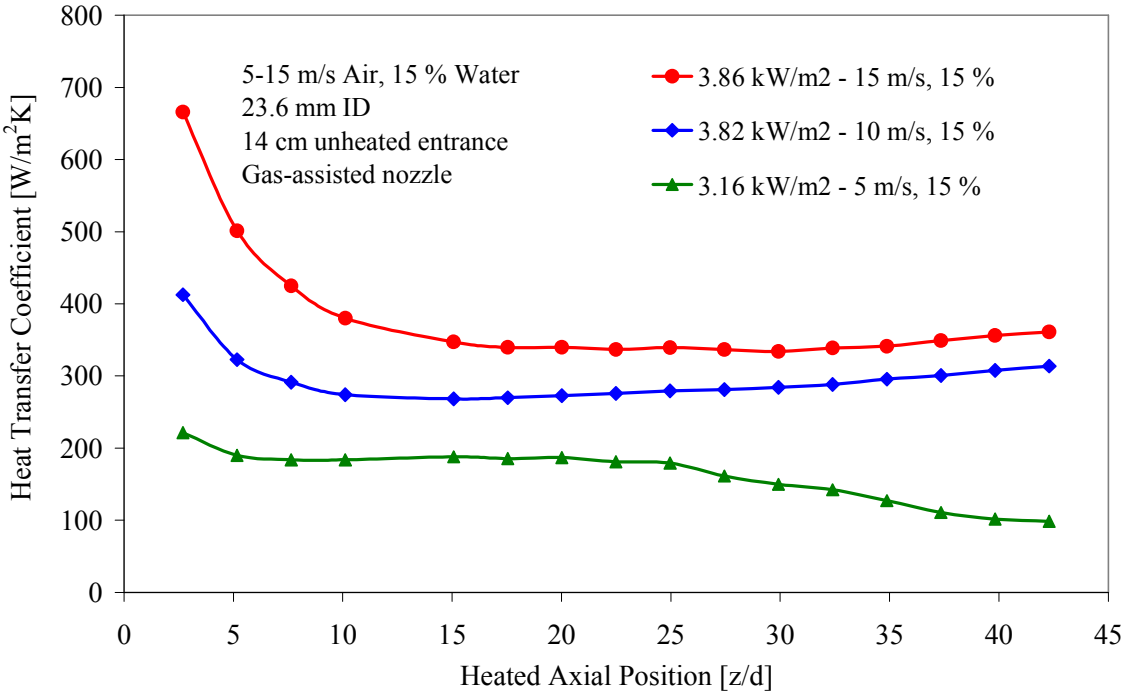

Figure 4.50 Variation of the local heat transfer coefficient with carrier gas velocity for downward mist flow in a circular pipe with a constant water mass fraction

The wall temperature distributions corresponding to the three experiments presented in Figure 4.50 are shown in Figure 4.51. As expected, lower wall temperatures are

obtained as the carrier gas velocity increased. Also, early film rupture and transition to rivulet flow can be readily seen for the lowest velocity (5 m/s) case.

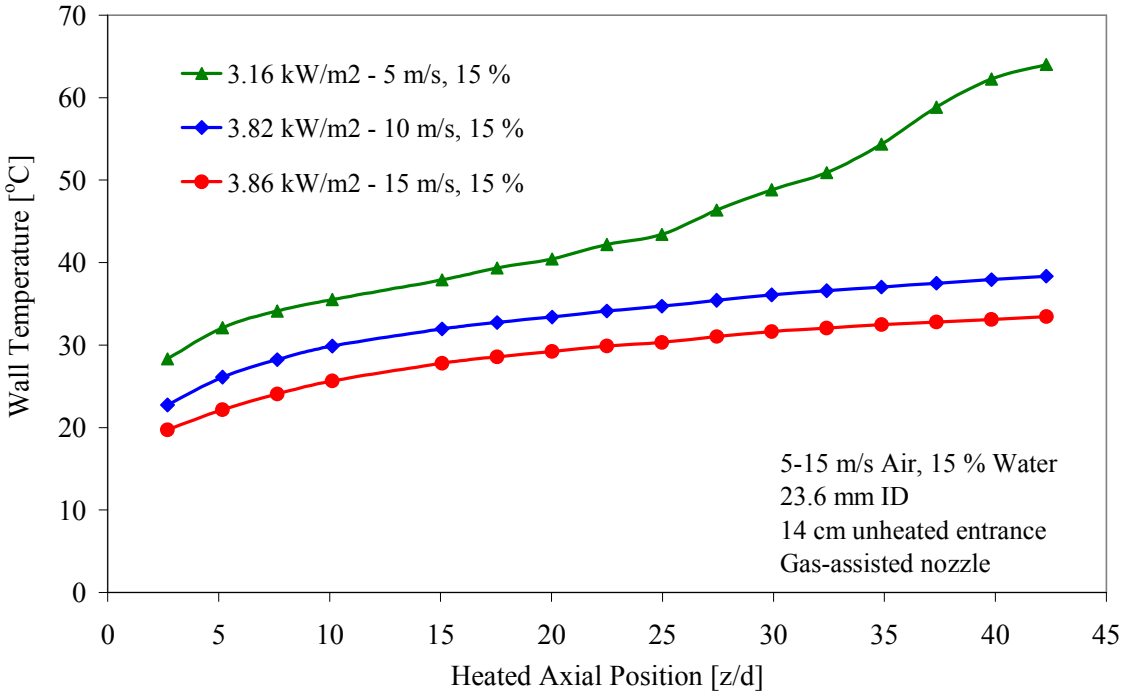

Figure 4.51 Variation of the wall temperature with carrier gas velocity for downward mist flow in a circular pipe with a constant water mass fraction

Experiments have also been conducted for the same three flow conditions (5, 10, and 15 m/s air velocity with 15 % water mass fraction) with progressively higher heat flux. The data have been used to determine the heat flux at which the first indications of film breakdown are observed. Heat flux values of 2.52, 6.38, and 12.74 kW/m^2 have been determined for the onset of film breakdown at carrier gas velocities of 5, 10, and 15 m/s, respectively. Figure 4.52 shows the local heat flux coefficients obtained in these three experiments. Significantly higher heat transfer coefficients are obtained as the carrier gas

velocity is increased; peak values of 181, 378, and 613 kW/m^{2}K were obtained at carrier gas velocities of 5, 10, and 15 m/s respectively. This is to be expected because of the higher heat flux at which the higher velocity (i.e. higher water flow rate) exhibits indications of film breakdown near the test section exit. Naturally, if the film thickness is really the same in these three cases, the enhanced evaporation obtained at the elevated heat flux (i.e. higher temperature) case will produce a higher heat transfer coefficient. This can be seen in Figure 4.53 where the wall temperature distributions for these three experiments are shown. Higher enhancement ratios are obtained as the gas velocity increases. The maximum enhancement ratio for the case of 15 m/s air velocity with 15 % water is nearly 9.0.

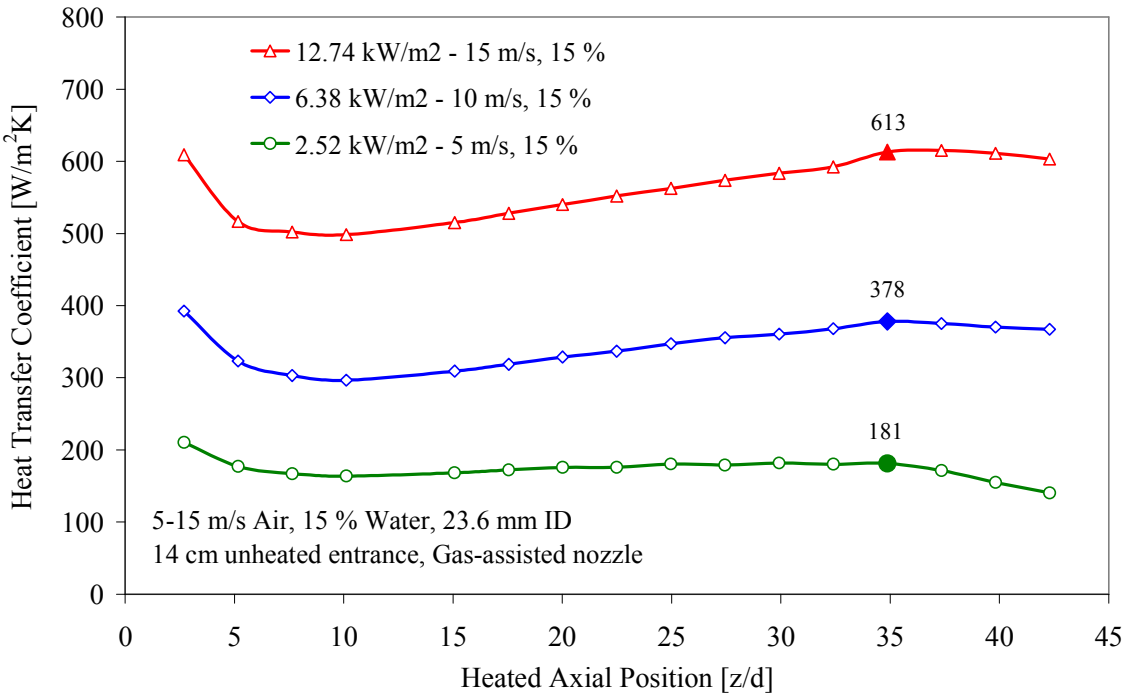

Figure 4.52 Variation of the local heat transfer coefficient with carrier gas velocity for downward mist flow in a circular pipe with a constant water injection mass fraction at the heat flux corresponding to the onset of film breakdown

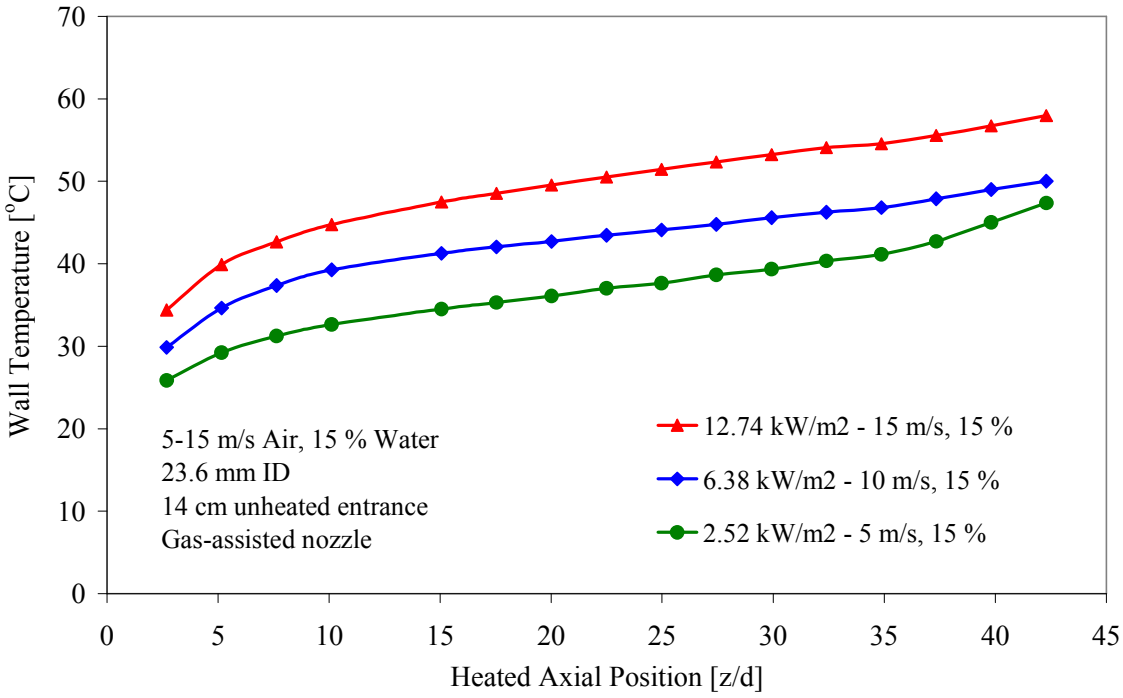

Figure 4.53 Variation of the wall temperature with carrier gas velocity for downward mist flow in a circular pipe with a constant water injection mass fraction at the heat flux corresponding to the onset of film breakdown

The maximum values for the local heat transfer coefficients corresponding to the three experiments presented in Figure 4.52 are plotted versus the corresponding carrier gas velocity (Figure 4.54). The data show a faster than linear increase in the peak heat transfer coefficient as the carrier gas velocity increases. Contrasting this result to the 0.8-power dependence of turbulent single-phase forced convection heat transfer coefficients points to the enhanced cooling potential of evaporative cooling as the carrier gas velocity is increased.

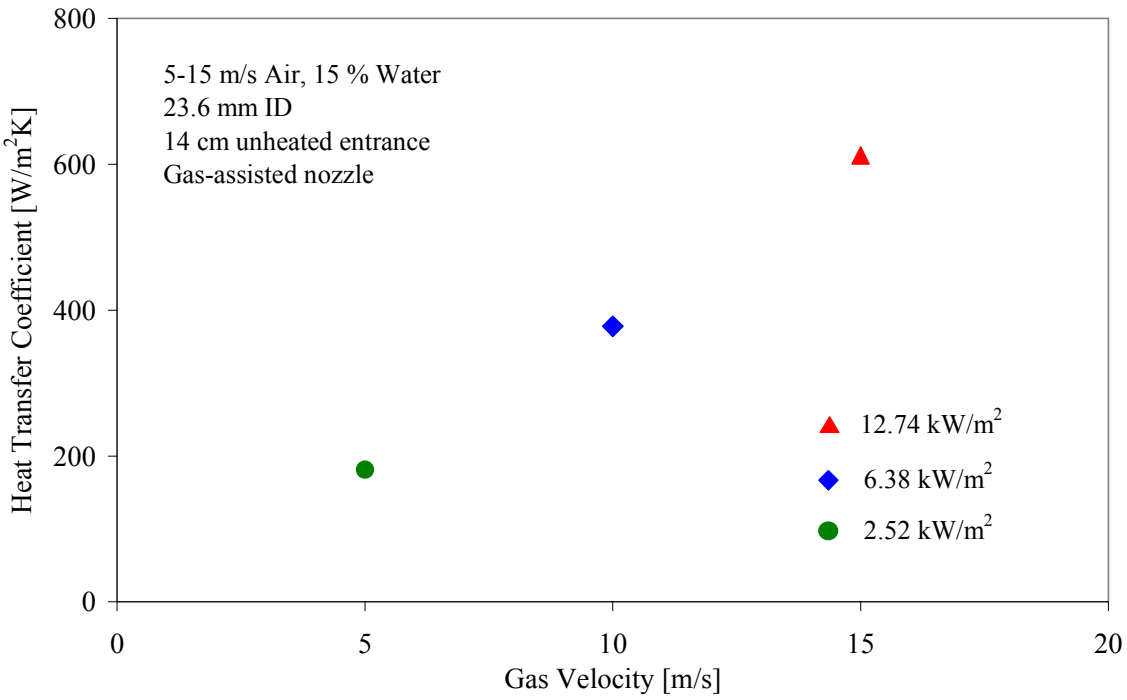

Figure 4.54 Variation of the peak value of the local heat transfer coefficient at the onset of film breakdown with carrier gas velocity for downward mist flow in a circular pipe with constant injected water mass fraction

4.9 Effect of Injected Water Temperature

As already established, higher enhancement ratios are achieved at higher wall temperatures (i.e. film temperatures) due to enhanced evaporation. In order to more directly examine this effect experiments have been conducted to qualify the effect of injected water temperature on mist cooling effectiveness. Downward mist flow experiments have been conducted using a fixed carrier gas velocity (15 m/s), a fixed water mass fraction (15 %), and a fixed wall heat flux (~ 8.9 kW/m^2), while varying the injected water inlet temperature from 2 ^{o}C to 95 ^{o}C. For high water injections temperatures, the stored energy in the heated water is used to adiabatically humidify and

warm the carrier gas before entering the test section. For a water line temperature of 95 °C, the bulk temperature measured in the entrance instrument block is 25 °C, versus a value of 13 °C when room temperature water is injected at 22 °C. The measured inlet bulk temperatures for 2 °C and 55 °C injected water temperatures are 8 °C and 20 °C respectively.

Figure 4.55 shows the effect of injected water temperature on the local heat transfer coefficients. The data pertain to downward mist flow in a 23.6 mm ID circular tube (PIPE 3) with a short (14 cm) unheated entry length. The atomizing gas flow rate (i.e. pressure) supplied to the gas-assisted nozzle was adjusted to produce the optimum mean droplet diameter (42 μm SMD). The corresponding values for the measured wall temperatures and calculated bulk temperatures are shown in Figure 4.56.

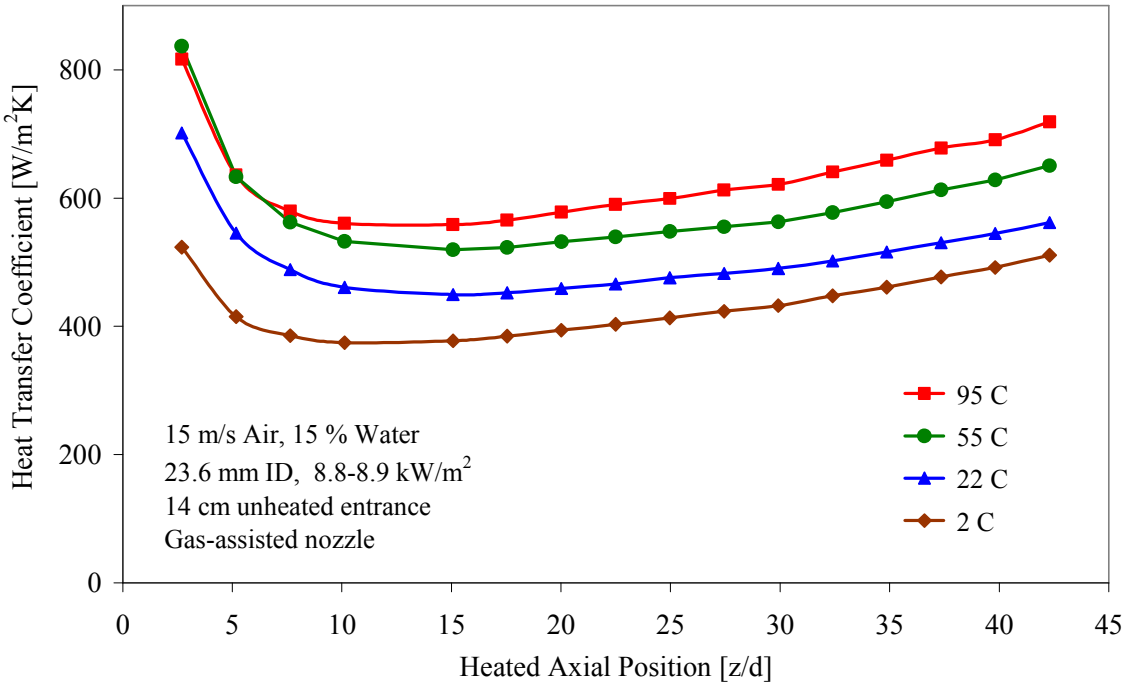

Figure 4.55 Effect of injected water temperature on the local heat transfer coefficient for downward mist flow in a circular tube

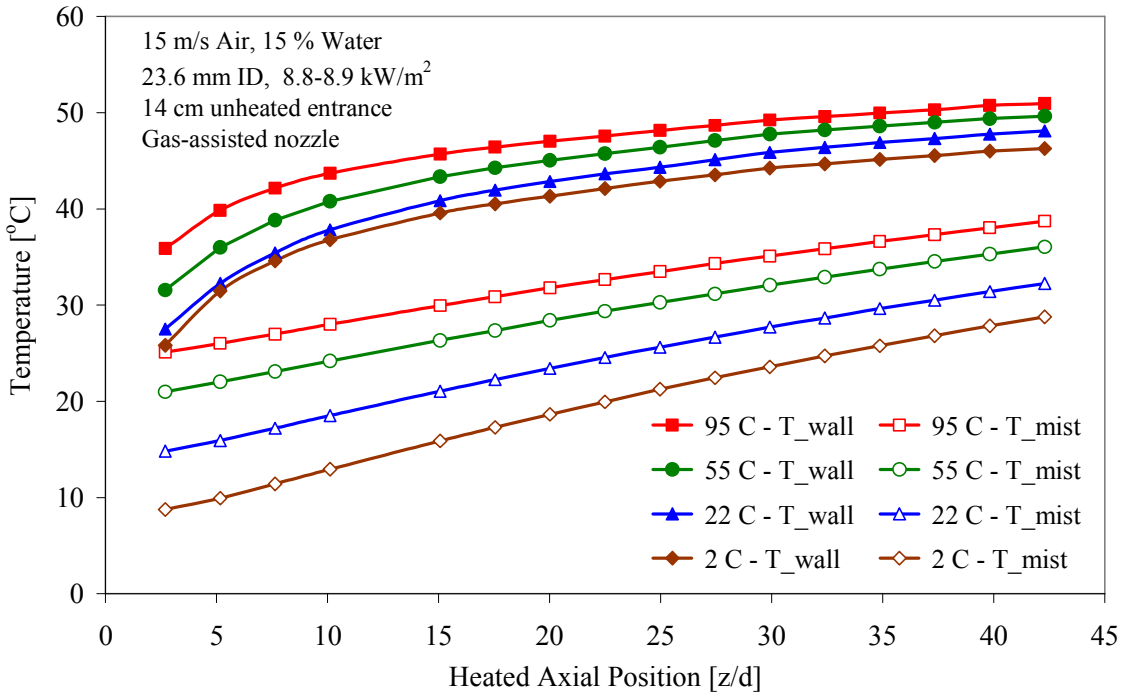

Figure 4.56 Effect of injected water temperature on the measured wall temperatures (top) and calculated bulk temperatures (bottom) for downward mist flow in a circular pipe

As expected, Figure 4.55 shows that higher injected water temperatures yield higher heat transfer coefficients at the same carrier gas velocity, water mass fraction, and wall heat flux. This is directly related to the enhanced evaporation. It should be noted, however, that despite the increase in heat transfer coefficient, the use of higher water injection temperature will increase the wall temperature. However, as can be seen from Figure 4.56, the increase in wall temperature is significantly smaller than the increase in the inlet bulk temperature caused by the elevated temperature of the water. As stated earlier, this is due to the non-linear relationship between the evaporation rate and the film temperature. The enhanced evaporation can also be discerned from the reduced rise in bulk temperature (i.e. lower slope in Figure 4.56) as the water injection temperature is

increased. Data for experiments performed at higher heat fluxes are shown in Figure 4.57. Here, the heat fluxes are elevated to the point where film breakdown becomes clearly evident near the test section exit. The data shows that increasing the injected water temperature causes film rupture to occur at a lower heat flux. The higher film temperature coupled with thinner films (due to higher evaporation) makes the liquid film more susceptible to thermocapillary instability and rupture. For lower injected water temperatures (2 ^{o}C and 22 ^{o}C), heat fluxes in excess of 15 kW/m^2 are reached before film rupture is observed near the test section exit.

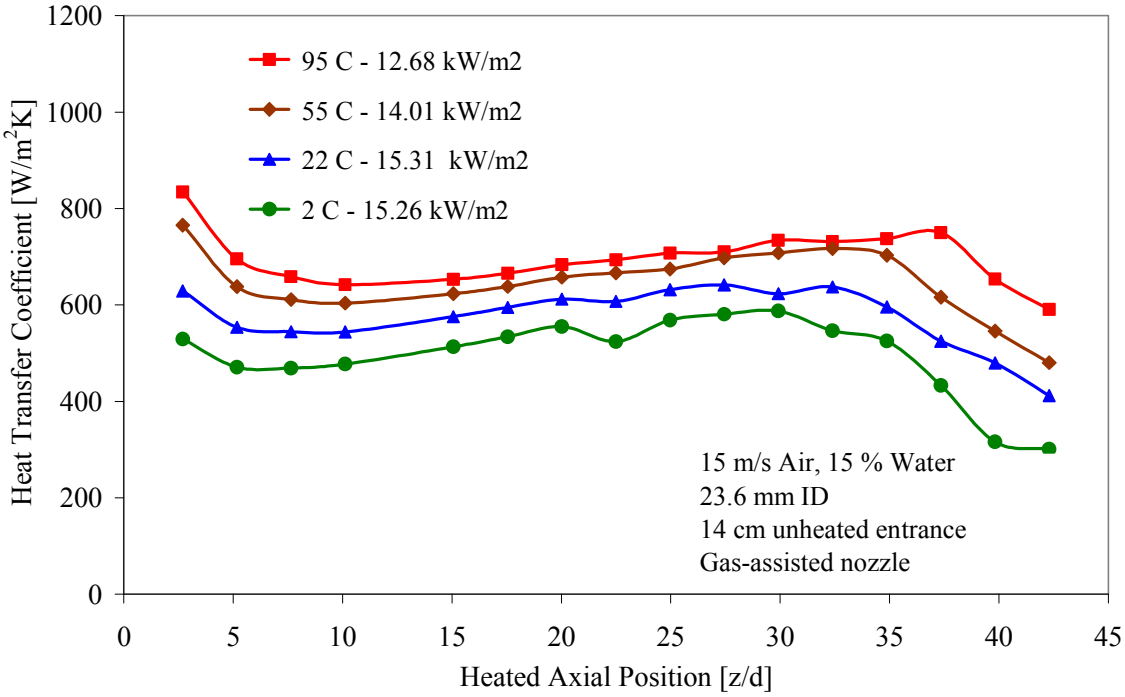

Figure 4.57 Effect of injected water temperature on the local heat transfer coefficients for downward mist cooling in a circular tube with elevated heat fluxes resulting in film rupture

The measured wall temperatures corresponding to these experiments are shown in Figure 4.58. The data clearly indicate the rapid increase in wall temperature following film rupture. It is interesting to note, however, that despite the relatively large differences among the heat flux values for these four experiments, the measured wall temperature distributions prior to film breakdown are nearly identical.

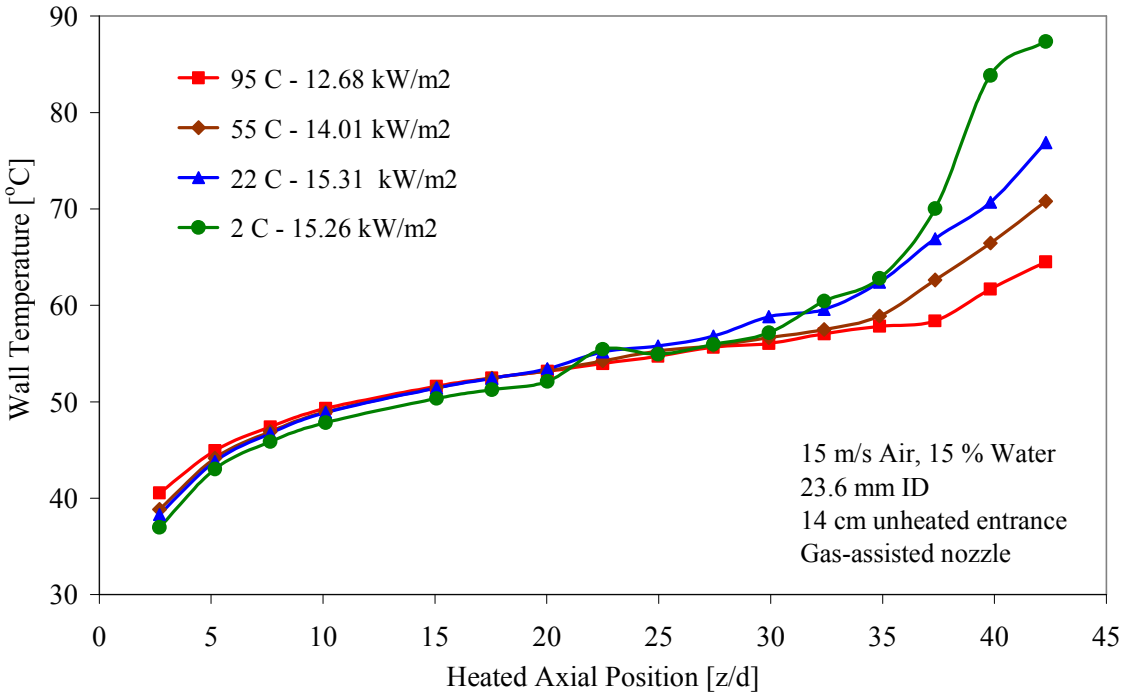

Figure 4.58 Effect of injected water temperature on the measured wall temperatures for downward mist flow in a circular tube with elevated heat fluxes resulting in film rupture

Nevertheless, one should not assume that film rupture is affected only by the wall temperature; several other parameters including film thickness, temperature gradient, and carrier gas flow conditions will impact the onset of film instability.

4.10 Effect of Carrier Gas Temperature

Similar to the injected water temperature, changing the inlet carrier gas temperature is expected to affect the heat transfer coefficient through its effect on evaporation. However, unlike the effect of injected water temperature, a change of only a few degrees in the inlet carrier gas temperature is expected to produce a significant change in the heat transfer coefficient. This can be seen in Figure 4.59, where the local heat transfer coefficients for downward mist flow in a 17.3 mm ID circular tube (PIPE 2) with a short (14 cm) unheated entry length are shown. The carrier gas inlet velocity is 15 m/s, while the injected water mass fraction is 15 %. A constant heat flux of 6.84 is used with two slightly different inlet carrier gas temperatures, viz. 19 ^{o}C and 23 ^{o}C. The atomizing gas flow rate (i.e. pressure) supplied to the gas-assisted nozzle was adjusted to produce the optimum mean droplet diameter (42 μm SMD). The data clearly show that a slight increase in inlet carrier gas temperature results in a significant increase in the local heat transfer coefficient. The difference in the heat transfer coefficients becomes larger as the mist proceeds along the heated length because of the non-linear increase in evaporation with temperature.

Figure 4.60 shows the corresponding distributions of measured wall temperatures and calculated bulk temperatures for the two experiments presented in Figure 4.59. As expected, the increase in wall temperature is less than the increase in bulk temperature because of the enhanced heat transfer. Nevertheless, an increase in carrier gas inlet temperature, with all other parameters unchanged, will always result in a higher entrance wall temperature. The data shows that the wall temperature at the exit asymptotically reaches the same value for both experiments.

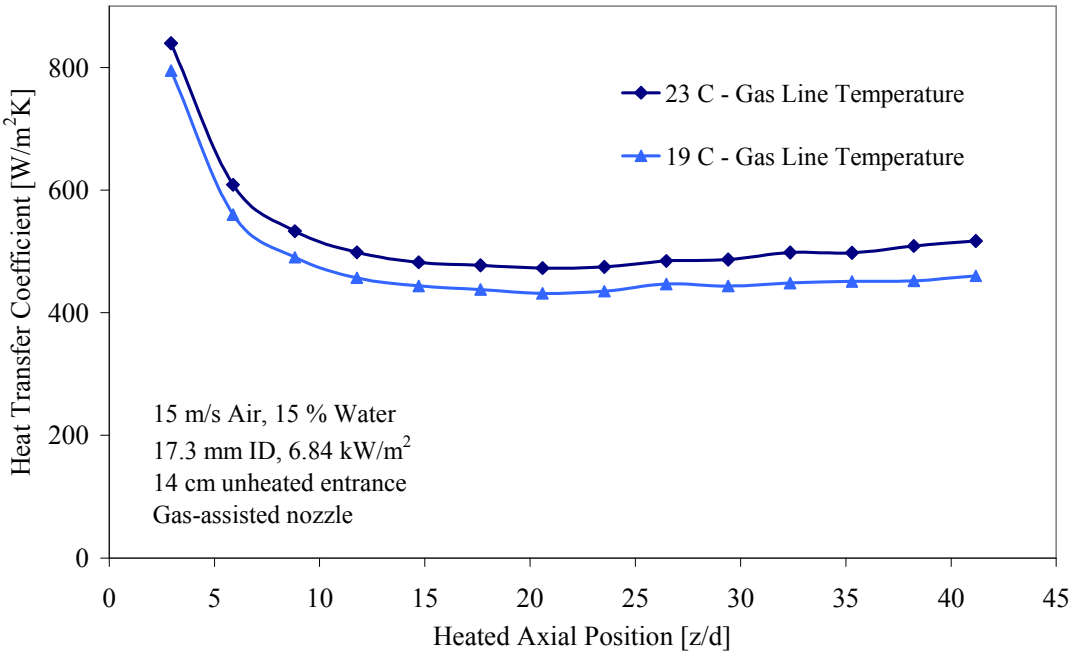

Figure 4.59 Effect of carrier gas inlet temperature on the local heat transfer coefficient for downward mist flow in a circular tube

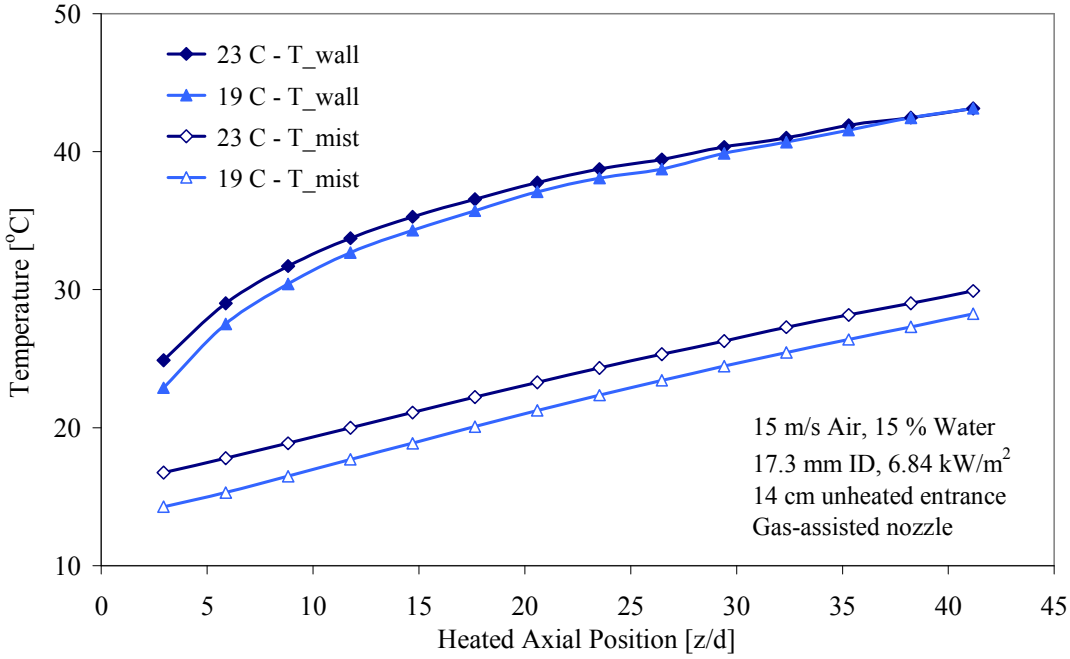

Figure 4.60 Effect of carrier gas inlet temperature on the measured wall temperature (top) and calculated bulk temperature (bottom) for downward mist flow in a circular pipe

4.11 Effect of Carrier Gas Humidity

The carrier gas supply humidity can have a significant effect on the performance of spray mist cooling. An adiabatic humidification of the carrier gas takes place within the inlet instrument block, and the unheated entry length. Therefore, depending on the supply gas relative humidity (RH), the bulk temperature of the carrier gas at the inlet of the heated section can vary considerably. If the carrier gas were to be fully humidified in the humidifier prior to reaching the test section inlet, it would require less water vapor from the droplets to reach saturation (i.e. 100 % relative humidity). Additional humidification is always required within the unheated entry length (even if the gas was fully humidified in the humidifier) because of the increase in bulk temperature between the humidifier and the test section inlet due to heat transfer from the ambient to the air supply lines. Nevertheless, if all other variables are unchanged, the pre-humidified gas would have a higher bulk temperature at the test section entrance. This, in turn, enhances heat transfer because of increased film evaporation as is the case with higher inlet water temperature and/or supply gas temperature. Typically, the relative humidity of the air reaching the mixer after being humidified is in the range of 31 – 34 %, while the supply line relative humidity is only a few percent. Figure 4.61 shows the effect of carrier gas inlet humidity on the heat transfer coefficient. The data correspond to downward mist flow in a 17.3 mm ID circular tube (PIPE 2) with a short (14 cm) unheated entry length. An average inlet velocity of 15 m/s and an injected water mass fraction of 15 % are used. The heat flux is kept constant and equal to 6.8 kW/m^2; this value is used since it corresponds to the case when the higher humidity case exhibits film breakdown near the test section exit. For the lower humidity case (6 % RH), the humidifier was bypassed, so

that air was supplied directly from the houseline. For the higher humidity case (33 % RH), the air was allowed to flow through the humidifier where it was fully humidified and cooled; subsequent heating reduced the relative humidity to 33 % while maintaining the same humidity ratio. Figure 4.62 shows the corresponding values for the measured wall temperatures and calculated bulk temperatures along the channel.

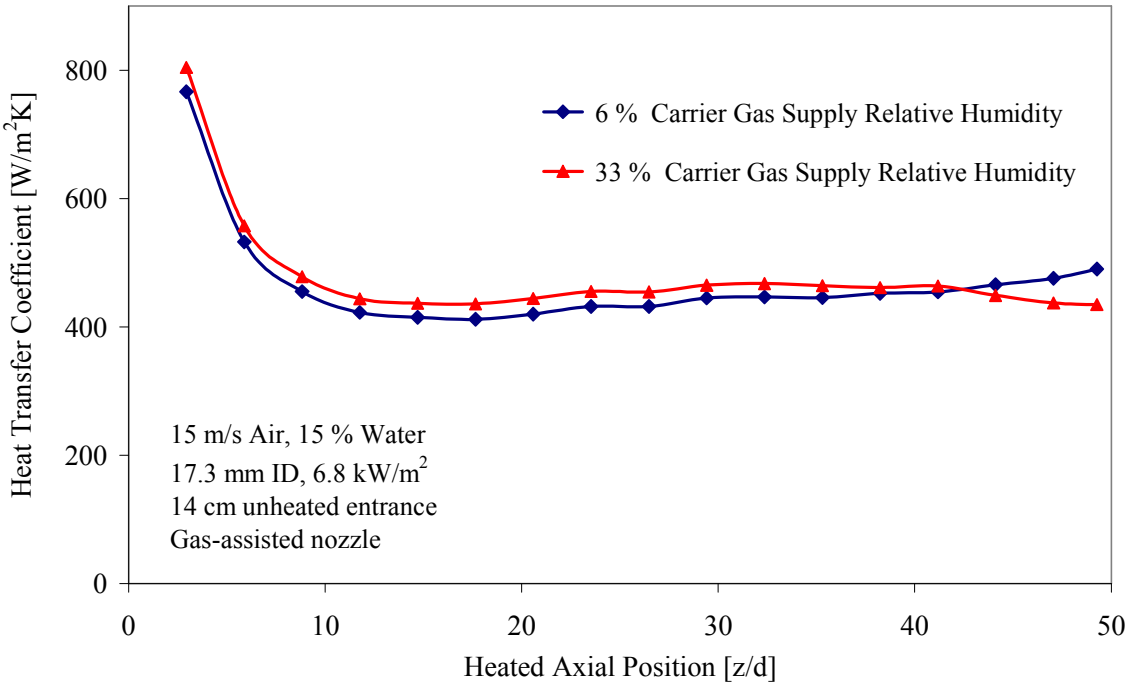

Figure 4.61 Effect of carrier gas inlet relative humidity on the local heat transfer coefficients for downward mist flow in a circular tube

As expected, a higher heat transfer coefficient is obtained for the higher relative humidity case because of the higher average bulk temperature at the heated test section inlet (see Figure 4.62). This, in turn, causes the film temperature to increase thereby increasing evaporation at the film/mist interface. The increase in inlet bulk temperature causes the

measured wall temperature to increase, albeit by a smaller amount, until the film becomes unstable. Film instability appears to take place near the test section exit for the higher inlet humidity case. This is primarily due to the slightly elevated wall temperature which increases the film's susceptibility to thermocapillary instability.

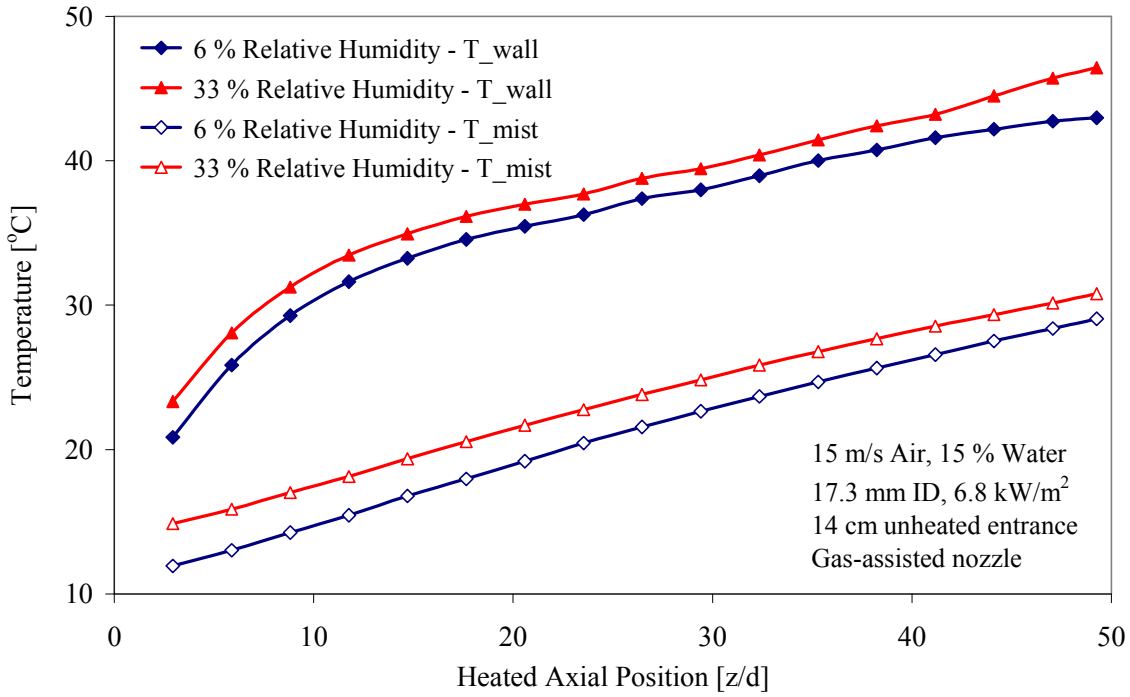

Figure 4.62 Effect of carrier gas inlet relative humidity on the measured wall temperature (top) and calculated bulk temperature (bottom) for downward mist flow in a circular tube

4.12 Effect of Carrier Gas

Helium/water mist has been proposed as a cooling medium for the Electra hibachi structure. The enhanced heat transfer characteristics of helium (vis-à-vis air), coupled with its lower beam absorption makes it preferable for such an application. A limited

number of experiments have been conducted to measure the heat transfer coefficient for helium/water mist flow. A helium gas inlet velocity of 30 m/s has been used; higher velocities were not possible because of test apparatus limitations. Different water flow rates corresponding to mass fractions of 21 %, 43 %, and 57 % have been used. These values have been selected to nearly match the water flow rates corresponding to these used for air/water mists with an air inlet velocity of 15 m/s and water mass fractions of 5, 10, and 15 %, respectively. Figure 4.63 shows variations of the local heat transfer coefficients for downward helium/water mist flow in a 17.3 mm ID circular tube (PIPE 2) with a short (14 cm) unheated entry length. Local heat transfer coefficients for single-phase forced convection of dry helium at the same average inlet velocity (30 m/s) are also shown. Progressively higher heat flux values are used as the injected water mass fraction is increased; heat fluxes of 5.17, 7.26, and 8.53 kW/m^2 are used for water mass fractions of 21 %, 43 %, and 57 %, respectively. These heat fluxes correspond to the values at which indications of film rupture are first observed near the test section exit. The atomizing gas flow rate (i.e. pressure) supplied to the gas assisted nozzle was selected to produce the desired optimal mean droplet size (42 μm SMD).

The helium mass flow rate corresponding to an average inlet velocity of 30 m/s is nearly equal to that for air at an inlet velocity of only 4.0 m/s. Figure 4.64 compares the heat transfer coefficients for downward helium/water mist flow with an inlet carrier velocity of 30 m/s and an injected water mass fraction of 64 % against values for air/water mists. The first air/water mist case has an inlet velocity of 15 m/s and a water mass fraction of 15 %; this corresponds to nearly four times the carrier gas mass flow rate with the same water injection rate.

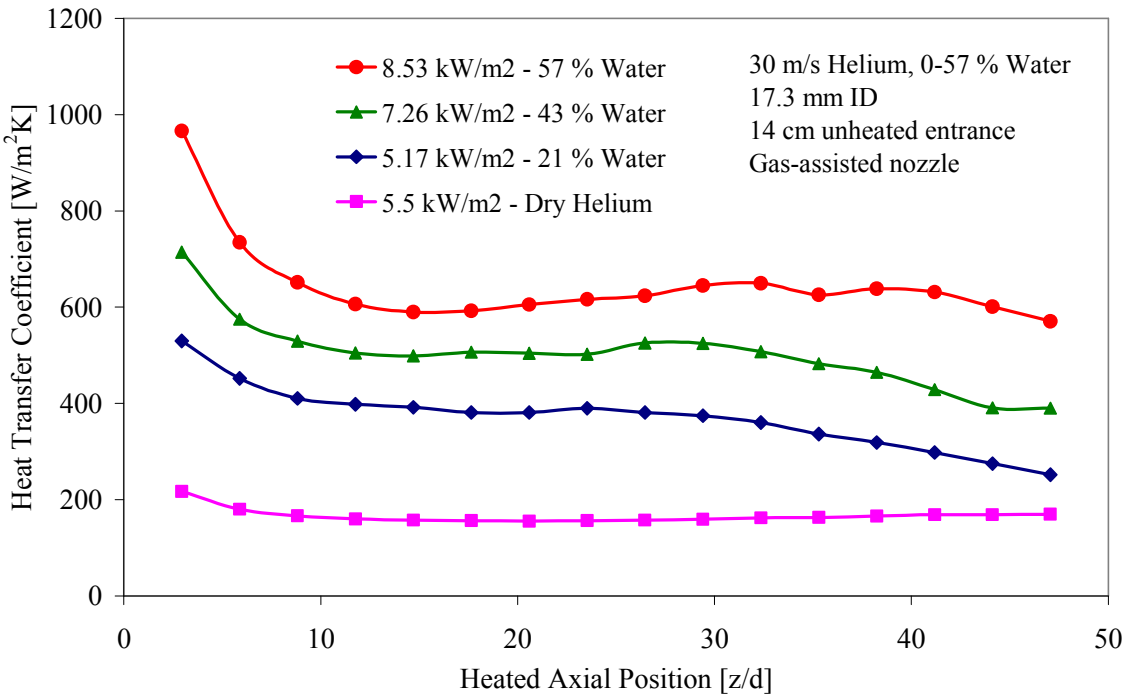

Figure 4.63 Effect of injected water mass fraction on the local heat transfer coefficients for downward helium/water mist flow in a circular tube at heat fluxes corresponding to the onset of film breakdown

The second air/water mist case corresponds to an inlet velocity of 6 m/s and a water mass fraction of 15 %. The heat flux values used in these experiments, namely, 9.09 kW/m^2 for helium, and 6.85 kW/m^2 and 1.49 kW/m^2, for air at 15 m/s and 6.0 m/s, respectively correspond to the point when indications of film breakdown are first observed near the test section exit. The data shown in Figure 4.64 demonstrates the superior heat transfer characteristics of helium/air mist cooling. Higher heat transfer coefficients are obtained because of the higher mass fractions required to saturate the helium performance. Despite the considerably higher heat transfer coefficients obtained with helium/water mists, the enhancement ratio is only ~ 4.0, because of the considerably higher single-phase forced convection heat transfer coefficient for dry helium.

The relatively high cost of operating the helium/water mist cooling experiments in a once-through mode imposed a limit on the number of experiments to be conducted. The possibility of using helium/water mist to cool the Electra hibachi structure using a closed helium recirculating system proved to be unfeasible because of the difficulty of operating helium recirculators with high gas moisture. Nevertheless, the limited amount of helium/water mist cooling data obtained here demonstrates its superior performance. These data can also be used to validate mechanistic mist cooling models since the physical and transport properties of the carrier gas significantly impact the predicted performance.

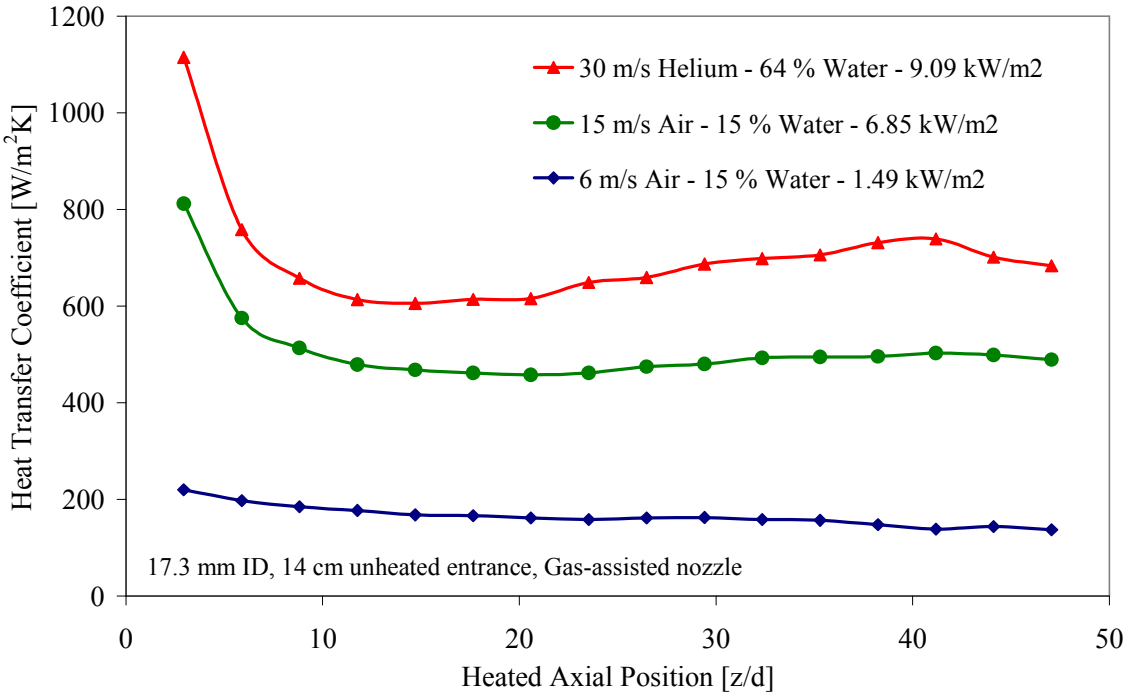

Figure 4.64 Comparison between the local heat transfer coefficients for downward helium/water and air/water mist flows in a circular tube

4.13 Effect of Channel Geometry

Experiments have been conducted using test sections with both circular and rectangular cross sections. Figure 4.65 shows variations of the local heat transfer coefficient for downward mist flow in circular tubes. Data are shown for a 23.6 mm ID (PIPE 3) and a 17.3 mm ID (PIPE 2) tube. In both cases the average carrier gas inlet velocity is 15 m/s, while the injected water mass fraction is 15 %. In both cases, the atomizing air flow rate (i.e. pressure) supplied to the nozzle has been selected to produce the optimum mean droplet diameter (~ 42 μm SMD). The heat fluxes have been selected to match the values at which indications of film breakdown are first observed at the test section exit; values of 6.85 kW/m^2 and 11.50 kW/m^2 are used for the 17.3 mm and the 23.6 mm, respectively. The fact that film breakdown requires a smaller heat flux as the tube diameter is reduced is not surprising since the thermocapillary forces depend on the surface curvature. Also the fact that higher heat transfer coefficients are obtained for the larger tube (Figure 4.65) is to be expected because of the higher surface heat flux. In general, however, for the same carrier gas velocity and water mass fraction, better performance will be obtained as the tube diameter increases since the flow area (i.e. the air and water flow rates) increases at a faster rate (proportional to D^2) than the total heat input (proportional to D). The increased vapor-carrying capacity of the gas makes it possible to operate at higher heat fluxes with commensurate increase in the heat transfer coefficient.

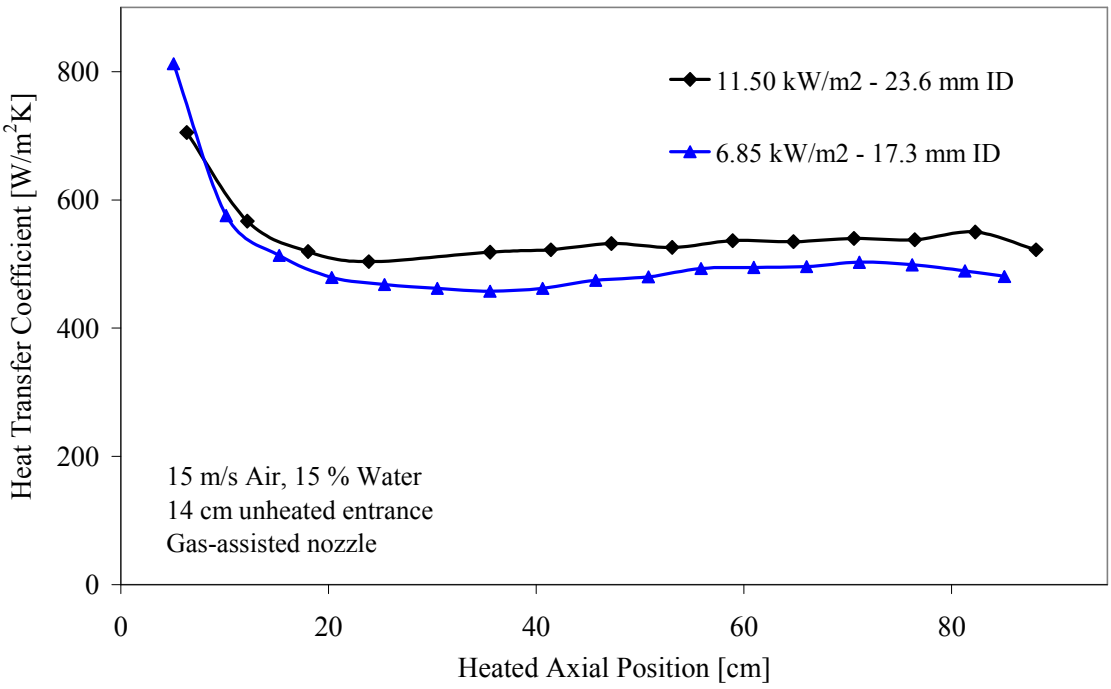

Figure 4.65 Effect of tube diameter on the local heat transfer coefficients for downward air/water mist flow in a circular tube

Figure 4.66 compares the local heat transfer coefficients obtained for downward mist flow in a 23.6 mm ID circular tube (PIPE 3) with these obtained using a (16.6 mm x 35.6 mm) rectangular channel (DUCT 2). In both cases, the average carrier gas inlet velocity is 15 m/s, while the injected water mass fraction is 15 %. While the rectangular channel has nearly the same hydraulic diameter (22.6 mm) as the circular tube (23.6 mm), its flow area is considerably larger (5.91 versus 4.37 cm^2). This means that the total air and water flow rates are higher for the rectangular channel. The heat transfer coefficients obtained using the rectangular channel are noticeably higher than those for the circular tube. The single-phase forced convection heat transfer coefficients for both channels (Figure 4.66) are nearly the same since they have the same hydraulic diameter, i.e. Reynolds number.

The data in Figure 4.66 also indicate that film breakdown occurs at a slightly lower heat flux in the circular tube than the rectangular channel. This effect may be attributed to the wall curvature effects on thermocapillary forces.

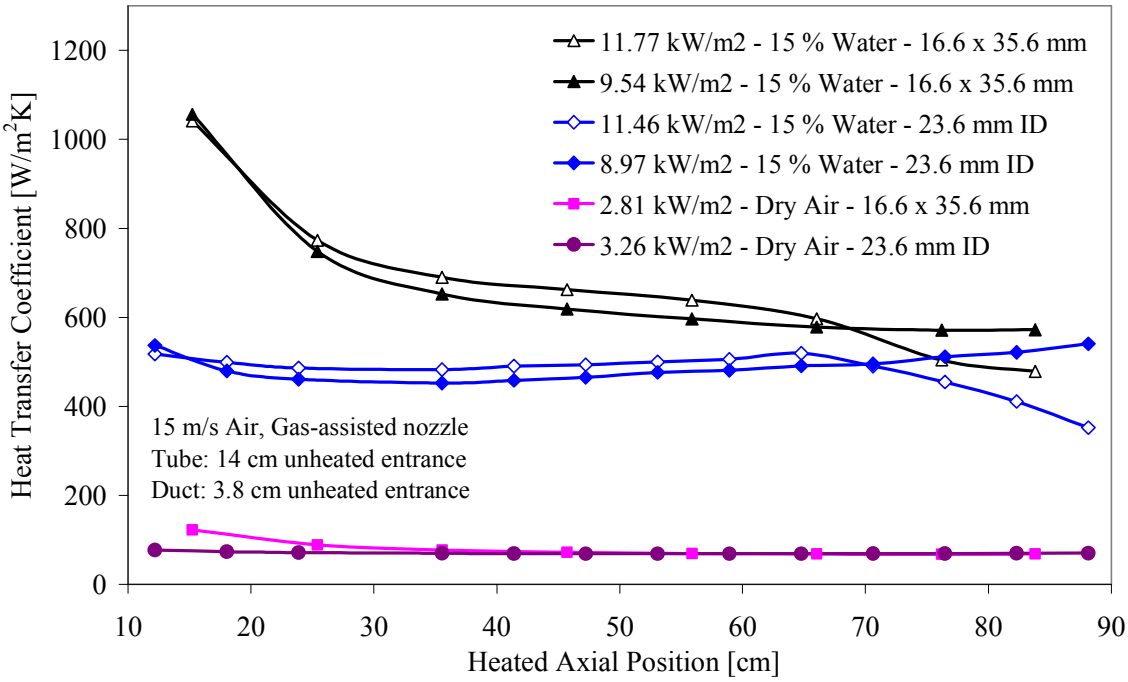

Figure 4.66 Comparison between the local heat transfer coefficients for downward air/water mist flow in circular and rectangular channels

To isolate the effect of carrier gas flow rate from that of the carrier gas velocity, comparison has been made between the heat transfer coefficients obtained for downward mist flow in the 17.3 mm ID tube (PIPE 2) and the 23.6 mm ID tube (PIPE 3). In this case a 10 m/s carrier gas inlet velocity is used for the larger tube, while a 15 m/s carrier gas velocity is used in the smaller tube; in both cases the water mass fraction is 15 %. Even though a lower velocity is used for the larger tube, the total carrier gas and water

flow rates are higher than those for the smaller tube. In this case, counter to the results shown in Figure 4.65, higher heat transfer coefficients are obtained with the smaller diameter tube (Figure 4.67) even though the heat flux was slightly lower (6.85 versus 7.61 kW/m^2). This suggests that the carrier gas velocity by itself has an impact on the resulting heat transfer coefficients. The higher gas velocities may result in higher shear stresses on the co-flowing film, which, in turn, may cause the film to be thinner thereby enhancing evaporation. The higher average liquid film velocity may also increase the convective heat transfer component to the liquid film thereby decreasing the overall thermal resistance between the wall and the mist core.

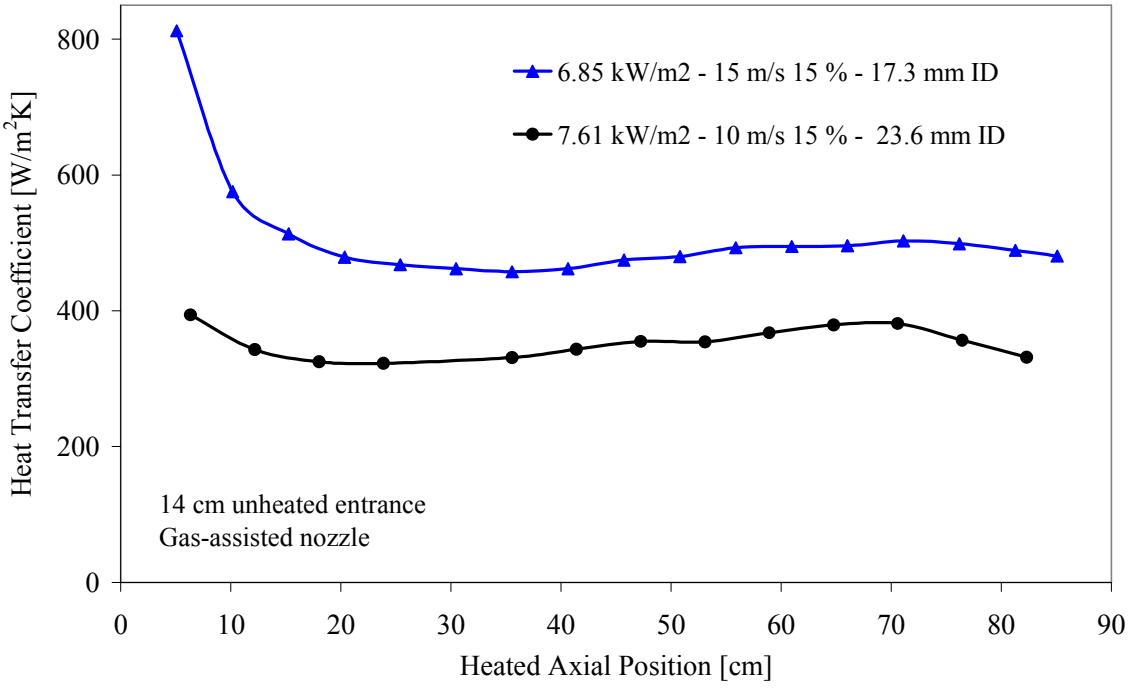

Figure 4.67 Effect of tube diameter and carrier gas velocity on the local heat transfer coefficients for downward mist flow in circular channels

The rectangular duct (DUCT 2) was instrumented to allow variations in the heat transfer coefficient around the channel periphery to be estimated. Such angular variations are to be expected because of the conical geometry of the spray produced by the nozzle. For a given heat flux, the narrower sides of channel are generally warmer than the wider sides. The local bulk temperature is evaluated using a one-dimensional energy balance between the inlet and each axial location along the channel. Therefore, a higher heat transfer coefficient is generally obtained for the wider channel sides than that for the narrower sides at the same axial location. This can be clearly seen in Figure 4.68 which pertains to downward mist flow with a carrier gas inlet velocity of 15 m/s and a 15 % injected water mass fraction. Only average values are reported in this study. Similar differences, albeit smaller, have also been observed for single-phase forced convection in rectangular channels.

Figure 4.69 shows the effect of heat flux on the local heat transfer coefficient for downward air/water mist flow in a rectangular channel (DUCT 2). The values shown correspond to the calculated average values at each axial location. As expected, the heat transfer coefficient increases as the heat flux increases as long as the entire surface is covered by a liquid film. As the heat flux increases, film breakdown occurs near the channel exit; the location of film breakdown moves farther upstream as the heat flux is further increased. It is noted however, that fully-developed conditions are reached at a point farther downstream ($z/d \approx 20$) than that for circular channels (see section 4.16). Here, "d" is the hydraulic diameter of the channel.

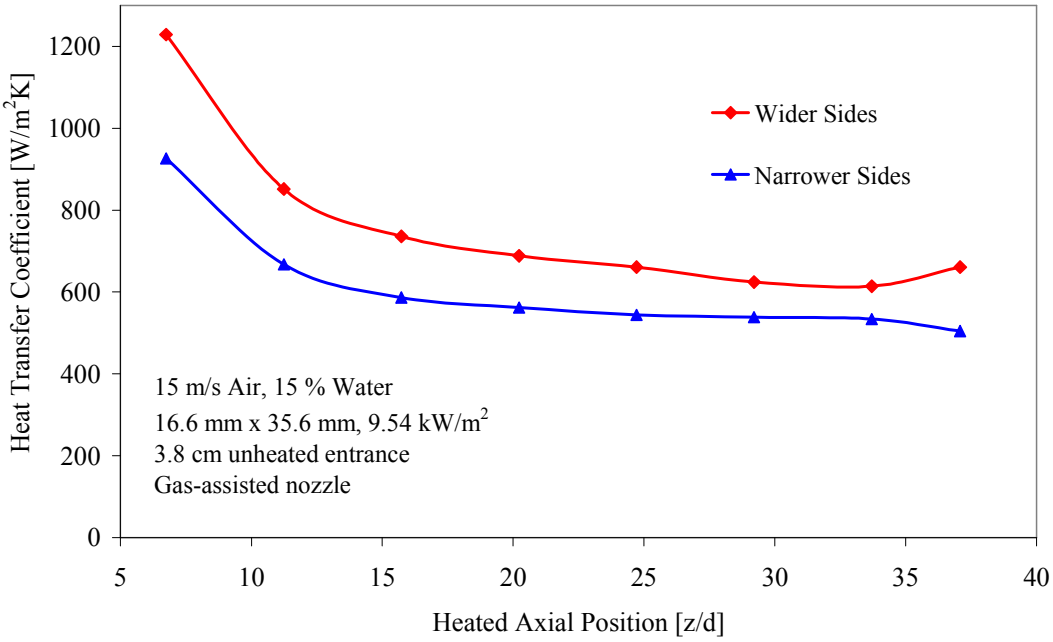

Figure 4.68 Comparison between the heat transfer coefficients along the wider and narrower sides of a rectangular channel (DUCT 2) for downward air/water mist flow

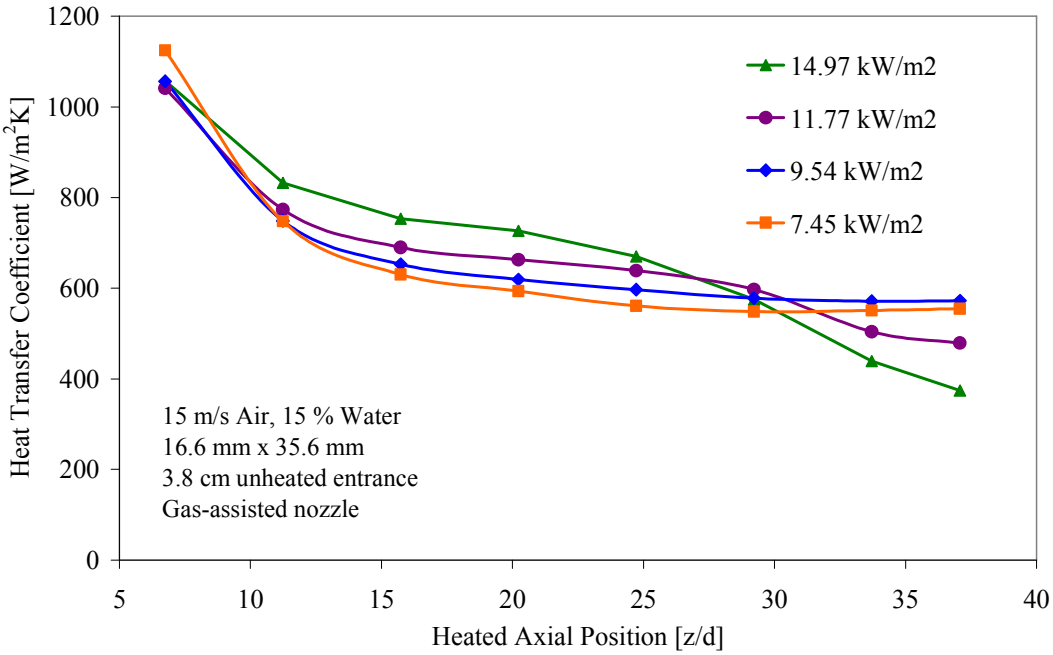

Figure 4.69 Effect of heat flux on the local average heat transfer coefficients for downward mist flow in a rectangular channel

4.14 Effect of Unheated Entry Length and its Wettability

As discussed earlier, the length of the test section plays an important role in mist cooling. Due to thermocapillary forces, a liquid film could break at significantly lower heat fluxes in a longer channel than it would in a shorter test section because of the increase in bulk temperature and wall temperature, coupled with the reduction in film thickness as the flow proceeds along the heated test section. In addition, a longer channel will likely experience a non-uniform droplet deposition near the exit, which produces a non-uniform film thereby increasing the chances for a film breakdown. In this study, the overall test section length can be changed by using either a short or a long unheated visualization tube upstream of the test section inlet. Changes in the unheated entry length produce significant effects on the heat transfer coefficients and the location of film breakdown. Figure 4.70 shows values of the local heat transfer coefficient for downward mist flow in a 23.6 mm ID circular tube with either a short (14 cm) or long (75 cm) unheated entry length. The axial location (z/d) on the horizontal axis represents the distance measured from the beginning of the heated length. The data correspond to an average carrier gas inlet velocity of 15 m/s and an injected water mass fraction of 15 %. These data show that as long as the film is intact, the fully-developed values of the heat transfer coefficients are nearly the same regardless of the unheated length. The data also show that hydraulically-developing flow coupled with nozzle-generated spray turbulence, yield higher local heat transfer coefficients for the shorter pipe. Additionally, channels with a longer unheated entry length experience film breakdown at significantly lower heat fluxes, as can be seen for the 10.22 kW/m^2 heat flux cases, where film breakdown occurs midway along the heated length of the channel with longer entry length, while the

channel with a shorter entry length exhibits no indications of film breakdown. By the time the shorter channel shows signs of film instability at the exit (12.74 kW/m^2), the longer channel has rivulet flow established at more than a half of its heated length.

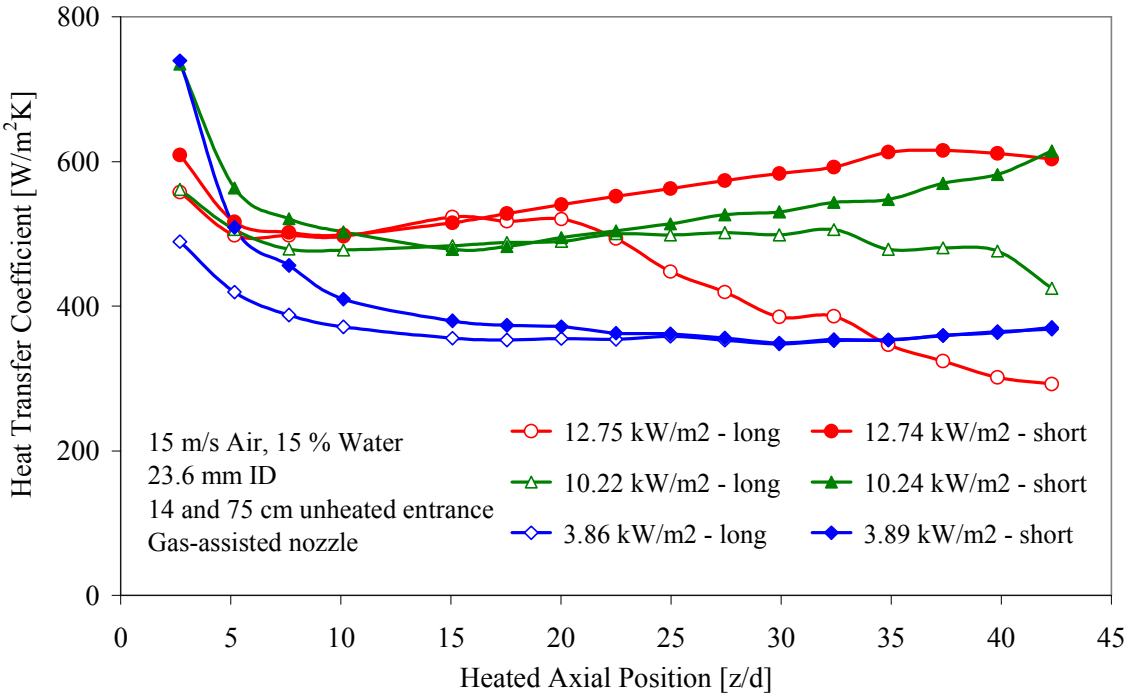

Figure 4.70 Effect of unheated entry length on the local heat transfer coefficients and film breakdown location for downward mist flow in a circular channel

Experimental observations suggest that film breakdown in longer channels does not always progress through all the usual instability steps typical for a shorter channel, namely, unstable dry patches followed by stable dry patches, and finally, rivulet flow formation. The appearance of stable dry patches at the exit is often absent, and the film quickly breaks down into rivulet flow. Occasionally, dry patches would appear farther upstream of the exit, while a uniform film is present at the exit; the dry patches then

progress towards the exit evolving to a full film breakdown, as shown in Figure 4.71. While the nozzles are accurately aligned, the second scenario is observed more frequently when the ultrasonic nozzle is used, suggesting that it has less uniform droplet deposition than the gas-assisted nozzle.

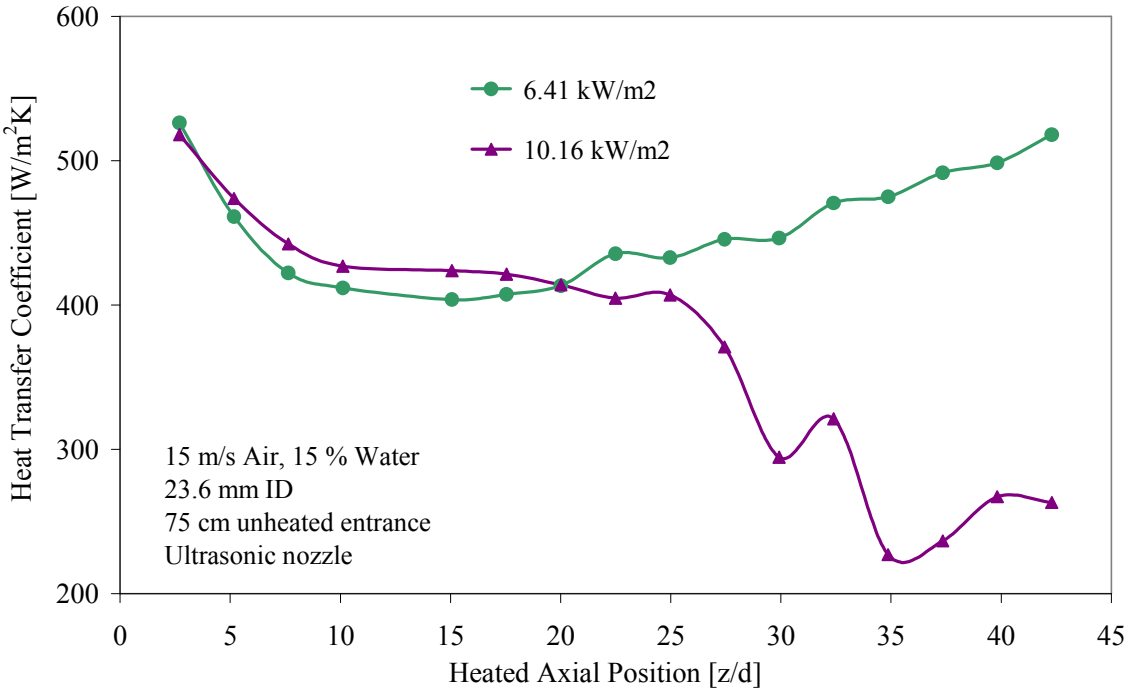

Figure 4.71 Film breakdown for downward air/water mist flow with an ultrasonic nozzle in a circular tube with a long unheated glass entry length

For experiments with a long unheated entry length, the wettability of the entry length (visualization tube) appears to play a significant role in liquid film stability. For example, when a long clear PVC tube with poor wettability is used, film breakdown would frequently occur in the PVC pipe itself prior to entering the heated length. Because of that, a long glass pipe with considerably better wettability is used for all experiments with a long unheated entry length. For experiments with a short unheated entry length

(visualization tube), the material of the unheated entry length (PVC versus glass) appears to have no effect on heat transfer along the heated length.

4.15 Effect of Flow Orientation

The flow orientation (upward versus downward flow) has a major effect on the behavior spray mist cooling. Various benefits in film stability and heat transfer enhancement are encountered in upward flow mist cooling. As already discussed, the optimum droplet size range for upward mist flow is significantly broader than that for downward flow. In essence, the droplet size has little effect on the effectiveness of upward mist flow, except for extremely small droplet diameters (few micros), which can be easily carried out of the channel by the nozzle generated jet, since velocities more than 200 m/s at the nozzle orifice are needed to produce that size droplet; a significant fraction of the injected liquid exits the channel without depositing on the heated wall. Bigger droplets than the optimal range for downward mist flow do not face the same problems as in downward case. As long as they reach the wall, gravitational effects help to spread them circumferentially and maintain a uniform film along the channel. These same benefits are also evident in case of a nozzle misalignment. Gravitational effects also result in a somewhat thicker liquid film than in the same downward flow case, i.e. they enhance droplet deposition as they combine with drag forces to rapidly reduce the relative velocity between the droplets and the much slower carrier gas. Higher droplet deposition rates enable the film to reach higher temperatures without rupturing. However, the film thickness increase is not significant enough to limit evaporation as evidenced by the high heat transfer coefficients. Dry patches are noticeably easier to be rewetted; the

gravity effect (possibly due to flooding) prevents their downstream spreading and tends to pull surrounding liquid toward such spots thereby rewetting them. Due to these factors, an upward-flowing mist provides superior cooling composed to a downward-flowing mist. However, the baseline case in this study is a downward-flowing mist, which is the desired flow configuration for the Electra foil cooling application. Hence, the majority of the data collected in this investigation pertains to downward mist flow. For completeness, however, a smaller number of experiments have been conducted for upward-flowing mists. These data are also used to validate the numerical model as described in Chapter V.

Figures 4.72 and 4.73 show the effect of heat flux on the local heat transfer coefficients for upward mist flow in a 17.3 mm ID circular tube with a short (14 cm) unheated entry length. Both sets of data use an average inlet carrier gas velocity of 15 m/s; water mass fractions of 15 % and 10 % are used, respectively. In both cases, the gas-assisted nozzle was used; the atomizing gas flow rate (i.e. pressure) corresponded to a mean droplet diameter of nearly 42 μm (SMD). The phenomena are similar to the downward flow case, except that the heat transfer coefficients are significantly higher as will be shown shortly. As expected, for a given set of flow conditions, the heat transfer coefficient increases as the heat flux increases as long as the film remains intact along the entire heated length. At a critical heat flux value, film breakdown occurs with subsequent rapid reduction in the heat transfer coefficient. For a given carrier gas inlet velocity, the heat flux corresponding to film breakdown increases as the water injection mass fraction increases.

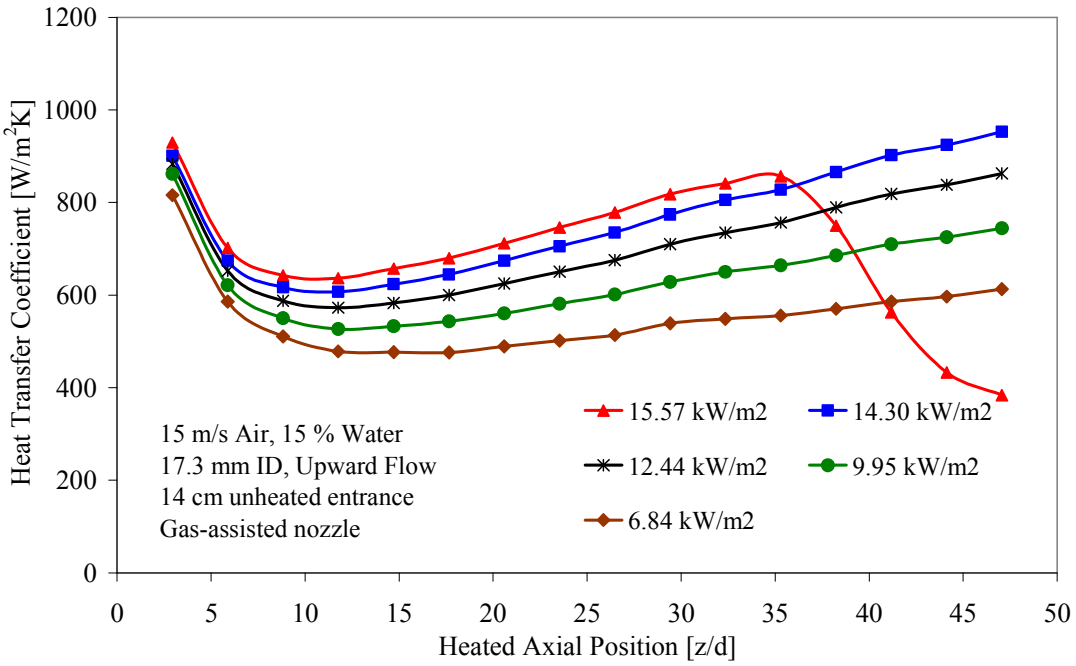

Figure 4.72 Effect of heat flux on the local heat transfer coefficients for upward air/water mist flow in a circular tube with a short entry length

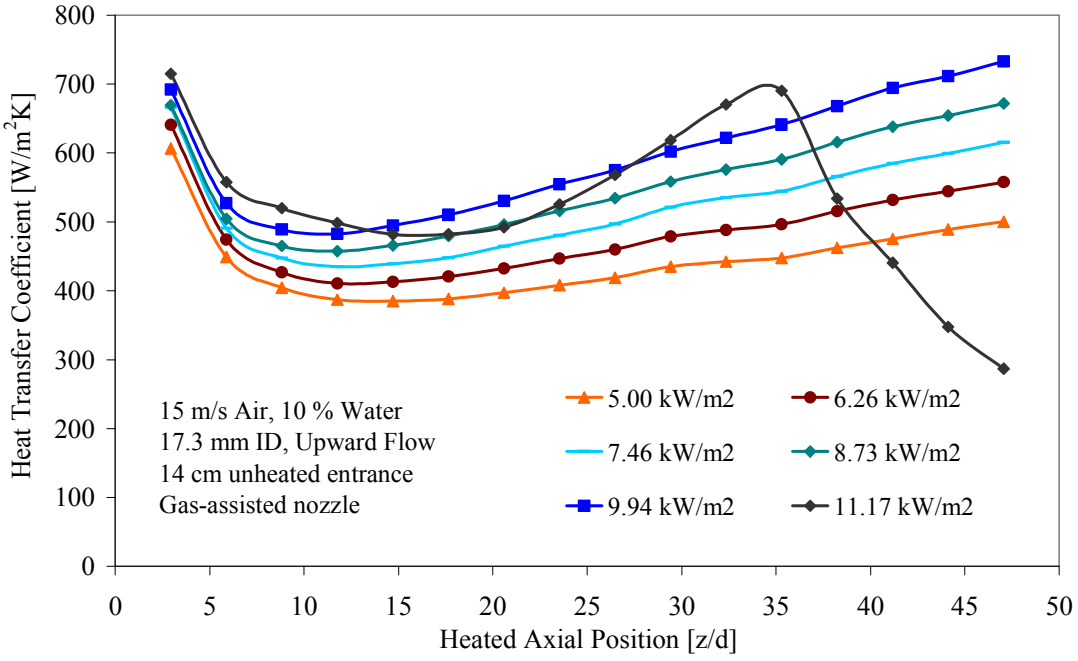

Figure 4.73 Effect of heat flux on the local heat transfer coefficients for upward air/water mist flow in a circular tube with a short entry length

An interesting result is shown in Figure 4. 73, where film breakdown is clearly evident at a heat flux of 11.17 kW/m^2. In this case, film instability appears to take place immediately after the entrance region. However, recovery and periodic rewetting takes place over a significant fraction of the heated length as evidenced by the continued presence of high heat transfer coefficients until complete film rupture takes place three quarters of the way along the heated length. This situation is not possible in downward flow mist cooling where dry patch formation would rapidly lead to film instability and transition to rivulet flow over the remainder of the heated length. For upward flow, dry patches formed early along the heated length may "slide" along the heated length until they exit the test section thereby returning the entire test section length to a fully-wetted condition. In other cases, film breakdown may occur near the test section exit resulting in significant temperature rise; reflooding would then rewet the dry region thereby restoring the wall temperatures to their pre-rupture conditions.

Figure 4.74 shows the effect of carrier gas velocity on the performance of upward mist flow. It also compares the local heat transfer coefficients for upward and downward flow at the same flow conditions. For upward flow, better cooling is achieved when the carrier gas velocity is reduced from 15 to 10 m/s with a 15 % injected water mass fraction. For the 10 m/s case, counter-current flow condition is nearly reached as evidenced by slight accumulation of liquid outflow; hence, the liquid film in that case is expected to be somewhat thicker and noticeably slower, and therefore able to sustain high heat fluxes and achieve higher wall temperatures without rupture (Figure 4.75) which enhance evaporation. Therefore, for this case film breakdown occurred at a much higher heat flux (23.0 kW/m^2); extremely high heat transfer coefficients were obtained (~ 1,700

W/m^{2}K) prior to film rupture near the test section exit. Figure 4.74 also shows the highest heat transfer coefficients obtained with downward mist flow at 15 m/s air velocity and 15 % water mass fraction. These are clearly much lower than the values obtained with upward mist flow. It is interesting to note that the enhancement ratio for the 10 m/s case with a heat flux of 23.0 kW/m^2 is nearly 30, while an enhancement ratio of only 13 is obtained for the 15 m/s case with a heat flux of 14.94 kW/m^2; the corresponding enhancement ratio for downward mist flow at 15 m/s is only 7.

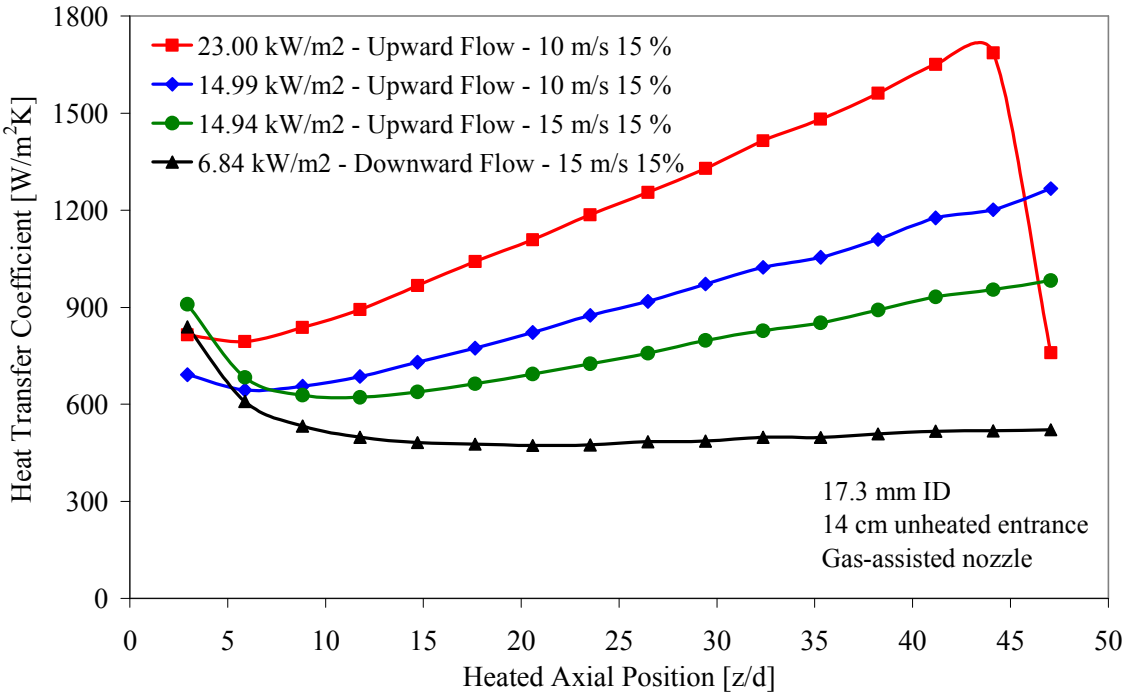

Figure 4.74 Comparison between the local heat transfer coefficients for upward and downward air/water mist flow in a circular tube with a short unheated entry length

Figure 4.75 shows the wall temperatures corresponding to the experiments described in Figure 4.74. As expected, the case producing the highest heat transfer

coefficients has the highest wall temperature followed by the other cases in order of heat transfer coefficients. It is interesting to compare the wall temperature distributions obtained for the 10 m/s and 15 m/s upward flow experiments at nearly the same heat flux (~ 15.0 kW/m^2). The wall temperature obtained for the low velocity case is higher, which corresponds to a higher heat transfer coefficients. The slight rise in wall temperatures is far smaller than the rise in the calculated bulk temperatures (Figure 4.76) as the air water flow rates were reduced by nearly a third while keeping the same heat flux.

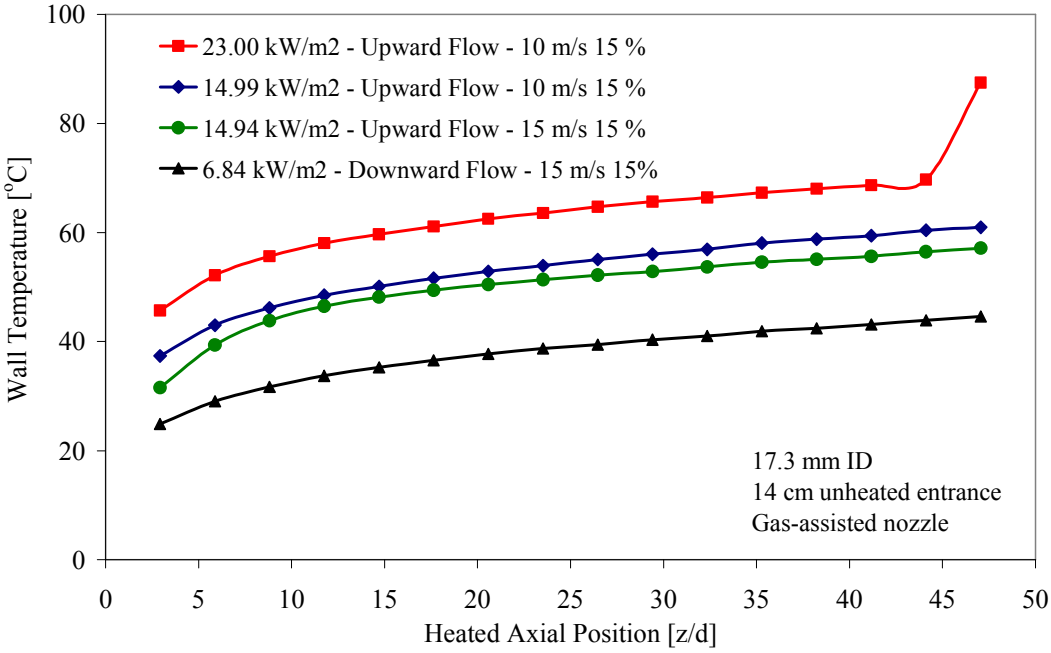

Figure 4.75 Effect of carrier gas velocity and flow direction on the measured wall temperatures for air/water mist flow in a circular tube with a short unheated entry length

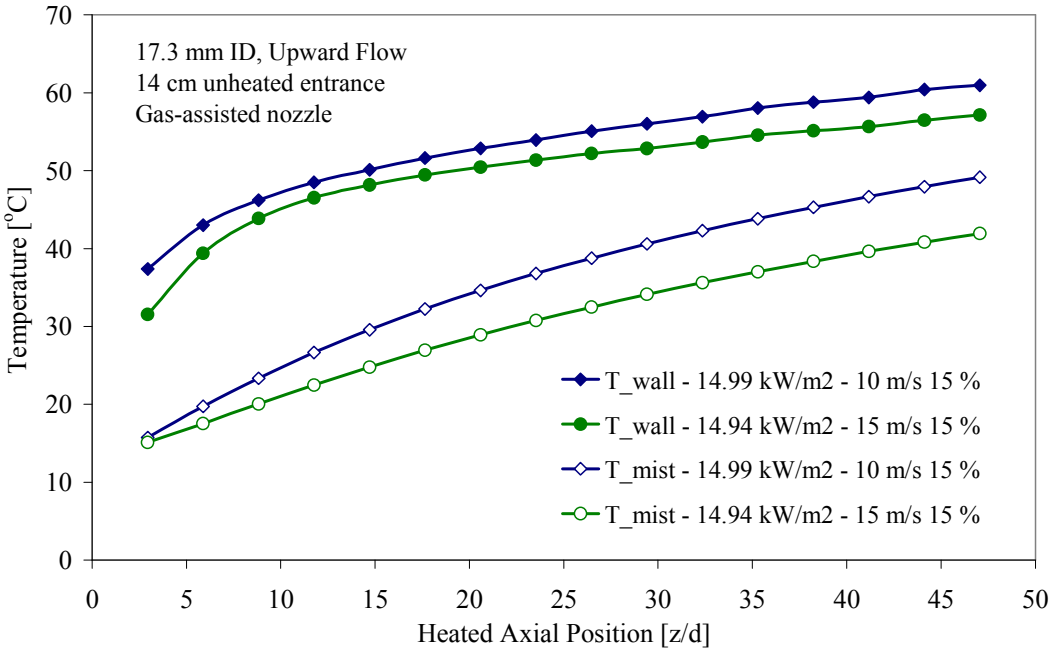

Figure 4.76 Effect of carrier gas velocity and flow direction on the calculated bulk temperatures and measured wall temperatures for air/water mist flow in a circular tube with a short unheated entry length

This is an example where the elevated wall temperature with a stable, continuous, liquid film is the main driver for the heat transfer enhancement caused by enhanced evaporation.

4.16 Thermal Entrance Region Effects

The data obtained in this investigation suggest that the thermal entrance region for spray mist cooling is generally longer than that for single-phase convection. This was the case for both short and long unheated entry lengths. This suggests that the increased entrance region length for mist flow is not solely due to the increased turbulence caused by the atomizing nozzle. Figures 4.77, 4.78, and 4.79 demonstrate this effect for downward mist flow in circular channels with either a gas-assisted or ultrasonic nozzles.

Figure 4.77 pertains to the case of downward air/water mist flow in a 23.6 mm ID circular tube (PIPE 3) with a short (14 cm) unheated entry length. The average carrier gas inlet velocity and wall heat flux are constant and equal to 15 m/s and 3.86 kW/m^2, respectively, while the injected water mass fraction is varied from 5 % to 15 %. Also shown is the case for single phase forced convection at the same carrier gas velocity. These experiments utilize the gas-assisted nozzle; the atomizing air flow rate (i.e. pressure) is adjusted to produce the optimal mean droplet diameter (42 μm SMD).

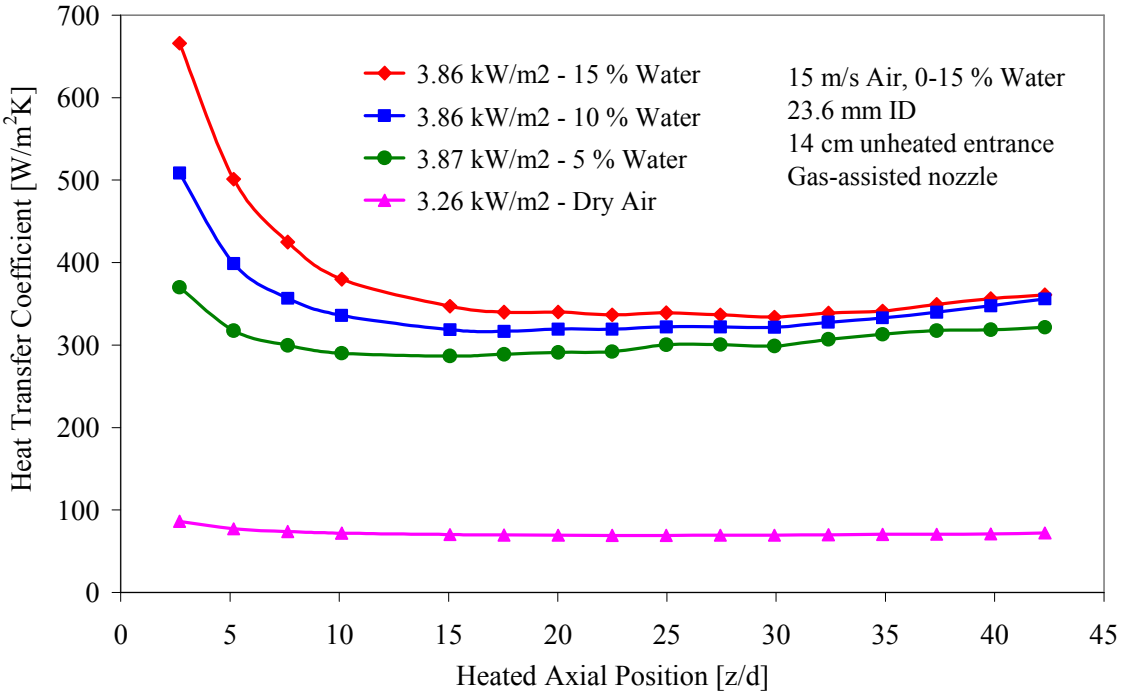

Figure 4.77 Effect of water mass fraction on the thermal entry length heat transfer for downward mist flow in a circular channel with a gas-assisted nozzle

These data clearly show that the thermal entry length is nearly equal to 15 pipe diameters regardless of the water injection mass fraction. In general, the heat transfer

coefficient rapidly decreases during the thermal entry length reaching a "fully-developed" value before gradually increasing as the wall temperature and bulk temperature continue to increase, thereby enhancing evaporation. At low heat fluxes, however, the "fully-developed" heat transfer coefficient remains essentially constant along the remainder of the tube as can be seen in Figure 4.78. These data pertain to downward mist flow in a smaller diameter tube (17.3 mm ID) with a lower carrier gas velocity (10 m/s) and different injection water mass fractions. Again, the entry length in this case is nearly 15 pipe diameters.

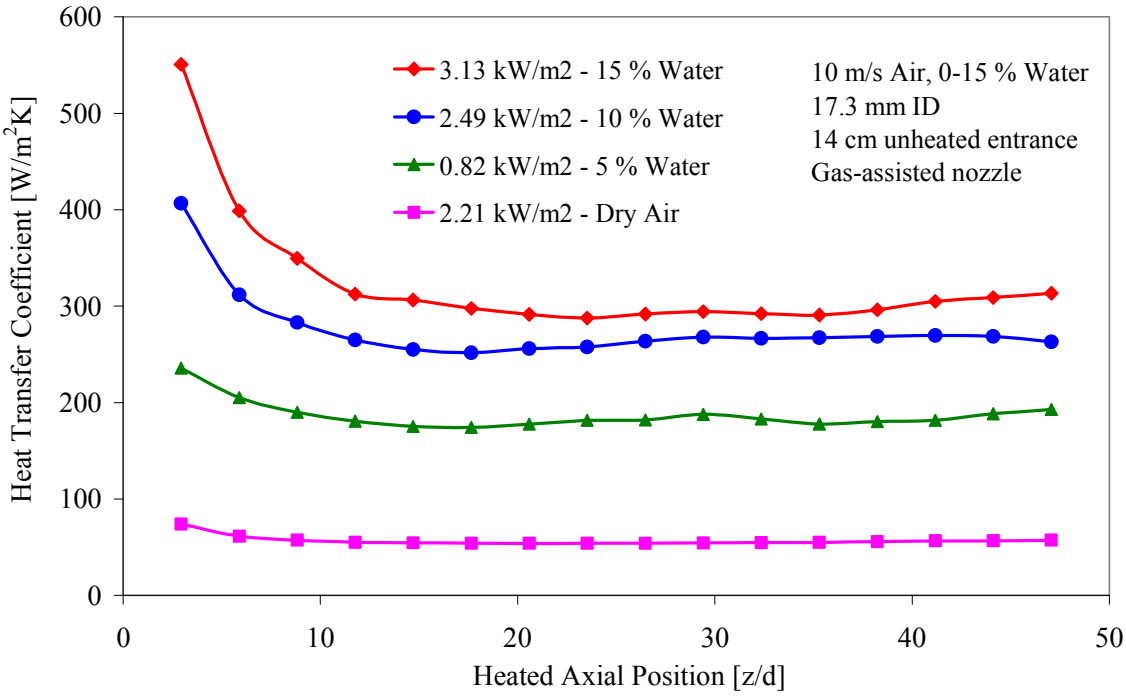

Figure 4.78 Thermal entry region heat transfer for downward mist flow in a circular tube with a short entry length and a gas-assisted nozzle

Figure 4.79 shows variations of the local heat transfer coefficient for downward air/water mist flow in a 23.6 mm ID circular tube. Here, a long (75 cm) unheated glass entry tube is used. Also, the mist is generated using the ultrasonic nozzle. An average carrier gas inlet velocity of 15 m/s is used with water mass fractions of 10 % and 15 % at a heat flux of 3.9 kW/m^2. These data are qualitatively and quantitatively similar to those shown in Figure 4.77 for the same size tube with a short PVC unheated entry length and a gas-assisted nozzle. The thermal entry length is again nearly equal to 15 times the pipe diameter.

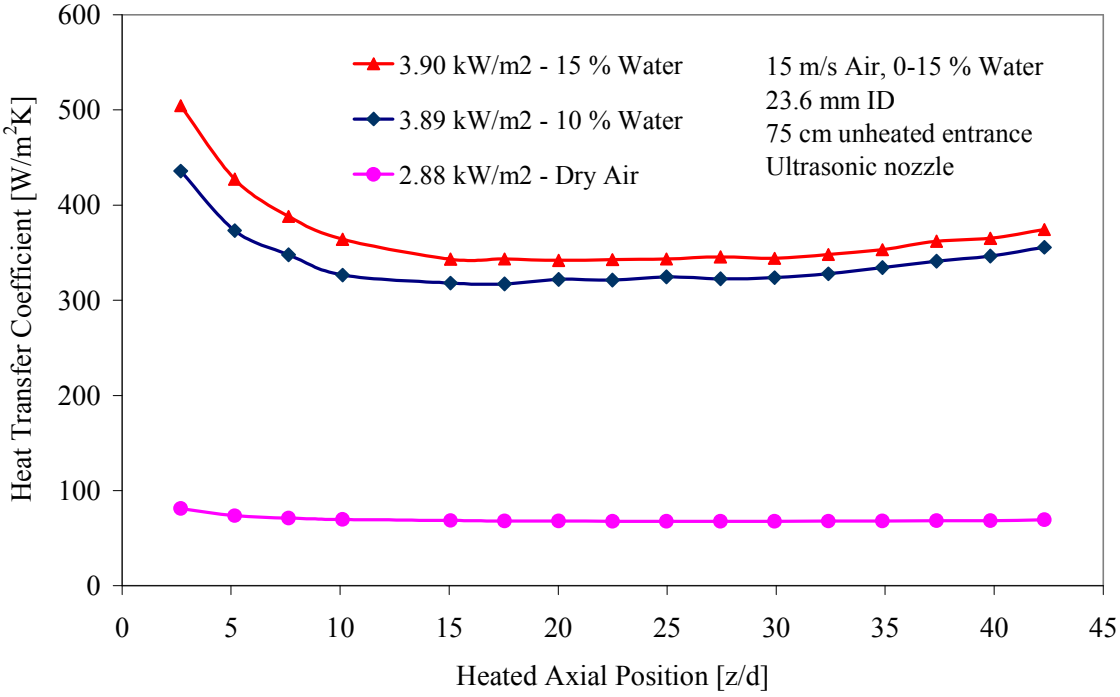

Figure 4.79 Effect of water mass fraction on the thermal entry length heat transfer for downward mist flow in a circular tube with a long unheated entry length and an ultrasonic nozzle

Figure 4.80 shows the effect of heat flux on the local heat transfer coefficients for downward air/water mist flow in a 23.6 mm ID circular tube (PIPE 3) with a short (14 cm) unheated PVC entry length. The data pertains to an inlet carrier gas velocity of 15 m/s and an injected water mass fraction of 15 %. The gas assisted nozzle is used with atomization air flow rate (i.e. pressure) corresponding to the optimum mean droplet diameter (42 μm SMD). Different values of heat flux ranging from 3.86 kW/m^2 to 11.44 kW/m^2 are used. In all cases, however, a stable liquid film is maintained along the entire heated length. The data shown in Figure 4.80 show that the thermal entry length can be easily determined at low heat fluxes where a nearly constant heat transfer coefficient is reached once fully-developed conditions are reached. At higher heat fluxes, however, it is difficult to determine the thermal entry length since the heat transfer coefficient gradually increases following the initial rapid drop near the beginning of the heated length. The gradual increase in the heat transfer coefficient is caused by enhanced evaporation due to the increasing wall temperature and bulk temperature as the mist proceeds along the channel length. The increase in the heat transfer coefficient begins closer to the heated length inlet as the heat flux is further increased making it difficult to pinpoint the thermal entry length and the point at which fully developed thermal conditions are reached. In essence, fully-developed conditions are never reached since the heat transfer coefficient increases throughout.

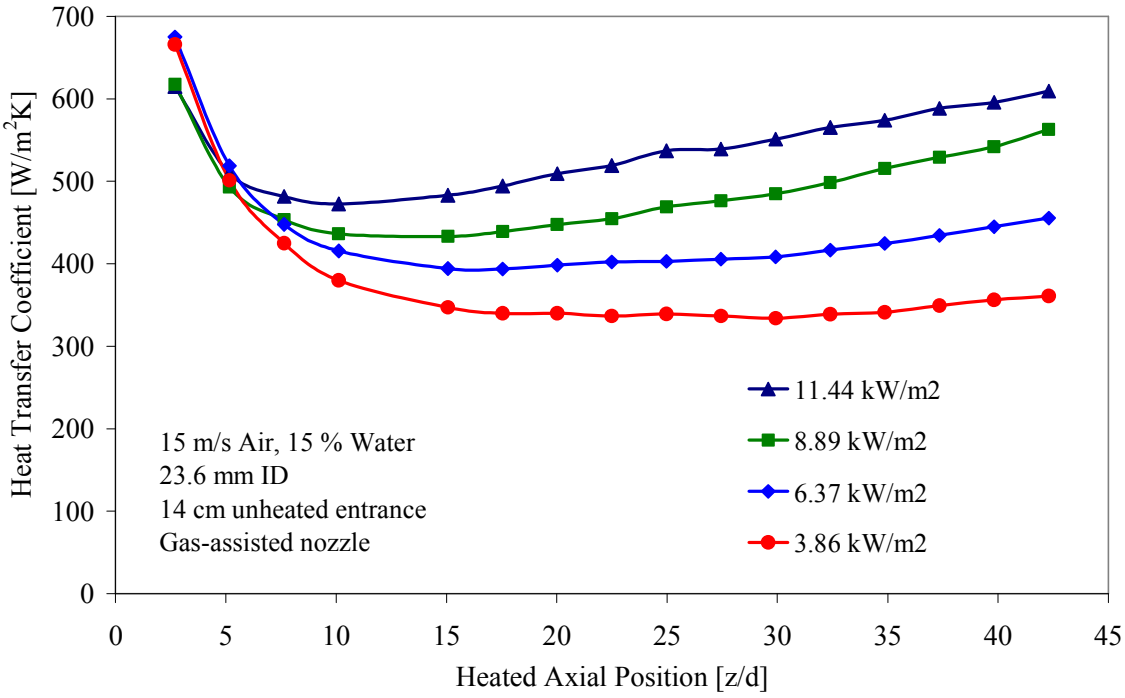

Figure 4.80 Effect of heat flux on the thermal entry length heat transfer of downward mist flow in a circular tube with a short unheated entry length and a gas-assisted nozzle

4.17 Summary

In this chapter, results showing the effect of various design and operational parameters on the effectiveness of mist cooling are presented. Local heat transfer coefficient data have been obtained for different nozzle designs, droplet sizes, heat fluxes, water injection rates, carrier gas velocities, injected water temperatures, carrier gas inlet temperatures and humidities, for both circular and rectangular cross sections with different unheated entry length and surface wettability. Both upward and downward flowing air/water mists have been tested. Experiments have also been conducted for downward flowing helium/water mists. The data indicate that the nozzle design has a significant impact on the heat transfer coefficients, gas-assisted nozzles provide the best

performance while the fixed geometry hydraulic nozzle produce the lowest heat transfer coefficients. For downward flow, optimum performance is achieved when the particle sizes are controlled within a relatively narrow range (~ 30 to 55 μm SMD). A much wider optimal droplet size range was obtained for upward mist flow (~ 20 to 100 μm SMD). The heat flux has a significant impact on the heat transfer coefficients. In general, as long as the liquid film remains intact along the entire heated length, higher heat transfer coefficients are obtained as the heat flux increases. This is directly related to the increased evaporation resulting from the higher wall (i.e. liquid film) temperatures. Increasing the water mass fraction generally enhances the heat transfer coefficients and delays film rupture; i.e. increases the heat flux at which film rupture is first observed. Increases in inlet water temperature, carrier gas inlet temperature and humidity generally increase the local heat transfer coefficients because of the increased wall temperatures and the corresponding increase in evaporation at the liquid film interface. The increases in wall temperature, however, is considerably smaller than the increase in bulk inlet temperature because of the non-linear relation between the evaporation rate and film temperature. Increasing the carrier gas velocity generally increase the heat transfer coefficient for downward mist flow; this however, is not always true for upward mist flow where higher heat transfer coefficients (and higher wall temperatures) can be obtained at lower gas velocities and water mass fractions.

In general, upward mist flow appears to be more effective than downward mist flow with the same flow conditions. Additionally, film breakdown for upward mist flow occurs at considerably higher heat fluxes than these for downward flow. Helium/water mist flow provides considerably higher heat transfer coefficients than air/water for the

same gas and water flow rates. The data suggest that the non-dimensional thermal entry length for mist flow is independent of the nozzle design, channel size, water mass fraction, and heat flux. It is also independent of the unheated hydrodynamic development entry length and its wettability.

In general, the performance of mist cooling can be optimized by operating at the highest carrier gas velocity subject to imposed constraints on the overall pressure drop in the system. Sufficient liquid should be injected to assure stability of the liquid film along the entire length of the heated channel at the highest expected wall heat flux. Mist cooling is clearly most suitable for high heat flux applications because of the enhanced evaporation to be attained as the film temperature increases.

CHAPTER V

NUMERICAL MODELING

The experimental data obtained in this investigation have been compared to predictions of the KIVA-3V code. This Chapter presents the results of that comparison. Section 5.1 provides an overview of the KIVA-3V code, while section 5.2 describes the modifications made to allow the code to model the experimental test conditions. Comparison between the experimental data and numerical model predictions is given in Section 5.3, while Section 5.4 presents the results of a parametric study aimed at identifying the sensitivity of model predictions to various parameters.

5.1 KIVA-3V Background

The KIVA-3V code has been developed by the Los Alamos National Laboratory for analysis of transient, three-dimensional, multiphase, multicomponent, chemically reacting flows with sprays. The code can be used from low speeds to supersonic flows for both laminar and turbulent regimes. Arbitrary numbers of species and chemical reactions are allowed. The original KIVA program was publicly released in 1985 [Amsden, *et al.* (1985)], and was followed by the improved KIVA-II in 1989 [Amsden, Butler, and O'Rourke (1987), and Amsden, O'Rourke, and Butler (1987)], and KIVA-3 in 1993 [Amsden (1993)], and KIVA-3V in 1997 [Amsden (1997)]. Here, the basic principal features of the KIVA-3V code will be discussed; a complete description of the code can be found in above mentioned publications.

The KIVA-3V code uses an Arbitrary Lagrangian Eulerian (ALE) methodology on a staggered grid. The code discretizes space using the finite-volume technique and uses an implicit time advancement, except for the advective terms which use an explicit time advancement. In order to avoid restricting the time step due to Courant conditions, the code can subcycle the convection calculations in the desired regions. A stochastic particle method is used to model evaporating liquid sprays, including aerodynamic breakups and droplet collisions effects. KIVA-3V bases liquid droplet evaporation on concentration gradients into a noncondensable gas, usually hot air, and uses the ideal gas assumption throughout its algorithm, as is done in all the major commercial computational fluid dynamics (CFD) codes. KIVA-3V is the first code version to incorporate a particle-based model for wall film dynamics, which models the dynamics and evaporation of liquid wall films. The basic model was described by O'Rourke and Amsden (1996). However, KIVA-3V Release 2 [see Amsden (1999)] contains a number of extensions to the basic model, e.g. splash velocities of secondary droplets, impingement pressure spreading, particle momentum and energy, gravitational terms, and other miscellaneous corrections to the basic wall film model. A generic version of KIVA-3V used in this study is dated December 22, 1998 and has all of the particle numerical wall film model corrections included in the latest KIVA code, i.e. KIVA-3V Release 2 issued in May 1999. A film formulation based on particles has the advantage of accurate calculation of convective transport of the film, and is compatible with the existing spray model. However, as stated by Amsden (1997),

"*It is important to note that the entire wall film model is still considered a work-in-progress and is expected to undergo further revisions and additions in the future. More comparison with experimental data will be required before the model can be considered validated.*"

The governing equations used in KIVA-3V for mass, momentum and energy for the continuous (gas) phase are:

$$\frac{\partial \rho}{\partial t} + \nabla \cdot (\rho \mathbf{u}) = \dot{\rho}^s \tag{5.1}$$

$$\frac{\partial (\rho \mathbf{u})}{\partial t} + \nabla \cdot (\rho \mathbf{u}\mathbf{u}) = -\nabla p - A_o \nabla \left(\frac{2}{3} \rho k \right) + \nabla \cdot \boldsymbol{\tau} + \mathrm{F}^s + \rho \mathbf{g} \tag{5.2}$$

$$\frac{\partial (\rho I)}{\partial t} + \nabla \cdot (\rho \mathbf{u} I) = -p \nabla \cdot \mathbf{u} + (1 - A_o) \boldsymbol{\tau} : \nabla \mathbf{u} + \nabla \cdot K \cdot \nabla T + \rho \varepsilon + \dot{Q}^s \tag{5.3}$$

The viscous stress tensor $\boldsymbol{\tau}$ is given by:

$$\boldsymbol{\tau} = \mu (\nabla \mathbf{u} + \nabla \mathbf{u}^T) + \lambda \nabla \cdot \mathbf{u} \mathbf{I} \tag{5.4}$$

Where μ and λ are the first and second coefficient of viscosity. The value of λ is equal to 2/3. The superscript T denotes the tensor transpose, while $\mathbf{I}$ is the unit dyadic second order tensor.

The equations for turbulent kinetic energy and its dissipation rate are

$$\frac{\partial (\rho k)}{\partial t} + \nabla \cdot (\rho \mathbf{u} k) = -\frac{2}{3} \rho k \nabla \cdot \mathbf{u} + \boldsymbol{\tau} : \nabla \mathbf{u} + \nabla \cdot \left(\frac{\mu}{\mathrm{Pr}_k} \nabla k \right) - \rho \varepsilon + \dot{W}^s \tag{5.5}$$

$$\frac{\partial (\rho \varepsilon)}{\partial t} + \nabla \cdot (\rho \mathbf{u} \varepsilon) =$$

$$-(\frac{2}{3} C_{\varepsilon 1} - C_{\varepsilon 3}) \rho \varepsilon \nabla \cdot \mathbf{u} + \nabla \cdot \left(\frac{\mu}{\mathrm{Pr}_\varepsilon} \nabla \varepsilon \right) + \frac{\varepsilon}{k} \left[C_{\varepsilon 1} \boldsymbol{\tau} : \nabla \mathbf{u} - C_{\varepsilon 2} \rho \varepsilon + C_s \dot{W}^s \right] \tag{5.6}$$

where the quantities $C_{\varepsilon 1}$, $C_{\varepsilon 2}$, $C_{\varepsilon 3}$, Pr_k, and Pr_ε are constants whose values are 1.44, 1.92, – 1.0, 1.0, and 1.3 respectively. They are determined from experiments and some theoretical considerations. The value C_s=1.5 is used as suggested by Amsden, O'Rourke and Butler (1989).

The transport coefficients (viscosity, μ and the thermal conductivity, K) represent their turbulent values, which are much larger than their laminar values due to the additional transport caused by turbulent fluctuations. They are:

$$\mu = \mu_g + C_\mu \frac{k^2}{\varepsilon}, \quad K = \frac{\mu C_p}{\mathrm{Pr}} \tag{5.7}$$

where C_μ is an empirical constant with the standard value of 0.09.

The source terms, such as $\dot{\rho}^s$, $\dot{W}^s$, F^s and $\dot{Q}^s$, are included due to the existence of the dispersed phase (droplets). Here, $\dot{\rho}^s$ is the rate of mass exchange due to droplet evaporation, $\dot{W}^s$ is the negative of the rate at which the turbulent eddies are doing work on dispersed droplets, F^s is the rate of momentum exchange between the two phases, and $\dot{Q}^s$ is the energy exchange rate due to spray which can be calculated in terms of total energy change of droplets and work done by the droplets to continuous phase.

The code solves finite-difference approximations of the governing equations. The general features and principles of the numerical scheme are as follows. Each differencing step has three Phases, i.e. Phase A, B, and C. Phase A is dedicated to the liquid phase. It uses the Lagrangian method in which computational cells move with the fluid. It tracks single particles within the computational domain and solves for their contribution to the mass, momentum and energy equations. The calculations of terms such as spray droplets

collision and oscillation/breakup are performed in this Phase. The governing equations in Phase A are the momentum and energy equations. Calculations for the gas phase are done in Phases B and C. Gas phase calculations use the Arbitrary Lagrangian-Eulerian method and have the ability of moving coordinates, necessary for modeling internal combustion engines, for which the KIVA-3V code was originally developed. Phase B uses the Lagrangian method, where diffusion is solved with the computational cells moving with the fluid, while convection is frozen. Phase C uses the Eulerian method, where diffusion is frozen, while the convective transport associate with moving computational mesh is solved and the flow field rezoned to a new mash. The governing equations for the gas phase are the continuity, momentum, and energy equations in addition to turbulence and species equations. A time step is calculated to satisfy the Courant condition, and the cycle is repeated. The types of boundary conditions modeled in KIVA-3V include, inlet boundary, outlet boundary, solid wall boundary, periodic boundary, along with boundary conditions for the particle phase. Because of its particular importance in modeling the experimental conditions used in this study, only the solid wall boundary is discussed further here. It consists of a velocity boundary condition, which can be slip, or no-slip boundary, and the temperature boundary. The temperature boundary condition can be either an adiabatic or a fixed temperature boundary. Initial conditions for the gas phase are velocity, temperature, pressure, turbulence and species, etc., while for the liquid phase they are the velocity, droplet temperature, size, etc.; they match the boundary conditions since the liquid phase is solved using the Lagrangian method.

The steps in running the code are as follows. First, the input preparation file is read, after which the grid is generated and boundary nodes specified, together making the

grid and boundary file. This file, together with the input operating condition file, is read by the main program, KIVA-3V. The main program then cycles through the liquid phase and gas phase solution steps until the specified convergence criteria are met, when the result file is generated.

Since the introduction of the original KIVA code in 1985, it has become the most widely used CFD program for multidimensional combustion modeling. Although KIVA-3V has been designed for internal combustion engine calculations, the modularity of the code allows for modifications that enable the code to be used in various problems with or without chemical reactions. To this end, the KIVA-3V has been modified to allow modeling of mist cooling with thin subcooled evaporating liquid films in heated channels.

5.2 KIVA-3V Modifications

Since the original KIVA-3V code can only accommodate either an isothermal or an adiabatic wall boundary condition, the original form of the code was not capable of modeling the mist cooling problem examined in this investigation where heat was added at the surface of the channel through which the mist is flowing. Therefore, it was necessary to modify the code to allow modeling of internal mist cooling with thin subcooled evaporating liquid films for channels with specified, non-zero heat flux at the wall and/or volumetric heating within the surrounding structures [Shin (2006)].

To identify the temperature boundary condition corresponding to volumetric heating within the surrounding structures (e.g. an ohmically heated channel wall), a separate heat conduction equation for the wall invoking a thin wall assumption has been

coupled to the conservation equations solved by KIVA-3V for the fluid domain. The heat conduction equation is given by:

$$\frac{1}{\alpha}\frac{\partial T_w}{\partial t} = \frac{\partial}{\partial x}\left(\frac{\partial T_w}{\partial x}\right) + \frac{\partial}{\partial z}\left(\frac{\partial T_w}{\partial z}\right) + \frac{q'''_w}{K} \qquad (5.8)$$

Here, T_w represents the wall temperature, α is thermal diffusivity, K is thermal conductivity, and q'''_w is a given thin wall heat generation (i.e. the volumetric heating rate within the wall structures). The wall material properties and thickness are specified as input variables. The conjugated equations (5.1-5.6) and (5.8) are simultaneously solved. The wall temperature T_w, from equation (5.8) is used as the boundary condition for the energy equation (5.3).

In addition to this modification, the input preparation file, i.e. iprep file, the input operating condition file, i.e. itape5 file, and the result file (i.e. output files Tsur, Tec, Par, Tavg, history and tsurmax) are modified for this particular application. The content of these files as well as the procedure of running the modified KIVA-3V code are explained in Appendix D. The important input variables in this study include, the flow direction, type of gas (air or helium), type of liquid (water or FC-72), inlet gas velocity, injected liquid mass flow rate and droplet velocity, entrance gas and water temperature, mass fraction of water vapor, oxygen and nitrogen, wall heat generation and its starting time, number, orientation and location of the nozzles, spray geometry, droplet size and time at which injection begins, turbulent Schmidt number (Sc_t) and turbulent kinetic energy, and time and space resolution. The numerical operating conditions are chosen to closely approximate the experimental conditions used in this study. The inlet velocity is assumed to be uniform and the velocity magnitude is calculated using the measured gas flow rate.

Another modification to KIVA-3V is in the manner in which liquid droplets are introduced into the system. A random liquid particle injection model has been developed. Here, the liquid droplets are injected randomly across the entire cross section of the entrance plane with specified injection velocity. In addition, KIVA-3V includes an injection routine with a cone type spray nozzle. Here, the cone angle, location of the point source of injection, and direction and velocity of injection can be defined. These two different injection types are shown in Figure 5.1. The calculations presented in this study assume the injected droplet size to be uniform. The wall heat generation rate can be set to be either constant or pulsed; the first models the conditions used in this experiment, while the latter can be used to model condition for the pulsed Electra KrF laser foils. The channel geometry can be set to either cylindrical or rectangular. If rectangular, all for sides could be heated, or only two opposite sides could be heated while the other two opposite sides are insulated. Again, the first models the conditions used in the experiment with the second rectangular test section, while the second models the conditions used in the first rectangular test section as well as those for the dual-foil hibachi structure in Electra.

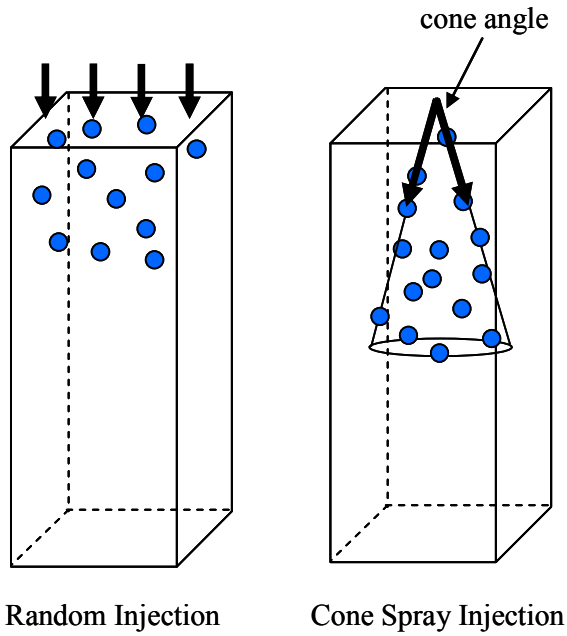

Figure 5.1 Droplet injection types

Figure 5.2 shows a typical simulation geometry and boundary condition used to model the first rectangular channel (i.e. DUCT 1) with heating only from the front and back surfaces. The inlet velocity of 15 m/s is set at the channel entrance, while an open boundary condition is used at the exit. The cross sectional channel dimensions in the *x* and *y* directions are 40 mm and 20 mm, respectively. The total heated channel length is 610 mm, while the unheated length, $z_{unheated}$ can be specified depending on the actual test condition.

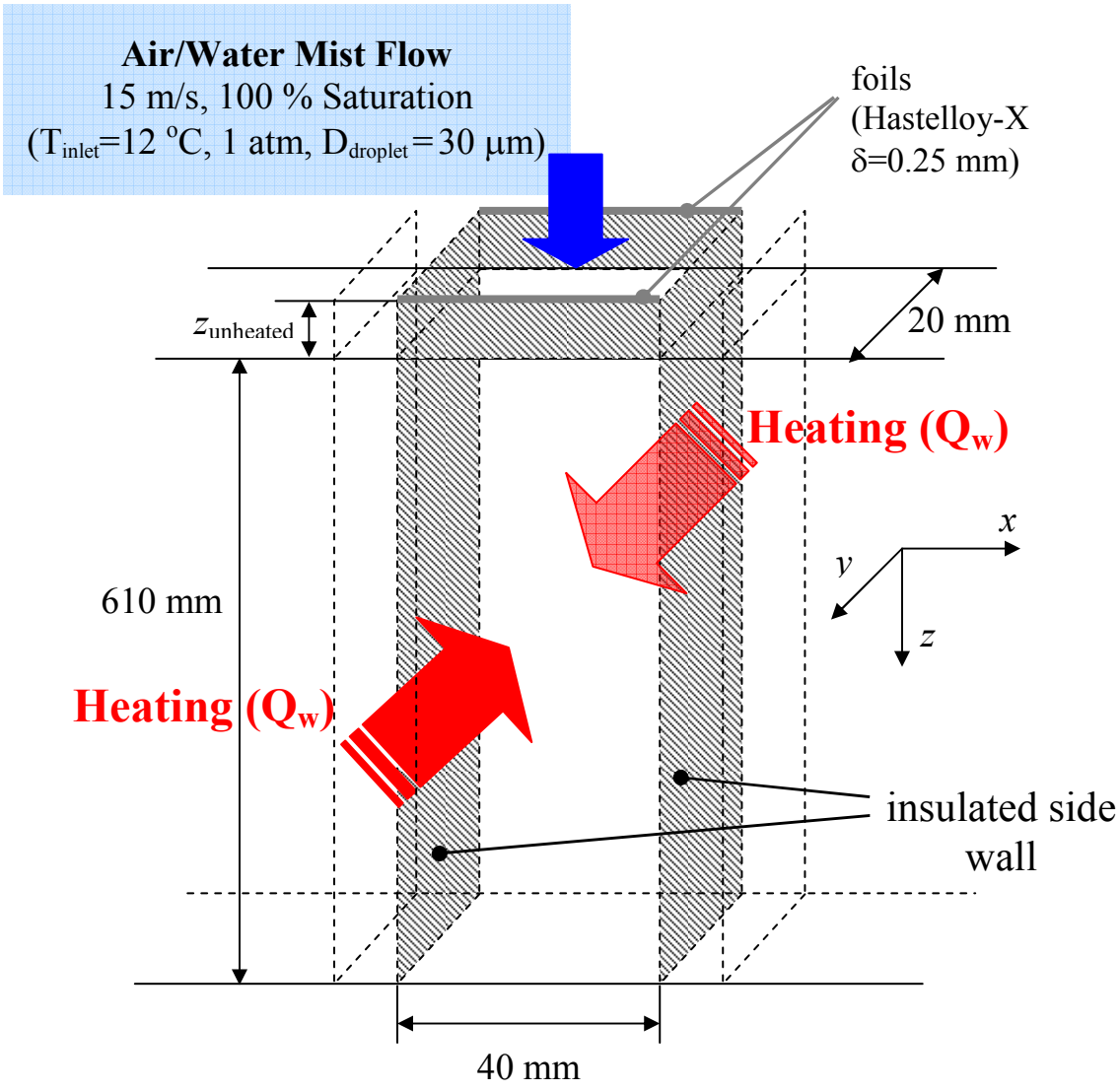

Figure 5.2 A typical simulation geometry and boundary conditions

5.3 Model Validation

In order to validate the modified KIVA-3V code, its predictions are compared with the experimental results obtained in this investigation for downward and upward mist flow. The comparisons are done for both, the gas-assisted and ultrasonic nozzles. For comparisons with the ultrasonic nozzle the random injection model is used, while for the gas-assisted nozzle the cone spray injection model is used. The droplet size used is the Sauter mean droplet diameter. The input variables are matched to the experimental variables as close as possible. Only the results obtained for the 23.6 mm ID circular tube (PIPE 3) with an average carrier gas inlet velocity of 15 m/s (air) and 15 % water mass fraction are presented here (Appendix C). Results for both downward and upward air/water mist flow are presented.

5.3.1 Downward Mist Flow

Comparisons have been made between the code predictions and experimental data for downward air/water mist flow obtained for cases with a long unheated channel entry length (70 cm). Such comparison should reduce the effect of the unknown gas velocity profile at the mixer and visualization tube connection. By using a long unheated channel length, it is believed that this effect is minimized.

Figure 5.3 shows a comparison between the experimental and predicted values for the inside wall temperature, gas bulk temperature, and local heat transfer coefficient. These results pertain to the case when the gas-assisted nozzle is used with a wall heat flux of 5.12 kW/m^2, which is significantly lower than the critical film breakdown heat flux

range. The droplet size at the inlet is assumed to be uniform and equal to 30 μm. Figure 5.4 shows the liquid film thickness predicted by the model for the same case.

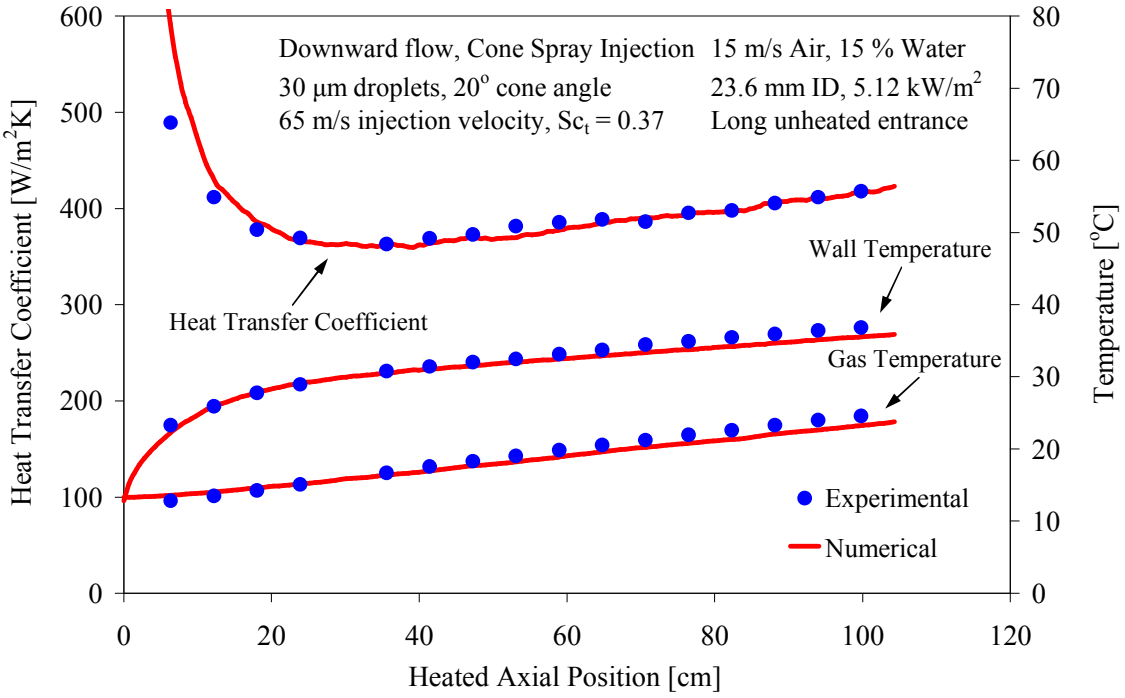

Figure 5.3 Comparison between experimental and predicted values of the local heat transfer coefficient, wall temperature, and gas bulk temperature for downward air/water mist flow in a circular tube with a gas-assisted nozzle at a low heat flux

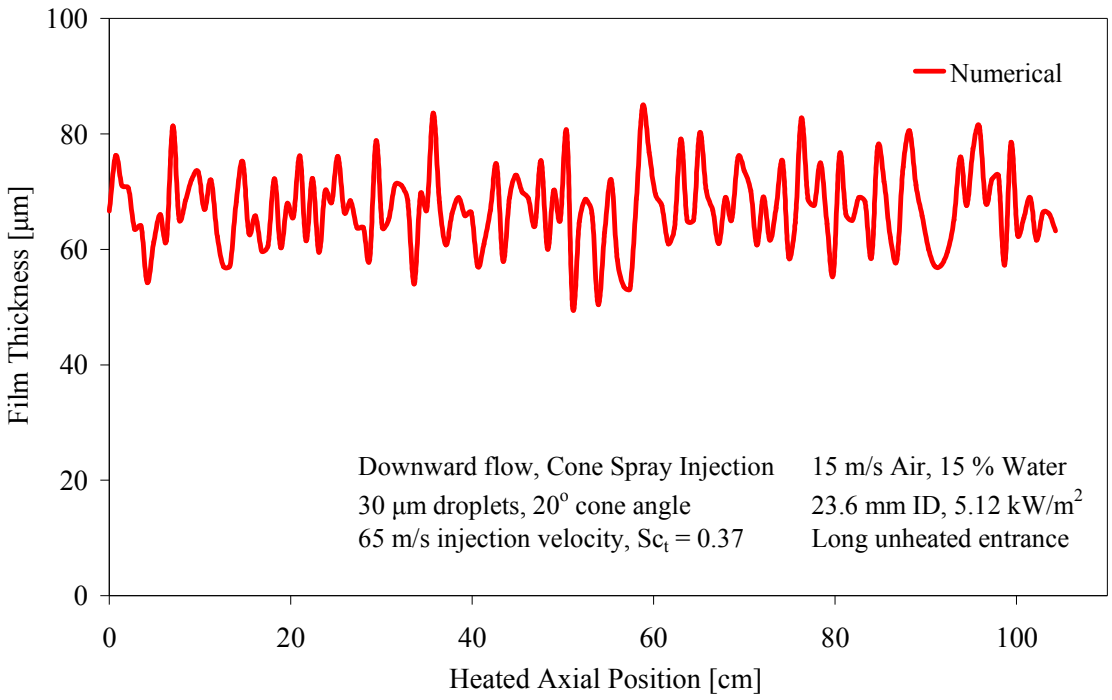

Figure 5.4 Predicted film thickness for downward air/water mist flow in a circular tube with a gas-assisted nozzle at a low heat flux

The results show remarkable agreement between the experimental and predicted values for the local heat transfer coefficient, wall temperatures, and gas temperatures. The average film thickness predicted by the code is approximately 68 μm. The experimental apparatus did not have the means to measure the film thickness; hence, independent verification of the predicted film thickness was not possible.

Figures 5.5 and 5.6 show similar results for the case of an ultrasonic nozzle. Here the droplet size at the inlet is assumed to be uniform and equal to 60 μm. The droplets are assumed to be randomly introduced into the test section.

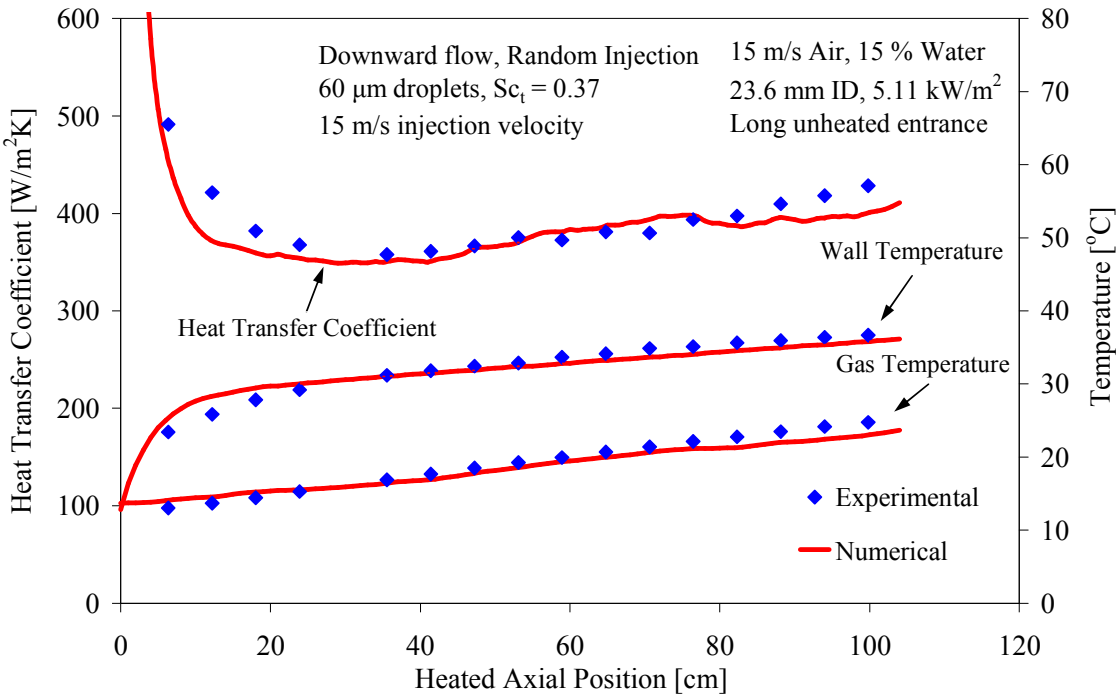

Figure 5.5 Comparison between experimental and predicted values of the local heat transfer coefficient, wall temperature, and gas bulk temperature for downward air/water mist flow in a circular tube with an ultrasonic nozzle at a low heat flux

Again, the results show remarkable agreement between the experimental and predicted values for the local heat transfer coefficient, wall temperatures and gas temperatures. Deviations between experimental and predicted values of the local heat transfer coefficients are present primarily near the entrance region. These deviations can be attributed to uncertainties in the manner by which the droplets are introduced into the channel; the actual manner in which the ultrasonic nozzle introduces the drops into the channel is clearly different than the random droplet introduction model used in the simulations. There are also uncertainties in the velocity distribution of the carrier gas at

the channel inlet because of the mixer geometry. Here, however, the model assumes the inlet velocity to be uniform.

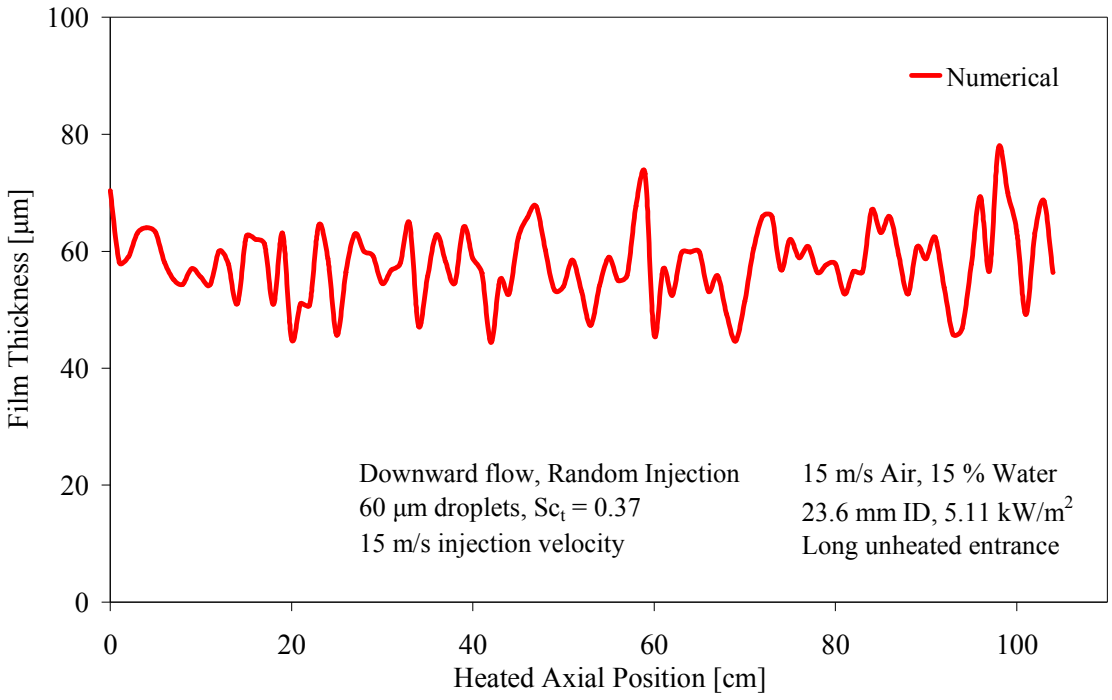

Figure 5.6 Predicted film thickness for downward air/water mist flow in a circular tube with an ultrasonic nozzle at a low heat flux

The predicted average liquid film thickness in this case is nearly 58 µm. Again, the value cannot be independently verified. Interaction between the low velocity droplets generated by the ultrasonic nozzle and the possibly non-uniform carrier gas velocity distribution at the inlet may result in preferential droplet deposition near the channel inlet. This would significantly increase the liquid film thickness along the channel. In contrast, the high velocity droplets generated by the gas-assisted nozzle may be less disrupted by interacting with the non-uniform, relatively slow, carrier gas at the inlet. This would

reduce the likelihood of droplet deposition near the channel inlet. Hence, the fact that the liquid film thickness predicted by the code for the ultrasonic nozzle is less than that for the gas-assisted nozzle may simply be traced to uncertainties in the inlet boundary conditions and may not reflect the actual experimental performance. Nevertheless, the experimental apparatus does not provide the means to directly measure the film thickness along the channel wall.

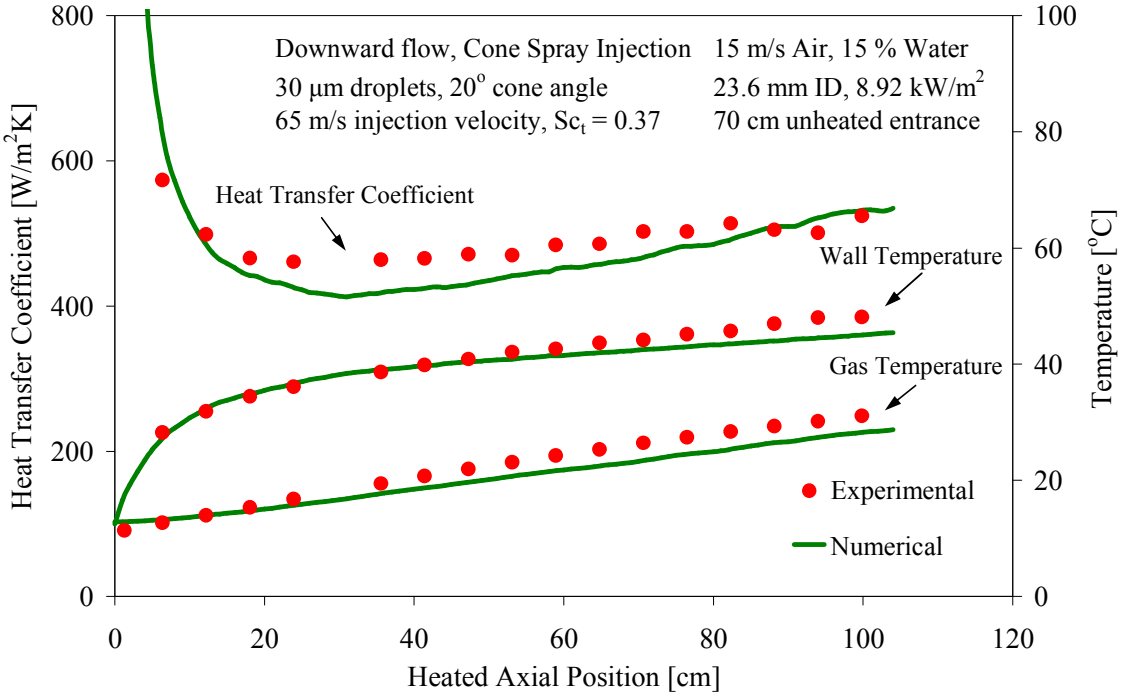

Figure 5.7 Comparison between experimental and predicted values of the local heat transfer coefficient, wall temperature, and gas bulk temperature for downward air/water mist flow in a circular tube with a gas-assisted nozzle at a high heat flux

Comparisons similar to those shown in Figure 5.3 for the gas-assisted nozzle have been conducted at an elevated wall heat flux near the point where film rupture is expected to begin near the test section exit. The results are shown in Figure 5.7 for a wall heat flux

of 8.92 kW/m2. The corresponding variation of liquid film thickness predicted by KIVA-3V is shown in Figure 5.8.

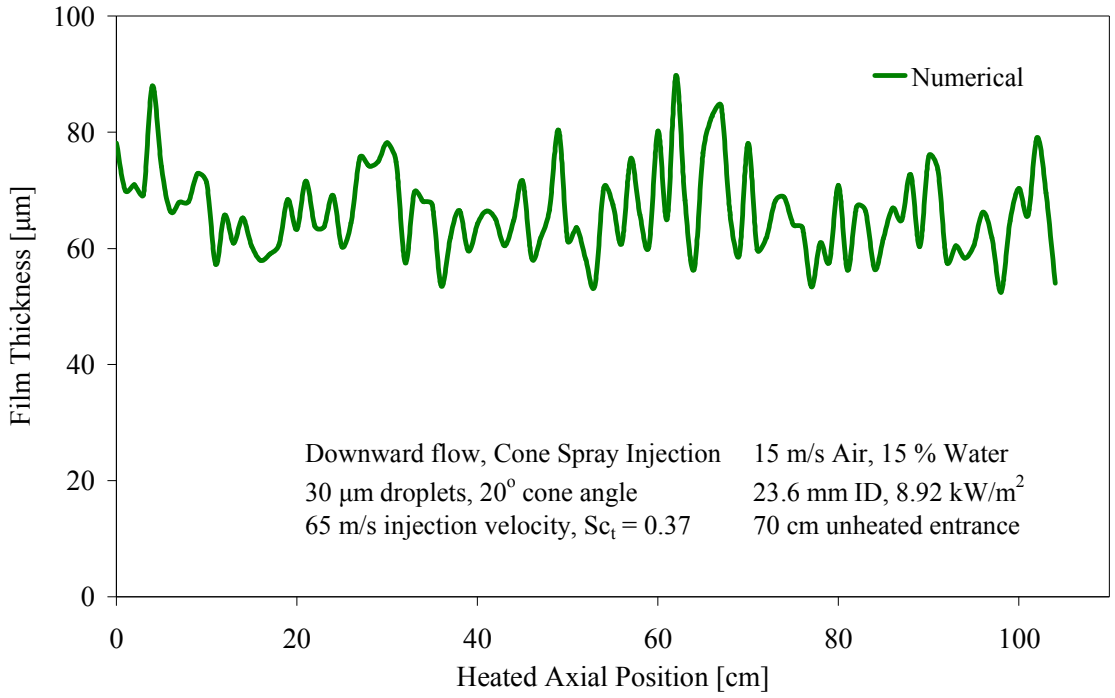

Figure 5.8 Predicted film thickness for downward air/water mist flow in a circular tube with a gas-assisted nozzle at a high heat flux

The results show reasonable agreement between the experimental and predicted values of the local heat transfer coefficients, wall temperatures, and gas bulk temperatures. The deviations are somewhat larger than those for the low heat flux case (Figure 5.3). The model appears to underpredict all three parameters. The predicted and measured wall temperatures show excellent agreement approximately half of the way along the heated length; after that the predicted wall temperature is lower which could suggest that at increased wall temperatures typical for the second half of the heated length the model

predicts a better cooling performance than experimentally observed. It is not clear why the model underpredicts the bulk temperature along most of the heated length. The macroscopic energy balance by which the experimental values are calculated is clearly different than the detailed integration scheme used in the model. The average liquid film thickness predicted by the model is nearly 66 μm which is comparable to the value predicted for the low heat flux simulation (68 μm). The model predicts the film to remain intact along the entire length of the heated test section.

In order to assess the model's ability to predict the onset of film rupture, the model was used to simulate high heat flux experiments where film rupture was clearly indicated by the experimental data. The predictions for the case when the ultrasonic nozzle is used are shown in Figures 5.9 and 5.10. The experimental data show a rapid decrease in the local heat transfer coefficient at a point approximately two thirds of the way along the heated length. The predicted values do not show any indication of film breakdown. As can be seen in Figure 5.10, the average film thickness is nearly 52 μm with no indications of film breakdown anywhere along the heated length. Clearly, this is a case where the model fails to predict the observed film behavior. The model predictions for the case when the gas-assisted nozzle is used also do not predict film breakdown. Modification of the KIVA-3V film model is outside the scope of this investigation.

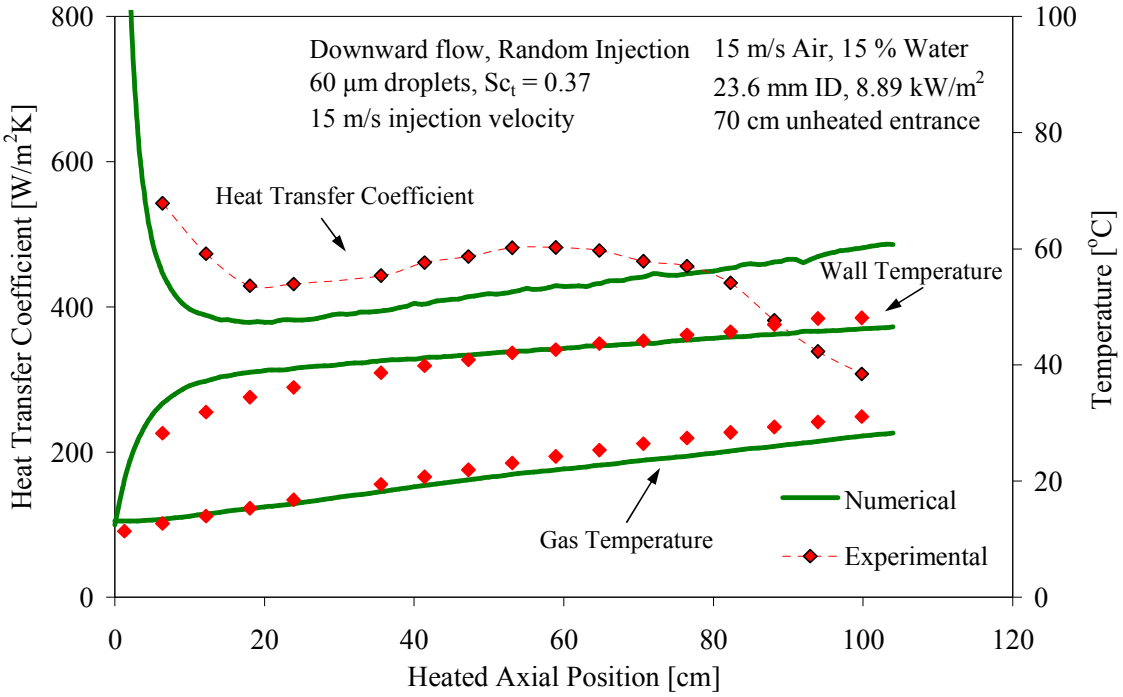

Figure 5.9 Comparison between experimental and predicted values of the local heat transfer coefficient, wall temperature, and gas bulk temperature for downward air/water mist flow in a circular tube with an ultrasonic nozzle at a high heat flux with film rupture

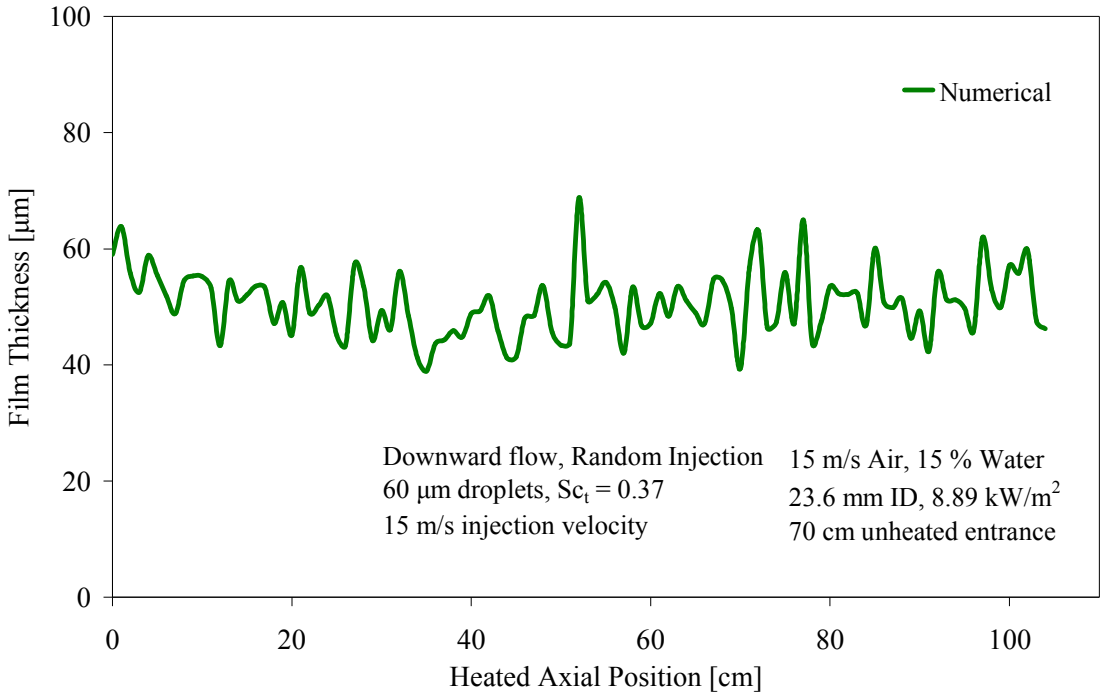

Figure 5.10 Predicted film thickness for downward air/water mist flow in a circular tube with an ultrasonic nozzle at a high heat flux

5.3.2 Upward Mist Flow

Comparison have been made between the KIVA-3V code predictions and experimental data for upward air/water mist flow. Experiments were only conducted using the gas-assisted nozzle with a short unheated entry length. While uncertainties remain regarding the inlet velocity distribution of the carrier gas when a short hydrodynamic entry length is used, these effects are believed to be small for upward flow. Also, the effect of the transition between the unheated visualization tube and the heated test section inlet is believed to be small for upward flow because of flooding effects. Two cases have been compared; the first corresponds to a low wall heat flux (6.38 kW/m^2) where the flow remains intact along the entire heated surface, while the

second corresponds to a higher wall heat flux (15.33 kW/m^2), which is still below the value corresponding to film breakdown. Figure 5.11 shows the experimental and predicted values of the local heat transfer coefficient, wall temperature, and bulk temperature for the lower heat flux case; the corresponding film thickness distribution predicted by KIVA-3V is shown in Figure 5.12. Results for the high heat flux case are shown in Figure 5.13 and 5.14, respectively.

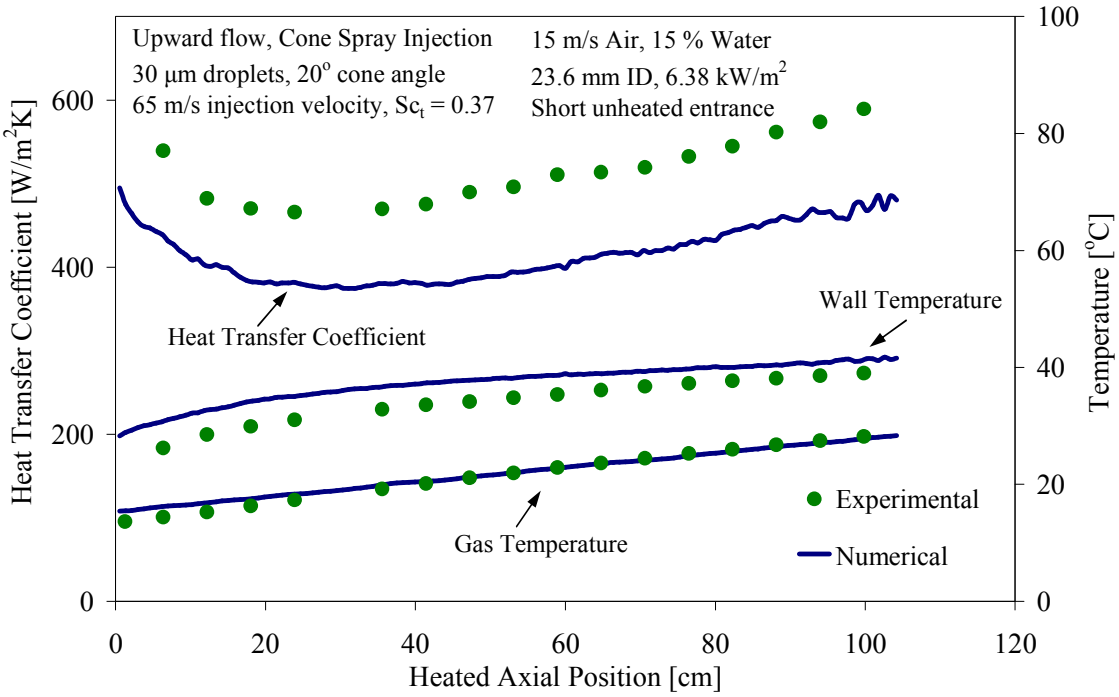

Figure 5.11 Comparison between experimental and predicted values of the local heat transfer coefficient, wall temperature, and gas bulk temperature for upward air/water mist flow in a circular tube with a gas-assisted nozzle at a low heat flux

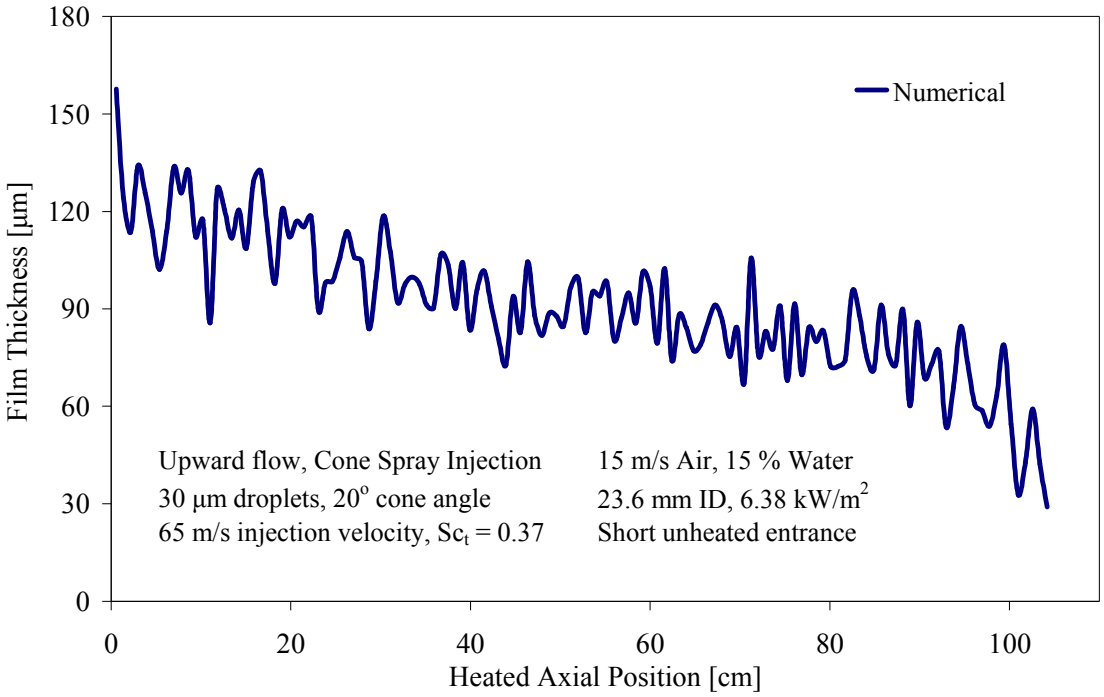

Figure 5.12 Predicted film thickness for upward air/water mist flow in a circular tube with a gas-assisted nozzle at a low heat flux

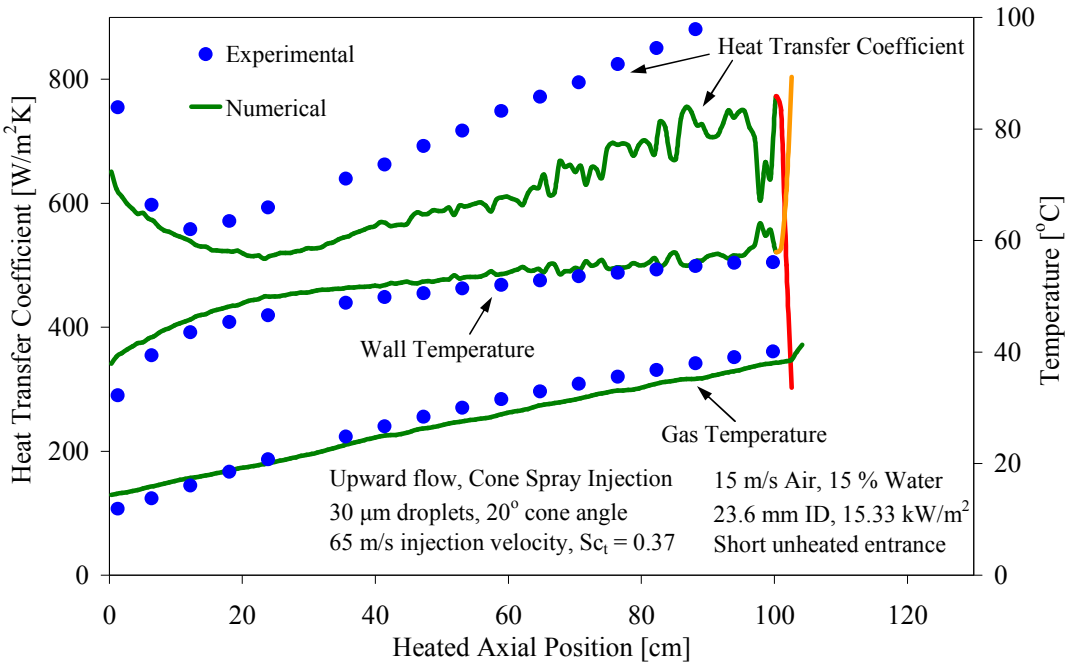

Figure 5.13 Comparison between experimental and predicted values of the local heat transfer coefficient, wall temperature, and gas bulk temperature for upward air/water mist flow in a circular tube with a gas-assisted nozzle at a high heat flux

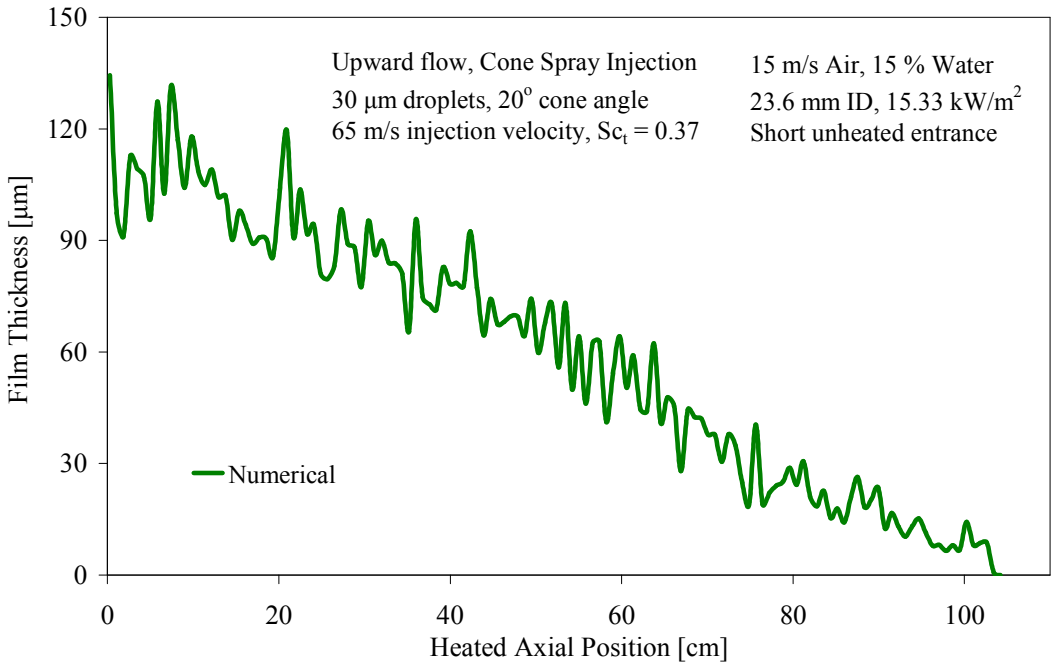

Figure 5.14 Predicted film thickness for upward air/water mist flow in a circular tube with a gas-assisted nozzle at a high heat flux

Referring to Figure 5.11 where the low heat flux case is presented, it is evident that the code significantly underpredicts the local heat transfer coefficient values over the entire length of the test sections. The fact that the model over-predicts the wall temperature indicates that the evaporation model may under-predict the evaporation massflux, thereby increasing the thermal resistance at the wall. Alternatively, the high thermal resistance predicted by the model may, in part, be do to the relatively large film thickness particularly near the test section inlet. The predicted film thickness ranges from 130 μm near the inlet to 48 μm near the exit. The model predicts that counter-current flow will occur near the channel inlet; negative (i.e. downward) liquid velocities were predicted. The accuracy of that is questionable since no liquid accumulation was observed in the inlet mixer at the conclusion of the experiment; liquid out flow due to counter-current conditions at the inlet was only observed at lower carrier gas velocities. The low heat transfer coefficient predicted by the model may be attributed to the "loss" of liquid through outflow at the inlet.

Referring to Figure 5.13 where the results of the high heat flux case are presented, it is again evident that the code significantly underpredicts the local heat transfer coefficient. More significant is the code's erroneous prediction that dryout will occur at the test section exit as can be seen in Figure 5.14, where the liquid film thickness is predicted to gradually decrease from an inlet value of 120 μm to zero at the exit. At the dryout point, the wall temperature rapidly increases, while the heat transfer coefficient rapidly decreases toward the single-phase (air-only) forced convection value. The fact that the code is sufficiently robust to predict such a transition without "crashing" is admirable; nevertheless, the predictions are incorrect. Again, the model predicts that

counter-current flow will take place at the test section inlet as evidenced by the negative (i.e. downward) liquid velocities. It is possible that the predictions of early dryout is closely linked to the "loss" of liquid through outflow at the inlet. This result points to the possibility that the model may underestimate the shear force exerted by the upward moving carrier gas on the liquid film interface. The gravitational forces acting on the liquid may then dominate resulting in counter-current flow conditions at the inlet and liquid loss through outflow. The experimental data do not slow any indication of either dryout at the exit or liquid out flow at the inlet. It is interesting to note that the code's predictions for downward mist flow were generally reasonable since gravitational forces and shear stress forces exerted by the gas at the liquid film surface are co-directional. The above results point to the need for closer examination of the constitutive relations used in the code for momentum exchange between the flowing gas core and the liquid film. Such examination is out side the scope of this investigation.

5.4 Parametric Analysis

A parametric study has been conducted to examine the sensitivity of the model's predictions to variations in different parameters. The analysis performed earlier for downward air/water mist flow in a circular tube with an ultrasonic nozzle at a low heat flux (Figure 5.5) has been repeated by parametrically varying the inlet droplet diameter within the range of 15 μm to 100 μm. The results are shown in Figure 5.15. These results indicate that the assumed droplet diameter has a significant impact on the predicted behavior within the thermally developing region. Larger droplets produce a considerably shorter entry length as evidenced by the rapid approach to the "fully-developed" value of

the local heat transfer coefficient. The droplet diameter appears to have little impact on the predicted behavior beyond the entrance region; the predicted values of the local heat transfer coefficient, wall temperature, and bulk temperature are virtually the same for droplet sizes between 15 μm and 100 μm.

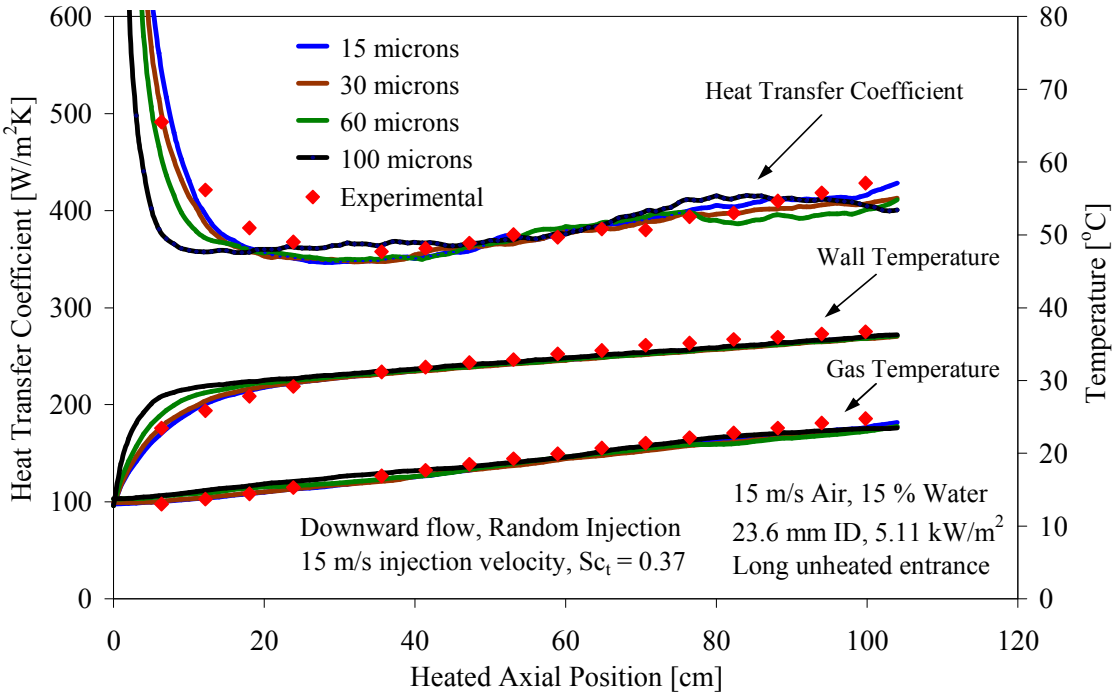

Figure 5.15 Effect of droplet size on the predicted values of local heat transfer coefficients, wall temperature, and bulk temperature for downward air/water mist flow in a circular tube with an ultrasonic nozzle at low heat flux

A similar parametric analysis has been performed for the downward air/water mist flow case in a circular tube with a gas-assisted nozzle at a low heat flux. Droplet diameters ranging from 15 μm to 100 μm have been used. The results (Figure 5.16) for 15 μm to 50 μm droplets indicate that the assumed droplet diameter has little impact on the local heat transfer coefficient, wall temperature, and bulk temperature. However, 100 μm droplets

show a significant impact on the predicted behavior within the thermally developing region. They produce a considerably longer entry length and higher local heat transfer coefficient. Similar behavior within the thermally developing region was observed in experiments using droplets near the upper limit of the examined droplet size range. Beyond the entrance region the examined droplet diameters appear to have little impact on the predicted values of the local heat transfer coefficient, wall temperature, and bulk temperature. Nevertheless, these results point to the importance of accurate representation of the model by which the droplets are introduced into the channel.

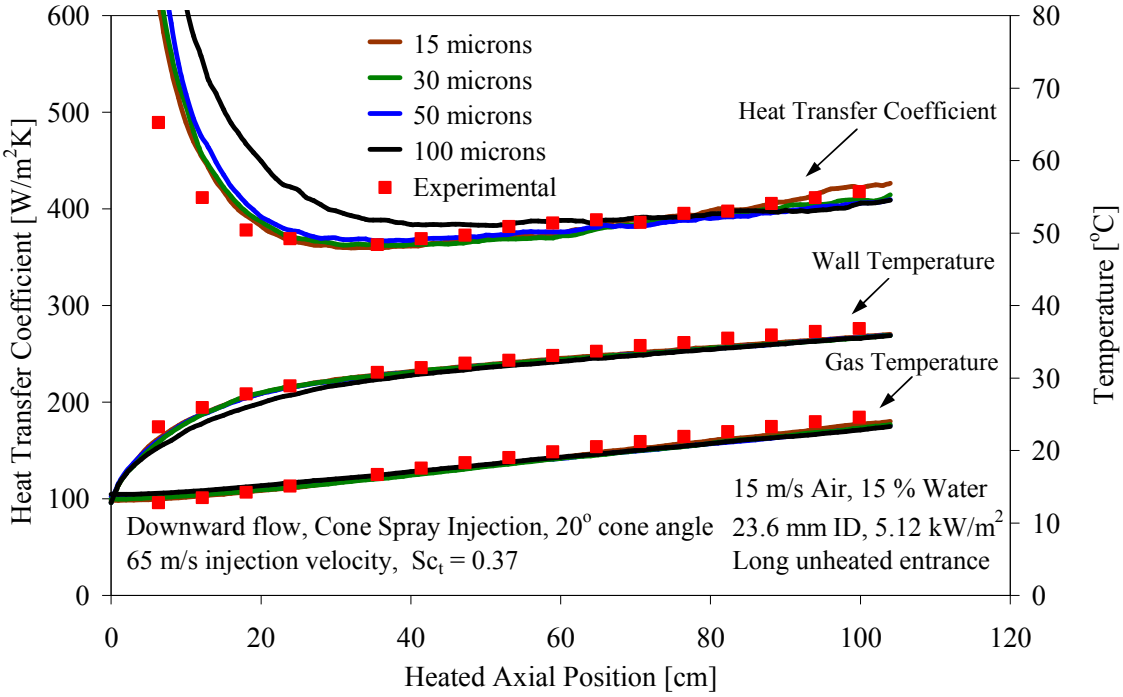

Figure 5.16 Effect of droplet size on the predicted values of local heat transfer coefficients, wall temperature, and bulk temperature for downward air/water mist flow in a circular tube with a gas-assisted nozzle at low heat flux

Among the parameters used in this model which significantly impacts the evaporation process is the turbulent Schmidt number, Sc_t. Parametric calculations have been performed to assess the sensitivity of the model predictions to the assumed value of Sc_t. The two cases presented above for downward air/water mist flow with either an ultrasonic nozzle (Figure 5.15) or a gas-assisted nozzle (Figure 5.16) were repeated using different values of Sc_t. The corresponding results are shown in Figure 5.17 and 5.18, respectively. The results for both cases indicate that the predicted values of the local heat transfer coefficient are sensitive to changes in the turbulent Schmidt number. As expected, higher values of the turbulent Schmidt number, i.e. reduction in the evaporation rate due to turbulence, results in a lower heat transfer coefficients.

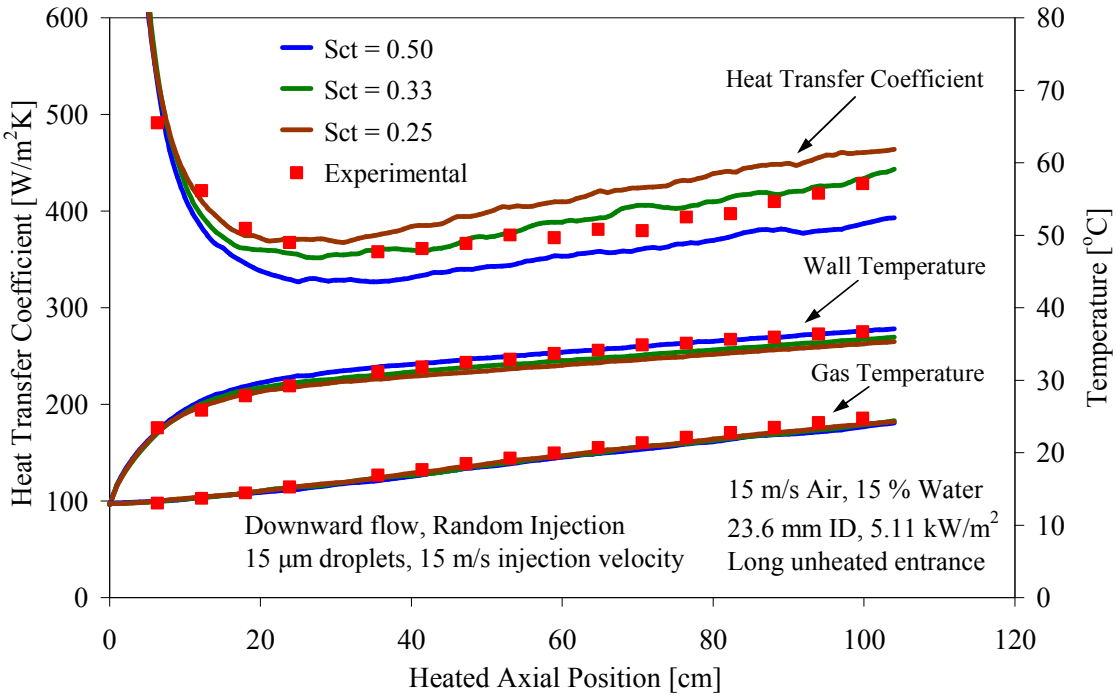

Figure 5.17 Effect of Turbulent Schmidt number on predicted performance for downward air/water mist flow in a circular tube with an ultrasonic nozzle at low heat flux

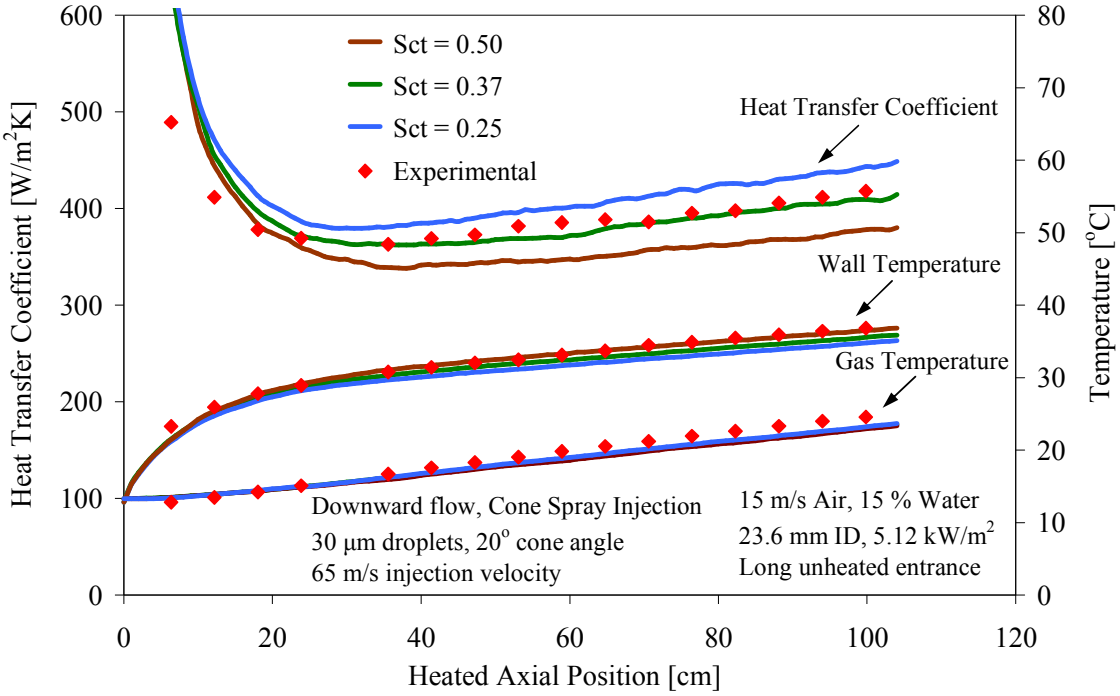

Figure 5.18 Effect of turbulent Schmidt number on predicted performance for downward air/water mist flow in a circular tube with a gas-assisted nozzle at low heat flux

The effect of spray cone angle on the predicted performance for the gas-assisted nozzle case discussed above was examined (Figure 5.19). Cone angle of 20° and 40° were assumed. The results indicate that for this set of conditions, the cone angle has little effect on the predicted performance. Independent confirmation of this observation was not possible since the gas-assisted nozzle design does not allow the cone angle to be varied.

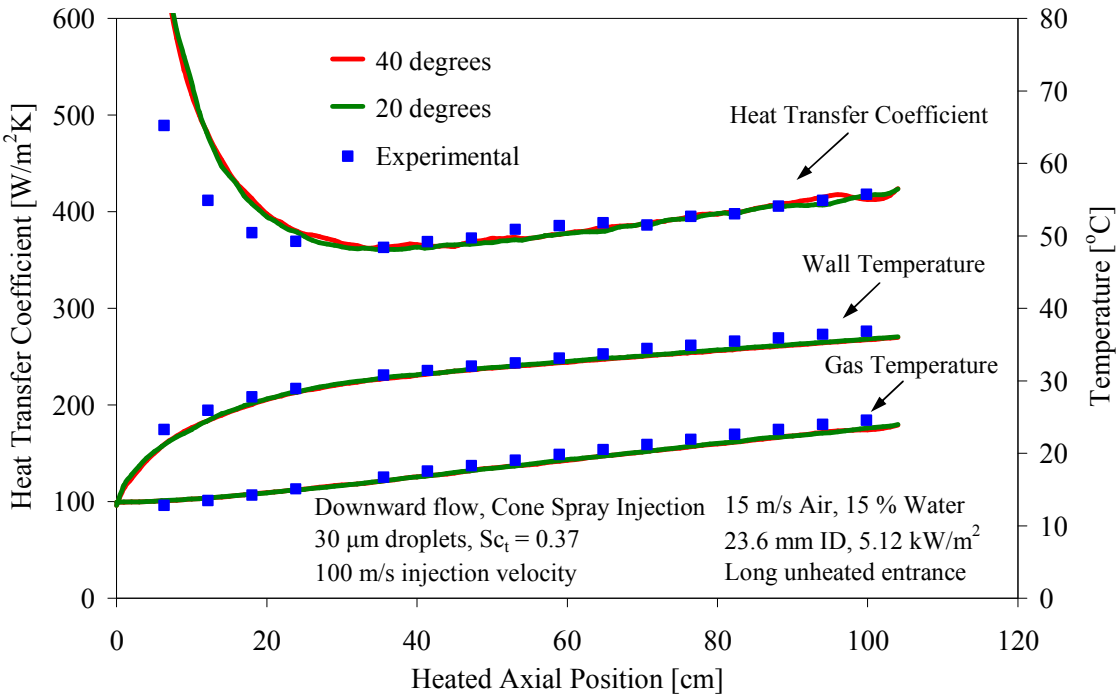

Figure 5.19 Effect of spray cone angle on predicted performance for downward air/water mist flow in a circular tube with a gas-assisted nozzle at low heat flux

The effect of droplet injection velocity on the predicted performance has been parametrically examined. The analysis performed earlier for downward air/water mist flow in a circular tube with an ultrasonic nozzle at a low heat flux (Figure 5.5) has been repeated by parametrically varying the droplet injection velocity from 1.5 to 150 m/s. Figure 5.20 shows variations of the predicted values of the local heat transfer coefficient, wall temperature, and bulk temperature. As described earlier, the droplets are assumed to be randomly injected through the entire inlet cross section. The results indicate that for this particle injection mode, the injection velocity has little effect on the predicted performance. This, however, is not the case for the point source, solid cone, spray model used to model the gas-assisted nozzle. The analysis performed earlier for downward

air/water mist flow in a circular tube with a gas-assisted nozzle at a high heat flux (Figure 5.7) has been repeated by parametrically varying the droplet injection velocity. Here, the droplet injection velocity was varied slightly from only 15 m/s to 65 m/s; the results are shown in Figure 5.21. This change in droplet injection velocity produced large changes in the predicted values of local heat transfer coefficients and wall temperature particularly in the thermal entrance region. However, for droplet injection velocities higher than 65 m/s changes in the predicted values are not as significant.

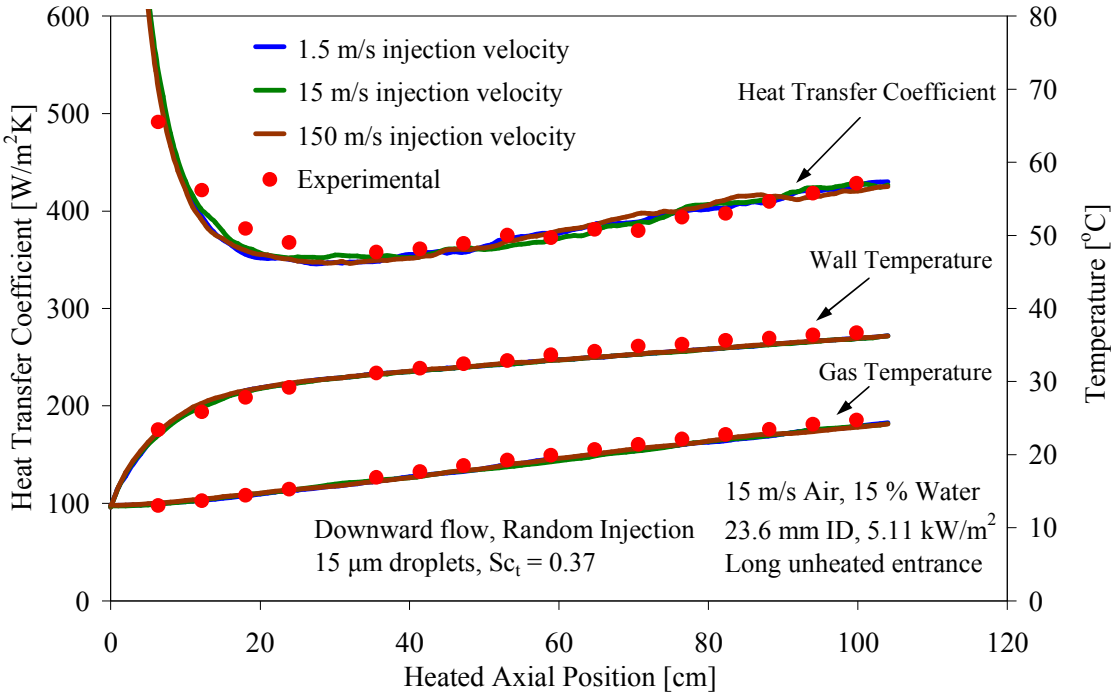

Figure 5.20 Effect of droplet injection velocity on the predicted values of local heat transfer coefficients, wall temperature, and bulk temperature for downward air/water mist flow in a circular tube with an ultrasonic nozzle at low heat flux

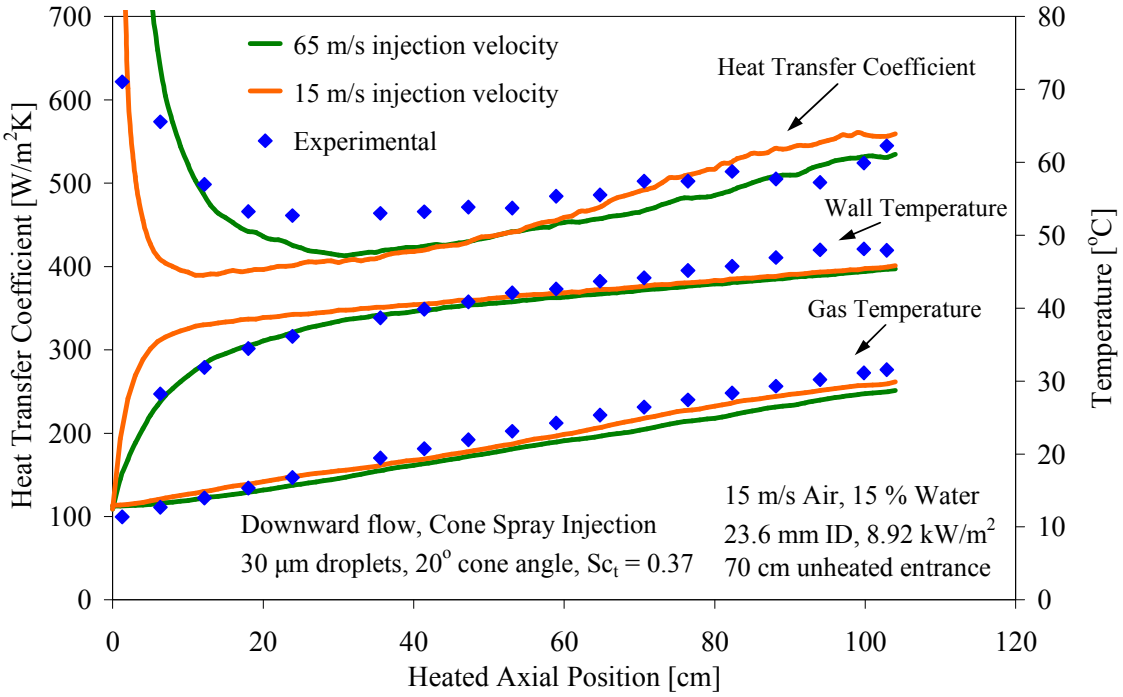

Figure 5.21 Effect of droplet injection velocity on the predicted values of local heat transfer coefficients, wall temperature, and bulk temperature for downward air/water mist flow in a circular tube with a gas-assisted nozzle at high heat flux

CHAPTER VI

CONCLUSIONS AND RECOMMENDATIONS

6.1 Conclusions

An experimental and numerical investigation has been conducted to examine the effects of various operating and design parameters on the cooling effectiveness of steady, internal, nozzle-generated, gas/liquid mist flow in vertical channels with ultra-thin, evaporating subcooled liquid films. This cooling method yields high heat transfer coefficients due to the phase change at the interface between the evaporating liquid film and the flowing mist core. The effectiveness of this cooling mechanism depends on the ability to maintain a stable liquid film over the entire heated surface through droplet deposition from the mist flowing through the channel. The high heat transfer coefficients, along with the low wall temperatures, obtained with this technique make it ideally suitable to high heat flux applications. Interest in this work has been motivated by the need for such an effective cooling scheme for the Electra high power laser developed for inertial fusion application.

Among the operating and design parameters impacting mist cooling effectiveness examined in this investigation are: the liquid atomization nozzle design (i.e. spray geometry, droplet size distribution, and droplet velocity/spray momentum), heat flux, gas/liquid combinations, carrier gas velocity, temperature, and humidity, liquid mass fraction, film thickness, injected liquid temperature, flow direction, test section geometry and length, and unheated entrance length and its surface wettability. A fully-instrumented experimental test facility has been designed and constructed. The facility includes three

cylindrical and two rectangular electrically-heated test sections with different unheated entry lengths. Water is used as the mist liquid with air, or helium, as the carrier gas. Three types of mist generating nozzles with significantly different spray characteristics are used. Over 1,500 experiments have been conducted to quantify the effect of these parameters on mist cooling effectiveness. A list of the parameter ranges used in this investigation is given in Table 6.1. Of particular interest is the effect of these parameters on the local heat transfer coefficient along the channel and likelihood of film rupture prior to the channel exit for both upward and downward flow. In addition, comparison has been made between the experimental data and predictions of a modified version of the KIVA-3V code [Amsden (1997) and (1999)], a mechanistic, three-dimensional computer program for internal, transient, dispersed two-phase flow applications. The original KIVA-3V code can only accommodate either an isothermal or an adiabatic boundary condition. The code has been modified to allow modeling of the test geometry, as well as the actual Electra hibachi geometry by simultaneously solving the heat conduction equation in the surrounding structure with either steady or pulsed heat generation.

Table 6.1 List and ranges of operating and design parameters used in this investigation

Nozzles	Gas-atomized nozzle Ultrasonic nozzle Fixed geometry hydraulic nozzle
Droplet Size Distribution	30-55 μm droplet size optimization for the gas-atomized nozzle
Heat Flux	Nearly zero - 51 kW/m2
Carrier Gas	Air Helium
Gas Velocity	Air: 5 m/s, 6 m/s, 10 m/s, 15 m/s, 30 m/s Helium: 24 m/s, 30m/s
Inlet Gas Temperature	Nearly 19 ^{o}C - 24 ^{o}C
Inlet Gas Relative Humidity	Nearly zero - 40 %
Mist Liquid elsewhere	Distilled water
Water Fraction	Air: 5 %. 10 %, 15 %, 19 %, (up to 209 %) Helium: ~ 20 %, 40 %, 60 %
Water Injection Temperature	2 ^{o}C, 22 ^{o}C, 55 ^{o}C, 95 ^{o}C
Flow Direction	Upward flow Downward flow
Cylindrical Channels ID and Length Effects Rectangular Channels Cross section and Length Effects	16 mm ID – 610 mm long 17.3 mm ID – 882 mm long 23.6 mm ID – 1052 long 20 mm x 40 mm – 622 mm long 16.6 mm x 35.6 mm – 889 mm long
Unheated Entry Length and Wettability	3.8 cm - 75 cm; acrylic, PVC, and glass

The data obtained in this investigation will allow designers of mist-cooled high flux engineering systems to predict their performance over a wide range of design and operational parameters.

Based on the results of this investigation, the following conclusions can be drawn:

1. Mist cooling is an effective cooling mechanism provided that the liquid film can remain stable over the entire surface of the heated channel. Order of magnitude enhancements in the heat transfer coefficient compared to turbulent forced convection of the carrier gas alone can be readily attained.
2. The nozzle design (i.e. spray characteristics) has a significant impact on mist cooling effectiveness. The narrow-angled cone and high velocity spray produced by the gas-assisted nozzle provides the fastest and most uniform droplet film deposition mechanism ensuring film stability over the entire length of the test section. The ultrasonic nozzle has a narrow angle spray; however, the mist produced by that nozzle has considerably less forward momentum compared to that produced by the gas-assisted nozzle. This provides less uniform droplet deposition along the channel length, which in return, may result in an uneven film thickness and possible thermocapillary breakdown prior to the test section exit. This is believed to be the reason for the somewhat poorer performance of the ultrasonic nozzle. The wide-angled cone with low velocity spray generated by the fixed geometry hydraulic nozzle produced significantly poorer cooling performance than the narrow-angled cone and low velocities spray generated by the ultrasonic nozzle. The significant drop in performance is believed to be due to the highly non-uniform droplet deposition along the heated channel length.

3. Droplet size plays a major role in cooling performance of the gas-assisted nozzle. The optimal droplet size range for downward mist flow is nearly 30-55 μm. Below and above that, liquid film breakdown occurred at lower heat fluxes. Smaller droplets (typical for extremely high atomizing gas velocities) tend to be carried out of the channel without depositing on the heated surface, while larger droplets (typical for low atomizing gas velocities) tend to deposit early along the channel resulting in a non-uniform film thickness. The optimum droplet size range for upward mist flow is considerably wider (20 to 100+ μm).
4. The wall heat flux significantly impacts mist cooling performance. Increasing the heat flux significantly increases the local heat transfer coefficient as long as the liquid film remains intact. A higher heat flux increases the inside wall surface temperature, and therefore, the liquid film surface temperature which enhances evaporation at the liquid film/gas interface and increases cooling performance. All other factors being equal, a higher heat flux will always produce a higher wall temperature; however, increased evaporation considerably limits the increase in wall temperature. The liquid film breaks and rivulet flow is established when the heat flux exceeds a critical value corresponding to the flow conditions. Film breakdown results in significant and rapid reduction in the local heat transfer coefficients.
5. Helium/water mist produces significantly higher heat transfer coefficient than air/water mist for the same gas and liquid flow rates.
6. A higher gas velocity for nearly the same liquid film flow rate and heat flux provides a more stable liquid film. This is due to a combination of two things, a lower wall temperature at the higher gas flow rate, as well as a higher shearing force

at the film/gas interface. A higher carrier gas enhances evaporation at the gas/film interface, and, therefore, produces higher heat transfer coefficients. However, the enhancement ratio, i.e. the ratio between the resulting heat transfer coefficients and those for the carrier gas alone, may not always increase with increasing carrier gas velocity.

7. For nearly the same liquid film flow rate and wall temperature, a lower gas velocity provided a more stable liquid film. This suggests that a thicker liquid film is more resistant to film breakdown than a thinner film, for the same wall temperature and film flow rate. However, a higher gas velocity provides a more stable liquid film when the film thickness, i.e. the water mass fraction, and heat flux are kept constant. For the same liquid film thickness, i.e. water mass fraction, and maximum heat fluxes, a higher gas velocity provides better cooling performance. Higher heat fluxes can be achieved without film breakdown. In general, for the same mist characteristics, higher heat transfer coefficients, and significantly higher heat fluxes can be attained without film rupture, by increasing the carrier gas flow rate and liquid mass fraction.

8. A lower carrier gas inlet temperature results in lower wall temperatures and higher achievable heat fluxes. However, it does not yield higher heat transfer coefficients due to the reduction in evaporation at the gas/film interface. Higher inlet gas temperature will always increase the wall temperature despite the increase in heat transfer coefficients due to increased evaporation. Additionally, increasing the carrier gas inlet temperature will limit the maximum achievable heat flux prior to film breakdown and establishment of rivulet flow.

9. A lower carrier gas inlet relative humidity (before mixing with the spray droplets) due to the reduction in gas temperature following adiabatic humidification by the spray droplets yields lower wall temperatures, despite the lower heat transfer coefficients. Increasing the gas inlet relative humidity (before combining with the spray droplets) will increase the wall temperature and decrease the gas/wall temperature difference, since the gas enters the test section at a higher temperature than in a lower gas inlet humidity case. The local heat transfer coefficients will also increase due to increased evaporation at higher temperatures.
10. For the water mass fractions used in this study, i.e. 5 %, 10 % and 15 %, when all other variables are kept the same, the thermal resistance of the film remains nearly constant as long as a stable liquid film can be maintained on the entire heated surface. However, with higher water fractions, higher heat fluxes could be achieved before film breakdown occurs. Additionally, as the water mass fraction increases, the entrance region heat transfer coefficients increase because of the increase in the convective component of the film heat transfer coefficient with increasing liquid film flow rates. For the same carrier gas velocity, the peak heat transfer coefficient at the highest achievable heat flux prior to film breakdown increases nearly linearly with water mass fraction. However, at extremely high liquid mass fractions, the liquid film thickness will significantly increase, thereby reducing the heat transfer coefficient, and increasing the wall temperatures.
11. An increase in the injection water temperature has the same effect as an increase in the carrier gas inlet temperature, i.e. it increases the wall temperature and the heat transfer coefficients due to enhanced evaporation. However, when all other

parameters are kept constant, an increase in the injection water temperature will decrease the maximum achievable heat flux prior to film breakdown.

12. For the same flow conditions and mist characteristics, upward flow mist cooling achieves significantly higher heat transfer coefficients than downward flow. The highest enhancement ratio achieved in this study for upward flow was nearly 30, while for downward flow it was nearly 18. Upward flow results in better circumferential film thickness uniformity and ensures liquid film uniformity as it flows along the channel. For this reason, it is less sensitive to droplets size variation (larger droplets are more tolerable) and nozzle misalignment compared to downward mist flow with the same flow conditions and mist characteristics; significantly higher heat fluxes can be achieved using upward mist flow before the onset of film breakdown.
13. For the same carrier gas velocity and liquid film mass fraction, higher heat transfer coefficients are achieved as the channel diameter increases. This is related to the higher moisture carrying capacity of the gas (proportional to D^2) than the increase in linear heat rate (proportional to D). However, for the same gas flow rates, a smaller diameter channel yields higher heat transfer coefficients even at somewhat lower water mass fractions. Nevertheless, for the same carrier gas velocity and mass fraction, film stability is enhanced as the tube diameter increases.
14. Rectangular test sections have higher local heat transfer coefficients on their wider sides than on the narrower sides for both single phase turbulent forced convection and air/water mist flow.

15. Shorter channels (compared to the thermal entry length) have higher heat transfer coefficients and can achieve higher heat fluxes before film rupture occurs. This is caused by the higher droplet deposition near the "point source" injection point, a more uniform film thickness along the entire channel length, and reduced thermocapillary forces.
16. A shorter unheated entry length results in a longer thermal entrance region, which increases the overall average heat transfer coefficient. Additionally, increasing the unheated entry length reduces the maximum achievable heat flux before film breakdown at the heated channel exit. The increase in unheated entry length reduces droplet deposition uniformity along the heated length.
17. For channels with a long unheated entry section, the wettability of the unheated entry significantly impacts liquid film stability. For lower wettability materials such as PVC, the liquid film tends to break earlier than the case of a wettable unheated entry section. For channels with a short unheated test section, surface wettability of the entry section has little impact on film stability when a gas-assisted nozzle was used; the high spray momentum produced by the gas-assisted nozzle tends to overcome the wettability effect.
18. Excellent agreement has been obtained between the experimental values of the local heat transfer coefficients, wall temperatures, and gas bulk temperatures and the corresponding values predicted by KIVA-3V for downward mist flow at low heat fluxes below the critical film breakdown range. At higher heat fluxes where film breakdown is experimentally observed, the code does not predict the onset of film breakdown, thereby overestimating the heat transfer coefficient in the ruptured film

region. In general, differences between experimental data and code predictions increase as the heat flux increases.

19. For upward mist flow, the code consistently underpredicts the local heat transfer coefficient. Counter-current annular flow is predicted near the test section inlet with significant loss of liquid through out-flow. At elevated heat fluxes, this leads to liquid film "starvation" and dryout near the heated channel exit. Neither of these effects was experimentally observed. These observations suggest that the model underestimates the shear force exerted on the liquid film thereby enhancing liquid loss through out-flow near the test section inlet.

6.2 Recommendations

Based on the results of this investigation, several recommendations can be made regarding future research in this area. These recommendation include:

- An investigation of nozzle-generated mist cooling with thin saturated evaporating liquid films should be undertaken in order to quantify the limiting performance of mist cooling heat transfer and the corresponding film breakdown limits.
- Experiments using considerably higher inlet carrier gas temperatures should be conducted to more systematically examine the gas inlet temperature effects on mist cooling performance. The test apparatus should be modified to allow pre-heating of the carrier gas well above room temperature before entering the test section.

- Experiments should be conducted at considerably higher gas velocities than those used in this study; considerably higher enhancement ratios can be attained as the carrier gas velocity is increased.
- Additional experiments need to be conducted at considerably higher water mass fractions; again, considerably higher enhancement ratios can be obtained as the water mass fraction is increased. Additionally, significantly higher heat fluxes can be attained prior to the onset of film rupture as the water injection rate is increased.
- Experiments should be conducted at different operating pressures, which may facilitate the development of a generalized empirical correlation for the heat transfer coefficient over a wide range of operating conditions.
- The experimental apparatus should be modified to allow the liquid film thickness to be measured, in order to confirm model predictions.
- Additional thermocouples should be used at each of the instrumented axial locations in order to better predict the azimuthal variations in the heat transfer coefficients particularly downstream of the film breakdown point.
- An investigation should be conducted to identify the reasons for the discrepancies between predictions of the KIVA-3V code and the experimental data particularly for the upward mist flow and for downward mist flow at elevated heat fluxes. Armed with the extensive data base generated in this investigation, code modifications can be tested to assess their success.

APPENDIX A

DATA ACQUISITION AND PROCESSING CODES

In this appendix, the codes used in data acquisition and initial processing (e.g. Visual Basic code) and the main experimental data processing (i.e. Engineering Equation Solver (EES) codes) are presented, respectively.

A.1 Data Acquisition Code

When steady state conditions are reached the Visual Basic code run from its Excel sheet is used to communicate, configure, and control all of the 60 channels of the Agilent data acquisition unit. The data acquisition procedure controlled by the Visual Basic code involves sequential scanning of all 60 channels which takes several seconds. The scanned data is then transferred to a PC and stored into its Excel sheet. As soon as this is done, the next sequential scan of the 60 channels is taken. The code repeats this cycle as many times as specified in the code's configuration subroutine. After the scanning is completed and all of the sequentially measured data are stored, the Visual Basic code time-averages the readings for each channel and redistributes them into a pre-designed table in the same Excel sheet. The code is shown below.

```
''''''''''''''''''''''''''''''''''''''''''''''''''''''''''''''''''''''''''''''''''''''''''''''''''''''''''''''''''''''''''''''''
'The programs and functions contained in this sheet, "RS232", can be used to
'send SCPI commands and receive data from the HP 34970A Data acquisition unit
'over an RS232 line.
''''''''''''''''''''''''''''''''''''''''''''''''''''''''''''''''''''''''''''''''''''''''''''''''''''''''''''''''''''''''''''''''
Option Explicit
Private WithEvents mComm As MSCommWrapper.Ccomm
Public Function InitializeApp() As Boolean
   Set mComm = New MSCommWrapper.Ccomm     ' Create a new cComm object
   On Error GoTo InitializeApp_Error       ' Install an error handler
   With mComm
      .CommPort = 1&                   ' The port to use
      .SettingsAsString = "57600,N,8,1"   ' Comm settings
                                 ' Enable receive event on any char
      .EnableDataReceivedEvent lngThreshold:=1&
      .OpenPort                        ' Open the serial port
   End With
   InitializeApp = True                ' Success!
   Exit Function
InitializeApp_Error:
   ' On any error display an error message
   MsgBox "Error (" & CStr(Err.Number) & "): " & Err.Description
   InitializeApp = False               ' Failure!
   Set mComm = Nothing                    ' Release the cComm object
End Function
Public Sub TerminateApp()
   On Error Resume Next    ' Ignore errors
   mComm.ClosePort         ' Close the port if open
   Set mComm = Nothing     ' Release the cComm object
End Sub
Public Sub SendSCPI(TextToUnit)
   ' If the cComm object has not been initialized, initialize it
   If mComm Is Nothing Then
      If Not InitializeApp() Then Exit Sub
   End If
   ' Send the B3 cell contents out the port
   mComm.WriteToPort CStr(TextToUnit) + Chr(10)
End Sub
Function GetSCPI() As String
   Dim rngTextReceived As Excel.Range
   Dim strTextReceived As String
   ' If the cComm object has not been initialized, initialize it
   If mComm Is Nothing Then
      If Not InitializeApp() Then Exit Function
   End If
   ' If any characters are received, place them in cell B5
```

```
   If mComm.ReadFromPort(strTextReceived) > 0& Then
      GetSCPI = strTextReceived
   End If
End Function
```

```
''''''''''''''''''''''''''''''''''''''''''''''''''''''''''''''''''''''''''''''''''''''''''''''''''''''''''''''''''''''''''''''''
'The programs and functions contained in this sheet, "Module2", are used to configure,
'control, and acquire data from the HP 34970A data acquisition unit over an RS232 line.
'At the end of data acquisition the code time-averages and stores collected data into an
'Excel sheet.
''''''''''''''''''''''''''''''''''''''''''''''''''''''''''''''''''''''''''''''''''''''''''''''''''''''''''''''''''''''''''''''''


Sub Data Acquisition()
  Dim NScans As Integer           'Number of scan points to be taken
  Dim NScansAvg As Integer         'Number of scan points to be averaged
  Dim NChannels As Integer        'Number of channels in scan
  Dim RowOfTableHead As Integer      'Number of the row where Heading of the data
Table starts
  Dim FirstRowOfTable As Integer   'Number of the row where actual data starts
  Dim LastColumnOfTable As Integer 'Number of the column where data Table ends
  Dim Avg As Integer              'location of the average number
  Dim msgPrompt As String, msgTitle As String
  Dim msgButtons As Integer, msgResult As Integer
  NScans = 8
  RowOfTableHead = 50
  FirstRowOfTable = RowOfTableHead + 1
  LastColumnOfTable = 61
  NScansAvg = NScans - 0      'if written - 2 (instead - 0) than it would not include first 2
rows in the averaging routine
  Worksheets("Data").Activate

  'Initialize the scan and scan output
  RS232.SendSCPI ("*RST")           'Factory reset
  Delay (0.5)
  RS232.SendSCPI ("INPUT:IMPEDANCE:AUTO ON, (@101:120,201:220,301:320)")
'Seting Input resistance to >10GOmh
  Delay (0.5)
 ' RS232.SendSCPI ("SOURCE:VOLT 5.0,(@304)")     'Set DC voltage to 5.0V on
channel 304 on multifunction module
 ' Delay (0.5)
  RS232.SendSCPI  ("CONF:TEMP  TC,E,(@101:105,201:220,301:320)")  'Configure
channels for scan
  Delay (0.5)
  RS232.SendSCPI ("CONF:VOLT:DC (@106:118)")          'Configure channels for scan
  Delay (0.5)
```

```
  RS232.SendSCPI ("CONF:VOLT:AC (@119,120)")          'Configure channels for scan
  Delay (0.5)
  RS232.SendSCPI ("SENS:TEMP:NPLC 10, (@101,102,103)")
  Delay (0.5)
  RS232.SendSCPI ("SENS:TEMP:NPLC 2, (@104,105,201:220,301:320)")
  Delay (0.5)
  RS232.SendSCPI ("SENS:VOLT:DC:NPLC 10, (@106:112,117,118)")       'all the
pressure and DC voltage drop channels
  Delay (0.5)
  RS232.SendSCPI ("SENS:VOLT:DC:NPLC 2, (@113:116)") 'all the Humidity
channels
  Delay (0.5)
  RS232.SendSCPI ("SENS:VOLT:AC:BAND 20, (@119,120)")
  Delay (0.5)
    RS232.SendSCPI ("SENS:VOLT:DC:RANG 10, (@117)")
    Delay (0.5)
    RS232.SendSCPI ("SENS:VOLT:AC:RANG 10, (@120)")
    Delay (0.5)
    RS232.SendSCPI ("SENS:VOLT:DC:RANG 0.1, (@118)")
    Delay (0.5)
    RS232.SendSCPI ("SENS:VOLT:AC:RANG 0.1, (@119)")
    Delay (0.5)
  RS232.SendSCPI ("ROUT:SCAN (@101:120,201:220,301:320)")          'Channels to
include in scan
  Delay (0.5)
  RS232.SendSCPI ("FORM:READ:ALAR OFF")       'Channel alarm status with output,
off
  Delay (0.5)
  RS232.SendSCPI ("FORM:READ:CHAN ON")       'Channel number with output, on
  Delay (0.5)
  RS232.SendSCPI ("FORM:READ:TIME OFF")        'Channel timestamp with output,
off
  Delay (0.5)
  RS232.SendSCPI ("FORM:READ:UNIT OFF")      'Channel unit with output, off
  Delay (0.5)
  RS232.SendSCPI ("ROUTE:SCAN:SIZE?")         'Request the number of channels in a
scan
  Delay (1)
  NChannels = Val(RS232.GetSCPI)

  'Verify that the user wants to make the scan
  msgPrompt = "Ready to scan " & NChannels & " channels"
  msgButtons = vbOKCancel
  msgTitle = "Scan Ready"
  msgResult = MsgBox(msgPrompt, msgButtons, msgTitle)
  Select Case msgResult
```

```
    Case vbOK
        'Clear Averages from first row Contents
        Range("b1:bz1").Select
        Selection.ClearContents
        Delay (0.5)     'Unimportant delay
        'Clear All Previously Scanned Data Contents
        Range(Cells(FirstRowOfTable, 1), Cells(200, 150)).Select
        Selection.ClearContents
        Range("A1").Select
        Delay (0.5)     'Unimportant delay

         'Loop to take scans
        Application.ScreenUpdating = True  'True False
        For n = 1 To NScans
            Worksheets("Data").Cells(n + RowOfTableHead, 1).Value = n        'write to
worksheet scan number
            Call RunScan(NChannels, n + RowOfTableHead)
            Delay (0.6)     'Delay in-between two scans
        Next
        Application.ScreenUpdating = True
    Case vbCancel
        'any Cancel actions could go here
  End Select

  ' Averaging Macro
  ' Macro recorded by Mechanical Engineering
  '
  Avg = NScans + RowOfTableHead + 1  'mast have this one since Averages are written
just a row below the data
  Range(Cells(Avg, 1), Cells(Avg, 1)).Select
  ActiveCell.FormulaR1C1 = "Average"
  Range(Cells(Avg, 2), Cells(Avg, 2)).Select
  ActiveCell.FormulaR1C1 = "=SUM(R[-" & NScansAvg & "]C:R[-1]C)/" &
NScansAvg & " "
  Range(Cells(Avg, 2), Cells(Avg, 2)).Select
  Selection.AutoFill Destination:=Range(Cells(Avg, 2), Cells(Avg,
LastColumnOfTable)), Type:=xlFillDefault
  Range(Cells(Avg, 2), Cells(Avg, LastColumnOfTable)).Select
  Range("A1").Select

  ' Shifting Average values to the first row Macro
  ' Macro recorded 3/28/2003 by Mechanical Engineering
  '
  Range(Cells(Avg, 2), Cells(Avg, LastColumnOfTable)).Select
  Selection.Copy
  Range("B1").Select
```

```
 Selection.PasteSpecial Paste:=xlValues, Operation:=xlNone, SkipBlanks:= _
  False, Transpose:=False
 Range("A1").Select
 Application.CutCopyMode = False
 ActiveCell.FormulaR1C1 = ""
 Range("A1").Select
 RS232.SendSCPI ("*RST")     'Factory reset after everything is done
 Delay (0.5)
 End Sub

""""""""""""""""""""""""""""""""""""""""""""""""""""""""""""""""""""""""""""""""""""""""
'RunScan sub controls the initiation of a scan, waits for data to become
'available from the scan and then reads the data from the data acq. unit.
'"NChannels" is the total number of channels in the scan and "Row" is the
'spreadsheet row on which the data will be written
""""""""""""""""""""""""""""""""""""""""""""""""""""""""""""""""""""""""""""""""""""""""
Sub RunScan(NChannels As Integer, Row As Integer)
  RS232.SendSCPI ("INIT")
  For i = 1 To NChannels
    Do 'wait for data to be available
      RS232.SendSCPI ("DATA:POINTS?")
      Delay (0.12)    'First half Delay in-between two writings
      ready = Val(RS232.GetSCPI)
    Loop Until ready >= 1
    ' Request the available data and read it to "data" sheet
    RS232.SendSCPI ("DATA:REM? 1")
    Delay (0.12)    'Second half Delay in-between two writings
    Cells(1, 1) = RS232.GetSCPI
    Range("a1").TextToColumns Destination:=Range("a1"), comma:=True
    Cells(Row, 1 + i).Value = Cells(1, 1)
    Range("a1:ba1").ClearContents
  Next i
End Sub
```

A.2 Main Mist Cooling Processing Code

The main version of the mist cooling Engineering Equation Solver (EES) experimental data processing code is used to determine the thermodynamic state at each experimental measurement location, the gas and water flow rates, and the heating power. The input into the code include all of the averaged electronically and visually recorded

data saved in a corresponding Visual Basic code Excel sheet (i.e. various pressure/pressure drop readings, flow and inside wall temperatures, humidities, electrical power, and water rotameter reading). The code is shown below along with an example of the calculated results.

```
{!  The Main Mist Cooling Processing Code  }
"  ********************************************************************** "
"! INPUT - Experimental Data"

p_dif_orf = 2.651556496 *convert(psi,Pa) "[Pa]"       "Differential pressure at orifice"
p_orf1=  4.344633926 *convert(psi,Pa) + p_amb  "[Pa]"  "!abs. pres. in front of Orifice"
p_1=  1.967462286 *convert(psi,Pa) + p_amb     "[Pa]"  "!abs. pressure at Inst. block 1"
p_2=   0.123710186 *convert(psi,Pa) + p_amb     "[Pa]"  "! abs. pressure at Inst. block 2"
p_3=   0.092262074 *convert(psi,Pa) + p_amb   "[Pa]"    "!abs. pressure at Inst. block 3"
p_vnt1=  41.56299414  *convert(psi,Pa) + p_amb  "[Pa]"  "!abs. pres. in front of Venturi"
p_dif_vnt= 0.170  *convert(inH2O,Pa)     "[Pa]"       "Differential pressure at Venturi"
p_amb=  14.6    *convert(psi,Pa)      "[Pa]"  "Ambient pressure"

T_1=          17.89     "[°C]"  "Mist center-line temperature at the Instrument Block 1"
T_2WB =   13.13      "[°C]"  "Mist center-line temperature at the Instrument Block 2"
T_orf=    17.26         "[°C]"  "Air temp. after the orifice, also the same as before orifice"
 T_vnt=   21.88       "[°C]"  "Air temp. after the Venturi, also the same as before Venturi"
T_surface_room = 2.69     "[C]" "Surface Temperature - Room Temperature"
      T_2WB = WETBULB(AirH2O,T=T_2,P=p_2,R=RH_2) "[°C]" "this gives the Bulk"

RH_1 = 35.6/100     "! [fraction]" "relative humidity at Inst. Block 1"
RH_2 = 97.2  /100      "! [fraction]" "relative humidity at Inst. Block 2"
RH_vnt1=  9.8 /100     "relative humidity after the Venturi"
      RH_3 = 100 /100      "! [fraction]" "relative humidity at Inst. Block 3"
      RH_test = 100 /100    "! [fraction]"

Electrical_Power = 1150.29    "[W]"  "not the same as heating power"
RM= 4.09     "! Water Rotameter reading, steel ball (heavy ball)"

Tw_M1 = 26 "[°C]" "the average inside surface wall temperature at the location M1"
Tw_M2 = 33 "[°C]" "the average inside surface wall temperature at the location M2"
Tw_M3 = 37 "[°C]" "the average inside surface wall temperature at the location M3"
Tw_M4 = 42 "[°C]" "the average inside surface wall temperature at the location M4"
Tw_M5 = 46 "[°C]" "the average inside surface wall temperature at the location M5"
Tw_M6 = 47 "[°C]" "the average inside surface wall temperature at the location M6"
Tw_M7 = 49 "[°C]" "the average inside surface wall temperature at the location M7"
```

```
Tw_M8 = 51 "[°C]" "the average inside surface wall temperature at the location M8"
Tw_M9 = 53 "[°C]" "the average inside surface wall temperature at the location M9"
Tw_M10 = 55 "[°C]" "the average inside surface wall temperature at the location M10"
Tw_M11 = 60 "[°C]" "the average inside surface wall temperature at the location M11"
Tw_M12 = 65 "[°C]" "the average inside surface wall temperature at the location M12"
Tw_M13 = 70 "[°C]" "the average inside surface wall temperature at the location M13"
Tw_M14 = 74 "[°C]" "the average inside surface wall temperature at the location M14"
Tw_M15 = 80 "[°C]" "the average inside surface wall temperature at the location M15"
Tw_M16 = 83 "[°C]" "the average inside surface wall temperature at the location M16"
Tw_M17 = 85 "[°C]" "the average inside surface wall temperature at the location M17"
Tw_M18 = 86 "[°C]" "the average inside surface wall temperature at the location M18"
Tw_M19 = 88 "[°C]" "the average inside surface wall temperature at the location M19"
Tw_M20 = 82 "[°C]" "the average inside surface wall temperature at the location M20"

RH_M1=RH_test; RH_M2=RH_test; RH_M3=RH_test ; RH_M4=RH_test ;
RH_M5=RH_test ; RH_M6= RH_test; RH_M7=RH_test ; RH_M8= RH_test;
RH_M9=RH_test ; RH_M10=RH_test; RH_M11=RH_test ; RH_M12=RH_test ;
RH_M13=RH_test ; RH_M14=RH_test ; RH_M15=RH_test ; RH_M16=RH_test ;
RH_M17=RH_test ; RH_M18=RH_test ; RH_M19=RH_test; RH_M20= RH_test

" ********************************************************************** "
"! CALCULATIONS"

"! Venturi"
d_vnt=0.340 *convert(in,m)   "[m]"
Dpvc_vnt=0.714  *convert(in,m)   "[m]"   "PVC  SCH80 pipe ID"
Beta_vnt=d_vnt/Dpvc_vnt
c_p_vnt1=CP(AirH2O,T=T_vnt,P=p_vnt1,R=RH_vnt1)  "[kJ/kg-K]"
c_v_vnt1=CV(AirH2O,T=T_vnt,P=p_vnt1,R=RH_vnt1)  "[kJ/kg-K]"
c_p_vnt2=CP(AirH2O,T=T_vnt,P=p_vnt2,R=RH_vnt2)  "[kJ/kg-K]"
c_v_vnt2=CV(AirH2O,T=T_vnt,P=p_vnt2,R=RH_vnt2)  "[kJ/kg-K]"
Kappa_vnt=(c_p_vnt1/c_v_vnt1 + c_p_vnt2/c_v_vnt2) / 2
p_vnt2=  p_vnt1 - p_dif_vnt
Rho_vnt1=DENSITY(AirH2O,T=T_vnt,P=p_vnt1,R=RH_vnt1) "[kg/m3]""air density
before Venturi"
Rho_vnt2=DENSITY(AirH2O,T=T_vnt,P=p_vnt2,R=RH_vnt2)   "[kg/m3]" "air density
after Venturi"
Omega_vnt= 100*  m_dot_vapor_vnt/m_dot_dryair_vnt   "![%]  in calculations must be
fraction"
m_dot_dryair_vnt=m_dot_humidair_vnt - m_dot_vapor_vnt   "[kg/s]"
RH_vnt1=RELHUM(AirH2O,T=T_vnt,P=p_vnt1,w=(Omega_vnt/100))  "! [fraction]"
RH_vnt2=RELHUM(AirH2O,T=T_vnt,P=p_vnt2,w=(Omega_vnt/100))   "! [fraction]"

"! Venturi Flowmeter, Air Flowrate"
m_dot_humidair_vnt=  pi/4*C_vnt*Y_vnt1*d_vnt^2 * sqrt(2*p_dif_vnt*Rho_vnt1/(1-
Beta_vnt^4))  "[kg/s]"
```

```
{m_dot_humidair_vnt=pi/4*C_vnt*Y_vnt2*d_vnt^2 * sqrt(2*p_dif_vnt*Rho_vnt2/(1-
Beta_vnt^4))  "[kg/s]"   "Flow rate is the same at vnt1 and vnt2 if you have correct
RH_vnt1 & RH_vnt2"}
 Y_vnt1= ( ( (1-Beta_vnt^4)*(Kappa_vnt/(Kappa_vnt-
1))*(p_vnt2/p_vnt1)^(2/Kappa_vnt)*(1-(p_vnt2/p_vnt1)^((Kappa_vnt-1)/Kappa_vnt)) ) /
( (1-Beta_vnt^4*(p_vnt2/p_vnt1)^(2/Kappa_vnt))*(1-p_vnt2/p_vnt1) ) )^(1/2)  "this is
exact theoretical adiabatic gas expansion factor"
{ Y_vnt2= ( ( (1-Beta_vnt^4)*(Kappa_vnt/(Kappa_vnt-
1))*(p_vnt2/p_vnt1)^(2/Kappa_vnt)*(1-(p_vnt2/p_vnt1)^((Kappa_vnt-1)/Kappa_vnt)) ) /
( (1-Beta_vnt^4*(p_vnt2/p_vnt1)^(2/Kappa_vnt))*(1-p_vnt2/p_vnt1) ) )^(1/2) *
sqrt(1+(p_dif_vnt/p_vnt2))  "this is exact theoretical adiabatic gas expansion factor"  }
C_vnt= 1.005 - 0.471*Beta_vnt + 0.546*Beta_vnt^2 -0.514*Beta_vnt^3   "discharge
coefficient C"

"! Orifice"
Beta_orf=d_orf/Dpvc_orf
d_orf=0.315  *convert(in,m)    "[m]"  "Orifice bore diameter"
Dinch_pvc_orf=0.714             "[in]"   "PVC  SCH80 pipe ID"
Dpvc_orf=Dinch_pvc_orf  *convert(in,m)   "[m]"  "PVC  SCH80 pipe ID"
Omega_orf=Omega_1  "! [%]  in calculations must be fraction"
Omega_orf= 100*  m_dot_vapor_orf/m_dot_dryair_orf   "[%]  in calculations must be
fraction"
m_dot_dryair_orf=m_dot_humidair_orf - m_dot_vapor_orf   "[kg/s]"
RH_orf1=RELHUM(AirH2O,T=T_orf,P=p_orf1,w=(Omega_orf/100))  "! [fraction]"
RH_orf2=RELHUM(AirH2O,T=T_orf,P=p_orf2,w=(Omega_orf/100))   "[fraction]"
p_orf2 = p_orf1 - p_dif_orf    "[Pa]"   "Orifice absolute pressure after the orifice"
 P_ratio=p_orf2/p_orf1    "should be bigger than 0.75"
 Re_Dorf1=m_dot_humidair_orf/(pi/4*Mu_orf1*Dpvc_orf)    "Reynolds number in front
of the orifice"
Re_Dorf2=m_dot_humidair_orf/(pi/4*Mu_orf2*Dpvc_orf)      "Reynolds number after
the orifice"
 Mu_orf1=VISCOSITY(AirH2O,T=T_orf,P=p_orf1,R=RH_orf1)  "[kg/m-s]"  "dynamic
viscosity of air in front orifice"
 Rho_orf1=DENSITY(AirH2O,T=T_orf,P=p_orf1,R=RH_orf1)    "[kg/m3]"   "density of
the air in front of the orifice"
Mu_orf2=VISCOSITY(AirH2O,T=T_orf,P=p_orf2,R=RH_orf2)   "[kg/m-s]"  "dynamic
viscosity of air after the orifice"
Rho_orf2=DENSITY(AirH2O,T=T_orf,P=p_orf2,R=RH_orf2)    "[kg/m3]"   "density of
the air after the orifice"
c_p_orf1=CP(AirH2O,T=T_orf,P=p_orf1,R=RH_orf1)  "[kJ/kg-K]"
c_v_orf1=CV(AirH2O,T=T_orf,P=p_orf1,R=RH_orf1)  "[kJ/kg-K]"
c_p_orf2=CP(AirH2O,T=T_orf,P=p_orf2,R=RH_orf2)  "[kJ/kg-K]"
c_v_orf2=CV(AirH2O,T=T_orf,P=p_orf2,R=RH_orf2)  "[kJ/kg-K]"
Kappa_orf=(c_p_orf1/c_v_orf1 + c_p_orf2/c_v_orf2) / 2
```

```
"! Orifice Flowmeter, Humid Air Flowrate"
{ m_dot_humidair_orf=pi/4*C_orf*Y_orf1*d_orf^2 * sqrt(2*p_dif_orf*Rho_orf1/(1-
Beta_orf^4))  "[kg/s]"  "Flow rate is the same at Orf1 and Orf2 if you have correct
RH_orf1 and RH_orf2" }
m_dot_humidair_orf_uncal=pi/4*C_orf*Y_orf2*d_orf^2*sqrt(2*p_dif_orf*Rho_orf2/(1-
Beta_orf^4))  "[kg/s]"
m_dot_humidair_orf_first = -6756724.46484375*m_dot_humidair_orf_uncal^6 +
490503.813531536*m_dot_humidair_orf_uncal^5 -
2292.74125644001*m_dot_humidair_orf_uncal^4 -
651.021633245378*m_dot_humidair_orf_uncal^3
m_dot_humidair_orf_second = 20.8378664487055*m_dot_humidair_orf_uncal^2 +
0.757532645897201*m_dot_humidair_orf_uncal + 0.000960935656272423   "this is
good up to 60 scfm or about 65 m/s in ID=23.6mm pipe"
m_dot_humidair_orf = m_dot_humidair_orf_first + m_dot_humidair_orf_second
{ Y_orf1= ((( (1-Beta_orf^4)*(Kappa_orf/(Kappa_orf-
1))*(p_orf2/p_orf1)^(2/Kappa_orf)*(1-(p_orf2/p_orf1)^((Kappa_orf-1)/Kappa_orf)) ) / (
(1-Beta_orf^4*(p_orf2/p_orf1)^(2/Kappa_orf))*(1-p_orf2/p_orf1) ) )^(1/2)   "this is exact
theoretical adiabatic gas expansion factor" }
Y_orf2= ( ( (1-Beta_orf^4)*(Kappa_orf/(Kappa_orf-
1))*(p_orf2/p_orf1)^(2/Kappa_orf)*(1-(p_orf2/p_orf1)^((Kappa_orf-1)/Kappa_orf)) ) / (
(1-Beta_orf^4*(p_orf2/p_orf1)^(2/Kappa_orf))*(1-p_orf2/p_orf1) ) )^(1/2) *
sqrt(1+(p_dif_orf/p_orf2))  "this is exact theoretical adiabatic gas expansion factor"
C_orf=(0.5980+0.468*(Beta_orf^4+10*Beta_orf^12)+(0.87+8.1*Beta_orf^4)/sqrt(Re_D
orf2) ) * sqrt(1-Beta_orf^4)  "discharge coefficient C"

 "! Water Rotameter"
 m_dot_liquid_noz= -0.000000024040384158 6891*RM^4 +
0.000000878061665584196*RM^3 - 0.000018282335702 9557*RM^2 +
0.0004112099033291*RM - 0.0002687620937642  "[kg/s]"  "heavy ball equation for a
water flow rate through the nozzle"
{ m_dot_liquid_noz = 0.000000000926088784380507*RM^6 -
0.000000051398001643 4866*RM^5 + 0.000001128788608 54524*RM^4 -
0.000012361992473536 6*RM^3 + 0.000067574176423 0794*RM^2 -
0.000086905038332 0928*RM + 0.000046284424313 4104
"[kg/s]"  "light ball equation for a water flow rate through the nozzle" }
 m_dot_liquid_noz_KIVA =  m_dot_liquid_noz * convert(kg/s,g/s)

"! Instrument Block 1"
Omega_1 = 100* HUMRAT(AirH2O,T=T_1,P=p_1,R=RH_1)  "[%]  in calculations
must be fraction"

"! Instrument Block 2"
m_dot_dryair_total=m_dot_dryair_orf+m_dot_dryair_vnt
m_dot_totalwater=m_dot_liquid_noz+m_dot_vapor_orf+m_dot_vapor_vnt     "[kg/s]"
Omega_total=100 * m_dot_totalwater/m_dot_dryair_total   "[%]  in calculations must be
fraction"  "humidity ratio of total water"
```

Omega_vapor_2=100*HUMRAT(AirH2O,T=T_2,P=p_2,R=RH_2) "[%]" "humidity ratio of vapor water at Mist 1 location"
Omega_vapor_2=100 * m_dot_vapor_2/m_dot_dryair_total "[%]" "humidity ratio of vapor water at Mist 1 location"
m_dot_dryair_total=m_dot_humidair_2 - m_dot_vapor_2 "[kg/s]"
m_dot_totalwater=m_dot_liquid_2+m_dot_vapor_2 "[kg/s]"
Mu_2=VISCOSITY(AirH2O,T=T_2,P=p_2,R=RH_2) "[kg/m-s]" "dynamic viscosity at Inst. Block 2 location"
Rho_2=DENSITY(AirH2O,T=T_2,P=p_2,R=RH_2) "[kg/m3]" "density of the air at Inst. Block 2 location"
Re_2_hydraulic=(Velocity_2*d_test*Rho_2/Mu_2) "Reynolds number at Inst. Block 2 location based on Hydraulic diameter"
Velocity_2 = m_dot_humidair_2/(Rho_2*A_cross_test) "[m/s]" "Average Velocity in test section"
Velocity_2_orifice = m_dot_humidair_orf/(Rho_2*A_cross_test)
Velocity_2_venturi = m_dot_humidair_vnt/(Rho_2*A_cross_test)
Velocity_air_nozzle_jet = m_dot_humidair_vnt/(Rho_2*A_cross_air_nozzle_orifice)

"! Mist 1 Thermocouple"
Omega_vapor_M1=100*HUMRAT(AirH2O,T=T_M1,P=(p_2-(p_2-p_3)*0.5/41.4),R=RH_M1) "[%]" "humidity ratio of vapor water at Mist 1 location"
Omega_vapor_M1=100 * m_dot_vapor_M1/m_dot_dryair_total "[%]" "humidity ratio of vapor water at Mist 1 location"
m_dot_dryair_total=m_dot_humidair_M1 - m_dot_vapor_M1 "[kg/s]"
m_dot_totalwater=m_dot_liquid_M1+m_dot_vapor_M1 "[kg/s]"

"! Mist 2 Thermocouple"
Omega_vapor_M2=100*HUMRAT(AirH2O,T=T_M2,P=(p_2-(p_2-p_3)*1.5/41.4),R=RH_M2) "[%]" "humidity ratio of vapor water at Mist 2 location"
Omega_vapor_M2=100 * m_dot_vapor_M2/m_dot_dryair_total "[%]" "humidity ratio of vapor water at Mist 2 location"
m_dot_dryair_total=m_dot_humidair_M2 - m_dot_vapor_M2 "[kg/s]"
m_dot_totalwater=m_dot_liquid_M2+m_dot_vapor_M2 "[kg/s]"

"! Mist 3 Thermocouple"
Omega_vapor_M3=100*HUMRAT(AirH2O,T=T_M3,P=(p_2-(p_2-p_3)*2.5/41.4),R=RH_M3) "[%]" "humidity ratio of vapor water at Mist 2 location"
Omega_vapor_M3=100 * m_dot_vapor_M3/m_dot_dryair_total "[%]" "humidity ratio of vapor water at Mist 3 location"
m_dot_dryair_total=m_dot_humidair_M3 - m_dot_vapor_M3 "[kg/s]"
m_dot_totalwater=m_dot_liquid_M3+m_dot_vapor_M3 "[kg/s]"

"! Mist 4 Thermocouple"
Omega_vapor_M4=100*HUMRAT(AirH2O,T=T_M4,P=(p_2-(p_2-p_3)*4.8/41.4),R=RH_M4) "[%]" "humidity ratio of vapor water at Mist 4 location"

Omega_vapor_M4=100 * m_dot_vapor_M4/m_dot_dryair_total "[%]" "humidity ratio of vapor water at Mist 4 location"
m_dot_dryair_total=m_dot_humidair_M4 - m_dot_vapor_M4 "[kg/s]"
m_dot_totalwater=m_dot_liquid_M4+m_dot_vapor_M4 "[kg/s]"

"! Mist 5 Thermocouple"
Omega_vapor_M5=100*HUMRAT(AirH2O,T=T_M5,P=(p_2-(p_2-p_3)*7.1/41.4),R=RH_M5) "[%]" "humidity ratio of vapor water at Mist 5 location"
Omega_vapor_M5=100 * m_dot_vapor_M5/m_dot_dryair_total "[%]" "humidity ratio of vapor water at Mist 5 location"
m_dot_dryair_total=m_dot_humidair_M5 - m_dot_vapor_M5 "[kg/s]"
m_dot_totalwater=m_dot_liquid_M5+m_dot_vapor_M5 "[kg/s]"

"! Mist 6 Thermocouple"
Omega_vapor_M6=100*HUMRAT(AirH2O,T=T_M6,P=(p_2-(p_2-p_3)*9.4/41.4),R=RH_M6) "[%]" "humidity ratio of vapor water at Mist 6 location"
Omega_vapor_M6=100 * m_dot_vapor_M6/m_dot_dryair_total "[%]" "humidity ratio of vapor water at Mist 6 location"
m_dot_dryair_total=m_dot_humidair_M6 - m_dot_vapor_M6 "[kg/s]"
m_dot_totalwater=m_dot_liquid_M6+m_dot_vapor_M6 "[kg/s]"

"! Mist 7 Thermocouple"
Omega_vapor_M7=100*HUMRAT(AirH2O,T=T_M7,P=(p_2-(p_2-p_3)*11.7/41.4),R=RH_M7) "[%]" "humidity ratio of vapor water at Mist 7 location"
Omega_vapor_M7=100 * m_dot_vapor_M7/m_dot_dryair_total "[%]" "humidity ratio of vapor water at Mist 7 location"
m_dot_dryair_total=m_dot_humidair_M7 - m_dot_vapor_M7 "[kg/s]"
m_dot_totalwater=m_dot_liquid_M7+m_dot_vapor_M7 "[kg/s]"

"! Mist 8 Thermocouple"
Omega_vapor_M8=100*HUMRAT(AirH2O,T=T_M8,P=(p_2-(p_2-p_3)*14.0/41.4),R=RH_M8) "[%]" "humidity ratio of vapor water at Mist 8 location"
Omega_vapor_M8=100 * m_dot_vapor_M8/m_dot_dryair_total "[%]" "humidity ratio of vapor water at Mist 8 location"
m_dot_dryair_total=m_dot_humidair_M8 - m_dot_vapor_M8 "[kg/s]"
m_dot_totalwater=m_dot_liquid_M8+m_dot_vapor_M8 "[kg/s]"

"! Mist 9 Thermocouple"
Omega_vapor_M9=100*HUMRAT(AirH2O,T=T_M9,P=(p_2-(p_2-p_3)*16.3/41.4),R=RH_M9) "[%]" "humidity ratio of vapor water at Mist 9 location"
Omega_vapor_M9=100 * m_dot_vapor_M9/m_dot_dryair_total "[%]" "humidity ratio of vapor water at Mist 9 location"
m_dot_dryair_total=m_dot_humidair_M9 - m_dot_vapor_M9 "[kg/s]"
m_dot_totalwater=m_dot_liquid_M9+m_dot_vapor_M9 "[kg/s]"

"! Mist 10 Thermocouple"
Omega_vapor_M10=100*HUMRAT(AirH2O,T=T_M10,P=(p_2-(p_2-p_3)*18.6/41.4),R=RH_M10) "[%]" "humidity ratio of vapor water at Mist 10 location"
Omega_vapor_M10=100 * m_dot_vapor_M10/m_dot_dryair_total "[%]" "humidity ratio of vapor water at Mist 10 location"
m_dot_dryair_total=m_dot_humidair_M10 - m_dot_vapor_M10 "[kg/s]"
m_dot_totalwater=m_dot_liquid_M10+m_dot_vapor_M10 "[kg/s]"

"! Mist 11 Thermocouple"
Omega_vapor_M11=100*HUMRAT(AirH2O,T=T_M11,P=(p_2-(p_2-p_3)*20.9/41.4),R=RH_M11) "[%]" "humidity ratio of vapor water at Mist 11 location"
Omega_vapor_M11=100 * m_dot_vapor_M11/m_dot_dryair_total "[%]" "humidity ratio of vapor water at Mist 11 location"
m_dot_dryair_total=m_dot_humidair_M11 - m_dot_vapor_M11 "[kg/s]"
m_dot_totalwater=m_dot_liquid_M11+m_dot_vapor_M11 "[kg/s]"

"! Mist 12 Thermocouple"
Omega_vapor_M12=100*HUMRAT(AirH2O,T=T_M12,P=(p_2-(p_2-p_3)*23.2/41.4),R=RH_M12) "[%]" "humidity ratio of vapor water at Mist 12 location"
Omega_vapor_M12=100 * m_dot_vapor_M12/m_dot_dryair_total "[%]" "humidity ratio of vapor water at Mist 12 location"
m_dot_dryair_total=m_dot_humidair_M12 - m_dot_vapor_M12 "[kg/s]"
m_dot_totalwater=m_dot_liquid_M12+m_dot_vapor_M12 "[kg/s]"

"! Mist 13 Thermocouple"
Omega_vapor_M13=100*HUMRAT(AirH2O,T=T_M13,P=(p_2-(p_2-p_3)*25.5/41.4),R=RH_M13) "[%]" "humidity ratio of vapor water at Mist 13 location"
Omega_vapor_M13=100 * m_dot_vapor_M13/m_dot_dryair_total "[%]" "humidity ratio of vapor water at Mist 13 location"
m_dot_dryair_total=m_dot_humidair_M13 - m_dot_vapor_M13 "[kg/s]"
m_dot_totalwater=m_dot_liquid_M13+m_dot_vapor_M13 "[kg/s]"

"! Mist 14 Thermocouple"
Omega_vapor_M14=100*HUMRAT(AirH2O,T=T_M14,P=(p_2-(p_2-p_3)*27.8/41.4),R=RH_M14) "[%]" "humidity ratio of vapor water at Mist 14 location"
Omega_vapor_M14=100 * m_dot_vapor_M14/m_dot_dryair_total "[%]" "humidity ratio of vapor water at Mist 14 location"
m_dot_dryair_total=m_dot_humidair_M14 - m_dot_vapor_M14 "[kg/s]"
m_dot_totalwater=m_dot_liquid_M14+m_dot_vapor_M14 "[kg/s]"

"! Mist 15 Thermocouple"
Omega_vapor_M15=100*HUMRAT(AirH2O,T=T_M15,P=(p_2-(p_2-p_3)*30.1/41.4),R=RH_M15) "[%]" "humidity ratio of vapor water at Mist 15 location"
Omega_vapor_M15=100 * m_dot_vapor_M15/m_dot_dryair_total "[%]" "humidity ratio of vapor water at Mist 15 location"
m_dot_dryair_total=m_dot_humidair_M15 - m_dot_vapor_M15 "[kg/s]"

m_dot_totalwater=m_dot_liquid_M15+m_dot_vapor_M15 "[kg/s]"

"! Mist 16 Thermocouple"
Omega_vapor_M16=100*HUMRAT(AirH2O,T=T_M16,P=(p_2-(p_2-p_3)*32.4/41.4),R=RH_M16) "[%]" "humidity ratio of vapor water at Mist 16 location"
Omega_vapor_M16=100 * m_dot_vapor_M16/m_dot_dryair_total "[%]" "humidity ratio of vapor water at Mist 16 location"
m_dot_dryair_total=m_dot_humidair_M16 - m_dot_vapor_M16 "[kg/s]"
m_dot_totalwater=m_dot_liquid_M16+m_dot_vapor_M16 "[kg/s]"

"! Mist 17 Thermocouple"
Omega_vapor_M17=100*HUMRAT(AirH2O,T=T_M17,P=(p_2-(p_2-p_3)*34.7/41.4),R=RH_M17) "[%]" "humidity ratio of vapor water at Mist 17 location"
Omega_vapor_M17=100 * m_dot_vapor_M17/m_dot_dryair_total "[%]" "humidity ratio of vapor water at Mist 17 location"
m_dot_dryair_total=m_dot_humidair_M17 - m_dot_vapor_M17 "[kg/s]"
m_dot_totalwater=m_dot_liquid_M17+m_dot_vapor_M17 "[kg/s]"

"! Mist 18 Thermocouple"
Omega_vapor_M18=100*HUMRAT(AirH2O,T=T_M18,P=(p_2-(p_2-p_3)*37.0/41.4),R=RH_M18) "[%]" "humidity ratio of vapor water at Mist 18 location"
Omega_vapor_M18=100 * m_dot_vapor_M18/m_dot_dryair_total "[%]" "humidity ratio of vapor water at Mist 18 location"
m_dot_dryair_total=m_dot_humidair_M18 - m_dot_vapor_M18 "[kg/s]"
m_dot_totalwater=m_dot_liquid_M18+m_dot_vapor_M18 "[kg/s]"

"! Mist 19 Thermocouple"
Omega_vapor_M19=100*HUMRAT(AirH2O,T=T_M19,P=(p_2-(p_2-p_3)*39.3/41.4),R=RH_M19) "[%]" "humidity ratio of vapor water at Mist 19 location"
Omega_vapor_M19=100 * m_dot_vapor_M19/m_dot_dryair_total "[%]" "humidity ratio of vapor water at Mist 19 location"
m_dot_dryair_total=m_dot_humidair_M19 - m_dot_vapor_M19 "[kg/s]"
m_dot_totalwater=m_dot_liquid_M19+m_dot_vapor_M19 "[kg/s]"

"! Mist 20 Thermocouple"
Omega_vapor_M20=100*HUMRAT(AirH2O,T=T_M20,P=(p_2-(p_2-p_3)*40.5/41.4),R=RH_M20) "[%]" "humidity ratio of vapor water at Mist 20 location"
Omega_vapor_M20=100 * m_dot_vapor_M20/m_dot_dryair_total "[%]" "humidity ratio of vapor water at Mist 20 location"
m_dot_dryair_total=m_dot_humidair_M20 - m_dot_vapor_M20 "[kg/s]"
m_dot_totalwater=m_dot_liquid_M20+m_dot_vapor_M20 "[kg/s]"

"! Control volume ENERGY balance"
Power = Electrical_Power - h_natural_convection*(T_surface_room)*Insulation_perimeter*L - 0.002*Electrical_Power "[W]" "True Heating Power"

PW = Power /1000 "[kW]"
PP = (p_2-p_3) "had to be done to make energy equation work, otherwise too long equations"

zL1= 0.5/41.4
PW*(zL1)=m_dot_dryair_total*(ENTHALPY(AirH2O,T=T_M1,P=(p_2-(p_2-p_3)*zL1),R=RH_M1)-ENTHALPY(AirH2O,T=T_2,P=p_2,R=RH_2))+m_dot_liquid_M1*ENTHALPY(Water,T=((T_M1+Tw_M1)/2),P=(p_2-(p_2-p_3)*zL1))-m_dot_liquid_2*ENTHALPY(Water,T=T_2WB,P=p_2)
"from here T_M1 is calculated which is the Bulk Temperature of the Gas/Mist together"

zL2=1.5/41.4
PW*(zL2)=m_dot_dryair_total*(ENTHALPY(AirH2O,T=T_M2,P=(p_2-(p_2-p_3)*zL2),R=RH_M2)-ENTHALPY(AirH2O,T=T_2,P=p_2,R=RH_2))+m_dot_liquid_M2*ENTHALPY(Water,T=((T_M2+Tw_M2)/2),P=(p_2-(p_2-p_3)*zL2))-m_dot_liquid_2*ENTHALPY(Water,T=T_2WB,P=p_2)
"from here T_M2 is calculated which is the Bulk Temperature of the Gas/Mist together"

zL3= 2.5/41.4
PW*(zL3)=m_dot_dryair_total*(ENTHALPY(AirH2O,T=T_M3,P=(p_2-(p_2-p_3)*zL3),R=RH_M3)-ENTHALPY(AirH2O,T=T_2,P=p_2,R=RH_2))+m_dot_liquid_M3*ENTHALPY(Water,T=((T_M3+Tw_M3)/2),P=(p_2-(p_2-p_3)*zL3))-m_dot_liquid_2*ENTHALPY(Water,T=T_2WB,P=p_2)
"from here T_M3 is calculated which is the Bulk Temperature of the Gas/Mist together"

zL4= 4.8/41.4
PW*(zL4)=m_dot_dryair_total*(ENTHALPY(AirH2O,T=T_M4,P=(p_2-(p_2-p_3)*zL4),R=RH_M4)-ENTHALPY(AirH2O,T=T_2,P=p_2,R=RH_2))+m_dot_liquid_M4*ENTHALPY(Water,T=((T_M4+Tw_M4)/2),P=(p_2-(p_2-p_3)*zL4))-m_dot_liquid_2*ENTHALPY(Water,T=T_2WB,P=p_2)
"from here T_M4 is calculated which is the Bulk Temperature of the Gas/Mist together"

zL5= 7.1/41.4
PW*(zL5)=m_dot_dryair_total*(ENTHALPY(AirH2O,T=T_M5,P=(p_2-(p_2-p_3)*zL5),R=RH_M5)-ENTHALPY(AirH2O,T=T_2,P=p_2,R=RH_2))+m_dot_liquid_M5*ENTHALPY(Water,T=((T_M5+Tw_M5)/2),P=(p_2-(p_2-p_3)*zL5))-m_dot_liquid_2*ENTHALPY(Water,T=T_2WB,P=p_2)
"from here T_M5 is calculated which is the Bulk Temperature of the Gas/Mist together"

zL6= 9.4/41.4

PW*(zL6)=m_dot_dryair_total*(ENTHALPY(AirH2O,T=T_M6,P=(p_2-(p_2-p_3)*zL6),R=RH_M6)-ENTHALPY(AirH2O,T=T_2,P=p_2,R=RH_2))+m_dot_liquid_M6*ENTHALPY(Water,T=((T_M6+Tw_M6)/2),P=(p_2-(p_2-p_3)*zL6))-m_dot_liquid_2*ENTHALPY(Water,T=T_2WB,P=p_2)
"from here T_M6 is calculated which is the Bulk Temperature of the Gas/Mist together"

zL7= 11.7/41.4
PW*(zL7)=m_dot_dryair_total*(ENTHALPY(AirH2O,T=T_M7,P=(p_2-(p_2-p_3)*zL7),R=RH_M7)-ENTHALPY(AirH2O,T=T_2,P=p_2,R=RH_2))+m_dot_liquid_M7*ENTHALPY(Water,T=((T_M7+Tw_M7)/2),P=(p_2-(p_2-p_3)*zL7))-m_dot_liquid_2*ENTHALPY(Water,T=T_2WB,P=p_2)
"from here T_M7 is calculated which is the Bulk Temperature of the Gas/Mist together"

zL8= 14.0/41.4
PW*(zL8)=m_dot_dryair_total*(ENTHALPY(AirH2O,T=T_M8,P=(p_2-(p_2-p_3)*zL8),R=RH_M8)-ENTHALPY(AirH2O,T=T_2,P=p_2,R=RH_2))+m_dot_liquid_M8*ENTHALPY(Water,T=((T_M8+Tw_M8)/2),P=(p_2-(p_2-p_3)*zL8))-m_dot_liquid_2*ENTHALPY(Water,T=T_2WB,P=p_2)
"from here T_M8 is calculated which is the Bulk Temperature of the Gas/Mist together"

zL9= 16.3/41.4
PW*(zL9)=m_dot_dryair_total*(ENTHALPY(AirH2O,T=T_M9,P=(p_2-(p_2-p_3)*zL9),R=RH_M9)-ENTHALPY(AirH2O,T=T_2,P=p_2,R=RH_2))+m_dot_liquid_M9*ENTHALPY(Water,T=((T_M9+Tw_M9)/2),P=(p_2-(p_2-p_3)*zL9))-m_dot_liquid_2*ENTHALPY(Water,T=T_2WB,P=p_2)
"from here T_M9 is calculated which is the Bulk Temperature of the Gas/Mist together"

zL10= 18.6/41.4
PW*(zL10)=m_dot_dryair_total*(ENTHALPY(AirH2O,T=T_M10,P=(p_2-PP*zL10),R=RH_M10)-ENTHALPY(AirH2O,T=T_2,P=p_2,R=RH_2))+m_dot_liquid_M10*ENTHALPY(Water,T=((T_M10+Tw_M10)/2),P=(p_2-PP*zL10))-m_dot_liquid_2*ENTHALPY(Water,T=T_2WB,P=p_2)
"from here T_M10 is calculated which is the Bulk Temperature of the Gas/Mist together"

zL11= 20.9/41.4
PW*(zL11)=m_dot_dryair_total*(ENTHALPY(AirH2O,T=T_M11,P=(p_2-PP*zL11),R=RH_M11)-ENTHALPY(AirH2O,T=T_2,P=p_2,R=RH_2))+m_dot_liquid_M11*ENTHALPY(Water,T=((T_M11+Tw_M11)/2),P=(p_2-PP*zL11))-m_dot_liquid_2*ENTHALPY(Water,T=T_2WB,P=p_2)
"from here T_M11 is calculated which is the Bulk Temperature of the Gas/Mist together"

zL12= 23.2/41.4
PW*(zL12)=m_dot_dryair_total*(ENTHALPY(AirH2O,T=T_M12,P=(p_2-PP*zL12),R=RH_M12)-ENTHALPY(AirH2O,T=T_2,P=p_2,R=RH_2))+m_dot_liquid_M12*ENTHALPY(Water,T=((T_M12+Tw_M12)/2),P=(p_2-PP*zL12))-m_dot_liquid_2*ENTHALPY(Water,T=T_2WB,P=p_2)
"from here T_M12 is calculated which is the Bulk Temperature of the Gas/Mist together"

zL13= 25.5/41.4
PW*(zL13)=m_dot_dryair_total*(ENTHALPY(AirH2O,T=T_M13,P=(p_2-PP*zL13),R=RH_M13)-ENTHALPY(AirH2O,T=T_2,P=p_2,R=RH_2))+m_dot_liquid_M13*ENTHALPY(Water,T=((T_M13+Tw_M13)/2),P=(p_2-PP*zL13))-m_dot_liquid_2*ENTHALPY(Water,T=T_2WB,P=p_2)
"from here T_M13 is calculated which is the Bulk Temperature of the Gas/Mist together"

zL14= 27.8/41.4
PW*(zL14)=m_dot_dryair_total*(ENTHALPY(AirH2O,T=T_M14,P=(p_2-PP*zL14),R=RH_M14)-ENTHALPY(AirH2O,T=T_2,P=p_2,R=RH_2))+m_dot_liquid_M14*ENTHALPY(Water,T=((T_M14+Tw_M14)/2),P=(p_2-PP*zL14))-m_dot_liquid_2*ENTHALPY(Water,T=T_2WB,P=p_2)
"from here T_M14 is calculated which is the Bulk Temperature of the Gas/Mist together"

zL15= 30.1/41.4
PW*(zL15)=m_dot_dryair_total*(ENTHALPY(AirH2O,T=T_M15,P=(p_2-PP*zL15),R=RH_M15)-ENTHALPY(AirH2O,T=T_2,P=p_2,R=RH_2))+m_dot_liquid_M15*ENTHALPY(Water,T=((T_M15+Tw_M15)/2),P=(p_2-PP*zL15))-m_dot_liquid_2*ENTHALPY(Water,T=T_2WB,P=p_2)
"from here T_M15 is calculated which is the Bulk Temperature of the Gas/Mist together"

zL16= 32.4/41.4
PW*(zL16)=m_dot_dryair_total*(ENTHALPY(AirH2O,T=T_M16,P=(p_2-PP*zL16),R=RH_M16)-ENTHALPY(AirH2O,T=T_2,P=p_2,R=RH_2))+m_dot_liquid_M16*ENTHALPY(Water,T=((T_M16+Tw_M16)/2),P=(p_2-PP*zL16))-m_dot_liquid_2*ENTHALPY(Water,T=T_2WB,P=p_2)
"from here T_M16 is calculated which is the Bulk Temperature of the Gas/Mist together"

zL17= 34.7/41.4
PW*(zL17)=m_dot_dryair_total*(ENTHALPY(AirH2O,T=T_M17,P=(p_2-PP*zL17),R=RH_M17)-ENTHALPY(AirH2O,T=T_2,P=p_2,R=RH_2))+m_dot_liquid_M17*ENTHALPY(Wate

```
r,T=((T_M17+Tw_M17)/2),P=(p_2-PP*zL17))-
m_dot_liquid_2*ENTHALPY(Water,T=T_2WB,P=p_2)
"from here T_M17 is calculated which is the Bulk Temperature of the Gas/Mist together"

zL18= 37.0/41.4
PW*(zL18)=m_dot_dryair_total*(ENTHALPY(AirH2O,T=T_M18,P=(p_2-
PP*zL18),R=RH_M18)-
ENTHALPY(AirH2O,T=T_2,P=p_2,R=RH_2))+m_dot_liquid_M18*ENTHALPY(Wate
r,T=((T_M18+Tw_M18)/2),P=(p_2-PP*zL18))-
m_dot_liquid_2*ENTHALPY(Water,T=T_2WB,P=p_2)
"from here T_M18 is calculated which is the Bulk Temperature of the Gas/Mist together"

zL19=39.3/41.4
PW*(zL19)=m_dot_dryair_total*(ENTHALPY(AirH2O,T=T_M19,P=(p_2-
PP*zL19),R=RH_M19)-
ENTHALPY(AirH2O,T=T_2,P=p_2,R=RH_2))+m_dot_liquid_M19*ENTHALPY(Wate
r,T=((T_M19+Tw_M19)/2),P=(p_2-PP*zL19))-
m_dot_liquid_2*ENTHALPY(Water,T=T_2WB,P=p_2)
"from here T_M19 is calculated which is the Bulk Temperature of the Gas/Mist together"

zL20=40.5/41.4
PW*(zL20)=m_dot_dryair_total*(ENTHALPY(AirH2O,T=T_M20,P=(p_2-(p_2-
p_3)*zL20),R=RH_M20)-
ENTHALPY(AirH2O,T=T_2,P=p_2,R=RH_2))+m_dot_liquid_M20*ENTHALPY(Wate
r,T=((T_M20+Tw_M20)/2),P=(p_2-(p_2-p_3)*zL20))-
m_dot_liquid_2*ENTHALPY(Water,T=T_2WB,P=p_2)
"from here T_M20 is calculated which is the Bulk Temperature of the Gas/Mist together"

PW20_IU = PW*(zL20)   "[kW]"

"! Natural Convection from outside"
Insulation_perimeter = 0.2286      "[m]"  "this is measured"
h_natural_convection = 15  "[W/m2K]"
Loss_nat_conv=(Electrical_Power-Power)/(Electrical_Power) * 100  "[%]"

"! Test Section Geometry and stuff"
d_test = 23.6  *convert(mm,m)  "[m]"  "inner diameter of the test section"
d_air_nozzle_orifice = 0.110  *convert(in,m)  "[m]" "air-assisted nozzle orifice"
A_cross_test = (d_test^2*pi)/4  "[m2]"  " test cross section area"
A_cross_air_nozzle_orifice = (d_air_nozzle_orifice^2*pi)/4    "[m2]"
L = 1.0516      "[m]"    "test section length"
D_policarbonate = 1 "[in]"


"! Mass Fractions for KIVA-3V code"
"Mass fractions in dry air: O2 = 0.24;  N2 = 0.76"
```

"m_dot_humidair_2 is the total gas phase flowrate at the inlet of the test section"

O2_mass = 0.24*m_dot_dryair_total
N2_mass = 0.76*m_dot_dryair_total
H2Ov_mass = m_dot_vapor_2

O2_mass_fraction = O2_mass/m_dot_humidair_2
N2_mass_fraction = N2_mass/m_dot_humidair_2
H2Ov_mass_fraction = H2Ov_mass/m_dot_humidair_2

ONE = O2_mass_fraction + N2_mass_fraction + H2Ov_mass_fraction

" ** "
{AIRH2O
Substance AIRH2O implements air-water vapor mixture (psychrometric) properties using thermodynamic data from the built-in AIR and WATER property relations
The reference state sets the specific enthalpy of dry air to 0 at 0 °C in (SI units) for consistency with most psychrometric charts. The reference state for enthalpy of water vapor is based on the traditional water table reference state.

WATER
Thermodynamic properties of WATER substance have been implemented using the thermodynamic property correlation
Enthalpy values are referred to 0 for saturated liquid at 0 °C.

AIR_ha and AIR
Enthalpy values are referred to 0 at 0 K.}
" ** "

An example of the calculated results is shown below.

A_cross_air_nozzle_orifice=0.000006131 [m2]
A_cross_test=0.0004374 [m2]
Beta_orf=0.4412 [-]
Beta_vnt=0.4762 [-]
C_orf=0.6112 [-]
c_p_orf1=1.014 [kJ/kg-K]
c_p_orf2=1.014 [kJ/kg-K]
c_p_vnt1=1.007 [kJ/kg-K]
c_p_vnt2=1.007 [kJ/kg-K]
C_vnt=0.849 [-]
c_v_orf1=0.7251 [kJ/kg-K]
c_v_orf2=0.7251 [kJ/kg-K]
c_v_vnt1=0.7202 [kJ/kg-K]
c_v_vnt2=0.7202 [kJ/kg-K]

Dinch_pvc_orf=0.714 [in]
Dpvc_orf=0.01814 [m]
Dpvc_vnt=0.01814 [m]
d_air_nozzle_orifice=0.002794 [m]
d_orf=0.008001 [m]
D_policarbonate=1 [in]
d_test=0.0236 [m]
d_vnt=0.008636 [m]
Electrical_Power=802.8 [W]
H2Ov_mass=0.00007338 [kg/s]
H2Ov_mass_fraction=0.00916 [-]
h_natural_convection=15 [W/m2K]
Insulation_perimeter=0.2286 [m]
ONE=1 [-]
Kappa_orf=1.398 [-]
Kappa_vnt=1.399 [-]
L=1.052 [m]
Loss_nat_conv=1.022 [%]
Mu_2=0.00001789 [kg/m-s]
Mu_orf1=0.00001812 [kg/m-s]
Mu_orf2=0.00001812 [kg/m-s]
m_dot_dryair_orf=0.006935537 [kg/s]
m_dot_dryair_total=0.007939440 [kg/s]
m_dot_dryair_vnt=0.001003903 [kg/s]
m_dot_humidair_2=0.008013 [kg/s]
m_dot_humidair_M1=0.00801 [kg/s]
m_dot_humidair_M10=0.008085 [kg/s]
m_dot_humidair_M11=0.008097 [kg/s]
m_dot_humidair_M12=0.008109 [kg/s]
m_dot_humidair_M13=0.008121 [kg/s]
m_dot_humidair_M14=0.008135 [kg/s]
m_dot_humidair_M15=0.008148 [kg/s]
m_dot_humidair_M16=0.008161 [kg/s]
m_dot_humidair_M17=0.008175 [kg/s]
m_dot_humidair_M18=0.008189 [kg/s]
m_dot_humidair_M19=0.008203 [kg/s]
m_dot_humidair_M2=0.008011 [kg/s]
m_dot_humidair_M20=0.008210284 [kg/s]
m_dot_humidair_M3=0.008015 [kg/s]
m_dot_humidair_M4=0.008022 [kg/s]
m_dot_humidair_M5=0.008031 [kg/s]
m_dot_humidair_M6=0.00804 [kg/s]
m_dot_humidair_M7=0.008052 [kg/s]
m_dot_humidair_M8=0.008062 [kg/s]
m_dot_humidair_M9=0.008073 [kg/s]
m_dot_humidair_orf=0.006963 [kg/s]

m_dot_humidair_orf_first=-0.0002117 [kg/s]
m_dot_humidair_orf_second=0.007175 [kg/s]
m_dot_humidair_orf_uncal=0.006895 [kg/s]
m_dot_humidair_vnt=0.001004 [kg/s]
m_dot_liquid_2=0.001118615 [kg/s]
m_dot_liquid_M1=0.001122 [kg/s]
m_dot_liquid_M10=0.001047 [kg/s]
m_dot_liquid_M11=0.001035 [kg/s]
m_dot_liquid_M12=0.001023 [kg/s]
m_dot_liquid_M13=0.00101 [kg/s]
m_dot_liquid_M14=0.0009967 [kg/s]
m_dot_liquid_M15=0.0009838 [kg/s]
m_dot_liquid_M16=0.00097 [kg/s]
m_dot_liquid_M17=0.0009566 [kg/s]
m_dot_liquid_M18=0.0009424 [kg/s]
m_dot_liquid_M19=0.0009287 [kg/s]
m_dot_liquid_M2=0.001121 [kg/s]
m_dot_liquid_M20=0.0009211 [kg/s]
m_dot_liquid_M3=0.001116 [kg/s]
m_dot_liquid_M4=0.00111 [kg/s]
m_dot_liquid_M5=0.001101 [kg/s]
m_dot_liquid_M6=0.001091 [kg/s]
m_dot_liquid_M7=0.001079 [kg/s]
m_dot_liquid_M8=0.00107 [kg/s]
m_dot_liquid_M9=0.001058 [kg/s]
m_dot_liquid_noz=0.001164 [kg/s]
m_dot_liquid_noz_KIVA=1.163596 [g/s]
m_dot_totalwater=0.001192 [kg/s]
m_dot_vapor_2=0.00007338 [kg/s]
m_dot_vapor_M1=0.00007031 [kg/s]
m_dot_vapor_M10=0.0001453 [kg/s]
m_dot_vapor_M11=0.0001572 [kg/s]
m_dot_vapor_M12=0.0001695 [kg/s]
m_dot_vapor_M13=0.0001819 [kg/s]
m_dot_vapor_M14=0.0001953 [kg/s]
m_dot_vapor_M15=0.0002082 [kg/s]
m_dot_vapor_M16=0.000222 [kg/s]
m_dot_vapor_M17=0.0002354 [kg/s]
m_dot_vapor_M18=0.0002496 [kg/s]
m_dot_vapor_M19=0.0002633 [kg/s]
m_dot_vapor_M2=0.00007141 [kg/s]
m_dot_vapor_M20=0.0002708 [kg/s]
m_dot_vapor_M3=0.0000756 [kg/s]
m_dot_vapor_M4=0.00008241 [kg/s]
m_dot_vapor_M5=0.00009113 [kg/s]
m_dot_vapor_M6=0.0001008 [kg/s]

m_dot_vapor_M7=0.0001125 [kg/s]
m_dot_vapor_M8=0.0001224 [kg/s]
m_dot_vapor_M9=0.0001337 [kg/s]
m_dot_vapor_orf=0.00002794 [kg/s]
m_dot_vapor_vnt=4.597E-07 [kg/s]
N2_mass=0.006034 [kg/s]
N2_mass_fraction=0.75304 [-]
O2_mass=0.001905 [kg/s]
O2_mass_fraction=0.23780 [-]
Omega_1=0.4028 [%]
Omega_orf=0.402810551 [%]
Omega_total=15.014 [%]
Omega_vapor_2=0.9242 [%]
Omega_vapor_M1=0.8856 [%]
Omega_vapor_M10=1.83 [%]
Omega_vapor_M11=1.98 [%]
Omega_vapor_M12=2.134 [%]
Omega_vapor_M13=2.291 [%]
Omega_vapor_M14=2.46 [%]
Omega_vapor_M15=2.623 [%]
Omega_vapor_M16=2.796 [%]
Omega_vapor_M17=2.965 [%]
Omega_vapor_M18=3.143 [%]
Omega_vapor_M19=3.316 [%]
Omega_vapor_M2=0.8995 [%]
Omega_vapor_M20=3.411 [%]
Omega_vapor_M3=0.9523 [%]
Omega_vapor_M4=1.038 [%]
Omega_vapor_M5=1.148 [%]
Omega_vapor_M6=1.269 [%]
Omega_vapor_M7=1.418 [%]
Omega_vapor_M8=1.541 [%]
Omega_vapor_M9=1.684 [%]
Omega_vnt=0.04579 [%]
Power=794.546 [W]
PP=179.9 [Pa]
PW=0.7945 [kW]
PW20_IU=0.7773 [kW]
p_1=114277 [Pa]
p_2=101507 [Pa]
p_3=101327 [Pa]
p_amb=100663 [Pa]
p_dif_orf=18457 [Pa]
p_dif_vnt=42.34 [Pa]
p_orf1=130797 [Pa]
p_orf2=112340 [Pa]

P_ratio=0.8589 [-]
p_vnt1=387230 [Pa]
p_vnt2=387188 [Pa]
Re_2_hydraulic=24165 [m2]
Re_Dorf1=26976 [-]
Re_Dorf2=26976 [-]
Rho_2=1.219 [kg/m3]
Rho_orf1=1.558 [kg/m3]
Rho_orf2=1.338 [kg/m3]
Rho_vnt1=4.569 [kg/m3]
Rho_vnt2=4.568 [kg/m3]
RH_1=0.354 [fraction]
RH_2=1 [fraction]
RH_3=1 [fraction]
RH_M1=1 [fraction]
RH_M10=1 [fraction]
RH_M11=1 [fraction]
RH_M12=1 [fraction]
RH_M13=1 [fraction]
RH_M14=1 [fraction]
RH_M15=1 [fraction]
RH_M16=1 [fraction]
RH_M17=1 [fraction]
RH_M18=1 [fraction]
RH_M19=1 [fraction]
RH_M2=1 [fraction]
RH_M20=1 [fraction]
RH_M3=1 [fraction]
RH_M4=1 [fraction]
RH_M5=1 [fraction]
RH_M6=1 [fraction]
RH_M7=1 [fraction]
RH_M8=1 [fraction]
RH_M9=1 [fraction]
RH_orf1=0.420 [fraction]
RH_orf2=0.361 [fraction]
RH_test=1 [fraction]
RH_vnt1=0.107 [fraction]
RH_vnt2=0.107 [fraction]
RM=4.1 (reading of the water rotameter)
Tw_M1=23 [°C]
Tw_M10=44 [°C]
Tw_M11=45 [°C]
Tw_M12=46 [°C]
Tw_M13=47 [°C]
Tw_M14=47 [°C]

Tw_M15=48 [°C]
Tw_M16=48 [°C]
Tw_M17=49 [°C]
Tw_M18=49 [°C]
Tw_M19=50 [°C]
Tw_M2=29 [°C]
Tw_M20=50 [°C]
Tw_M3=29 [°C]
Tw_M4=35 [°C]
Tw_M5=38 [°C]
Tw_M6=40 [°C]
Tw_M7=39 [°C]
Tw_M8=42 [°C]
Tw_M9=43 [°C]
T_1=18.03 [°C]
T_2=12.82 [°C]
T_2WB=12.82 [°C]
T_M1=12.18 [°C]
T_M10=23.45 [°C]
T_M11=24.72 [°C]
T_M12=25.94 [°C]
T_M13=27.1 [°C]
T_M14=28.27 [°C]
T_M15=29.33 [°C]
T_M16=30.4 [°C]
T_M17=31.38 [°C]
T_M18=32.36 [°C]
T_M19=33.27 [°C]
T_M2=12.41 [°C]
T_M20=33.75 [°C]
T_M3=13.27 [°C]
T_M4=14.57 [°C]
T_M5=16.11 [°C]
T_M6=17.67 [°C]
T_M7=19.39 [°C]
T_M8=20.71 [°C]
T_M9=22.11 [°C]
T_orf=17.45 [°C]
T_surface_room=1.83 [C]
T_vnt=21.91 [°C]
Velocity_2=15.03 [m/s]
Velocity_2_orifice=13.06 [m/s]
Velocity_2_venturi=1.884 [m/s]
Velocity_air_nozzle_jet=134.4 [m/s]
Y_orf2=0.9902 [-]
Y_vnt1=0.9999 [-]

```
zL1=0.01208 [-]
zL10=0.4493 [-]
zL11=0.5048 [-]
zL12=0.5604 [-]
zL13=0.6159 [-]
zL14=0.6715 [-]
zL15=0.7271 [-]
zL16=0.7826 [-]
zL17=0.8382 [-]
zL18=0.8937 [-]
zL19=0.9493 [-]
zL2=0.03623 [-]
zL20=0.9783 [-]
zL3=0.06039 [-]
zL4=0.1159 [-]
zL5=0.1715 [-]
zL6=0.2271 [-]
zL7=0.2826 [-]
zL8=0.3382 [-]
zL9=0.3937[-]
```

A.3 First Single-Phase Convection Processing Code

This Engineering Equation Solver (EES) experimental data processing code calculates the heat transfer coefficient for air single-phase forced convection experiments by using a correlation proposed by Reynolds, Swearingen and McEligot (1969). It follows the same procedure as the main mist cooling processing code (see section A.2), however the water flow rate through the water rotameter is set to zero. Only the parts of this code that are different from the main mist cooling processing code are shown below.

```
{! The First Single-phase Convection Processing Code  }
"! This code uses Reynolds et al. correlation; Thermally Developing Flow"
"  ********************************************************************** "
"! INPUT - Experimental Data"

p_dif_orf = 9.965405882 *convert(psi,Pa)     "[Pa]"  "Differential pressure at orifice"
p_orf1=  19.22555144  *convert(psi,Pa) + p_amb   "[Pa]"  "!abs. pres. in front of Orifice"
```

```
p_1=  10.08700961 *convert(psi,Pa) + p_amb "[Pa]" "! abs. presure at Inst. block 1"
p_2=   0.469463391 *convert(psi,Pa) + p_amb "[Pa]" "! abs. presure at Inst. block 2"
p_3=   0.347110982 *convert(psi,Pa) + p_amb "[Pa]" "! abs. presure at Inst. block 3"
p_vnt1=  0.000 *convert(psi,Pa) + p_amb  "[Pa]"    "!abs. pressure in front of Venturi"
p_amb=  14.6 *convert(psi,Pa)      "[Pa]"  "Ambient pressure"
p_dif_vnt= 0.0000001 *convert(inH2O,Pa) "[Pa]" "actually zero, diff. pres. at Venturi"

T_1=  21.46 "[°C]"  "Mist center-line temperature at the Instrument Block 1"
T_2=  21.90 "[°C]"  "Mist center-line temperature at the Instrument Block 2"
T_tc3  = 35.00 "[°C]" "Mist center-line temperature at the Inst. Block 3 or above it"
T_orf= 21.77 "[°C]"  "Air temp. after the orifice, also the same as before the orifice"
T_vnt=  22.12   "[°C]"  "Air temp. after the Venturi, also the same as before the Venturi"
T_surface_room = 3.42    "[C]" "Surface Tepmerature - Room Temperature"

RH_1 = 6.1 /100     "! [fraction]" "relative humidity at Inst. Block 1"   {3.7 /100}
RH_2 = 3.0 /100      "! [fraction]" "relative humidity at Inst. Block 2"    {2.9 /100}
RH_vnt1=  10 /100  "relative humidity after the Venturi"

Electrical_Power = 434.35   "[W]"  "not the same as heating power"
RM=   0.00     "! Water Rotameter reading"

"  ************************************************************ "
"! CALCULATIONS"

"! Water Rotameter"
 m_dot_liquid_noz= 0

"! Instrument Block 2"
Omega_2 = 100* HUMRAT(AirH2O,T=T_2,P=p_2,R=RH_2)  "[%]  in calculations
must be fraction, should be the same as Omega_1"
m_dot_dryair_total=m_dot_dryair_orf+m_dot_dryair_vnt
m_dot_humidair_total = m_dot_humidair_orf + m_dot_humidair_vnt
Mu_2=VISCOSITY(AirH2O,T=T_2,P=p_2,R=RH_2)   "[kg/m-s]"    "dynamic viscosity
at Inst. Block 2 location"
Rho_2=DENSITY(AirH2O,T=T_2,P=p_2,R=RH_2)    "[kg/m3]"    "density of the air at
Inst. Block 2 location"
Re_2_hydraulic=(Velocity_2*d_test*Rho_2/Mu_2)  "Reynolds number at Inst. Block 2
location based on Hydraulic diameter"
Velocity_2 = m_dot_humidair_total/(Rho_2*A_cross_test) "[m/s]" "Average Velocity in
test section"
Velocity_2_orifice = m_dot_humidair_orf/(Rho_2*A_cross_test)
Velocity_2_venturi = m_dot_humidair_vnt/(Rho_2*A_cross_test)


"! Check if Re >20,000 and  IF  Nu_fd = Nu_fd_Dittus_Boelter  or  {
Nu_fd_Dittus_Boelter  or  Nu_fd_Gnielinski  or  Nu_fd_Graetz_uniform_flux } "
```

```
"! Local Nusselt number at Fully Developed location with constant heat flux or constant wall temperature (same solution) by Notter and Sleicher exact solution, plus Dittus-Boelter correlation and Gnielinski correlation"

at0_10=64.38; at1_10= 646.8; at2_10=1870;
Bt0_10=7.596; Bt1_10=1.829; Bt2_10=1.217
at0_20=109; at1_20= 1119; at2_20=3240;    Bt0_20=13.06; Bt1_20=2.95; Bt2_20=1.784
at0_50=219; at1_50= 2350; at2_50=6808;    Bt0_50=26.6; Bt1_50=5.63; Bt2_50=3.32
{
"! If  10,00< Re <20,000 use this"
    at0_M10 = at0_10 + (at0_20 - at0_10)*((Re_M10-10000)/(20000-10000));
    at1_M10 = at1_10 + (at1_20 - at1_10)*((Re_M10-10000)/(20000-10000));
    at2_M10 = at2_10 + (at2_20 - at2_10)*((Re_M10-10000)/(20000-10000));
    Bt0_M10 = Bt0_10 + (Bt0_20 - Bt0_10)*((Re_M10-10000)/(20000-10000));
    Bt1_M10 = Bt1_10 + (Bt1_20 - Bt1_10)*((Re_M10-10000)/(20000-10000));
    Bt2_M10 = Bt2_10 + (Bt2_20 - Bt2_10)*((Re_M10-10000)/(20000-10000))
}
"! If  20,000< Re <50,000 use this"
    at0_M10 = at0_20 + (at0_50 - at0_20)*((Re_M10-20000)/(50000-20000));
    at1_M10 = at1_20 + (at1_50 - at1_20)*((Re_M10-20000)/(50000-20000));
    at2_M10 = at2_20 + (at2_50 - at2_20)*((Re_M10-20000)/(50000-20000));
    Bt0_M10 = Bt0_20 + (Bt0_50 - Bt0_20)*((Re_M10-20000)/(50000-20000));
    Bt1_M10 = Bt1_20 + (Bt1_50 - Bt1_20)*((Re_M10-20000)/(50000-20000));
    Bt2_M10 = Bt2_20 + (Bt2_50 - Bt2_20)*((Re_M10-20000)/(50000-20000))

Nu_fd_Graetz_uniform_flux = 1/ ( 16* (Bt0_M10/at0_M10^2 + Bt1_M10/at1_M10^2 + Bt2_M10/at2_M10^2 ) )
h_fd_Graetz_uniform_flux=Nu_fd_Graetz_uniform_flux*k_fd/d_test   "[W/m2-K]"
"Local heat transfer coefficient"

 Nu_fd_Gnielinski=( (f1_Blausius/8)*(Re_fd_hydraulic-1000)*Pr_fd ) / (1+12.7*sqrt(f1_Blausius/8)*(Pr_fd^(2/3)-1))   "Nusselt number using Gnielinski corelation valid for Re>3000  has 10%error"
 Nu_fd_Dittus_Boelter=0.023*Re_fd_hydraulic^(4/5)*Pr_fd^0.4    "Nusselt number using Dittus-Boelter eqn valid for Re>10,000  has 25%error"
 f1_Blausius=0.316/(Re_fd_hydraulic)^0.25  "Blausius formula for friction factor for Re < 20,000"
  f1_Petukhov=(0.790*ln(Re_fd_hydraulic)-1.64)^(-2)  "Petukhov formula for small and larg Re,  Re<20,000<Re  "
  Re_fd_hydraulic=(Velocity_fd*d_test*Rho_fd/Mu_fd)          "Reynolds number at fully developed location based on Hydraulic diameter"
     Mu_fd=VISCOSITY(AirH2O,T=T_M10,P=(p_2+p_3)/2,R=RH_M10)   "[kg/m-s]"
"dynamic viscosity at fully developed location"
     Rho_fd=DENSITY(AirH2O,T=T_M10,P=(p_2+p_3)/2,R=RH_M10)    "[kg/m3]"
"density of the air at fully developed location"
```

```
    Velocity_fd = m_dot_humidair_total/(Rho_fd*A_cross_test) "[m/s]" "Average
Velocity in test section at fully developed location"
  Pr_fd=PRANDTL(Air_ha,T=T_M10,P=(p_2+p_3)/2)       "Prandtl number"
  k_fd=CONDUCTIVITY(AirH2O,T=T_M10,P=(p_2+p_3)/2,R=RH_M10)   "[W/m-K]"
"Conductivity"
 h_fd_Dittus_Boelter=Nu_fd_Dittus_Boelter*k_fd/d_test   "[W/m2-K]"  "Local heat
transfer coeficient"
 h_fd_Gnielinski=Nu_fd_Gnielinski*k_fd/d_test   "[W/m2-K]"  "Local heat transfer
coeficient"

Nu_fd = Nu_fd_Gnielinski        { Nu_fd_Dittus_Boelter   Nu_fd_Gnielinski
Nu_fd_Graetz_uniform_flux  }

"!  Reynolds et al. correlation for entrance region with constant heat flux, Thermally
Developing Flow"

Nu_M1 / Nu_fd = 1+ (0.8*(1+70000* (Re_M1)^(-3/2))) / (0.5/d_in_test );
h_M1 = Nu_M1 * k_M1/d_test
    Re_M1 = (Velocity_M1*d_test*Rho_M1/Mu_M1) "Reynolds numb. at location M1"
    Mu_M1=VISCOSITY(AirH2O,T=T_M1,P=(p_2-(p_2-p_3)*0.5/41.4),R=RH_M1)
      "[kg/m-s]"    "dynamic viscosity at location M1"
    Rho_M1=DENSITY(AirH2O,T=T_M1,P=(p_2-(p_2-p_3)*0.5/41.4),R=RH_M1)
      "[kg/m3]"    "density of the air at location M1"
    Velocity_M1 = m_dot_humidair_total/(Rho_M1*A_cross_test) "[m/s]"
      "Average velocity in test section at location M1"
      {Pr_M1=PRANDTL(Air_ha,T=T_M1,P=(p_2-(p_2-p_3)*0.5/41.4)) Prandtl numb.}
    k_M1=CONDUCTIVITY(AirH2O,T=T_M1,P=(p_2-(p_2-
    p_3)*0.5/41.4),R=RH_M1)   "[W/m-K]" "Conductivity"

Nu_M2 / Nu_fd = 1+ (0.8*(1+70000* (Re_M2)^(-3/2))) / (1.5/d_in_test );
h_M2 = Nu_M2 * k_M2/d_test
    Re_M2 = (Velocity_M2*d_test*Rho_M2/Mu_M2)
    Mu_M2=VISCOSITY(AirH2O,T=T_M2,P=(p_2-(p_2-p_3)*1.5/41.4),R=RH_M2)
    Rho_M2=DENSITY(AirH2O,T=T_M2,P=(p_2-(p_2-p_3)*1.5/41.4),R=RH_M2)
    Velocity_M2 = m_dot_humidair_total/(Rho_M2*A_cross_test)
    k_M2=CONDUCTIVITY(AirH2O,T=T_M2,P=(p_2-(p_2-
    p_3)*1.5/41.4),R=RH_M2)

Nu_M3 / Nu_fd = 1+ (0.8*(1+70000* (Re_M3)^(-3/2))) / (2.5/d_in_test );
h_M3 = Nu_M3 * k_M3/d_test
    Re_M3 = (Velocity_M3*d_test*Rho_M3/Mu_M3)
    Mu_M3=VISCOSITY(AirH2O,T=T_M3,P=(p_2-(p_2-p_3)*2.5/41.4),R=RH_M3)
    Rho_M3=DENSITY(AirH2O,T=T_M3,P=(p_2-(p_2-p_3)*2.5/41.4),R=RH_M3)
    Velocity_M3 = m_dot_humidair_total/(Rho_M3*A_cross_test)
    k_M3=CONDUCTIVITY(AirH2O,T=T_M3,P=(p_2-(p_2-
    p_3)*2.5/41.4),R=RH_M3)
```

```
Nu_M4 / Nu_fd = 1+ (0.8*(1+70000* (Re_M4)^(-3/2))) / (4.8/d_in_test );
h_M4 = Nu_M4 * k_M4/d_test
    Re_M4 = (Velocity_M4*d_test*Rho_M4/Mu_M4)
    Mu_M4=VISCOSITY(AirH2O,T=T_M4,P=(p_2-(p_2-p_3)*4.8/41.4),R=RH_M4)
    Rho_M4=DENSITY(AirH2O,T=T_M4,P=(p_2-(p_2-p_3)*4.8/41.4),R=RH_M4)
    Velocity_M4 = m_dot_humidair_total/(Rho_M4*A_cross_test)
    k_M4=CONDUCTIVITY(AirH2O,T=T_M4,P=(p_2-(p_2-
    p_3)*4.8/41.4),R=RH_M4)

Nu_M5 / Nu_fd = 1+ (0.8*(1+70000* (Re_M5)^(-3/2))) / (7.1/d_in_test );
h_M5 = Nu_M5 * k_M5/d_test
    Re_M5 = (Velocity_M5*d_test*Rho_M5/Mu_M5)
    Mu_M5=VISCOSITY(AirH2O,T=T_M5,P=(p_2-(p_2-p_3)*7.1/41.4),R=RH_M5)
    Rho_M5=DENSITY(AirH2O,T=T_M5,P=(p_2-(p_2-p_3)*7.1/41.4),R=RH_M5)
    Velocity_M5 = m_dot_humidair_total/(Rho_M5*A_cross_test)
    k_M5=CONDUCTIVITY(AirH2O,T=T_M5,P=(p_2-(p_2-
    p_3)*7.1/41.4),R=RH_M5)

Nu_M6 / Nu_fd = 1+ (0.8*(1+70000* (Re_M6)^(-3/2))) / (9.4/d_in_test );
h_M6 = Nu_M6 * k_M6/d_test
    Re_M6 = (Velocity_M6*d_test*Rho_M6/Mu_M6)
    Mu_M6=VISCOSITY(AirH2O,T=T_M6,P=(p_2-(p_2-p_3)*9.4/41.4),R=RH_M6)
    Rho_M6=DENSITY(AirH2O,T=T_M6,P=(p_2-(p_2-p_3)*9.4/41.4),R=RH_M6)
    Velocity_M6 = m_dot_humidair_total/(Rho_M6*A_cross_test)
    k_M6=CONDUCTIVITY(AirH2O,T=T_M6,P=(p_2-(p_2-
    p_3)*9.4/41.4),R=RH_M6)

Nu_M7 / Nu_fd = 1+ (0.8*(1+70000* (Re_M7)^(-3/2))) / (11.7/d_in_test );
h_M7 = Nu_M7 * k_M7/d_test
    Re_M7 = (Velocity_M7*d_test*Rho_M7/Mu_M7)
    Mu_M7=VISCOSITY(AirH2O,T=T_M7,P=(p_2-(p_2-p_3)*11.7/41.4),R=RH_M7)
    Rho_M7=DENSITY(AirH2O,T=T_M7,P=(p_2-(p_2-p_3)*11.7/41.4),R=RH_M7)
    Velocity_M7 = m_dot_humidair_total/(Rho_M7*A_cross_test)
    k_M7=CONDUCTIVITY(AirH2O,T=T_M7,P=(p_2-(p_2-
    p_3)*11.7/41.4),R=RH_M7)

Nu_M8 / Nu_fd = 1+ (0.8*(1+70000* (Re_M8)^(-3/2))) / (14.0/d_in_test );
h_M8 = Nu_M8 * k_M8/d_test
    Re_M8 = (Velocity_M8*d_test*Rho_M8/Mu_M8)
    Mu_M8=VISCOSITY(AirH2O,T=T_M8,P=(p_2-(p_2-p_3)*14.0/41.4),R=RH_M8)
    Rho_M8=DENSITY(AirH2O,T=T_M8,P=(p_2-(p_2-p_3)*14.0/41.4),R=RH_M8)
    Velocity_M8 = m_dot_humidair_total/(Rho_M8*A_cross_test)
    k_M8=CONDUCTIVITY(AirH2O,T=T_M8,P=(p_2-(p_2-
    p_3)*14.0/41.4),R=RH_M8)
```

```
Nu_M9 / Nu_fd = 1+ (0.8*(1+70000* (Re_M9)^(-3/2))) / (16.3/d_in_test );
h_M9 = Nu_M9 * k_M9/d_test
    Re_M9 = (Velocity_M9*d_test*Rho_M9/Mu_M9)
    Mu_M9=VISCOSITY(AirH2O,T=T_M9,P=(p_2-(p_2-p_3)*16.3/41.4),R=RH_M9)
    Rho_M9=DENSITY(AirH2O,T=T_M9,P=(p_2-(p_2-p_3)*16.3/41.4),R=RH_M9)
    Velocity_M9 = m_dot_humidair_total/(Rho_M9*A_cross_test)
    k_M9=CONDUCTIVITY(AirH2O,T=T_M9,P=(p_2-(p_2-
    p_3)*16.3/41.4),R=RH_M9)

"! At location 10 it is assumed to be fully developed flow"
Nu_M10 / Nu_fd = 1+ (0.8*(1+70000* (Re_M10)^(-3/2))) / (18.6/d_in_test );
h_M10 = Nu_M10 * k_M10/d_test
    Re_M10 = (Velocity_M10*d_test*Rho_M10/Mu_M10) "Reynolds numb. at fully
       developed location based on Hydraulic diameter"
    Mu_M10=VISCOSITY(AirH2O,T=T_M10,P=(p_2-(p_2-
    p_3)*18.6/41.4),R=RH_M10)   "[kg/m-s]" "dynamic viscosity at fully developed loc."
    Rho_M10=DENSITY(AirH2O,T=T_M10,P=(p_2-(p_2-
    p_3)*18.6/41.4),R=RH_M10)    "[kg/m3]" "density of the air at fully developed loc."
    Velocity_M10 = m_dot_humidair_total/(Rho_M10*A_cross_test) "[m/s]"
      "Average velocity in test section at fully developed location"
      {Pr_M10=PRANDTL(Air_ha,T=T_M10,P=(p_2-(p_2-p_3)*18.6/41.4)) Prandtl #}
    k_M10=CONDUCTIVITY(AirH2O,T=T_M10,P=(p_2-(p_2-
    p_3)*18.6/41.4),R=RH_M10)   "[W/m-K]" "Conductivity"

Nu_M11 / Nu_fd = 1+ (0.8*(1+70000* (Re_M11)^(-3/2))) / (20.9/d_in_test );
h_M11 = Nu_M11 * k_M11/d_test
    Re_M11 = (Velocity_M11*d_test*Rho_M11/Mu_M11)
    Mu_M11=VISCOSITY(AirH2O,T=T_M11,P=(p_2-(p_2-
    p_3)*20.9/41.4),R=RH_M11)
    Rho_M11=DENSITY(AirH2O,T=T_M11,P=(p_2-(p_2-p_3)*20.9/41.4),R=RH_M11)
    Velocity_M11 = m_dot_humidair_total/(Rho_M11*A_cross_test)
    k_M11=CONDUCTIVITY(AirH2O,T=T_M11,P=(p_2-(p_2-
    p_3)*20.9/41.4),R=RH_M11)

Nu_M12 / Nu_fd = 1+ (0.8*(1+70000* (Re_M12)^(-3/2))) / (23.2/d_in_test );
h_M12 = Nu_M12 * k_M12/d_test
    Re_M12 = (Velocity_M12*d_test*Rho_M12/Mu_M12)
    Mu_M12=VISCOSITY(AirH2O,T=T_M12,P=(p_2-(p_2-
    p_3)*23.2/41.4),R=RH_M12)
    Rho_M12=DENSITY(AirH2O,T=T_M12,P=(p_2-(p_2-
    p_3)*23.2/41.4),R=RH_M12)
    Velocity_M12 = m_dot_humidair_total/(Rho_M12*A_cross_test)
    k_M12=CONDUCTIVITY(AirH2O,T=T_M12,P=(p_2-(p_2-
    p_3)*23.2/41.4),R=RH_M12)

Nu_M13 / Nu_fd = 1+ (0.8*(1+70000* (Re_M13)^(-3/2))) / (25.5/d_in_test );
```

```
h_M13 = Nu_M13 * k_M13/d_test
    Re_M13 = (Velocity_M13*d_test*Rho_M13/Mu_M13)
    Mu_M13=VISCOSITY(AirH2O,T=T_M13,P=(p_2-(p_2-
    p_3)*25.5/41.4),R=RH_M13)
    Rho_M13=DENSITY(AirH2O,T=T_M13,P=(p_2-(p_2-p_3)*25.5/41.4),R=RH_M13)
    Velocity_M13 = m_dot_humidair_total/(Rho_M13*A_cross_test)
    k_M13=CONDUCTIVITY(AirH2O,T=T_M13,P=(p_2-(p_2-
    p_3)*25.5/41.4),R=RH_M13)

Nu_M14 / Nu_fd = 1+ (0.8*(1+70000* (Re_M14)^(-3/2))) / (27.8/d_in_test );
h_M14 = Nu_M14 * k_M14/d_test
    Re_M14 = (Velocity_M14*d_test*Rho_M14/Mu_M14)
    Mu_M14=VISCOSITY(AirH2O,T=T_M14,P=(p_2-(p_2-
    p_3)*27.8/41.4),R=RH_M14)
    Rho_M14=DENSITY(AirH2O,T=T_M14,P=(p_2-(p_2-p_3)*27.8/41.4),R=RH_M14)
    Velocity_M14 = m_dot_humidair_total/(Rho_M14*A_cross_test)
    k_M14=CONDUCTIVITY(AirH2O,T=T_M14,P=(p_2-(p_2-
    p_3)*27.8/41.4),R=RH_M14)

Nu_M15 / Nu_fd = 1+ (0.8*(1+70000* (Re_M15)^(-3/2))) / (30.1/d_in_test );
h_M15 = Nu_M15 * k_M15/d_test
    Re_M15 = (Velocity_M15*d_test*Rho_M15/Mu_M15)
    Mu_M15=VISCOSITY(AirH2O,T=T_M15,P=(p_2-(p_2-
    p_3)*30.1/41.4),R=RH_M15)
    Rho_M15=DENSITY(AirH2O,T=T_M15,P=(p_2-(p_2-
    p_3)*30.1/41.4),R=RH_M15)
    Velocity_M15 = m_dot_humidair_total/(Rho_M15*A_cross_test)
    k_M15=CONDUCTIVITY(AirH2O,T=T_M15,P=(p_2-(p_2-
    p_3)*30.1/41.4),R=RH_M15)

Nu_M16 / Nu_fd = 1+ (0.8*(1+70000* (Re_M16)^(-3/2))) / (32.4/d_in_test );
h_M16 = Nu_M16 * k_M16/d_test
    Re_M16 = (Velocity_M16*d_test*Rho_M16/Mu_M16)
    Mu_M16=VISCOSITY(AirH2O,T=T_M16,P=(p_2-(p_2-
    p_3)*32.4/41.4),R=RH_M16)
    Rho_M16=DENSITY(AirH2O,T=T_M16,P=(p_2-(p_2-
    p_3)*32.4/41.4),R=RH_M16)
    Velocity_M16 = m_dot_humidair_total/(Rho_M16*A_cross_test)
    k_M16=CONDUCTIVITY(AirH2O,T=T_M16,P=(p_2-(p_2-
    p_3)*32.4/41.4),R=RH_M16)

Nu_M17 / Nu_fd = 1+ (0.8*(1+70000* (Re_M17)^(-3/2))) / (34.7/d_in_test );
h_M17 = Nu_M17 * k_M17/d_test
    Re_M17 = (Velocity_M17*d_test*Rho_M17/Mu_M17)
    Mu_M17=VISCOSITY(AirH2O,T=T_M17,P=(p_2-(p_2-
    p_3)*34.7/41.4),R=RH_M17)
```

```
    Rho_M17=DENSITY(AirH2O,T=T_M17,P=(p_2-(p_2-
    p_3)*34.7/41.4),R=RH_M17)
    Velocity_M17 = m_dot_humidair_total/(Rho_M17*A_cross_test)
    k_M17=CONDUCTIVITY(AirH2O,T=T_M17,P=(p_2-(p_2-
    p_3)*34.7/41.4),R=RH_M17)

Nu_M18 / Nu_fd = 1+ (0.8*(1+70000* (Re_M18)^(-3/2))) / (37.0/d_in_test );
h_M18 = Nu_M18 * k_M18/d_test
    Re_M18 = (Velocity_M18*d_test*Rho_M18/Mu_M18)
    Mu_M18=VISCOSITY(AirH2O,T=T_M18,P=(p_2-(p_2-
    p_3)*37.0/41.4),R=RH_M18)
    Rho_M18=DENSITY(AirH2O,T=T_M18,P=(p_2-(p_2-
    p_3)*37.0/41.4),R=RH_M18)
    Velocity_M18 = m_dot_humidair_total/(Rho_M18*A_cross_test)
    k_M18=CONDUCTIVITY(AirH2O,T=T_M18,P=(p_2-(p_2-
    p_3)*37.0/41.4),R=RH_M18)

Nu_M19 / Nu_fd = 1+ (0.8*(1+70000* (Re_M19)^(-3/2))) / (39.3/d_in_test );
h_M19 = Nu_M19 * k_M19/d_test
    Re_M19 = (Velocity_M19*d_test*Rho_M19/Mu_M19)
    Mu_M19=VISCOSITY(AirH2O,T=T_M19,P=(p_2-(p_2-
    p_3)*39.3/41.4),R=RH_M19)
    Rho_M19=DENSITY(AirH2O,T=T_M19,P=(p_2-(p_2-
    p_3)*39.3/41.4),R=RH_M19)
    Velocity_M19 = m_dot_humidair_total/(Rho_M19*A_cross_test)
    k_M19=CONDUCTIVITY(AirH2O,T=T_M19,P=(p_2-(p_2-
    p_3)*39.3/41.4),R=RH_M19)

"! DO NOT USE CALCULATIONS FOR:
   Mist XX Thermocouple (as in the main mist cooling code)"
"! Control volume ENERGY balance"

RH_M1=  RELHUM(AirH2O,T=T_M1,P=(p_2-(p_2-
p_3)*0.5/41.4),w=(Omega_2/100))    "relative humidity at location Mist 1"
RH_M2 =  RELHUM(AirH2O,T=T_M2,P=(p_2-(p_2-
p_3)*1.5/41.4),w=(Omega_2/100))    "relative humidity at location Mist 2"
RH_M3 =  RELHUM(AirH2O,T=T_M3,P=(p_2-(p_2-
p_3)*2.5/41.4),w=(Omega_2/100))    "relative humidity at location Mist 3"
RH_M4 =  RELHUM(AirH2O,T=T_M4,P=(p_2-(p_2-
p_3)*4.8/41.4),w=(Omega_2/100))    "relative humidity at location Mist 4"
RH_M5 =  RELHUM(AirH2O,T=T_M5,P=(p_2-(p_2-
p_3)*7.1/41.4),w=(Omega_2/100))    "relative humidity at location Mist 5"
RH_M6 =  RELHUM(AirH2O,T=T_M6,P=(p_2-(p_2-
p_3)*9.4/41.4),w=(Omega_2/100))    "relative humidity at location Mist 6"
RH_M7 =  RELHUM(AirH2O,T=T_M7,P=(p_2-(p_2-
p_3)*11.7/41.4),w=(Omega_2/100))  "relative humidity at location Mist 7"
```

```
RH_M8 =  RELHUM(AirH2O,T=T_M8,P=(p_2-(p_2-
p_3)*14.0/41.4),w=(Omega_2/100))  "relative humidity at location Mist 8"
RH_M9 =  RELHUM(AirH2O,T=T_M9,P=(p_2-(p_2-
p_3)*16.3/41.4),w=(Omega_2/100))  "relative humidity at location Mist 9"
RH_M10 =  RELHUM(AirH2O,T=T_M10,P=(p_2-(p_2-
p_3)*18.6/41.4),w=(Omega_2/100))  "relative humidity at location Mist 10"
RH_M11 =  RELHUM(AirH2O,T=T_M11,P=(p_2-(p_2-
p_3)*20.9/41.4),w=(Omega_2/100))  "relative humidity at location Mist 11"
RH_M12 =  RELHUM(AirH2O,T=T_M12,P=(p_2-(p_2-
p_3)*23.2/41.4),w=(Omega_2/100))  "relative humidity at location Mist 12"
RH_M13 =  RELHUM(AirH2O,T=T_M13,P=(p_2-(p_2-
p_3)*25.5/41.4),w=(Omega_2/100))  "relative humidity at location Mist 13"
RH_M14 =  RELHUM(AirH2O,T=T_M14,P=(p_2-(p_2-
p_3)*27.8/41.4),w=(Omega_2/100))  "relative humidity at location Mist 14"
RH_M15 =  RELHUM(AirH2O,T=T_M15,P=(p_2-(p_2-
p_3)*30.1/41.4),w=(Omega_2/100))  "relative humidity at location Mist 15"
RH_M16 =  RELHUM(AirH2O,T=T_M16,P=(p_2-(p_2-
p_3)*32.4/41.4),w=(Omega_2/100))  "relative humidity at location Mist 16"
RH_M17 =  RELHUM(AirH2O,T=T_M17,P=(p_2-(p_2-
p_3)*34.7/41.4),w=(Omega_2/100))  "relative humidity at location Mist 17"
RH_M18 =  RELHUM(AirH2O,T=T_M18,P=(p_2-(p_2-
p_3)*37.0/41.4),w=(Omega_2/100))  "relative humidity at location Mist 18"
RH_M19 =  RELHUM(AirH2O,T=T_M19,P=(p_2-(p_2-
p_3)*39.3/41.4),w=(Omega_2/100))  "relative humidity at location Mist 19"
RH_M20 =  RELHUM(AirH2O,T=T_M20,P=(p_2-(p_2-p_3)*40.5
/41.4),w=(Omega_2/100))              "relative humidity at location Mist 20"

Power = Electrical_Power -
h_natural_convection*(T_surface_room)*Insulation_perimeter*L -
0.002*Electrical_Power  "[W]"  "True Heating Power"

Power/1000 * (0.5/41.4) = m_dot_dryair_total*(ENTHALPY(AirH2O,T=T_M1,P=(p_2-
(p_2-p_3)*0.5/41.4),R=RH_M1) - ENTHALPY(AirH2O,T=T_2,P=p_2,R=RH_2))

Power/1000 * (1.5/41.4) = m_dot_dryair_total*(ENTHALPY(AirH2O,T=T_M2,P=(p_2-
(p_2-p_3)*1.5/41.4),R=RH_M2) - ENTHALPY(AirH2O,T=T_2,P=p_2,R=RH_2))

Power/1000 * (2.5/41.4) = m_dot_dryair_total*(ENTHALPY(AirH2O,T=T_M3,P=(p_2-
(p_2-p_3)*2.5/41.4),R=RH_M3) - ENTHALPY(AirH2O,T=T_2,P=p_2,R=RH_2))

Power/1000 * (4.8/41.4) = m_dot_dryair_total*(ENTHALPY(AirH2O,T=T_M4,P=(p_2-
(p_2-p_3)*4.8/41.4),R=RH_M4) - ENTHALPY(AirH2O,T=T_2,P=p_2,R=RH_2))

Power/1000 * (7.1/41.4) = m_dot_dryair_total*(ENTHALPY(AirH2O,T=T_M5,P=(p_2-
(p_2-p_3)*7.1/41.4),R=RH_M5) - ENTHALPY(AirH2O,T=T_2,P=p_2,R=RH_2))
```

Power/1000 * (9.4/41.4) = m_dot_dryair_total*(ENTHALPY(AirH2O,T=T_M6,P=(p_2-(p_2-p_3)*9.4/41.4),R=RH_M6) - ENTHALPY(AirH2O,T=T_2,P=p_2,R=RH_2))

Power/1000 * (11.7/41.4) =
m_dot_dryair_total*(ENTHALPY(AirH2O,T=T_M7,P=(p_2-(p_2-p_3)*11.7/41.4),R=RH_M7) - ENTHALPY(AirH2O,T=T_2,P=p_2,R=RH_2))

Power/1000 * (14.0/41.4) =
m_dot_dryair_total*(ENTHALPY(AirH2O,T=T_M8,P=(p_2-(p_2-p_3)*14.0/41.4),R=RH_M8) - ENTHALPY(AirH2O,T=T_2,P=p_2,R=RH_2))

Power/1000 * (16.3/41.4) =
m_dot_dryair_total*(ENTHALPY(AirH2O,T=T_M9,P=(p_2-(p_2-p_3)*16.3/41.4),R=RH_M9) - ENTHALPY(AirH2O,T=T_2,P=p_2,R=RH_2))

Power/1000 * (18.6/41.4) =
m_dot_dryair_total*(ENTHALPY(AirH2O,T=T_M10,P=(p_2-(p_2-p_3)*18.6/41.4),R=RH_M10) - ENTHALPY(AirH2O,T=T_2,P=p_2,R=RH_2))

Power/1000 * (20.9/41.4) =
m_dot_dryair_total*(ENTHALPY(AirH2O,T=T_M11,P=(p_2-(p_2-p_3)*20.9/41.4),R=RH_M11) - ENTHALPY(AirH2O,T=T_2,P=p_2,R=RH_2))

Power/1000 * (23.2/41.4) =
m_dot_dryair_total*(ENTHALPY(AirH2O,T=T_M12,P=(p_2-(p_2-p_3)*23.2/41.4),R=RH_M12) - ENTHALPY(AirH2O,T=T_2,P=p_2,R=RH_2))

Power/1000 * (25.5/41.4) =
m_dot_dryair_total*(ENTHALPY(AirH2O,T=T_M13,P=(p_2-(p_2-p_3)*25.5/41.4),R=RH_M13) - ENTHALPY(AirH2O,T=T_2,P=p_2,R=RH_2))

Power/1000 * (27.8/41.4) =
m_dot_dryair_total*(ENTHALPY(AirH2O,T=T_M14,P=(p_2-(p_2-p_3)*27.8/41.4),R=RH_M14) - ENTHALPY(AirH2O,T=T_2,P=p_2,R=RH_2))

Power/1000 * (30.1/41.4) =
m_dot_dryair_total*(ENTHALPY(AirH2O,T=T_M15,P=(p_2-(p_2-p_3)*30.1/41.4),R=RH_M15) - ENTHALPY(AirH2O,T=T_2,P=p_2,R=RH_2))

Power/1000 * (32.4/41.4) =
m_dot_dryair_total*(ENTHALPY(AirH2O,T=T_M16,P=(p_2-(p_2-p_3)*32.4/41.4),R=RH_M16) - ENTHALPY(AirH2O,T=T_2,P=p_2,R=RH_2))

Power/1000 * (34.7/41.4) =
m_dot_dryair_total*(ENTHALPY(AirH2O,T=T_M17,P=(p_2-(p_2-p_3)*34.7/41.4),R=RH_M17) - ENTHALPY(AirH2O,T=T_2,P=p_2,R=RH_2))

```
Power/1000 * (37.0/41.4) =
m_dot_dryair_total*(ENTHALPY(AirH2O,T=T_M18,P=(p_2-(p_2-
p_3)*37.0/41.4),R=RH_M18) - ENTHALPY(AirH2O,T=T_2,P=p_2,R=RH_2))

Power/1000 * (39.3/41.4) =
m_dot_dryair_total*(ENTHALPY(AirH2O,T=T_M19,P=(p_2-(p_2-
p_3)*39.3/41.4),R=RH_M19) - ENTHALPY(AirH2O,T=T_2,P=p_2,R=RH_2))

Power/1000 * (40.5/41.4) =
m_dot_dryair_total*(ENTHALPY(AirH2O,T=T_M20,P=(p_2-(p_2-
p_3)*40.5/41.4),R=RH_M20) - ENTHALPY(AirH2O,T=T_2,P=p_2,R=RH_2))
```

A.4 Second Single-Phase Convection Processing Code

This Engineering Equation Solver (EES) experimental data processing code calculates the heat transfer coefficient for air single-phase forced convection experiments by using a theoretical turbulent Graetz problem solution by Notter and Sleicher (1972). It follows the same procedure as the first single-phase convection processing code (see section A.3). Only the parts of this code that are different from the first single-phase convection processing code are shown below.

```
{! The Second Single-phase Convection Processing Code  }
"! This code uses Graetz problem Exact solution for turbulent flow;
   Thermally Developing Flow"
"  ********************************************************************** "

"! Graetz problem for turbulent flow in smooth circular ducts with constant heat flux
   exact solution by Notter and Sleicher; Thermally Developing Flow"

"! These values are for Re = 10,000 and 50,000"
b1_10=519.5; b2_10= 1624; b3_10=3202;
A1_10=-0.0123; A2_10=-0.00738; A3_10=-0.00653
b1_50=1952; b2_50= 6154; b3_50=12480;
A1_50=-0.00296; A2_50=-0.00147; A3_50=-0.00106

    X_M1 = 0.5/(d_in_test * Re_M1 * Pr_M1)
```

```
b1_M1 = b1_10 + (b1_50 - b1_10)*((Re_M1-10000)/(50000-10000));
b2_M1 = b2_10 + (b2_50 - b2_10)*((Re_M1-10000)/(50000-10000))
b3_M1 = b3_10 + (b3_50 - b3_10)*((Re_M1-10000)/(50000-10000));
A1_M1 = A1_10 + (A1_50 - A1_10)*((Re_M1-10000)/(50000-10000))
A2_M1 = A2_10 + (A2_50 - A2_10)*((Re_M1-10000)/(50000-10000));
A3_M1 = A3_10 + (A3_50 - A3_10)*((Re_M1-10000)/(50000-10000))
Nu_M1 = 2 / (2/Nu_fd + A1_M1*exp(-2*b1_M1*X_M1) + A2_M1*exp(-
2*b2_M1*X_M1) + A3_M1*exp(-2*b3_M1*X_M1) )
h_M1 = Nu_M1 * k_M1/d_test
Re_M1 = (Velocity_M1*d_test*Rho_M1/Mu_M1) "Reynolds number at location M1
  based on Hydraulic diameter"
Mu_M1=VISCOSITY(AirH2O,T=T_M1,P=(p_2-(p_2-p_3)*0.5/41.4),R=RH_M1)
  "[kg/m-s]"   "Dynamic viscosity at fully developed location"
Rho_M1=DENSITY(AirH2O,T=T_M1,P=(p_2-(p_2-p_3)*0.5/41.4),R=RH_M1)
  "[kg/m3]"   "density of the air at fully developed location"
Velocity_M1 = m_dot_humidair_total/(Rho_M1*A_cross_test) "[m/s]"
  "Average Velocity in test section at fully developedlovation"
Pr_M1=PRANDTL(Air_ha,T=T_M1,P=(p_2-(p_2-p_3)*0.5/41.4)) "Prandtl number"
k_M1=CONDUCTIVITY(AirH2O,T=T_M1,P=(p_2-(p_2-
p_3)*0.5/41.4),R=RH_M1)  "[W/m-K]" "Conductivity"

X_M2 = 1.5/(d_in_test * Re_M2 * Pr_M2)
b1_M2 = b1_10 + (b1_50 - b1_10)*((Re_M2-10000)/(50000-10000));
b2_M2 = b2_10 + (b2_50 - b2_10)*((Re_M2-10000)/(50000-10000))
b3_M2 = b3_10 + (b3_50 - b3_10)*((Re_M2-10000)/(50000-10000));
A1_M2 = A1_10 + (A1_50 - A1_10)*((Re_M2-10000)/(50000-10000))
A2_M2 = A2_10 + (A2_50 - A2_10)*((Re_M2-10000)/(50000-10000));
A3_M2 = A3_10 + (A3_50 - A3_10)*((Re_M2-10000)/(50000-10000))
Nu_M2 = 2 / (2/Nu_fd + A1_M2*exp(-2*b1_M2*X_M2) + A2_M2*exp(-
2*b2_M2*X_M2) + A3_M2*exp(-2*b3_M2*X_M2) )
h_M2 = Nu_M2 * k_M2/d_test
Re_M2 = (Velocity_M2*d_test*Rho_M2/Mu_M2)
Mu_M2=VISCOSITY(AirH2O,T=T_M2,P=(p_2-(p_2-p_3)*1.5/41.4),R=RH_M2)
Rho_M2=DENSITY(AirH2O,T=T_M2,P=(p_2-(p_2-p_3)*1.5/41.4),R=RH_M2)
Velocity_M2 = m_dot_humidair_total/(Rho_M2*A_cross_test)
Pr_M2=PRANDTL(Air_ha,T=T_M2,P=(p_2-(p_2-p_3)*1.5/41.4))
k_M2=CONDUCTIVITY(AirH2O,T=T_M2,P=(p_2-(p_2-
p_3)*1.5/41.4),R=RH_M2)

X_M3 = 2.5/(d_in_test * Re_M3 * Pr_M3)
b1_M3 = b1_10 + (b1_50 - b1_10)*((Re_M3-10000)/(50000-10000));
b2_M3 = b2_10 + (b2_50 - b2_10)*((Re_M3-10000)/(50000-10000))
b3_M3 = b3_10 + (b3_50 - b3_10)*((Re_M3-10000)/(50000-10000));
A1_M3 = A1_10 + (A1_50 - A1_10)*((Re_M3-10000)/(50000-10000))
A2_M3 = A2_10 + (A2_50 - A2_10)*((Re_M3-10000)/(50000-10000));
A3_M3 = A3_10 + (A3_50 - A3_10)*((Re_M3-10000)/(50000-10000))
```

```
Nu_M3 = 2 / (2/Nu_fd + A1_M3*exp(-2*b1_M3*X_M3) + A2_M3*exp(-
    2*b2_M3*X_M3) + A3_M3*exp(-2*b3_M3*X_M3) )
    h_M3 = Nu_M3 * k_M3/d_test
    Re_M3 = (Velocity_M3*d_test*Rho_M3/Mu_M3)
    Mu_M3=VISCOSITY(AirH2O,T=T_M3,P=(p_2-(p_2-p_3)*2.5/41.4),R=RH_M3)
    Rho_M3=DENSITY(AirH2O,T=T_M3,P=(p_2-(p_2-p_3)*2.5/41.4),R=RH_M3)
    Velocity_M3 = m_dot_humidair_total/(Rho_M3*A_cross_test)
    Pr_M3=PRANDTL(Air_ha,T=T_M3,P=(p_2-(p_2-p_3)*2.5/41.4))
    k_M3=CONDUCTIVITY(AirH2O,T=T_M3,P=(p_2-(p_2-
    p_3)*2.5/41.4),R=RH_M3)

    X_M4 = 4.8/(d_in_test * Re_M4 * Pr_M4)
    b1_M4 = b1_10 + (b1_50 - b1_10)*((Re_M4-10000)/(50000-10000));
    b2_M4 = b2_10 + (b2_50 - b2_10)*((Re_M4-10000)/(50000-10000))
    b3_M4 = b3_10 + (b3_50 - b3_10)*((Re_M4-10000)/(50000-10000));
    A1_M4 = A1_10 + (A1_50 - A1_10)*((Re_M4-10000)/(50000-10000))
    A2_M4 = A2_10 + (A2_50 - A2_10)*((Re_M4-10000)/(50000-10000));
    A3_M4 = A3_10 + (A3_50 - A3_10)*((Re_M4-10000)/(50000-10000))
Nu_M4 = 2 / (2/Nu_fd + A1_M4*exp(-2*b1_M4*X_M4) + A2_M4*exp(-
    2*b2_M4*X_M4) + A3_M4*exp(-2*b3_M4*X_M4) )
    h_M4 = Nu_M4 * k_M4/d_test
    Re_M4 = (Velocity_M4*d_test*Rho_M4/Mu_M4)
    Mu_M4=VISCOSITY(AirH2O,T=T_M4,P=(p_2-(p_2-p_3)*4.8/41.4),R=RH_M4)
    Rho_M4=DENSITY(AirH2O,T=T_M4,P=(p_2-(p_2-p_3)*4.8/41.4),R=RH_M4)
    Velocity_M4 = m_dot_humidair_total/(Rho_M4*A_cross_test)
    Pr_M4=PRANDTL(Air_ha,T=T_M4,P=(p_2-(p_2-p_3)*4.8/41.4))
    k_M4=CONDUCTIVITY(AirH2O,T=T_M4,P=(p_2-(p_2-
    p_3)*4.8/41.4),R=RH_M4)

    X_M5 = 7.1/(d_in_test * Re_M5 * Pr_M5)
    b1_M5 = b1_10 + (b1_50 - b1_10)*((Re_M5-10000)/(50000-10000));
    b2_M5 = b2_10 + (b2_50 - b2_10)*((Re_M5-10000)/(50000-10000))
    b3_M5 = b3_10 + (b3_50 - b3_10)*((Re_M5-10000)/(50000-10000));
    A1_M5 = A1_10 + (A1_50 - A1_10)*((Re_M5-10000)/(50000-10000))
    A2_M5 = A2_10 + (A2_50 - A2_10)*((Re_M5-10000)/(50000-10000));
    A3_M5 = A3_10 + (A3_50 - A3_10)*((Re_M5-10000)/(50000-10000))
Nu_M5 = 2 / (2/Nu_fd + A1_M5*exp(-2*b1_M5*X_M5) + A2_M5*exp(-
    2*b2_M5*X_M5) + A3_M5*exp(-2*b3_M5*X_M5) )
    h_M5 = Nu_M5 * k_M5/d_test
    Re_M5 = (Velocity_M5*d_test*Rho_M5/Mu_M5)
    Mu_M5=VISCOSITY(AirH2O,T=T_M5,P=(p_2-(p_2-p_3)*7.1/41.4),R=RH_M5)
    Rho_M5=DENSITY(AirH2O,T=T_M5,P=(p_2-(p_2-p_3)*7.1/41.4),R=RH_M5)
    Velocity_M5 = m_dot_humidair_total/(Rho_M5*A_cross_test)
    Pr_M5=PRANDTL(Air_ha,T=T_M5,P=(p_2-(p_2-p_3)*7.1/41.4))
    k_M5=CONDUCTIVITY(AirH2O,T=T_M5,P=(p_2-(p_2-
    p_3)*7.1/41.4),R=RH_M5)
```

```
X_M6 = 9.4/(d_in_test * Re_M6 * Pr_M6)
b1_M6 = b1_10 + (b1_50 - b1_10)*((Re_M6-10000)/(50000-10000));
b2_M6 = b2_10 + (b2_50 - b2_10)*((Re_M6-10000)/(50000-10000))
b3_M6 = b3_10 + (b3_50 - b3_10)*((Re_M6-10000)/(50000-10000));
A1_M6 = A1_10 + (A1_50 - A1_10)*((Re_M6-10000)/(50000-10000))
A2_M6 = A2_10 + (A2_50 - A2_10)*((Re_M6-10000)/(50000-10000));
A3_M6 = A3_10 + (A3_50 - A3_10)*((Re_M6-10000)/(50000-10000))
Nu_M6 = 2 / (2/Nu_fd + A1_M6*exp(-2*b1_M6*X_M6) + A2_M6*exp(-
2*b2_M6*X_M6) + A3_M6*exp(-2*b3_M6*X_M6) )
h_M6 = Nu_M6 * k_M6/d_test
Re_M6 = (Velocity_M6*d_test*Rho_M6/Mu_M6)
Mu_M6=VISCOSITY(AirH2O,T=T_M6,P=(p_2-(p_2-p_3)*9.4/41.4),R=RH_M6)
Rho_M6=DENSITY(AirH2O,T=T_M6,P=(p_2-(p_2-p_3)*9.4/41.4),R=RH_M6)
Velocity_M6 = m_dot_humidair_total/(Rho_M6*A_cross_test)
Pr_M6=PRANDTL(Air_ha,T=T_M6,P=(p_2-(p_2-p_3)*9.4/41.4))
k_M6=CONDUCTIVITY(AirH2O,T=T_M6,P=(p_2-(p_2-
p_3)*9.4/41.4),R=RH_M6)

X_M7 = 11.7/(d_in_test * Re_M7 * Pr_M7)
b1_M7 = b1_10 + (b1_50 - b1_10)*((Re_M7-10000)/(50000-10000));
b2_M7 = b2_10 + (b2_50 - b2_10)*((Re_M7-10000)/(50000-10000))
b3_M7 = b3_10 + (b3_50 - b3_10)*((Re_M7-10000)/(50000-10000));
A1_M7 = A1_10 + (A1_50 - A1_10)*((Re_M7-10000)/(50000-10000))
A2_M7 = A2_10 + (A2_50 - A2_10)*((Re_M7-10000)/(50000-10000));
A3_M7 = A3_10 + (A3_50 - A3_10)*((Re_M7-10000)/(50000-10000))
Nu_M7 = 2 / (2/Nu_fd + A1_M7*exp(-2*b1_M7*X_M7) + A2_M7*exp(-
2*b2_M7*X_M7) + A3_M7*exp(-2*b3_M7*X_M7) )
h_M7 = Nu_M7 * k_M7/d_test
Re_M7 = (Velocity_M7*d_test*Rho_M7/Mu_M7)
Mu_M7=VISCOSITY(AirH2O,T=T_M7,P=(p_2-(p_2-p_3)*11.7/41.4),R=RH_M7)
Rho_M7=DENSITY(AirH2O,T=T_M7,P=(p_2-(p_2-p_3)*11.7/41.4),R=RH_M7)
Velocity_M7 = m_dot_humidair_total/(Rho_M7*A_cross_test)
Pr_M7=PRANDTL(Air_ha,T=T_M7,P=(p_2-(p_2-p_3)*11.7/41.4))
k_M7=CONDUCTIVITY(AirH2O,T=T_M7,P=(p_2-(p_2-
p_3)*11.7/41.4),R=RH_M7)

X_M8 = 14.0/(d_in_test * Re_M8 * Pr_M8)
b1_M8 = b1_10 + (b1_50 - b1_10)*((Re_M8-10000)/(50000-10000));
b2_M8 = b2_10 + (b2_50 - b2_10)*((Re_M8-10000)/(50000-10000))
b3_M8 = b3_10 + (b3_50 - b3_10)*((Re_M8-10000)/(50000-10000));
A1_M8 = A1_10 + (A1_50 - A1_10)*((Re_M8-10000)/(50000-10000))
A2_M8 = A2_10 + (A2_50 - A2_10)*((Re_M8-10000)/(50000-10000));
A3_M8 = A3_10 + (A3_50 - A3_10)*((Re_M8-10000)/(50000-10000))
Nu_M8 = 2 / (2/Nu_fd + A1_M8*exp(-2*b1_M8*X_M8) + A2_M8*exp(-
2*b2_M8*X_M8) + A3_M8*exp(-2*b3_M8*X_M8) )
```

```
    h_M8 = Nu_M8 * k_M8/d_test
    Re_M8 = (Velocity_M8*d_test*Rho_M8/Mu_M8)
    Mu_M8=VISCOSITY(AirH2O,T=T_M8,P=(p_2-(p_2-p_3)*14.0/41.4),R=RH_M8)
    Rho_M8=DENSITY(AirH2O,T=T_M8,P=(p_2-(p_2-p_3)*14.0/41.4),R=RH_M8)
    Velocity_M8 = m_dot_humidair_total/(Rho_M8*A_cross_test)
    Pr_M8=PRANDTL(Air_ha,T=T_M8,P=(p_2-(p_2-p_3)*14.0/41.4))
    k_M8=CONDUCTIVITY(AirH2O,T=T_M8,P=(p_2-(p_2-
    p_3)*14.0/41.4),R=RH_M8)

    X_M9 = 16.3/(d_in_test * Re_M9 * Pr_M9)
    b1_M9 = b1_10 + (b1_50 - b1_10)*((Re_M9-10000)/(50000-10000));
    b2_M9 = b2_10 + (b2_50 - b2_10)*((Re_M9-10000)/(50000-10000))
    b3_M9 = b3_10 + (b3_50 - b3_10)*((Re_M9-10000)/(50000-10000));
    A1_M9 = A1_10 + (A1_50 - A1_10)*((Re_M9-10000)/(50000-10000))
    A2_M9 = A2_10 + (A2_50 - A2_10)*((Re_M9-10000)/(50000-10000));
    A3_M9 = A3_10 + (A3_50 - A3_10)*((Re_M9-10000)/(50000-10000))
Nu_M9 = 2 / (2/Nu_fd + A1_M9*exp(-2*b1_M9*X_M9) + A2_M9*exp(-
    2*b2_M9*X_M9) + A3_M9*exp(-2*b3_M9*X_M9) )
    h_M9 = Nu_M9 * k_M9/d_test
    Re_M9 = (Velocity_M9*d_test*Rho_M9/Mu_M9)
    Mu_M9=VISCOSITY(AirH2O,T=T_M9,P=(p_2-(p_2-p_3)*16.3/41.4),R=RH_M9)
    Rho_M9=DENSITY(AirH2O,T=T_M9,P=(p_2-(p_2-p_3)*16.3/41.4),R=RH_M9)
    Velocity_M9 = m_dot_humidair_total/(Rho_M9*A_cross_test)
    Pr_M9=PRANDTL(Air_ha,T=T_M9,P=(p_2-(p_2-p_3)*16.3/41.4))
    k_M9=CONDUCTIVITY(AirH2O,T=T_M9,P=(p_2-(p_2-
    p_3)*16.3/41.4),R=RH_M9)

"! At location 10 it is assumed to be fully developed flow"
    X_M10 = 18.6/(d_in_test * Re_M10 * Pr_M10)
    b1_M10 = b1_10 + (b1_50 - b1_10)*((Re_M10-10000)/(50000-10000));
    b2_M10 = b2_10 + (b2_50 - b2_10)*((Re_M10-10000)/(50000-10000))
    b3_M10 = b3_10 + (b3_50 - b3_10)*((Re_M10-10000)/(50000-10000));
    A1_M10 = A1_10 + (A1_50 - A1_10)*((Re_M10-10000)/(50000-10000))
    A2_M10 = A2_10 + (A2_50 - A2_10)*((Re_M10-10000)/(50000-10000));
    A3_M10 = A3_10 + (A3_50 - A3_10)*((Re_M10-10000)/(50000-10000))
Nu_M10 = 2 / (2/Nu_fd + A1_M10*exp(-2*b1_M10*X_M10) + A2_M10*exp(-
    2*b2_M10*X_M10) + A3_M10*exp(-2*b3_M10*X_M10) )
    h_M10 = Nu_M10 * k_M10/d_test
    Re_M10 = (Velocity_M10*d_test*Rho_M10/Mu_M10)
    Mu_M10=VISCOSITY(AirH2O,T=T_M10,P=(p_2-(p_2-
    p_3)*18.6/41.4),R=RH_M10)
    Rho_M10=DENSITY(AirH2O,T=T_M10,P=(p_2-(p_2-
    p_3)*18.6/41.4),R=RH_M10)
    Velocity_M10 = m_dot_humidair_total/(Rho_M10*A_cross_test)
    Pr_M10=PRANDTL(Air_ha,T=T_M10,P=(p_2-(p_2-p_3)*18.6/41.4))
    k_M10=CONDUCTIVITY(AirH2O,T=T_M10,P=(p_2-(p_2-
```

```
    p_3)*18.6/41.4),R=RH_M10)

    X_M11 = 20.9/(d_in_test * Re_M11 * Pr_M11)
    b1_M11 = b1_10 + (b1_50 - b1_10)*((Re_M11-10000)/(50000-10000));
    b2_M11 = b2_10 + (b2_50 - b2_10)*((Re_M11-10000)/(50000-10000))
    b3_M11 = b3_10 + (b3_50 - b3_10)*((Re_M11-10000)/(50000-10000));
    A1_M11 = A1_10 + (A1_50 - A1_10)*((Re_M11-10000)/(50000-10000))
    A2_M11 = A2_10 + (A2_50 - A2_10)*((Re_M11-10000)/(50000-10000));
    A3_M11 = A3_10 + (A3_50 - A3_10)*((Re_M11-10000)/(50000-10000))
Nu_M11 = 2 / (2/Nu_fd + A1_M11*exp(-2*b1_M11*X_M11) + A2_M11*exp(-
    2*b2_M11*X_M11) + A3_M11*exp(-2*b3_M11*X_M11) )
    h_M11 = Nu_M11 * k_M11/d_test
    Re_M11 = (Velocity_M11*d_test*Rho_M11/Mu_M11)
    Mu_M11=VISCOSITY(AirH2O,T=T_M11,P=(p_2-(p_2-
    p_3)*20.9/41.4),R=RH_M11)
    Rho_M11=DENSITY(AirH2O,T=T_M11,P=(p_2-(p_2-
    p_3)*20.9/41.4),R=RH_M11)
    Velocity_M11 = m_dot_humidair_total/(Rho_M11*A_cross_test)
    Pr_M11=PRANDTL(Air_ha,T=T_M11,P=(p_2-(p_2-p_3)*20.9/41.4))
    k_M11=CONDUCTIVITY(AirH2O,T=T_M11,P=(p_2-(p_2-
    p_3)*20.9/41.4),R=RH_M11)

    X_M12 = 23.2/(d_in_test * Re_M12 * Pr_M12)
    b1_M12 = b1_10 + (b1_50 - b1_10)*((Re_M12-10000)/(50000-10000));
    b2_M12 = b2_10 + (b2_50 - b2_10)*((Re_M12-10000)/(50000-10000))
    b3_M12 = b3_10 + (b3_50 - b3_10)*((Re_M12-10000)/(50000-10000));
    A1_M12 = A1_10 + (A1_50 - A1_10)*((Re_M12-10000)/(50000-10000))
    A2_M12 = A2_10 + (A2_50 - A2_10)*((Re_M12-10000)/(50000-10000));
    A3_M12 = A3_10 + (A3_50 - A3_10)*((Re_M12-10000)/(50000-10000))
Nu_M12 = 2 / (2/Nu_fd + A1_M12*exp(-2*b1_M12*X_M12) + A2_M12*exp(-
    2*b2_M12*X_M12) + A3_M12*exp(-2*b3_M12*X_M12) )
    h_M12 = Nu_M12 * k_M12/d_test
    Re_M12 = (Velocity_M12*d_test*Rho_M12/Mu_M12)
    Mu_M12=VISCOSITY(AirH2O,T=T_M12,P=(p_2-(p_2-
    p_3)*23.2/41.4),R=RH_M12)
    Rho_M12=DENSITY(AirH2O,T=T_M12,P=(p_2-(p_2-p_3)*23.2/41.4),R=RH_M12)
    Velocity_M12 = m_dot_humidair_total/(Rho_M12*A_cross_test)
    Pr_M12=PRANDTL(Air_ha,T=T_M12,P=(p_2-(p_2-p_3)*23.2/41.4))
    k_M12=CONDUCTIVITY(AirH2O,T=T_M12,P=(p_2-(p_2-
    p_3)*23.2/41.4),R=RH_M12)

    X_M13 = 25.5/(d_in_test * Re_M13 * Pr_M13)
    b1_M13 = b1_10 + (b1_50 - b1_10)*((Re_M13-10000)/(50000-10000));
    b2_M13 = b2_10 + (b2_50 - b2_10)*((Re_M13-10000)/(50000-10000))
    b3_M13 = b3_10 + (b3_50 - b3_10)*((Re_M13-10000)/(50000-10000));
    A1_M13 = A1_10 + (A1_50 - A1_10)*((Re_M13-10000)/(50000-10000))
```

```
    A2_M13 = A2_10 + (A2_50 - A2_10)*((Re_M13-10000)/(50000-10000));
    A3_M13 = A3_10 + (A3_50 - A3_10)*((Re_M13-10000)/(50000-10000))
Nu_M13 = 2 / (2/Nu_fd + A1_M13*exp(-2*b1_M13*X_M13) + A2_M13*exp(-
    2*b2_M13*X_M13) + A3_M13*exp(-2*b3_M13*X_M13) )
    h_M13 = Nu_M13 * k_M13/d_test
    Re_M13 = (Velocity_M13*d_test*Rho_M13/Mu_M13)
    Mu_M13=VISCOSITY(AirH2O,T=T_M13,P=(p_2-(p_2-
    p_3)*25.5/41.4),R=RH_M13)
    Rho_M13=DENSITY(AirH2O,T=T_M13,P=(p_2-(p_2-
    p_3)*25.5/41.4),R=RH_M13)
    Velocity_M13 = m_dot_humidair_total/(Rho_M13*A_cross_test)
    Pr_M13=PRANDTL(Air_ha,T=T_M13,P=(p_2-(p_2-p_3)*25.5/41.4))
    k_M13=CONDUCTIVITY(AirH2O,T=T_M13,P=(p_2-(p_2-
    p_3)*25.5/41.4),R=RH_M13)

    X_M14 = 27.8/(d_in_test * Re_M14 * Pr_M14)
    b1_M14 = b1_10 + (b1_50 - b1_10)*((Re_M14-10000)/(50000-10000));
    b2_M14 = b2_10 + (b2_50 - b2_10)*((Re_M14-10000)/(50000-10000))
    b3_M14 = b3_10 + (b3_50 - b3_10)*((Re_M14-10000)/(50000-10000));
    A1_M14 = A1_10 + (A1_50 - A1_10)*((Re_M14-10000)/(50000-10000))
    A2_M14 = A2_10 + (A2_50 - A2_10)*((Re_M14-10000)/(50000-10000));
    A3_M14 = A3_10 + (A3_50 - A3_10)*((Re_M14-10000)/(50000-10000))
Nu_M14 = 2 / (2/Nu_fd + A1_M14*exp(-2*b1_M14*X_M14) + A2_M14*exp(-
    2*b2_M14*X_M14) + A3_M14*exp(-2*b3_M14*X_M14) )
    h_M14 = Nu_M14 * k_M14/d_test
    Re_M14 = (Velocity_M14*d_test*Rho_M14/Mu_M14)
    Mu_M14=VISCOSITY(AirH2O,T=T_M14,P=(p_2-(p_2-
    p_3)*27.8/41.4),R=RH_M14)
    Rho_M14=DENSITY(AirH2O,T=T_M14,P=(p_2-(p_2-
    p_3)*27.8/41.4),R=RH_M14)
    Velocity_M14 = m_dot_humidair_total/(Rho_M14*A_cross_test)
    Pr_M14=PRANDTL(Air_ha,T=T_M14,P=(p_2-(p_2-p_3)*27.8/41.4))
    k_M14=CONDUCTIVITY(AirH2O,T=T_M14,P=(p_2-(p_2-
    p_3)*27.8/41.4),R=RH_M14)

    X_M15 = 30.1/(d_in_test * Re_M15 * Pr_M15)
    b1_M15 = b1_10 + (b1_50 - b1_10)*((Re_M15-10000)/(50000-10000));
    b2_M15 = b2_10 + (b2_50 - b2_10)*((Re_M15-10000)/(50000-10000))
    b3_M15 = b3_10 + (b3_50 - b3_10)*((Re_M15-10000)/(50000-10000));
    A1_M15 = A1_10 + (A1_50 - A1_10)*((Re_M15-10000)/(50000-10000))
    A2_M15 = A2_10 + (A2_50 - A2_10)*((Re_M15-10000)/(50000-10000));
    A3_M15 = A3_10 + (A3_50 - A3_10)*((Re_M15-10000)/(50000-10000))
Nu_M15 = 2 / (2/Nu_fd + A1_M15*exp(-2*b1_M15*X_M15) + A2_M15*exp(-
    2*b2_M15*X_M15) + A3_M15*exp(-2*b3_M15*X_M15) )
    h_M15 = Nu_M15 * k_M15/d_test
```

```
Re_M15 = (Velocity_M15*d_test*Rho_M15/Mu_M15)
Mu_M15=VISCOSITY(AirH2O,T=T_M15,P=(p_2-(p_2-
p_3)*30.1/41.4),R=RH_M15)
Rho_M15=DENSITY(AirH2O,T=T_M15,P=(p_2-(p_2-
p_3)*30.1/41.4),R=RH_M15)
Velocity_M15 = m_dot_humidair_total/(Rho_M15*A_cross_test)
Pr_M15=PRANDTL(Air_ha,T=T_M15,P=(p_2-(p_2-p_3)*30.1/41.4))
k_M15=CONDUCTIVITY(AirH2O,T=T_M15,P=(p_2-(p_2-
p_3)*30.1/41.4),R=RH_M15)

X_M16 = 32.4/(d_in_test * Re_M16 * Pr_M16)
b1_M16 = b1_10 + (b1_50 - b1_10)*((Re_M16-10000)/(50000-10000));
b2_M16 = b2_10 + (b2_50 - b2_10)*((Re_M16-10000)/(50000-10000))
b3_M16 = b3_10 + (b3_50 - b3_10)*((Re_M16-10000)/(50000-10000));
A1_M16 = A1_10 + (A1_50 - A1_10)*((Re_M16-10000)/(50000-10000))
A2_M16 = A2_10 + (A2_50 - A2_10)*((Re_M16-10000)/(50000-10000));
A3_M16 = A3_10 + (A3_50 - A3_10)*((Re_M16-10000)/(50000-10000))
Nu_M16 = 2 / (2/Nu_fd + A1_M16*exp(-2*b1_M16*X_M16) + A2_M16*exp(-
2*b2_M16*X_M16) + A3_M16*exp(-2*b3_M16*X_M16) )
h_M16 = Nu_M16 * k_M16/d_test
Re_M16 = (Velocity_M16*d_test*Rho_M16/Mu_M16)
Mu_M16=VISCOSITY(AirH2O,T=T_M16,P=(p_2-(p_2-
p_3)*32.4/41.4),R=RH_M16)
Rho_M16=DENSITY(AirH2O,T=T_M16,P=(p_2-(p_2-p_3)*32.4/41.4),R=RH_M16)
Velocity_M16 = m_dot_humidair_total/(Rho_M16*A_cross_test)
Pr_M16=PRANDTL(Air_ha,T=T_M16,P=(p_2-(p_2-p_3)*32.4/41.4))
k_M16=CONDUCTIVITY(AirH2O,T=T_M16,P=(p_2-(p_2-
p_3)*32.4/41.4),R=RH_M16)

X_M17 = 34.7/(d_in_test * Re_M17 * Pr_M17)
b1_M17 = b1_10 + (b1_50 - b1_10)*((Re_M17-10000)/(50000-10000));
b2_M17 = b2_10 + (b2_50 - b2_10)*((Re_M17-10000)/(50000-10000))
b3_M17 = b3_10 + (b3_50 - b3_10)*((Re_M17-10000)/(50000-10000));
A1_M17 = A1_10 + (A1_50 - A1_10)*((Re_M17-10000)/(50000-10000))
A2_M17 = A2_10 + (A2_50 - A2_10)*((Re_M17-10000)/(50000-10000));
A3_M17 = A3_10 + (A3_50 - A3_10)*((Re_M17-10000)/(50000-10000))
Nu_M17 = 2 / (2/Nu_fd + A1_M17*exp(-2*b1_M17*X_M17) + A2_M17*exp(-
2*b2_M17*X_M17) + A3_M17*exp(-2*b3_M17*X_M17) )
h_M17 = Nu_M17 * k_M17/d_test
Re_M17 = (Velocity_M17*d_test*Rho_M17/Mu_M17)
Mu_M17=VISCOSITY(AirH2O,T=T_M17,P=(p_2-(p_2-
p_3)*34.7/41.4),R=RH_M17)
Rho_M17=DENSITY(AirH2O,T=T_M17,P=(p_2-(p_2-
p_3)*34.7/41.4),R=RH_M17)
```

```
    Velocity_M17 = m_dot_humidair_total/(Rho_M17*A_cross_test)
    Pr_M17=PRANDTL(Air_ha,T=T_M17,P=(p_2-(p_2-p_3)*34.7/41.4))
    k_M17=CONDUCTIVITY(AirH2O,T=T_M17,P=(p_2-(p_2-
    p_3)*34.7/41.4),R=RH_M17)

    X_M18 = 37.0/(d_in_test * Re_M18 * Pr_M18)
    b1_M18 = b1_10 + (b1_50 - b1_10)*((Re_M18-10000)/(50000-10000));
    b2_M18 = b2_10 + (b2_50 - b2_10)*((Re_M18-10000)/(50000-10000))
    b3_M18 = b3_10 + (b3_50 - b3_10)*((Re_M18-10000)/(50000-10000));
    A1_M18 = A1_10 + (A1_50 - A1_10)*((Re_M18-10000)/(50000-10000))
    A2_M18 = A2_10 + (A2_50 - A2_10)*((Re_M18-10000)/(50000-10000));
    A3_M18 = A3_10 + (A3_50 - A3_10)*((Re_M18-10000)/(50000-10000))
Nu_M18 = 2 / (2/Nu_fd + A1_M18*exp(-2*b1_M18*X_M18) + A2_M18*exp(-
    2*b2_M18*X_M18) + A3_M18*exp(-2*b3_M18*X_M18) )
    h_M18 = Nu_M18 * k_M18/d_test
    Re_M18 = (Velocity_M18*d_test*Rho_M18/Mu_M18)
    Mu_M18=VISCOSITY(AirH2O,T=T_M18,P=(p_2-(p_2-
    p_3)*37.0/41.4),R=RH_M18)
    Rho_M18=DENSITY(AirH2O,T=T_M18,P=(p_2-(p_2-
    p_3)*37.0/41.4),R=RH_M18)
    Velocity_M18 = m_dot_humidair_total/(Rho_M18*A_cross_test)
    Pr_M18=PRANDTL(Air_ha,T=T_M18,P=(p_2-(p_2-p_3)*37.0/41.4))
    k_M18=CONDUCTIVITY(AirH2O,T=T_M18,P=(p_2-(p_2-
    p_3)*37.0/41.4),R=RH_M18)

    X_M19 = 39.3/(d_in_test * Re_M19 * Pr_M19)
    b1_M19 = b1_10 + (b1_50 - b1_10)*((Re_M19-10000)/(50000-10000));
    b2_M19 = b2_10 + (b2_50 - b2_10)*((Re_M19-10000)/(50000-10000))
    b3_M19 = b3_10 + (b3_50 - b3_10)*((Re_M19-10000)/(50000-10000));
    A1_M19 = A1_10 + (A1_50 - A1_10)*((Re_M19-10000)/(50000-10000))
    A2_M19 = A2_10 + (A2_50 - A2_10)*((Re_M19-10000)/(50000-10000));
    A3_M19 = A3_10 + (A3_50 - A3_10)*((Re_M19-10000)/(50000-10000))
Nu_M19 = 2 / (2/Nu_fd + A1_M19*exp(-2*b1_M19*X_M19) + A2_M19*exp(-
    2*b2_M19*X_M19) + A3_M19*exp(-2*b3_M19*X_M19) )
    h_M19 = Nu_M19 * k_M19/d_test
    Re_M19 = (Velocity_M19*d_test*Rho_M19/Mu_M19)
    Mu_M19=VISCOSITY(AirH2O,T=T_M19,P=(p_2-(p_2-
    p_3)*39.3/41.4),R=RH_M19)
    Rho_M19=DENSITY(AirH2O,T=T_M19,P=(p_2-(p_2-
    p_3)*39.3/41.4),R=RH_M19)
    Velocity_M19 = m_dot_humidair_total/(Rho_M19*A_cross_test)
    Pr_M19=PRANDTL(Air_ha,T=T_M19,P=(p_2-(p_2-p_3)*39.3/41.4))
    k_M19=CONDUCTIVITY(AirH2O,T=T_M19,P=(p_2-(p_2-
    p_3)*39.3/41.4),R=RH_M19)
```

A.5 Heat Flux Measurement Accuracy Check Code

This version of the processing code is used to check the accuracy of the power and the heat flux measurements. It is essentially the same as the main mist cooling processing code (see section A.2), except for the control volume energy balance calculations. Instead of calculating the total heating power by multiplying the effective current and voltage drop along the test section length, the local heating rate (power input per unit length) is calculated by multiplying the square of the effective current by the appropriate test section resistance evaluated at the local wall temperature. In the first method which is used in the main mist cooling processing code the average heat flux is calculated while in the second method the local heat flux is calculated. Only the parts of this code that are different from the main mist cooling processing code are shown below.

```
{!  The Power Measurement accuracy Check Code  }
"  ************************************************************** "
"! INPUT - Experimental Data"

p_dif_orf = 2.651556496 *convert(psi,Pa) "[Pa]"       "Differential pressure at orifice"
p_orf1=  4.344633926 *convert(psi,Pa) + p_amb  "[Pa]"  "!abs. pres. in front of Orifice"
p_1=  1.967462286 *convert(psi,Pa) + p_amb     "[Pa]"  "!abs. pressure at Inst. block 1"
p_2=   0.123710186 *convert(psi,Pa) + p_amb     "[Pa]"  "! abs. pressure at Inst. block 2"
p_3=   0.092262074 *convert(psi,Pa) + p_amb   "[Pa]"    "!abs. pressure at Inst. block 3"
p_vnt1=  41.56299414  *convert(psi,Pa) + p_amb  "[Pa]"  "!abs. pres. in front of Venturi"
p_dif_vnt= 0.170  *convert(inH2O,Pa)     "[Pa]"       "Differential pressure at Venturi"
p_amb=  14.6    *convert(psi,Pa)      "[Pa]"  "Ambient pressure"

T_1=          17.89     "[°C]"  "Mist center-line temperature at the Instrument Block 1"
T_2WB =   13.13      "[°C]"  "Mist center-line temperature at the Instrument Block 2"
T_orf=    17.26         "[°C]"  "Air temp. after the orifice, also the same as before orifice"
 T_vnt=   21.88       "[°C]"  "Air temp. after the Venturi, also the same as before Venturi"
T_surface_room = 2.69     "[C]" "Surface Temperature - Room Temperature"
      T_2WB = WETBULB(AirH2O,T=T_2,P=p_2,R=RH_2) "[°C]" "this gives the Bulk"

RH_1 = 35.6/100     "! [fraction]" "relative humidity at Inst. Block 1"
RH_2 = 97.2  /100      "! [fraction]" "relative humidity at Inst. Block 2"
RH_vnt1=  9.8 /100     "relative humidity after the Venturi"
```

```
RH_3 = 100 /100      "! [fraction]" "relative humidity at Inst. Block 3"
RH_test = 100 /100    "! [fraction]"

Electrical_Power = 1150.29    "[W]"  "not the same as heating power"
Current = 263.0   "[A]"  "! Effective current measured using the 4-wire method"
RM= 4.09     "! Water Rotameter reading, steel ball (heavy ball)"

Tw_M1 = 26 "[°C]" "the average inside surface wall temperature at the location M1"
Tw_M2 = 33 "[°C]" "the average inside surface wall temperature at the location M2"
Tw_M3 = 37 "[°C]" "the average inside surface wall temperature at the location M3"
Tw_M4 = 42 "[°C]" "the average inside surface wall temperature at the location M4"
Tw_M5 = 46 "[°C]" "the average inside surface wall temperature at the location M5"
Tw_M6 = 47 "[°C]" "the average inside surface wall temperature at the location M6"
Tw_M7 = 49 "[°C]" "the average inside surface wall temperature at the location M7"
Tw_M8 = 51 "[°C]" "the average inside surface wall temperature at the location M8"
Tw_M9 = 53 "[°C]" "the average inside surface wall temperature at the location M9"
Tw_M10 = 55 "[°C]" "the average inside surface wall temperature at the location M10"
Tw_M11 = 60 "[°C]" "the average inside surface wall temperature at the location M11"
Tw_M12 = 65 "[°C]" "the average inside surface wall temperature at the location M12"
Tw_M13 = 70 "[°C]" "the average inside surface wall temperature at the location M13"
Tw_M14 = 74 "[°C]" "the average inside surface wall temperature at the location M14"
Tw_M15 = 80 "[°C]" "the average inside surface wall temperature at the location M15"
Tw_M16 = 83 "[°C]" "the average inside surface wall temperature at the location M16"
Tw_M17 = 85 "[°C]" "the average inside surface wall temperature at the location M17"
Tw_M18 = 86 "[°C]" "the average inside surface wall temperature at the location M18"
Tw_M19 = 88 "[°C]" "the average inside surface wall temperature at the location M19"
Tw_M20 = 82 "[°C]" "the average inside surface wall temperature at the location M20"

RH_M1=RH_test; RH_M2=RH_test; RH_M3=RH_test ; RH_M4=RH_test ;
RH_M5=RH_test ; RH_M6= RH_test; RH_M7=RH_test ; RH_M8= RH_test;
RH_M9=RH_test ; RH_M10=RH_test; RH_M11=RH_test ; RH_M12=RH_test ;
RH_M13=RH_test ; RH_M14=RH_test ; RH_M15=RH_test ; RH_M16=RH_test ;
RH_M17=RH_test ; RH_M18=RH_test ; RH_M19=RH_test; RH_M20= RH_test

"  ********************************************************************** "
"! CALCULATIONS"

"! Control volume ENERGY balance"
Power = Electrical_Power -
h_natural_convection*(T_surface_room)*Insulation_perimeter*L -
0.002*Electrical_Power  "[W]"  "True Heating Power"
PW = Power /1000    "[kW]"
PP = (p_2-p_3)  "had to be done to make energy equation work, otherwise too long
equations"
```

" Calcutaling alfa - Temperature Coeficient of Resistivity "
T1200 = CONVERTTEMP('F', 'C', 1200)
T68 = CONVERTTEMP('F', 'C', 68)
116 = 74*(1+alfa*(T1200-T68)) "[1/C]"

zL1=0.5/41.4
sec1= 0.5 "[in]"
Resistivity1 = 74 * (1 + alfa * (Tw_M1 - T68)) "[microhm-cm]"
Resistance1 = (Resistivity1 * (sec1 * 2.54) / A_cross_metal_tube) / (10^6) "[Ohm]"
PW_sec1 = Resistance1 * Current^2 /1000 "[kW]"
Heat_fl_1 = PW_sec1/ (sec1*convert(in,m) * d_test*pi)
PW1 = PW_sec1
PW1=m_dot_dryair_total*(ENTHALPY(AirH2O,T=T_M1,P=(p_2-(p_2-
p_3)*zL1),R=RH_M1)-
ENTHALPY(AirH2O,T=T_2,P=p_2,R=RH_2))+m_dot_liquid_M1*
ENTHALPY(Water,T=((T_M1+Tw_M1)/2),P=(p_2-(p_2-p_3)*zL1))-
m_dot_liquid_2*ENTHALPY(Water,T=T_2WB,P=p_2)
"from here T_M1 is calculated which is the Bulk Temperature of the Gas/Mist together"

zL2=1.5/41.4
sec2= 1 "[in]"
Resistivity2 = 74 * (1 + alfa * (Tw_M2 - T68)) "[microhm-cm]"
Resistance2 = (Resistivity2 * (sec2 * 2.54) / A_cross_metal_tube) / (10^6) "[Ohm]"
PW_sec2 = Resistance2 * Current^2 /1000 "[kW]"
Heat_fl_2 = PW_sec2/ (sec2*convert(in,m) * d_test*pi)
PW2 = PW1 + PW_sec2
PW2=m_dot_dryair_total*(ENTHALPY(AirH2O,T=T_M2,P=(p_2-(p_2-
p_3)*zL2),R=RH_M2)-
ENTHALPY(AirH2O,T=T_2,P=p_2,R=RH_2))+m_dot_liquid_M2*
ENTHALPY(Water,T=((T_M2+Tw_M2)/2),P=(p_2-(p_2-p_3)*zL2))-
m_dot_liquid_2*ENTHALPY(Water,T=T_2WB,P=p_2)
"from here T_M2 is calculated which is the Bulk Temperature of the Gas/Mist together"

zL3= 2.5/41.4
sec3= 1 "[in]"
Resistivity3 = 74 * (1 + alfa * (Tw_M3 - T68)) "[microhm-cm]"
Resistance3 = (Resistivity3 * (sec3 * 2.54) / A_cross_metal_tube) / (10^6) "[Ohm]"
PW_sec3 = Resistance3 * Current^2 /1000 "[kW]"
Heat_fl_3 = PW_sec3/ (sec3*convert(in,m) * d_test*pi)
PW3 = PW2 + PW_sec3
PW3=m_dot_dryair_total*(ENTHALPY(AirH2O,T=T_M3,P=(p_2-(p_2-
p_3)*zL3),R=RH_M3)-
ENTHALPY(AirH2O,T=T_2,P=p_2,R=RH_2))+m_dot_liquid_M3*
ENTHALPY(Water,T=((T_M3+Tw_M3)/2),P=(p_2-(p_2-p_3)*zL3))-
m_dot_liquid_2*ENTHALPY(Water,T=T_2WB,P=p_2)
"from here T_M3 is calculated which is the Bulk Temperature of the Gas/Mist together"

```
zL4= 4.8/41.4
sec4= 2.3   "[in]"
Resistivity4 = 74 * ( 1 + alfa * ( Tw_M4 - T68) )   "[microhm-cm]"
Resistance4 = ( Resistivity4 * (sec4 * 2.54) / A_cross_metal_tube ) / (10^6)   "[Ohm]"
PW_sec4 = Resistance4 * Current^2 /1000    "[kW]"
Heat_fl_4 = PW_sec4/ ( sec4*convert(in,m) * d_test*pi)
PW4 = PW3 + PW_sec4
PW4=m_dot_dryair_total*(ENTHALPY(AirH2O,T=T_M4,P=(p_2-(p_2-
p_3)*zL4),R=RH_M4)-
ENTHALPY(AirH2O,T=T_2,P=p_2,R=RH_2))+m_dot_liquid_M4*
ENTHALPY(Water,T=((T_M4+Tw_M4)/2),P=(p_2-(p_2-p_3)*zL4))-
m_dot_liquid_2*ENTHALPY(Water,T=T_2WB,P=p_2)
"from here T_M4 is calculated which is the Bulk Temperature of the Gas/Mist together"

zL5= 7.1/41.4
sec5= 2.3   "[in]"
Resistivity5 = 74 * ( 1 + alfa * ( Tw_M5 - T68) )   "[microhm-cm]"
Resistance5 = ( Resistivity5 * (sec5 * 2.54) / A_cross_metal_tube ) / (10^6)   "[Ohm]"
PW_sec5 = Resistance5 * Current^2 /1000    "[kW]"
Heat_fl_5 = PW_sec5/ ( sec5*convert(in,m) * d_test*pi)
PW5 = PW4 + PW_sec5
PW5=m_dot_dryair_total*(ENTHALPY(AirH2O,T=T_M5,P=(p_2-(p_2-
p_3)*zL5),R=RH_M5)-
ENTHALPY(AirH2O,T=T_2,P=p_2,R=RH_2))+m_dot_liquid_M5*
ENTHALPY(Water,T=((T_M5+Tw_M5)/2),P=(p_2-(p_2-p_3)*zL5))-
m_dot_liquid_2*ENTHALPY(Water,T=T_2WB,P=p_2)
"from here T_M5 is calculated which is the Bulk Temperature of the Gas/Mist together"

zL6= 9.4/41.4
sec6= 2.3   "[in]"
Resistivity6 = 74 * ( 1 + alfa * ( Tw_M6 - T68) )   "[microhm-cm]"
Resistance6 = ( Resistivity6 * (sec6 * 2.54) / A_cross_metal_tube ) / (10^6)   "[Ohm]"
PW_sec6 = Resistance6 * Current^2 /1000    "[kW]"
Heat_fl_6 = PW_sec6/ ( sec6*convert(in,m) * d_test*pi)
PW6 = PW5 + PW_sec6
PW6=m_dot_dryair_total*(ENTHALPY(AirH2O,T=T_M6,P=(p_2-(p_2-
p_3)*zL6),R=RH_M6)-
ENTHALPY(AirH2O,T=T_2,P=p_2,R=RH_2))+m_dot_liquid_M6*
ENTHALPY(Water,T=((T_M6+Tw_M6)/2),P=(p_2-(p_2-p_3)*zL6))-
m_dot_liquid_2*ENTHALPY(Water,T=T_2WB,P=p_2)
"from here T_M6 is calculated which is the Bulk Temperature of the Gas/Mist together"

zL7= 11.7/41.4
sec7= 2.3   "[in]"
Resistivity7 = 74 * ( 1 + alfa * ( Tw_M7 - T68) )   "[microhm-cm]"
```

```
Resistance7 = ( Resistivity7 * (sec7 * 2.54) / A_cross_metal_tube ) / (10^6)   "[Ohm]"
PW_sec7 = Resistance7 * Current^2 /1000    "[kW]"
Heat_fl_7 = PW_sec7/ ( sec7*convert(in,m) * d_test*pi)
PW7 = PW6 + PW_sec7
PW7=m_dot_dryair_total*(ENTHALPY(AirH2O,T=T_M7,P=(p_2-(p_2-
p_3)*zL7),R=RH_M7)-
ENTHALPY(AirH2O,T=T_2,P=p_2,R=RH_2))+m_dot_liquid_M7*
ENTHALPY(Water,T=((T_M7+Tw_M7)/2),P=(p_2-(p_2-p_3)*zL7))-
m_dot_liquid_2*ENTHALPY(Water,T=T_2WB,P=p_2)
"from here T_M7 is calculated which is the Bulk Temperature of the Gas/Mist together"

zL8= 14.0/41.4
sec8= 2.3   "[in]"
Resistivity8 = 74 * ( 1 + alfa * ( Tw_M8 - T68) )   "[microhm-cm]"
Resistance8 = ( Resistivity8 * (sec8 * 2.54) / A_cross_metal_tube ) / (10^6)   "[Ohm]"
PW_sec8 = Resistance8 * Current^2 /1000    "[kW]"
Heat_fl_8 = PW_sec8/ ( sec8*convert(in,m) * d_test*pi)
PW8 = PW7 + PW_sec8
PW8=m_dot_dryair_total*(ENTHALPY(AirH2O,T=T_M8,P=(p_2-(p_2-
p_3)*zL8),R=RH_M8)-
ENTHALPY(AirH2O,T=T_2,P=p_2,R=RH_2))+m_dot_liquid_M8*
ENTHALPY(Water,T=((T_M8+Tw_M8)/2),P=(p_2-(p_2-p_3)*zL8))-
m_dot_liquid_2*ENTHALPY(Water,T=T_2WB,P=p_2)
"from here T_M8 is calculated which is the Bulk Temperature of the Gas/Mist together"

zL9= 16.3/41.4
sec9= 2.3   "[in]"
Resistivity9 = 74 * ( 1 + alfa * ( Tw_M9 - T68) )   "[microhm-cm]"
Resistance9 = ( Resistivity9 * (sec9 * 2.54) / A_cross_metal_tube ) / (10^6)   "[Ohm]"
PW_sec9 = Resistance9 * Current^2 /1000    "[kW]"
Heat_fl_9 = PW_sec9/ ( sec9*convert(in,m) * d_test*pi)
PW9 = PW8 + PW_sec9
PW9=m_dot_dryair_total*(ENTHALPY(AirH2O,T=T_M9,P=(p_2-(p_2-
p_3)*zL9),R=RH_M9)-
ENTHALPY(AirH2O,T=T_2,P=p_2,R=RH_2))+m_dot_liquid_M9*
ENTHALPY(Water,T=((T_M9+Tw_M9)/2),P=(p_2-(p_2-p_3)*zL9))-
m_dot_liquid_2*ENTHALPY(Water,T=T_2WB,P=p_2)
"from here T_M9 is calculated which is the Bulk Temperature of the Gas/Mist together"

zL10= 18.6/41.4
sec10= 2.3   "[in]"
Resistivity10 = 74 * ( 1 + alfa * ( Tw_M10 - T68) )   "[microhm-cm]"
Resistance10 = ( Resistivity10 * (sec10 * 2.54) / A_cross_metal_tube ) / (10^6)
"[Ohm]"
PW_sec10 = Resistance10 * Current^2 /1000    "[kW]"
Heat_fl_10 = PW_sec10/ ( sec10*convert(in,m) * d_test*pi)
```

```
PW10 = PW9 + PW_sec10
PW10=m_dot_dryair_total*(ENTHALPY(AirH2O,T=T_M10,P=(p_2-
PP*zL10),R=RH_M10)-
ENTHALPY(AirH2O,T=T_2,P=p_2,R=RH_2))+m_dot_liquid_M10*
ENTHALPY(Water,T=((T_M10+Tw_M10)/2),P=(p_2-PP*zL10))-
m_dot_liquid_2*ENTHALPY(Water,T=T_2WB,P=p_2)
"from here T_M10 is calculated which is the Bulk Temperature of the Gas/Mist together"

zL11= 20.9/41.4
sec11= 2.3   "[in]"
Resistivity11 = 74 * ( 1 + alfa * ( Tw_M11 - T68) )   "[microhm-cm]"
Resistance11 = ( Resistivity11 * (sec11 * 2.54) / A_cross_metal_tube ) / (10^6)
"[Ohm]"
PW_sec11 = Resistance11 * Current^2 /1000    "[kW]"
Heat_fl_11 = PW_sec11/ ( sec11*convert(in,m) * d_test*pi)
PW11 = PW10 + PW_sec11
PW11=m_dot_dryair_total*(ENTHALPY(AirH2O,T=T_M11,P=(p_2-
PP*zL11),R=RH_M11)-
ENTHALPY(AirH2O,T=T_2,P=p_2,R=RH_2))+m_dot_liquid_M11*
ENTHALPY(Water,T=((T_M11+Tw_M11)/2),P=(p_2-PP*zL11))-
m_dot_liquid_2*ENTHALPY(Water,T=T_2WB,P=p_2)
"from here T_M11 is calculated which is the Bulk Temperature of the Gas/Mist together"

zL12= 23.2/41.4
sec12= 2.3   "[in]"
Resistivity12 = 74 * ( 1 + alfa * ( Tw_M12 - T68) )   "[microhm-cm]"
Resistance12 = ( Resistivity12 * (sec12 * 2.54) / A_cross_metal_tube ) / (10^6)
"[Ohm]"
PW_sec12 = Resistance12 * Current^2 /1000    "[kW]"
Heat_fl_12 = PW_sec12/ ( sec12*convert(in,m) * d_test*pi)
PW12 = PW11 + PW_sec12
PW12=m_dot_dryair_total*(ENTHALPY(AirH2O,T=T_M12,P=(p_2-
PP*zL12),R=RH_M12)-
ENTHALPY(AirH2O,T=T_2,P=p_2,R=RH_2))+m_dot_liquid_M12*
ENTHALPY(Water,T=((T_M12+Tw_M12)/2),P=(p_2-PP*zL12))-
m_dot_liquid_2*ENTHALPY(Water,T=T_2WB,P=p_2)
"from here T_M12 is calculated which is the Bulk Temperature of the Gas/Mist together"

zL13= 25.5/41.4
sec13= 2.3   "[in]"
Resistivity13 = 74 * ( 1 + alfa * ( Tw_M13 - T68) )   "[microhm-cm]"
Resistance13 = ( Resistivity13 * (sec13 * 2.54) / A_cross_metal_tube ) / (10^6)
"[Ohm]"
PW_sec13 = Resistance13 * Current^2 /1000    "[kW]"
Heat_fl_13 = PW_sec13/ ( sec13*convert(in,m) * d_test*pi)
PW13 = PW12 + PW_sec13
```

PW13=m_dot_dryair_total*(ENTHALPY(AirH2O,T=T_M13,P=(p_2-PP*zL13),R=RH_M13)-ENTHALPY(AirH2O,T=T_2,P=p_2,R=RH_2))+m_dot_liquid_M13*ENTHALPY(Water,T=((T_M13+Tw_M13)/2),P=(p_2-PP*zL13))-m_dot_liquid_2*ENTHALPY(Water,T=T_2WB,P=p_2)
"from here T_M13 is calculated which is the Bulk Temperature of the Gas/Mist together"

zL14= 27.8/41.4
sec14= 2.3 "[in]"
Resistivity14 = 74 * (1 + alfa * (Tw_M14 - T68)) "[microhm-cm]"
Resistance14 = (Resistivity14 * (sec14 * 2.54) / A_cross_metal_tube) / (10^6) "[Ohm]"
PW_sec14 = Resistance14 * Current^2 /1000 "[kW]"
Heat_fl_14 = PW_sec14/ (sec14*convert(in,m) * d_test*pi)
PW14 = PW13 + PW_sec14
PW14=m_dot_dryair_total*(ENTHALPY(AirH2O,T=T_M14,P=(p_2-PP*zL14),R=RH_M14)-ENTHALPY(AirH2O,T=T_2,P=p_2,R=RH_2))+m_dot_liquid_M14*ENTHALPY(Water,T=((T_M14+Tw_M14)/2),P=(p_2-PP*zL14))-m_dot_liquid_2*ENTHALPY(Water,T=T_2WB,P=p_2)
"from here T_M14 is calculated which is the Bulk Temperature of the Gas/Mist together"

zL15= 30.1/41.4
sec15= 2.3 "[in]"
Resistivity15 = 74 * (1 + alfa * (Tw_M15 - T68)) "[microhm-cm]"
Resistance15 = (Resistivity15 * (sec15 * 2.54) / A_cross_metal_tube) / (10^6) "[Ohm]"
PW_sec15 = Resistance15 * Current^2 /1000 "[kW]"
Heat_fl_15 = PW_sec15/ (sec15*convert(in,m) * d_test*pi)
PW15 = PW14 + PW_sec15
PW15=m_dot_dryair_total*(ENTHALPY(AirH2O,T=T_M15,P=(p_2-PP*zL15),R=RH_M15)-ENTHALPY(AirH2O,T=T_2,P=p_2,R=RH_2))+m_dot_liquid_M15*ENTHALPY(Water,T=((T_M15+Tw_M15)/2),P=(p_2-PP*zL15))-m_dot_liquid_2*ENTHALPY(Water,T=T_2WB,P=p_2)
"from here T_M15 is calculated which is the Bulk Temperature of the Gas/Mist together"

zL16= 32.4/41.4
sec16= 2.3 "[in]"
Resistivity16 = 74 * (1 + alfa * (Tw_M16 - T68)) "[microhm-cm]"
Resistance16 = (Resistivity16 * (sec16 * 2.54) / A_cross_metal_tube) / (10^6) "[Ohm]"
PW_sec16 = Resistance16 * Current^2 /1000 "[kW]"
Heat_fl_16 = PW_sec16/ (sec16*convert(in,m) * d_test*pi)
PW16 = PW15 + PW_sec16

```
PW16=m_dot_dryair_total*(ENTHALPY(AirH2O,T=T_M16,P=(p_2-
PP*zL16),R=RH_M16)-
ENTHALPY(AirH2O,T=T_2,P=p_2,R=RH_2))+m_dot_liquid_M16*
ENTHALPY(Water,T=((T_M16+Tw_M16)/2),P=(p_2-PP*zL16))-
m_dot_liquid_2*ENTHALPY(Water,T=T_2WB,P=p_2)
"from here T_M16 is calculated which is the Bulk Temperature of the Gas/Mist together"

zL17= 34.7/41.4
sec17= 2.3   "[in]"
Resistivity17 = 74 * ( 1 + alfa * ( Tw_M17 - T68) )   "[microhm-cm]"
Resistance17 = ( Resistivity17 * (sec17 * 2.54) / A_cross_metal_tube ) / (10^6)
"[Ohm]"
PW_sec17 = Resistance17 * Current^2 /1000    "[kW]"
Heat_fl_17 = PW_sec17/ ( sec17*convert(in,m) * d_test*pi)
PW17 = PW16 + PW_sec17
PW17=m_dot_dryair_total*(ENTHALPY(AirH2O,T=T_M17,P=(p_2-
PP*zL17),R=RH_M17)-
ENTHALPY(AirH2O,T=T_2,P=p_2,R=RH_2))+m_dot_liquid_M17*
ENTHALPY(Water,T=((T_M17+Tw_M17)/2),P=(p_2-PP*zL17))-
m_dot_liquid_2*ENTHALPY(Water,T=T_2WB,P=p_2)
"from here T_M17 is calculated which is the Bulk Temperature of the Gas/Mist together"

zL18= 37.0/41.4
sec18= 2.3   "[in]"
Resistivity18 = 74 * ( 1 + alfa * ( Tw_M18 - T68) )   "[microhm-cm]"
Resistance18 = ( Resistivity18 * (sec18 * 2.54) / A_cross_metal_tube ) / (10^6)
"[Ohm]"
PW_sec18 = Resistance18 * Current^2 /1000    "[kW]"
Heat_fl_18 = PW_sec18/ ( sec18*convert(in,m) * d_test*pi)
PW18 = PW17 + PW_sec18
PW18=m_dot_dryair_total*(ENTHALPY(AirH2O,T=T_M18,P=(p_2-
PP*zL18),R=RH_M18)-
ENTHALPY(AirH2O,T=T_2,P=p_2,R=RH_2))+m_dot_liquid_M18*
ENTHALPY(Water,T=((T_M18+Tw_M18)/2),P=(p_2-PP*zL18))-
m_dot_liquid_2*ENTHALPY(Water,T=T_2WB,P=p_2)
"from here T_M18 is calculated which is the Bulk Temperature of the Gas/Mist together"

zL19=39.3/41.4
sec19= 2.3   "[in]"
Resistivity19 = 74 * ( 1 + alfa * ( Tw_M19 - T68) )   "[microhm-cm]"
Resistance19 = ( Resistivity19 * (sec19 * 2.54) / A_cross_metal_tube ) / (10^6)
"[Ohm]"
PW_sec19 = Resistance19 * Current^2 /1000    "[kW]"
Heat_fl_19 = PW_sec19/ ( sec19*convert(in,m) * d_test*pi)
PW19 = PW18 + PW_sec19
```

```
PW19=m_dot_dryair_total*(ENTHALPY(AirH2O,T=T_M19,P=(p_2-
PP*zL19),R=RH_M19)-
ENTHALPY(AirH2O,T=T_2,P=p_2,R=RH_2))+m_dot_liquid_M19*
ENTHALPY(Water,T=((T_M19+Tw_M19)/2),P=(p_2-PP*zL19))-
m_dot_liquid_2*ENTHALPY(Water,T=T_2WB,P=p_2)
"from here T_M19 is calculated which is the Bulk Temperature of the Gas/Mist together"

zL20=40.5/41.4
sec20= 1.2   "[in]"
Resistivity20 = 74 * ( 1 + alfa * ( Tw_M20 - T68) )   "[microhm-cm]"
Resistance20 = ( Resistivity20 * (sec20 * 2.54) / A_cross_metal_tube ) / (10^6)
"[Ohm]"
PW_sec20 = Resistance20 * Current^2 /1000    "[kW]"
Heat_fl_20 = PW_sec20/ ( sec20*convert(in,m) * d_test*pi)
PW20 = PW19 + PW_sec20
PW20=m_dot_dryair_total*(ENTHALPY(AirH2O,T=T_M20,P=(p_2-(p_2-
p_3)*zL20),R=RH_M20)-
ENTHALPY(AirH2O,T=T_2,P=p_2,R=RH_2))+m_dot_liquid_M20*
ENTHALPY(Water, T=((T_M20+Tw_M20)/2),P=(p_2-(p_2-p_3)*zL20))-
m_dot_liquid_2*ENTHALPY(Water,T=T_2WB,P=p_2)
"from here T_M20 is calculated which is the Bulk Temperature of the Gas/Mist together"

zL21=41.4/41.4
sec21= 0.9  "[in]"
Resistivity21 = 74 * ( 1 + alfa * ( Tw_M21 - T68) )   "[microhm-cm]"
Resistance21 = ( Resistivity21 * (sec21 * 2.54) / A_cross_metal_tube ) / (10^6)
"[Ohm]"
PW_sec21 = Resistance21 * Current^2 /1000    "[kW]"
Heat_fl_21 = PW_sec21/ ( sec21*convert(in,m) * d_test*pi)
PW21 = PW20 + PW_sec21

PW20_IU = PW*(zL20)   "[kW]"
PW20_RI2 = PW20   "[kW]"
```

APPENDIX B

EXPERIMENTAL DATA

In this appendix, the experimental data obtained in this investigation are listed. Because of the large number of experiments conducted, only experiments discussed in the body of the thesis will be tabulated. Each experiment will be identified by a unique number which indicates the test conditions at which it was conducted. The identification number takes the form:

$$\alpha - \beta - \gamma\gamma - \delta\delta - \varepsilon - \sigma\sigma\sigma - xx - yyy - zz.zz - aa.a - bbb$$

Here:

α can be either "A" for air/water experiments or "H" for helium/water experiments

β can be either "D" for downward flow or "U" for upward flow

$\gamma\gamma$ can be "GA" for gas-assisted nozzle, "US" for ultrasonic nozzle, "FG" for fixed geometry hydraulic nozzle, or "NA" (not available) for single-phase experiments

$\delta\delta$ can be either "P1", "P2", or "P3" for the first, second, and third cylindrical test section, and "D1", or "D2" for the first and second rectangular test section, respectively

ε can be either "S" for the short unheated entry length or "L" for the long unheated entry length

$\sigma\sigma\sigma$ can be either "PVC", "GLS", or "ACR" for the unheated PVC, glass, or acrylic visualization tubes, respectively or "NON" for the second rectangular test section.

xx represents the average gas inlet velocity in m/s (e.g. 05, 10, 15, etc.)

yyy represents the injected water mass fraction in percent (e.g. 000, 005, 010, etc.)

zz.zz represents the wall heat flux in kW/m^2

aa.a represents the inlet relative humidity measured at the inlet instrument block

bbb represents the inlet wet bulb temperature for gas/liquid mist flow or the inlet gas temperature for single-phase flow measured at the inlet instrument block

Unless otherwise specified, the gas and water inlet temperatures are equal to the ambient temperature. Any other important information not identified by the unique number is also additionally specified. The experimental data obtained in this investigation are listed first for the second and third cylindrical test section, followed by the second rectangular test section, respectively. For each test section the data are listed in the order in which they are presented in this thesis. Experiments that are repeated in several figures may not be tabulated each time they are graphed. Single-phase convection results are additionally tabulated at the beginning of each test channel section in order be easily found if the enhancement ratio is to be calculated. All of the locally measured wall temperatures are shown.

Table B.1 Experimental Data A-D-NA-P2-S-ACR-15-000-03.18-20.0-003

z/d	Twall [°C]		Tbulk [°C]	h [W/m^{2}K]	z/d	Twall [°C]		Tbulk [°C]	h [W/m^{2}K]
2.9	54.5	54.4	22.10	98.2	26.5	81.5	81.3	38.85	74.7
5.9	61.9	62.2	24.20	84.0	29.4	83.5	83.3	40.94	74.9
8.8	66.5	66.4	26.29	79.2	32.4	85.6	84.9	43.03	75.3
11.8	69.8	69.7	28.38	76.8	35.3	87.4	87.0	45.13	75.5
14.7	72.4	72.4	30.48	75.8	38.2	89.2	88.5	47.22	76.3
17.6	74.9	74.8	32.57	75.2	41.2	90.3	90.6	49.31	77.3
20.6	77.4	77.1	34.66	74.7	44.1	92.5	92.5	51.40	77.3
23.5	79.3	79.4	36.75	74.6	47.1	94.4	94.5	53.50	77.6

Table B.2 Experimental Data A-D-NA-P2-S-ACR-10-000-02.21-20.5-003

z/d	Twall [°C]		Tbulk [°C]	h [W/m^{2}K]	z/d	Twall [°C]		Tbulk [°C]	h [W/m^{2}K]
2.9	53.1	53.0	23.14	73.92	26.5	81.5	81.3	40.69	54.26
5.9	61.2	61.4	25.34	61.43	29.4	83.5	83.4	42.89	54.48
8.8	66.2	66.0	27.53	57.24	32.4	85.7	85.0	45.08	54.91
11.8	69.7	69.6	29.73	55.35	35.3	87.5	87.1	47.27	55.13
14.7	72.4	72.3	31.92	54.63	38.2	89.4	88.7	49.47	55.82
17.6	74.9	74.7	34.11	54.27	41.2	90.5	90.8	51.66	56.64
20.6	77.3	77.0	36.31	54.04	44.1	92.8	92.8	53.85	56.74
23.5	79.2	79.4	38.50	54.12	47.1	94.6	94.7	56.05	57.28

Table B.3 Experimental Data A-D-NA-P2-S-ACR-06-000-01.44-20.6-004

z/d	Twall [°C]		Tbulk [°C]	h [W/m^{2}K]	z/d	Twall [°C]		Tbulk [°C]	h [W/m^{2}K]
2.9	52.0	51.4	23.05	50.22	26.5	81.5	81.4	42.42	36.86
5.9	60.5	60.4	25.47	41.11	29.4	83.5	83.5	44.84	37.26
8.8	65.6	65.4	27.89	38.26	32.4	85.6	85.0	47.26	37.81
11.8	69.3	69.1	30.32	37.02	35.3	87.5	87.2	49.69	38.17
14.7	72.1	72.1	32.74	36.55	38.2	89.4	88.8	52.11	38.89
17.6	74.7	74.7	35.16	36.38	41.2	90.6	91.0	54.53	39.71
20.6	77.3	77.1	37.58	36.33	44.1	92.9	92.9	56.95	40.04
23.5	79.2	79.5	40.00	36.55	47.1	94.3	94.4	59.37	41.11

Table B.4 Experimental Data H-D-NA-P2-S-ACR-30-000-05.50-21.6-000

z/d	Twall [°C]		Tbulk [°C]	h [W/m^{2}K]	z/d	Twall [°C]		Tbulk [°C]	h [W/m^{2}K]
2.9	49.5	49.5	24.19	216.91	26.5	79.8	79.7	44.87	157.38
5.9	57.2	57.3	26.77	180.06	29.4	82.0	81.9	47.45	159.38
8.8	62.5	62.3	29.36	166.22	32.4	84.4	83.6	50.04	161.94
11.8	66.3	66.3	31.94	159.86	35.3	86.6	86.1	52.62	163.04
14.7	69.4	69.4	34.53	157.57	38.2	88.7	88.0	55.21	165.95
17.6	72.3	72.3	37.11	156.30	41.2	90.1	90.6	57.79	168.78
20.6	75.2	74.8	39.7	155.59	44.1	92.9	93.0	60.38	168.70
23.5	77.2	77.6	42.28	156.40	47.1	95.3	95.5	62.96	169.64

Table B.5 Experimental Data A-D-GA-P2-S-ACR-15-015-06.79-15.5-097 Troom = 25 °C

z/d	Twall [°C]		Tbulk [°C]	h [W/m²K]	z/d	Twall [°C]		Tbulk [°C]	h [W/m²K]
2.9	23.5	25.2	16.05	816.59	26.5	38.7	39.5	24.82	474.13
5.9	27.6	28.9	17.2	613.92	29.4	39.6	40.5	25.79	475.52
8.8	30.4	31.4	18.21	535.40	32.4	40.5	41.0	26.73	485.68
11.8	32.7	33.5	19.44	495.69	35.3	41.2	41.9	27.63	488.41
14.7	34.4	35.2	20.54	476.94	38.2	41.8	42.4	28.56	500.71
17.6	35.8	36.5	21.68	469.72	41.2	42.3	43.2	29.4	508.50
20.6	37.1	37.8	22.7	460.06	44.1	43.0	44.0	30.21	512.44
23.5	38.0	38.8	23.75	463.26	47.1	43.6	45.1	31	507.68

Table B.6 Experimental Data A-D-GA-P2-S-ACR-15-015-06.84-13.7-081 Troom = 20 °C

z/d	Twall [°C]		Tbulk [°C]	h [W/m²K]	z/d	Twall [°C]		Tbulk [°C]	h [W/m²K]
2.9	22.9	22.8	14.3	794.8	26.5	38.5	38.9	23.4	446.8
5.9	28.1	26.9	15.3	560.0	29.4	39.4	40.4	24.5	443.5
8.8	30.9	30.0	16.5	490.4	32.4	40.1	41.3	25.4	448.5
11.8	33.0	32.4	17.7	456.7	35.3	40.9	42.2	26.4	450.9
14.7	34.3	34.3	18.9	443.7	38.2	41.6	43.3	27.3	451.8
17.6	35.7	35.7	20.1	437.7	41.2	42.2	44.1	28.3	459.9
20.6	37.0	37.2	21.2	431.6	44.1	42.8	46.5	29.1	439.7
23.5	37.9	38.3	22.4	435.0	47.1	43.8	48.2	29.9	424.8

Table B.7 Experimental Data A-U-GA-P2-S-ACR-15-015-15.57-13.6-100

z/d	Twall [°C]		Tbulk [°C]	h [W/m²K]	z/d	Twall [°C]		Tbulk [°C]	h [W/m²K]
2.9	30.7	33.3	15.24	907.43	26.5	53.0	53.1	33.07	763.12
5.9	38.9	41.0	17.77	688.78	29.4	53.7	53.9	34.74	800.47
8.8	43.8	45.3	20.34	632.02	32.4	54.8	54.8	36.25	822.67
11.8	46.8	47.8	22.84	625.83	35.3	55.9	55.8	37.68	837.82
14.7	48.6	49.3	25.25	645.85	38.2	61.2	58.2	38.94	735.07
17.6	50.1	50.5	27.41	667.98	41.2	65.1	70.3	40.03	554.40
20.6	51.3	51.4	29.44	698.68	44.1	66.9	87.1	41.06	428.20
23.5	52.0	52.4	31.33	731.65	47.1	66.8	98.6	42.12	379.87

Table B.8 Experimental Data A-U-GA-P2-S-ACR-15-015-14.30-13.5-100

z/d	Twall [°C]		Tbulk [°C]	h [W/m²K]	z/d	Twall [°C]		Tbulk [°C]	h [W/m²K]
2.9	30.0	31.6	14.96	901.11	26.5	51.3	51.2	31.79	735.32
5.9	37.9	39.0	17.25	673.92	29.4	52.0	51.8	33.4	774.06
8.8	42.6	43.2	19.7	616.67	32.4	52.9	52.3	34.87	805.39
11.8	45.4	45.8	22.03	607.03	35.3	53.8	53.3	36.25	827.92
14.7	47.1	47.3	24.25	623.61	38.2	54.4	53.8	37.59	865.79
17.6	48.5	48.5	26.35	644.85	41.2	54.6	54.8	38.82	902.14
20.6	49.6	49.4	28.3	674.61	44.1	55.5	55.4	39.99	924.16
23.5	50.3	50.4	30.11	705.65	47.1	56.1	56.1	41.1	952.63

Table B.9 Experimental Data A-U-GA-P2-S-ACR-15-015-09.95-13.4-100

z/d	Twall [°C]		Tbulk [°C]	h [W/m^{2}K]	z/d	Twall [°C]		Tbulk [°C]	h [W/m^{2}K]
2.9	25.3	26.6	14.43	861.74	26.5	43.7	43.6	27.13	601.14
5.9	31.7	32.4	16.02	621.48	29.4	44.3	44.2	28.44	628.35
8.8	35.7	36.0	17.71	549.83	32.4	45.2	44.8	29.73	650.23
11.8	38.2	38.4	19.39	526.99	35.3	46.1	45.7	30.91	663.93
14.7	39.7	39.9	21.12	532.44	38.2	46.8	46.3	32.03	685.42
17.6	41.0	41.1	22.76	543.28	41.2	47.1	47.3	33.15	710.20
20.6	42.2	42.0	24.3	560.41	44.1	47.9	47.9	34.17	724.75
23.5	42.8	42.9	25.75	581.58	47.1	48.5	48.5	35.16	744.41

Table B.10 Experimental Data A-U-GA-P2-S-ACR-15-015-06.84-13.5-100

z/d	Twall [°C]		Tbulk [°C]	h [W/m^{2}K]	z/d	Twall [°C]		Tbulk [°C]	h [W/m^{2}K]
2.9	22.1	23.0	14.15	815.71	26.5	36.8	36.7	23.41	513.61
5.9	26.7	27.2	15.27	586.08	29.4	37.2	37.1	24.49	538.70
8.8	29.7	30.0	16.44	510.49	32.4	38.1	37.7	25.47	548.65
11.8	31.8	32.0	17.65	478.53	35.3	38.9	38.6	26.41	555.84
14.7	33.2	33.3	18.9	476.61	38.2	39.5	39.1	27.32	570.21
17.6	34.4	34.4	20.02	476.02	41.2	39.8	40.0	28.25	585.95
20.6	35.3	35.1	21.25	489.15	44.1	40.6	40.5	29.1	596.68
23.5	35.9	36.0	22.35	501.39	47.1	41.1	41.1	29.97	612.66

Table B.11 Experimental Data A-U-FG-P2-S-ACR-15-015-12.39-13.1-100

z/d	Twall [°C]		Tbulk [°C]	h [W/m^{2}K]	z/d	Twall [°C]		Tbulk [°C]	h [W/m^{2}K]
2.9	26.5	33.7	14.25	782.90	26.5	49.4	62.8	29.26	461.92
5.9	33.1	49.2	15.91	491.80	29.4	50.6	61.2	30.82	494.31
8.8	37.6	54.2	18.01	443.70	32.4	52.9	64.5	32.15	466.30
11.8	40.8	56.3	20.13	435.85	35.3	57.0	67.7	33.38	428.20
14.7	43.2	59.4	22.11	424.91	38.2	61.5	67.5	34.63	415.28
17.6	45.1	61.6	24.02	423.22	41.2	65.2	69.1	35.81	396.01
20.6	46.5	60.3	25.93	451.58	44.1	70.0	74.8	36.81	348.18
23.5	47.6	60.1	27.71	474.27	47.1	78.9	73.6	37.84	322.92

Table B.12 Experimental Data A-U-FG-P2-S-ACR-15-015-10.01-13.9-100

z/d	Twall [°C]		Tbulk [°C]	h [W/m^{2}K]	z/d	Twall [°C]		Tbulk [°C]	h [W/m^{2}K]
2.9	25.0	29.7	14.79	798.36	26.5	43.8	44.0	27.51	609.24
5.9	30.3	34.7	16.46	623.28	29.4	44.5	44.7	28.8	633.76
8.8	34.2	37.2	18.21	571.89	32.4	45.6	45.5	30.03	645.64
11.8	37.1	38.8	19.95	556.07	35.3	46.5	46.4	31.2	655.90
14.7	39.0	40.1	21.58	556.66	38.2	47.2	47.0	32.36	679.07
17.6	40.6	41.2	23.19	564.16	41.2	47.6	47.9	33.42	698.80
20.6	41.9	42.2	24.71	577.77	44.1	48.5	48.5	34.44	709.79
23.5	42.7	43.2	26.15	594.84	47.1	49.2	49.2	35.42	726.22

Table B.13 Experimental Data A-U-FG-P2-S-ACR-15-015-06.89-14.1-100

z/d	Twall [°C]		Tbulk [°C]	h [W/m²K]	z/d	Twall [°C]		Tbulk [°C]	h [W/m²K]
2.9	22.0	25.2	14.69	770.10	26.5	36.8	37.0	23.89	529.15
5.9	25.8	29.0	15.79	591.77	29.4	37.4	37.6	24.89	547.45
8.8	28.7	31.1	17.03	535.39	32.4	38.3	38.3	25.86	552.55
11.8	30.9	32.4	18.23	512.05	35.3	39.2	39.2	26.85	557.66
14.7	32.5	33.5	19.46	508.33	38.2	40.0	39.7	27.74	569.44
17.6	33.9	34.5	20.63	508.02	41.2	40.3	40.5	28.61	583.26
20.6	35.0	35.3	21.76	513.38	44.1	41.1	41.1	29.5	593.78
23.5	35.9	36.3	22.85	521.71	47.1	41.7	41.7	30.31	605.05

Table B.14 Experimental Data A-D-GA-P2-S-ACR-15-015-06.83-13.0-100 9 μm droplets

z/d	Twall [°C]		Tbulk [°C]	h [W/m²K]	z/d	Twall [°C]		Tbulk [°C]	h [W/m²K]
2.9	18.5	27.4	13.59	729.92	26.5	35.3	40.0	23.02	467.43
5.9	22.7	31.5	14.74	552.56	29.4	36.1	41.1	24.06	469.41
8.8	26.0	33.8	15.94	489.03	32.4	37.3	42.7	25.07	457.38
11.8	28.8	35.4	17.19	457.23	35.3	38.6	45.1	25.97	429.12
14.7	30.9	36.6	18.39	444.45	38.2	39.8	47.1	26.85	410.74
17.6	32.0	37.6	19.62	449.77	41.2	40.7	49.5	27.76	394.56
20.6	33.0	38.4	20.8	458.06	44.1	41.9	52.9	28.53	362.26
23.5	33.8	39.5	21.93	464.71	47.1	42.3	55.5	29.38	349.74

Table B.15 Experimental Data A-D-GA-P2-S-ACR-15-015-06.82-12.5-100 15 μm droplets

z/d	Twall [°C]		Tbulk [°C]	h [W/m²K]	z/d	Twall [°C]		Tbulk [°C]	h [W/m²K]
2.9	17.9	28.1	12.97	678.57	26.5	34.5	40.1	22.48	460.44
5.9	22.0	32.1	14.13	529.13	29.4	35.2	41.2	23.6	466.64
8.8	25.3	34.1	15.35	475.18	32.4	36.3	42.7	24.55	456.94
11.8	28.0	35.6	16.6	450.00	35.3	37.6	44.4	25.53	441.59
14.7	30.1	36.7	17.81	437.38	38.2	38.8	45.9	26.41	427.26
17.6	31.3	37.6	19.05	442.67	41.2	39.3	48.1	27.32	416.39
20.6	32.2	38.4	20.24	452.17	44.1	40.5	51.5	28.15	382.06
23.5	33.0	39.4	21.46	462.82	47.1	41.3	55.5	28.9	349.74

Table B.16 Experimental Data A-D-GA-P2-S-ACR-15-015-06.82-12.5-100 25 μm droplets

z/d	Twall [°C]		Tbulk [°C]	h [W/m²K]	z/d	Twall [°C]		Tbulk [°C]	h [W/m²K]
2.9	18.1	27.8	13.05	688.29	26.5	35.1	39.3	22.59	467.28
5.9	22.3	32.0	14.2	527.46	29.4	36.2	40.3	23.64	467.17
8.8	25.3	33.9	15.41	480.59	32.4	37.0	41.1	24.65	473.62
11.8	27.8	35.4	16.66	457.34	35.3	37.9	42.6	25.62	466.75
14.7	29.8	36.5	17.95	448.84	38.2	38.7	43.4	26.56	470.49
17.6	31.6	37.4	19.1	443.95	41.2	39.4	45.1	27.46	461.85
20.6	33.0	38.1	20.29	448.19	44.1	40.2	47.2	28.29	442.52
23.5	34.1	38.9	21.43	452.54	47.1	41.0	49.0	29.13	429.84

Table B.17 Experimental Data A-D-GA-P2-S-ACR-15-015-06.82-15.0-100 41 μm droplets

z/d	Twall [°C]		Tbulk [°C]	h [W/m^{2}K]	z/d	Twall [°C]		Tbulk [°C]	h [W/m^{2}K]
2.9	22.6	25.3	15.66	823.15	26.5	38.5	39.8	24.48	463.97
5.9	27.8	29.2	16.64	575.72	29.4	39.5	40.8	25.47	465.70
8.8	30.5	32.2	17.76	501.31	32.4	40.2	41.2	26.42	476.56
11.8	32.8	34.5	18.93	464.22	35.3	40.9	42.1	27.33	480.03
14.7	34.2	36.0	20.13	456.33	38.2	41.5	42.9	28.27	490.02
17.6	35.5	37.2	21.21	449.71	41.2	42.0	43.8	29.13	494.75
20.6	36.8	38.3	22.32	446.71	44.1	42.7	44.3	29.95	502.55
23.5	37.9	39.2	23.39	449.82	47.1	43.3	45.4	30.75	501.58

Table B.18 Experimental Data A-D-GA-P2-S-ACR-15-015-06.85-15.8-095 48 μm droplets

z/d	Twall [°C]		Tbulk [°C]	h [W/m^{2}K]	z/d	Twall [°C]		Tbulk [°C]	h [W/m^{2}K]
2.9	23.7	26.2	16.49	812.31	26.5	39.0	40.2	25.2	474.75
5.9	28.9	29.8	17.46	575.43	29.4	39.8	41.1	26.17	480.02
8.8	31.6	32.4	18.65	513.35	32.4	40.5	41.6	27.17	493.01
11.8	33.7	34.5	19.8	479.14	35.3	41.1	42.7	28.07	494.71
14.7	35.0	36.1	20.91	468.16	38.2	41.7	43.8	28.94	495.91
17.6	36.3	37.5	22.05	462.01	41.2	42.3	44.6	29.79	502.87
20.6	37.5	38.7	23.14	457.82	44.1	42.8	45.8	30.6	498.80
23.5	38.4	39.6	24.19	462.06	47.1	43.5	47.3	31.39	489.22

Table B.19 Experimental Data A-D-GA-P2-S-ACR-15-015-06.84-15.7-097 61 μm droplets

z/d	Twall [°C]		Tbulk [°C]	h [W/m^{2}K]	z/d	Twall [°C]		Tbulk [°C]	h [W/m^{2}K]
2.9	24.5	25.8	16.4	779.99	26.5	39.6	39.8	25.1	469.20
5.9	29.3	29.7	17.37	563.66	29.4	40.8	41.5	26.08	454.08
8.8	32.0	32.1	18.56	506.60	32.4	41.9	42.4	27.01	451.85
11.8	33.8	34.0	19.71	482.91	35.3	43.6	44.8	27.86	418.20
14.7	35.0	35.4	20.89	477.00	38.2	44.7	47.0	28.69	398.12
17.6	36.2	36.6	21.95	472.87	41.2	47.4	51.1	29.44	345.30
20.6	37.5	37.6	23.04	472.14	44.1	49.1	56.2	30.12	303.77
23.5	38.6	38.8	24.09	468.29	47.1	53.0	59.8	30.78	266.97

Table B.20 Experimental Data A-D-GA-P2-L-GLS-15-015-06.83-13.3-087 22 μm droplets

z/d	Twall [°C]		Tbulk [°C]	h [W/m^{2}K]	z/d	Twall [°C]		Tbulk [°C]	h [W/m^{2}K]
2.9	23.8	25.6	13.9	631.20	26.5	42.4	40.8	23.06	368.84
5.9	28.7	29.8	15.03	480.76	29.4	45.6	40.6	24.1	359.55
8.8	31.1	32.2	16.21	442.44	32.4	48.7	42.7	24.98	329.56
11.8	32.9	34.1	17.44	424.53	35.3	52.5	44.2	25.83	303.51
14.7	34.1	35.8	18.71	420.40	38.2	56.6	46.8	26.65	272.20
17.6	35.7	37.1	19.84	413.00	41.2	60.5	49.2	27.45	248.97
20.6	37.6	37.8	21.01	408.78	44.1	66.4	51.6	28.18	221.37
23.5	40.8	39.2	22.05	379.29	47.1	71.2	54.8	28.89	200.02

Table B.21 Experimental Data A-D-GA-P2-L-GLS-15-015-06.85-13.1-087 28 μm droplets

z/d	Twall [°C]		Tbulk [°C]	h [W/m^{2}K]	z/d	Twall [°C]		Tbulk [°C]	h [W/m^{2}K]
2.9	23.5	24.6	13.77	666.42	26.5	38.8	40.6	23.06	412.41
5.9	28.3	29.7	14.82	482.64	29.4	39.9	41.4	24.11	414.46
8.8	30.3	32.4	16.01	447.08	32.4	40.8	43.7	25.11	399.31
11.8	32.0	34.5	17.34	430.63	35.3	42.8	43.5	26.07	400.36
14.7	33.2	36.3	18.53	421.82	38.2	44.2	44.5	26.95	393.05
17.6	34.6	37.8	19.76	416.92	41.2	46.6	46.1	27.8	369.27
20.6	36.5	38.5	20.85	411.47	44.1	49.9	46.2	28.67	353.28
23.5	38.1	39.7	21.98	404.99	47.1	52.4	49.4	29.41	318.96

Table B.22 Experimental Data A-D-GA-P2-L-GLS-15-015-06.81-13.8-085 34 μm droplets

z/d	Twall [°C]		Tbulk [°C]	h [W/m^{2}K]	z/d	Twall [°C]		Tbulk [°C]	h [W/m^{2}K]
2.9	21.8	25.5	14.6	749.42	26.5	37.5	39.9	23.73	454.74
5.9	26.3	30.0	15.71	548.98	29.4	38.8	40.5	24.74	457.00
8.8	28.2	32.8	16.87	499.07	32.4	39.9	41.8	25.72	450.34
11.8	30.3	35.0	18.08	467.88	35.3	40.9	43.3	26.66	441.17
14.7	31.8	36.5	19.32	460.49	38.2	42.2	44.0	27.57	438.34
17.6	33.3	37.8	20.43	451.29	41.2	43.5	46.1	28.4	415.66
20.6	34.9	38.3	21.57	452.86	44.1	44.5	47.4	29.25	407.91
23.5	36.4	39.3	22.67	447.78	47.1	46.7	47.2	30.07	403.28

Table B.23 Experimental Data A-D-GA-P2-L-GLS-15-015-06.86-12.9-087 41 μm droplets

z/d	Twall [°C]		Tbulk [°C]	h [W/m^{2}K]	z/d	Twall [°C]		Tbulk [°C]	h [W/m^{2}K]
2.9	23.3	25.4	13.47	629.76	26.5	36.9	38.3	23.08	472.82
5.9	27.5	29.4	14.62	497.22	29.4	38.3	39.1	24.12	471.61
8.8	29.3	31.7	15.93	470.55	32.4	39.1	40.3	25.12	470.66
11.8	31.0	33.5	17.26	457.92	35.3	40.3	41.5	26.09	462.63
14.7	32.1	34.8	18.46	457.18	38.2	41.1	42.5	27.02	465.05
17.6	33.6	35.8	19.69	457.39	41.2	42.3	43.9	27.92	452.41
20.6	35.0	36.3	20.86	463.76	44.1	43.5	44.9	28.79	444.87
23.5	36.3	37.2	21.99	463.75	47.1	45.1	46.2	29.58	426.38

Table B.24 Experimental Data A-D-GA-P2-L-GLS-15-015-06.83-13.2-082 48 μm droplets

z/d	Twall [°C]		Tbulk [°C]	h [W/m^{2}K]	z/d	Twall [°C]		Tbulk [°C]	h [W/m^{2}K]
2.9	21.2	25.2	14.18	758.71	26.5	36.3	41.0	23.31	445.53
5.9	26.0	29.9	15.2	536.70	29.4	37.7	41.8	24.33	443.16
8.8	27.8	32.7	16.47	496.36	32.4	38.9	44.4	25.26	416.66
11.8	29.9	34.9	17.6	462.16	35.3	40.2	46.7	26.16	394.54
14.7	31.1	36.5	18.85	457.06	38.2	40.9	48.9	27.08	383.49
17.6	32.5	37.9	20.05	451.67	41.2	42.0	52.0	27.92	358.17
20.6	34.0	38.6	21.13	450.50	44.1	43.0	55.1	28.73	336.43
23.5	35.6	39.9	22.24	439.84	47.1	44.7	56.0	29.52	328.33

Table B.25 Experimental Data A-D-GA-P2-L-GLS-15-015-06.83-13.2-082 56 μm droplets

z/d	Twall [°C]		Tbulk [°C]	h [W/m^{2}K]	z/d	Twall [°C]		Tbulk [°C]	h [W/m^{2}K]
2.9	24.0	25.8	13.92	611.25	26.5	37.5	42.2	23.18	405.84
5.9	28.3	30.3	14.95	469.22	29.4	38.9	43.3	24.21	399.80
8.8	29.9	33.0	16.22	442.75	32.4	39.8	47.0	25.07	369.21
11.8	31.3	35.0	17.53	431.81	35.3	41.2	50.5	25.98	340.42
14.7	32.5	36.7	18.71	424.85	38.2	42.4	52.6	26.85	328.02
17.6	33.8	38.4	19.91	417.46	41.2	43.8	55.5	27.69	308.16
20.6	35.4	39.2	21.07	416.87	44.1	45.8	60.6	28.46	273.97
23.5	36.8	40.9	22.11	404.02	47.1	47.5	64.4	29.2	253.88

Table B.26 Experimental Data A-U-GA-P2-S-ACR-15-015-12.90-13.4-100 8 μm droplets

z/d	Twall [°C]		Tbulk [°C]	h [W/m^{2}K]	z/d	Twall [°C]		Tbulk [°C]	h [W/m^{2}K]
2.9	26.0	35.7	14.58	793.82	26.5	51.0	78.7	29.74	367.27
5.9	32.9	41.6	16.72	628.31	29.4	53.8	77.4	31.31	375.97
8.8	37.3	45.9	18.97	571.20	32.4	58.7	86.1	32.53	323.47
11.8	40.6	49.9	21.07	534.02	35.3	66.1	92.5	33.7	282.92
14.7	42.8	55.7	23.02	491.65	38.2	73.7	97.9	34.87	253.32
17.6	44.7	62.3	24.84	450.23	41.2	79.2	107.8	35.91	223.97
20.6	46.7	68.6	26.56	414.42	44.1	91.9	112.0	36.93	198.34
23.5	48.2	73.8	28.22	393.75	47.1	95.7	115.3	38.06	191.36

Table B.27 Experimental Data A-U-GA-P2-S-ACR-15-015-14.28-13.4-100 16 μm droplets

z/d	Twall [°C]		Tbulk [°C]	h [W/m^{2}K]	z/d	Twall [°C]		Tbulk [°C]	h [W/m^{2}K]
2.9	28.2	35.0	14.75	848.12	26.5	51.1	51.5	31.7	728.80
5.9	36.0	41.6	17.13	659.42	29.4	51.8	52.2	33.32	765.55
8.8	41.1	44.6	19.59	612.92	32.4	52.8	52.9	34.79	790.89
11.8	44.3	46.7	21.93	606.09	35.3	53.7	53.8	36.18	813.79
14.7	46.3	47.9	24.15	621.97	38.2	54.4	54.3	37.48	845.45
17.6	47.9	49.0	26.26	642.83	41.2	54.7	55.3	38.75	878.57
20.6	49.2	49.8	28.21	671.26	44.1	55.7	56.0	39.92	897.98
23.5	50.0	50.9	30.02	699.37	47.1	56.3	56.7	41.03	922.58

Table B.28 Experimental Data A-U-GA-P2-S-ACR-15-015-14.27-13.6-100 42 μm droplets

z/d	Twall [°C]		Tbulk [°C]	h [W/m^{2}K]	z/d	Twall [°C]		Tbulk [°C]	h [W/m^{2}K]
2.9	28.6	34.5	14.96	861.56	26.5	51.1	51.2	31.88	740.55
5.9	36.3	41.2	17.34	667.95	29.4	51.7	51.9	33.49	780.07
8.8	41.3	44.2	19.79	621.95	32.4	52.7	52.5	34.96	808.63
11.8	44.4	46.2	22.13	616.69	35.3	53.6	53.5	36.35	828.98
14.7	46.4	47.5	24.41	633.09	38.2	54.4	54.1	37.65	860.94
17.6	47.9	48.7	26.45	652.71	41.2	54.6	55.1	38.91	895.07
20.6	49.2	49.5	28.4	681.19	44.1	55.6	55.8	40.08	915.05
23.5	50.0	50.6	30.2	710.03	47.1	56.3	56.5	41.19	940.62

Table B.29 Experimental Data A-U-GA-P2-S-ACR-15-015-14.30-13.8-100 58 μm droplets

z/d	Twall [°C]		Tbulk [°C]	h [W/m^{2}K]	z/d	Twall [°C]		Tbulk [°C]	h [W/m^{2}K]
2.9	29.3	32.2	15.28	923.44	26.5	51.0	51.1	32.1	754.67
5.9	36.6	39.5	17.56	696.92	29.4	51.7	51.8	33.66	791.19
8.8	41.4	43.3	20.01	640.71	32.4	52.7	52.4	35.12	820.44
11.8	44.4	45.7	22.41	631.45	35.3	53.5	53.4	36.5	844.21
14.7	46.4	47.2	24.61	645.04	38.2	54.2	53.9	37.83	880.90
17.6	47.9	48.4	26.64	665.55	41.2	54.5	54.9	39.06	914.98
20.6	49.2	49.3	28.58	692.64	44.1	55.5	55.6	40.23	935.68
23.5	49.9	50.4	30.38	723.77	47.1	56.2	56.3	41.33	960.17

Table B.30 Experimental Data A-U-GA-P2-S-ACR-15-015-14.28-13.5-100 100+ μm droplets

z/d	Twall [°C]		Tbulk [°C]	h [W/m^{2}K]	z/d	Twall [°C]		Tbulk [°C]	h [W/m^{2}K]
2.9	30.4	33.9	14.76	821.46	26.5	50.8	50.8	31.88	753.98
5.9	37.1	39.9	17.25	671.16	29.4	51.6	51.5	33.45	788.86
8.8	41.5	42.7	19.71	637.84	32.4	52.6	52.3	34.92	816.46
11.8	44.3	44.8	22.13	636.87	35.3	53.6	53.2	36.31	835.01
14.7	46.1	46.5	24.34	651.18	38.2	54.3	53.8	37.65	870.60
17.6	47.6	47.8	26.45	672.13	41.2	54.5	54.8	38.88	903.46
20.6	48.9	48.8	28.4	697.92	44.1	55.5	55.6	40.05	920.21
23.5	49.7	50.0	30.2	726.75	47.1	56.3	56.3	41.16	942.97

Table B.31 Experimental Data A-D-GA-P2-S-ACR-06-010-00.62-10.9-096-10.9-096

z/d	Twall [°C]		Twall average [°C]	z/d	Twall [°C]		Twall average [°C]
2.9	14.3	14.9	14.6	26.5	18.6	18.4	18.5
5.9	15.4	15.6	15.5	29.4	18.8	18.6	18.7
8.8	16.1	16.0	16.1	32.4	19.2	19.0	19.1
11.8	16.8	16.6	16.7	35.3	19.5	19.5	19.5
14.7	17.3	17.1	17.2	38.2	19.9	19.8	19.8
17.6	17.7	17.4	17.6	41.2	20.0	20.2	20.1
20.6	18.1	17.9	18.0	44.1	20.3	20.3	20.3
23.5	18.4	18.2	18.3	47.1	20.5	20.7	20.6

Table B.32 Experimental Data A-D-GA-P2-S-ACR-06-034-00.62-13.3-100

z/d	Twall [°C]		Twall average [°C]	z/d	Twall [°C]		Twall average [°C]
2.9	14.4	15.3	14.9	26.5	18.9	17.1	18.0
5.9	15.5	16.0	15.7	29.4	19.0	17.8	18.4
8.8	15.9	16.4	16.2	32.4	19.4	18.3	18.8
11.8	16.6	16.5	16.5	35.3	19.8	18.7	19.2
14.7	17.3	16.5	16.9	38.2	20.1	18.8	19.4
17.6	17.8	16.6	17.2	41.2	20.4	18.8	19.6
20.6	18.3	16.6	17.5	44.1	20.5	19.5	20.0
23.5	18.6	16.8	17.7	47.1	20.6	19.8	20.2

Table B.33 Experimental Data A-D-GA-P2-S-ACR-06-053-00.62-14.5-100

z/d	Twall [°C]		Twall average [°C]	z/d	Twall [°C]		Twall average [°C]
2.9	14.8	15.7	15.3	26.5	17.4	17.9	17.7
5.9	15.3	16.1	15.7	29.4	17.6	18.2	17.9
8.8	15.7	16.4	16.0	32.4	18.0	18.6	18.3
11.8	16.1	16.7	16.4	35.3	18.5	19.0	18.7
14.7	16.4	17.1	16.7	38.2	18.8	19.2	19.0
17.6	16.7	17.3	17.0	41.2	19.0	19.4	19.2
20.6	17.0	17.4	17.2	44.1	19.1	19.5	19.3
23.5	17.2	17.7	17.4	47.1	19.3	19.7	19.5

Table B.34 Experimental Data A-D-GA-P2-S-ACR-06-146-00.62-17.6-100

z/d	Twall [°C]		Twall average [°C]	z/d	Twall [°C]		Twall average [°C]
2.9	17.4	17.7	17.6	26.5	18.5	18.7	18.6
5.9	17.7	18.0	17.8	29.4	18.6	18.7	18.6
8.8	17.8	18.1	18.0	32.4	18.8	19.1	19.0
11.8	18.0	18.3	18.1	35.3	19.1	19.4	19.3
14.7	18.1	18.4	18.3	38.2	19.3	19.5	19.4
17.6	18.3	18.5	18.4	41.2	19.4	19.6	19.5
20.6	18.4	18.5	18.4	44.1	19.5	19.7	19.6
23.5	18.4	18.6	18.5	47.1	19.5	19.7	19.6

Table B.35 Experimental Data A-D-GA-P2-S-ACR-06-209-00.62-18.5-100

z/d	Twall [°C]		Twall average [°C]	z/d	Twall [°C]		Twall average [°C]
2.9	18.3	18.4	18.4	26.5	19.1	19.1	19.1
5.9	18.5	18.7	18.6	29.4	19.0	19.2	19.1
8.8	18.6	18.7	18.7	32.4	19.3	19.5	19.4
11.8	18.8	18.8	18.8	35.3	19.5	19.8	19.7
14.7	18.8	19.0	18.9	38.2	19.7	19.8	19.8
17.6	18.9	19.0	19.0	41.2	19.8	19.9	19.9
20.6	19.0	19.0	19.0	44.1	19.8	19.9	19.9
23.5	19.0	19.0	19.0	47.1	19.9	20.0	19.9

Table B.36 Experimental Data A-D-GA-P2-S-ACR-15-015-06.84-16.1-072 Tgas_line = 23 °C

z/d	Twall [°C]		Tbulk [°C]	h [W/m^{2}K]	z/d	Twall [°C]		Tbulk [°C]	h [W/m^{2}K]
2.9	23.7	26.1	16.74	839.27	26.5	38.9	40.0	25.32	484.45
5.9	28.2	29.8	17.78	608.68	29.4	39.8	40.9	26.28	486.63
8.8	31.1	32.3	18.87	533.02	32.4	40.6	41.4	27.27	498.20
11.8	33.2	34.2	20	498.39	35.3	41.4	42.4	28.16	497.56
14.7	34.7	35.9	21.09	482.06	38.2	42.0	42.9	29.02	508.77
17.6	36.1	37.0	22.21	477.09	41.2	42.5	43.8	29.9	516.89
20.6	37.3	38.2	23.29	472.84	44.1	43.1	44.7	30.71	518.26
23.5	38.2	39.2	24.33	474.75	47.1	43.7	45.5	31.48	521.22

Table B.37 Experimental Data A-D-GA-P2-S-ACR-15-015-06.84-13.7-081 Tgas_line = 19 °C

z/d	Twall [°C]		Tbulk [°C]	h [W/m²K]	z/d	Twall [°C]		Tbulk [°C]	h [W/m²K]
2.9	22.9	22.8	14.3	794.8	26.5	38.5	38.9	23.4	446.8
5.9	28.1	26.9	15.3	560.0	29.4	39.4	40.4	24.5	443.5
8.8	30.9	30.0	16.5	490.4	32.4	40.1	41.3	25.4	448.5
11.8	33.0	32.4	17.7	456.7	35.3	40.9	42.2	26.4	450.9
14.7	34.3	34.3	18.9	443.7	38.2	41.6	43.3	27.3	451.8
17.6	35.7	35.7	20.1	437.7	41.2	42.2	44.1	28.3	459.9
20.6	37.0	37.2	21.2	431.6	44.1	42.8	46.5	29.1	439.7
23.5	37.9	38.3	22.4	435.0	47.1	43.8	48.2	29.9	424.8

Table B.38 Experimental Data A-D-GA-P2-S-ACR-15-015-06.83-11.4-091 RHgas_line = 6 %

z/d	Twall [°C]		Tbulk [°C]	h [W/m²K]	z/d	Twall [°C]		Tbulk [°C]	h [W/m²K]
2.9	19.2	22.5	11.94	766.36	26.5	36.9	37.8	21.56	431.91
5.9	24.4	27.3	13.02	532.37	29.4	37.5	38.5	22.64	445.00
8.8	28.2	30.3	14.25	454.92	32.4	38.7	39.3	23.68	446.70
11.8	30.8	32.5	15.45	422.27	35.3	39.7	40.3	24.68	445.60
14.7	32.4	34.1	16.78	414.97	38.2	40.6	40.9	25.64	452.17
17.6	33.8	35.3	17.97	411.85	41.2	41.2	42.0	26.57	454.38
20.6	34.9	36.0	19.19	419.94	44.1	41.9	42.5	27.52	465.70
23.5	35.5	37.0	20.44	431.71	47.1	42.7	42.8	28.38	475.67

Table B.39 Experimental Data A-D-GA-P2-S-ACR-15-015-06.80-14.2-091 RHgas_line= 33 %

z/d	Twall [°C]		Tbulk [°C]	h [W/m²K]	z/d	Twall [°C]		Tbulk [°C]	h [W/m²K]
2.9	21.7	24.9	14.87	804.46	26.5	38.3	39.2	23.81	454.39
5.9	26.7	29.5	15.87	557.35	29.4	39.0	39.9	24.82	465.01
8.8	30.3	32.2	17.02	478.19	32.4	40.1	40.7	25.85	467.56
11.8	32.7	34.3	18.13	443.69	35.3	41.2	41.7	26.78	464.02
14.7	34.2	35.7	19.36	436.70	38.2	42.6	42.3	27.68	461.40
17.6	35.4	36.9	20.54	435.85	41.2	43.1	43.4	28.55	463.70
20.6	36.5	37.5	21.68	444.25	44.1	44.7	44.3	29.35	448.93
23.5	36.9	38.5	22.76	455.41	47.1	46.1	45.4	30.16	437.10

Table B.40 Experimental Data H-D-NA-P2-S-ACR-30-000-05.50-21.6-000

z/d	Twall [°C]		Tbulk [°C]	h [W/m²K]	z/d	Twall [°C]		Tbulk [°C]	h [W/m²K]
2.9	49.5	49.5	24.19	216.91	26.5	79.8	79.7	44.87	157.38
5.9	57.2	57.3	26.77	180.06	29.4	82.0	81.9	47.45	159.38
8.8	62.5	62.3	29.36	166.22	32.4	84.4	83.6	50.04	161.94
11.8	66.3	66.3	31.94	159.86	35.3	86.6	86.1	52.62	163.04
14.7	69.4	69.4	34.53	157.57	38.2	88.7	88.0	55.21	165.95
17.6	72.3	72.3	37.11	156.30	41.2	90.1	90.6	57.79	168.78
20.6	75.2	74.8	39.7	155.59	44.1	92.9	93.0	60.38	168.70
23.5	77.2	77.6	42.28	156.40	47.1	95.3	95.5	62.96	169.64

Table B.41 Experimental Data H-D-GA-P2-S-ACR-30-021-05.17-09.8-077

z/d	Twall [°C]		Tbulk [°C]	h [W/m^{2}K]	z/d	Twall [°C]		Tbulk [°C]	h [W/m^{2}K]
2.9	18.7	18.3	8.72	529.99	26.5	29.2	27.9	14.98	381.17
5.9	21.4	20.6	9.57	451.95	29.4	29.8	29.1	15.67	374.41
8.8	23.7	22.3	10.39	410.35	32.4	31.5	29.9	16.35	360.31
11.8	24.5	23.2	11.22	398.00	35.3	33.7	31.0	16.99	336.25
14.7	26.0	24.5	12.01	391.76	38.2	36.1	31.6	17.63	318.79
17.6	27.0	25.7	12.77	381.26	41.2	38.7	32.5	18.24	298.10
20.6	27.9	26.4	13.54	380.94	44.1	41.0	34.3	18.84	275.00
23.5	27.6	27.4	14.27	389.82	47.1	43.1	36.9	19.43	251.84

Table B.42 Experimental Data H-D-GA-P2-S-ACR-30-043-07.26-09.7-087

z/d	Twall [°C]		Tbulk [°C]	h [W/m^{2}K]	z/d	Twall [°C]		Tbulk [°C]	h [W/m^{2}K]
2.9	19.8	18.9	9.18	714.61	26.5	32.3	29.5	17.08	525.66
5.9	23.9	21.8	10.22	575.05	29.4	32.5	31.1	17.94	524.83
8.8	26.2	23.8	11.27	529.26	32.4	34.9	31.2	18.76	507.55
11.8	28.0	25.4	12.29	504.71	35.3	36.8	32.4	19.53	482.41
14.7	29.2	26.5	13.31	498.99	38.2	38.8	33.1	20.31	464.62
17.6	29.6	27.7	14.3	506.35	41.2	41.6	34.3	21.03	428.66
20.6	31.0	28.3	15.25	504.31	44.1	44.3	36.3	21.71	390.55
23.5	31.8	29.4	16.16	502.20	47.1	44.4	37.7	22.45	390.36

Table B.43 Experimental Data H-D-GA-P2-S-ACR-30-057-08.53-10.2-097

z/d	Twall [°C]		Tbulk [°C]	h [W/m^{2}K]	z/d	Twall [°C]		Tbulk [°C]	h [W/m^{2}K]
2.9	20.2	18.8	10.67	966.54	26.5	33.7	31.6	19	623.61
5.9	24.4	22.2	11.71	734.68	29.4	33.9	32.4	19.95	645.08
8.8	27.0	24.9	12.84	651.34	32.4	35.0	32.9	20.82	649.76
11.8	29.1	26.9	13.93	606.13	35.3	36.5	34.0	21.62	625.91
14.7	30.5	28.3	14.97	590.05	38.2	37.4	34.3	22.48	638.36
17.6	31.5	29.3	16.03	592.51	41.2	38.3	35.2	23.26	631.45
20.6	32.0	30.3	17.09	605.24	44.1	40.1	36.4	24.03	601.12
23.5	32.7	31.1	18.06	616.19	47.1	42.0	37.4	24.73	570.82

Table B.44 Experimental Data H-D-GA-P2-S-ACR-30-064-09.09-10.9-100

z/d	Twall [°C]		Tbulk [°C]	h [W/m^{2}K]	z/d	Twall [°C]		Tbulk [°C]	h [W/m^{2}K]
2.9	19.5	20.0	11.64	1115.21	26.5	34.4	33.1	20	659.41
5.9	25.5	23.7	12.61	758.52	29.4	34.4	33.9	20.96	687.23
8.8	28.8	26.2	13.69	657.79	32.4	35.0	34.7	21.84	698.57
11.8	31.0	28.2	14.79	613.74	35.3	35.5	35.7	22.69	706.06
14.7	32.1	29.7	15.91	605.70	38.2	36.4	35.5	23.55	731.51
17.6	32.6	30.9	16.98	614.32	41.2	36.7	36.5	24.34	739.39
20.6	33.6	31.9	18.01	615.72	44.1	38.2	37.9	25.11	701.44
23.5	33.4	32.7	19.05	649.09	47.1	39.6	38.7	25.85	683.64

Table B.45 Experimental Data A-D-GA-P2-S-ACR-15-015-06.85-15.8-095

z/d	Twall [°C]		Tbulk [°C]	h [W/m^{2}K]	z/d	Twall [°C]		Tbulk [°C]	h [W/m^{2}K]
2.9	23.7	26.2	16.49	812.31	26.5	39.0	40.2	25.2	474.75
5.9	28.9	29.8	17.46	575.43	29.4	39.8	41.1	26.17	480.02
8.8	31.6	32.4	18.65	513.35	32.4	40.5	41.6	27.17	493.01
11.8	33.7	34.5	19.8	479.14	35.3	41.1	42.7	28.07	494.71
14.7	35.0	36.1	20.91	468.16	38.2	41.7	43.8	28.94	495.91
17.6	36.3	37.5	22.05	462.01	41.2	42.3	44.6	29.79	502.87
20.6	37.5	38.7	23.14	457.82	44.1	42.8	45.8	30.6	498.80
23.5	38.4	39.6	24.19	462.06	47.1	43.5	47.3	31.39	489.22

Table B.46 Experimental Data A-D-GA-P2-S-ACR-06-015-01.49-12.3-100

z/d	Twall [°C]		Tbulk [°C]	h [W/m^{2}K]	z/d	Twall [°C]		Tbulk [°C]	h [W/m^{2}K]
2.9	19.2	19.3	12.42	219.95	26.5	27.8	26.8	18.07	161.75
5.9	21.2	20.1	13.08	197.58	29.4	28.2	27.6	18.71	162.74
8.8	22.8	21.0	13.83	184.71	32.4	29.1	28.4	19.34	158.55
11.8	23.8	22.2	14.57	177.30	35.3	29.9	29.0	19.95	156.76
14.7	25.0	23.3	15.28	168.20	38.2	31.6	29.7	20.55	147.90
17.6	25.5	24.5	15.98	166.33	41.2	33.4	30.4	21.14	138.45
20.6	26.5	25.3	16.67	161.69	44.1	33.5	30.8	21.78	144.05
23.5	27.1	26.4	17.34	158.72	47.1	34.9	31.5	22.34	137.49

Table B.47 Experimental Data A-U-GA-P2-S-ACR-15-015-06.84-13.5-100

z/d	Twall [°C]		Tbulk [°C]	h [W/m^{2}K]	z/d	Twall [°C]		Tbulk [°C]	h [W/m^{2}K]
2.9	22.1	23.0	14.15	815.71	26.5	36.8	36.7	23.41	513.61
5.9	26.7	27.2	15.27	586.08	29.4	37.2	37.1	24.49	538.70
8.8	29.7	30.0	16.44	510.49	32.4	38.1	37.7	25.47	548.65
11.8	31.8	32.0	17.65	478.53	35.3	38.9	38.6	26.41	555.84
14.7	33.2	33.3	18.9	476.61	38.2	39.5	39.1	27.32	570.21
17.6	34.4	34.4	20.02	476.02	41.2	39.8	40.0	28.25	585.95
20.6	35.3	35.1	21.25	489.15	44.1	40.6	40.5	29.1	596.68
23.5	35.9	36.0	22.35	501.39	47.1	41.1	41.1	29.97	612.66

Table B.48 Experimental Data A-U-GA-P2-S-ACR-15-015-09.95-13.4-100

z/d	Twall [°C]		Tbulk [°C]	h [W/m^{2}K]	z/d	Twall [°C]		Tbulk [°C]	h [W/m^{2}K]
2.9	25.3	26.6	14.43	861.74	26.5	43.7	43.6	27.13	601.14
5.9	31.7	32.4	16.02	621.48	29.4	44.3	44.2	28.44	628.35
8.8	35.7	36.0	17.71	549.83	32.4	45.2	44.8	29.73	650.23
11.8	38.2	38.4	19.39	526.99	35.3	46.1	45.7	30.91	663.93
14.7	39.7	39.9	21.12	532.44	38.2	46.8	46.3	32.03	685.42
17.6	41.0	41.1	22.76	543.28	41.2	47.1	47.3	33.15	710.20
20.6	42.2	42.0	24.3	560.41	44.1	47.9	47.9	34.17	724.75
23.5	42.8	42.9	25.75	581.58	47.1	48.5	48.5	35.16	744.41

Table B.49 Experimental Data A-U-GA-P2-S-ACR-15-015-12.44-13.4-100

z/d	Twall [°C]		Tbulk [°C]	h [W/m^{2}K]	z/d	Twall [°C]		Tbulk [°C]	h [W/m^{2}K]
2.9	27.9	29.6	14.7	883.33	26.5	48.4	48.2	29.87	675.42
5.9	35.2	36.4	16.71	652.37	29.4	49.0	48.8	31.39	710.18
8.8	39.7	40.4	18.85	587.60	32.4	49.9	49.5	32.77	734.99
11.8	42.4	42.9	20.92	572.58	35.3	50.7	50.3	34.09	756.72
14.7	44.1	44.4	22.91	583.08	38.2	51.3	50.9	35.36	789.57
17.6	45.5	45.6	24.83	600.18	41.2	51.6	51.9	36.54	818.32
20.6	46.6	46.5	26.63	624.62	44.1	52.5	52.5	37.66	838.27
23.5	47.4	47.5	28.3	650.50	47.1	53.1	53.2	38.73	862.60

Table B.50 Experimental Data A-U-GA-P2-S-ACR-15-015-14.30-13.5-100

z/d	Twall [°C]		Tbulk [°C]	h [W/m^{2}K]	z/d	Twall [°C]		Tbulk [°C]	h [W/m^{2}K]
2.9	30.0	31.6	14.96	901.11	26.5	51.3	51.2	31.79	735.32
5.9	37.9	39.0	17.25	673.92	29.4	52.0	51.8	33.4	774.06
8.8	42.6	43.2	19.7	616.67	32.4	52.9	52.3	34.87	805.39
11.8	45.4	45.8	22.03	607.03	35.3	53.8	53.3	36.25	827.92
14.7	47.1	47.3	24.25	623.61	38.2	54.4	53.8	37.59	865.79
17.6	48.5	48.5	26.35	644.85	41.2	54.6	54.8	38.82	902.14
20.6	49.6	49.4	28.3	674.61	44.1	55.5	55.4	39.99	924.16
23.5	50.3	50.4	30.11	705.65	47.1	56.1	56.1	41.1	952.63

Table B.51 Experimental Data A-U-GA-P2-S-ACR-15-015-15.57-13.6-100

z/d	Twall [°C]		Tbulk [°C]	h [W/m^{2}K]	z/d	Twall [°C]		Tbulk [°C]	h [W/m^{2}K]
2.9	30.7	33.3	15.24	907.43	26.5	53.0	53.1	33.07	763.12
5.9	38.9	41.0	17.77	688.78	29.4	53.7	53.9	34.74	800.47
8.8	43.8	45.3	20.34	632.02	32.4	54.8	54.8	36.25	822.67
11.8	46.8	47.8	22.84	625.83	35.3	55.9	55.8	37.68	837.82
14.7	48.6	49.3	25.25	645.85	38.2	61.2	58.2	38.94	735.07
17.6	50.1	50.5	27.41	667.98	41.2	65.1	70.3	40.03	554.40
20.6	51.3	51.4	29.44	698.68	44.1	66.9	87.1	41.06	428.20
23.5	52.0	52.4	31.33	731.65	47.1	66.8	98.6	42.12	379.87

Table B.52 Experimental Data A-U-GA-P2-S-ACR-15-010-05.00-12.7-100

z/d	Twall [°C]		Tbulk [°C]	h [W/m^{2}K]	z/d	Twall [°C]		Tbulk [°C]	h [W/m^{2}K]
2.9	20.6	22.4	13.29	606.33	26.5	32.9	33.0	20.98	418.97
5.9	24.8	25.9	14.2	448.86	29.4	33.3	33.4	21.83	434.91
8.8	27.2	28.0	15.21	404.34	32.4	34.0	34.0	22.7	442.15
11.8	28.9	29.5	16.25	386.92	35.3	34.7	34.7	23.49	447.35
14.7	30.0	30.5	17.25	385.11	38.2	35.2	35.0	24.3	462.19
17.6	30.9	31.3	18.22	388.01	41.2	35.5	35.7	25.05	475.05
20.6	31.7	31.8	19.15	397.17	44.1	36.1	36.1	25.82	488.64
23.5	32.2	32.5	20.06	407.97	47.1	36.5	36.5	26.52	500.19

Table B.53 Experimental Data A-U-GA-P2-S-ACR-15-010-06.26-12.8-097

z/d	Twall [°C]		Tbulk [°C]	h [W/m^{2}K]	z/d	Twall [°C]		Tbulk [°C]	h [W/m^{2}K]
2.9	22.4	24.2	13.52	640.89	26.5	36.5	36.5	22.86	459.95
5.9	27.3	28.6	14.71	474.27	29.4	37.0	37.0	23.9	478.84
8.8	30.2	31.0	15.92	426.64	32.4	37.8	37.6	24.86	488.21
11.8	32.1	32.7	17.15	410.50	35.3	38.5	38.3	25.78	496.15
14.7	33.3	33.8	18.38	413.01	38.2	39.0	38.7	26.71	515.43
17.6	34.3	34.6	19.56	420.42	41.2	39.3	39.5	27.58	531.71
20.6	35.2	35.2	20.73	432.41	44.1	39.9	40.0	28.44	544.12
23.5	35.7	36.0	21.82	446.52	47.1	40.5	40.5	29.24	557.58

Table B.54 Experimental Data A-U-GA-P2-S-ACR-15-010-07.46-12.8-100

z/d	Twall [°C]		Tbulk [°C]	h [W/m^{2}K]	z/d	Twall [°C]		Tbulk [°C]	h [W/m^{2}K]
2.9	24.0	25.9	13.74	666.04	26.5	39.6	39.5	24.5	496.73
5.9	29.7	30.9	15.06	490.74	29.4	40.0	39.9	25.66	521.29
8.8	32.9	33.6	16.58	447.55	32.4	40.8	40.5	26.73	535.09
11.8	34.9	35.4	18.02	434.84	35.3	41.6	41.4	27.76	544.27
14.7	36.1	36.6	19.39	439.18	38.2	42.1	41.8	28.78	565.91
17.6	37.3	37.5	20.75	448.00	41.2	42.4	42.6	29.73	584.68
20.6	38.1	38.1	22.09	464.65	44.1	43.1	43.1	30.67	599.07
23.5	38.8	38.9	23.32	480.41	47.1	43.7	43.7	31.55	615.34

Table B.55 Experimental Data A-U-GA-P2-S-ACR-15-010-08.73-12.7-094

z/d	Twall [°C]		Tbulk [°C]	h [W/m^{2}K]	z/d	Twall [°C]		Tbulk [°C]	h [W/m^{2}K]
2.9	25.7	27.9	13.8	669.21	26.5	42.4	42.4	26.07	534.18
5.9	32.0	33.4	15.41	504.37	29.4	43.0	43.0	27.34	558.37
8.8	35.4	36.3	17.12	464.89	32.4	43.8	43.5	28.52	575.96
11.8	37.6	38.2	18.79	457.38	35.3	44.5	44.3	29.64	590.57
14.7	38.9	39.4	20.41	465.68	38.2	45.1	44.7	30.74	615.53
17.6	40.0	40.3	21.94	479.37	41.2	45.3	45.6	31.77	638.03
20.6	41.0	41.0	23.39	495.90	44.1	46.1	46.1	32.77	654.03
23.5	41.5	41.8	24.76	515.98	47.1	46.7	46.7	33.72	671.86

Table B.56 Experimental Data A-U-GA-P2-S-ACR-15-010-09.94-12.8-092

z/d	Twall [°C]		Tbulk [°C]	h [W/m^{2}K]	z/d	Twall [°C]		Tbulk [°C]	h [W/m^{2}K]
2.9	27.3	29.5	14.03	691.68	26.5	44.9	44.9	27.64	575.10
5.9	34.0	35.6	15.9	526.97	29.4	45.5	45.4	28.97	601.86
8.8	37.7	38.6	17.83	488.98	32.4	46.4	46.1	30.23	621.70
11.8	39.9	40.6	19.64	482.50	35.3	47.1	46.8	31.46	641.01
14.7	41.2	41.8	21.44	494.60	38.2	47.7	47.3	32.6	668.01
17.6	42.4	42.8	23.13	510.15	41.2	47.9	48.2	33.71	694.34
20.6	43.5	43.4	24.71	530.38	44.1	48.7	48.7	34.74	711.24
23.5	44.0	44.3	26.24	554.64	47.1	49.3	49.3	35.74	732.77

Table B.57 Experimental Data A-U-GA-P2-S-ACR-15-010-11.17-12.9-094

z/d	Twall [°C]		Tbulk [°C]	h [W/m^{2}K]	z/d	Twall [°C]		Tbulk [°C]	h [W/m^{2}K]
2.9	28.8	31.2	14.34	714.80	26.5	46.5	51.0	29.1	568.23
5.9	35.6	37.3	16.4	557.49	29.4	47.1	50.1	30.54	618.27
8.8	38.8	41.3	18.55	519.81	32.4	48.0	49.1	31.89	670.31
11.8	41.2	44.8	20.55	498.27	35.3	49.1	49.5	33.15	690.19
14.7	42.7	48.5	22.42	481.90	38.2	52.8	57.6	34.24	533.77
17.6	44.0	50.7	24.21	482.12	41.2	59.4	61.9	35.31	440.62
20.6	45.1	52.1	25.92	492.22	44.1	66.7	70.1	36.27	347.52
23.5	45.7	52.0	27.56	525.34	47.1	73.2	79.1	37.21	286.74

Table B.58 Experimental Data A-U-GA-P2-S-ACR-15-015-14.94-13.6-100

z/d	Twall [°C]		Tbulk [°C]	h [W/m^{2}K]	z/d	Twall [°C]		Tbulk [°C]	h [W/m^{2}K]
2.9	30.2	32.9	15.1	908.73	26.5	52.2	52.2	32.48	757.75
5.9	38.3	40.4	17.51	683.16	29.4	52.9	52.8	34.12	797.57
8.8	43.2	44.5	20.06	628.23	32.4	53.9	53.5	35.62	827.74
11.8	46.0	47.0	22.48	621.73	35.3	54.7	54.4	37.02	852.00
14.7	47.8	48.5	24.77	639.02	38.2	55.3	54.9	38.35	891.76
17.6	49.2	49.6	26.93	663.75	41.2	55.5	55.8	39.62	931.86
20.6	50.5	50.4	28.92	693.67	44.1	56.4	56.5	40.81	954.11
23.5	51.2	51.5	30.77	725.79	47.1	57.1	57.2	41.93	982.68

Table B.59 Experimental Data A-U-GA-P2-S-ACR-10-015-14.99-13.2-100

z/d	Twall [°C]		Tbulk [°C]	h [W/m^{2}K]	z/d	Twall [°C]		Tbulk [°C]	h [W/m^{2}K]
2.9	37.1	37.7	15.72	691.76	26.5	55.1	55.0	38.75	918.50
5.9	43.0	43.0	19.75	644.61	29.4	56.1	56.0	40.6	971.90
8.8	46.3	46.1	23.35	655.96	32.4	57.1	56.7	42.28	1023.52
11.8	48.6	48.4	26.65	685.85	35.3	58.2	57.9	43.84	1054.64
14.7	50.1	50.1	29.58	729.92	38.2	59.0	58.6	45.29	1109.53
17.6	51.7	51.5	32.24	773.31	41.2	59.2	59.6	46.65	1176.32
20.6	53.0	52.7	34.63	821.79	44.1	60.3	60.5	47.93	1201.43
23.5	53.8	54.1	36.8	874.60	47.1	60.9	61.0	49.14	1266.92

Table B.60 Experimental Data A-U-GA-P2-S-ACR-10-015-23.00-13.1-100

z/d	Twall [°C]		Tbulk [°C]	h [W/m^{2}K]	z/d	Twall [°C]		Tbulk [°C]	h [W/m^{2}K]
2.9	45.7	45.7	17.46	814.79	26.5	64.7	64.7	46.38	1254.82
5.9	52.1	52.2	23.2	793.93	29.4	65.7	65.6	48.35	1328.76
8.8	55.7	55.5	28.16	837.37	32.4	66.8	66.1	50.15	1414.59
11.8	58.1	58.0	32.31	892.65	35.3	67.6	67.1	51.8	1481.42
14.7	59.7	59.7	35.92	967.61	38.2	68.4	67.7	53.32	1561.50
17.6	61.2	61.1	39.02	1041.33	41.2	68.5	68.8	54.74	1650.10
20.6	62.7	62.3	41.76	1109.07	44.1	69.7	69.7	56.04	1686.01
23.5	63.4	63.7	44.19	1185.90	47.1	89.5	85.6	57.24	759.85

Table B.61 Experimental Data A-D-GA-P2-S-ACR-15-015-06.84-16.1-072

z/d	Twall [°C]		Tbulk [°C]	h [W/m^{2}K]	z/d	Twall [°C]		Tbulk [°C]	h [W/m^{2}K]
2.9	23.7	26.1	16.74	839.27	26.5	38.9	40.0	25.32	484.45
5.9	28.2	29.8	17.78	608.68	29.4	39.8	40.9	26.28	486.63
8.8	31.1	32.3	18.87	533.02	32.4	40.6	41.4	27.27	498.20
11.8	33.2	34.2	20	498.39	35.3	41.4	42.4	28.16	497.56
14.7	34.7	35.9	21.09	482.06	38.2	42.0	42.9	29.02	508.77
17.6	36.1	37.0	22.21	477.09	41.2	42.5	43.8	29.9	516.89
20.6	37.3	38.2	23.29	472.84	44.1	43.1	44.7	30.71	518.26
23.5	38.2	39.2	24.33	474.75	47.1	43.7	45.5	31.48	521.22

Table B.62 Experimental Data A-D-NA-P2-S-ACR-10-000-02.21-20.5-003

z/d	Twall [°C]		Tbulk [°C]	h [W/m^{2}K]	z/d	Twall [°C]		Tbulk [°C]	h [W/m^{2}K]
2.9	53.1	53.0	23.14	73.92	26.5	81.5	81.3	40.69	54.26
5.9	61.2	61.4	25.34	61.43	29.4	83.5	83.4	42.89	54.48
8.8	66.2	66.0	27.53	57.24	32.4	85.7	85.0	45.08	54.91
11.8	69.7	69.6	29.73	55.35	35.3	87.5	87.1	47.27	55.13
14.7	72.4	72.3	31.92	54.63	38.2	89.4	88.7	49.47	55.82
17.6	74.9	74.7	34.11	54.27	41.2	90.5	90.8	51.66	56.64
20.6	77.3	77.0	36.31	54.04	44.1	92.8	92.8	53.85	56.74
23.5	79.2	79.4	38.50	54.12	47.1	94.6	94.7	56.05	57.28

Table B.63 Experimental Data A-D-GA-P2-S-ACR-10-005-00.82-11.4-079

z/d	Twall [°C]		Tbulk [°C]	h [W/m^{2}K]	z/d	Twall [°C]		Tbulk [°C]	h [W/m^{2}K]
2.9	14.5	16.0	11.75	235.81	26.5	18.6	18.7	14.09	181.97
5.9	15.6	16.5	12.03	205.21	29.4	18.7	18.9	14.39	187.76
8.8	16.4	16.9	12.32	189.88	32.4	19.1	19.3	14.68	183.07
11.8	17.0	17.4	12.63	180.69	35.3	19.5	19.7	14.94	177.74
14.7	17.4	17.8	12.91	175.26	38.2	19.8	19.8	15.23	180.25
17.6	17.8	18.1	13.22	174.29	41.2	20.0	20.1	15.51	181.52
20.6	18.1	18.2	13.52	177.68	44.1	20.1	20.2	15.8	188.40
23.5	18.3	18.4	13.83	181.48	47.1	20.3	20.4	16.07	192.79

Table B.64 Experimental Data A-D-GA-P2-S-ACR-10-010-02.49-13.5-086

z/d	Twall [°C]		Tbulk [°C]	h [W/m^{2}K]	z/d	Twall [°C]		Tbulk [°C]	h [W/m^{2}K]
2.9	19.5	20.9	14.08	406.64	26.5	29.2	29.4	19.86	263.82
5.9	22.3	23.1	14.75	311.94	29.4	29.7	29.9	20.51	267.95
8.8	24.0	24.7	15.53	283.02	32.4	30.4	30.6	21.15	266.71
11.8	25.4	25.9	16.28	265.00	35.3	31.0	31.3	21.82	267.32
14.7	26.5	27.0	16.97	255.23	38.2	31.5	31.8	22.43	268.63
17.6	27.4	27.7	17.69	251.67	41.2	32.0	32.6	23.06	269.52
20.6	28.1	28.2	18.45	255.98	44.1	32.6	33.2	23.65	268.79
23.5	28.7	28.9	19.14	257.71	47.1	33.1	34.3	24.21	263.06

Table B.65 Experimental Data A-D-GA-P2-S-ACR-10-015-03.13-14.0-092

z/d	Twall [°C]		Tbulk [°C]	h [W/m^{2}K]	z/d	Twall [°C]		Tbulk [°C]	h [W/m^{2}K]
2.9	18.8	21.7	14.59	550.70	26.5	31.7	31.8	21.03	291.93
5.9	21.7	24.6	15.34	398.73	29.4	32.4	32.4	21.78	294.42
8.8	23.8	26.4	16.15	349.63	32.4	33.5	33.1	22.58	292.23
11.8	26.0	27.9	16.95	312.48	35.3	34.1	34.0	23.28	290.77
14.7	27.3	28.7	17.81	306.46	38.2	34.7	34.4	23.98	296.21
17.6	28.7	29.6	18.65	297.69	41.2	35.0	35.0	24.71	304.93
20.6	30.0	30.4	19.46	291.50	44.1	35.4	35.6	25.37	308.97
23.5	31.1	31.2	20.25	287.77	47.1	36.2	36.0	26.07	313.39

Table B.66 Experimental Data A-D-NA-P3-S-PVC-05-000-01.20-21.9-003

z/d	Twall [°C]		Tbulk [°C]	h [W/m^{2}K]	z/d	Twall [°C]		Tbulk [°C]	h [W/m^{2}K]
2.7	57.7	57.8	24.08	35.67	25.0	86.6	86.5	41.86	26.89
5.2	66.2	66.2	26.05	29.96	27.4	88.4	88.3	43.84	27.01
7.6	71.0	71.1	28.03	27.96	29.9	90.1	90.2	45.82	27.15
10.1	74.5	74.4	30.01	27.08	32.4	91.8	91.9	47.79	27.31
15.1	79.3	78.9	33.96	26.64	34.9	93.3	93.8	49.77	27.49
17.5	81.4	81.0	35.94	26.56	37.3	95.1	95.3	51.74	27.67
20.0	83.3	82.9	37.91	26.62	39.8	96.7	97.1	53.72	27.83
22.5	85.1	84.8	39.89	26.71	42.3	96.26	96.50	55.7	29.57

Table B.67 Experimental Data A-D-NA-P3-S-PVC-10-000-02.22-21.5-003

z/d	Twall [°C]		Tbulk [°C]	h [W/m^{2}K]	z/d	Twall [°C]		Tbulk [°C]	h [W/m^{2}K]
2.7	59.7	59.8	23.43	61.01	25.0	86.3	86.0	39.84	47.84
5.2	66.7	66.7	25.25	53.49	27.4	88.0	87.7	41.66	47.93
7.6	70.7	70.7	27.08	50.80	29.9	89.6	89.6	43.48	48.05
10.1	73.9	73.6	28.9	49.40	32.4	91.1	91.3	45.31	48.27
15.1	78.8	78.1	32.55	48.24	34.9	92.5	93.1	47.13	48.53
17.5	81.0	80.2	34.37	47.89	37.3	94.2	94.6	48.95	48.74
20.0	82.9	82.2	36.19	47.81	39.8	95.8	96.4	50.77	48.86
22.5	84.7	84.1	38.01	47.76	42.3	96.51	96.96	52.6	50.20

Table B.68 Experimental Data A-D-NA-P3-S-PVC-15-000-03.26-21.3-003

z/d	Twall [°C]		Tbulk [°C]	h [W/m^{2}K]	z/d	Twall [°C]		Tbulk [°C]	h [W/m^{2}K]
2.7	61.0	61.1	23.23	86.25	25.0	86.5	86.1	39.27	69.27
5.2	67.2	67.2	25.01	77.32	27.4	88.2	87.8	41.05	69.42
7.6	70.9	70.9	26.79	73.89	29.9	89.7	89.6	42.83	69.60
10.1	74.1	73.7	28.57	71.96	32.4	91.1	91.3	44.61	69.92
15.1	79.0	78.1	32.14	70.19	34.9	92.4	93.0	46.4	70.37
17.5	81.2	80.2	33.92	69.64	37.3	94.1	94.5	48.18	70.69
20.0	83.1	82.2	35.7	69.47	39.8	95.6	96.2	49.96	70.92
22.5	84.9	84.1	37.49	69.32	42.3	96.62	97.10	51.74	72.23

Table B.69 Experimental Data A-D-NA-P3-S-PVC-30-000-04.52-22.1-005

z/d	Twall [°C]		Tbulk [°C]	h [W/m^{2}K]	z/d	Twall [°C]		Tbulk [°C]	h [W/m^{2}K]
2.7	53.2	53.3	23.41	86.25	25.0	71.3	70.7	34.55	69.27
5.2	57.2	57.1	24.64	77.32	27.4	72.5	72.0	35.79	69.42
7.6	59.8	59.6	25.88	73.89	29.9	73.6	73.5	37.03	69.60
10.1	62.1	61.6	27.12	71.96	32.4	74.6	74.7	38.27	69.92
15.1	65.9	64.9	29.6	70.19	34.9	75.4	76.0	39.5	70.37
17.5	67.5	66.3	30.84	69.64	37.3	76.6	77.0	40.74	70.69
20.0	68.9	67.8	32.07	69.47	39.8	77.6	78.2	41.98	70.92
22.5	70.3	69.2	33.31	69.32	42.3	78.50	79.08	43.22	72.23

Table B.70 Experimental Data A-D-NA-P3-L-GLS-05-000-01.14-23.6-003

z/d	Twall [°C]		Tbulk [°C]	h [W/m^{2}K]	z/d	Twall [°C]		Tbulk [°C]	h [W/m^{2}K]
2.7	59.1	59.1	25.59	33.93	25.0	84.7	84.5	42.43	26.98
5.2	66.7	66.6	27.46	29.03	27.4	86.6	86.3	44.3	26.99
7.6	70.4	70.3	29.33	27.72	29.9	88.2	88.2	46.17	27.04
10.1	73.2	72.7	31.21	27.25	32.4	89.9	90.0	48.04	27.16
15.1	77.5	76.6	34.95	27.02	34.9	91.3	91.7	49.91	27.32
17.5	79.5	78.7	36.82	26.93	37.3	93.1	93.2	51.78	27.47
20.0	81.2	80.6	38.69	26.93	39.8	94.6	95.1	53.65	27.61
22.5	83.1	82.5	40.56	26.93	42.3	94.21	94.51	55.52	29.29

Table B.71 Experimental Data A-D-NA-P3-L-GLS-10-000-02.00-21.7-003

z/d	Twall [°C]		Tbulk [°C]	h [W/m^{2}K]	z/d	Twall [°C]		Tbulk [°C]	h [W/m^{2}K]
2.7	58.3	58.3	23.52	57.41	25.0	81.2	80.8	38.33	46.81
5.2	64.4	64.3	25.16	51.01	27.4	82.9	82.5	39.97	46.76
7.6	67.7	67.3	26.81	49.07	29.9	84.3	84.4	41.62	46.74
10.1	70.4	69.7	28.46	48.04	32.4	85.8	86.1	43.26	46.82
15.1	74.5	73.5	31.75	47.26	34.9	87.2	87.8	44.91	46.94
17.5	76.4	75.4	33.39	47.00	37.3	88.9	89.2	46.56	47.05
20.0	78.1	77.2	35.04	46.93	39.8	90.3	91.0	48.2	47.08
22.5	79.8	79.0	36.68	46.76	42.3	90.99	91.57	49.85	48.23

Table B.72 Experimental Data A-D-NA-P3-L-GLS-15-000-02.88-20.8-003

z/d	Twall [°C]		Tbulk [°C]	h [W/m^{2}K]	z/d	Twall [°C]		Tbulk [°C]	h [W/m^{2}K]
2.7	58.1	58.0	22.53	81.21	25.0	79.6	78.9	36.65	67.70
5.2	63.4	63.2	24.09	73.48	27.4	81.1	80.6	38.21	67.64
7.6	66.5	66.0	25.66	70.95	29.9	82.4	82.3	39.78	67.67
10.1	69.1	68.3	27.23	69.52	32.4	83.7	83.9	41.35	67.84
15.1	73.2	71.8	30.37	68.40	34.9	85.0	85.6	42.92	68.07
17.5	75.0	73.6	31.94	68.06	37.3	86.5	86.9	44.49	68.25
20.0	76.5	75.3	33.51	67.97	39.8	87.9	88.6	46.06	68.33
22.5	78.2	77.1	35.08	67.72	42.3	88.83	89.49	47.63	69.40

Table B.73 Experimental Data A-D-NA-P3-L-GLS-30-000-05.40-21.9-003

z/d	Twall [°C]		Tbulk [°C]	h [W/m^{2}K]	z/d	Twall [°C]		Tbulk [°C]	h [W/m^{2}K]
2.7	61.1	60.9	23.5	144.10	25.0	81.2	79.7	36.77	123.62
5.2	65.7	65.2	24.98	133.60	27.4	82.6	81.4	38.24	123.53
7.6	68.6	67.6	26.45	129.84	29.9	83.8	83.1	39.72	123.66
10.1	71.1	69.6	27.93	127.45	32.4	84.9	84.7	41.19	123.97
15.1	75.1	72.9	30.87	125.37	34.9	85.9	86.2	42.67	124.55
17.5	76.9	74.5	32.35	124.70	37.3	87.3	87.5	44.14	124.86
20.0	78.3	76.1	33.82	124.46	39.8	88.6	89.1	45.62	125.14
22.5	79.9	77.9	35.3	123.86	42.3	89.63	90.15	47.09	126.27

Table B.74 Experimental Data A-D-GA-P3-S-PVC-15-015-10.20-12.8-100 P = UI

z/d	Twall [°C]		Tbulk [°C]	h [W/m^{2}K]	z/d	Twall [°C]		Tbulk [°C]	h [W/m^{2}K]
2.7	32.4	25.2	13.27	657.71	25.0	47.0	44.4	25.95	516.36
5.2	37.3	31.8	14.57	511.28	27.4	47.7	45.4	27.11	524.72
7.6	40.0	35.9	16.11	466.85	29.9	48.5	46.3	28.28	534.12
10.1	42.1	37.6	17.67	459.71	32.4	48.7	47.0	29.34	550.53
15.1	44.4	40.1	20.71	473.17	34.9	49.1	47.6	30.41	567.28
17.5	45.3	41.1	22.12	483.20	37.3	49.4	48.2	31.39	585.78
20.0	46.0	42.6	23.45	490.015	39.8	49.9	48.8	32.37	600.29
22.5	46.6	43.6	24.73	500.62	42.3	49.97	49.37	33.27	621.72

Table B.75 Experimental Data A-D-GA-P3-S-PVC-15-015-10.20-12.8-100 P = I^{2}R

z/d	Twall [°C]		Tbulk [°C]	h [W/m^{2}K]	z/d	Twall [°C]		Tbulk [°C]	h [W/m^{2}K]
2.7	32.4	25.2	13.24	647.0	25.0	47.0	44.4	25.89	515.0
5.2	37.3	31.8	14.53	505.5	27.4	47.7	45.4	27.06	524.1
7.6	40.0	35.9	16.06	462.8	29.9	48.5	46.3	28.23	533.5
10.1	42.1	37.6	17.61	456.4	32.4	48.7	47.0	29.3	550.6
15.1	44.4	40.1	20.64	470.0	34.9	49.1	47.6	30.37	567.3
17.5	45.3	41.1	22.05	480.4	37.3	49.4	48.2	31.35	586.4
20.0	46.0	42.6	23.39	487.8	39.8	49.9	48.8	32.34	601.2
22.5	46.6	43.6	24.67	498.9	42.3	49.97	49.37	33.25	623.6

Table B.76 Experimental Data A-D-GA-P3-S-PVC-15-015-03.86-13.8-086

z/d	Twall [°C]		Tbulk [°C]	h [W/m^{2}K]	z/d	Twall [°C]		Tbulk [°C]	h [W/m^{2}K]
2.7	20.9	18.6	13.94	666.09	25.0	31.1	29.6	18.96	339.26
5.2	23.6	20.8	14.46	501.29	27.4	31.7	30.4	19.56	336.73
7.6	25.4	22.7	14.98	425.00	29.9	32.2	31.1	20.08	334.14
10.1	27.0	24.3	15.48	379.97	32.4	32.6	31.6	20.67	338.81
15.1	28.9	26.6	16.66	347.11	34.9	32.8	32.1	21.16	341.24
17.5	29.6	27.5	17.22	339.79	37.3	33.2	32.4	21.73	349.27
20.0	30.2	28.3	17.87	340.02	39.8	33.4	32.8	22.28	356.18
22.5	30.8	29.0	18.42	336.80	42.3	33.67	33.21	22.75	361.21

Table B.77 Experimental Data A-D-GA-P3-S-PVC-15-015-03.85-13.3-089

z/d	Twall [°C]		Tbulk [°C]	h [W/m^{2}K]	z/d	Twall [°C]		Tbulk [°C]	h [W/m^{2}K]
2.7	20.0	18.4	13.48	668.99	25.0	30.4	29.0	18.53	345.97
5.2	22.3	20.5	13.91	512.95	27.4	31.0	29.7	19.07	340.59
7.6	24.1	22.3	14.52	443.04	29.9	31.6	30.4	19.67	339.66
10.1	25.7	23.9	15.03	392.90	32.4	32.0	31.0	20.18	340.79
15.1	27.9	26.1	16.21	356.13	34.9	32.3	31.5	20.76	345.97
17.5	28.7	27.0	16.79	348.20	37.3	32.6	31.8	21.33	353.38
20.0	29.3	27.7	17.35	345.36	39.8	32.9	32.3	21.81	357.78
22.5	30.0	28.4	17.99	343.30	42.3	33.19	32.64	22.36	365.05

Table B.78 Experimental Data A-D-GA-P3-S-PVC-15-015-06.43-13.2-090

z/d	Twall [°C]		Tbulk [°C]	h [W/m^{2}K]	z/d	Twall [°C]		Tbulk [°C]	h [W/m^{2}K]
2.7	24.4	22.6	13.37	633.85	25.0	38.5	37.0	21.74	401.85
5.2	28.2	26.2	14.28	498.71	27.4	39.1	37.9	22.58	403.59
7.6	30.8	28.8	15.16	439.49	29.9	39.7	38.6	23.46	408.97
10.1	33.0	30.9	16.11	406.75	32.4	40.2	39.3	24.25	415.05
15.1	35.6	33.6	18.02	387.59	34.9	40.4	39.8	25.07	426.30
17.5	36.6	34.6	18.98	386.95	37.3	40.8	40.3	25.82	436.00
20.0	37.3	35.5	19.9	390.24	39.8	41.2	40.8	26.6	446.77
22.5	38.1	36.4	20.8	391.62	42.3	41.42	41.22	27.3	458.22

Table B.79 Experimental Data A-D-GA-P3-S-PVC-15-015-06.37-13.2-087

z/d	Twall [°C]		Tbulk [°C]	h [W/m^{2}K]	z/d	Twall [°C]		Tbulk [°C]	h [W/m^{2}K]
2.7	24.1	22.0	13.56	675.17	25.0	38.5	36.7	21.76	403.12
5.2	27.8	25.5	14.36	518.90	27.4	39.2	37.4	22.59	405.83
7.6	30.4	28.5	15.23	447.96	29.9	39.8	38.4	23.46	408.27
10.1	32.8	30.2	16.18	415.80	32.4	40.2	38.9	24.25	416.59
15.1	35.5	33.0	18.07	394.35	34.9	40.5	39.7	25.07	424.84
17.5	36.5	33.9	19.02	393.69	37.3	40.9	40.1	25.81	434.60
20.0	37.1	34.9	20.01	398.51	39.8	41.2	40.6	26.59	445.06
22.5	37.9	35.6	20.9	402.33	42.3	41.49	41.06	27.28	455.50

Table B.80 Experimental Data A-D-GA-P3-S-PVC-15-015-08.89-13.1-091

z/d	Twall [°C]		Tbulk [°C]	h [W/m^{2}K]	z/d	Twall [°C]		Tbulk [°C]	h [W/m^{2}K]
2.7	29.0	26.7	13.46	617.60	25.0	44.3	43.0	24.7	469.16
5.2	33.6	31.7	14.62	493.17	27.4	45.0	43.8	25.76	476.43
7.6	36.5	34.6	15.94	453.67	29.9	45.6	44.6	26.78	485.05
10.1	38.6	36.7	17.29	436.48	32.4	46.0	45.3	27.82	498.69
15.1	41.3	39.5	19.9	433.24	34.9	46.2	45.9	28.82	515.60
17.5	42.3	40.5	21.16	439.14	37.3	46.7	46.4	29.73	529.37
20.0	43.1	41.4	22.37	447.53	39.8	47.1	47.0	30.65	542.11
22.5	43.9	42.3	23.53	454.64	42.3	47.24	47.34	31.5	563.06

Table B.81 Experimental Data A-D-GA-P3-S-PVC-15-015-08.91-13.7-094

z/d	Twall [°C]		Tbulk [°C]	h [W/m^{2}K]	z/d	Twall [°C]		Tbulk [°C]	h [W/m^{2}K]
2.7	29.6	27.1	14.01	621.68	25.0	44.7	43.4	25.13	470.49
5.2	34.5	31.2	15.26	506.46	27.4	45.3	44.3	26.24	479.59
7.6	37.3	34.2	16.55	463.82	29.9	45.9	45.1	27.25	488.43
10.1	39.5	36.9	17.79	436.50	32.4	46.3	45.8	28.27	502.25
15.1	41.9	39.6	20.46	438.43	34.9	46.5	46.4	29.21	517.82
17.5	42.9	40.7	21.7	443.36	37.3	46.9	46.8	30.16	534.37
20.0	43.5	41.6	22.89	452.21	39.8	47.2	47.3	31.02	547.88
22.5	44.3	42.7	24.03	457.27	42.3	47.45	47.68	31.91	569.22

Table B.82 Experimental Data A-D-GA-P3-S-PVC-15-015-12.74-13.1-091

z/d	Twall [°C]		Tbulk [°C]	h [W/m^{2}K]	z/d	Twall [°C]		Tbulk [°C]	h [W/m^{2}K]
2.7	35.1	33.7	13.48	609.12	25.0	52.4	50.5	28.83	562.71
5.2	40.4	39.5	15.25	516.53	27.4	53.4	51.3	30.15	573.86
7.6	43.2	42.2	17.29	501.99	29.9	53.8	52.7	31.4	583.49
10.1	45.7	43.9	19.21	498.42	32.4	55.6	52.6	32.6	592.38
15.1	48.6	46.4	22.76	515.30	34.9	54.9	54.2	33.77	612.95
17.5	49.6	47.5	24.42	528.04	37.3	56.0	55.1	34.85	615.34
20.0	50.6	48.6	25.98	540.39	39.8	57.1	56.4	35.89	611.16
22.5	51.4	49.7	27.44	551.95	42.3	58.01	57.92	36.85	603.38

Table B.83 Experimental Data A-D-GA-P3-S-PVC-15-015-12.73-13.3-087

z/d	Twall [°C]		Tbulk [°C]	h [W/m^{2}K]	z/d	Twall [°C]		Tbulk [°C]	h [W/m^{2}K]
2.7	33.9	30.9	13.94	689.37	25.0	52.1	51.0	28.98	564.46
5.2	39.5	36.4	15.69	571.67	27.4	53.4	52.7	30.24	557.83
7.6	42.6	40.4	17.61	532.92	29.9	54.3	56.7	31.44	528.35
10.1	45.3	43.5	19.42	509.16	32.4	66.4	60.6	32.33	408.82
15.1	48.4	46.6	22.95	519.07	34.9	66.9	66.5	33.41	382.74
17.5	49.7	47.4	24.59	530.32	37.3	68.1	68.7	34.47	375.06
20.0	50.5	48.6	26.14	543.87	39.8	73.6	70.9	35.43	345.63
22.5	51.8	49.8	27.6	549.35	42.3	76.81	79.26	36.28	304.85

Table B.84 Experimental Data A-D-GA-P3-S-PVC-15-015-14.00-13.2-087

z/d	Twall [°C]		Tbulk [°C]	h [W/m^{2}K]	z/d	Twall [°C]		Tbulk [°C]	h [W/m^{2}K]
2.7	35.8	33.0	13.9	681.89	25.0	57.1	58.7	29.93	500.57
5.2	41.5	38.0	15.96	588.89	27.4	60.9	65.6	31.14	435.82
7.6	44.0	43.2	17.99	546.58	29.9	65.1	72.4	32.3	384.08
10.1	46.9	46.0	19.98	528.16	32.4	72.3	74.2	33.41	351.48
15.1	50.3	49.4	23.72	535.42	34.9	73.8	81.4	34.52	324.74
17.5	52.2	52.7	25.41	517.42	37.3	78.6	84.0	35.58	306.44
20.0	53.5	54.1	27.07	523.60	39.8	80.3	91.8	36.57	282.99
22.5	56.1	55.7	28.51	511.13	42.3	81.33	93.87	37.65	280.24

Table B.85 Experimental Data A-D-GA-P3-S-PVC-15-015-14.03-13.1-091

z/d	Twall [°C]		Tbulk [°C]	h [W/m^{2}K]	z/d	Twall [°C]		Tbulk [°C]	h [W/m^{2}K]
2.7	36.2	35.0	13.62	639.25	25.0	55.2	53.1	30.08	583.41
5.2	41.9	40.7	15.62	546.92	27.4	56.8	54.1	31.46	585.21
7.6	45.0	44.1	17.77	524.17	29.9	60.9	55.6	32.69	549.53
10.1	45.8	46.2	19.86	536.40	32.4	64.6	64.0	33.74	459.17
15.1	50.4	48.6	23.69	544.49	34.9	67.2	70.4	34.83	413.37
17.5	52.5	49.6	25.39	546.72	37.3	72.8	67.9	35.95	408.32
20.0	53.3	50.6	27.05	563.25	39.8	75.9	70.8	36.98	385.82
22.5	55.3	52.0	28.61	560.65	42.3	72.87	74.02	38.07	396.70

Table B.86 Experimental Data A-D-GA-P3-S-PVC-15-015-14.05-13.1-089

z/d	Twall [°C]		Tbulk [°C]	h [W/m^{2}K]	z/d	Twall [°C]		Tbulk [°C]	h [W/m^{2}K]
2.7	36.3	34.7	13.68	644.27	25.0	59.5	63.6	29.78	442.80
5.2	41.5	40.2	15.68	557.83	27.4	62.1	71.9	30.96	389.60
7.6	43.4	44.4	17.82	538.73	29.9	66.0	76.2	32.18	361.31
10.1	47.2	46.5	19.83	519.42	32.4	68.3	86.5	33.26	318.51
15.1	50.9	47.8	23.75	549.26	34.9	74.5	92.2	34.31	286.75
17.5	53.3	51.2	25.39	523.09	37.3	74.9	90.2	35.57	299.15
20.0	54.0	51.1	27.11	551.87	39.8	78.9	92.0	36.63	287.95
22.5	55.9	56.7	28.5	505.70	42.3	82.29	90.28	37.72	289.35

Table B.87 Experimental Data A-D-GA-P3-S-PVC-05-005-00.66-12.1-056

z/d	Twall [°C]		Tbulk [°C]	h [W/m^{2}K]	z/d	Twall [°C]		Tbulk [°C]	h [W/m^{2}K]
2.7	17.3	16.6	12.34	142.60	25.0	22.0	21.4	15.72	109.77
5.2	18.6	17.6	12.72	122.17	27.4	22.5	21.9	16.09	107.40
7.6	19.4	18.4	13.09	112.63	29.9	22.9	22.5	16.43	105.59
10.1	20.1	19.1	13.46	107.33	32.4	23.2	22.7	16.79	106.69
15.1	21.0	20.0	14.23	104.84	34.9	23.4	23.1	17.14	107.41
17.5	21.3	20.4	14.61	105.38	37.3	23.7	23.3	17.46	108.88
20.0	21.5	20.7	15	107.33	39.8	24.0	23.7	17.81	108.97
22.5	21.9	21.1	15.35	107.08	42.3	24.19	23.89	18.15	111.58

Table B.88 Experimental Data A-D-GA-P3-S-PVC-05-005-00.65-11.9-060

z/d	Twall [°C]		Tbulk [°C]	h [W/m^{2}K]	z/d	Twall [°C]		Tbulk [°C]	h [W/m^{2}K]
2.7	17.5	16.6	12.2	134.59	25.0	21.9	21.3	15.58	108.08
5.2	18.7	17.6	12.58	117.38	27.4	22.3	21.8	15.95	107.09
7.6	19.5	18.4	12.95	109.05	29.9	22.7	22.2	16.28	105.23
10.1	20.2	19.0	13.33	104.25	32.4	23.0	22.5	16.64	106.73
15.1	21.0	20.0	14.09	102.10	34.9	23.3	22.8	17.00	107.97
17.5	21.2	20.3	14.47	103.29	37.3	23.5	23.0	17.35	110.45
20.0	21.5	20.7	14.86	105.26	39.8	23.7	23.3	17.67	112.41
22.5	21.8	21.0	15.23	105.88	42.3	23.78	23.49	18.01	115.94

Table B.89 Experimental Data A-D-GA-P3-S-PVC-05-005-01.25-12.0-056

z/d	Twall [°C]		Tbulk [°C]	h [W/m^{2}K]	z/d	Twall [°C]		Tbulk [°C]	h [W/m^{2}K]
2.7	21.7	19.3	12.58	158.98	25.0	35.1	30.3	18.65	89.13
5.2	23.9	21.4	13.3	134.13	27.4	37.0	32.3	19.24	81.26
7.6	25.4	23.1	14.03	123.06	29.9	38.5	33.6	19.83	77.31
10.1	26.6	24.3	14.71	116.90	32.4	39.4	34.8	20.42	75.10
15.1	29.0	26.1	16.1	109.17	34.9	42.5	35.9	20.97	68.74
17.5	30.9	27.0	16.76	103.03	37.3	44.6	37.7	21.51	63.86
20.0	31.7	27.9	17.41	101.23	39.8	46.0	39.2	22.04	61.09
22.5	33.8	29.2	18.03	93.16	42.3	46.42	40.33	22.6	60.35

Table B.90 Experimental Data A-D-GA-P3-S-PVC-05-005-01.26-12.0-060

z/d	Twall [°C]		Tbulk [°C]	h [W/m^{2}K]	z/d	Twall [°C]		Tbulk [°C]	h [W/m^{2}K]
2.7	21.4	19.4	12.52	159.85	25.0	34.6	30.1	18.64	91.83
5.2	23.7	21.7	13.24	133.71	27.4	36.4	31.9	19.23	84.22
7.6	25.2	23.3	13.98	123.05	29.9	38.7	33.1	19.81	78.32
10.1	26.4	24.5	14.67	116.80	32.4	39.7	34.3	20.4	75.82
15.1	28.4	26.3	16.08	111.77	34.9	42.2	35.7	20.95	70.02
17.5	30.0	27.0	16.72	106.60	37.3	44.2	37.4	21.49	65.18
20.0	31.2	27.9	17.38	103.54	39.8	45.1	38.7	22.05	63.47
22.5	33.4	29.1	18.02	95.31	42.3	47.22	40.10	22.57	59.73

Table B.91 Experimental Data A-D-GA-P3-S-PVC-05-005-01.84-12.0-060

z/d	Twall [°C]		Tbulk [°C]	h [W/m^{2}K]	z/d	Twall [°C]		Tbulk [°C]	h [W/m^{2}K]
2.7	24.9	22.0	12.88	173.90	25.0	54.5	43.2	21.17	66.56
5.2	28.0	25.4	13.92	144.29	27.4	57.4	47.6	21.94	60.25
7.6	30.4	27.4	14.95	132.06	29.9	60.5	49.6	22.73	56.96
10.1	32.8	29.1	15.94	122.76	32.4	63.4	52.1	23.48	53.76
15.1	38.9	33.4	17.82	100.37	34.9	65.8	53.7	24.22	51.77
17.5	42.8	36.5	18.67	87.90	37.3	68.5	56.8	24.93	48.83
20.0	46.4	39.7	19.53	78.22	39.8	70.3	59.3	25.64	47.03
22.5	50.9	43.3	20.34	68.78	42.3	71.53	61.00	26.34	46.12

Table B.92 Experimental Data A-D-GA-P3-S-PVC-05-005-01.86-12.0-056

z/d	Twall [°C]		Tbulk [°C]	h [W/m^{2}K]	z/d	Twall [°C]		Tbulk [°C]	h [W/m^{2}K]
2.7	25.3	21.9	12.87	173.54	25.0	55.9	45.0	21.21	63.69
5.2	28.3	25.0	13.92	145.86	27.4	59.5	48.8	22	57.86
7.6	30.6	27.2	14.96	133.51	29.9	61.8	50.4	22.8	55.83
10.1	33.9	29.3	15.94	118.73	32.4	64.8	51.4	23.57	53.86
15.1	40.3	34.7	17.81	94.42	34.9	66.8	52.8	24.32	52.40
17.5	46.0	38.9	18.65	78.29	37.3	69.2	56.3	25.04	49.31
20.0	50.3	42.0	19.52	69.81	39.8	71.0	59.0	25.75	47.36
22.5	53.3	45.3	20.37	64.27	42.3	71.93	61.02	26.44	46.47

Table B.93 Experimental Data A-D-GA-P3-S-PVC-15-015-11.44-13.2-091 aligned

z/d	Twall [°C]		Tbulk [°C]	h [W/m^{2}K]	z/d	Twall [°C]		Tbulk [°C]	h [W/m^{2}K]
2.7	32.8	31.5	13.52	615.19	25.0	49.5	48.2	27.58	537.16
5.2	38.1	37.1	15.15	509.85	27.4	50.9	49.0	28.76	539.35
7.6	40.8	40.4	16.88	481.81	29.9	51.5	50.0	29.99	551.38
10.1	43.3	42.3	18.61	472.65	32.4	52.0	50.7	31.12	565.32
15.1	46.3	44.7	21.86	483.32	34.9	52.5	51.7	32.2	574.09
17.5	47.4	45.6	23.39	494.34	37.3	53.1	52.3	33.27	588.61
20.0	48.1	46.5	24.84	509.22	39.8	53.5	53.4	34.26	595.77
22.5	49.0	47.5	26.21	519.33	42.3	53.69	54.26	35.21	609.57

Table B.94 Experimental Data A-D-GA-P3-S-PVC-15-015-11.50-13.3-088 misaligned

z/d	Twall [°C]		Tbulk [°C]	h [W/m^{2}K]	z/d	Twall [°C]		Tbulk [°C]	h [W/m^{2}K]
2.7	31.6	28.5	13.84	709.52	25.0	50.7	49.6	27.61	511.03
5.2	37.3	33.1	15.46	581.72	27.4	51.0	49.4	28.91	540.46
7.6	40.6	37.7	17.1	521.29	29.9	51.9	50.4	30.09	546.24
10.1	43.1	40.1	18.83	505.08	32.4	53.1	52.8	31.17	527.91
15.1	46.0	42.7	22.08	516.38	34.9	52.8	53.8	32.3	548.06
17.5	47.1	44.5	23.6	518.83	37.3	54.1	62.1	33.17	461.65
20.0	47.9	45.5	25.05	531.08	39.8	55.2	59.1	34.25	502.33
22.5	49.2	49.7	26.3	497.14	42.3	56.46	63.15	35.18	467.18

Table B.95 Experimental Data A-D-FG-P3-S-PVC-15-010-02.58-10.9-057

z/d	Twall [°C]		Tbulk [°C]	h [W/m^{2}K]	z/d	Twall [°C]		Tbulk [°C]	h [W/m^{2}K]
2.7	21.0	17.1	10.88	315.86	25.0	27.2	24.4	15.03	239.54
5.2	22.1	18.9	11.27	279.24	27.4	27.5	25.1	15.5	239.08
7.6	22.9	20.2	11.74	262.40	29.9	26.9	25.7	15.97	249.18
10.1	23.6	21.0	12.27	256.36	32.4	27.0	26.0	16.38	255.78
15.1	25.1	22.2	13.17	246.48	34.9	27.4	26.5	16.83	255.05
17.5	25.7	23.0	13.68	242.53	37.3	28.3	27.0	17.22	247.12
20.0	26.2	23.2	14.11	243.54	39.8	31.0	27.5	17.61	221.89
22.5	26.6	24.0	14.61	241.15	42.3	32.80	28.30	17.93	204.41

Table B.96 Experimental Data A-D-FG-P3-S-PVC-15-010-05.08-11.3-056

z/d	Twall [°C]		Tbulk [°C]	h [W/m^{2}K]	z/d	Twall [°C]		Tbulk [°C]	h [W/m^{2}K]
2.7	24.9	21.8	11.51	429.07	25.0	44.2	55.4	18.43	161.97
5.2	28.4	26.1	12.34	341.60	27.4	46.5	59.3	19.11	150.28
7.6	30.4	29.2	13.16	305.81	29.9	51.4	62.9	19.73	135.82
10.1	32.0	31.1	14.03	290.13	32.4	47.5	66.0	20.53	140.49
15.1	33.4	33.5	15.82	288.18	34.9	48.5	71.5	21.17	130.86
17.5	36.2	38.0	16.55	247.25	37.3	52.5	74.7	21.74	121.49
20.0	38.0	43.4	17.21	216.35	39.8	61.9	77.9	22.21	106.59
22.5	40.7	48.1	17.86	191.63	42.3	69.34	81.83	22.68	96.09

Table B.97 Experimental Data A-D-US-P3-S-PVC-15-010-05.08-12.9-061

z/d	Twall [°C]		Tbulk [°C]	h [W/m^{2}K]	z/d	Twall [°C]		Tbulk [°C]	h [W/m^{2}K]
2.7	27.2	23.1	13.14	424.41	25.0	35.3	34.3	20.65	358.80
5.2	29.4	26.0	13.95	370.30	27.4	35.9	35.0	21.38	361.20
7.6	30.7	27.9	14.8	349.90	29.9	36.4	35.7	22.14	365.45
10.1	31.9	29.5	15.7	338.86	32.4	36.7	36.2	22.83	372.71
15.1	33.4	31.6	17.41	337.14	34.9	37.0	36.7	23.55	382.71
17.5	34.0	32.3	18.28	341.47	37.3	37.4	37.0	24.25	392.80
20.0	34.4	33.0	19.08	346.97	39.8	37.7	37.5	24.89	400.75
22.5	35.0	33.7	19.85	349.99	42.3	37.87	37.83	25.55	413.42

Table B.98 Experimental Data A-D-US-P3-S-PVC-15-010-07.64-12.2-061

z/d	Twall [°C]		Tbulk [°C]	h [W/m^{2}K]	z/d	Twall [°C]		Tbulk [°C]	h [W/m^{2}K]
2.7	32.9	27.9	12.59	429.27	25.0	41.8	41.1	23.58	427.78
5.2	35.3	32.0	13.92	387.90	27.4	42.5	41.7	24.62	437.03
7.6	36.7	34.4	15.26	376.73	29.9	43.6	42.5	25.58	437.30
10.1	38.0	36.1	16.6	374.37	32.4	44.7	43.0	26.5	441.17
15.1	39.6	38.3	19.11	385.40	34.9	45.0	43.6	27.4	452.56
17.5	40.3	39.1	20.28	394.62	37.3	46.0	44.1	28.29	455.56
20.0	40.8	39.8	21.41	405.49	39.8	47.4	44.7	29.13	452.03
22.5	41.4	40.4	22.54	416.07	42.3	47.88	45.88	29.93	450.95

Table B.99 Experimental Data A-D-GA-P3-S-PVC-15-010-05.13-12.2-084

z/d	Twall [°C]		Tbulk [°C]	h [W/m^{2}K]	z/d	Twall [°C]		Tbulk [°C]	h [W/m^{2}K]
2.7	23.1	20.7	12.67	555.22	25.0	35.1	33.8	20.08	357.12
5.2	26.4	23.7	13.48	442.14	27.4	35.7	34.6	20.87	359.63
7.6	28.5	26.2	14.27	391.80	29.9	36.2	35.3	21.59	361.70
10.1	30.3	28.1	15.18	365.04	32.4	36.6	35.8	22.3	367.99
15.1	32.6	30.7	16.85	346.78	34.9	36.9	36.4	23.03	376.57
17.5	33.4	31.6	17.68	345.70	37.3	37.2	36.8	23.73	386.97
20.0	34.1	32.4	18.48	347.44	39.8	37.5	37.2	24.38	394.47
22.5	34.7	33.2	19.32	350.65	42.3	37.76	37.61	25.05	405.91

Table B.100 Experimental Data A-D-GA-P3-S-PVC-15-010-07.66-12.1-082

z/d	Twall [°C]		Tbulk [°C]	h [W/m^{2}K]	z/d	Twall [°C]		Tbulk [°C]	h [W/m^{2}K]
2.7	28.4	24.6	12.68	553.91	25.0	42.2	40.6	23.38	425.74
5.2	32.5	28.7	13.92	459.25	27.4	43.0	41.4	24.38	430.25
7.6	34.9	31.8	15.18	421.35	29.9	43.6	42.2	25.38	437.46
10.1	36.8	34.1	16.46	402.59	32.4	43.8	42.8	26.31	449.59
15.1	39.4	36.9	18.91	398.31	34.9	44.4	43.4	27.24	459.81
17.5	40.3	38.0	20.08	401.26	37.3	44.8	43.9	28.1	471.56
20.0	41.0	38.9	21.26	408.91	39.8	45.4	44.5	28.97	477.60
22.5	41.7	39.9	22.34	414.96	42.3	45.18	46.65	29.77	474.19

Table B.101 Experimental Data A-D-GA-P3-L-GLS-15-015-03.86-12.9-083

z/d	Twall [°C]		Tbulk [°C]	h [W/m^{2}K]	z/d	Twall [°C]		Tbulk [°C]	h [W/m^{2}K]
2.7	24.6	16.8	12.81	489.17	25.0	31.1	26.9	18.21	358.38
5.2	26.2	18.9	13.34	419.42	27.4	31.6	27.8	18.75	353.01
7.6	27.3	20.6	13.97	387.78	29.9	32.1	28.7	19.27	347.83
10.1	28.3	21.6	14.58	371.33	32.4	32.4	29.3	19.87	352.14
15.1	29.6	23.7	15.78	355.88	34.9	32.6	30.0	20.38	353.47
17.5	30.0	24.6	16.36	353.40	37.3	33.0	30.5	20.95	359.19
20.0	30.4	25.4	17.02	355.14	39.8	33.2	31.0	21.52	364.56
22.5	30.9	26.1	17.58	354.08	42.3	33.43	31.53	21.99	368.34

Table B.102 Experimental Data A-D-GA-P3-L-GLS-15-015-06.40-13.1-086

z/d	Twall [°C]		Tbulk [°C]	h [W/m^{2}K]	z/d	Twall [°C]		Tbulk [°C]	h [W/m^{2}K]
2.7	31.0	20.0	13.12	515.82	25.0	38.9	34.4	21.72	427.18
5.2	33.1	24.7	14.03	430.15	27.4	39.5	34.8	22.62	440.31
7.6	34.4	28.0	14.91	392.70	29.9	40.0	36.0	23.43	439.13
10.1	35.6	29.7	15.96	383.22	32.4	40.3	36.1	24.21	457.16
15.1	37.1	31.7	17.95	389.22	34.9	40.6	37.2	25.03	461.23
17.5	37.7	32.3	18.98	400.23	37.3	41.0	37.5	25.77	474.37
20.0	38.0	33.1	19.9	408.55	39.8	41.3	38.3	26.55	483.04
22.5	38.6	33.0	20.86	428.42	42.3	41.56	38.74	27.3	497.74

Table B.103 Experimental Data A-D-GA-P3-L-GLS-15-015-08.92-12.5-087

z/d	Twall [°C]		Tbulk [°C]	h [W/m^{2}K]	z/d	Twall [°C]		Tbulk [°C]	h [W/m^{2}K]
2.7	32.6	23.2	12.7	588.01	25.0	44.0	40.5	24.25	494.74
5.2	35.8	27.2	13.99	509.65	27.4	44.6	42.0	25.33	496.12
7.6	37.7	30.4	15.33	475.68	29.9	44.8	42.8	26.43	513.64
10.1	38.7	32.8	16.8	470.42	32.4	45.5	44.0	27.43	513.64
15.1	40.8	35.7	19.45	473.27	34.9	45.8	44.9	28.38	525.54
17.5	41.7	37.2	20.73	475.41	37.3	46.8	46.3	29.31	516.40
20.0	42.8	38.2	21.96	481.20	39.8	47.7	46.8	30.2	521.77
22.5	43.5	39.9	23.13	479.90	42.3	48.19	47.29	31.11	536.19

Table B.104 Experimental Data A-D-US-P3-L-GLS-15-015-03.90-12.1-070

z/d	Twall [°C]		Tbulk [°C]	h [W/m^{2}K]	z/d	Twall [°C]		Tbulk [°C]	h [W/m^{2}K]
2.7	22.0	17.5	12.03	504.50	25.0	30.0	27.5	17.4	343.46
5.2	23.9	19.5	12.58	427.25	27.4	30.6	28.1	18.04	345.45
7.6	25.2	21.3	13.22	388.18	29.9	31.1	28.9	18.67	344.15
10.1	26.4	22.5	13.75	364.20	32.4	31.5	29.3	19.2	348.18
15.1	28.0	24.7	14.99	343.21	34.9	31.8	29.9	19.8	353.21
17.5	28.6	25.4	15.68	343.38	37.3	32.0	30.3	20.39	361.96
20.0	29.1	26.2	16.26	341.95	39.8	32.4	30.7	20.89	365.30
22.5	29.7	26.6	16.8	342.85	42.3	32.60	31.13	21.46	374.39

Table B.105 Experimental Data A-D-US-P3-L-GLS-15-015-06.41-13.1-072

z/d	Twall [°C]		Tbulk [°C]	h [W/m^{2}K]	z/d	Twall [°C]		Tbulk [°C]	h [W/m^{2}K]
2.7	30.5	20.4	13.24	526.32	25.0	38.9	34.6	21.96	432.77
5.2	32.6	23.7	14.27	461.28	27.4	39.5	34.9	22.8	445.67
7.6	34.0	26.7	15.16	422.18	29.9	40.0	36.0	23.68	446.40
10.1	35.3	28.3	16.22	411.93	32.4	40.3	36.0	24.54	470.68
15.1	36.8	31.4	18.23	403.84	34.9	40.6	37.0	25.3	475.01
17.5	37.4	32.4	19.19	407.48	37.3	41.0	37.2	26.1	491.72
20.0	37.8	33.4	20.12	413.49	39.8	41.5	37.9	26.83	498.59
22.5	38.5	33.1	21.09	435.64	42.3	41.56	38.34	27.58	518.03

Table B.106 Experimental Data A-D-US-P3-L-GLS-15-015-08.89-12.4-072

z/d	Twall [°C]		Tbulk [°C]	h [W/m^{2}K]	z/d	Twall [°C]		Tbulk [°C]	h [W/m^{2}K]
2.7	35.1	22.0	12.54	555.80	25.0	46.5	38.2	24.3	492.05
5.2	37.7	26.8	13.85	483.12	27.4	47.5	39.7	25.39	487.70
7.6	39.4	31.7	15.21	437.16	29.9	49.3	41.1	26.37	472.50
10.1	41.2	32.6	16.69	439.52	32.4	49.7	43.3	27.38	465.22
15.1	43.3	34.8	19.38	451.70	34.9	51.7	45.2	28.29	441.38
17.5	44.1	35.2	20.75	470.50	37.3	55.4	48.7	29.12	387.72
20.0	44.8	36.4	21.99	479.02	39.8	59.1	52.5	29.88	343.64
22.5	45.8	36.7	23.17	491.74	42.3	62.87	55.44	30.62	311.69

Table B.107 Experimental Data A-D-GA-P3-S-PVC-10-010-05.06-12.3-100 18 μm droplets

z/d	Twall [°C]		Tbulk [°C]	h [W/m^{2}K]	z/d	Twall [°C]		Tbulk [°C]	h [W/m^{2}K]
2.7	27.7	26.2	12.91	360.19	25.0	42.8	40.7	23.44	276.43
5.2	31.7	30.6	14.13	297.78	27.4	45.2	42.2	24.38	262.18
7.6	34.2	32.9	15.37	278.23	29.9	47.2	44.7	25.3	244.75
10.1	36.2	34.5	16.62	269.71	32.4	49.3	48.8	26.14	220.82
15.1	38.7	37.1	19.08	269.26	34.9	52.4	54.7	26.89	189.88
17.5	39.7	38.0	20.24	272.42	37.3	55.5	57.6	27.69	175.35
20.0	40.8	38.9	21.35	274.24	39.8	58.9	59.9	28.47	163.81
22.5	42.2	39.6	22.41	273.38	42.3	58.34	60.51	29.32	168.22

Table B.108 Experimental Data A-D-GA-P3-S-PVC-10-010-05.07-12.3-097 28 μm droplets

z/d	Twall [°C]		Tbulk [°C]	h [W/m^{2}K]	z/d	Twall [°C]		Tbulk [°C]	h [W/m^{2}K]
2.7	28.1	26.4	12.85	352.14	25.0	42.3	40.6	23.45	281.37
5.2	32.1	30.6	14.07	292.86	27.4	43.8	41.6	24.44	277.72
7.6	34.5	33.1	15.38	275.42	29.9	45.8	42.9	25.35	267.16
10.1	36.5	34.8	16.63	266.79	32.4	49.0	44.8	26.23	244.76
15.1	38.7	37.0	19.09	269.66	34.9	52.1	47.9	27.05	220.42
17.5	39.9	38.0	20.25	271.27	37.3	55.0	49.7	27.85	206.96
20.0	40.5	38.8	21.36	277.03	39.8	59.0	51.5	28.62	190.35
22.5	42.1	39.6	22.42	274.51	42.3	60.26	53.96	29.43	183.02

Table B.109 Experimental Data A-D-GA-P3-S-PVC-10-010-05.07-12.5-088 41 μm droplets

z/d	Twall [°C]		Tbulk [°C]	h [W/m^{2}K]	z/d	Twall [°C]		Tbulk [°C]	h [W/m^{2}K]
2.7	28.8	27.2	13.1	339.84	25.0	42.5	40.1	23.66	287.99
5.2	32.9	31.0	14.31	287.48	27.4	42.8	40.9	24.69	295.83
7.6	35.2	33.4	15.55	271.12	29.9	43.4	41.6	25.63	300.65
10.1	36.8	35.0	16.86	266.34	32.4	44.0	42.2	26.58	306.66
15.1	38.9	37.0	19.32	271.76	34.9	44.7	43.2	27.46	307.02
17.5	39.8	37.8	20.47	276.56	37.3	47.6	43.9	28.28	290.45
20.0	40.4	38.6	21.58	282.80	39.8	50.5	45.3	29.07	269.89
22.5	41.3	39.5	22.64	285.69	42.3	51.49	46.32	29.87	266.39

Table B.110 Experimental Data A-D-GA-P3-S-PVC-10-010-05.07-12.9-075 55 μm droplets

z/d	Twall [°C]		Tbulk [°C]	h [W/m^{2}K]	z/d	Twall [°C]		Tbulk [°C]	h [W/m^{2}K]
2.7	29.5	26.8	13.47	344.49	25.0	42.4	40.1	23.98	293.57
5.2	33.3	30.8	14.68	291.88	27.4	44.2	40.8	24.96	289.03
7.6	35.5	33.1	15.91	275.58	29.9	45.4	41.7	25.9	287.47
10.1	37.1	34.7	17.22	270.96	32.4	45.9	42.3	26.85	294.13
15.1	39.2	37.0	19.66	274.67	34.9	46.8	42.8	27.73	296.99
17.5	40.1	37.9	20.8	278.81	37.3	48.1	43.5	28.57	294.01
20.0	41.6	38.7	21.9	278.13	39.8	49.9	44.3	29.39	286.17
22.5	42.3	39.4	22.96	283.14	42.3	50.82	44.72	30.19	288.41

Table B.111 Experimental Data A-D-GA-P3-S-PVC-10-010-05.07-13.0-068 61 μm droplets

z/d	Twall [°C]		Tbulk [°C]	h [W/m^{2}K]	z/d	Twall [°C]		Tbulk [°C]	h [W/m^{2}K]
2.7	30.3	27.4	13.52	331.35	25.0	44.1	39.9	24.07	282.45
5.2	33.6	31.4	14.74	285.22	27.4	46.0	40.7	25	276.57
7.6	35.6	33.7	16.03	271.91	29.9	49.6	41.7	25.91	256.82
10.1	37.2	35.3	17.27	267.24	32.4	53.0	43.3	26.78	237.44
15.1	39.4	37.2	19.71	272.36	34.9	57.3	46.4	27.56	208.76
17.5	40.4	37.9	20.91	277.47	37.3	62.6	50.8	28.28	178.66
20.0	41.5	38.5	22	281.82	39.8	64.8	53.5	29.09	168.79
22.5	42.8	39.4	23.06	280.76	42.3	69.93	56.47	29.81	151.87

Table B.112 Experimental Data A-D-GA-P3-S-PVC-10-015-06.39-13.2-100 20 μm droplets

z/d	Twall [°C]		Tbulk [°C]	h [W/m^{2}K]	z/d	Twall [°C]		Tbulk [°C]	h [W/m^{2}K]
2.7	29.9	28.6	13.49	405.17	25.0	49.0	41.5	25.54	324.13
5.2	35.3	33.6	14.78	324.72	27.4	51.1	43.5	26.59	308.74
7.6	38.2	36.5	16.21	302.77	29.9	55.5	43.7	27.61	290.58
10.1	40.3	38.2	17.67	295.85	32.4	58.5	46.2	28.54	268.36
15.1	43.0	39.6	20.55	307.77	34.9	61.9	47.1	29.48	255.79
17.5	44.2	39.8	21.95	319.34	37.3	64.7	48.0	30.4	246.35
20.0	45.6	39.8	23.22	328.45	39.8	68.7	49.5	31.28	229.71
22.5	47.6	40.8	24.37	322.24	42.3	75.34	53.47	31.96	196.94

Table B.113 Experimental Data A-D-GA-P3-S-PVC-10-015-06.35-13.2-100 29 µm droplets

z/d	Twall [°C]		Tbulk [°C]	h [W/m^{2}K]	z/d	Twall [°C]		Tbulk [°C]	h [W/m^{2}K]
2.7	31.2	28.2	13.43	389.87	25.0	45.7	42.6	25.5	339.62
5.2	35.6	32.3	14.81	330.95	27.4	47.3	43.8	26.61	335.78
7.6	38.4	35.2	16.23	308.70	29.9	48.6	44.5	27.67	336.22
10.1	40.4	36.9	17.68	302.75	32.4	49.9	45.5	28.7	333.45
15.1	42.7	39.5	20.54	308.32	34.9	52.2	46.2	29.63	323.70
17.5	43.7	41.2	21.79	307.27	37.3	55.9	47.1	30.53	302.21
20.0	44.4	41.7	23.13	318.98	39.8	60.0	47.9	31.4	281.40
22.5	45.2	42.4	24.34	325.93	42.3	63.46	49.16	32.2	263.30

Table B.114 Experimental Data A-D-GA-P3-S-PVC-10-015-06.40-13.2-100 35 µm droplets

z/d	Twall [°C]		Tbulk [°C]	h [W/m^{2}K]	z/d	Twall [°C]		Tbulk [°C]	h [W/m^{2}K]
2.7	31.2	26.9	13.58	413.87	25.0	45.9	43.7	25.59	333.29
5.2	35.7	31.3	14.87	343.72	27.4	46.8	43.9	26.7	343.30
7.6	38.2	33.7	16.39	326.56	29.9	47.4	44.4	27.82	353.81
10.1	40.1	35.8	17.84	318.24	32.4	48.4	44.7	28.85	361.75
15.1	42.6	40.3	20.54	305.88	34.9	49.3	45.3	29.83	367.26
17.5	43.5	41.7	21.87	308.55	37.3	49.9	46.5	30.77	366.93
20.0	44.2	42.4	23.15	317.54	39.8	50.6	47.8	31.68	365.15
22.5	45.0	43.2	24.43	325.33	42.3	52.95	48.24	32.56	354.79

Table B.115 Experimental Data A-D-GA-P3-S-PVC-10-015-06.39-13.3-096 42 µm droplets

z/d	Twall [°C]		Tbulk [°C]	h [W/m^{2}K]	z/d	Twall [°C]		Tbulk [°C]	h [W/m^{2}K]
2.7	31.1	27.8	13.6	402.45	25.0	45.6	43.7	25.66	335.96
5.2	35.6	32.5	14.98	334.61	27.4	46.2	44.5	26.77	343.76
7.6	38.2	35.2	16.4	314.85	29.9	46.9	45.1	27.89	352.56
10.1	40.3	36.8	17.85	308.73	32.4	48.2	45.6	28.9	354.81
15.1	42.6	39.0	20.7	317.37	34.9	48.0	45.8	29.93	376.30
17.5	43.5	40.6	22.03	318.92	37.3	48.9	46.4	30.87	380.04
20.0	44.2	41.7	23.29	325.22	39.8	49.8	47.4	31.78	379.72
22.5	45.0	43.0	24.5	327.47	42.3	50.71	47.82	32.65	384.38

Table B.116 Experimental Data A-D-GA-P3-S-PVC-10-015-06.38-13.5-088 48 µm droplets

z/d	Twall [°C]		Tbulk [°C]	h [W/m^{2}K]	z/d	Twall [°C]		Tbulk [°C]	h [W/m^{2}K]
2.7	32.2	28.5	13.63	381.93	25.0	45.5	43.3	25.74	341.54
5.2	36.5	33.9	14.92	313.99	27.4	46.6	44.0	26.84	345.74
7.6	38.9	36.7	16.43	298.46	29.9	47.1	44.5	27.96	357.69
10.1	40.7	38.2	17.88	295.64	32.4	47.7	44.9	28.97	367.36
15.1	42.9	40.5	20.73	304.31	34.9	48.1	45.5	30	380.42
17.5	43.7	41.3	22.05	311.81	37.3	48.6	46.7	30.93	381.91
20.0	44.3	42.1	23.31	321.04	39.8	49.6	48.0	31.84	375.57
22.5	45.1	42.7	24.59	329.97	42.3	50.07	48.54	32.71	384.33

Table B.117 Experimental Data A-D-GA-P3-S-PVC-10-015-06.39-13.6-080 55 µm droplets

z/d	Twall [°C]		Tbulk [°C]	h [W/m^{2}K]	z/d	Twall [°C]		Tbulk [°C]	h [W/m^{2}K]
2.7	33.0	29.4	13.85	369.17	25.0	45.8	43.3	25.93	343.32
5.2	37.1	34.7	15.13	308.28	27.4	46.5	43.9	27.03	351.95
7.6	39.3	37.2	16.55	294.96	29.9	47.9	44.6	28.08	351.60
10.1	40.9	38.6	18.08	294.84	32.4	48.3	44.8	29.15	367.34
15.1	43.0	40.5	20.93	306.80	34.9	48.8	45.3	30.17	378.38
17.5	43.8	41.2	22.25	315.85	37.3	49.1	46.1	31.11	387.64
20.0	44.4	41.9	23.58	326.83	39.8	50.8	47.2	32.01	376.37
22.5	45.2	42.6	24.78	335.11	42.3	51.97	49.32	32.84	358.99

Table B.118 Experimental Data A-D-GA-P3-S-PVC-10-015-06.38-13.6-077 61 µm droplets

z/d	Twall [°C]		Tbulk [°C]	h [W/m^{2}K]	z/d	Twall [°C]		Tbulk [°C]	h [W/m^{2}K]
2.7	33.0	29.4	13.74	364.48	25.0	46.6	43.4	25.89	333.69
5.2	36.9	34.4	15.12	310.54	27.4	48.4	44.1	26.93	329.66
7.6	39.2	37.1	16.63	296.77	29.9	50.0	44.9	27.99	327.62
10.1	40.8	38.6	18.06	295.01	32.4	52.1	44.9	29.01	326.76
15.1	42.9	40.5	20.9	306.93	34.9	55.8	45.7	29.94	306.12
17.5	43.7	41.0	22.22	316.56	37.3	61.6	49.6	30.69	255.84
20.0	44.5	41.7	23.55	326.39	39.8	67.6	52.2	31.47	224.28
22.5	45.9	42.6	24.68	325.84	42.3	72.12	53.83	32.27	207.69

Table B.119 Experimental Data A-D-GA-P3-S-PVC-10-015-06.28-13.5-072 67 µm droplets

z/d	Twall [°C]		Tbulk [°C]	h [W/m^{2}K]	z/d	Twall [°C]		Tbulk [°C]	h [W/m^{2}K]
2.7	34.2	27.8	13.65	361.58	25.0	65.6	54.0	24.69	179.01
5.2	37.3	32.0	15.02	319.88	27.4	73.0	63.1	25.4	147.21
7.6	39.4	33.5	16.51	314.79	29.9	76.5	57.1	26.64	156.46
10.1	41.2	34.2	18.02	319.72	32.4	70.9	62.1	27.77	162.20
15.1	44.0	35.4	20.82	332.60	34.9	86.2	63.3	28.41	135.51
17.5	48.0	37.2	21.98	305.15	37.3	91.8	62.5	29.37	131.50
20.0	53.4	42.3	22.96	252.89	39.8	94.1	68.0	30.19	123.47
22.5	61.5	52.1	23.63	189.46	42.3	99.61	66.16	31.08	121.27

Table B.120 Experimental Data A-D-GA-P3-S-PVC-15-010-08.94-11.9-097 20 µm droplets

z/d	Twall [°C]		Tbulk [°C]	h [W/m^{2}K]	z/d	Twall [°C]		Tbulk [°C]	h [W/m^{2}K]
2.7	31.0	29.6	12.52	503.22	25.0	46.4	44.4	24.87	435.67
5.2	35.4	34.0	14.02	431.56	27.4	46.0	45.1	25.98	457.02
7.6	37.9	36.8	15.51	409.26	29.9	47.0	45.8	27.04	461.60
10.1	39.9	38.8	17	399.81	32.4	47.8	46.4	28.05	469.44
15.1	42.2	41.2	19.86	409.14	34.9	48.4	47.1	29.06	478.80
17.5	43.0	42.1	21.19	418.41	37.3	49.9	48.1	30	470.26
20.0	44.2	42.8	22.46	424.74	39.8	50.4	50.1	30.88	461.44
22.5	45.0	43.6	23.67	433.39	42.3	51.41	52.80	31.73	438.55

Table B.121 Experimental Data A-D-GA-P3-S-PVC-15-010-08.94-12.2-089 30 μm droplets

z/d	Twall [°C]		Tbulk [°C]	h [W/m^{2}K]	z/d	Twall [°C]		Tbulk [°C]	h [W/m^{2}K]
2.7	31.4	28.0	12.88	530.41	25.0	45.3	44.2	25.07	454.55
5.2	35.7	32.4	14.36	453.83	27.4	45.9	45.0	26.17	463.60
7.6	38.1	35.5	15.84	427.16	29.9	46.6	45.8	27.22	471.51
10.1	40.0	38.0	17.31	411.91	32.4	47.0	46.4	28.27	485.13
15.1	42.3	40.8	20.1	416.83	34.9	47.6	46.9	29.24	495.64
17.5	43.2	41.8	21.42	424.60	37.3	47.8	47.5	30.2	512.34
20.0	43.8	42.6	22.68	436.01	39.8	48.5	48.2	31.1	518.49
22.5	44.5	43.4	23.92	446.18	42.3	48.63	48.72	31.99	535.80

Table B.122 Experimental Data A-D-GA-P3-S-PVC-15-010-08.87-12.3-078 42 μm droplets

z/d	Twall [°C]		Tbulk [°C]	h [W/m^{2}K]	z/d	Twall [°C]		Tbulk [°C]	h [W/m^{2}K]
2.7	31.4	28.9	12.9	513.69	25.0	45.0	44.0	25.07	457.24
5.2	35.7	33.8	14.37	435.47	27.4	45.6	44.7	26.17	467.52
7.6	38.1	36.5	15.84	414.14	29.9	46.4	45.5	27.25	473.73
10.1	40.0	38.3	17.31	406.48	32.4	47.5	46.1	28.25	478.42
15.1	42.3	40.8	20.13	414.14	34.9	47.6	46.6	29.22	496.21
17.5	43.2	41.7	21.44	422.57	37.3	47.9	47.1	30.18	512.99
20.0	43.9	42.5	22.69	432.82	39.8	48.4	47.6	31.1	525.16
22.5	44.6	43.3	23.93	443.73	42.3	48.58	47.91	31.96	544.80

Table B.123 Experimental Data A-D-GA-P3-S-PVC-15-010-08.93-12.5-071 56 μm droplets

z/d	Twall [°C]		Tbulk [°C]	h [W/m^{2}K]	z/d	Twall [°C]		Tbulk [°C]	h [W/m^{2}K]
2.7	33.8	30.2	13.05	471.76	25.0	45.4	43.9	25.31	462.53
5.2	37.2	34.8	14.53	416.87	27.4	46.2	44.6	26.4	469.74
7.6	39.1	37.1	16.01	404.94	29.9	46.8	45.5	27.45	477.69
10.1	40.6	38.7	17.53	404.31	32.4	47.3	46.2	28.49	489.69
15.1	42.6	40.8	20.36	418.34	34.9	48.2	46.9	29.46	494.11
17.5	43.4	41.6	21.68	428.99	37.3	50.2	47.7	30.39	482.25
20.0	44.0	42.3	22.93	441.44	39.8	54.1	48.7	31.23	443.32
22.5	44.9	43.5	24.13	445.19	42.3	58.36	50.42	32.04	399.71

Table B.124 Experimental Data A-D-GA-P3-S-PVC-15-015-08.91-13.0-081 44 μm droplets

z/d	Twall [°C]		Tbulk [°C]	h [W/m^{2}K]	z/d	Twall [°C]		Tbulk [°C]	h [W/m^{2}K]
2.7	29.5	26.5	13.3	605.21	25.0	44.7	42.2	24.68	475.08
5.2	34.2	31.5	14.48	485.01	27.4	45.4	43.1	25.75	481.57
7.6	37.1	34.8	15.82	443.51	29.9	46.0	43.9	26.84	492.25
10.1	39.1	36.7	17.19	430.41	32.4	46.4	44.6	27.83	503.59
15.1	41.8	38.8	19.83	435.90	34.9	46.8	45.3	28.83	517.86
17.5	42.8	39.7	21.11	443.11	37.3	47.1	45.9	29.75	531.66
20.0	43.4	40.8	22.33	450.95	39.8	47.9	46.5	30.63	537.76
22.5	44.2	41.6	23.56	459.98	42.3	47.14	46.98	31.57	575.32

Table B.125 Experimental Data A-D-GA-P3-S-PVC-15-015-08.89-12.8-071 69 μm droplets

z/d	Twall [°C]		Tbulk [°C]	h [W/m^{2}K]	z/d	Twall [°C]		Tbulk [°C]	h [W/m^{2}K]
2.7	27.3	23.7	13.35	730.40	25.0	49.4	58.4	23.85	296.22
5.2	32.8	27.7	14.52	564.26	27.4	52.1	53.3	25.09	322.05
7.6	37.0	30.7	15.84	494.42	29.9	53.1	59.6	25.96	292.15
10.1	39.4	32.9	17.11	466.89	32.4	58.1	63.8	26.81	260.64
15.1	42.8	36.4	19.74	447.52	34.9	59.2	65.7	27.75	255.93
17.5	44.3	38.8	20.94	430.85	37.3	62.2	67.2	28.65	246.66
20.0	46.5	42.7	22.01	394.03	39.8	64.0	70.8	29.48	234.31
22.5	47.3	47.6	23.05	364.22	42.3	66.81	72.56	30.33	225.85

Table B.126 Experimental Data A-D-GA-P3-S-PVC-15-015-03.86-13.8-086

z/d	Twall [°C]		Tbulk [°C]	h [W/m^{2}K]	z/d	Twall [°C]		Tbulk [°C]	h [W/m^{2}K]
2.7	20.9	18.6	13.94	666.09	25.0	31.1	29.6	18.96	339.26
5.2	23.6	20.8	14.46	501.29	27.4	31.7	30.4	19.56	336.73
7.6	25.4	22.7	14.98	425.00	29.9	32.2	31.1	20.08	334.14
10.1	27.0	24.3	15.48	379.97	32.4	32.6	31.6	20.67	338.81
15.1	28.9	26.6	16.66	347.11	34.9	32.8	32.1	21.16	341.24
17.5	29.6	27.5	17.22	339.79	37.3	33.2	32.4	21.73	349.27
20.0	30.2	28.3	17.87	340.02	39.8	33.4	32.8	22.28	356.18
22.5	30.8	29.0	18.42	336.80	42.3	33.67	33.21	22.75	361.21

Table B.127 Experimental Data A-D-GA-P3-S-PVC-15-015-06.37-13.2-087

z/d	Twall [°C]		Tbulk [°C]	h [W/m^{2}K]	z/d	Twall [°C]		Tbulk [°C]	h [W/m^{2}K]
2.7	24.1	22.0	13.56	675.17	25.0	38.5	36.7	21.76	403.12
5.2	27.8	25.5	14.36	518.90	27.4	39.2	37.4	22.59	405.83
7.6	30.4	28.5	15.23	447.96	29.9	39.8	38.4	23.46	408.27
10.1	32.8	30.2	16.18	415.80	32.4	40.2	38.9	24.25	416.59
15.1	35.5	33.0	18.07	394.35	34.9	40.5	39.7	25.07	424.84
17.5	36.5	33.9	19.02	393.69	37.3	40.9	40.1	25.81	434.60
20.0	37.1	34.9	20.01	398.51	39.8	41.2	40.6	26.59	445.06
22.5	37.9	35.6	20.9	402.33	42.3	41.49	41.06	27.28	455.50

Table B.128 Experimental Data A-D-GA-P3-S-PVC-15-015-08.89-13.1-091

z/d	Twall [°C]		Tbulk [°C]	h [W/m^{2}K]	z/d	Twall [°C]		Tbulk [°C]	h [W/m^{2}K]
2.7	29.0	26.7	13.46	617.60	25.0	44.3	43.0	24.7	469.16
5.2	33.6	31.7	14.62	493.17	27.4	45.0	43.8	25.76	476.43
7.6	36.5	34.6	15.94	453.67	29.9	45.6	44.6	26.78	485.05
10.1	38.6	36.7	17.29	436.48	32.4	46.0	45.3	27.82	498.69
15.1	41.3	39.5	19.9	433.24	34.9	46.2	45.9	28.82	515.60
17.5	42.3	40.5	21.16	439.14	37.3	46.7	46.4	29.73	529.37
20.0	43.1	41.4	22.37	447.53	39.8	47.1	47.0	30.65	542.11
22.5	43.9	42.3	23.53	454.64	42.3	47.24	47.34	31.5	563.06

Table B.129 Experimental Data A-D-GA-P3-S-PVC-15-015-11.44-13.2-091 aligned

z/d	Twall [°C]		Tbulk [°C]	h [W/m^{2}K]	z/d	Twall [°C]		Tbulk [°C]	h [W/m^{2}K]
2.7	32.8	31.5	13.52	615.19	25.0	49.5	48.2	27.58	537.16
5.2	38.1	37.1	15.15	509.85	27.4	50.9	49.0	28.76	539.35
7.6	40.8	40.4	16.88	481.81	29.9	51.5	50.0	29.99	551.38
10.1	43.3	42.3	18.61	472.65	32.4	52.0	50.7	31.12	565.32
15.1	46.3	44.7	21.86	483.32	34.9	52.5	51.7	32.2	574.09
17.5	47.4	45.6	23.39	494.34	37.3	53.1	52.3	33.27	588.61
20.0	48.1	46.5	24.84	509.22	39.8	53.5	53.4	34.26	595.77
22.5	49.0	47.5	26.21	519.33	42.3	53.69	54.26	35.21	609.57

Table B.130 Experimental Data A-D-GA-P3-S-PVC-15-015-14.03-13.1-091

z/d	Twall [°C]		Tbulk [°C]	h [W/m^{2}K]	z/d	Twall [°C]		Tbulk [°C]	h [W/m^{2}K]
2.7	36.2	35.0	13.62	639.25	25.0	55.2	53.1	30.08	583.41
5.2	41.9	40.7	15.62	546.92	27.4	56.8	54.1	31.46	585.21
7.6	45.0	44.1	17.77	524.17	29.9	60.9	55.6	32.69	549.53
10.1	45.8	46.2	19.86	536.40	32.4	64.6	64.0	33.74	459.17
15.1	50.4	48.6	23.69	544.49	34.9	67.2	70.4	34.83	413.37
17.5	52.5	49.6	25.39	546.72	37.3	72.8	67.9	35.95	408.32
20.0	53.3	50.6	27.05	563.25	39.8	75.9	70.8	36.98	385.82
22.5	55.3	52.0	28.61	560.65	42.3	72.87	74.02	38.07	396.70

Table B.131 Experimental Data A-D-GA-P3-S-PVC-15-015-14.61-13.1-089

z/d	Twall [°C]		Tbulk [°C]	h [W/m^{2}K]	z/d	Twall [°C]		Tbulk [°C]	h [W/m^{2}K]
2.7	36.7	37.3	13.61	623.96	25.0	62.1	67.7	30.19	420.76
5.2	41.3	42.6	15.81	559.02	27.4	66.7	74.1	31.46	374.84
7.6	45.5	45.6	18.04	530.76	29.9	69.7	78.0	32.71	355.10
10.1	48.2	46.3	20.2	540.37	32.4	74.2	81.6	33.91	332.05
15.1	51.8	50.1	24.08	543.45	34.9	76.7	89.1	35.01	305.24
17.5	53.2	53.6	25.84	529.63	37.3	77.5	93.4	36.18	296.55
20.0	55.4	55.2	27.48	524.48	39.8	77.6	94.4	37.33	300.24
22.5	57.7	62.4	28.87	468.61	42.3	79.95	96.62	38.4	292.80

Table B.132 Experimental Data A-D-GA-P3-S-PVC-32-019-12.35-12.7-100

z/d	Twall [°C]		Tbulk [°C]	h [W/m^{2}K]	z/d	Twall [°C]		Tbulk [°C]	h [W/m^{2}K]
2.7	21.0	21.7	12.67	1423.08	25.0	35.0	35.6	19.78	795.57
5.2	23.8	24.7	13.36	1135.00	27.4	35.9	36.4	20.53	790.40
7.6	26.0	27.0	14.15	998.18	29.9	36.7	37.2	21.27	789.02
10.1	28.3	29.2	14.93	894.26	32.4	37.2	37.7	22.08	801.95
15.1	31.3	32.0	16.55	818.25	34.9	37.7	38.3	22.77	810.95
17.5	32.5	33.0	17.39	804.46	37.3	38.2	38.7	23.54	828.73
20.0	33.3	33.9	18.21	804.19	39.8	38.6	39.2	24.29	846.90
22.5	34.3	34.8	19	795.40	42.3	38.92	39.54	24.93	863.63

Table B.133 Experimental Data A-D-GA-P3-S-PVC-32-019-25.38-12.7-100

z/d	Twall [°C]		Tbulk [°C]	h [W/m^{2}K]	z/d	Twall [°C]		Tbulk [°C]	h [W/m^{2}K]
2.7	30.2	30.6	12.55	1423.20	25.0	51.1	50.9	26.53	1035.93
5.2	35.5	36.2	14.1	1166.62	27.4	52.0	51.7	27.82	1055.22
7.6	39.3	40.2	15.71	1055.49	29.9	52.7	52.6	29.06	1076.89
10.1	42.8	43.3	17.35	987.66	32.4	53.2	53.2	30.3	1108.58
15.1	46.9	46.9	20.61	965.63	34.9	53.6	53.8	31.43	1139.12
17.5	48.4	48.1	22.21	975.05	37.3	54.1	54.2	32.56	1175.56
20.0	49.3	49.1	23.73	996.23	39.8	54.4	54.8	33.59	1207.71
22.5	50.4	50.1	25.16	1012.17	42.3	54.77	55.07	34.62	1250.14

Table B.134 Experimental Data A-D-GA-P3-S-PVC-32-019-38.25-12.8-100

z/d	Twall [°C]		Tbulk [°C]	h [W/m^{2}K]	z/d	Twall [°C]		Tbulk [°C]	h [W/m^{2}K]
2.7	39.0	39.3	12.74	1447.87	25.0	61.3	60.7	32.36	1335.19
5.2	45.7	46.7	15.12	1231.13	27.4	62.1	61.4	34.01	1381.04
7.6	49.9	51.0	17.69	1167.36	29.9	62.6	62.1	35.5	1423.37
10.1	53.5	53.8	20.17	1141.00	32.4	63.0	62.7	36.9	1474.28
15.1	57.4	57.0	24.76	1178.68	34.9	63.2	63.3	38.26	1528.99
17.5	58.8	58.1	26.88	1212.94	37.3	63.7	63.6	39.55	1587.35
20.0	59.6	59.0	28.84	1256.39	39.8	64.0	64.1	40.73	1639.99
22.5	60.6	59.8	30.67	1295.05	42.3	64.24	64.30	41.89	1709.34

Table B.135 Experimental Data A-D-GA-P3-S-PVC-32-019-51.11-12.9-100

z/d	Twall [°C]		Tbulk [°C]	h [W/m^{2}K]	z/d	Twall [°C]		Tbulk [°C]	h [W/m^{2}K]
2.7	47.1	47.2	12.97	1495.00	25.0	68.4	67.4	37.27	1668.28
5.2	54.3	55.1	16.27	1330.77	27.4	69.0	67.9	39.02	1735.09
7.6	58.3	59.1	19.71	1311.25	29.9	69.4	68.6	40.68	1802.79
10.1	61.6	61.5	22.89	1322.60	32.4	69.7	69.1	42.19	1877.10
15.1	65.1	64.1	28.56	1418.02	34.9	69.8	69.6	43.64	1958.08
17.5	66.2	65.1	31.03	1476.43	37.3	70.2	69.8	44.99	2041.53
20.0	67.0	65.9	33.27	1541.02	39.8	70.5	70.3	46.24	2118.41
22.5	67.9	66.6	35.38	1605.09	42.3	70.63	70.35	47.44	2217.38

Table B.136 Experimental Data A-D-GA-P3-S-PVC-15-015-03.86-12.1-082

z/d	Twall [°C]		Tbulk [°C]	h [W/m^{2}K]	z/d	Twall [°C]		Tbulk [°C]	h [W/m^{2}K]
2.7	20.6	19.5	12.43	508.68	25.0	30.6	29.7	18.21	322.06
5.2	23.2	22.2	13	398.85	27.4	31.2	30.4	18.79	322.18
7.6	24.9	24.1	13.63	356.69	29.9	31.7	31.0	19.37	321.67
10.1	26.3	25.3	14.31	336.04	32.4	32.1	31.4	19.98	327.60
15.1	28.3	27.2	15.62	318.61	34.9	32.4	32.0	20.58	332.95
17.5	29.0	27.9	16.26	316.75	37.3	32.7	32.3	21.11	339.86
20.0	29.5	28.6	16.95	319.34	39.8	32.9	32.7	21.69	347.60
22.5	30.2	29.1	17.56	319.32	42.3	33.22	33.00	22.25	355.98

Table B.137 Experimental Data A-D-GA-P3-S-PVC-15-010-05.13-12.2-084

z/d	Twall [°C]		Tbulk [°C]	h [W/m²K]	z/d	Twall [°C]		Tbulk [°C]	h [W/m²K]
2.7	23.1	20.7	12.67	555.22	25.0	35.1	33.8	20.08	357.12
5.2	26.4	23.7	13.48	442.14	27.4	35.7	34.6	20.87	359.63
7.6	28.5	26.2	14.27	391.80	29.9	36.2	35.3	21.59	361.70
10.1	30.3	28.1	15.18	365.04	32.4	36.6	35.8	22.3	367.99
15.1	32.6	30.7	16.85	346.78	34.9	36.9	36.4	23.03	376.57
17.5	33.4	31.6	17.68	345.70	37.3	37.2	36.8	23.73	386.97
20.0	34.1	32.4	18.48	347.44	39.8	37.5	37.2	24.38	394.47
22.5	34.7	33.2	19.32	350.65	42.3	37.76	37.61	25.05	405.91

Table B.138 Experimental Data A-D-GA-P3-S-PVC-15-010-06.36-12.1-082

z/d	Twall [°C]		Tbulk [°C]	h [W/m²K]	z/d	Twall [°C]		Tbulk [°C]	h [W/m²K]
2.7	24.5	22.9	12.68	576.63	25.0	38.5	37.3	21.73	392.63
5.2	28.5	26.5	13.67	460.32	27.4	39.2	38.0	22.61	397.50
7.6	31.2	29.7	14.69	404.43	29.9	39.8	38.9	23.45	400.20
10.1	32.9	31.5	15.75	386.33	32.4	40.2	39.4	24.32	410.89
15.1	35.5	34.1	17.87	375.47	34.9	40.5	40.0	25.11	419.29
17.5	36.5	35.1	18.87	376.46	37.3	40.8	40.4	25.92	432.09
20.0	37.3	35.9	19.84	378.88	39.8	41.2	41.0	26.71	441.99
22.5	38.1	36.6	20.78	384.52	42.3	41.40	41.32	27.43	456.62

Table B.139 Experimental Data A-D-GA-P3-S-PVC-15-010-07.66-12.1-082

z/d	Twall [°C]		Tbulk [°C]	h [W/m²K]	z/d	Twall [°C]		Tbulk [°C]	h [W/m²K]
2.7	28.4	24.6	12.68	553.91	25.0	42.2	40.6	23.38	425.74
5.2	32.5	28.7	13.92	459.25	27.4	43.0	41.4	24.38	430.25
7.6	34.9	31.8	15.18	421.35	29.9	43.6	42.2	25.38	437.46
10.1	36.8	34.1	16.46	402.59	32.4	43.8	42.8	26.31	449.59
15.1	39.4	36.9	18.91	398.31	34.9	44.4	43.4	27.24	459.81
17.5	40.3	38.0	20.08	401.26	37.3	44.8	43.9	28.1	471.56
20.0	41.0	38.9	21.26	408.91	39.8	45.4	44.5	28.97	477.60
22.5	41.7	39.9	22.34	414.96	42.3	45.18	46.65	29.77	474.19

Table B.140 Experimental Data A-D-GA-P3-S-PVC-15-010-08.94-12.1-082

z/d	Twall [°C]		Tbulk [°C]	h [W/m²K]	z/d	Twall [°C]		Tbulk [°C]	h [W/m²K]
2.7	31.6	26.2	12.86	558.39	25.0	46.4	43.4	25.01	448.95
5.2	35.6	30.8	14.28	472.55	27.4	47.5	44.2	26.12	452.54
7.6	38.1	34.1	15.76	440.04	29.9	48.8	45.2	27.17	451.61
10.1	40.2	36.3	17.24	425.77	32.4	50.2	46.2	28.15	446.09
15.1	42.5	39.4	20.08	428.53	34.9	51.8	46.9	29.13	441.84
17.5	43.9	40.5	21.35	428.96	37.3	52.7	47.9	30.07	441.66
20.0	45.0	41.7	22.62	431.30	39.8	55.3	48.9	30.94	421.63
22.5	45.6	42.6	23.86	442.53	42.3	56.47	49.65	31.84	421.29

Table B.141 Experimental Data A-D-GA-P3-S-PVC-15-010-10.16-12.1-084

z/d	Twall [°C]		Tbulk [°C]	h [W/m^{2}K]	z/d	Twall [°C]		Tbulk [°C]	h [W/m^{2}K]
2.7	32.2	30.9	12.9	545.11	25.0	52.4	48.2	26.35	424.27
5.2	36.5	35.4	14.62	475.68	27.4	54.0	51.8	27.51	400.51
7.6	39.8	36.7	16.31	463.71	29.9	57.0	59.5	28.49	341.54
10.1	42.1	38.5	17.97	454.97	32.4	60.0	63.6	29.53	315.21
15.1	45.9	41.9	21.07	445.03	34.9	62.6	66.3	30.54	299.82
17.5	47.5	43.0	22.48	446.37	37.3	70.4	75.7	31.34	243.75
20.0	49.0	43.6	23.86	452.61	39.8	63.7	97.2	32.17	210.47
22.5	50.3	45.4	25.17	447.68	42.3	84.80	79.98	33.12	206.24

Table B.142 Experimental Data A-D-GA-P3-S-PVC-15-010-10.82-12.0-084

z/d	Twall [°C]		Tbulk [°C]	h [W/m^{2}K]	z/d	Twall [°C]		Tbulk [°C]	h [W/m^{2}K]
2.7	33.4	30.9	12.88	561.30	25.0	65.8	48.4	26.85	357.76
5.2	37.1	36.5	14.72	489.79	27.4	70.4	50.2	28.04	335.16
7.6	41.1	38.7	16.53	462.56	29.9	74.5	57.6	29.08	292.51
10.1	42.7	40.4	18.28	464.21	32.4	83.6	64.2	30.05	246.47
15.1	46.4	43.2	21.55	465.49	34.9	86.4	63.8	31.14	245.98
17.5	49.7	44.3	22.99	450.73	37.3	91.8	75.6	32.02	209.37
20.0	51.4	45.5	24.43	450.06	39.8	91.6	96.4	32.81	176.68
22.5	59.8	47.0	25.65	389.84	42.3	90.55	99.55	33.82	176.68

Table B.143 Experimental Data A-D-GA-P3-S-PVC-15-005-03.87-11.1-070

z/d	Twall [°C]		Tbulk [°C]	h [W/m^{2}K]	z/d	Twall [°C]		Tbulk [°C]	h [W/m^{2}K]
2.7	22.6	21.5	11.62	370.01	25.0	31.5	30.5	18.1	300.41
5.2	25.0	24.1	12.35	317.54	27.4	32.1	31.1	18.74	300.71
7.6	26.5	25.6	13.12	299.62	29.9	32.5	32.2	19.37	298.88
10.1	27.8	26.7	13.88	290.16	32.4	33.1	32.1	20	307.08
15.1	29.5	28.2	15.34	286.83	34.9	33.1	32.9	20.62	313.05
17.5	30.1	28.8	16.04	289.02	37.3	33.7	33.1	21.2	317.78
20.0	30.7	29.4	16.76	291.08	39.8	34.2	33.7	21.79	318.59
22.5	31.4	29.9	17.43	292.07	42.3	34.72	34.03	22.34	321.65

Table B.144 Experimental Data A-D-GA-P3-S-PVC-15-005-05.10-11.1-069

z/d	Twall [°C]		Tbulk [°C]	h [W/m^{2}K]	z/d	Twall [°C]		Tbulk [°C]	h [W/m^{2}K]
2.7	25.8	24.4	11.77	382.52	25.0	35.6	34.6	20.06	337.95
5.2	28.4	27.4	12.76	336.72	27.4	36.3	35.2	20.85	341.29
7.6	30.2	29.2	13.74	319.25	29.9	36.6	36.2	21.62	344.11
10.1	31.6	30.5	14.73	312.59	32.4	37.5	36.6	22.38	347.72
15.1	33.5	32.2	16.6	314.38	34.9	37.7	37.2	23.1	355.59
17.5	34.2	32.8	17.5	318.94	37.3	38.2	37.7	23.82	361.02
20.0	34.9	33.4	18.39	323.62	39.8	39.9	38.1	24.51	352.05
22.5	35.5	34.0	19.23	328.32	42.3	40.67	38.41	25.17	354.61

Table B.145 Experimental Data A-D-GA-P3-S-PVC-15-005-06.36-11.1-069

z/d	Twall [°C]		Tbulk [°C]	h [W/m^{2}K]	z/d	Twall [°C]		Tbulk [°C]	h [W/m^{2}K]
2.7	28.5	25.6	12.05	424.13	25.0	42.7	39.2	21.96	334.73
5.2	31.6	29.4	13.26	368.97	27.4	44.4	40.9	22.86	321.69
7.6	33.5	31.7	14.48	350.89	29.9	45.5	42.2	23.75	316.47
10.1	35.4	33.2	15.65	341.37	32.4	48.1	43.9	24.6	297.19
15.1	37.4	35.4	17.92	344.64	34.9	50.5	49.2	25.38	260.22
17.5	38.5	36.3	18.99	345.43	37.3	53.6	54.7	26.15	227.32
20.0	39.1	37.1	20.04	352.79	39.8	57.3	57.1	26.9	209.88
22.5	40.7	38.2	21	345.26	42.3	59.68	64.49	27.63	184.62

Table B.146 Experimental Data A-D-GA-P3-S-PVC-15-005-08.86-11.0-069

z/d	Twall [°C]		Tbulk [°C]	h [W/m^{2}K]	z/d	Twall [°C]		Tbulk [°C]	h [W/m^{2}K]
2.7	32.7	31.0	12.39	455.55	25.0	73.3	56.7	25.09	222.13
5.2	36.7	35.2	14.1	405.91	27.4	78.3	59.4	26.2	207.79
7.6	38.9	37.7	15.74	392.60	29.9	83.7	58.3	27.3	202.77
10.1	41.7	39.2	17.32	382.86	32.4	85.0	60.6	28.35	199.57
15.1	48.9	41.8	20.22	352.82	34.9	87.3	69.8	29.31	179.89
17.5	56.6	44.0	21.51	307.56	37.3	97.9	74.1	30.24	159.04
20.0	59.4	46.9	22.79	291.90	39.8	105.6	77.3	31.14	146.93
22.5	69.3	52.9	23.92	238.44	42.3	105.97	90.17	32.02	134.20

Table B.147 Experimental Data A-D-GA-P3-S-PVC-10-015-07.61-13.2-092

z/d	Twall [°C]		Tbulk [°C]	h [W/m^{2}K]	z/d	Twall [°C]		Tbulk [°C]	h [W/m^{2}K]
2.7	34.7	31.1	13.59	394.06	25.0	50.3	46.3	27.6	367.72
5.2	39.4	35.4	15.21	342.72	27.4	50.7	47.2	28.89	379.16
7.6	42.1	38.6	16.94	325.14	29.9	52.0	48.1	30.06	381.20
10.1	43.9	40.6	18.67	322.77	32.4	54.6	50.2	31.09	356.86
15.1	46.6	43.3	21.98	331.40	34.9	58.2	51.9	32.13	331.68
17.5	47.2	44.2	23.5	343.37	37.3	62.0	54.5	33.04	301.84
20.0	47.9	44.9	24.94	355.04	39.8	66.3	58.9	33.92	265.27
22.5	49.8	45.8	26.31	354.34	42.3	72.57	62.62	34.74	231.58

Table B.148 Experimental Data A-D-GA-P3-S-PVC-10-015-05.08-13.3-091

z/d	Twall [°C]		Tbulk [°C]	h [W/m^{2}K]	z/d	Twall [°C]		Tbulk [°C]	h [W/m^{2}K]
2.7	29.0	24.0	13.47	389.98	25.0	41.3	38.2	23.41	310.78
5.2	32.8	28.4	14.5	315.60	27.4	41.9	39.0	24.36	315.70
7.6	35.1	31.0	15.69	292.89	29.9	42.5	39.8	25.34	322.20
10.1	36.8	32.7	16.84	283.70	32.4	42.9	40.6	26.22	327.93
15.1	38.9	35.4	19.17	282.44	34.9	43.2	41.1	27.13	337.71
17.5	39.7	36.2	20.27	287.79	37.3	43.7	41.8	27.95	343.47
20.0	40.3	36.8	21.33	295.01	39.8	44.0	42.4	28.81	353.07
22.5	40.9	37.4	22.43	304.16	42.3	44.23	42.81	29.58	364.59

Table B.149 Experimental Data A-D-GA-P3-S-PVC-10-015-03.82-13.3-091

z/d	Twall [°C]		Tbulk [°C]	h [W/m^{2}K]	z/d	Twall [°C]		Tbulk [°C]	h [W/m^{2}K]
2.7	24.6	20.9	13.51	412.58	25.0	36.3	33.1	21.08	279.58
5.2	28.1	24.1	14.28	322.76	27.4	36.8	34.0	21.84	281.04
7.6	30.2	26.3	15.14	291.53	29.9	37.4	34.8	22.65	284.27
10.1	31.9	27.9	15.97	274.05	32.4	37.8	35.5	23.37	288.46
15.1	34.0	30.0	17.75	268.33	34.9	38.1	36.0	24.13	295.66
17.5	34.7	30.8	18.6	269.97	37.3	38.4	36.6	24.81	300.55
20.0	35.3	31.5	19.42	272.93	39.8	38.7	37.1	25.54	307.77
22.5	35.9	32.4	20.31	275.90	42.3	39.02	37.68	26.18	313.62

Table B.150 Experimental Data A-D-GA-P3-S-PVC-10-015-06.38-13.4-092

z/d	Twall [°C]		Tbulk [°C]	h [W/m^{2}K]	z/d	Twall [°C]		Tbulk [°C]	h [W/m^{2}K]
2.7	32.1	27.6	13.63	392.66	25.0	45.6	42.6	25.74	347.14
5.2	36.5	32.8	14.92	323.32	27.4	46.3	43.3	26.85	355.58
7.6	38.9	35.8	16.34	303.22	29.9	47.3	43.9	27.91	360.52
10.1	40.7	37.8	17.79	296.89	32.4	47.8	44.7	28.92	368.11
15.1	42.9	39.6	20.65	309.20	34.9	48.1	45.6	29.95	378.21
17.5	43.7	40.4	22.05	318.65	37.3	49.1	46.7	30.89	375.28
20.0	44.3	41.1	23.32	328.70	39.8	50.3	47.8	31.8	370.31
22.5	45.1	41.8	24.53	336.80	42.3	51.36	48.72	32.67	367.17

Table B.151 Experimental Data A-D-GA-P3-S-PVC-05-015-03.16-13.7-070

z/d	Twall [°C]		Tbulk [°C]	h [W/m^{2}K]	z/d	Twall [°C]		Tbulk [°C]	h [W/m^{2}K]
2.7	31.2	25.4	14.08	221.39	25.0	47.4	39.4	25.83	179.44
5.2	35.1	29.2	15.51	190.03	27.4	50.5	42.3	26.8	161.34
7.6	37.3	31.0	16.98	184.04	29.9	53.7	43.9	27.79	149.95
10.1	38.9	32.1	18.37	183.96	32.4	56.0	45.8	28.75	142.44
15.1	41.5	34.3	21.13	188.20	34.9	60.7	48.1	29.57	127.30
17.5	42.8	35.9	22.35	185.69	37.3	66.8	50.9	30.37	110.83
20.0	44.1	36.8	23.58	187.07	39.8	71.3	53.3	31.2	101.57
22.5	46.0	38.4	24.76	181.05	42.3	73.40	54.64	32.04	98.72

Table B.152 Experimental Data A-D-GA-P3-S-PVC-05-015-02.52-13.6-074

z/d	Twall [°C]		Tbulk [°C]	h [W/m^{2}K]	z/d	Twall [°C]		Tbulk [°C]	h [W/m^{2}K]
2.7	27.9	23.8	13.94	210.72	25.0	39.8	35.5	23.71	180.50
5.2	31.4	27.0	15.04	177.26	27.4	40.7	36.7	24.64	179.14
7.6	33.5	28.9	16.19	167.27	29.9	41.3	37.4	25.53	182.02
10.1	35.1	30.2	17.31	163.94	32.4	42.4	38.4	26.4	180.16
15.1	37.0	32.0	19.58	168.23	34.9	43.3	39.0	27.3	181.45
17.5	37.7	32.9	20.73	172.45	37.3	45.3	40.1	28.05	171.37
20.0	38.3	33.9	21.76	175.74	39.8	48.4	41.6	28.79	154.96
22.5	39.1	35.0	22.75	175.98	42.3	51.82	42.92	29.46	140.47

Table B.153 Experimental Data A-D-GA-P3-S-PVC-15-015-08.80-24.5-100 Twater = 95 °C

z/d	Twall [°C]		Tbulk [°C]	h [W/m²K]	z/d	Twall [°C]		Tbulk [°C]	h [W/m²K]
2.7	37.2	34.6	25.1	816.65	25.0	48.4	47.9	33.47	599.23
5.2	40.8	38.9	26.02	636.05	27.4	48.9	48.5	34.31	612.41
7.6	42.8	41.5	26.97	579.74	29.9	49.3	49.2	35.08	621.22
10.1	44.3	43.0	28	560.53	32.4	49.7	49.5	35.86	640.61
15.1	46.2	45.2	29.95	558.49	34.9	49.9	50.0	36.62	658.90
17.5	46.9	45.9	30.86	565.41	37.3	50.2	50.4	37.32	678.07
20.0	47.5	46.6	31.79	577.96	39.8	50.8	50.8	38.03	690.92
22.5	48.0	47.1	32.65	590.06	42.3	50.96	50.97	38.72	718.73

Table B.154 Experimental Data A-D-GA-P3-S-PVC-15-015-08.84-20.4-100 Twater = 55 °C

z/d	Twall [°C]		Tbulk [°C]	h [W/m²K]	z/d	Twall [°C]		Tbulk [°C]	h [W/m²K]
2.7	33.3	29.8	20.99	837.07	25.0	47.0	45.8	30.28	547.99
5.2	37.6	34.4	22.03	633.27	27.4	47.6	46.5	31.17	555.25
7.6	40.0	37.6	23.1	562.46	29.9	48.2	47.4	32.07	562.88
10.1	42.0	39.6	24.19	532.59	32.4	48.6	47.9	32.9	577.29
15.1	44.3	42.4	26.33	519.52	34.9	48.8	48.5	33.74	594.33
17.5	45.2	43.3	27.36	522.96	37.3	49.1	48.8	34.55	612.95
20.0	45.8	44.2	28.41	532.11	39.8	49.4	49.4	35.3	628.07
22.5	46.6	45.0	29.36	539.42	42.3	49.62	49.67	36.05	650.53

Table B.155 Experimental Data A-D-GA-P3-S-PVC-15-015-08.90-14.4-092 Twater = 22 °C

z/d	Twall [°C]		Tbulk [°C]	h [W/m²K]	z/d	Twall [°C]		Tbulk [°C]	h [W/m²K]
2.7	29.3	25.7	14.81	701.46	25.0	45.3	43.4	25.62	475.77
5.2	34.3	30.2	15.93	545.43	27.4	46.0	44.3	26.66	482.46
7.6	37.4	33.5	17.2	488.41	29.9	46.5	45.2	27.71	490.31
10.1	39.7	36.0	18.51	460.72	32.4	47.0	45.8	28.66	501.92
15.1	42.4	39.3	21.04	449.39	34.9	47.2	46.5	29.64	516.07
17.5	43.3	40.5	22.26	452.47	37.3	47.6	47.0	30.52	530.44
20.0	44.0	41.6	23.43	458.79	39.8	47.9	47.6	31.42	544.72
22.5	44.8	42.5	24.55	466.11	42.3	48.19	48.02	32.25	561.60

Table B.156 Experimental Data A-D-GA-P3-S-PVC-15-015-08.94-08.7-087 Twater = 2 °C

z/d	Twall [°C]		Tbulk [°C]	h [W/m²K]	z/d	Twall [°C]		Tbulk [°C]	h [W/m²K]
2.7	26.9	24.7	8.749	523.52	25.0	43.4	42.4	21.26	413.29
5.2	32.3	30.7	9.93	415.15	27.4	44.0	43.1	22.44	423.46
7.6	35.3	33.9	11.41	385.47	29.9	44.5	43.9	23.57	432.29
10.1	37.7	35.9	12.93	374.47	32.4	44.9	44.4	24.72	447.62
15.1	40.4	38.7	15.88	377.42	34.9	45.2	45.1	25.76	461.14
17.5	41.4	39.6	17.29	384.58	37.3	45.6	45.5	26.82	477.16
20.0	42.1	40.6	18.65	394.07	39.8	46.0	46.0	27.84	491.89
22.5	42.8	41.4	19.94	403.06	42.3	46.18	46.34	28.77	510.88

Table B.157 Experimental Data A-D-GA-P3-S-PVC-15-015-12.68-24.5-100 Twater = 95 °C

z/d	Twall [°C]		Tbulk [°C]	h [W/m²K]	z/d	Twall [°C]		Tbulk [°C]	h [W/m²K]
2.7	42.4	38.7	25.35	834.36	25.0	55.2	54.2	36.8	707.51
5.2	46.4	43.5	26.71	695.63	27.4	56.4	54.9	37.81	710.25
7.6	48.6	46.3	28.17	658.85	29.9	56.3	55.8	38.78	734.29
10.1	50.1	48.5	29.55	642.05	32.4	57.6	56.5	39.72	731.20
15.1	52.3	50.9	32.2	653.20	34.9	57.9	57.8	40.64	737.80
17.5	53.1	51.9	33.43	665.96	37.3	58.7	58.1	41.5	750.29
20.0	53.7	52.6	34.59	683.19	39.8	63.0	60.4	42.28	653.66
22.5	54.6	53.4	35.7	693.88	42.3	66.40	62.60	43.04	590.86

Table B.158 Experimental Data A-D-GA-P3-S-PVC-15-015-14.01-19.7-100 Twater = 55 °C

z/d	Twall [°C]		Tbulk [°C]	h [W/m²K]	z/d	Twall [°C]		Tbulk [°C]	h [W/m²K]
2.7	40.8	36.8	20.53	765.71	25.0	56.1	54.4	34.49	674.65
5.2	45.5	42.8	22.2	638.07	27.4	56.5	55.1	35.72	697.68
7.6	47.9	45.9	23.99	611.26	29.9	57.4	55.9	36.86	708.01
10.1	49.9	48.0	25.73	603.78	32.4	58.4	56.6	37.94	716.54
15.1	52.2	50.8	29	623.43	34.9	60.6	57.2	38.95	702.79
17.5	53.0	51.9	30.49	638.31	37.3	67.3	58.0	39.89	616.18
20.0	53.7	52.7	31.9	657.46	39.8	73.7	59.2	40.77	545.65
22.5	55.0	53.5	33.23	666.73	42.3	80.83	60.75	41.62	480.41

Table B.159 Experimental Data A-D-GA-P3-S-PVC-15-015-15.31-13.4-094 Twater = 22 °C

z/d	Twall [°C]		Tbulk [°C]	h [W/m²K]	z/d	Twall [°C]		Tbulk [°C]	h [W/m²K]
2.7	40.1	36.6	13.98	629.30	25.0	56.7	54.8	31.55	631.88
5.2	45.1	42.6	16.18	553.85	27.4	57.7	55.9	32.93	641.51
7.6	47.7	45.8	18.59	544.38	29.9	59.3	58.3	34.25	623.19
10.1	49.8	48.0	20.73	543.99	32.4	60.6	58.6	35.56	637.69
15.1	52.2	50.6	24.85	575.99	34.9	63.6	61.2	36.71	595.90
17.5	53.2	51.7	26.7	594.89	37.3	70.4	63.4	37.74	524.93
20.0	54.0	52.9	28.42	612.07	39.8	77.6	63.8	38.8	480.04
22.5	56.4	54.0	29.99	607.57	42.3	87.64	66.13	39.7	411.81

Table B.160 Experimental Data A-D-GA-P3-S-PVC-15-015-15.26-08.2-088 Twater = 2 °C

z/d	Twall [°C]		Tbulk [°C]	h [W/m²K]	z/d	Twall [°C]		Tbulk [°C]	h [W/m²K]
2.7	37.2	36.7	8.135	529.16	25.0	55.4	54.5	28.09	568.57
5.2	43.3	42.7	10.65	471.24	27.4	56.7	55.2	29.68	580.92
7.6	46.3	45.4	13.32	468.95	29.9	57.1	57.2	31.18	587.42
10.1	48.5	47.2	15.89	477.55	32.4	58.9	62.0	32.5	546.45
15.1	51.1	49.6	20.6	513.16	34.9	63.4	62.3	33.76	525.23
17.5	52.1	50.4	22.69	533.95	37.3	71.5	68.5	34.81	433.31
20.0	52.9	51.3	24.64	555.36	39.8	79.9	87.8	35.57	316.16
22.5	57.8	53.1	26.33	524.07	42.3	80.98	93.75	36.7	301.24

Table B.161 Experimental Data A-D-GA-P3-S-PVC-15-015-11.50-13.3-088

z/d	Twall [°C]		Tbulk [°C]	h [W/m²K]	z/d	Twall [°C]		Tbulk [°C]	h [W/m²K]
2.7	31.4	29.0	13.89	705.01	25.0	50.4	47.9	27.73	536.49
5.2	37.1	34.5	15.52	566.69	27.4	50.7	50.2	28.97	534.65
7.6	40.5	38.1	17.16	519.51	29.9	51.6	51.4	30.16	539.78
10.1	43.2	40.3	18.89	503.76	32.4	52.2	53.2	31.29	537.89
15.1	46.0	42.6	22.14	518.51	34.9	52.8	53.8	32.37	549.80
17.5	47.1	44.2	23.67	522.35	37.3	54.1	56.7	33.37	522.11
20.0	47.9	45.6	25.11	532.08	39.8	54.4	60.0	34.33	503.55
22.5	49.7	46.9	26.42	525.91	42.3	54.22	59.08	35.36	540.06

Table B.162 Experimental Data A-D-GA-P3-S-PVC-15-015-10.24-13.3-088

z/d	Twall [°C]		Tbulk [°C]	h [W/m²K]	z/d	Twall [°C]		Tbulk [°C]	h [W/m²K]
2.7	29.2	26.4	13.86	734.99	25.0	47.1	45.4	26.33	513.96
5.2	33.8	32.9	15.16	563.58	27.4	47.9	46.1	27.54	526.40
7.6	37.9	34.8	16.69	520.78	29.9	48.8	47.1	28.65	530.31
10.1	40.7	36.5	18.24	502.48	32.4	49.4	47.7	29.71	543.30
15.1	43.7	41.3	21.1	478.45	34.9	50.3	48.5	30.73	547.50
17.5	44.9	42.6	22.5	482.61	37.3	50.5	48.9	31.75	569.96
20.0	45.6	43.5	23.84	494.81	39.8	51.0	49.5	32.69	582.16
22.5	46.5	44.3	25.11	504.19	42.3	50.52	50.08	33.64	614.63

Table B.163 Experimental Data A-D-GA-P3-S-PVC-15-015-03.89-13.1-086

z/d	Twall [°C]		Tbulk [°C]	h [W/m²K]	z/d	Twall [°C]		Tbulk [°C]	h [W/m²K]
2.7	18.9	18.2	13.27	739.27	25.0	29.7	28.7	18.48	361.77
5.2	21.9	20.8	13.7	508.83	27.4	30.5	29.4	19.02	356.12
7.6	23.4	22.3	14.33	456.30	29.9	31.2	30.2	19.55	349.08
10.1	24.9	23.8	14.85	409.61	32.4	31.6	30.7	20.15	353.89
15.1	26.9	25.6	16.05	379.69	34.9	32.0	31.3	20.66	353.14
17.5	27.7	26.5	16.72	373.54	37.3	32.4	31.6	21.23	359.66
20.0	28.1	27.4	17.29	371.60	39.8	32.7	32.1	21.72	363.27
22.5	29.2	28.0	17.85	362.68	42.3	32.99	32.52	22.27	370.45

Table B.164 Experimental Data A-D-GA-P3-L-GLS-15-015-12.75-12.5-087

z/d	Twall [°C]		Tbulk [°C]	h [W/m²K]	z/d	Twall [°C]		Tbulk [°C]	h [W/m²K]
2.7	42.4	28.7	12.66	557.55	25.0	62.7	50.5	28.13	447.71
5.2	46.1	34.2	14.57	498.16	27.4	66.7	52.8	29.38	419.56
7.6	47.9	36.6	16.65	497.83	29.9	71.3	56.0	30.53	385.18
10.1	49.1	39.5	18.6	496.53	32.4	74.9	54.7	31.77	386.04
15.1	50.6	42.7	22.3	523.10	34.9	82.1	57.0	32.78	346.74
17.5	52.7	44.4	23.91	517.44	37.3	87.6	58.6	33.8	324.15
20.0	54.8	45.1	25.43	520.23	39.8	93.4	60.7	34.78	301.65
22.5	58.8	46.6	26.87	493.75	42.3	93.28	65.53	35.79	292.29

Table B.165 Experimental Data A-D-GA-P3-L-GLS-15-015-10.22-12.5-087

z/d	Twall [°C]		Tbulk [°C]	h [W/m^{2}K]	z/d	Twall [°C]		Tbulk [°C]	h [W/m^{2}K]
2.7	37.4	24.3	12.68	561.40	25.0	48.5	43.9	25.71	498.36
5.2	40.2	28.7	14.22	505.86	27.4	49.4	45.1	26.89	501.66
7.6	41.9	32.4	15.79	479.08	29.9	50.7	46.4	28.02	498.69
10.1	43.4	34.3	17.46	477.52	32.4	51.6	47.0	29.1	506.03
15.1	45.3	37.9	20.46	483.78	34.9	53.6	49.3	30.09	478.54
17.5	46.3	39.3	21.88	488.17	37.3	56.1	48.6	31.09	480.74
20.0	47.1	41.0	23.17	489.58	39.8	57.4	49.6	32.05	476.28
22.5	48.2	41.7	24.53	500.11	42.3	63.20	50.70	32.89	424.83

Table B.166 Experimental Data A-D-US-P3-L-GLS-15-015-10.16-12.3-073

z/d	Twall [°C]		Tbulk [°C]	h [W/m^{2}K]	z/d	Twall [°C]		Tbulk [°C]	h [W/m^{2}K]
2.7	33.1	30.8	12.34	518.01	25.0	53.2	47.5	25.36	407.01
5.2	36.7	34.0	13.91	473.91	27.4	56.7	51.0	26.45	370.89
7.6	39.9	37.0	15.5	442.45	29.9	62.9	60.5	27.21	294.58
10.1	43.0	38.8	17.1	427.02	32.4	67.6	52.6	28.45	321.21
15.1	45.4	42.7	20.08	423.94	34.9	70.9	76.4	28.9	226.97
17.5	47.1	44.2	21.53	421.35	37.3	75.9	70.1	30.07	236.68
20.0	49.4	45.4	22.85	413.96	39.8	68.7	69.9	31.27	267.19
22.5	51.3	47.1	24.1	404.75	42.3	74.69	67.00	32.24	263.20

Table B.167 Experimental Data A-D-US-P3-L-GLS-15-010-03.89-11.4-071

z/d	Twall [°C]		Tbulk [°C]	h [W/m^{2}K]	z/d	Twall [°C]		Tbulk [°C]	h [W/m^{2}K]
2.7	22.7	18.3	11.55	435.72	25.0	30.2	28.9	17.61	324.72
5.2	24.7	20.6	12.21	373.13	27.4	30.8	29.8	18.22	322.57
7.6	25.9	22.4	12.93	347.79	29.9	31.3	30.5	18.86	323.86
10.1	27.2	23.8	13.57	326.61	32.4	31.6	31.0	19.44	327.69
15.1	28.6	25.9	15.00	318.12	34.9	31.9	31.5	20.06	334.44
17.5	29.1	26.8	15.66	317.25	37.3	32.2	31.9	20.67	341.18
20.0	29.3	27.5	16.31	321.90	39.8	32.6	32.3	21.21	346.45
22.5	29.9	28.3	17.00	321.19	42.3	32.80	32.67	21.79	355.62

Table B.168 Experimental Data A-D-GA-P3-S-PVC-15-015-11.46-13.1-089

z/d	Twall [°C]		Tbulk [°C]	h [W/m^{2}K]	z/d	Twall [°C]		Tbulk [°C]	h [W/m^{2}K]
2.7	32.6	31.2	13.53	623.73	25.0	51.5	49.6	27.45	496.45
5.2	37.4	37.0	15.07	517.64	27.4	52.5	49.2	28.76	519.48
7.6	40.2	39.5	16.9	499.26	29.9	55.9	50.5	29.85	490.50
10.1	43.1	41.2	18.55	486.40	32.4	58.3	53.9	30.89	454.87
15.1	46.6	44.6	21.83	482.67	34.9	64.1	55.5	31.9	410.89
17.5	47.8	45.6	23.36	490.69	37.3	67.4	63.1	32.74	352.25
20.0	49.3	46.6	24.75	493.61	39.8	72.6	67.3	33.64	315.69
22.5	50.5	47.6	26.14	500.25	42.3	74.63	67.15	34.63	316.07

Table B.169 Experimental Data A-D-GA-P3-S-PVC-15-015-08.97-13.2-087

z/d	Twall [°C]		Tbulk [°C]	h [W/m^{2}K]	z/d	Twall [°C]		Tbulk [°C]	h [W/m^{2}K]
2.7	27.4	24.2	13.79	745.86	25.0	44.7	42.4	24.91	481.07
5.2	32.4	30.7	14.87	537.00	27.4	45.5	43.0	25.98	491.16
7.6	35.7	34.1	16.19	479.69	29.9	46.1	44.1	27.01	495.58
10.1	38.4	35.6	17.55	461.34	32.4	46.6	44.6	28.05	511.79
15.1	41.4	38.6	20.17	452.78	34.9	46.9	45.5	29	521.62
17.5	42.5	39.6	21.43	458.38	37.3	47.2	45.9	29.96	540.57
20.0	43.2	40.7	22.64	465.48	39.8	47.7	46.6	30.84	550.47
22.5	44.1	41.2	23.8	476.56	42.3	47.76	47.00	31.73	573.32

Table B.170 Experimental Data A-D-GA-D2-S-NON-15-000-02.81-21.3-000

z/d	Twall wider sides [°C]		Twall narrower sides [°C]		Tbulk [°C]	h [W/m^{2}K]
6.74	47.4	47.6	49.4	49.4	25.54	122.67
11.24	58.9		60.9	60.9	28.36	89.06
15.73	66.6	66.8	68.7	68.3	31.17	77.14
20.22	71.8	71.7	74.3	73.3	33.99	72.42
24.72	76.0	76.2	78.5		36.8	69.34
29.21	79.6	79.5	82.5	81.0	39.61	68.46
33.71	82.8	82.7	85.7	84.0	42.43	67.88
37.08	83.7	83.7	87.04		44.54	68.77

Table B.171 Experimental Data A-D-GA-D2-S-NON-15-015-11.77-16.4-100

z/d	Twall wider sides [°C]		Twall narrower sides [°C]		Tbulk [°C]	h [W/m^{2}K]
6.74	30.8	29.8	33.2	33.2	20.44	1040.98
11.24	36.6		40.2	39.6	23.06	773.47
15.73	41.8	40.5	44.4	44.2	25.65	690.06
20.22	44.7	43.9	47.6	47.1	28.07	662.87
24.72	47.0	49.1	49.4		30.29	638.66
29.21	50.5	53.2	52.6	51.6	32.28	597.01
33.71	62.7	57.2	56.4	53.6	34.09	504.05
37.08	64.2	58.2	58.81		35.4	478.71

Table B.172 Experimental Data A-D-GA-D2-S-NON-15-015-09.54-16.3-100

z/d	Twall wider sides [°C]		Twall narrower sides [°C]		Tbulk [°C]	h [W/m^{2}K]
6.74	27.9	27.0	30.1	29.8	19.67	1056.34
11.24	33.0		36.5	35.6	21.78	748.37
15.73	37.7	36.3	40.7	39.9	24.01	652.87
20.22	40.4	39.5	43.4	42.7	26.07	618.97
24.72	42.5	42.5	45.6		28.04	596.75
29.21	45.1	45.1	48.2	46.9	29.82	578.15
33.71	46.8	47.4	50.5	48.4	31.54	571.24
37.08	47.1	47.4	51.72		32.81	572.38

Table B.173 Experimental Data A-D-GA-D2-S-NON-15-015-09.54-16.3-100 wider sides

z/d	Twall wider sides [°C]		Twall narrower sides [°C]		Tbulk [°C]	h [W/m^{2}K]
6.74	27.9	27.0			19.67	1229.15
11.24	33.0				21.78	851.69
15.73	37.7	36.3			24.01	735.84
20.22	40.4	39.5			26.07	688.27
24.72	42.5	42.5			28.04	660.77
29.21	45.1	45.1			29.82	624.20
33.71	46.8	47.4			31.54	614.17
37.08	47.1	47.4			32.81	660.90

Table B.174 Experimental Data A-D-GA-D2-S-NON-15-015-09.54-16.3-100 narrower sides

z/d	Twall wider sides [°C]		Twall narrower sides [°C]		Tbulk [°C]	h [W/m^{2}K]
6.74			30.1	29.8	19.67	926.14
11.24			36.5	35.6	21.78	667.41
15.73			40.7	39.9	24.01	586.71
20.22			43.4	42.7	26.07	562.35
24.72			45.6		28.04	544.04
29.21			48.2	46.9	29.82	538.44
33.71			50.5	48.4	31.54	533.91
37.08			51.72		32.81	504.78

Table B.175 Experimental Data A-D-GA-D2-S-NON-15-015-07.45-16.3-100

z/d	Twall wider sides [°C]		Twall narrower sides [°C]		Tbulk [°C]	h [W/m^{2}K]
6.74	24.9	24.2	27.0	26.4	19	1124.68
11.24	29.2		32.7	31.4	20.64	747.88
15.73	33.2	32.0	36.6	35.2	22.42	630.27
20.22	35.7	34.2	39.1	37.8	24.16	593.22
24.72	37.5	37.4	40.7		25.8	561.03
29.21	39.7	39.4	42.6	41.7	27.28	548.30
33.71	41.1	40.7	44.4	43.1	28.79	550.79
37.08	41.4	41.3	45.31		29.91	554.48

Table B.176 Experimental Data A-D-GA-D2-S-NON-15-015-14.97-16.5-100

z/d	Twall wider sides [°C]		Twall narrower sides [°C]		Tbulk [°C]	h [W/m^{2}K]
6.74	34.3	33.8	36.8	38.0	21.57	1057.82
11.24	40.8		44.3	45.1	24.81	832.69
15.73	46.6	45.8	49.0	49.8	27.94	753.22
20.22	49.9	50.2	52.4	52.9	30.74	726.35
24.72	52.8	58.4	55.6		33.26	669.87
29.21	60.4	66.6	60.3	58.7	35.47	575.10
33.71	78.3	75.2	68.7	63.7	37.38	438.88
37.08	89.8	78.8	73.09		38.69	373.97

APPENDIX C

NUMERICAL RESULTS

In this appendix, the results of the numerical modeling performed using the KIVA-3V code will be tabulated. Because of the large number of numerical simulations conducted, only simulations discussed in the body of the thesis will be tabulated. Because of the large amount of output obtained in each simulation, only the parameters corresponding to the experimentally measured variables at the instrumented locations will be tabulated. Here, only the average wall temperatures are shown. The same identification code used in Appendix B will be used here for model predictions, except that information for the unheated visualization tubes is not included since it was not a variable. Any other important information not identified by the unique number is additionally specified. Standard resolution used was 8 x 8 x 175 for downward flow or 8 x 8 x 150 for upward flow. Some simulations were conducted using a higher resolution, i.e. 12 x 12 x 250. First, the experimental data used to validate the modified KIVA-3V code are listed in the order in which they appear in this thesis followed by the model predictions. Simulations that are repeated in several figures are also tabulated each time they are graphed.

Table C.1 Experimental Data A-D-GA-P3-L-GLS-15-015-05.12-13.1-085

z [cm]	Twall [^{o}C]	Tbulk [^{o}C]	h [W/m^{2}K]	z [cm]	Twall [^{o}C]	Tbulk [^{o}C]	h [W/m^{2}K]
6.4	23.3	12.82	489.29	58.9	33.1	19.84	385.58
12.2	25.9	13.49	411.80	64.8	33.7	20.54	388.69
18.0	27.8	14.24	378.14	70.6	34.5	21.22	386.20
23.9	28.9	15.08	369.36	76.5	34.9	21.95	395.37
35.6	30.8	16.69	362.97	82.3	35.5	22.6	397.86
41.4	31.4	17.56	369.05	88.1	35.9	23.3	405.62
47.2	32.0	18.31	372.83	94.0	36.4	23.99	411.79
53.1	32.5	19.04	381.66	99.8	36.8	24.59	417.93

Table C.2 Experimental Data A-D-US-P3-L-GLS-15-015-05.11-13.3-072

z [cm]	Twall [^{o}C]	Tbulk [^{o}C]	h [W/m^{2}K]	z [cm]	Twall [^{o}C]	Tbulk [^{o}C]	h [W/m^{2}K]
6.4	23.4	13.03	491.32	58.9	33.7	19.95	372.69
12.2	25.8	13.70	421.29	64.8	34.1	20.72	381.17
18.0	27.8	14.45	382.03	70.6	34.9	21.40	379.97
23.9	29.2	15.29	367.70	76.5	35.1	22.14	393.76
35.6	31.2	16.89	357.77	82.3	35.6	22.78	397.45
41.4	31.8	17.67	361.19	88.1	36.0	23.48	409.93
47.2	32.4	18.50	366.62	94.0	36.4	24.16	418.28
53.1	32.9	19.24	375.22	99.8	36.7	24.76	428.35

Table C.3 Experimental Data A-D-GA-P3-L-GLS-15-015-08.92-12.7-087

z [cm]	Twall [^{o}C]	Tbulk [^{o}C]	h [W/m^{2}K]	z [cm]	Twall [^{o}C]	Tbulk [^{o}C]	h [W/m^{2}K]
6.4	28.2	12.70	573.50	58.9	42.7	24.25	484.43
12.2	31.9	13.99	498.71	64.8	43.7	25.33	485.75
18.0	34.5	15.33	466.13	70.6	44.2	26.43	502.53
23.9	36.1	16.80	461.09	76.5	45.2	27.43	502.53
35.6	38.7	19.45	463.83	82.3	45.7	28.38	513.92
41.4	39.9	20.73	465.88	88.1	47.0	29.31	505.17
47.2	40.9	21.96	471.43	94.0	48.0	30.20	500.93
53.1	42.1	23.13	470.19	99.8	48.1	31.11	524.10

Table C.4 Experimental Data A-D-US-P3-L-GLS-15-015-08.89-12.7-072

z [cm]	Twall [^{o}C]	Tbulk [^{o}C]	h [W/m^{2}K]	z [cm]	Twall [^{o}C]	Tbulk [^{o}C]	h [W/m^{2}K]
6.4	28.9	12.54	542.81	58.9	42.8	24.3	481.85
12.2	32.6	13.85	473.28	64.8	44.0	25.39	477.67
18.0	35.9	15.21	429.09	70.6	45.6	26.37	463.08
23.9	37.3	16.69	431.35	76.5	46.9	27.38	456.09
35.6	39.5	19.38	443.09	82.3	48.8	28.29	433.15
41.4	40.0	20.75	461.16	88.1	52.4	29.12	381.36
47.2	40.9	21.99	469.35	94.0	56.1	29.88	338.63
53.1	41.6	23.17	481.55	99.8	59.5	30.62	307.56

Table C.5 Experimental Data A-U-GA-P3-S-PVC-15-015-06.38-14.5-100

z [cm]	Twall [^{o}C]	Tbulk [^{o}C]	h [W/m^{2}K]	z [cm]	Twall [^{o}C]	Tbulk [^{o}C]	h [W/m^{2}K]
6.4	26.2	14.40	539.27	58.9	35.4	22.86	510.73
12.2	28.5	15.28	482.21	64.8	36.1	23.66	513.56
18.0	29.9	16.32	470.15	70.6	36.7	24.44	519.26
23.9	31.0	17.32	465.87	76.5	37.3	25.26	532.41
35.6	32.8	19.23	469.72	82.3	37.7	25.99	544.84
41.4	33.6	20.15	475.28	88.1	38.1	26.77	561.54
47.2	34.2	21.11	489.58	94.0	38.6	27.46	573.92
53.1	34.8	21.96	495.85	99.8	39.0	28.19	589.36

Table C.6 Experimental Data A-U-GA-P3-S-PVC-15-015-15.33-13.3-100

z [cm]	Twall [^{o}C]	Tbulk [^{o}C]	h [W/m^{2}K]	z [cm]	Twall [^{o}C]	Tbulk [^{o}C]	h [W/m^{2}K]
6.4	39.4	13.78	597.58	58.9	52.0	31.56	749.01
12.2	43.6	16.08	558.06	64.8	52.8	32.98	772.05
18.0	45.4	18.56	571.33	70.6	53.6	34.31	795.10
23.9	46.6	20.78	593.45	76.5	54.2	35.62	824.52
35.6	48.8	24.87	639.81	82.3	54.8	36.81	850.59
41.4	49.8	26.70	662.70	88.1	55.4	37.99	880.85
47.2	50.5	28.41	692.80	94.0	56.0	39.07	906.28
53.1	51.4	30.06	717.43	99.8	56.1	40.13	959.52

Table C.7 Model Predictions A-D-GA-P3-L-15-015-05.12-13.1-085 Figure 5.3 High Resolution

z [cm]	Twall [^{o}C]	Tbulk [^{o}C]	h [W/m^{2}K]	z [cm]	Twall [^{o}C]	Tbulk [^{o}C]	h [W/m^{2}K]
6.3	22.2	13.57	592.52	58.8	32.5	18.88	377.19
11.9	25.8	14.00	434.86	65.1	33.0	19.66	385.19
18.2	27.9	14.62	385.28	70.7	33.4	20.24	390.33
23.8	29.1	15.14	367.24	76.3	33.8	20.76	393.85
35.7	30.5	16.39	361.89	83.3	34.3	21.40	397.89
41.3	31.0	16.95	363.66	88.2	34.7	22.06	405.19
46.9	31.5	17.63	370.08	93.8	35.1	22.62	409.83
53.2	32.1	18.23	370.00	100.1	35.5	23.28	417.38

Table C.8 Model Predictions A-D-US-P3-L-15-015-05.11-13.3-072 Figure 5.5

z [cm]	Twall [^{o}C]	Tbulk [^{o}C]	h [W/m^{2}K]	z [cm]	Twall [^{o}C]	Tbulk [^{o}C]	h [W/m^{2}K]
6.0	25.0	14.05	465.79	59.0	32.8	19.38	381.26
12.0	28.3	14.54	372.55	65.0	33.2	20.02	388.00
18.0	29.5	15.22	359.42	71.0	33.7	20.70	394.67
24.0	30.0	15.54	353.96	77.0	34.1	21.18	396.93
36.0	31.1	16.49	351.19	83.0	34.6	21.37	386.56
41.0	31.5	16.87	349.99	88.0	34.9	21.99	395.86
47.0	31.8	17.75	363.58	94.0	35.4	22.43	395.49
53.0	32.4	18.56	369.97	100	35.8	23.06	401.25

Table C.9 Model Predictions A-D-GA-P3-L-15-015-08.92-12.7-087 Figure 5.7

z [cm]	Twall [^{o}C]	Tbulk [^{o}C]	h [W/m^{2}K]	z [cm]	Twall [^{o}C]	Tbulk [^{o}C]	h [W/m^{2}K]
6.0	26.7	13.20	659.37	59.0	41.4	21.67	451.33
12.0	32.2	13.93	487.78	65.0	42.0	22.50	457.67
18.0	34.9	14.74	442.13	71.0	42.5	23.47	468.17
24.0	36.7	15.73	424.98	77.0	43.1	24.58	482.29
36.0	39.1	17.82	419.41	83.0	43.5	25.50	494.21
41.0	39.7	18.63	423.67	88.0	44.0	26.44	508.23
47.0	40.4	19.62	429.28	94.0	44.5	27.39	521.36
53.0	40.9	20.67	441.76	100.0	45.0	28.27	532.06

Table C.10 Model Predictions A-D-US-P3-L-15-015-08.89-12.7-072 Figure 5.9

z [cm]	Twall [^{o}C]	Tbulk [^{o}C]	h [W/m^{2}K]	z [cm]	Twall [^{o}C]	Tbulk [^{o}C]	h [W/m^{2}K]
6.0	32.9	13.40	455.94	59.0	42.7	21.95	429.10
12.0	37.2	14.32	389.05	65.0	43.3	22.77	432.63
18.0	38.8	15.27	378.53	71.0	43.8	23.65	442.31
24.0	39.4	16.12	381.77	77.0	44.3	24.38	446.22
36.0	40.8	18.26	394.96	83.0	44.9	25.30	454.82
41.0	41.2	19.16	403.50	88.0	45.2	25.97	461.69
47.0	41.7	20.17	413.66	94.0	45.8	26.85	469.39
53.0	42.3	21.13	420.62	100.0	46.3	27.78	481.30

Table C.11 Model Predictions A-U-GA-P3-S-15-015-06.38-14.5-100 Figure 5.11

z [cm]	Twall [^{o}C]	Tbulk [^{o}C]	h [W/m^{2}K]	z [cm]	Twall [^{o}C]	Tbulk [^{o}C]	h [W/m^{2}K]
6.2	30.7	16.18	439.48	59.2	38.7	22.80	401.74
12.6	32.8	16.89	401.01	64.8	38.9	23.57	415.55
18.2	34.2	17.55	382.33	70.5	39.3	24.06	419.87
23.9	35.0	18.31	381.56	76.9	39.8	24.96	430.99
35.9	36.7	19.97	380.46	83.3	40.1	25.77	445.16
41.5	37.4	20.49	378.25	88.1	40.4	26.43	455.68
47.2	37.8	21.22	385.36	93.8	40.8	27.07	465.59
52.8	38.1	21.94	394.09	99.4	41.1	27.73	477.51

Table C.12 Model Predictions A-U-GA-P3-S-15-015-15.33-13.3-100 Figure 5.13

z [cm]	Twall [^{o}C]	Tbulk [^{o}C]	h [W/m^{2}K]	z [cm]	Twall [^{o}C]	Tbulk [^{o}C]	h [W/m^{2}K]
7.4	43.5	16.19	562.59	59.8	54.2	29.07	610.87
13.8	46.7	17.73	530.20	65.3	54.3	30.59	646.59
19.3	48.4	19.11	523.51	70.9	54.9	31.73	660.66
24.9	50.0	20.32	516.84	77.2	55.2	33.15	696.78
36.8	51.6	23.77	551.23	83.6	55.9	34.64	722.96
42.3	52.4	25.12	563.11	88.3	56.4	35.24	725.84
47.9	52.7	26.41	583.06	93.9	57.3	36.57	738.31
53.4	53.4	27.66	595.08	99.4	61.9	37.95	640.44

Table C.13 Model Predictions A-D-US-P3-L-15-015-05.11-13.3-072 15 μm droplets

z [cm]	Twall [°C]	Tbulk [°C]	h [W/m^{2}K]	z [cm]	Twall [°C]	Tbulk [°C]	h [W/m^{2}K]
6.0	22.4	13.34	562.39	59.0	32.8	19.20	376.33
12.0	26.7	13.83	398.69	65.0	33.3	19.98	385.22
18.0	28.6	14.46	361.05	71.0	33.8	20.67	391.20
24.0	29.7	15.08	350.76	77.0	34.2	21.41	401.35
36.0	31.0	16.38	349.70	83.0	34.6	21.99	404.58
41.0	31.4	16.86	351.99	88.0	35.0	22.53	411.28
47.0	32.0	17.65	358.04	94.0	35.5	23.01	411.61
53.0	32.3	18.65	374.24	100.0	35.9	23.59	416.19

Table C.14 Model Predictions A-D-US-P3-L-15-015-05.11-13.3-072 30 μm droplets

z [cm]	Twall [°C]	Tbulk [°C]	h [W/m^{2}K]	z [cm]	Twall [°C]	Tbulk [°C]	h [W/m^{2}K]
6.0	23.3	13.37	515.71	59.0	32.7	19.10	376.22
12.0	27.1	13.91	388.91	65.0	33.1	19.73	382.06
18.0	28.8	14.51	357.89	71.0	33.6	20.41	388.70
24.0	29.7	15.14	351.36	77.0	34.0	21.12	396.16
36.0	30.9	16.19	347.54	83.0	34.5	21.59	397.55
41.0	31.3	16.96	356.10	88.0	34.8	22.11	401.76
47.0	31.8	17.69	362.32	94.0	35.3	22.71	405.96
53.0	32.3	18.28	365.82	100.0	35.8	23.19	407.16

Table C.15 Model Predictions A-D-US-P3-L-15-015-05.11-13.3-072 60 μm droplets

z [cm]	Twall [°C]	Tbulk [°C]	h [W/m^{2}K]	z [cm]	Twall [°C]	Tbulk [°C]	h [W/m^{2}K]
6.0	25.0	14.05	465.79	59.0	32.8	19.38	381.26
12.0	28.3	14.54	372.55	65.0	33.2	20.02	388.00
18.0	29.5	15.22	359.42	71.0	33.7	20.70	394.67
24.0	30.0	15.54	353.96	77.0	34.1	21.18	396.93
36.0	31.1	16.49	351.19	83.0	34.6	21.37	386.56
41.0	31.5	16.87	349.99	88.0	34.9	21.99	395.86
47.0	31.8	17.75	363.58	94.0	35.4	22.43	395.49
53.0	32.4	18.56	369.97	100	35.8	23.06	401.25

Table C.16 Model Predictions A-D-US-P3-L-15-015-05.11-13.3-072 100 μm droplets

z [cm]	Twall [°C]	Tbulk [°C]	h [W/m^{2}K]	z [cm]	Twall [°C]	Tbulk [°C]	h [W/m^{2}K]
6.0	27.6	14.17	380.84	59.0	33.0	19.37	376.66
12.0	29.2	14.89	357.57	65.0	33.5	20.25	385.89
18.0	29.9	15.53	357.24	71.0	33.9	21.06	400.28
24.0	30.3	16.15	362.50	77.0	34.3	21.85	410.95
36.0	31.3	17.29	365.56	83.0	34.8	22.39	414.11
41.0	31.7	17.68	366.50	88.0	35.2	22.72	411.28
47.0	32.1	18.13	366.11	94.0	35.5	23.11	411.64
53.0	32.6	18.74	369.81	100.0	36.0	23.39	404.65

Table C.17 Model Predictions A-D-GA-P3-L-15-015-05.12-13.1-085 15 μm droplets

z [cm]	Twall [°C]	Tbulk [°C]	h [W/m^{2}K]	z [cm]	Twall [°C]	Tbulk [°C]	h [W/m^{2}K]
6.0	21.4	13.29	633.04	59.0	32.6	18.90	373.34
12.0	25.0	13.72	455.35	65.0	33.1	19.70	382.69
18.0	27.3	14.29	393.36	71.0	33.6	20.37	388.23
24.0	28.8	14.85	367.29	77.0	34.0	20.99	393.79
36.0	30.5	16.28	359.50	83.0	34.5	21.65	399.13
41.0	31.0	16.87	361.81	88.0	34.8	22.18	405.22
47.0	31.6	17.61	366.97	94.0	35.2	22.89	415.18
53.0	32.1	18.35	372.20	100.0	35.8	23.61	421.82

Table C.18 Model Predictions A-D-GA-P3-L-15-015-05.12-13.1-085 30 μm droplets

z [cm]	Twall [°C]	Tbulk [°C]	h [W/m^{2}K]	z [cm]	Twall [°C]	Tbulk [°C]	h [W/m^{2}K]
6.0	21.3	13.50	660.22	59.0	32.4	18.59	370.08
12.0	25.1	13.90	458.21	65.0	32.9	19.38	379.40
18.0	27.3	14.38	397.45	71.0	33.3	20.04	385.31
24.0	28.7	14.96	372.04	77.0	33.8	20.66	390.04
36.0	30.3	16.24	362.84	83.0	34.3	21.37	396.22
41.0	30.9	16.80	363.40	88.0	34.6	21.83	400.09
47.0	31.5	17.42	364.62	94.0	35.1	22.45	404.55
53.0	32.0	18.08	369.17	100.0	35.6	23.07	409.21

Table C.19 Model Predictions A-D-GA-P3-L-15-015-05.12-13.1-085 50 μm droplets

z [cm]	Twall [°C]	Tbulk [°C]	h [W/m^{2}K]	z [cm]	Twall [°C]	Tbulk [°C]	h [W/m^{2}K]
6.0	21.1	13.82	701.66	59.0	32.4	18.83	376.08
12.0	24.9	14.16	475.53	65.0	32.9	19.46	381.24
18.0	27.3	14.65	405.93	71.0	33.4	19.99	382.86
24.0	28.7	15.17	377.80	77.0	33.8	20.65	388.03
36.0	30.4	16.45	367.24	83.0	34.3	21.20	391.95
41.0	30.8	16.99	369.36	88.0	34.6	21.69	395.83
47.0	31.4	17.63	370.80	94.0	35.1	22.39	401.76
53.0	32.0	18.27	373.53	100.0	35.6	22.98	406.12

Table C.20 Model Predictions A-D-GA-P3-L-15-015-05.12-13.1-085 100 μm droplets

z [cm]	Twall [°C]	Tbulk [°C]	h [W/m^{2}K]	z [cm]	Twall [°C]	Tbulk [°C]	h [W/m^{2}K]
6.0	20.2	14.10	834.28	59.0	32.2	19.00	387.76
12.0	23.6	14.46	558.40	65.0	32.7	19.50	387.64
18.0	25.9	14.97	467.67	71.0	33.2	20.11	391.53
24.0	27.7	15.54	422.58	77.0	33.7	20.66	391.74
36.0	29.8	16.65	388.35	83.0	34.2	21.31	397.95
41.0	30.5	17.17	383.87	88.0	34.6	21.72	397.48
47.0	31.1	17.77	383.75	94.0	35.1	22.22	398.38
53.0	31.7	18.39	384.01	100.0	35.5	22.87	405.83

Table C.21 Model Predictions A-D-US-P3-L-15-015-05.11-13.3-072 Sct = 0.50

z [cm]	Twall [°C]	Tbulk [°C]	h [W/m²K]	z [cm]	Twall [°C]	Tbulk [°C]	h [W/m²K]
6.0	22.6	13.31	551.90	59.0	33.8	19.27	353.59
12.0	27.1	13.80	385.63	65.0	34.2	19.91	358.17
18.0	29.2	14.37	346.23	71.0	34.7	20.52	361.51
24.0	30.4	14.86	329.13	77.0	35.2	21.24	367.13
36.0	31.9	16.22	327.18	83.0	35.6	21.96	375.20
41.0	32.3	16.91	332.86	88.0	35.9	22.47	380.33
47.0	32.8	17.78	340.02	94.0	36.4	22.88	379.40
53.0	33.3	18.45	343.92	100.0	36.8	23.59	387.15

Table C.22 Model Predictions A-D-US-P3-L-15-015-05.11-13.3-072 Sct = 0.33

z [cm]	Twall [°C]	Tbulk [°C]	h [W/m²K]	z [cm]	Twall [°C]	Tbulk [°C]	h [W/m²K]
6.0	22.4	13.26	562.14	59.0	32.6	19.44	388.44
12.0	26.6	13.77	397.73	65.0	33.0	20.01	393.06
18.0	28.6	14.46	361.48	71.0	33.5	20.89	405.99
24.0	29.6	15.22	356.45	77.0	34.0	21.35	405.38
36.0	30.7	16.55	360.64	83.0	34.4	22.09	415.89
41.0	31.2	16.99	359.17	88.0	34.8	22.53	417.86
47.0	31.7	17.86	369.94	94.0	35.2	23.16	426.13
53.0	32.2	18.62	378.28	100.0	35.7	23.87	433.86

Table C.23 Model Predictions A-D-US-P3-L-15-015-05.11-13.3-072 Sct = 0.25

z [cm]	Twall [°C]	Tbulk [°C]	h [W/m²K]	z [cm]	Twall [°C]	Tbulk [°C]	h [W/m²K]
6.0	22.5	13.29	554.05	59.0	32.0	19.49	409.67
12.0	26.3	13.89	413.04	65.0	32.4	20.27	420.78
18.0	28.1	14.43	374.71	71.0	32.9	20.84	424.68
24.0	29.0	15.20	370.29	77.0	33.4	21.50	431.59
36.0	30.2	16.59	376.44	83.0	33.9	22.23	440.43
41.0	30.6	17.30	385.28	88.0	34.2	22.77	448.49
47.0	31.0	18.07	394.39	94.0	34.6	23.35	455.39
53.0	31.6	18.90	403.98	100.0	35.0	23.93	460.76

Table C.24 Model Predictions A-D-GA-P3-L-15-015-05.12-13.1-085 Sct = 0.50

z [cm]	Twall [°C]	Tbulk [°C]	h [W/m²K]	z [cm]	Twall [°C]	Tbulk [°C]	h [W/m²K]
6.0	21.1	13.43	664.76	59.0	33.3	18.51	347.31
12.0	25.3	13.87	447.16	65.0	33.8	19.19	350.78
18.0	27.7	14.37	384.04	71.0	34.2	19.92	357.84
24.0	29.2	14.92	358.87	77.0	34.7	20.52	360.21
36.0	31.1	15.98	338.83	83.0	35.2	21.10	363.25
41.0	31.6	16.64	342.11	88.0	35.6	21.68	367.74
47.0	32.2	17.33	343.23	94.0	36.0	22.24	370.83
53.0	32.8	17.97	345.04	100.0	36.5	22.96	378.25

Table C.25 Model Predictions A-D-GA-P3-L-15-015-05.12-13.1-085 Sct = 0.37

z	Twall [°C]	Tbulk [°C]	h [W/m^{2}K]	z [cm]	Twall [°C]	Tbulk [°C]	h [W/m^{2}K]
6.0	21.3	13.50	660.22	59.0	32.4	18.59	370.08
12.0	25.1	13.90	458.21	65.0	32.9	19.38	379.40
18.0	27.3	14.38	397.45	71.0	33.3	20.04	385.31
24.0	28.7	14.96	372.04	77.0	33.8	20.66	390.04
36.0	30.3	16.24	362.84	83.0	34.3	21.37	396.22
41.0	30.9	16.80	363.40	88.0	34.6	21.83	400.09
47.0	31.5	17.42	364.62	94.0	35.1	22.45	404.55
53.0	32.0	18.08	369.17	100.0	35.6	23.07	409.21

Table C.26 Model Predictions A-D-GA-P3-L-15-015-05.12-13.1-085 Sct = 0.25

z [cm]	Twall [°C]	Tbulk [°C]	h [W/m^{2}K]	z [cm]	Twall [°C]	Tbulk [°C]	h [W/m^{2}K]
6.0	20.9	13.40	680.94	59.0	31.7	18.88	400.34
12.0	24.7	13.88	474.38	65.0	32.1	19.54	406.96
18.0	26.8	14.42	413.20	71.0	32.6	20.22	413.30
24.0	28.2	14.98	386.27	77.0	33.1	20.85	418.23
36.0	29.7	16.29	381.07	83.0	33.5	21.48	425.71
41.0	30.2	16.89	384.96	88.0	33.9	21.96	430.18
47.0	30.7	17.58	389.59	94.0	34.3	22.59	437.16
53.0	31.2	18.25	395.67	100.0	34.8	23.24	443.52

Table C.27 Model Predictions A-D-GA-P3-L-15-015-05.12-13.1-085 40° Cone Spray

z [cm]	Twall [°C]	Tbulk [°C]	h [W/m^{2}K]	z [cm]	Twall [°C]	Tbulk [°C]	h [W/m^{2}K]
6.0	20.9	13.43	684.31	59.0	32.5	18.92	376.58
12.0	24.4	13.84	483.20	65.0	33.0	19.65	383.61
18.0	26.7	14.37	413.74	71.0	33.5	20.33	388.88
24.0	28.4	14.97	379.91	77.0	33.9	21.00	396.35
36.0	30.3	16.26	363.71	83.0	34.4	21.60	399.84
41.0	30.9	16.85	365.14	88.0	34.8	22.20	407.06
47.0	31.5	17.60	368.42	94.0	35.2	22.89	415.01
53.0	32.0	18.28	373.53	100.0	35.7	23.26	412.50

Table C.28 Model Predictions A-D-GA-P3-L-15-015-05.12-13.1-085 20° Cone Spray

z [cm]	Twall [°C]	Tbulk [°C]	h [W/m^{2}K]	z [cm]	Twall [°C]	Tbulk [°C]	h [W/m^{2}K]
6.0	21.0	13.45	681.94	59.0	32.6	19.01	377.00
12.0	24.4	13.83	482.02	65.0	33.1	19.64	379.93
18.0	26.9	14.36	408.29	71.0	33.6	20.33	386.79
24.0	28.5	14.96	378.81	77.0	34.0	21.02	393.57
36.0	30.4	16.27	361.07	83.0	34.5	21.67	399.06
41.0	31.0	16.84	362.35	88.0	34.8	22.23	405.83
47.0	31.6	17.60	366.08	94.0	35.4	22.77	406.96
53.0	32.1	18.26	370.93	100.0	35.8	23.48	416.26

Table C.29 Model Predictions Data A-D-US-P3-L-15-015-05.11-13.3-072 1.5 m/s

z [cm]	Twall [°C]	Tbulk [°C]	h [W/m^{2}K]	z [cm]	Twall [°C]	Tbulk [°C]	h [W/m^{2}K]
6.0	22.6	13.28	550.60	59.0	32.9	19.35	376.72
12.0	26.6	13.72	396.28	65.0	33.3	20.07	386.91
18.0	28.7	14.36	356.05	71.0	33.8	20.64	389.41
24.0	29.7	15.09	350.21	77.0	34.2	21.45	400.09
36.0	31.1	16.43	348.73	83.0	34.7	22.01	404.46
41.0	31.5	17.11	355.73	88.0	35.1	22.56	408.82
47.0	32.0	17.68	357.39	94.0	35.5	23.37	421.19
53.0	32.4	18.61	371.12	100.0	35.9	23.89	425.67

Table C.30 Model Predictions Data A-D-US-P3-L-15-015-05.11-13.3-072 15 m/s

z [cm]	Twall [°C]	Tbulk [°C]	h [W/m^{2}K]	z [cm]	Twall [°C]	Tbulk [°C]	h [W/m^{2}K]
6.0	22.4	13.23	560.60	59.0	32.9	19.05	370.13
12.0	26.5	13.79	402.77	65.0	33.3	19.87	380.08
18.0	28.6	14.49	362.63	71.0	33.7	20.57	388.88
24.0	29.7	15.14	351.79	77.0	34.2	21.49	403.98
36.0	31.0	16.54	353.01	83.0	34.7	22.14	408.10
41.0	31.5	16.94	352.25	88.0	35.0	22.61	413.10
47.0	31.9	17.77	361.15	94.0	35.5	23.38	423.77
53.0	32.4	18.31	363.33	100.0	35.9	23.89	426.88

Table C.31 Model Predictions Data A-D-US-P3-L-15-015-05.11-13.3-072 150 m/s

z [cm]	Twall [°C]	Tbulk [°C]	h [W/m^{2}K]	z [cm]	Twall [°C]	Tbulk [°C]	h [W/m^{2}K]
6.0	22.8	13.38	544.04	59.0	32.9	19.39	377.86
12.0	27.0	13.92	392.73	65.0	33.3	20.10	386.53
18.0	28.8	14.53	359.75	71.0	33.8	20.92	397.95
24.0	29.8	15.19	350.59	77.0	34.2	21.47	401.73
36.0	31.0	16.38	349.63	83.0	34.7	22.30	413.27
41.0	31.5	17.01	352.18	88.0	35.1	22.78	414.91
47.0	32.0	17.81	360.66	94.0	35.5	23.15	414.34
53.0	32.5	18.61	369.09	100.0	35.9	23.77	420.26

Table C.32 Model Predictions A-D-GA-P3-L-15-015-08.92-12.7-087 65 m/s

z [cm]	Twall [°C]	Tbulk [°C]	h [W/m^{2}K]	z [cm]	Twall [°C]	Tbulk [°C]	h [W/m^{2}K]
6	26.7	13.2	659.37	59	41.4	21.67	451.33
12	32.2	13.93	487.78	65	42	22.5	457.67
18	34.9	14.74	442.13	71	42.5	23.47	468.17
24	36.7	15.73	424.98	77	43.1	24.58	482.29
36	39.1	17.82	419.41	83	43.5	25.5	494.21
41	39.7	18.63	423.67	88	44	26.44	508.23
47	40.4	19.62	429.28	94	44.5	27.39	521.36
53	40.9	20.67	441.76	100	45	28.27	532.06

Table C.33 Model Predictions A-D-GA-P3-L-15-015-08.92-12.7-087 15 m/s

z [cm]	Twall [^{o}C]	Tbulk [^{o}C]	h [W/m^{2}K]	z [cm]	Twall [^{o}C]	Tbulk [^{o}C]	h [W/m^{2}K]
6.0	35.4	13.75	411.69	59.0	42.1	22.50	455.43
12.0	37.7	14.82	389.45	65.0	42.6	23.68	472.21
18.0	38.5	15.89	394.90	71.0	43.1	24.97	492.60
24.0	39.2	16.93	401.12	77.0	43.5	26.05	510.79
36.0	40.1	18.52	412.62	83.0	44.0	27.18	529.50
41.0	40.5	19.25	419.05	88.0	44.3	27.88	541.56
47.0	41.1	20.28	428.11	94.0	44.9	28.69	548.82
53.0	41.6	21.38	441.30	100.0	45.4	29.44	558.23

APPENDIX D

MODIFIED KIVA-3V CODE MANUAL

In this appendix, the content of input and output files, nozzle geometry, coolant options, grid structure, as well as procedures of running the modified KIVA-3V code for mist cooling applications are explained. This is done by using Power Point slides in which the modified KIVA-3V code manual is written. The manual was originally written by Dr. Shin [Shin (2006)] and was slightly modified during the course of this investigation. The manual is presented below.

MIST COOLING MANUAL

FOR

MODIFIED KIVA-3V CODE

1

Setup grid

- Only two files (kiva3vprep.exe, iprep) are required to setup the grid
- Place these two files in the same directory after setting the iprep (input) file and then simply execute (double click) kiva3vprep.exe file
- After running kiva3vprep.exe, “otape17” will be generated. Simply changes it to itape17 and use it to run kiva3v.exe

Input variables (iprep)

- Bore : [cm] diameter of pipe (hydraulic in rectangular channel) (all KIVA units in are: “cm gram sec Kelvin” CGS system)
- Stroke : [cm] test section length (un-heated and heated together)
- nsx2 : resolution in x direction (nx in grid generation source code) (must be even number only for rectangular test section)
  (in case of circular pipe, nsx1=nsx2), (from 10x10 resolution to 20x20 about 8 times longer calculation time)
- nsx1 : resolution in y direction (this is ny in grid generation source code) (must be even number only for rectangular test section)
- nsy : resolution in z dir. (nz in grid generation source code) (not more than KIVA specified max, should be 3-4 times nsx1 x nsx2)
- itype_channel : channel type (cylinder=2, rectangle=4)
- 1.18 -1.18 0.0 : vertice#1 [cm]
- 1.18 1.18 0.0 : vertice#2 [cm]
- -1.18 1.18 0.0 : vertice#3 [cm]
- -1.18 -1.18 0.0 : vertice#4 [cm]
- 1.18 -1.18 175.0 : vertice#5 [cm]
- 1.18 1.18 175.0 : vertice#6 [cm]
- -1.18 1.18 175.0 : vertice#7 [cm]
- -1.18 -1.18 175.0 : vertice#8 [cm]

Grid geometry

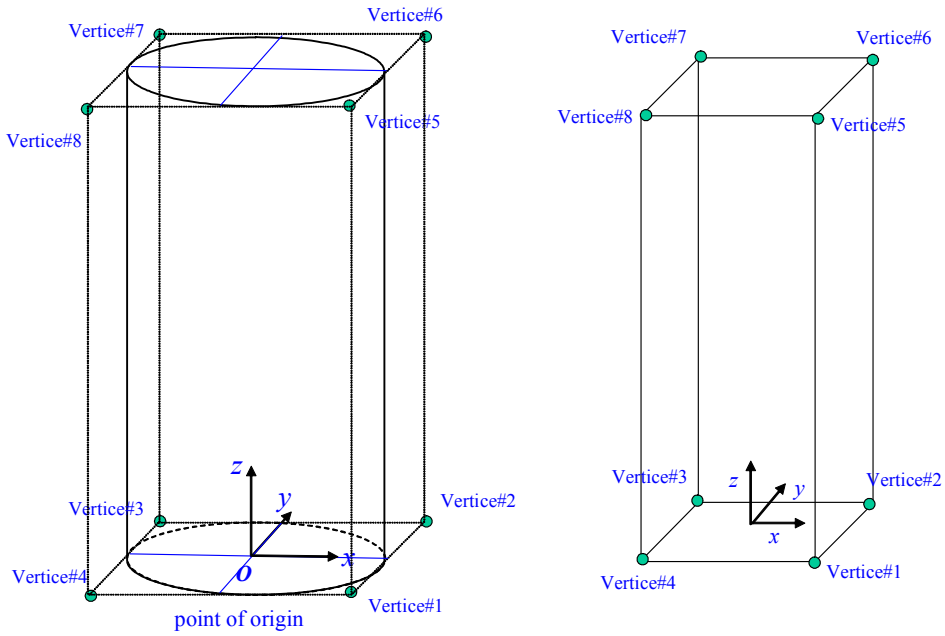

Running the code / Output files

- **Only three files (kiva3v.exe, itape5, and itape17) are required to run the simulation (for the very first time, i.e. not using restart option)**
- **Place these three files at the same directory after setting the input file itape5 for a given mist flow case (with irest=0, and choose the appropriate value for nctap8 to set the storing rate of the restart file) and then simply execute (double click) kiva3v.exe file**
- **After running, "Tsur###.dat", "Tec###.dat" and "Par###.dat" files are generated which are wall temperature, gas temperature and particle information data respectively. These files are teckplot ready.**
- **Also "Tavg###.dat", "history.dat" and "tsurmax.dat" files are generated. They represent average cross sectional data, time history and maximum surface temperature data, respectively. These files are in ascii format and can be loaded into matlab or excel.**

Output files

- **In case of pulsed heating, output file will be with three different indices A, B, and C. Each represent the status at following location:**

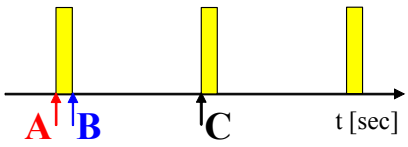

A : just before pulse
B : just after pulse
C : one pulse later

- **A is plotting at every "iplot_freq" pulse of heating**

- **Structure of "Tsur###.dat" file**

j i T_{sur} [i, j] : i, j is index in i and j direction (i=1,…, nsx, j=1,…,nsy)

Output files

- **Structure of "Tec###.dat" file**

x [cm]	y [cm]	z [cm]	u [cm]	v [cm]	w [cm]	T [K]	p [g/cm*s2]	ρ [g/cm3]
-.611647E+00	-.611647E+00	0.000000E+00	0.000000E+00	0.000000E+00	0.150000E+04	0.295011E+03	0.101592E+07	0.119306E-02

s(internal energy)	scl(turb length scale)	tke(turb kinetic energy)	eps(dissipation)
0.212746E+10	0.225481E+09	0.899388E+05	0.225481E+09

- **Structure of "Par###.dat" file**

x [cm]	y [cm]	z [cm]	u [cm]	v [cm]	w [cm]	T [K]	radius [cm]	i [index]
-.611647E+00	-.611647E+00	0.000000E+00	0.000000E+00	0.000000E+00	0.000000E+00	0.000000E+00	0.000000E+00	0.000000E+00

i = 0 particle is in the mist core **i = 1** particle is in the wall film

- **Structure of "Tavg###.dat" file**

z [cm]	T_{avg} [K]	P_{avg} [Pa*10]	ρ_{avg} [g/cm3]	T_{sur} [K]	par #	V_{par} [cm/s]	film thickness [cm]
0.000000E+00	0.295000E+03	0.101583E+07	0.119300E-02	0.295000E+03	0.000000E+00	0.000000E+00	0.000000E+00
0.104533E+01	0.295000E+03	0.101583E+07	0.119300E-02	0.295000E+03	0.000000E+00	0.000000E+00	0.000000E+00

par # : total number of particle (in film and core) V_{par} : film particle velocity

Output files

- **Structure of "history.dat" file**

A	B	C	D	E	F	G
0.2500000000E-03	0.5879920734E+05	0.0000000000E+00	1	0	1	0.2949274405E+03
0.5000000000E-03	-0.3821486961E+06	0.0000000000E+00	3	0	3	0.2948577969E+03
0.7500000000E-03	-0.1178778655E+07	0.0000000000E+00	4	0	4	0.2947901493E+03
0.1000000000E-02	-0.2240426354E+07	0.0000000000E+00	6	0	6	0.2947245051E+03
0.1250000000E-02	-0.3514564062E+07	0.0000000000E+00	7	0	7	0.2946608361E+03
0.1500000000E-02	-0.4968189140E+07	0.0000000000E+00	9	0	9	0.2945991062E+03
0.1750000000E-02	-0.6577515983E+07	0.0000000000E+00	10	0	10	0.2945392642E+03

A : time
B : heat removal from the wall by convection
C : heat removal from the wall by conduction
D : number of particle inside the channel
E : number of particle on the wall
F : total number of particle
G : bulk temperature of coolant at the exit

- **Structure of "tsurmax.dat" file**

X	Y
0.1000000000E-04	0.2950000179E+03
0.2000000000E-04	0.2950000357E+03
0.3000000000E-04	0.2950000536E+03

X : time Y : maximum wall temperature

During simulation

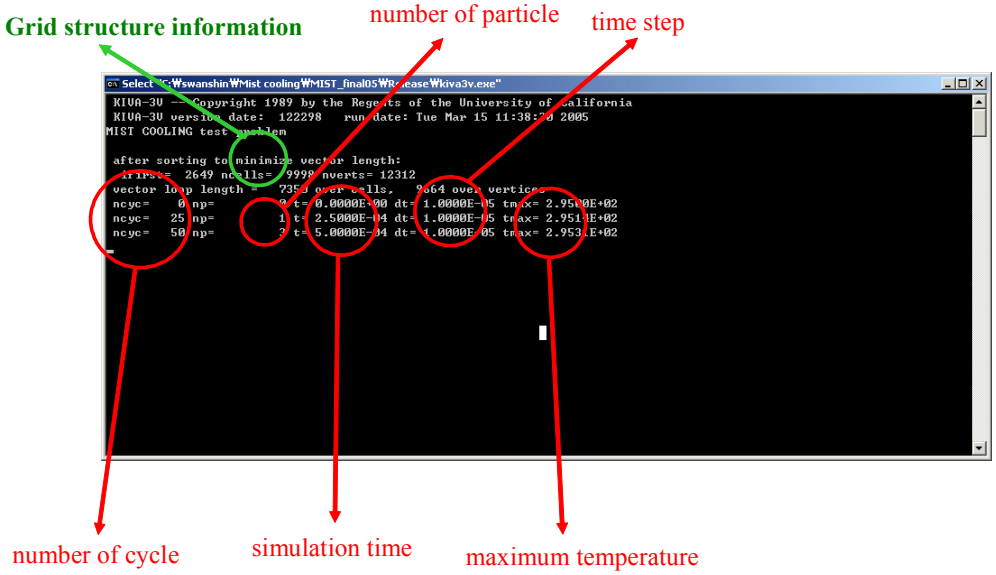

Restarting the code

- After running the code for the very first time (i.e. when irest=0) two restart files “otape8” and “restart.out” would be created (at the rate of every nctap8 time cycle)
- Change the file name “otape8” to “itape7”
- Place “itape7”, “restart.out”, “itape5”, “itape17” and kiva3v.exe files (total of 5 files) in the same directory; reset the “irest” value to 1 in “itape5” and then run the RESTART program by double clicking kiva3v.exe file

Input variables (itape5)

```
0                                   :irest
5000                                :ncfilm
5000                                :nctap8
5.0e-6                              :dt
2.36                                :bore
175.0                               :stroke
0.0                                 :gx
0.0                                 :gy
981.0                               :gz
285.81                              :tcylwl
1.457e-5                            :airmu1
110.0                               :airmu2
252.0                               :airla1
200.0                               :airla2
0.71                                :prl
2.7                                 :rpr
2.7                                 :rsc
1                                   :itype_inject
1                                   :numnoz
0.0                                 :t1inj
9.99d+9                             :tdinj
1.167                               :tspmas
11670.0                             :tnparc
0                                   :injdist
287.39                              :tpi
0.0                                 :drnoz
1.0                                 :dznoz
0.0                                 :dthnoz
0.0                                 :tiltxy
0.0                                 :tiltxz
10.0                                :cone
10.0                                :dcone
0.1                                 :anoz
1.50e-3                             :smr
```

```
6500.0                              :velinj
3                                   :nsp
h2o
    o2   mw2    32.000  htf2    0.0
    n2   mw3    28.016  htf3    0.0
1015520.0                           :presi
287.39                              :tempi
112500.0                            :tkei
0.00854                             :mfracfu
0.23795                             :mfraco2
0.75351                             :mfracn2
8.0d0                               :rowall
1.63d6                              :tkwall
5.0d6                               :cpwall
8.89d-2                             :thwall
3.9904d9                            :Qwall
70.0                                :zl_unheated
0                                   :itpye_channel
4.0                                 :x_length
2.0                                 :y_length
8                                   :nsx1
8                                   :nsx2
175                                 :nsy
0                                   :itype_Q
0.0d0                               :tini_Q
0.01d0                              :pulse_freq
0.0001d0                            :pusle_width
10                                  :iplot_freq
0                                   :itype_gas
0                                   :itype_liquid
175.0                               :distamb
1006630.0                           :pamb
11250.0                             :tkeamb
1500.0                              :velin
```

Input variables (itape5)-continued

- irest : restart flag (=0 : without restart i.e. only when you run it the very first time, =1: restart, i.e when you use saved date from the very first run and want to continue from there)
- ncfilm : # of cycles between screen outputs
- nctap8 : # of cycles between storing restarting file
- dt : initial simulation time step [sec] (in case of pulsed heating using fixed time step. dt should be smaller than pulse width, e.g. 1.0e-5 is good for pulse heating)
- bore : pipe diameter [cm]
- stroke : pipe length [cm]
- gx, gy, gz : gravitational acceleration vector, [g·cm/s^2]
- tcylwl : initial pipe wall temperature, [K]
- airmu1, airmu2 : molecular viscosity of ambient medium is given by airmu1*$temp^{1.5}$/(temp+airmu2)
- airla1, airla2 : molecular heat conduction coefficient of ambient medium is airla1*$temp^{1.5}$/(temp+airla2)
- prl : laminar prandtl number

Input variables (itape5)-continued

- rpr : 1.0/turbulent prandtl number (this is empirical and good for Air and Helium)
- rsc : 1.0/turbulent schmidt number (this is empirical and good for Air and Helium)
- itype_inject : type of injection (0 = random injection, 1 = injection from nozzle)
- numnoz : number of injection nozzles (effective only if itype_inject=1)
- t1inj : time injection begins [sec]
- tdinj : time injection ends [sec]
- tspmas : injected liquid mass flow rate [g/sec]
- tnparc : number of computation particles injected per second, (use "tspmas" * 10,000 – Dr. Seungwon Shin recommendation)
- injdist : 0=uniform droplet size, 1=follows specified droplet size distribution (e.g. Gaussian distribution)
- tpi : test section entrance water droplet temperature; after the nozzle [K]
- drnoz : radial location of nozzle from axial flow centerline [cm] (effective only if itype_inject=1); if there is more that one nozzle just make as many columns and separate them by space.

Input variables (itape5)-continued

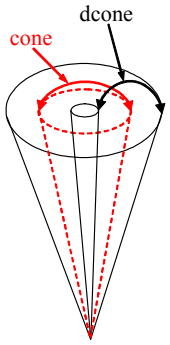

- **dznoz : location of nozzle relative to the inlet plane [cm] (effective only if itype_inject=1)**
- **dthnoz : azimuth angle of nozzle [degree] (effective only if itype_inject=1)**
- **tiltxy : nozzle rotation in the x-y plane [degree] (effective only if itype_inject=1)**
- **tiltxz : nozzle rotation in the x-z plane [degree] (effective only if itype_inject=1)**
- **cone : mean spray cone angle [degree] (effective only if itype_inject =1)**
- **dcone : spray thickness [degree], for solid code = cone (effective only if itype_inject =1)**
- **anoz : actual nozzle flow area [cm^2] (effective only if itype_inject=1)**
- **smr : sauter mean *RADIUS* of droplet [cm]**
- **velinj : droplet injection velocity [cm/s] (Seungwon recommends same velocity as air velocity even if you use nozzle)**
- **nsp : number of species**

Input variables (itape5)-continued

- **o2, n2, h2o : species chemical formula, used as identifier (mw#: molecular weight of species, htf#: heat of formation of species – not important for here), h2o and FC72 set automatically in subroutine fuel**
- **presi : initial pressure [$g/cm{\cdot}s^2$], (Pa * 10)**
- **tempi : test section entrance gas temperature; after the nozzle [K]**
- **tkei : initial turbulent kinetic energy $V^2/2$ [cm^2/s^2]. Use 1-10% of the mean flow kinetic energy (even up to 25% for air-assisted nozzle case)**
- **mfrac : *MASS* fraction of species (should be provided for nsp species)**
- **rowall : density of the wall material**
- **tkwall : conductivity of the wall material**
- **cpwall : capacity of the wall material**
- **rowall : thickness of the wall material [cm]**
- **Qwall : heat power into the flow [power in CGS sys] [W *d7]**
- **zl_unheated : unheated inlet length [cm]**

Input variables (itape5)-continued

- itype_channel : cylinder = 0; rectangular channel = 1 for two opposite side heated, and 3 for four side heated
- x_length : rectangular test section dimension in x direction [cm] (used only if itype_channel =1)
- y_length : rectangular test section dimension in y direction [cm] (used only if itype_channel =1)
- nsx1 : ny in grid generation (must be even number only for rectangular test section) (in case of circular pipe, nsx1=nsx2)
- nsx2 : nx in grid generation (must be even number only for rectangular test section) – these are the two heated sides in rectangular channel in the case of itype_channel = 1
- nsy : nz in grid generation
- itype_Q : heat generation type (0 continuous, 1 pulsed)
- tini_Q : starting time of heat generation [sec]
- pulse_freq : pulse frequency [sec] (effective only if itype_Q=1)
- pulse_width : pulse width [sec] (effective only if itype_Q =1)
- iplot_freq : plotting frequency for pulsed heating [plots every XX pulse] (effective only if itype_Q=1)

Input variables (itape5)-continued

- itype_gas : type of gas (0 air, 1 helium)
- itype_liq : type of liquid (0 water, 1 FC72) (effective only if itype_gas=1, cannot run air and FC72)
- distamb : outflow pressure distance [cm]. Usually use the size of pipe length or at least half of the pipe length
- pamb : ambient pressure [g/cm·s^2], (Pa * 10)
- tkeamb : ambient turbulent kinetic energy $V^2/2$ [cm^2/s^2]
- velin : inlet velocity [cm/s]

- For Air: airmu1 = 1.457d-5, airmu2 = 110.0, airla1 = 252.0, airla2 = 200.0
- For helium: airmu1 = 1.5d-5, airmu2 = 80.0, airla1 = 1220.0, airla2 = 120.0

Choosing the coolant

- **Number of species is made up of coolant and injecting liquid. Injection liquid comes first (it is called fuel), then coolant.**
- **mw#: molecular weight of species, htf#: heat of formation of species**
- **Various options are available for injection liquid (fuel), in case of water, use identification "h2o". FC72 can be used as injection liquid by using identification "gasoline" (btw FC72 molecular mass is 338 but there is not need to write it in the "itape5" file). h2o as well as FC72 set automatically in subroutine fuel. Other injection liquids are also available, see KIVA code references.**
- **In case of air, use two gases (n_2 and o_2, identification "n2" and "o2") with *mass* fraction (0.76 and 0.24). Heat of formation is not important since there is no chemical reaction occurring.**
- **In case of helium, use identification "h" and molecular weight of 4, Heat of formation - again not important**
- **Other "materials" are also available, see KIVA code references**

Nozzle geometry

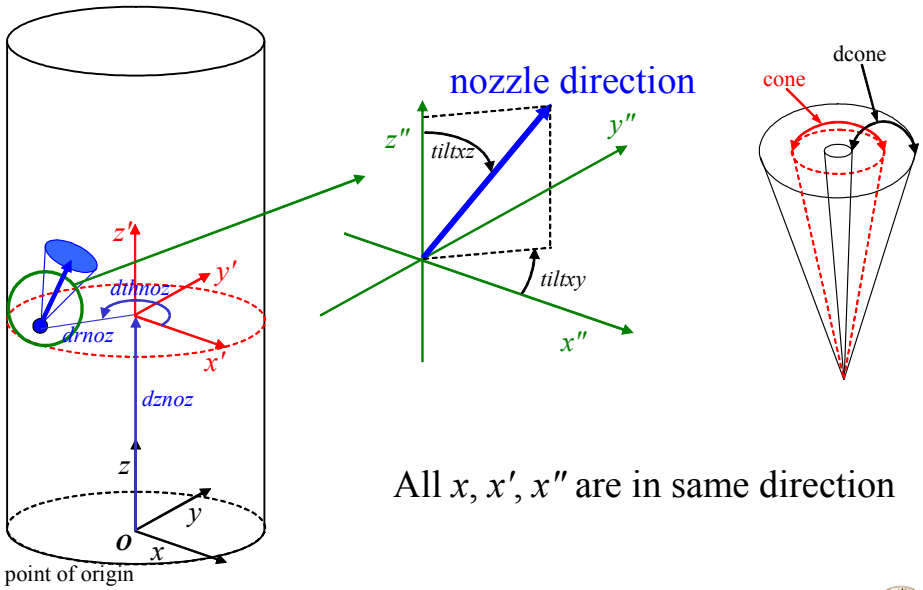

All x, x', x'' are in same direction

APPENDIX E

DROPLET SIZE DISTRIBUTION

In this appendix, droplet size distribution for the gas-assisted nozzle (Spray Systems 1/8J-SS+SU22B-SS), and the fixed geometry hydraulic nozzle (HAGO M1) used in this study are presented.

Table E.1 Sauter Mean Diameter [μm] for the gas-assisted nozzle (Spray Systems 1/8J-SS+SU22B-SS), (extrapolated diameters shown in bold)

Pressure	Liquid			
Gas	1	2	5	10
1	**70**	**73**		
2	**63**	**66**		
3	**56**	**59**		
4	**49**	**52**	64	
5	**42**	**45**		
6	**35**	**38**	47	62
7	**28**	**31**		
8	**21**	**24**	34	50
9	**17**	**20**		
10	**13**	**16**	26	42

Table E.2 Sauter Mean Diameter [μm] for the fixed geometry nozzle (HAGO M1)

Liquid Pressure [PSI]	Sauter Mean Diameter [μm]
40	39.4
60	34.1
80	30.3
100	28.4
200	22.6

APPENDIX F

CALIBRATIONS

This appendix presents the calibrations for the thermocouples, pressure transducers, humidity sensors, orifice flowmeter and water rotameter used in this thesis.

F.1 Thermocouples

The thermocouples located at the Teflon instrument block #1 (T102, since it was connected to the channel #102 in the Agilent 34970A data acquisition unit), Teflon instrument block #2 (T101), Teflon instrument block #3 (T103), upstream of the Venturi flowmeter (T104), and upstream of the orifice flowmeter (T105) (all of them: Omega EMQSS-062E-12) were calibrated using a block calibrator (Techne Laboratory Equipment DB-35L) and a platinum resistance temperature detector (RTD) with manufacturer-supplied uncertainty of 0.005 ^{o}C (ASL T100-250, SN 440037). The rest of the thermocouples used in experiments with second and third cylindrical test sections (TUBE 2 and TUBE 3, respectively) and second rectangular test section (DUCT 2) were not calibrated due to the fact that they had self-adhesive patch which would be damaged during the calibration. In addition to this thermocouples used to measure water line temperature immediately before the nozzle, room and outside insulation surface temperature were not calibrated. However, all of the uncelebrated thermocouples are manufactured as high accuracy thermocouples with manufacturer-supplied calibrations and uncertainty of 1 ^{o}C. Thermocouples used for wall temperature measurements for the first rectangular and cylindrical test sections were individually calibrated; however since

data of those test sections were not presented in this thesis the calibration details are not shown here either.

The calibration data of the five thermocouples mentioned above were taken over a range from approximately 5 to 110 ^{o}C. All five thermocouples are calibrated simultaneously by tying them to the RTD and inserting the sensor into the crucible for the block calibrator. The crucible was filled with glycerin in order to reduce thermal variations between the sensors. The temperature was allowed to stabilize for approximately ten minutes between adjustments to the block calibration unit. For each data point 100 Power Line Cycle (PLC) measurements were taken. The measured parameter for the thermocouples was in degrees Celsius since they were connected to the Agilent 34970A and the channels were set up as a type T thermocouples. The output of the RTD in Ohms was measured by an Agilent 34401A Digital Multimeter and converted to temperature by a ninth order equation provided by the RTD manufacturer. Table F.1 shows data taken for the calibration. The results of the linear calibrations are summarized in Table F.2. The uncertainty of the calibration is taken to be the standard error of the calibration, standard error of estimate (SEE), times the student-t value for a confidence level of 95 percent.

Table F.1 The thermocouples calibration data

Calibrator T [°C]	RTD [OHM]	RTD [°C]	T101 [°C]	T102 [°C]	T103 [°C]	T104 [°C]	T105 [°C]
5	102.046	5.013	4.365	4.457	4.608	4.678	4.447
10	104.046	10.037	9.119	9.278	9.418	9.594	9.479
15	106.045	15.067	14.164	14.318	14.473	14.629	14.557
20	108.033	20.077	19.301	19.465	19.611	19.713	19.571
25	110.027	25.109	24.046	24.246	24.395	24.564	24.553
30	112.042	30.202	29.091	29.291	29.443	29.623	29.657
35	114.027	35.228	34.412	34.573	34.706	34.826	34.769
40	116.016	40.271	39.446	39.646	39.774	39.905	39.846
45	117.992	45.289	44.204	44.389	44.535	44.720	44.807
50	119.998	50.391	49.461	49.640	49.744	49.878	49.920
55	121.980	55.440	54.205	54.391	54.533	54.717	54.880
60	123.940	60.441	59.275	59.483	59.589	59.770	59.917
65	125.930	65.526	64.335	64.531	64.675	64.871	65.021
70	127.930	70.644	69.671	69.828	69.932	70.083	70.194
75	129.900	75.694	74.682	74.853	74.959	75.137	75.241
80	131.890	80.803	79.546	79.734	79.879	80.073	80.315
85	133.840	85.817	84.739	84.946	85.058	85.209	85.378
90	135.780	90.813	89.703	89.912	90.023	90.187	90.386
95	137.770	95.946	94.697	94.886	95.019	95.226	95.506
100	139.710	100.957	99.813	99.975	100.121	100.276	100.544
105	141.700	106.106	105.021	105.205	105.319	105.448	105.689
109	143.230	110.071	108.810	109.015	109.156	109.304	109.632

Table F.2 Summary of the thermocouple calibrations

Thermocouple	Slope	Intercept [°C]	SEE t_{95} [°C]
T101	1.00367952	0.82856117	0.260
T102	1.00329213	0.67008303	0.235
T103	1.00353513	0.52369092	0.221
T104	0.99651002	-0.11946465	0.167
T105	0.99883233	0.55048024	0.073
Other with manufacturer-supplied calibrations	1	0	1

F.2 Pressure Transducers

The calibrations of the pressure transducers were performed using a tube with series of tees where the pressure transducers and the standard pressure instrument (a Bourdon Tube or water U manometer) were attached. Data was taken by adjusting the static pressure in the tube with the pressure regulator and allowing the tube pressure to stabilize. At each stabilized pressure, the output of the pressure transducers were read using 100 Power Line Cycle (PLC) measurements, and the pressure was read off of the standard pressure instrument. The uncertainty of calibration is taken to be the standard error of the calibration, SEE, times the student-t value for a confidence level of 95 percent. A differential pressure transducer (P106, since it was connected to the channel #106 in the Agilent 34970A data acquisition unit) (Omega PX26-015DV) used for measuring the pressure difference across the orifice flowmeter (Gerrand Engineering, model ¾" B-5) was calibrated using the Bourdon tube (HEISE cc-99976, Bourdon tube 403) as the standard with uncertainty of 0.2 psi (provided by the manufacturer) and the range of 0 to 200 psig. The calibration data for this transducer are shown in Table F.3, while the results of the calibration are summarized in Table F.7. A gage pressure transducer (P107) (Omega PX180-060GV) used for measuring the upstream gage pressure at the Venturi flowmeter (Lambda Square CBV075) was calibrated using the Bourdon tube (HEISE cc-99976, Bourdon tube 403) as the standard with uncertainty of 0.2 psi (provided by the manufacturer) and the range of 0 to 200 psig. The calibration data for this transducer are shown in Table F.4, while the results of the calibration are summarized in Table F.7. Gage pressure transducers used for measuring gage pressure in the Teflon instrument block #1 (P108), Teflon instrument block #2 (P109), and Teflon

instrument block #3 (P110) (all of them: Omega PX180-015GV) were calibrated using a test gage with accuracy grade 3A (ASHCROFT Q-8638, AISI 316 tube) as the standard with uncertainty of 0.25 % over the entire scale (0-15 psig) provided by the manufacturer. The calibration data for this transducer are shown in Table F.5, while the results of the calibration are summarized in Table F.7. A differential pressure transducer (P111) (Omega PX26-030DV) used for measuring the upstream gage pressure at the orifice flowmeter (Gerrand Engineering, model ¾" B-5) was calibrated using the Bourdon tube (HEISE cc-99976, Bourdon tube 403) as the standard with uncertainty of 0.2 psi (provided by the manufacturer) and the range of 0 to 200 psig. The calibration data for this transducer are shown in Table F.6, while the results of the calibration are summarized in Table F.7. An absolute pressure transducer (P112) (Omega PX302-015AV) used for measuring the room pressure had manufacturer-supplied calibration and uncertainty of 0.25% (summarized in Table F.7).

Table F.3 P106 differential pressure transducer calibration data

Standard [PSIG]	P106 [VDC]
0.00	-0.00015160
2.01	0.01464178
4.00	0.02762814
6.02	0.04275206
8.00	0.05522872
10.00	0.06704992
12.10	0.08211704
13.98	0.09408812
15.35	0.10391110

Table F.4 P107 gage pressure transducer calibration data

Standard [PSIG]	P107 [VDC]
0.00	-0.0001039
2.01	0.00357348
4.00	0.00679647
6.02	0.01056282
8.00	0.01368117
10.00	0.01664067
12.10	0.02043731
13.98	0.02347289
15.35	0.02597812
18.55	0.03133188
22.35	0.0376187
25.60	0.04310071
28.35	0.0476544
30.65	0.05146156
35.65	0.05987458
40.50	0.06803335
45.40	0.07634521
49.85	0.08378106
55.20	0.09262472
60.00	0.1006332

Table F.5 P108-P110 gage pressure transducers calibration data

Standard [PSIG]	P108 [VDC]	P109 [VDC]	P110 [VDC]
1.79	0.011422	0.011249	0.012022
1.73	0.011083	0.010905	0.011680
1.59	0.010129	0.009951	0.010725
1.50	0.009499	0.009319	0.010090
1.43	0.009028	0.008851	0.009631
1.33	0.008369	0.008189	0.008972
1.24	0.007810	0.007628	0.008409
1.11	0.006874	0.006692	0.007472
1.02	0.006330	0.006143	0.006929
0.92	0.005651	0.005464	0.006253
0.81	0.004929	0.004741	0.005525
0.73	0.004425	0.004236	0.005021
0.61	0.003596	0.003404	0.004187
0.53	0.003089	0.002894	0.003680
0.45	0.002535	0.002341	0.003133
0.38	0.002059	0.001868	0.002660
0.31	0.001610	0.001416	0.002204
0.25	0.001182	0.000987	0.001777
0.14	0.000509	0.000311	0.001098
0.06	-0.000073	-0.000274	0.000520
0.00	-0.000457	-0.000658	0.000140
1.80	0.011934	0.011757	0.012528
2.20	0.014738	0.014568	0.015339
2.60	0.017335	0.017174	0.017941
2.80	0.018789	0.018629	0.019390
3.09	0.020586	0.020431	0.021194
4.21	0.028200	0.028058	0.028803
4.68	0.031497	0.031356	0.032095
4.81	0.032376	0.032238	0.032973
5.00	0.033588	0.033450	0.034185
3.24	0.021749	0.021576	0.022345
3.52	0.023585	0.023420	0.024185
3.70	0.024793	0.024633	0.025389
4.04	0.027055	0.026901	0.027654

Table F.6 P111 differential pressure transducer calibration data

Standard [PSIG]	P111 [VDC]
0.00	-0.00014974
2.01	0.00717311
4.00	0.01361189
6.02	0.02113096
8.00	0.02734538
10.00	0.03321107
12.10	0.04078701
13.98	0.04680237
15.35	0.05177413
18.55	0.06243385
22.35	0.07492502
25.60	0.08582071
28.35	0.09485773
30.65	0.10242640

Table F.7 Summary of the pressure transducer calibrations

Pressure transducer	Slope	Intercept [PSI]	SEE t_{95} [PSI]
P106	149.0525956	-0.129794935	0.30
P107	596.5708971	-0.08747232	0.17
P108	150.4481915	0.069475096	0.037
P109	150.1268083	0.09933616	0.037
P110	150.3799541	-0.01989733	0.037
P111	299.7942714	-0.110624518	0.20
P112	152.4758343	-0.1628678	0.25 %

F.3 Humidity Sensors

Relative humidity sensors (all of them: Honeywell HIH-3610-003) used in this thesis had manufacturer-supplied calibration and uncertainty of 2 %. A relative humidity sensor (P113, since it was connected to the channel #113 in the Agilent 34970A data acquisition unit) was used to measure relative humidity upstream of the Venturi flowmeter (Lambda Square CBV075). Differential pressure transducers (P114-P116) were used to measure relative humidity in the Teflon instrument block # 1, Teflon instrument block # 2, and Teflon instrument block # 3, respectively. The results of the relative humidity sensor calibrations are summarized in Table F.8. After applying the calibration formula to the humidity sensors' voltage readings a temperature compensation was taken into account using the manufacturer-supplied formula (True RH = (Sensor RH)/(1.0546 - 0.00216 x Temperature), Temperature in ^{o}C).

Table F.8 Summary of the relative humidity sensor calibrations

Humidity sensor	Slope	Intercept [%]	SEE t_{95} [% RH]
P113	31.64556962	-27.72151899	2
P114	31.446541	-26.761006	2
P115	31.34796	-27.89968652	2
P116	31.34796	-27.86833856	2

F.4 Orifice Flowmeter

An orifice flowmeter (Gerrand Engineering, model ¾" B-5) used in this thesis was calibrated against the Venturi flowmeter (Lambda Square CBV075). The Venturi flowmeter had manufacturer-supplied uncertainty of 1 %. The calibration data for the orifice flowmeter are shown in Table F.9. After the 0.007184 kg/s flow rate it is assumed that the orifice and the Venturi flowmeters read the same flow rate. Sixth order trendline is obtained in Excel:

$$y = -6756724.46484375x^6 + 490503.813531536x^5 - 2292.74125644001x^4 - 651.021633245378x^3 + 20.8378664487055x^2 + 0.757532645897201x + 0.000960935656272423 \quad \text{(F.1)}$$

with $R^2 = 0.999995271607303$. Here "x" is the original reading of the orifice flowmeter, while "y" is the corrected flowrate by using the calibration against the Venturi flowmeter. Uncertainty B with 95 % confidence limit (see Jeter and Donnell (2004)) for the gas flow rate through the orifice flowmeter was calculated to be 5.4 % of the total flow rate by using an Engineering Equation Solver (EES) code via the built in error propagation analysis which is known to be reliable, see Kline and McClintock (1953).

Table F.9 The orifice flowmeter calibration data

Orifice kg/s	Venturi kg/s
0.000964	0.001732
0.001915	0.002447
0.002570	0.002983
0.003046	0.003445
0.003857	0.004210
0.004555	0.004847
0.005198	0.005397
0.005748	0.005889
0.006247	0.006352
0.006743	0.006784
0.007184	0.007183
0.0076	0.0076
0.0082	0.0082
0.0087	0.0087
0.0093	0.0093
0.0098	0.0098
0.0103	0.0103
0.0113	0.0113
0.0123	0.0123
0.0133	0.0133
0.0143	0.0143
0.0153	0.0153
0.0163	0.0163
0.0173	0.0173
0.0183	0.0183
0.0193	0.0193
0.0203	0.0203
0.0213	0.0213
0.0223	0.0223
0.0233	0.0233
0.0243	0.0243
0.0253	0.0253
0.0263	0.0263
0.0273	0.0273
0.0283	0.0283
0.0293	0.0293
0.0303	0.0303
0.0313	0.0313
0.0323	0.0323
0.0333	0.0333
0.0343	0.0343
0.0348	0.0348

F.5 Water Rotameter

A water rotameter (Brooks Instrument Division 1355K1BH0F6CG) used in this thesis was calibrated using weighing tank method. The water rotameter has two measuring balls, i.e. light and heavy. The weighing scale had manufacturer-supplied uncertainty of 0.1 kg. The timer had manufacturer-supplied uncertainty of 0.01 sec. The calibration data for the water rotameter light ball are shown in Table F.10, while for the heavy ball the data are shown in Table F.11. Sixth order trendline is obtained for the light ball in Excel:

$$a = 0.000000000926088784380507b^6 - 0.000000051398001643486 6b^5 + 0.000011287886085452 4b^4 - 0.000012361992473536 6b^3 + 0.000067574176423079 4b^2 - 0.000086905038332092 8b + 0.000046284424313410 4 \quad (F.2)$$

with $R^2 = 0.999970930599769$. Here "b" is the light ball reading, while "a" is the calibrated mass water flowrate. Fourth order trendline is obtained for the heavy ball in Excel:

$$c = -0.000000024040384158689 1d^4 + 0.000000878061665584196d^3 - 0.000018282335702955 7d^2 + 0.000411209903329 1d - 0.000268762093764 2 \quad (F.3)$$

with $R^2 = 0.99998201091188$. Here "d" is the heavy ball reading, while "c" is the calibrated mass water flowrate.

As in section F.4 the uncertainty B with 95 % confidence limit for the water flow rate was calculated to be 1.1 % of the total flow rate by using an Engineering Equation Solver (EES) code via the built in error propagation analysis.

Table F.10 The light ball water rotameter calibration data

Rotameter light ball	Flow rate [kg/s]
0	0
1.55	3.44104E-05
2.72	0.000112673
3.3	0.000169063
4.05	0.000233266
5	0.000315543
6.35	0.00041732
7.75	0.000513778
8.95	0.000586765
11.1	0.000707013
13	0.000803333
14.8	0.00087973

Table F.11 The heavy ball water rotameter calibration data

Rotameter heavy ball	Flow rate [kg/s]
0	0
1.3	0.000233266
1.52	0.000315543
1.8	0.00041732
2.04	0.000513778
2.3	0.000586765
2.65	0.000707013
2.95	0.000803333
3.18	0.00087973
4.5	0.00127686
6	0.001702
8	0.002205839
10	0.002647222
12.25	0.003100342
14.75	0.00349845

APPENDIX G

UNCERTAINTY ANALYSIS

This appendix summarizes the methods used to obtain the uncertainty for the wall and bulk temperatures, uniform wall heat flux, and local heat transfer coefficient. Uncertainty A (U_A) also known as imprecision is obtained using the generic formula,

$$U_A = k_c \text{ SSD} \tag{G.1}$$

where k_c is coverage factor and is computed from the t-distribution using the auxiliary parameter called the degrees of freedom (see Jeter and Donnell (2004)); SSD is sample standard deviation. The uncertainty A (U_A) has 95 % confidence limit.

Uncertainty B (U_B) also known as inaccuracy is determined by propagation of error. Error propagation was always calculated by following generic equation,

$$\left(U_B(b)\right)^2 = \sum_{n=1}^{m}\left(\frac{\partial b}{\partial a_n} U_B(a_n)\right)^2 \tag{G.2}$$

where,

$$b = b(a_1, a_2, a_3, \ldots, a_m) \tag{G.3}$$

and m is the total number of independent parameters. The uncertainty B (U_B) also has 95 % confidence limit.

Combined uncertainty (U_C) is calculated using the rule for combining uncertainties, where the square combined uncertainty is a sum of the square of the two contributing uncertainties, or

$$U_C = \sqrt{U_A^2 + U_B^2} \tag{G.4}$$

G.1 Wall Temperature

The uncertainty B for wall thermocouples ($U_B(T_w)$) was estimated from manufacturer-supplied calibrations (1.0 ^{o}C). T_w is the local value of the average inside surface temperature.

G.2 Uniform Wall Heat Flux

The uncertainty B for the calculated uniform wall heat flux ($U_B(q_w)$) was calculated with an Engineering Equation Solver (EES) code by using the built in error propagation analysis which is known to be reliable, see Kline and McClintock (1953). Equation used in calculating the inside wall surface uniform heat flux in the heated test section is,

$$q_w = \frac{V_{eff} I_{eff}}{A_w} \tag{G.5}$$

where, q_w is the calculated inside wall surface uniform heat flux in the heated test section; V_{eff} is the effective voltage drop along the heated test section measured by an Agilent 34970A data acquisition unit and $U_B(V_{eff})$ is the corresponding uncertainty B provided by the manufacturer (0.01 % of the measurement); I_{eff} is the effective current measured by DC shunt (Deltec Company MKB-600-100) and $U_B(I_{eff})$ is the corresponding uncertainty B provided by the manufacturer (0.25 % of the measurement); A_w is the inside wall area of the heated test section calculated from the test section measurements and $U_B(A_w)$ is the corresponding uncertainty B calculated by using the resolution of the length and inner diameter measurements (1.4 % of the calculated area). The uncertainties of these three measurements and the calculated uncertainty of the uniform heat flux by using the error propagation analysis are shown in Table G.1. The representative experiment used in calculating the uncertainty B of the calculated uniform wall heat flux $U_B(q_w)$ is downward air/water mist flow with an average inlet air velocity of 15 m/s and injected water mass fraction of 15 % with 10.20 kW/m^2 heat flux in the 23.6 mm ID circular test section (PIPE 3) with a 7.5 cm long unheated acrylic visualization section (see Figure 4.4 in Chapter IV).

Table G.1 Uncertainties used in calculating the heat flux uncertainty

Variable	Uncertainty B	Source
Effective voltage V_{eff}	0.03 V	Provided by manufacturer
Effective current I_{eff}	0.70 A	Provided by manufacturer
Inside wall area A_w	0.0011 m^2	Calculated from measurements
Uniform heat flux q_w	180 W/m^2	

Calculated uncertainty B for the calculated uniform heat flux is equivalent to ~ 1.8 % of the total heat flux used in this experiment.

G.3 Bulk Temperature

The uncertainty B for bulk thermocouples ($U_B(T_b)$) was calculated with an Engineering Equation Solver (EES) code by using the built in error propagation analysis as in section G.2. T_b is the calculated mean bulk temperature of the mist. The uncertainties of the variables used in the error propagation analysis and the calculated uncertainty of the bulk temperature are shown in Table G.2. The representative experiment used in calculating the uncertainty B of the bulk temperature was the same as in section G.2.

Table G.2 Uncertainties used in calculating the bulk temperature uncertainty

Variable	Uncertainty B	Source
Uniform heat flux q_w	1.8 %	Calculated (see section G.2)
Gas flowrate $\dot{m}_{gas}$	5.6 %	Calibration
Water flowrate $\dot{m}_{water}$	1.1 %	Calibration
Inlet temperature T_{inlet}	0.26 ^{o}C	Calibration
Wall temperature T_w	1.0 ^{o}C	Calibration
Bulk Temperature T_b	0.58 ^{o}C	

q_w is the inside wall surface uniform heat flux in the heated test section, its uncertainty B is discussed in section G.2; $\dot{m}_{gas}$ is the carrier gas flow rate through the heated test section and its corresponding uncertainty B is obtained by calibration (5.6 % of the measured flow rate); $\dot{m}_{water}$ is the water flow rate through the heated test section and its corresponding uncertainty B is obtained by calibration (1.1 % of the measured flow rate); T_{inlet} is the inlet gas and water temperature at 100 % relative humidity and its corresponding uncertainty B is obtained by calibration (i.e. 0.26 ^{o}C); T_w is the wall temperature and its corresponding uncertainty B is estimated from manufacturer-supplied calibrations (i.e. 1.0 ^{o}C).

G.4 Local Heat Transfer Coefficient

As discussed in Chapter III the heat transfer coefficient h is calculated using the relation,

$$h = \frac{q_w}{\left(T_w - T_b\right)} \tag{G.6}$$

where q_w is the heated test section wall heat flux based on the inside surface area, T_w is the local value of the average inside surface temperature, and T_b is the calculated mean bulk temperature of the mist at the same axial location. The representative experiment used in calculating the three uncertainties of the heat transfer coefficient was the same as in section G.2.

The uncertainty A for the local heat transfer coefficient (U_A) is calculated using the equation (G.1). The calculation for the uncertainty A of the local heat transfer coefficient for the same representative experiment as in section G.2 is shown in Table G.3. The values of heat transfer coefficient h used in calculating the uncertainty A (U_A) are taken at the instrumented location z/d = 20. It is assumed that the calculated uncertainty A is the same for all of the instrumented test section locations where the local heat transfer coefficient is calculated.

Table G.3 Uncertainty A of the calculated local heat transfer coefficient

Data index	Heat transfer coefficient h, $\frac{W^2}{m^4K^2}$	
1	486.8	
2	481.7	
3	489.3	
4	495.4	
5	490.7	
6	490.1	
7	495.0	
8	491.6	
	490	= average h
	4.4	= calculated SSD
	2.36	= calculated k_c
	11	= calculated U_A

The uncertainty B for the local heat transfer coefficient (U_B) is calculated using the following error propagation equation (also see equation (G.2)),

$$U_B^2 = \left(\frac{1}{T_w - T_b} U_B(q_w)\right)^2 + \left(-\frac{q_w}{(T_w - T_b)^2} U_B(T_w)\right)^2 + \left(\frac{q_w}{(T_w - T_b)^2} U_B(T_b)\right)^2 \quad \text{(G.7)}$$

This equation can be also written as,

$$U_B^2 = \left(\frac{h}{q_w} U_B(q_w)\right)^2 + \left(-\frac{h}{(T_w - T_b)} U_B(T_w)\right)^2 + \left(\frac{h}{(T_w - T_b)} U_B(T_b)\right)^2 \qquad \text{(G.8)}$$

where $U_B(T_w)$ is the uncertainty B for the wall temperatures (see section G.1); $U_B(q_w)$ is the uncertainty B for the calculated heat flux (see section G.2); $U_B(T_b)$ is the uncertainty B for the calculated bulk temperatures (see section G.3). The calculation steps for the uncertainty B of the calculated local heat transfer coefficient for the same representative experiment as in section G.2 is shown in Table G.4. The values for h, T_w, and T_b used in calculating the influence coefficients $\frac{\partial b}{\partial a_n}$, i.e. $\frac{h}{(T_w - T_b)}$ and $\frac{h}{q_w}$ are taken at the instrumented location z/d = 20; their values are,

$$\frac{h}{(T_w - T_b)} = -\frac{490 \frac{\mathrm{W}}{\mathrm{m^2 K}}}{(44^{\circ}\mathrm{C} - 23^{\circ}\mathrm{C})} = 23 \frac{\mathrm{W}}{\mathrm{m^2 K^2}} \qquad \text{(G.9)}$$

$$\frac{h}{q_w} = \frac{490 \frac{\mathrm{W}}{\mathrm{m^2 K}}}{10200 \frac{\mathrm{W}}{\mathrm{m^2}}} = 0.048 \frac{1}{\mathrm{K}} \qquad \text{(G.10)}$$

It is assumed that the calculated uncertainty B (U_B) is the same for all of the instrumented test section locations where the local heat transfer coefficient is calculated.

Table G.4 Uncertainty B of the calculated local heat transfer coefficient

Variable	Uncertainty B $(U_B(a_n))$	Influence coefficient, $\frac{\partial b}{\partial a_n}$	$\left(\frac{\partial b}{\partial a_n}U_B(a_n)\right)^2$
Wall temperature T_w	1.0 °C	$-23\frac{\mathrm{W}}{\mathrm{m^2K^2}}$	$530\ \frac{\mathrm{W^2}}{\mathrm{m^4K^2}}$
Wall heat flux q_w	$180\ \frac{\mathrm{W}}{\mathrm{m^2}}$	$0.048\frac{1}{\mathrm{K}}$	$8.6\ \frac{\mathrm{W^2}}{\mathrm{m^4K^2}}$
Bulk temperature T_b	0.58 °C	$23\frac{\mathrm{W}}{\mathrm{m^2K^2}}$	$180\ \frac{\mathrm{W^2}}{\mathrm{m^4K^2}}$
		Sum of $(U_B(b))^2$ =	$720\ \frac{\mathrm{W^2}}{\mathrm{m^4K^2}}$
		Uncertainty B (U_B) =	$27\ \frac{\mathrm{W}}{\mathrm{m^2K}}$

Finally the combine uncertainty (U_C) is calculated using the equation (G.4),

$$U_C = \sqrt{\left(11\frac{\mathrm{W}}{\mathrm{m^2K}}\right)^2 + \left(27\frac{\mathrm{W}}{\mathrm{m^2K}}\right)^2} = 29\frac{\mathrm{W}}{\mathrm{m^2K}} \qquad \text{(G.11)}$$

The combined uncertainty for the local heat transfer coefficient of 29 W/m^{2}K is equivalent to 6 % of the calculated heat transfer coefficient at the instrumented location z/d = 20. Since it is assumed that the calculated uncertainty A (U_A) and uncertainty B (U_B) are the same for all of the instrumented test section locations where the local heat transfer coefficient is calculated, it is also assumed that the combined uncertainty C (U_C)

is the same for all of the instrumented test section locations. The uncertainty A and uncertainty C of the local heat transfer coefficient for the same representative experiment as in section G.2 are shown in Figure 4.4 for the case in which the heat flux is calculated using the equation (G.5) (see Chapter IV).

REFERENCES

Amsden, A. A., "KIVA-3: A KIVA Program with Block-Structured Mesh for Complex Geometries," Los Alamos National Laboratory report LA-12503-MS, March 1993.

Amsden, A. A., "KIVA-3V: A Block-Structured KIVA Program for Engines with Vertical or Canted Valves," Los Alamos National Laboratory report LA-13313-MS, July 1997.

Amsden, A. A., "KIVA-3V, Release 2, Improvements to KIVA-3V," Los Alamos National Laboratory report LA-13608-MS, May 1999.

Amsden, A. A., Butler, T. D., and O'Rourke, P. J., "The KIVA-II Computer Program for Transient Multidimensional Chemically Reactive Flows with Sprays," SAE Technical Paper 872072, 1987.

Amsden, A. A., Butler, T. D., O'Rourke, P. J., and Ramshaw, J. D., "KIVA: A Comprehensive Model for 2-D and 3-D Engine Simulations," SAE Technical Paper 850554, 1985.

Amsden, A. A., O'Rourke, P. J., and Butler, T. D., "KIVA-II: A Computer Program for Chemically Reactive Flows with Sprays," Los Alamos National Laboratory report LA-11560-MS, May 1989.

Amsden, A. A., Ramshaw, J. D., Cloutman, L. D., and O'Rourke, P. J., "Improvements and Extensions to the KIVA Computer Program," Los Alamos National Laboratory report LA-10534-MS, October 1985.

Amsden, A. A., Ramshaw, J. D., O'Rourke, P. J., and Dukowicz, J. K., "KIVA: A Computer Program for Two- and Three-Dimensional Fluid Flows with Chemical Reactions and Fuel Sprays," Los Alamos National Laboratory report LA-10245-MS, February 1985.

Akagawa, K., Fujii, T., Murata, K. and Mugitani, N., "Studies of Swirling Annular-Mist Two-Phase Flow (3rd Report, Characteristics of Liquid Film)," *Bulletin of JSME,* Vol. 27, No. 226, April 1984.

Barbosa, J. R., Kandlbinder, T. and Hewitt, G. F., "Forced Convection boiling of Ternary Mixture at High Qualities," *International Journal of Heat and Mass Transfer,* 45, pp. 2655-2665, 2002.

Barbosa Jr., J. R., Hewitt, G. F. and Richardson, S. M., "A Note on the Influence of Droplet Interchange on Evaporation and Condensation of Multicomponent Mixtures in Annular Flow," *Int. J. Heat Mass Transfer,* Vol. 46, pp. 2505-2509, 2003.

Dengler, C. E. and Addoms, J. N., "Heat Transfer Mechanism for Vaporization of Water in a Vertical Tube," *Chem. Eng. Prog. Symp. Series*, **52**, 95, 1956.

Dukler, A. E., "Fluid Mechanics and Heat Transfer in Falling Film Systems," paper presented at the ASME-AIChE 3rd National Heat Transfer Conference, August 1959. See also *Chem. Eng. Prog. Symp. Series,* **56,** 30, pp. 1-10, 1960.

El-Genk, M. S. and Saber, H. H., "An Investigation of the Breakup of an Evaporating Liquid Film, Falling Down a Vertical, Uniformly Heated Wall," *Journal of Heat Transfer, Transactions of the ASME*, Vol. 124, Feb, pp. 39-50, 2002.

Fore, L. B., Ibrahim, B. B. and Beus, S. G., "Visual Measurements of Droplet Size in Gas-Liquid Annular Flow," *International Journal of Multiphase Flow,* v 28, pp. 1895-1910, 2002.

Fu, F. and Klausner, J. F., "A Separated Flow Model for Predicting Two-Phase Pressure Drop and Evaporative Heat Transfer for Vertical Annular Flow," *Int. J. Heat Mass Transfer,* Vol. 18, pp. 541-549, 1997.

Fujita, T. and Ueda, T., "Heat Transfer to Falling Liquid Films and Film Breakdown – I; Subcooled Liquid Films," *Int. J. Heat Mass Transfer,* Vol. 21, pp. 97-108, 1978.

Fujita, T. and Ueda, T., "Heat Transfer to Falling Liquid Films and Film Breakdown – II; Saturated Liquid Films with Nucleate Boiling," *Int. J. Heat Mass Transfer,* Vol. 21, pp. 109-118, 1978.

Ganić, E. N. and Rohsenow, W. M., "Dispersed Flow Heat Transfer," *Int. J. Heat Mass Transfer,* Vol. 20, pp. 855-866. Pergamon Press, 1977.

Ganić, E. N. and Getachew, D., "Effects of Surface Condition and working Fluid on Liquid Film Breakdown During Heat Transfer," *8th Int. HTC*, Washington, D.C., Vol. 4, pp. 1931-1936, 1986.

Ghiaasiaan, S. M., "ME 7301 – Transport Phenomena in Multiphase Flow," Georgia Institute of Technology, class notes, fall semester 2003.

Giuliani, J. L., Hegeler, F., Sethian, J. D., Wolford, M. F., Myers, M. C., Abdel-Khalik, S. I., Sadowski, D., Schoonover, K., Novak, V., "Foil Cooling for Rep-rated Electron Beam Pumped KrF Lasers," *Submitted to International Fusion Science and Applications 2005 Conference Proceedings*, Biarritz, France, Sep. 4-9, 2005.

Guerrieri, S. A. and Talty, R. D., "A Study of Heat Transfer to Organic Liquids in Single Tube, Natural Circulation Vertical Tube Boilers," *Chem. Eng. Prog. Series,* Heat Transfer, Louisville, **52,** 18, pp. 69-77, 1956.

Halbleib, J. A., Kensek, R. P., Valdez, G. D., Seltzer, S. M. and Berger, M. J., "ITS: The Integrated TIGER Series of Electron/Photon Transport Codes – Version 3.0," *IEEE Transactions on Nuclear Science*, Vol. 39. No. 4, pp. 1025-1030, 1992.

Hartley, D. E. and Murgatroyd, W., "Criteria for the Break-up of Thin Liquid Layers Flowing Isothermally Over Solid Surfaces," *Int. J. Heat Mass Transfer,* Vol. 7, pp. 1003-1015, 1964.

Hewitt, G. F., "Analysis of Annular Two-Phase Flow; Application of the Dukler Analysis to Vertical Upward Flow in a Tube," AERE-R 3680, H.M.S.O., 1961.

Hewitt, G. F. and Lacey, P. M. C., "The Breakdown of the Liquid Film in Annular Two-phase Flow," *Int. J. Heat Mass Transfer,* Vol. 8, pp. 781-791, 1965.

Hewitt, G. F. and Hall-Taylor, N. S., "Annular Two-Phase Flow," *Chemical Engineering Devision, A.E.R.E.,* Harwell, England, Pergamon Press, 1970.

Hoke, B. C. and Chen. J. C., "Thermocapillary Breakdown of Subcooled Falling Liquid Films," *Ind. Eng. Chem. Res.*, Vol. 31, No. 3, pp. 688-694, 1992.

Hughes, D. T. and Bott, T. R., "Minimum Thickness of a Liquid Film Flowing Down a Vertical Tube," *Int. J. Heat Mass Transfer,* Vol. 41, No. 2, pp. 253-260, 1998.

Incropera, F. P. and DeWitt, D. P., "Fundamentals of Heat and Mass Transfer," Fourth Edition, John Wiley & Sons, Inc., ISBN 0-471-30460-3, 1996.

Jayanti, S. and Hewitt, G. F., "Hydrodynamics and Heat Transfer of Wavy Thin Film Flow," *Int. J. Heat Mass Transfer,* Vol. 40, No. 1, pp. 179-190, 1997.

Jayanti, S. and Hewitt, G. F., "Hydrodynamics and Heat Transfer in Wavy Annular Gas-Liquid Flow : a Computational Fluid Dynamics Study," *International Journal of Heat and Mass Transfer,* Vol. 40, No. 10, pp. 2445-2460, 1997.

Jeter, S. and Donnell, J., "Writing Style and Standards in Undergraduate Reports," College Publishing, Virginia, ISBN: 0-9679121-7-2, 2004.

Kakac, S., Shah, R. K. and Aung, W., "Handbook of Single-phase Convective Heat Transfer," *Publisher: New York, Wiley,* Chapter 4: Turbulent and Transition Flow Convective Heat Transfer in Ducts, 1987.

Kataoka, I, Ishii, M. and Mishima, K., "Generation and Size Distribution of Droplet in Annular Two-Phase Flow," *Journal of Fluids Engineering, Transactions of the ASME*, v 105, n 2, Jun, pp. 230-238, 1983.

Kitagawa, T., Torii, K. and Nishino, K., "Heat Transfer of Air-Water Dispersed Flow in a Vertical Pipe," *Heat Transfer – Japanese Research,* 27, (4), 1998.

Kline, S. A. and McClintock, F. A., "Describing Uncertainties in Single-Sample Experiments," *Mechanical Engineering*, Vol. 75, pp. 3-8, 1953

Kocamustafaogullari, G., Smits, S. R. and Razi, J., "Maximum and Mean Droplet Sizes in Annular Two-Phase Flow," *Int. J. Heat Mass Transfer,* Vol. 37, No. 6, pp. 955-965, 1994.

Lawrence Livermore National Laboratory, "Internal Fusion Energy: Opportunity for Fusion Innovation," report UCRL-MI-125743, January 1997.

Lee, M. M. and Hanratty, T. J., "The Inhibition of Droplet Deposition by the Presence of a Liquid Wall Film," *Int. J. Multiphase Flow*, Vol. 14, No. 2, pp.129-140, 1988.

Lee, S. L., Issapour, I., Yang, Z. H., Cho, S. K., "Supercooling by Evaporation of an Extra Thin Film Maintained by Micro Droplet Deposition," *Heat Transfer, Proceedings of the International Heat Transfer Conference,* pp. 217-222, 1990.

Lee, S. L., Yang, Z. H. and Hsyua, Y., "Cooling of a Heated Surface by Mist Flow," *Journal of Heat Transfer, Transactions ASME*, v 116, n 1, Feb, p 167-172, 1994.

Mastanaiah, K. and Ganić, E. N., "Heat Transfer in Two-Component Dispersed Flow," *Transactions of the ASME. Journal of Heat Transfer*, v 103, n 2, May 1981, p 300-306, 1981.

Matida, E. A. and Torii, K., "Droplet Deposition and Heat Transfer Simulations of Turbulent Air-Water Dispersed Flow in a Vertical Tube," *JSME International Journal, Series B*, v 38, n 4, Nov, p 628-636, 1995.

McPherson, G. D., "Axial Stability of the Dry Patch Formed in Dryout of a Two-Phase Annular Flow," *Int. J. Heat Mass Transfer,* Vol. 13, pp. 1133-1152, 1970.

Mesler, R. B., "An Alternative to the Dengler and Addoms Convection Concept of Forced Convection Boiling Heat Transfer," *AIChE Journal*, v 23, pp. 448-453, 1977.

Miller, R. W., (1996), "Flow Measurements Engineering Handbook," Third Edition, McGraw-Hill Book Company, 1996.

Mori, Y., Hijikata, K. and Yasunaga, T., "Mist Cooling of Very Hot Tubules with Reference to Through-Hole Cooling of Gas Turbine Blades," *Int. J. Heat Mass Transfer,* Vol. 25, No. 9, pp. 1271-1278, 1982.

Murgatroyd, W., "The Role of Shear and Form Force in the Stability of a Dry Patch in Two-Phase Film Flow," *Int. J. Heat Mass Transfer,* Vol. 8, pp. 297-301, 1965.

Notter, R. H. and Sleicher, C. A., "A solution to the Turbulent Graetz Problem – III Fully Developed and Entry Region Heat Transfer Rates," *Chemical Engineering Science*, Vol. 27, pp. 2073-2093, 1972.

Novak, V., Sadowski, D., Shin, S., Schoonover, K., Abdel-Khalik, S. I., "Experimental and Numerical Investigation of Mist Cooling for the Electra Hibachi," *Fusion Science and Technology*, Vol. 47, pp. 610-615, 2005.

O'Rourke, P. J. and Amsden, A. A., "A Particle Numerical Model for Wall Film Dynamics in Port-Injection Engines," Los Alamos National Lab report 961961, Copyright 1996 Society of Automotive Engineers Inc., 1996.

Petukhov, V. V. and Zlokazov, A. B., "Mist-Annular Flow in Heated Vertical Channels," *Heat transfer – Soviet Research,* Vol. 23, No. 1, pp. 107-116, 1991.

Pletcher, R. H. and McManus Jr., H. N., "Heat Transfer and Pressure Drop in Horizontal Annular Two-Phase, Two-Component Flow," *Int. J. Heat Mass Transfer,* Vol. 11, pp. 1087-1104, 1968.

Reynolds, H. C., Swearingen, T. B. and McEligot, D. M., "Thermal Entry for Low Reynolds Number Turbulent Flow," *J. Basic Eng.*, Vol. 91, pp. 87-94, 1969.

Sethian, J. D., Myers, M. C., Giuliani, J. L., Lehmberg, R. H., Kepple, P. C., Obenschain, S. P., Hegeler, F., Friedman, M., Wolford, M. F., Smilgys, R. V., Swanekamp, S. B., Weidenheimer, D., Giorgi, D., Welch, D. R., Rose, D. V., Searles, S., "Electron Beam Pumped Krypton Fluoride Lasers for Fusion Energy," *Proceedings of the IEEE*, Vol. 92. No. 7, 2004.

Shin, S., Georgia Institute of Technology, private communication, 2006.

Šikalo, Š., Delalić, N. and Ganić, E. N., "Hydrodynamics and Heat Transfer Investigation of Air-Water Dispersed Flow," *Experimental Thermal and Fluid Science,* 25, p 511-521, 2002.

Sun, G. and Hewitt, G. F., "Evaporation and Condensation of Steam-Water in a Vertical Tube," *Nuclear Engineering and Design,* 207, pp. 137-145. 2001.

Suzuki, K., Hagiwara, Y. and Sato, T., "Heat Transfer and Flow Characteristics of Two-Phase Two-Component Annular-Flow," *International Journal of Heat and Mass Transfer,* Vol. 26, No. 4, pp. 597-605, 1983.

Suzuki, K., Nakabe, K. and Yamanaka, T., "Heat Transfer Accompanied by Evaporation to a Recirculating Turbulent Disperesed Flow," *PCH, PhysicoChemical Hydrodynamics*, v 6, n 3, pp. 311-327, 1985.

Swanekamp, S., Naval Research Laboratory, private communication, 2004.

Tatterson, D. F., Dallman, J. C. and Hanratty, T. J., "Drop Sizes in Annular Gas-Liquid Flows," *AIChE Journal*, v 23, n 1, Jan, pp. 68-76, 1977.

Ueda, T. and Tanaka, T., "Studies of Liquid Film Flow in Two-phase Annular and Annular-Mist Flow Regions (Part 1, Downflow in a Vertical Tube)," *Bulletin of the JSME*, Vol. 17, No. 107, May, pp. 603-613, 1974.

Ueda, T. and Nose, S., "Studies of Liquid Film Flow in Two-phase Annular and Annular-Mist Flow Regions (Part 2, Upflow in a Vertical Tube)," *Bulletin of the JSME*, Vol. 17, No. 107, May, pp. 614-624, 1974.

Verberk, J. Q. J. C., "Application of air in membrane filtration," *Ph.D. thesis, Delft University of Technology*, ISBN 90-9019344-8, 2005.

Yang, Z. H. and Lee, S. L., "On the Droplet Deposition and Mist Supercooling in a Turbulent Channel Flow," *Particle and Particle Systems Characterization,* v 8, n 1, pp. 72-78, 1991.

Zuber, N. and Staub, F. W., "Stability of Dry Patches Forming in Liquid Films Flowing Over Heated Surfaces," *Int. J. Heat Mass Transfer,* Vol. 9, pp. 897-905, 1966.